Lecture Notes in Mechanical Engineering

Yu Zhou
Motoaki Kimura
Guoyi Peng
A. D. Lucey
Lixi Huang *Editors*

Fluid-Structure-Sound Interactions and Control

Proceedings of the 4th Symposium on Fluid-Structure-Sound Interactions and Control

Springer

Lecture Notes in Mechanical Engineering

Lecture Notes in Mechanical Engineering (LNME) publishes the latest developments in Mechanical Engineering—quickly, informally and with high quality. Original research reported in proceedings and post-proceedings represents the core of LNME. Also considered for publication are monographs, contributed volumes and lecture notes of exceptionally high quality and interest. Volumes published in LNME embrace all aspects, subfields and new challenges of mechanical engineering. Topics in the series include:

- Engineering Design
- Machinery and Machine Elements
- Mechanical Structures and Stress Analysis
- Automotive Engineering
- Engine Technology
- Aerospace Technology and Astronautics
- Nanotechnology and Microengineering
- Control, Robotics, Mechatronics
- MEMS
- Theoretical and Applied Mechanics
- Dynamical Systems, Control
- Fluid Mechanics
- Engineering Thermodynamics, Heat and Mass Transfer
- Manufacturing
- Precision Engineering, Instrumentation, Measurement
- Materials Engineering
- Tribology and Surface Technology

More information about this series at http://www.springer.com/series/11236

Yu Zhou · Motoaki Kimura
Guoyi Peng · A. D. Lucey
Lixi Huang
Editors

Fluid-Structure-Sound Interactions and Control

Proceedings of the 4th Symposium on Fluid-Structure-Sound Interactions and Control

Springer

Editors
Yu Zhou
Shenzhen Graduate School
Harbin Institute of Technology
Shenzhen
China

Motoaki Kimura
Nihon University
Tokyo
Japan

Guoyi Peng
Nihon University
Tokyo
Japan

A. D. Lucey
Curtin University
Perth, WA
Australia

Lixi Huang
The University of Hong Kong
Hong Kong
China

ISSN 2195-4356 ISSN 2195-4364 (electronic)
Lecture Notes in Mechanical Engineering
ISBN 978-981-10-7541-4 ISBN 978-981-10-7542-1 (eBook)
https://doi.org/10.1007/978-981-10-7542-1

Library of Congress Control Number: 2018935208

Printed on acid-free paper

This Springer imprint is published by the registered company Springer Nature Singapore Pte Ltd.
part of Springer Nature
The registered company address is: 152 Beach Road, #21-01/04 Gateway East, Singapore 189721, Singapore

Contents

Part I
Turbulence and Unsteady Fluid Dynamics

K41 Versus K62: Recent Developments

R. A. Antonia, S. L. Tang, L. Danaila, L. Djenidi and Y. Zhou

Abstract For the past 50 years or so, Kolmogorov's (1962) correction (K62) to his 1941 hypotheses (K41) has been embraced by an overwhelming majority of turbulence researchers. Our recent work suggests that there are no valid reasons for abandoning K41. In particular, analytical considerations, based on the NS equations, which take into account the finite Reynolds number (FRN) effect, together with the available experimental laboratory data, seem to confirm a tendency towards the simple and elegant predictions of K41 as the Reynolds number increases. This is especially true when the focus is on the length scales which lie in the dissipative range. Incorrectly accounting for the FRN effect and the inclusion of the atmospheric surface layer (ASL) data, likely to have been affected by the proximity to the surface, appear to be the major factors which have contributed to a nearly unchallenged acceptance of K62.

1 Introduction

The theory of small scale turbulence has benefited immensely from the contributions of Taylor [1], who introduced the concept of isotropy and obtained a simplified expression for the mean energy dissipation rate $\bar{\varepsilon}$, and Karman and Kowarth [2] who derived a transport equation (hereafter referred to as the KH equation) for the two-point velocity correlation function in isotropic turbulence. Further significant progress was made in 1941 when Kolmogorov [3] introduced two important hypotheses, specifically the first and second similarity hypotheses dealing with

R. A. Antonia · S. L. Tang (✉) · Y. Zhou
Institute for Turbulence-Noise-Vibration Interaction and Control, Shenzhen Graduate School, Harbin Institute of Technology, Shenzhen 518055, People's Republic of China
e-mail: shunlin.tang88@gmail.com

L. Djenidi
School of Engineering, University of Newcastle, NSW 2308, Australia

L. Danaila
CORIA CNRS UMR 6614, Université de Rouen Normandie, 76801 Saint Etienne du Rouvray, France

Y. Zhou et al. (eds.), *Fluid-Structure-Sound Interactions and Control*, Lecture Notes in Mechanical Engineering,
https://doi.org/10.1007/978-981-10-7542-1_1

turbulence scales in the dissipative (DR) and inertial (IR) ranges at very large Reynolds number. In a separate paper, Kolmogorov [4] also derived, starting with the KH equation rewritten in terms of δu, a simple expression for $\overline{(\delta u)^3}/\bar{\varepsilon} r$, which is generally interpreted as the energy flux or mean rate of transfer of energy down the cascade at a scale r within the IR, viz.

$$-\frac{\overline{(\delta u)^3}}{\bar{\varepsilon} r} = \frac{4}{5}, \tag{1}$$

where $\delta u = u(x + r) - u(x)$ is the increment between velocity fluctuations at two points in space, separated by a distance r. The overbar denotes time averaging. Equation (1) has become known as the "4/5 th" law and represents an exact result for isotropic turbulence at very large Reynolds numbers. Further notable contributions in the 1940 s included Batchelor's [6] thorough appraisal of Kolmogorov's theory and his papers with Townsend [7, 8] dealing with the transport equation for $\bar{\varepsilon}$ (or equivalently the mean enstrophy) in isotropic turbulence and the intermittent nature of the fine-scale structure of turbulence.

Kolmogorov's phenomenology [3] or K41 led to the exciting prospect that small scale turbulence could be universal at sufficiently large Reynolds number. Kolmogorov postulated that $\bar{\varepsilon}$ and the kinematic viscosity ν are the governing parameters in the DR. The main outcome of the first similarity hypothesis is

$$\overline{(\delta u^*)^n} = f_{un}(r^*), \tag{2}$$

where the asterisk denotes normalization by the Kolmogorov velocity and length scales, $u_K = (\nu\bar{\varepsilon})^{1/4}$ and $\eta = (\nu^3/\bar{\varepsilon})^{1/4}$ respectively. The function f_{un} is a universal. A consequence of (2) when $r \to 0$ is that the normalized velocity derivative moments should all be constant, i.e. independent of R_λ,

$$S_n = \frac{\overline{(\partial u/\partial x)^n}}{\overline{(\partial u/\partial x)^2}^{n/2}} = const. \tag{3}$$

Note that S_3 and S_4 are the skewness and flatness factor (or kurtosis) of $\partial u/\partial x$. The second similarity hypothesis argues that in the IR ($\eta \ll r \ll L$, where L is the integral length scale), the local Reynolds number is sufficiently large to allow the effect of viscosity to be ignored and yields the well-known result

$$\overline{(\delta u^*)^n} = C_{un} r^{*n/3} \tag{4}$$

where C_{un} are universal constants. The main outcomes of K41, Eqs. (2)–(4), were to a large extent undermined by the third (revised) hypothesis introduced by Kolmogorov 20 years after K41 [5, 9].

The revision was made to take into account the spatio-temporal intermittency of fluctuations in ε and assumed a log-normal model for ε_r, the subscript denoting

averaging over a volume of linear dimension r, i.e. the probability distribution of $\ln \epsilon_r$ is Gaussian. Two consequences of the third hypothesis are

(i) S_n is no longer constant. The magnitude of S_n for $n \geq 3$ is now expected to increase indefinitely with R_λ

$$|S_n| \sim R_\lambda^{\alpha(n)} \qquad (\alpha > 0), \tag{5}$$

(ii) Relation (4) now becomes

$$\overline{(\delta u^*)^n} \sim r^{*\zeta_{un}}, \tag{6}$$

where the exponent ζ_{un} may depart from $n/3$, except when $n = 3$ (since the exact result, Eq. (1), needs to be preserved). The log-normal and subsequent probabilistic models indicate that the departure from $n/3$ increases as n increases, albeit at a rate which may differ between models. Predictions from physical models, based on generally simplistic proposals of how ϵ is localized in space, have not always qualitatively agreed with (5) (see for example Van Atta and Antonia [10], Sreenivasan and Antonia [11], Wyngaard [12]).

It is fair to assert that experimental support for both (5) and (6) has been nothing short of considerable. We do not wish to embark on a detailed discussion here; we refer the reader to Van Atta and Antonia [10] and the reviews by Sreenivasan and Antonia [11], Anselmet et al. [13], and Ishihara et al. [14]. Notwithstanding a few dissentions, objections or doubts about K62 (e.g. [15–18]), the experimental evidence has strongly pointed to K41 having to be abandoned in favour of K62. If we leave aside the results from the ASL and recall that the most "damning" evidence against K41, in the context of (6), came from the laboratory investigation of Anselmet et al. [19], a major criticism that can be levelled at nearly all the laboratory studies is the failure to properly recognise the influence of the Reynolds number, especially since R_λ has seldom exceeded 1000, on the statistics of velocity derivatives as well as on the moments of δu in the IR; the fact that the latter was never satisfactorily established should have been cause for concern, if not alarm. The realization that the FRN effect has to be taken into account came to the fore in 1997 (Qian [20]) and a little later (Qian [21], Danaila et al. [22], and Lindborg [23]). The essence of the approach was to revisit the KH equation (or the Karman-Lin equation [24] in the case of Qian [21] who adopted a spectral approach) which includes the nonstationarity (or $\partial u/\partial t$ term) that was ignored by Kolmogorov [4]. The inclusion of the nonstationarity permits an assessment of how the large scale inhomogeneity can affect the small scales and hence an estimation of how large R_λ should be before Eq. (1) is satisfied. Such an estimation was also carried out by Lundgren [25] and Antonia and Burattini [26]. The latter authors showed that "4/5" is approached more rapidly for forced than for decaying turbulence; for a substantial IR to exist, the results indicated that R_λ may need to exceed 10^3 in the former case and 10^6 in the latter. These results, obtained via a scale-by-scale energy budget, were confirmed by Tchoufag et al. [27] using the Eddy-Damped Quasi-Normal Markovian (EDQNM) method. One natural inference

from the previous results is that the approach to "4/5" is expected to depend on the flow since each flow may have different levels of inhomogeneity at large scales.

The above considerations lead to only one conclusion: previous evidence in support of K62 needs to be critically reexamined in the context of the FRN effect since this latter effect appears to have been incorrectly mistaken for the intermittency effect. Note that intermittency was not explicitly taken into account in the previously described work since xit is intrinsic to the N-S equations.

One objective of this paper is to first point out likely flaws in the approach used hitherto for examining consequences of K41 and K62. This is done in Sect. 2. A second is to highlight recent advances in understanding the behaviour of S_3 with R_λ, underpinned by the transport equation for $\overline{(\delta u)^2}$ or scale-by-scale energy budget. The limiting form of this budget has provided valuable insight into the Reynolds number dependence of S as well as that of $\overline{(\delta u)^3}$ in the scaling range. Some analytical considerations are briefly given in Sect. 3. Results associated the DR and IR are presented in Sects. 4 and 5 resepctively. Conclusions are given in Sect. 6.

2 Shortcomings in Previous Approaches Used to Test K41 and K62

Fig. 1, taken from Wyngaard and Tennekes (WT) [28], highlights the impact that the ASL data has had on bolstering the validity of K62 and provides incisive insight into how subsequent researchers may have been misled into accepting, if not

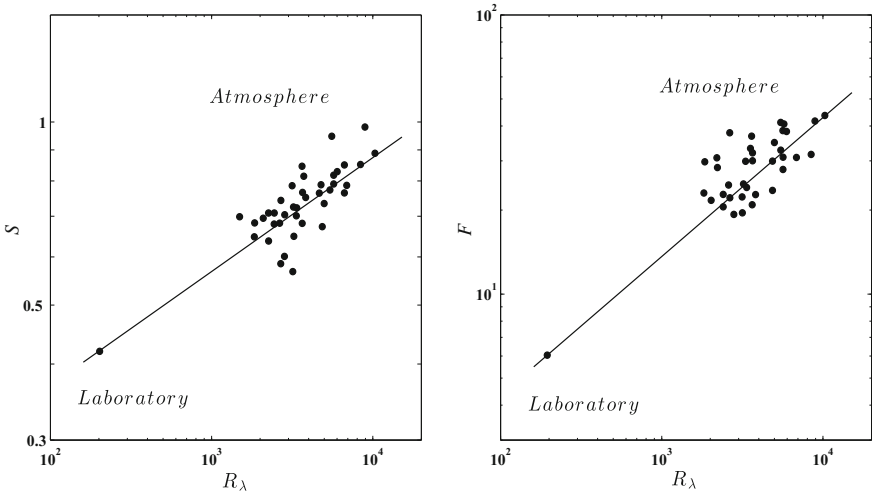

Fig. 1 Dependence of S and F on R_λ reproduced from Figs. 5 and 6 of Wyngaard and Tennekes [28]

wholeheartedly embracing, K62. WT compared virtually a single measurement in the laboratory (a mixing layer between plane jets, confined in a curved channel) at a relatively modest value of R_λ (<200) with data obtained in the 1968 Air Force Cambridge Research Laboratory Study of the boundary layer above a flat, homogeneous plain in southwest Kansas. The straight lines in Fig. 1 are predictions of S ($\equiv S_3$) and F ($\equiv S_4$) based on particular choices for the characteristic length r (here $r = \lambda$) of the averaging volume and the universal constant μ (here $\mu = 1/2$) in the Kolmogorov-Obukhov expression for the variance σ^2 of $\ln \varepsilon_r$, viz.

$$\sigma^2 = A + \mu \ln \frac{L}{r} \tag{7}$$

in the lognormal model; A depends on the large scale (L is the integral scale). WT concluded that the dependence of S and F on R_λ contradicts K41 or the universal equilibrium theory, whilst recognizing that the good agreement with the prediction from the lognormal model may need reappraisal due to the choice made for r, the neglect of A and the uncertainty in the value of μ (0.5 was used; the present day consensus value for μ is about 0.2). With the benefit of hindsight, the methodology embodied in Fig. 1 can now be criticized on at least three major levels. Firstly, it ignores the FRN effect (this will be addressed in Sect. 3) which can affect the laboratory data in a significant way and, to a lesser extent, the ASL data. Secondly, the FRN effect, through the very nature from which it arises (it mainly reflects the inhomogeneity associated with the large scale motion; the latter has been shown to depend on the flow), is expected to affect different flows differently. This expectation is completely ignored in Fig. 1. The compilation by Van Atta and Antonia [10] of how S and F vary with R_λ and its subsequent reappraisal (Sreenivasan and Antonia, [11]) do indeed show that the laboratory values exhibit "apparent" scatter (our recent work, [29–32], confirms that, at least for S, there is a systematic dependence on R_λ which can be explained analytically). Clearly, one cannot afford to indiscriminately use data obtained from various flows unless the Reynolds number is large enough to allow the FRN effect in each of theses flows to be dismissed. The need to achieve a sufficiently high Reynolds number in any given laboratory flow so that Eq. (1) is approximately satisfied in the IR should, strictly speaking, be considered as a minimum requirement before examining the consequences of K41 and K62. This seems to have been largely overlooked. Thirdly, the inclusion of the ASL data when testing K41 and K62 needs, at the very least, to be discussed or scrutinized more objectively than in the past. For example, the Kansas data in Fig. 1 were collected at three heights ($z = 5.66$, 11.3 and 22.6m) above the ground; with a few exceptions, the ASL data used to test the dependence of S and F on R_λ have generally been obtained below a height of 30m. Often, no information for the stability conditions is given. Under "neutral" conditions, the ASL ought to be comparable (at similar values of z/δ) with the laboratory boundary layer provided the nature of the surface is also comparable. It is difficult to estimate with confidence the thickness δ of the neutral ASL. Wyngaard [12] suggests that, under neutral conditions, δ may scale with U_τ/f (U_τ is the friction velocity and f is the Coriolis parameter) and estimates, for

mid-latitudes, δ to be within the range 250–2500 m. This implies that the majority of the neutral ASL data for S and F were taken in the region $z/\delta < 0.1$. It is not difficult to conclude that there is significant uncertainty in the estimation of δ, e.g. a value of δ smaller than 100 m was found by Metzger et al. [33] based on experiments in Utah's western desert under almost "exactly" neutral conditions; the authors stressed however the difficulties associated in making measurements under those conditions. In any case, it is not clear if any the published ASL data were obtained under "exactly" neutral conditions. Certainly, it is difficult to believe that measurements of S and F in region $z/\delta < 0.1$ have not been affected by the proximity to the surface. Recent measurements (Djenidi et al. [34]) in a laboratory boundary layer over smooth and rough walls indicate that both S and F are approximately constant (with respect to z/δ) in the region $0.3 < z/\delta < 0.6$ (R_λ is also approximately constant with respect to z/δ in this region). However, the magnitudes of S and F can increase, perhaps by as much as a factor of 3, as the wall is approached. In the region $z/\delta > 0.6$, S and F are affected by the intermittency associated with the turbulent/irrotational interface. The implication of these observations is that it would be unwise to use data outside the range $0.3 < z/\delta < 0.6$ when testing K41 and K62. Naturally, one should also check that there are no major departures from local isotropy in this range due to the probable effects of the mean shear. In the region $z/\delta < 0.1$, a larger departure from local isotropy is expected due to the combined effect of an increase in mean shear and the "blockage" caused by the presence of the surface. Notwithstanding the large values of R_λ that can be achieved in the ASL (the ASL results of Sreenivasan and Dhrava [35] at $z \approx 35$m illustrate the difficulty in unambiguously estimating power-law exponents for $\overline{(\delta u)^2}$ and $\overline{(\delta u)^4}$ in the scaling range even when R_λ is in the range 10000–20000), it would be preferable to err on the side of caution and exclude all the previously obtained ASL data when examining the R_λ dependence of S and F and examining the behaviour of $\overline{(\delta u)^n}$ in the scaling range. We do not rule out the potential viability of data, collected for example in the region $0.3 < z/\delta < 0.6$ in a near-neutral ASL (this may entail making airborne measurements e.g. Sheih et al. [36]; flying can circumvent, if not minimize, the effect any possible nonstationarity and facilitate the convergence of statistics) or data collected away from boundaries as in the tidal channel experiment of Grant et al. [37].

3 Analytical Considerations

For homogeneous isotropic turbulence at very large Reynolds number, the transport equation for $\overline{(\delta u)^2}$ is given by

$$-\overline{(\delta u)^3} + 6\nu \frac{\partial}{\partial r} \overline{(\delta u)^2} = \frac{4}{5} \bar{\varepsilon} r. \tag{8}$$

If we divide all terms in Eq. (8) by $\overline{\varepsilon}r$, the above relation states, in essence, that the energy flux $-\overline{(\delta u)^3}/\overline{\varepsilon}r$ in the IR, where the viscous term is negligible, remains constant (see Eq. (1)). In small to moderate Reynolds number, this equation is usually not satisfied except at small r since Eq. (8) does not contain any large-scale term. For example, [22] showed that Eq. (8) is satisfied only for $r/\eta \leq 5$ for grid turbulence at $R_\lambda = 66$, suggesting that the large-scale term contributes to Eq. (8) for $r/\eta > 5$. After including such as term, $I_u(r)$ say, Eq. (8) becomes

$$-\overline{(\delta u)^3} + 6\nu \frac{\partial}{\partial r}\overline{(\delta u)^2} = \frac{4}{5}\overline{\varepsilon}r - I_u \tag{9}$$

where I_u differs from flow to flow, e.g. in decaying HIT [22, 38], along the axis in the far field of an axisymmetric jet flow [39], and along the centreline of a fully developed channel flow [40]. This equation is of fundamental importance since it is an equilibrium relation between second- and third-order moments. Further, Eq. (9) provides a viable platform for quantifying the FRN effect on $\overline{(\delta u)^3}$ since it provides insight into the budget of energy at each scale. As $r \to 0$, Eq. (9) becomes the transport equation for the mean enstrophy or $\overline{\varepsilon}$, which can be written in the generic form [29–32]

$$S + 2\frac{G}{R_\lambda} = \frac{C}{R_\lambda}, \tag{10}$$

where $G\left(= \overline{u^2}\frac{\overline{(\partial^2 u/\partial x^2)^2}}{\overline{(\partial u/\partial x)^2}}\right)$ is the enstrophy destruction coefficient and C is a constant which depends on the flow and may vary across regions of the same flow. Equation (10) represents, in essence, a constraint on how S varies with R_λ in different flows. Since the ratio G/R_λ approaches a constant relatively rapidly with increasing R_λ [29–32] and the terms on the right side of (10) must eventually vanish, Eq. (10) implies that the magnitude of S should become constant at sufficiently large R_λ. This expectation has been confirmed [29–32] and will be discussed briefly in the next section.

4 Results for the Dissipative Range

There has been strong support for K41 in the DR for the second-order statistics. For example, Kolmogorov-normalized one-dimensional velocity spectra $\phi_u^*(k_1^*)$ collapse very well in the high wavenumber region [41]. In contrast to the stipulations of K41 and K62, viz. R_λ must be very large and local isotropy should hold, this collapse does not require R_λ to be large [41], not does it require local isotropy to be satisfied rigorously; it does however break down [42] when R_λ is sufficiently small, typically when it falls below about 40. Pearson et al. [43] showed that $\overline{(\delta u^*)^2}$ also collapses reasonably well in the DR over a large range of R_λ ($40 < R_\lambda < 4250$). In flows con-

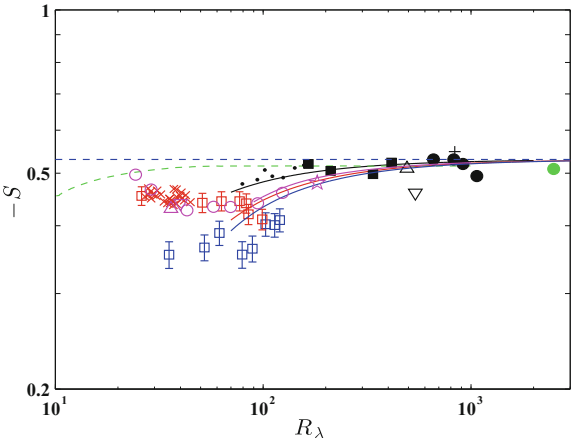

Fig. 2 Dependence of S on R_λ in different flows. The 4 solid curves (black, red, blue and pink), inferred from Eq. (10) by assuming that $2G/R_\lambda$ = constant (≈ 0.53 for $R_\lambda \geq 70$ in all flows except the far-wake where $R_\lambda \geq 100$), correspond to the flow the axis in the far-field of a round jet, decaying grid turbulence, the centerline of a fully developed channel flow and the axis in the far-wake of a circular cylinder; corresponding measurements in each flow are shown as symbols with the same color without identifying the sources [29–32]. The green dashed curve is the prediction by Qian [16]; the solid green symbol was obtained in the ONERA wind tunnel [45]. The horizontal dashed line indicates the value of 0.53

sidered in Sect. 3, simple analytical expressions for C can be obtained [29–31] in different flows or for specific regions of a given flow. For example, in decaying grid turbulence, $C = \frac{90}{7(1+2R)}\left(\frac{n+1}{n}\right)$ with $R = \overline{v^2}/\overline{u^2}$, whilst along the axis in the far-field of a round jet, $C = \frac{90}{7(2+R)}$. Since C differs from flow to flow, it is clear that C/R_λ will approach zero along different paths. Since $2G/R_\lambda$ becomes constant ($\approx$0.53) at $R_\lambda = 70$–100 [29–31], we have already shown in several papers [29–32] that S depends on both the type of flow and R_λ at small to moderate R_λ (Fig. 2); it will reach a universal constant when R_λ is sufficiently large (in general, R_λ only needs to exceed about 300, allowing for the uncertainty in measuring S). Antonia et al. [32] also examined the variation of S_n with R_λ (Eq. (3)), up to $n = 6$, on the axis of a plane jet, and found that S_n for $n = 3$–6 is constant (by definition, $S_2 = 1$) over a range of R_λ ($500 < R_\lambda < 1100$), suggesting that the FRN effect is not observed in this range. Antonia et al. [32] further examined $\overline{(\delta u^*)^n}$ ($n = 2$–6) for the plane jet data at $R_\lambda =$ 550, 696, 826, 914, and 1067 respectively and found that there is relatively good collapse for all the structure functions at small r^* (DR). All these results associated with the DR favour K41 over K62 and hence imply an absence of intermittency-related corrections over this range of R_λ.

5 Results for the Scaling Range

A completely developed IR exists when R_λ is very large. When R_λ is not sufficiently large, the scaling range cannot be identified with IR. Antonia and Burattini [26] showed that only when $I_u(r)$ becomes negligible over a sufficiently large range of r can the scaling range be correctly identified with the IR. In reality, $\overline{(\delta u)^3}/(\bar{\varepsilon} r)$ approaches a plateau with a value 4/5 as R_λ increases, while this approach is more rapid for forced than for decaying turbulence [26]. Similar results have been obtained by Refs. [20, 23, 27] using different types of closures applied to either Eq. (9) or the Karman-Lin spectral equation [24]. When assessing the scaling range exponents of $\phi_u(k_1)$, the pressure spectrum $E_p(k_1)$, or higher-order structure functions, particular attention needs to be paid to the FRN effect. For example, Fig. 6.29 of [44], which is a compilation of different values of the power-law exponent for $\phi_u(k_1)$ measured in grid turbulence, shows that the $-5/3$ power-law scaling (K41) is approached slowly as R_λ increases. [46] measured pressure spectra ($E_p(k_1)$) on the centreline of a round jet over a large range of R_λ ($= 200 \sim 1250$). They showed that the $-7/3$ power-law scaling (K41) for $E_p(k_1)$ is approached as R_λ increases and is confirmed for $R_\lambda \geq 600$. Using EDQNM in decaying HIT, Meldi and Sagaut [47] further confirmed the FRN effect on the pressure spectrum and revealed that $R_\lambda \sim 10000$ is needed before the pressure spectrum exhibits a IR with an extent of one decade. Recently, the FRN effect on the scaling range exponents of structure functions, up to order 8, has been assessed critically either via experiments (axes of plane and circular jets, wake centreline) or DNS [32, 48]. In all cases, the magnitude of the exponent increases as R_λ increases and the rate of increase depends on n. For a fixed R_λ, the exponent can vary from flow to flow and for a given flow, the larger R_λ is, the closer the exponent is to the K41 value. As an example, Fig. 3 shows the scaling exponents on the axis of the plane jet at R_λ=550 and 1067 respectively [48]. The latter authors concluded

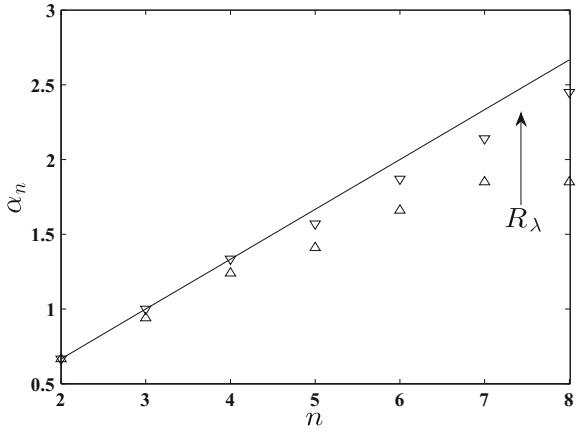

Fig. 3 Scaling exponents α_n, defined from the power-law $\overline{(\delta u)^n} \sim r^{\alpha_n}$ in the SR, on the axis of the plane jet at R_λ=550 ($\triangle$) and 1067 ($\triangledown$) respectively [48]. Solid line is the K41 prediction, i.e. $\alpha_n = n/3$, Eq. (4)

that the FRN effect, which depends on the flow, needs to be properly accounted for before determining whether corrections to K41 are required.

6 Conclusions

We, once again, recall that both K41 and K62 are asymptotic $R_\lambda \to \infty$ phenomenologies. As such, we may never be able to decide if K62 provides a realistic alternative to K41 when $R_\lambda \to \infty$. What is of paramount importance however is to critically appraise the manner with which K41 and K62 have been tested. In Sect. 2, we put forward plausible arguments for excluding ASL data obtained in the region $z/\delta < 0.1$ when testing K41 and K62. Laboratory boundary layer data obtained in a similar region are not suitable for this purpose, given the likely effect of the strong shear and the departure from LI, and have not, to our knowledge, been used. If we set aside the ASL data, the laboratory data for S and F are consistent with K41, at least when R_λ approaches 10^3, i.e. S and F approach constant values. Our recent analytical work [29–32] has allowed a reliable estimation of the way S is affected by the FRN effect in a variety of flows. This has confirmed that S does indeed approach a constant along different paths in different flows, thus debunking the practice of indiscriminately lumping together values of S obtained in various flows before testing the dependence of S on R_λ. The analytical approach adopted is based on the scale-by-scale energy budget, derived from the N-S equations, which allows important physical constraints to be satisfied, namely the energy and enstrophy budgets at large and small r respectively, in each flow. The challenge ahead of us is to now extend this approach to examine how F varies in each flow; we believe this should be feasible, see for example [49], with the help of DNS. The laboratory data for F [32, 50] indicate that, like S, F also becomes constant at sufficiently large R_λ (this value is not much larger than 10) thus further supporting K41; of course, confirmation of this observation, underpinned by the N-S equations, is essential. Further, we have observed, using only laboratory data, that the scaling range exponents tends towards the K41 value of $n/3$, at least for $2, 3, 4$, as R_λ increases. The scaling exponent α_n approaches $n/3$ (the K41 value), more slowly as n increases. Naturally, it is highly desirable that we continue to scrutinize this trend by trying to further increase R_λ, preferably within the controlled environment of the laboratory.

Acknowledgements SL Tang wishes to acknowledge support given to him from NSFC through grant 11702074.

References

1. Taylor GI (1935) Statistical theory of turbulence. Proc R Soc Lond A 151:421–444
2. De Karman T, Howarth L (1938) On the statistical theory of isotropic turbulence. Proc R Soc Lond A 164:192–215
3. Kolmogorov AN (1941) Local structure of turbulence in an incompressible fluid for very large Reynolds numbers. Dokl Akad Nauk SSSR 30:299–303
4. Kolmogorov AN (1941) Dissipation of energy in the locally isotropic turbulence. Dokl Akad Nauk SSSR 32:19–21
5. Kolmogorov AN (1962) A refinement of previous hypotheses concerning the local structure of turbulence in a viscous incompressible fluid at high Reynolds number. J Fluid Mech 13:82–85
6. Batchelor GK (1947) Kolmogoroff's theory of locally isotropic turbulence. Proc Carnb Phil Soc 43:533–559
7. Batchelor GK, Townsend AA (1947) Decay of vorticity in isotropic turbulence. Proc R Soc Lond A 190:534–550
8. Batchelor GK, Townsend AA (1949) The nature of turbulent motion at large wave-numbers. Proc R Soc Lond A 199:238–255
9. Obukhov AM (1962) Some specific features of atmospheric turbulence. J Fluid Mech 13:77–81
10. Van Atta CW, Antonia RA (1980) Reynolds number dependence of skewness and flatness factors of turbulent velocity derivatives. Phys Fluids 23:252–257
11. Sreenivasan K, Antonia RA (1997) The phenomenology of small-scale turbulence. Ann Rev Fluid Mech 29:435–472
12. Wyngaard JC (2010) Turbulence in the atmosphere. Cambridge University Press
13. Anselmet F, Antonia RA, Danaila L (2001) Turbulent flows and intermittency in laboratory experiments. Planet Sp Sci 49:1177–1191
14. Ishihara T, Gotoh T, Kaneda Y (2009) Study of high-Reynolds number isotropic turbulence by direct numerical simulation. Ann Rev Fluid Mech 41:165–180
15. Frisch U (1995) Turbulence: the legacy of A. N. Kolmogorov. Cambridge University Press
16. Qian J (1994) Skewness factor of turbulent velocity derivative. Acta Mech Sin 10:12–15
17. Grossmann S, Lohse D (1994) Scale resolved intermittency in turbulence. Phys Fluids 6:611–617
18. Qian J (1998) Normal and anomalous scaling of turbulence. Phys Rev E 58:7325
19. Anselmet F, Gagne Y, Hopfinger EJ, Antonia RA (1984) High-order velocity structure functions in turbulent shear flows. J Fluid Mech 140:63–89
20. Qian J (1997) Inertial range and the finite Reynolds number effect of turbulence. Phys Rev E 55:337–342
21. Qian J (1999) Slow decay of the finite Reynolds number effect of turbulence. Phys Rev E 60:3409
22. Danaila L, Anselmet F, Zhou T, Antonia RA (1999) A generalization of Yaglom?s equation which accounts for the large-scale forcing in heated decaying turbulence. J Fluid Mech 391:359–372
23. Lindborg E (1999) Correction to the four-fifths law due to variations of the dissipation. Phys Fluids 11:510
24. Von Karman T, Lin CC (1949) On the concept of similiarity in the theory of isotropic turbulence. Rev Mod Phys 21:516
25. Lundgren TS (2003) Kolmogorov turbulence by matched asymptotic expansions. Phys Fluids 15:1074–1081
26. Antonia RA, Burattini P (2006) Approach to the 4/5 law in homogeneous isotropic turbulence. J Fluid Mech 550:175–184
27. Tchoufag J, Sagaut P, Cambon C (2012) Spectral approach to finite Reynolds number effects on Kolmogorov's 4/5 law in isotropic turbulence. Phys Fluids 24:015107
28. Wyngaard JC, Tennekes H (1970) Measurements of the small-scale structure of turbulence at moderate Reynolds numbers. Phys Fluids 13:1962–1969

29. Antonia RA, Tang SL, Djenidi L, Danaila L (2015) Boundedness of the velocity derivative skewness in various turbulent flows. J Fluid Mech 781:727–744
30. Tang SL, Antonia RA, Djenidi L, Abe H, Zhou T, Danaila L, Zhou Y (2015) Transport equation for the mean turbulent energy dissipation rate on the centreline of a fully developed channel flow. J Fluid Mech 777:151–177
31. Tang SL, Antonia RA, Djenidi L, Zhou Y (2015) Transport equation for the isotropic turbulent energy dissipation rate in the far-wake of a circular cylinder. J Fluid Mech 784:109–129
32. Antonia RA, Djenidi L, Danaila L, Tang SL (2017) Small scale turbulence and the finite Reynolds number effect. Phys Fluids 29:020715
33. Metzger M, McKeon BJ, Holmes H (2007) The near-neutral atmospheric surface layer: turbulence and non-stationarity. Phil Trans R Soc Lond A 365:859–876
34. Djenidi L, Antonia RA, Talluru MK, Abe H (2017) Skewness and flatness factors of the longitudinal velocity derivative in wall-bounded flows. Phys Rev Fluids 2:064608
35. Sreenivasan KR, Dhruva B (1998) Is there scaling in high-Reynolds-number turbulence? Prog Theor Phys Suppl 130:103–120
36. Sheih CM, Tennekes H, Lumley JL (1971) Airborne hot-wire measurements of the small-scale structure of atmospheric turbulence. Phys Fluids 14:201–215
37. Grant HL, Stewart RW, Moilliet A (1962) Turbulence spectra from a tidal channel. J Fluid Mech 12:241–268
38. Antonia RA, Zhou T, Danaila L, Anselmet F (2000) Streamwise inhomogeneity of decaying grid turbulence. Phys Fluids 12:3086
39. Thiesset F, Antonia RA, Djenidi L (2014) Consequences of self-preservation on the axis of a turbulent round jet. J Fluid Mech 748(R2)
40. Danaila L, Anselmet F, Zhou T, Antonia RA (2001) Turbulent energy scale-budget equations in a fully developed channel flow. J Fluid Mech 430:87–109
41. Antonia RA, Djenidi L, Danaila L (2014) Collapse of the turbulent dissipation range on Kolmogorov scales. Phys Fluids 26:045105
42. Djenidi L, Tardu SF, Antonia RA, Danaila L (2014) Breakdown of Kolmogorov's first similarity hypothesis in grid turbulence. J Turb 15:596–610
43. Pearson BR, Antonia RA (2001) Reynolds-number dependence of turbulent velocity and pressure increments. J Fluid Mech 444:343–382
44. Pope SB (2000) Turbulent flows. Cambridge University Press
45. Bos WJT, Chevillard L, Scott JF, Rubinstein R (2012) Reynolds number effect on the velocity increment skewness in isotropic turbulence. Phys Fluids 24:015108
46. Tsuji Y, Ishihara T (2003) Similarity scaling of pressure fluctuation in turbulence. Phys Rev E 68:026309
47. Meldi M, Sagaut P (2013) Pressure statistics in self-similar freely decaying isotropic turbulence. J Fluid Mech 717:R2
48. Tang SL, Antonia RA, Djenidi L, Danaila L, Zhou Y (2017) Finite Reynolds number effect on the scaling range behavior of turbulent longitudinal velocity structure functions. J Fluid Mech 820:341–369
49. Djenidi L, Antonia RA, Danaila L, Tang SL (2017) A note on the velocity derivative flatness factor in decaying HIT. Phys Fluids 29:051702
50. Tang SL, Antonia RA, Djenidi L, Danaila L, Zhou Y (2017) Reappraisal of the velocity derivative flatness factor in various turbulent flows. J Fluid Mech (in revision)

Jets and Waves Generated by an Obstacle in Stratified or Homogeneous Fluids

Hideshi Hanazaki

Abstract Jets and waves, whose origin is in gravity force, are often observed in fluids. When the fluid has a vertical density stratification, both can be generated due to the buoyancy force. The jet appears when an obstacle descends vertically in a stratified fluid. The generation is supported by the molecular diffusion of the stratifying scalar such as salt. If there is no scalar/density diffusion, the density must be conserved along the fluid motion, and the originally horizontal isopycnal surfaces are simply deformed as they are dragged down by the obstacle, so that the dragged fluid will move downward indefinitely and will never go back to its original height. If the diffusion exists, the fluid can change its original density, and move away from the isopycnal surface to which the fluid originally belonged. In this study, we demonstrate the generation process of the jet, along with its interaction with the internal gravity waves. As another example of waves in fluids, water waves with capillary effects in a homogeneous fluid are numerically simulated, showing the excitation of short capillary waves by a long solitary wave. The phenomenon has been predicted by a weakly nonlinear theory, but has not yet been observed.

Keywords Stratified fluid · Jet · Internal gravity wave · Capillary gravity wave

1 Jets and Waves in a Stratified Fluid

There have been uncountably many studies on stratified flows, but most of them are on horizontal flows, since many of the applications of stratified flows are in the large-scale atmospheric or oceanic flows in which the horizontal velocity is usually much larger than the vertical velocity. However, importance of the vertical flow generated by a vertical movement of an obstacle in stratified fluid has been recently recognized, particularly in smaller-scale flows. For example, accurate control of the

H. Hanazaki (✉)
Department of Mechanical Engineering and Science, Kyoto University,
4 Kyoto daigaku-katsura, Nishikyo-ku, Kyoto 615-8540, Japan
e-mail: hanazaki.hideshi.5w@kyoto-u.ac.jp

Y. Zhou et al. (eds.), *Fluid-Structure-Sound Interactions and Control*, Lecture Notes in Mechanical Engineering,
https://doi.org/10.1007/978-981-10-7542-1_2

vertical movement of floats used for the abyssal observation is necessary to develop a reliable float, and the prediction of the vertical movement of zoo-planktons is essential to estimate the carbon circulation in the ocean, which is important in the climate model to predict the global warming of the earth.

In this study, we consider a sphere moving vertically at constant speed in a linearly stratified fluid. Both the experiments and numerical simulations are performed, and various jet/wake patterns are observed and the essential mechanisms of the flow, including the mechanism of the jet formation, are investigated.

1.1 Water-Tank Experiments

A schematic figure of the experimental facilities is presented in Fig. 1 [1]. An acrylic sphere of radius a ($0.3\,\text{cm} \le a \le 2.5\,\text{cm}$) is sustained by eight thin wires (diameter $= 0.1\,\text{mm}$) and it moves downward at constant speed W. The flow is visualised by shadowgraph method, dye visualisation, particle image velocimetry (PIV) and laser induced fluorescence (LIF). For PIV, a double pulse laser (15 Hz, 532 nm) is used [4], and for LIF, a continuous wave (CW) laser (488 nm) is used. In PIV and LIF, velocity and dye concentration (salinity) in the vertical plane across the sphere centre

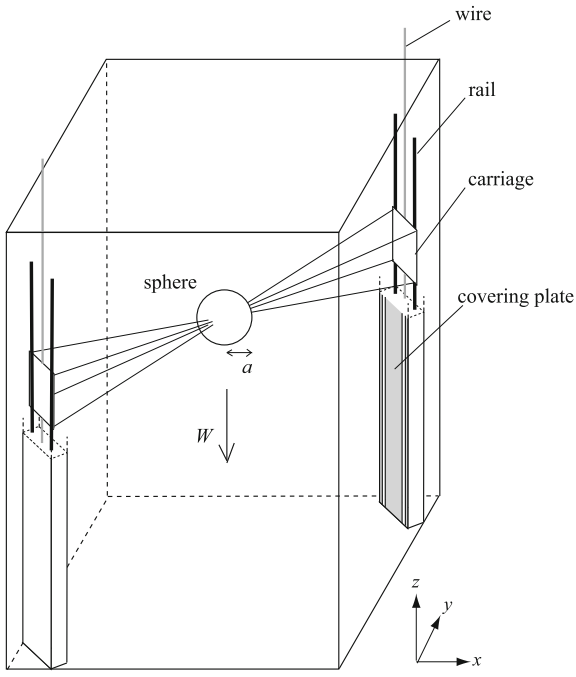

Fig. 1 Schematic figure of the test tank. Reproduced from [1] https://doi.org/10.1017/S0022112009990498

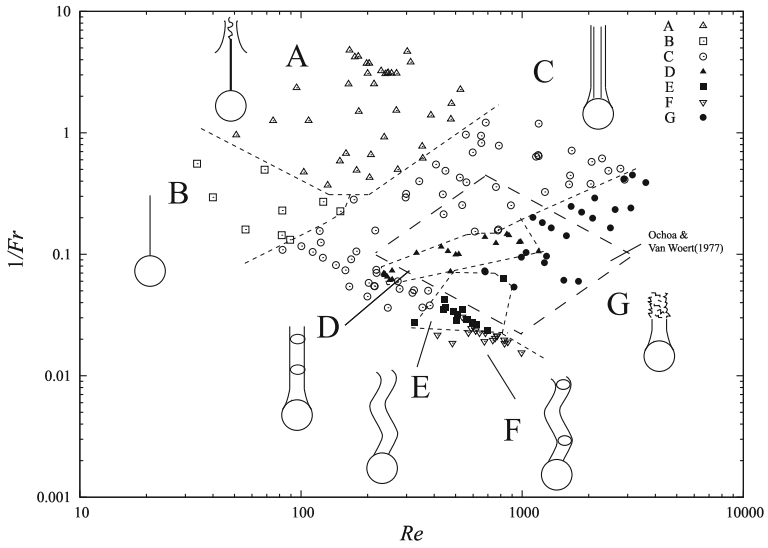

Fig. 2 Parameter range (Re, $1/Fr$) investigated in the experiments. A ∼ G denote the regions where wake patterns A ∼ G (cf. Fig. 5) have been observed. Reproduced from [1] https://doi.org/10.1017/S0022112009990498

are measured. In this paper, the results of shadowgraph and dye visualisation are demonstrated, while the results of PIV and LIF are omitted.

There are three non-dimensional parameters in the present problem. Among them, the Froude number is defined by $Fr = W/Na$ and the Reynolds number is defined by $Re = 2aW/\nu$, where W is the descending velocity of the sphere, N is the buoyancy frequency, a is the radius of the sphere and ν is the dynamic viscosity of fluid. The last parameter, i.e. the Schmidt number $Sc = \nu/\kappa$ (κ: diffusion coefficient of the scalar) is also an important non-dimensional parameter, but we consider only the salt-stratified fluid here. Therefore, it is fixed at 700.

Experiments show that, except for the very low Froude-number cases ($Fr < 0.1$) where unstable and unsteady jet appears, the jet/wake structures in the parameter space of Fr and Re are classified into seven types (Fig. 2). Those include two types of thin jets observed under strong stratification, one of which is topped by a peculiar 'bell-shaped' structure (Fig. 3a), while the other has a simple straight jet without the bell-shaped structure (Fig. 3b). Type C is a straight broad jet observed at weaker stratification (Fig. 3c). Type D, E and F are observed at weak stratification. Type D has periodically generated knots in the jet which would correspond to the vortex shedding in homogeneous fluid (Fig. 3d). Indeed, the shedding frequency corresponds to the Strouhal number for the usual vortex shedding from the sphere. Type E is a slightly meandering jet (Fig. 3e) and type F is another jet with periodic knots but with a spiral structure (Fig. 3f). Finally, type G is a turbulent jet which appears at high Reynolds numbers (Fig. 3g).

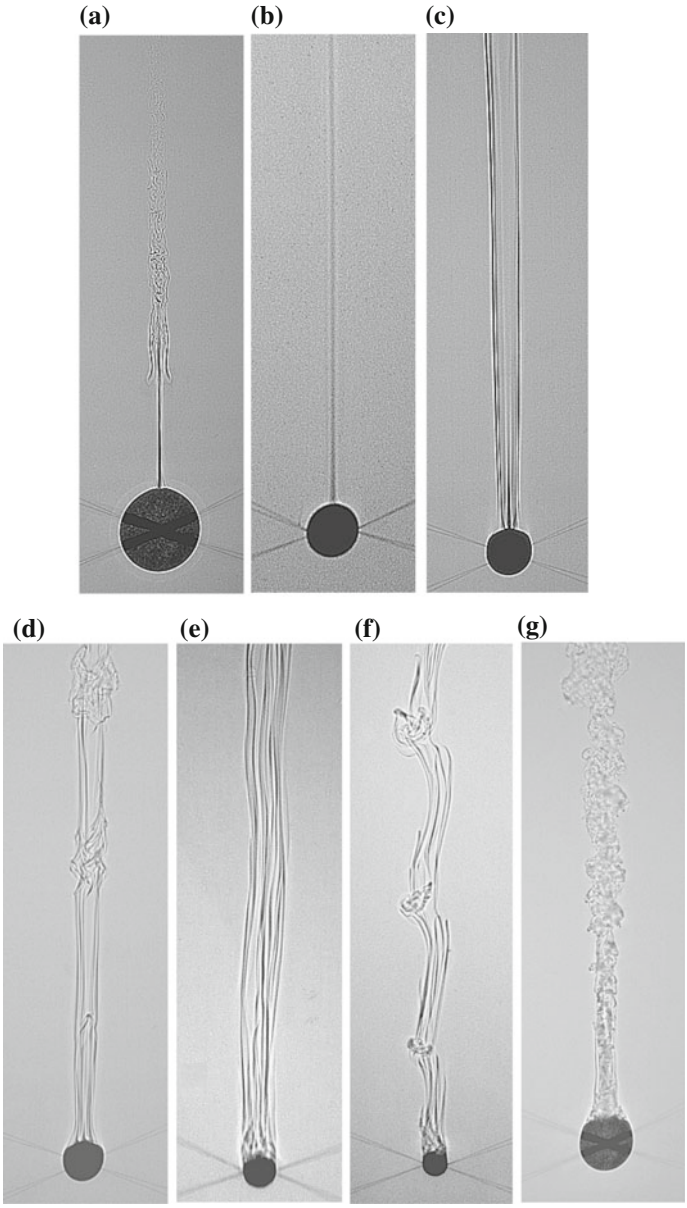

Fig. 3 Shadowgraph images of type A ∼ G. The values of (Re, Fr) are **a** type A, (199, 0.32) ; **b** type B, (126, 3.7); **c** type C, (610, 6.5); **d** type D, (678, 7.2); **e** type E, (567, 34.6); **f** type F, (589, 40.6); **g** type G, (2637, 4.3). Reproduced from [1] https://doi.org/10.1017/S0022112009990498

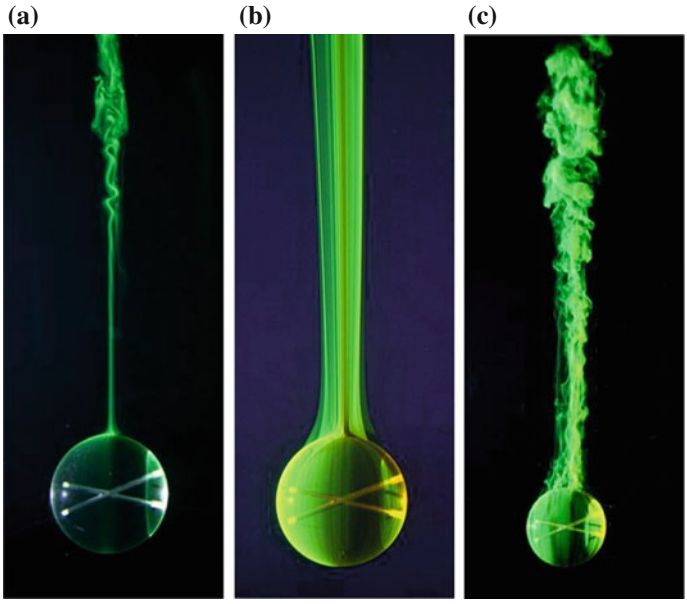

Fig. 4 Dye visualisation of the wake structures of type A, C, and G. The values of (*Re*, *Fr*) are **a** type A, (230, 0.30); **b** type C, (1189, 1.55); **c** type G, (3101, 4.17). Reproduced from [1] https://doi.org/10.1017/S0022112009990498

We have performed also dye visualisation using fluorescein sodium (or uranine). The dye is released from the vicinity of lower/upstream stagnation point of the sphere by injecting a drop of strong solution of dye using a syringe. The dye visualizes flows near the sphere surface and along the rear vertical axis of the flow. The results for type A, C and G are presented in Fig. 4, which correspond to the shadowgraph observations presented in Fig. 3. In type A (Fig. 4a), the bell-shaped structure is not well visualised by the dye since the dye would move up very near the centre of the jet, and it does not move along the bell-shaped structure.

1.2 Numerical Simulations

Numerical simulations corresponding to the water-tank experiments also have been performed to investigate the mechanisms of the jet formation [2]. Since the essential mechanisms of the jet formation would be in the axisymmetric aspects of the flow, and the simulation is limited to the Reynolds number less than 200, we have assumed the axisymmetry of the flow. Numerical method is the finite difference method with generalised curvilinear coordinates so that a computational grid line runs along the sphere surface. Since the Schmidt number is very high ($Sc = 700$) for the salt, the scalar/density boundary layer on the sphere is very thin compared to the velocity boundary layer, typically $1/\sqrt{Sc} \sim 1/28$ of the velocity boundary layer. Therefore,

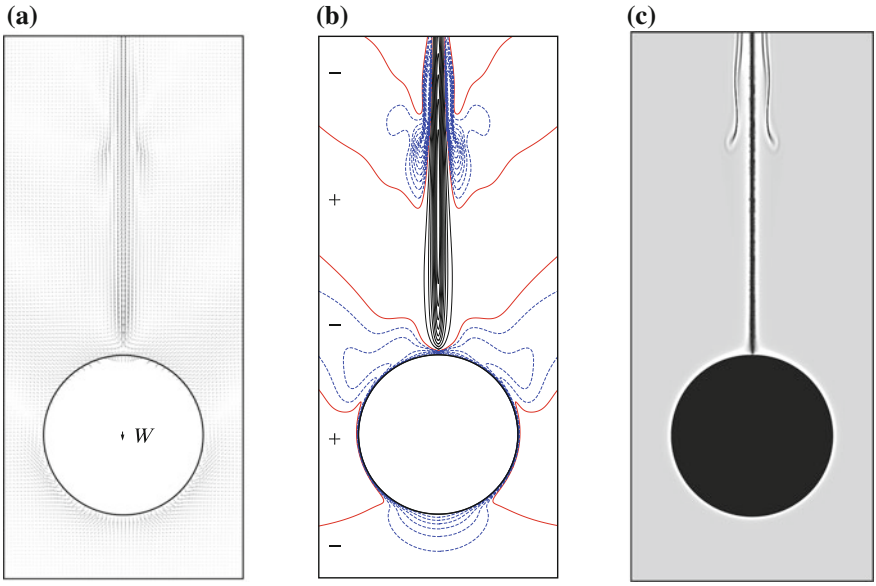

Fig. 5 Typical results at a low Froude number ($Fr = 0.3$, $Re = 247$, steady state at $t = 30$). **a** Velocity vectors in laboratory/stationary frame. Arrow at the centre of the sphere shows the downward velocity of the sphere. **b** Contours of vertical velocity in laboratory/stationary frame, i.e. $(w - 1)$, drawn at the interval of $\Delta(w - 1) = (w_{max} - 1)/10$ for $w - 1 > 0$ (solid lines), and $|w_{min} - 1|/10$ for $w - 1 < 0$ (dashed lines). Broad lines represent $w - 1 = 0$. **c** Gray-scale image of the distribution of molecular diffusion of density $\nabla^2\rho'/ReSc$. Reproduced from [2] https://doi.org/10.1017/jfm.2014.737

a very small grid size is necessary near the sphere. The small grid size would be necessary also in and near the jet, where large scalar/density variation is expected.

Typical results at low Froude numbers ($Fr = 0.3$, $Re = 247$) are shown in Fig. 5. The bell-shaped structure observed in the experiments in type A (Fig. 3a) is reproduced in three different physical quantities, i.e., velocity vector (Fig. 5a), vertical velocity component in laboratory/stationary frame (Fig. 5b) and molecular diffusion of density (Fig. 5c). In these figures, Fig. 5c directly corresponds to the shadowgraph results which visualise the Laplacian of density, and it gives the most clear image of the bell-shaped structure. We note in Fig. 5a, b that there is a diverging pattern of internal gravity waves (bold solid lines), and the bell corresponds to the downward flow due to the internal gravity waves.

The position of the bell-shaped structure moves upward as the Froude number increases. This has been observed both in the experiments and numerical simulations (Fig. 6), verifying that the bell-shaped structure is indeed the result of an internal wave which generates the maximum downward velocity near and above the sphere. Indeed, the height from the upper/rear stagnation point of the sphere is proportional to Fr, and the distance between the two contours of $w = 0$ is in agreement with the linear internal wave theory [5].

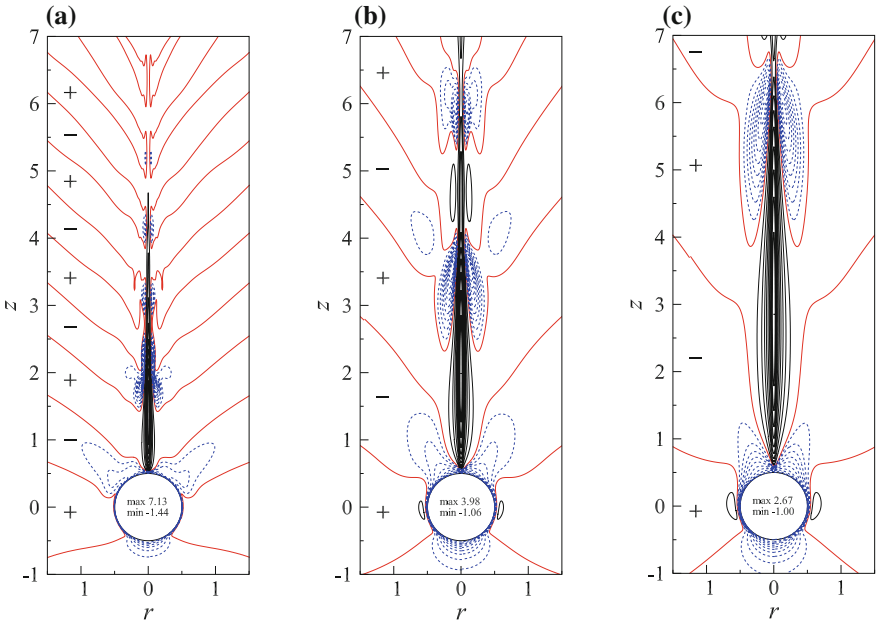

Fig. 6 Contours of steady vertical velocity in laboratory frame, i.e. $(w-1)$, at $t=30$. Broad solid lines denote $w-1=0$, thin solid lines denote $w-1>0$ at the interval of $(w_{max}-1)/10$, and dashed lines denote $w-1<0$ at the interval of $\mid w_{min}-1 \mid /10$. Values written on the sphere are the maximum and minimum velocity in each figure. **a** $Fr=0.3$; **b** $Fr=0.8$; **c** $Fr=1.5$. Reproduced from [2] https://doi.org/10.1017/jfm.2014.737

2 Water Waves with Capillary Effects

In the fluid with uniform density, surface water wave would be the most commonly observed wave, and it may be excited by an obstacle located on the bottom of the channel. When the wavelength is much longer than the water depth and the slow-time development is considered, we would observe solitary waves or solitons. The solitons are excited periodically by the obstacle, and propagate upstream of the obstacle. When capillary effects exist, large-amplitude solitons can generate short capillary waves, which propagate faster than the solitons (Fig. 7). We investigate these processes by numerical solutions of the Euler equations, and compare the results with the predictions by the weakly nonlinear theory, i.e. the forced Korteweg-de Vries equation with a higher (fifth)-order term which represents the capillary effect [3]. The weakly nonlinear theory can predict the upstream generation of the capillary waves by solitary waves, but it significantly overestimates the wavelength of the capillary waves and their propagation speed since the theory assumes a long wavelength and would not properly predict the capillary waves which have short wavelengths.

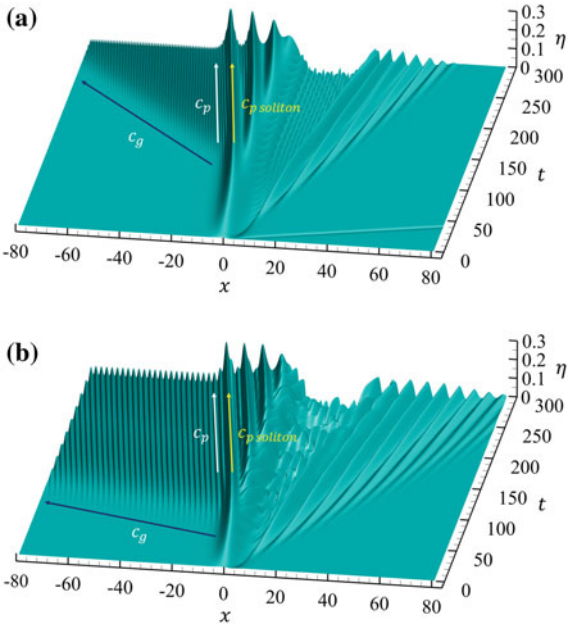

Fig. 7 Time development of the water waves excited by an obstacle located at x = 0 and on the bottom of the channel. Free-surface displacement is denoted by $\eta(x, t)$. **a** Euler equations; **b** fifth-order fKdV equation. Large-amplitude and long-wave solitons are excited periodically and propagate upstream (x < 0), and they generate short capillary waves which propagate upstream faster than the solitons since the group velocity C_g of the capillary wave is larger than its phase velocity C_p. Reproduced from [3] https://doi.org/10.1017/jfm.2016.702

References

1. Hanazaki H, Kashimoto K, Okamura T (2009) Jets generated by a sphere moving vertically in a stratified fluid. J Fluid Mech 638:173–197
2. Hanazaki H, Nakamura S, Yoshikawa H (2015) Numerical simulation of jets generated by a sphere moving vertically in a stratified fluid. J Fluid Mech 765:424–451
3. Hirata M, Okino S, Hanazaki H (2017) Radiation of short waves from the resonantly excited capillary-gravity waves. J Fluid Mech 810:5–24
4. Okino S, Akiyama S, Hanazaki H (2017) Velocity distribution around a sphere descending in a linearly stratified fluid. J Fluid Mech 826:759–780
5. Torres CR, Hanazaki H, Ochoa J, Castillo J, Van Woert M (2000) Flow past a sphere moving vertically in a stratified diffusive fluid. J Fluid Mech 417:217–236

Closed-Loop Turbulence Control-From Human to Machine Learning (and Retour)

Bernd R. Noack

Abstract Feedback turbulence control is a rapidly evolving, interdisciplinary field of research. The range of current and future engineering applications of closed-loop turbulence control has truly epic proportions, including cars, trains, airplanes, noise, air conditioning, medical applications, wind turbines, combustors, and energy systems. A key feature, opportunity and technical challenge of closed-loop turbulence control is the inherent nonlinearity of the actuation response. For instance, excitation at a given frequency will affect also other frequencies. This frequency crosstalk is not accessible in any linear control framework. This paper will address these nonlinear actuation mechanisms in three parts. First, success stories of human learning in turbulence control are presented, i.e. cases in which the nonlinear actuation mechanism has been modelled and understood. A large class of literature studies can be categorized in terms of surprisingly few mechanisms. Second, we discuss model-free machine learning control (MLC) and selected applications. MLC detects and exploits the winning actuation mechanisms in the experiment in an unsupervised manner. In all studies MLC has reproduced or outperformed existing optimized control strategies. Finally, future directions of turbulence control are outlined. Methods of machine learning are a disruptive technology will contribute to rapidly accelerating progress in turbulence control—both for performance and for physical understanding.

B. R. Noack (✉)
LIMSI-CNRS, Rue John von Neumann, Campus Universitaire d'Orsay,
Bât 508, 91403 Orsay, France
e-mail: Bernd.Noack@limsi.fr

B. R. Noack
Harbin Institute of Technology, Shenzhen Campus, Shenzhen, People's Republic of China

B. R. Noack
Technische Universität Braunschweig, Braunschweig, Germany

B. R. Noack
Technische Universität Berlin, Berlin, Germany

B. R. Noack
Institute PPRIME, Chasseneuil-du-Poitou, France

Y. Zhou et al. (eds.), *Fluid-Structure-Sound Interactions and Control*, Lecture Notes in Mechanical Engineering,
https://doi.org/10.1007/978-981-10-7542-1_3

Keywords Turbulence control · Control design · Machine learning
Reduced-order modeling

1 Closed-Loop Turbulence Control—Applications and Challenges

Features of turbulent flows have a large effect on the performance of engineering applications, like ground, maritime or airborne transport and energy systems. In numerous studies, feedback control has been shown to change these features employing small modern actuators and corresponding sensors. Thereby the performance has been significantly improved. Examples include drag reduction of cars and trucks, lift increase of airplanes, gust mitigation of wind turbines and NOX reduction in combustors—just to name a few.

A key challenge for control design is the inherent nonlinearity of turbulence dynamics. For instance, excitation at a given frequency will affect also other frequencies. Dominant vortex shedding at one frequency may be mitigated by a low- or high-frequency actuation [1]. This frequency crosstalk is not accessible in any linear control framework and has many qualitatively different characteristics [2]. Yet, virtually all turbulence control experiments exploit frequency crosstalk [3].

This contribution addresses these nonlinear actuation mechanisms in three parts. First (Sect. 2), success stories of turbulence control are presented in which the nonlinear actuation mechanism has been modelled. Second (Sect. 3), we discuss machine learning control (MLC) and selected applications. MLC detects and exploits the winning actuation mechanisms in the experiment in an unsupervised model-free manner. Finally (Sect. 4), future developments of turbulence control are outlined.

2 Control with Human Learning—Building Blocks of Understanding

Myriad control design method have been proposed for flow control. These methods can be attributed to numerous categories: model-free, model-based with black, gray and white box models, and open-loop versus adaptive feedback versus in-time response—just to name a few. Yet, only few actuation mechanisms have been exploited in the vast majority of flow control applications and the chosen control design is typically a corollary to that mechanism:

- **Opposition control (direct, in-time)**: This mechanism is encapsulated in the simple example

$$da/dt = a + b, \tag{1}$$

where a represents the state with unstable fixed point $a_s = 0$ and b is the control. Obviously $b = -2a$ stabilizes the plant. Several skin friction reductions [4] and Tollmien-Schlichting wave suppressions [5] are based on this mechanism: the wall-normal velocity is counteracted by a membrane or by suction/blowing.

- **Phasor control (direct, in-time)**: Let us consider following dynamical system coupling a self-amplified amplitude limited oscillator (a_1, a_2) and a stable linear oscillator at 10-fold frequency (a_3, a_4):

$$\begin{aligned} da_1/dt &= \sigma a_1 - a_2, & da_3/dt &= -0.1a_3 - 10a_4, \\ da_2/dt &= \sigma a_2 + a_1 + b_1, & da_4/dt &= -0.1a_4 + 10a_3 + b_3, \\ \sigma &= 0.1 - a_1^2 - a_2^2 - a_3^2 - a_4^2 - b_2. \end{aligned} \tag{2}$$

  Without control, $b_1 = b_2 = b_3 \equiv 0$, the first oscillator converges to the limit cycle $a_1^2 + a_2^2 = 0.1$ with unit frequency, while the second one vanishes, $a_3 = a_4 = 0$. We will ignore the stable oscillator (a_3, a_4) unless it is excited with b_3. The first oscillator can be stabilized with phasor control $b_1 = -0.4\, a_2$. This can be considered as opposition control for the evolution equation of the energy $E = (a_1^2 + a_2^2)/2$. Many cavity noise mitigations [6] and low-Reynolds number wake stabilizations [7, 8] belong to this category.
- **Constant forcing (indirect, open-loop)**: The first oscillator of (2) may be stabilized with $b_2 = 0.2$. Physically, this corresponds to an enforced change of the baseflow towards a more stable regime. Such a stabilization has, for instance, been realized for mitigating vortex shedding behind high-lift airfoil via Coanda blowing [9].
- **Periodic forcing at high or low frequency (indirect, open-loop)**: The first oscillator of (2) can also be stabilized exploiting the frequency crosstalk with the stable one: Now $b = \cos 10t$ can be seen to excite the second oscillator which stabilizes the first one via σ. Physically, this corresponds to baseflow change via an induced Reynolds stress at a new frequency, ideally exploiting a weakly damped instability. The actuation frequency may be higher or lower than the natural one. Such high- and low-frequency stabilization of vortex shedding has been observed numerous times for wakes, jets and shear-layers [1]. Figure 1 illustrates the drag reduction by low-frequency forcing of a D-shaped cylinder and high-frequency actuation of an Ahmed body.

We shall not pause to list obvious variations, like a closed-loop destabilization in the last example. In addition, adaptive generalizations, e.g. extremum or slope seeking, may allow to adjust open- and closed-loop control to slowly varying operating conditions. Once, the actuation mechanism and corresponding model is identified, the nonlinear control design is typically straightforward. We refer to the literature for the Navier-Stokes based derivation of such models and examples, e.g. our review article [3] and our books [12, 13]. We also refer to exquisite reviews on specific topics, like linear control [6, 14, 15], wake control [16] and actuators [17].

The above discussion focusses on nonlinear dynamical models. An alternative approach follows Brockett's idea of control design for the equivalent linear

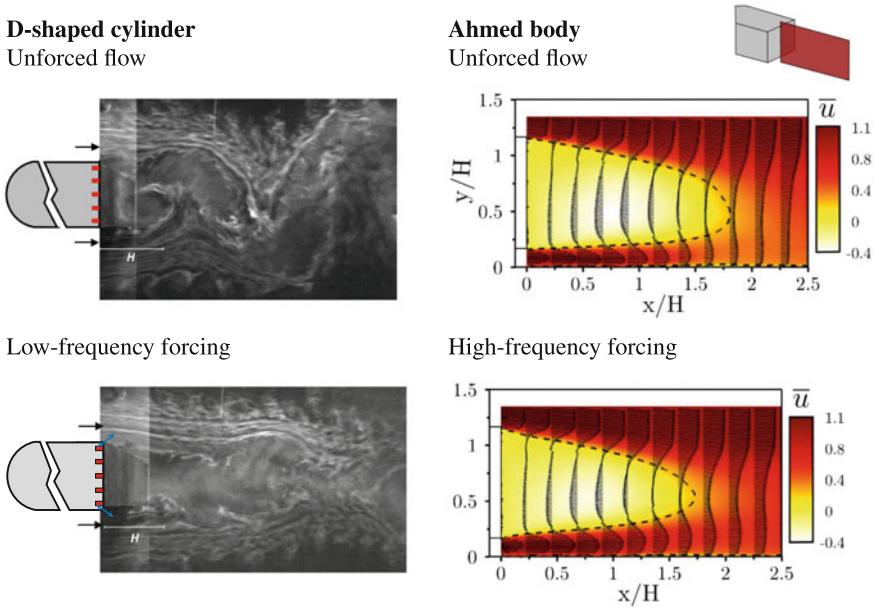

Fig. 1 Flow visualization behind bluff bodies with significant drag reductions in wind-tunnel experiments. Left: D-shaped cylinder ($Re_D = 40,000$) with symmetric low-frequency forcing [10]. The D-shaped body is indicated in gray, the red squares mark the location of the pressure sensors and the blue arrows indicated the employed zero-net-mass-flux actuators. The flow is visualized with smoke without forcing (top) and with forcing (bottom). Note the delayed vortex shedding by actuation. Right: Ahmed body ($Re_H = 3 \times 10^5$) with high-frequency Coanda blowing at all four rearward edges [11]. The mean flow is displayed in the near-wake symmetry plane from PIV data without forcing (top) and with forcing (bottom). The top right figure indicates the displayed flow region (brown) and the Ahmed body (gray). Note the more streamlined form of the forced wake region (fluidic boat tailing). The subfigures are adapted from [3, 11]

Liouville equation for the probability distribution [18]. A practical data-driven realization is based on clustering of snapshot data and the resulting Markov transition model [19, 20].

3 Control with Machine Learning—Often Faster, More Flexible and Better

The bald eagle can perform impressive flight maneuvers under gusty wind conditions with closed-loop control—yet without apparent knowledge of Navier-Stokes equations and control design. Nature has found another strategy: control design by evolution with smart trial and error. This approach has been pioneered by Rechenberg [21] and Schwefel [22] for shape optimization at the TU Berlin over 50 years

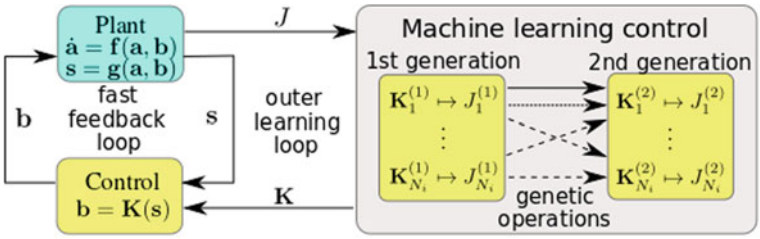

Fig. 2 Principle sketch of MLC using genetic programming. MLC consists of a fast inner feedback loop for testing the performance J and a slow outer learning loop for evolving the control law $\boldsymbol{K}$. After the learning phase, the best individual of the last generation is taken as control law

ago. Nature's way of control design is mimicked in the recently discovered *Machine Learning Control (MLC)*. Control design is framed as *regression problem of second kind*: Find the control law $\boldsymbol{b} = \boldsymbol{K}(\boldsymbol{s}, t)$ which minimizes the cost function J, $\boldsymbol{K}^\star = \arg\min_{\boldsymbol{K}} J\,[\boldsymbol{K}(\boldsymbol{s}, t)]$. Here, t represents time, $\boldsymbol{s}$ comprises the sensor signals and $\boldsymbol{b}$ analogously the actuation commands. The chosen form of the control law includes periodic excitation $b = B\cos\Omega t$, multi-frequency forcing, sensor-based feedback $\boldsymbol{b} = \boldsymbol{K}(\boldsymbol{s})$ and combinations thereof.

Genetic programming [23] is chosen as a powerful regression technique for general nonlinear control laws of unknown structure. It is particularly suited for exploring a complex J landscape with several local minima. MLC with genetic programming as regression method consists of following steps (see also Fig. 2):

- **First generation**: Let $\boldsymbol{b} = \boldsymbol{K}_i^{(1)}$, $i = 1, \ldots, N_i$ be random control laws, also called individuals. A typical population size is $N_i = 100$. These control laws are tested and graded in the plant $J_i^{(1)}$. Without loss of generality, the individuals are sorted after testing, $J_1^{(1)} \leq J_2^{(1)} \leq \ldots \leq J_{N_i}^{(1)}$. The first step of genetic programming is a simple Monte-Carlo search.
- **Second generation**: The second generation $\boldsymbol{b} = \boldsymbol{K}_i^{(2)}$, $i = 1, \ldots, N_i$ is created from the first by three stochastic genetic operations mimicking natural selection: Crossover of two individuals shall produce better individuals; mutations shall explore potentially new unpopulated minima; and replication shall memorize successful individuals. In addition, elitism copies the best N_e individuals directly in the new generation. Typically, only the best individual ($N_e = 1$) is saved. The selection probabilities of crossover, mutation and replication are typically chosen to be $P_c = 0.7$, $P_m = 0.2$ and $P_r = 0.1$.
- **Next generations and termination**: Analogously, more generations are produced until a convergence or another stop criterion is reached. In all experiments, convergence is reached before $N_g = 10$ generations. The best individual $\boldsymbol{K}_1^{N_g}$ of the last generation yields the desired MLC law.

Genetic programming has numerous parameters. Fortunately, a single set of parameters was found to produce the winning control in over a dozen different experiments

[13]. In addition, the MLC laws have been found to be reproducible modulo small unavoidable uncertainty.

MLC has been studied in a number of experiments.

- **Mixing layer energetization (TUCOROM wind tunnel, France** [24]). In this first MLC experiment, a turbulent mixing layer is forced upstream with 96 synchronously operated streamwise fluid jets (b) in the separating plate and monitored downstream with a vertical array of 24 hot-wire probes $\boldsymbol{s}$. The Reynolds number based on initial mixing layer thickness is 500, yielding a laminar boundary layer for the learning phase. The testing for off-design conditions is done at $Re = 2000$ with a turbulent boundary layer. The goal J is to increase the mixing layer width as measured by the hot-wire rag. The best periodic forcing yields a 55% increase of shear-layer width. MLC yields reproducibly a direct sensor feedback $b = K(\boldsymbol{s}')$ which increases this width by 67% and at only 54% of cost of optimal periodic forcing. In addition, MLC is more robust to large changes of the freestream velocities as compared to the periodic benchmark. An important enabler of this control is the feedback of the velocity *fluctuations* to reduce sensitivity to slow baseflow changes. MLC converges after few generations with 100 individuals. The actuation mechanism is based on phase synchronization (phasor control). Despite the simple actuation mechanism, we could not identify a linear ERA-OKID model for the actuation response—even in a narrow frequency range: Sensor response could hardly be correlated with the actuation command.
- **Reduction of a circulation bubble behind a backward facing step (PMMH water tunnel, France** [25]). In this MLC experiment, a flow over backward-facing step is forced upstream with slot actuator (blowing and suction) and monitored in the dead-water region with in-time PIV. The sensor signal is the size of the reverse flow region, which is 'blind' to the Kelvin-Helmholtz shedding phase. The Reynolds number based on step height is 1350 for the learning phase and is varied between 900 and 1800 for testing off-design conditions. The goal is to minimize the recirculation zone with an actuation penalty. MLC yields a direct sensor feedback $b = K(s)$ which excites a low-frequency flapping mode. The cost is similar to an optimal periodic forcing exciting the Kelvin-Helmholtz shedding for the reference condition. However, MLC is much more robust for a range of (untested) oncoming velocities resulting in cumulative cost $J = 0.43$ (MLC) versus $J = 0.77$ for the periodic benchmark. $J = 1$ would correspond to the unforced flow at reference conditions. MLC is converged after 8 generations with 500 individuals. The actuation mechanism exploits frequency crosstalk with feedback destabilization of the flapping mode at low frequency.
- **Drag reduction of a car model (wind tunnel Beton, PPRIME, France** [26]). The drag of a wall-mounted Ahmed body at $Re_H = 3 \times 10^5$ is reduced with 4 independent on/off Coanda jets at the rear edges ($\boldsymbol{b} \in R^4$). The flow is sensed with 12 pressure sensors distributed over the rear side ($\boldsymbol{s} \in R^{12}$). The optimal periodic forcing is found to be at high frequency and low duty cycle, yielding 19% drag reduction at an estimated actuation power of only 1/7 of the saved drag power [11]. MLC rapidly converges with a population size $N_i = 50$ in $N_g = 5$

generations (250 runs). MLC depends on the assumed control law. Sensor-based feedback $\boldsymbol{b} = \boldsymbol{K}(\bar{\boldsymbol{s}}, \boldsymbol{s}')$ reproduces high-frequency forcing with similar drag reduction. Note that the sensor signals have been decomposed into a short-term mean $\bar{\boldsymbol{s}}$ (not used by MLC) and a fluctuation $\boldsymbol{s}'$. The performance is remarkable since the time delay from actuation to sensing is two (!) periods and since the signature of high-frequency actuation is below the noise level in most sensors. MLC chooses the only sensor with good high-frequency signal to noise level, i.e. performs sensor selection for the optimal control law. With the ansatz $\boldsymbol{b} = \boldsymbol{K}(\boldsymbol{s}', h(t))$, h being a harmonic signal at optimal high-frequency forcing, MLC chooses the slightly better performing open-loop control. Given an open-loop multi-frequency ansatz $\boldsymbol{b} = \boldsymbol{K}(\boldsymbol{h}(t))$, MLC improves drag reduction by 22% with a 2-frequency forcing. The employed actuation mechanism is based on frequency crosstalk in all cases.

- **Separation mitigation of a turbulent boundary layer (wind tunnel, LML and PRISME, France** [13, 27]). The separation of a turbulent boundary layer over a smooth ramp is mitigated by an upstream array of synchronously operated jets in two geometrically similar wind-tunnel experiments at different Reynolds numbers based on step height: 13,000 at LML and 130,000 at PRISME. The flow is monitored with skin-friction and pressure sensors. The goal is to mitigate the separation, as measured by a cost function J with actuation penalization. The optimal open-loop forcing laws are found to be constant blowing (LML) and periodic actuation (PRISME). The ansatz for the control laws is sensor feedback $\boldsymbol{b} = K(\boldsymbol{s})$. The optimal MLC laws found intermittent forcing (LML) and high-frequency actuation (PRISME)—outperforming the optimized open-loop benchmark.
- **Other MLC studies.** Applications to other plants with the author include:
  - Stabilization of a noisy unstable oscillator [13]. Here the optimal control solution is almost exactly reproduced using random filters.
  - Chaos maximization of a Lorenz system [28].
  - Stabilization of two coupled oscillators, Eq. (2) [13].
  - Stabilization of three nonlinearly coupled oscillators [26].
  - Energetization of a 2D mixing layer in a direct numerical simulation.
  - Lift-increase of a NACA0015 airfoil with an emulated plasma actuator in a direct numerical simulation. Intriguingly, MLC found intermittent actuation leading to a series of small vortices moving over the top side of the airfoil. This actuation increases lift beyond constant and periodic forcing while reducing the actuation power [Joint work with H. Fukumoto and A. Oyama].
  - Stabilization of a fluidic pinball in a wind-tunnel experiment [29].
  - Mixing increase behind a backward-facing step in a wind-tunnel experiment [31].
  - Drag reduction of a D-shaped cylinder in a wind-tunnel experiment [30].
  - Symmetrization of the Ahmed body wake to mitigate bimodal behavior. The problem and benchmark feedback controller are described in [32].

  In all cases, MLC has reproduced or outperformed the optimized benchmark control in some 1,000 test runs using the same parameters of genetic programming.

In the mentioned studies, we have used genetic programming as powerful regression method for arbitrary nonlinear control laws. MLC may also be performed with other regression techniques. Starting from an assumed linear control law, the gains may also be optimized with a simpler genetic algorithm [33]. A further simplification is achieved in the rare case that the optimal actuation for given flow state can be computed with a full-state simulation. In this case, the search for a mapping from known sensor signals to know actuation commands constitutes a *regression problem of the first kind*. A sensor-based feedback law may, for instance, be obtained with a neural network [34].

4 Conquering Terra Incognita—Paradigm Shifts by Machine Learning

Presented results indicate that methods of machine learning will dramatical change and accelerate progress in turbulence control in the coming years. Here are few expected future directions.

- The control laws to be explored will go far beyond constant and periodic actuation (or small variations thereof). MLC makes it easy to explore control laws of the form

$$\boldsymbol{b} = \boldsymbol{K}(\boldsymbol{s}, \boldsymbol{h}, \boldsymbol{n})$$

  where $\boldsymbol{h}$ comprises harmonic functions and $\boldsymbol{n}$ noise terms for stochastic forcing.
- The traditional paradigm: *'From understanding to modeling to control'* will largely be replaced by the new paradigm *'From control to modeling to understanding'*. The winning control tends to be too complex to be predicted by any model. Moreover, identified models will be much more powerful and predictive if they incorporate many different control laws.
- Also modeling will be strongly affected. Modern data-driven regression techniques may allow to derive simple human-interpretable dynamical models from data. For instance, SINDy [35] has been shown to derive first-principle based generalized mean-field models—similar to (2)—from properly prepared simulation data. The traditional paradigm *'From first principles to modes to dynamics'* is likely to be replaced by the new paradigm *'From (controlled) dynamics to modes (or more general flow estimators) to a first-principles based understanding'*. The old paradigm assumes, for instance, that the optimal actuation mechanism is correctly predicted. However, the mentioned MLC studies have, more oven than not, surprised with unexpected better mechanisms. We show the potential of the new paradigm for a transient wake flow [36].
- As consequence of machine-learned models, we can expect many new qualitatively different nonlinear dynamics models enabling more a powerful control.
- A key task of turbulence control includes to estimate achievable performance with control for a new configuration and to predict the right choice and location of

actuators. These are likely to remain a challenging topic in the first principles domain until the performance data of actuators in different configurations is becoming very rich.

Acknowledgements This material presented here was only possible through the hard and enthusiastic work of my former PhD students Diogo Barros, Eurika Kaiser, Ruiying Li, Mark Luchtenburg and Mark Pastoor, my former Postdocs Thomas Duriez and Vladimir Parezanović, other members of the former TUCOROM Team (Jean-Paul Bonnet, Jacques Borée, Laurent Cordier, and Andreas Spohn) and the fruitful collaborations with Markus Abel, Jean-Luc Aider, Steven Brunton, Camila Chovet, Guy Yoslan Cornejo Maceda, Nan Deng, Hiroaki Fukumoto, Nicolas Gautiers, Rudibert King, Laurent Keirsbulck, Azeddine Kourta, François Lusseyran, Lionel Mathelin, Robert Martinuzzi, Marek Morzyński, Robert Niven, Akira Oyama, Luc Pastur, Cedric Raibaudo, Richard Semaan and Michel Stanislas. Three PhD theses have been supported by the OpenLab Fluidics between PSA Peugeot-Citroën and Institute Pprime (Fluidics@poitiers) and L'Ecole Doctorale SMeMAG at LIMSI-CNRS. This work is also supported by a public grant overseen by the French National Research Agency (ANR) as part of the "Investissement dAvenir" program, through the "iCODE Institute project" funded by the IDEX Paris-Saclay, ANR-11-IDEX-0003-02.

References

1. Glezer A, Amitay M, Honohan AM (2005) Aspects of low- and high-frequency actuation for aerodynamic flow control. AIAA J 43(7):1501–1511
2. Noack BR, Schlegel M, Ahlborn B, Mutschke G, Morzyński M, Comte P, Tadmor G (2008) A finite-time thermodynamics of unsteady fluid flows. J Non-Equilib Thermodyn 33(2):103–148
3. Brunton SL, Noack, BR (2015) Closed-loop turbulence control: progress and challenges. Appl Mech Rev 67(5):050801:01–48
4. Choi H, Moin P, Kim J (1994) Active turbulence control for drag reduction in wall-bounded flows. J Fluid Mech 262:75–110
5. Airiau C, Bottaro A, Walther S, Legendre D (2003) A methodology for optimal laminar flow control: application to the damping of Tollmien-Schlichting waves in a boundary layer. Phys Fluids 15(5):1131–1145
6. Rowley CW, Williams DR (2006) Dynamics and control of high-Reynolds number flows over open cavities. Ann Rev Fluid Mech 38:251–276
7. Zhang MM, Cheng L, Zhou Y (2004) Closed-loop control of fluid-structure interactions on a flexibly supported cylinder. Eur J Mech B 23:189–197
8. Protas B (2004) Linear feedback stabilization of laminar vortex shedding based on a point vortex model. Phys Fluids 16(12):4473–4488
9. Semaan R, Kumar P, Burnazzi M, Tissot G, Cordier L, Noack BR (2016) Reduced-order modeling of the flow around a high-lift configuration with unsteady Coanda blowing. J Fluid Mech 800:71–110
10. Pastoor M, Henning L, Noack BR, King R, Tadmor G (2008) Feedback shear layer control for bluff body drag reduction. J Fluid Mech 608:161–196
11. Barros D, Borée J, Noack BR, Spohn A, Ruiz T (2016) Bluff body drag manipulation using pulsed jets and Coanda effect. J Fluid Mech 805:442–459
12. Noack BR, Morzyński M, Tadmor G (2011) Reduced-order modelling for flow control, volume 528 of CISM courses and lectures. Springer
13. Duriez T, Brunton S, Noack BR (2016) Machine learning control—taming nonlinear dynamics and turbulence, volume 116 of fluid mechanics and its applications. Springer
14. Kim J, Bewley TR (2007) A linear systems approach to flow control. Ann Rev Fluid Mech 39:383–417

15. Bagheri S, Hoepffner J, Schmid PJ, Henningson DS (2009). Input-output analysis and control design applied to a linear model of spatially developing flows. Appl Mech Rev 62(2):020803: 1–27
16. Choi H, Jeon W-P, Kim J (2008) Control of flow over a bluff body. Ann Rev Fluid Mech 40:113–139
17. Cattafesta L, Shelpak M (2011) Actuators for active flow control. Ann Rev Fluid Mech 43:247–272
18. Brockett R (2012) Notes on the control of the Liouville equation. In Alabau-Boussouira F, Brockett R, Glass O, Le Rousseau J, Zuazua E (eds) Control of partial differential equations, volume 2048 of lecture notes in mathematics. Springer, pp 101–130
19. Kaiser E, Noack BR, Cordier L, Spohn A, Segond M, Abel MW, Daviller G, Östh J, Krajnović S, Niven RK (2014) Cluster-based reduced-order modelling of a mixing layer. J Fluid Mech 754:365–414
20. Kaiser E, Noack BR, Spohn A, Cattafesta LN, Morzyński M (2017) Cluster-based control of nonlinear dynamics. Theor Comput Fluid Dyn (online) 1–15
21. Rechenberg I (1973) Evolutionsstrategie: optimierung technischer systeme nach prinzipien der biologischen evolution. Frommann-Holzboog, Stuttgart
22. Schwefel H-P (1965) Kybernetische Evolution als Strategie der experimentellen Forschung in der Strömunstechnik. Master thesis, Hermann-Föttinger-Institut für Strömungstechnik, Technische Universität Berlin, Germany
23. Koza JR (1992) Genetic programming: on the programming of computers by means of natural selection. The MIT Press, Boston
24. Parezanović V, Cordier L, Spohn A, Duriez T, Noack BR, Bonnet J-P, Segond M, Abel M, Brunton SL (2016) Frequency selection by feedback control in a turbulent shear flow. J Fluid Mech 797:247–283
25. Gautier N, Aider J-L, Duriez T, Noack BR, Segond M, Abel MW (2015) Closed-loop separation control using machine learning. J Fluid Mech 770:424–441
26. Li R, Noack BR, Cordier L, Borée J, Harambat F (2017) Drag reduction of a car model by linear genetic programming control. Exp Fluids 58:103:1–20
27. Debien A, von Krbek KAFF, Mazellier N, Duriez T, Cordier L, Noack BR, Abel MW, Kourta A (2016) Closed-loop separation control over a sharp-edge ramp using genetic programming. Exp Fluids 57(3):40:1–19
28. Duriez T, Parezanović V, Laurentie J-C, Fourment C, Delville J, Bonnet J-P, Cordier L, Noack BR, Segond M, Abel MW, Gautier N, Aider J-L, Raibaudo C, Cuvier C, Stanislas M, Brunton S (2014) Closed-loop control of experimental shear layers using machine learning (invited). In: 7th AIAA flow control conference. Atlanta, Georgia, USA, pp 1–16
29. Raibaudo C, Zhong P, Martinuzzi RJ, Noack BR (2017) Closed-loop control of a triangular bluff body using rotating cylinders. In: The 20th World Congress of the International Federation of Automatic Control (IFAC), Toulouse, France, pp 1–6
30. Ostwald P (2017) Experimental investigations of active and passive drag-reducing devices over a D-shaped bluff body. Master thesis 445, Technische Universität Braunschweig
31. Chovet C, Keirsbulck L, Noack BR, Lippert M, Foucaut JM (2017) Machine learning control for experimental shear flows targeting the reduction of a recirculation bubble. In: The 20th World Congress of the International Federation of Automatic Control (IFAC)
32. Li R, Barros D, Borée J, Cadot O, Noack BR, Cordier L (2016) Feedback control of bi-modal wake dynamics. Exp Fluids 57(158):1–6
33. Benard N, Pons-Prats J, Periaux J, Bugeda G, Braud P, Bonnet JP, Moreau E (2016) Turbulent separated shear flow control by surface plasma actuator: experimental optimization by genetic algorithm approach. Exp Fluids 57:22:1–17
34. Lee C, Kim J, Babcock D, Goodman R (1997) Application of neural networks to turbulence control for drag reduction. Phys Fluids 9(6):1740–1747
35. Brunton SL, Proctor JL, Kutz NJ (2016) Discovering governing equations from data by sparse identification of nonlinear dynamical systems. Proc Natl Acad Sci USA 113(5):3932–3937
36. Loiseau J-Ch, Noack BR, Brunton SL (2017) Sparse reduced-order modeling: sensor-based dynamics to full-state estimation. J Fluid Mech 1–28 (in print)

Exploring a Universal Wake Number for Finite-Height Bluff Bodies

S. Unnikrishnan and D. Sumner

Abstract The suitability of two universal wake numbers, namely Roshko's universal Strouhal number and the Griffin number, was explored for surface-mounted finite-height bluff bodies. Mean drag force coefficient, Strouhal number, and mean base pressure coefficient data for finite cylinders and finite square prisms, for various Reynolds numbers and aspect ratios, were considered. Comparison was made to established values for the two-dimensional cylinder and square prism for Reynolds numbers in the range of $10^4 < \mathrm{Re} < 10^5$. The Griffin number was found to be the most suitable universal wake number, and was reasonably successful at collapsing data for finite cylinders and finite square prisms for a wide range of aspect ratios and incidence angles, particularly if the body's aspect ratio was higher than the critical aspect ratio.

Keywords Bluff body · Wake · Vortex shedding · Finite square prism
Finite cylinder · Base pressure

1 Introduction

Vortex shedding occurs from many types of bluff bodies and the vortex street wakes of different bodies are often similar. The vortex shedding frequency is closely related to the size of the near-wake region, including the lateral spacing of the shear layers, the length and width of the near-wake recirculation zone, and the vortex formation length. For two-dimensional (2D) bluff bodies, the similarity in the vortex street wakes and the inter-relationship between the vortex shedding frequency, base pressure, and drag force, have led to the development of various

S. Unnikrishnan (✉) · D. Sumner (✉)
Department of Mechanical Engineering, University of Saskatchewan,
Saskatoon, SK, Canada
e-mail: sau443@mail.usask.ca

D. Sumner
e-mail: david.sumner@usask.ca

Y. Zhou et al. (eds.), *Fluid-Structure-Sound Interactions and Control*, Lecture Notes in Mechanical Engineering,
https://doi.org/10.1007/978-981-10-7542-1_4

"universal wake numbers", which can be used to characterize bluff body vortex wakes independent of the body geometry or flow regime.

The universal Strouhal number of Roshko [15], St_R, and the universal wake number of Griffin [4], G, have been reasonably successful at scaling and collapsing vortex shedding frequency (f), base pressure (P_B), and drag force (F_D) data from a wide range of 2D bluff bodies, including stationary and oscillating cylinders and prisms [1, 4, 9], as well as groups of cylinders [16], over a wide range of Reynolds number, Re (= $U_\infty D/\nu$, where U_∞ is the freestream velocity, D is the body width, and ν is the kinematic viscosity). Collapse of the data is obtained by using theoretical or semi-empirical length and velocity scales associated with the near wake instead of the body geometry or upstream flow conditions. Both St_R (Eq. 1) and G (Eq. 2) are functions of the Strouhal number, St (= fD/U_∞), base pressure coefficient, C_{PB} (= $2(P_B - P_\infty)/(\rho U_\infty^2)$, where P_∞ is the freestream static pressure, and ρ is the fluid density), and mean drag coefficient, C_D (= $2F_D/(\rho U_\infty^2 A)$, where A is the frontal area), as shown below (where $K = (1 - C_{PB})^{1/2}$).

$$St_R = -\frac{St}{K}\frac{C_D}{C_{PB}} \tag{1}$$

$$G = \frac{StC_D}{K^3} \tag{2}$$

In the present study, the suitability of St_R and G is explored for the flow around surface-mounted finite-height square prisms and cylinders, where the flow field is strongly three-dimensional (3D).

2 Experimental Approach

The data come from three sets of wind tunnel experiments for surface-mounted finite-height square prisms and cylinders of aspect ratio AR = H/D = 9, 7, 5, and 3 (where H is the body height). The C_D and St data for the finite square prisms were taken from McClean and Sumner [6] at Re = 7.4×10^4, for incidence angles from $\alpha = 0°$ to 45°; C_{PB} data for AR = 3 were obtained from near-wake seven-hole-probe measurements at Re = 3.7×10^4 by Ogunremi and Sumner [14]; the C_{PB} data for the other aspect ratios were obtained in similar experiments (unpublished). The C_D, St and C_{PB} data for the finite cylinders, at Re = 6×10^4, were taken from Sumner et al. [17]. The C_{PB} data were obtained at a streamwise location of $x \sim 1.2D$ downstream of the body. Since the vortex formation length, and therefore C_{PB}, vary along the height of the 3D bodies, a representative value of C_{PB} was needed to scale the data. Here, the average value of C_{PB} between z/H = 0.1 and 0.9 (where z is the wall-normal or vertical coordinate) was used.

3 Results and Discussion

Figure 1a shows the variation of St_R and G with Re for a 2D cylinder and a 2D square prism at $\alpha = 0°$ for $10^4 < Re < 10^5$. For the 2D bluff bodies, the data collapse to the same value of $St_R = 0.124$ (Table 1) for both the cylinder and the prism, and to comparable values of $G = 0.069$ and $G = 0.073$ for the cylinder and prism, respectively. For the 2D bodies, the two wake numbers are therefore independent of the body shape and may be considered "universal".

Also shown in Fig. 1a are data for the finite cylinder. The St_R data for the finite cylinders of AR = 9, 7, and 5 ($St_R = 0.131$, 0.120, and 0.119, respectively) are close to the 2D cylinder value of $St_R = 0.124$ (Table 1). However, for the finite cylinder of AR = 3, a higher value of $St_R = 0.161$ is obtained. It is noted that the finite cylinder of AR = 3 lies below the critical aspect ratio, and has a distinct vortex wake compared to finite cylinders of higher aspect ratio [17]. In contrast to the St_R data for the finite cylinder, the Griffin number is relatively insensitive to AR, ranging from G = 0.051 to 0.056 for the four finite cylinders (Fig. 1a, Table 1). However, the G values for the finite cylinder are slightly lower than the 2D cylinder value of G = 0.069, a result that suggests different physical mechanisms may be influencing vortex shedding from the finite cylinder, such as variation of the separation angle and near-wake width along the cylinder height.

Figure 1a also shows data for the finite square prism at $\alpha = 0°$. Again, the results are similar to those of the finite cylinder discussed above. The finite square prism of AR = 3 lies below the critical aspect ratio [6], with a different wake structure, and hence distinct universal wake numbers of $St_R = 0.109$ and G = 0.051 are obtained compared to the finite prisms of AR = 9, 7, and 5 (Table 1). Moreover, both St_R and G attain different values for the finite prism compared to the 2D prism, which, again, suggests different physical mechanisms (related to the free end) are influencing the vortex wake.

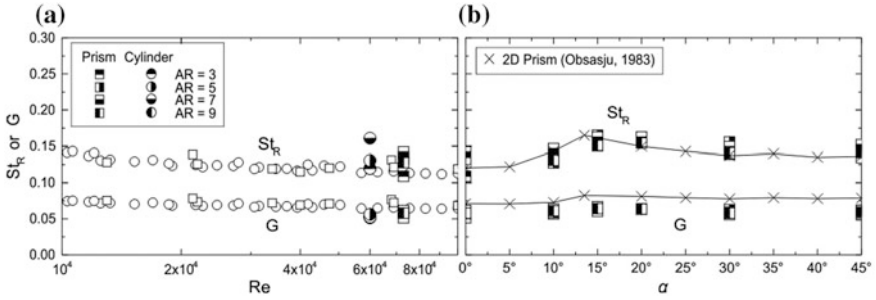

Fig. 1 Universal wake number data for finite-height square prisms and cylinders: **a** as a function of Reynolds number; **b** data for square prisms as a function of incidence angle. 2D cylinder data: ◯, from Norberg [12]. 2D square prism data: □, from Bearman and Trueman [3], Bearman and Obasaju [2], Luo et al. [5], Minguez et al. [7], Nakaguchi et al. [8], Noda and Nakayama [10], Norberg [11], Obasaju [13] and Vickery [18]

Table 1 Summary of universal wake number data (for $10^4 < Re < 10^5$)

Cylinders	St_R	Std. dev.	G	Std. dev.
2D Cylinder [12], Fig. 1a	0.124	7%	0.069	5%
Finite cylinder, AR = 9	0.131		0.056	
Finite cylinder, AR = 7	0.120		0.052	
Finite cylinder, AR = 5	0.119		0.051	
Finite cylinder, AR = 3	0.161		0.053	
Square prisms ($\alpha = 0°$ only)	St_R	Std. dev.	G	Std. dev.
2D square prism (various studies, Fig. 1a)	0.124	6%	0.073	4%
Finite square prism, AR = 9	0.128		0.058	
Finite square prism, AR = 7	0.142		0.061	
Finite square prism, AR = 5	0.133		0.060	
Finite square prism, AR = 3	0.109		0.051	
Square prisms ($\alpha = 0°$–45°)	St_R	Std. dev. (%)	G	Std. dev. (%)
2D Square Prism (Obasaju [13], Fig. 1b)	0.139	9	0.077	5
Finite square prism, AR = 9	0.141	7	0.060	5
Finite square prism, AR = 7	0.152	5	0.063	4
Finite square prism, AR = 5	0.149	10	0.062	4
Finite square prism, AR = 3	0.133	11	0.056	6

Figure 1b shows St_R and G as functions of α for both 2D and finite square prisms. Peak values of St_R and G at $\alpha = 13.5°$ and 15° for the 2D and finite prisms, respectively, correspond to the critical incidence angle associated with minimum C_D, maximum lift coefficient magnitude, maximum St, and greatest wake asymmetry [14]. At non-zero α (over the range $\alpha = 0°$– 45°) the average values of St_R and G are different than those obtained at $\alpha = 0°$, both numbers becoming slightly higher when the prism is no longer oriented at 0° (Table 1). This may be caused by asymmetry in the near wake of the prism, the distinct behaviours of the two separated shear layers, and the different wake flow patterns observed as α is varied [6]. Of the two universal numbers, the Griffin number is better at collapsing the 2D and finite prism data to common values that are sensibly independent of α. Lower values of G are again obtained for the finite prism of AR = 3, which is below the critical AR (Table 1).

4 Conclusions

This study suggests that the universal wake number concept, introduced by Roshko [15] and extended by Griffin [4] and others, may be applicable to the flow around surface-mounted finite-height cylinders and square prisms, particularly if the body's

aspect ratio is greater than the critical aspect ratio, at least within the Reynolds number range of $10^4 < Re < 10^5$. Of the two universal wake numbers considered here, the Griffin number (G) was more successful in collapsing finite-height bluff body data compared to Roshko's universal Strouhal number (St_R); this result is consistent with the findings of other studies (e.g., [16]. Differences in the values of St_R and G between the 2D and finite-height bodies may be attributed to different physical influences on vortex shedding.

References

1. Adachi T (1997) Effects of surface roughness on the universal Strouhal number over the wide Reynolds number range. J Wind Eng Ind Aerod 69–71:399–412
2. Bearman PW, Obasaju ED (1982) An experimental study of pressure fluctuations on fixed and oscillating square-section cylinders. J Fluid Mech 119:297–321
3. Bearman PW, Trueman DM (1972) An investigation of the flow around rectangular cylinders. Aero Quart 23:229–237
4. Griffin OM (1981) Universal similarity in the wakes of stationary and vibrating bluff structures. J Fluid Eng-T ASME 103:52–58
5. Luo SC, Yazdani MG, Chew YT, Lee TS (1994) Effects of incidence and afterbody shape on flow past bluff cylinders. J Wind Eng Ind Aerod 53:375–399
6. McClean JF, Sumner D (2014) An experimental investigation of aspect ratio and incidence angle effects for the flow around surface-mounted finite-height square prisms. J Fluid Eng-T ASME 136:081206
7. Minguez M, Brun C, Pasquetti R, Serre E (2011) Experimental and high-order LES analysis of the flow in near-wall region of a square cylinder. Int J Heat Fluid Fl 32:558–566
8. Nakaguchi H, Hashimoto K, Muto S (1968) An experimental study on aerodynamic drag of rectangular cylinders. J Japan Soc Aero Space Sci 16:1–5
9. Nakamura Y (1996) Vortex shedding from bluff bodies and a universal Strouhal number. J Fluid Struct 10:159–171
10. Noda H, Nakayama A (2003) Free-stream turbulence effects on the instantaneous pressure and forces on cylinders of rectangular cross section. Exp Fluids 34:332–344
11. Norberg C (1993) Flow around rectangular cylinders: pressure forces and wake frequencies. J Wind Eng Ind Aerod 49:187–196
12. Norberg C (1987) Reynolds number and freestream turbulence effects on the flow and fluid forces for a circular cylinder in cross flow. PhD thesis, Chalmers University of Technology
13. Obasaju ED (1983) An investigation of the effects of incidence on the flow around a square section cylinder. Aero Quart 34:243–259
14. Ogunremi A, Sumner D (2015) On the effects of incidence angle on the mean wake of a surface-mounted finite-height square prism. In: 2015 Joint Fluids Engineering Conference on ASME/JSME/KSME, July 26–31, Seoul, Korea, Paper No. AJK Fluids 2015-15011
15. Roshko A (1955) On the wake and drag of bluff bodies. J Aero Sci 22:124–132
16. Sumner D (2004) Closely spaced circular cylinders in cross-flow and a universal wake number. J Fluid Eng-T ASME 126:245–249
17. Sumner D, Heseltine JL, Dansereau OJP (2004) Wake structure of a finite circular cylinder of small aspect ratio. Exp Fluids 37:720–730
18. Vickery BJ (1966) Fluctuating lift and drag on a long cylinder of square cross-section in a smooth and in a turbulent stream. J Fluid Mech 25:481–494

Numerical Investigation of the Post-stall Flow Patterns over a NACA 0021 Hydrofoil with Sinusoidal Leading Edge

Julien Cisonni and Andrew J. C. King

Abstract As passive flow-control devices disrupting flow separation, leading-edge protuberances can provide superior hydrodynamic performance to hydrofoils at high angles of attack. Most experimental and numerical investigations carried out for low Reynolds number conditions have related the relative improvements observed post-stall to "bi-periodic" flow structures, developing over tubercles pairs. In this study, a numerical approach is employed to show the emergence of higher-order patterns in the flow over a stalling NACA 0021 hydrofoil with sinusoidal leading edge. The effect of the number of sinusoidal tubercles defining the leading edge of the hydrofoil model on the prediction of "bi-periodic" or "tri-periodic" flow structures is particularly analyzed to interpret the uncertainty found on the resulting hydrodynamic performance.

1 Introduction

Initially inspired from the pectoral flipper of the humpback whale [4], hydrofoil designs including leading-edge protuberances have been investigated for their potential benefits in terms of hydrodynamic performance and flow control, particularly for low Reynolds number conditions [2, 5]. In general, most experimental and numerical studies have shown that scalloped leading edges allow mitigating the drop in lift generated on an hydrofoil occurring at high angles of attack with an unmodified leading edge. This relative performance improvement has been linked to complex flow patterns generated by the tubercles that disrupt flow separation on the suction surface of the hydrofoil. In particular, "bi-periodic" flow structures developing over tubercles pairs at high angles of attack have been observed both experimentally [3], with high aspect-ratio airfoils spanning over the entire width of the wind-tunnel test section, and numerically [1, 2], with symmetric or cyclic boundary conditions used to dis-

J. Cisonni (✉) · A. J. C. King
Fluid Dynamics Research Group, Department of Mechanical Engineering,
Curtin University, Perth, WA 6845, Australia
e-mail: julien.cisonni@curtin.edu.au

Y. Zhou et al. (eds.), *Fluid-Structure-Sound Interactions and Control*, Lecture Notes in Mechanical Engineering,
https://doi.org/10.1007/978-981-10-7542-1_5

count the effects of tip vortices on the flow properties. Further numerical analyses have indicated that the lift curves predicted for scalloped leading edges were fluctuating over the post-stall range of angles of attack [1]. This numerical study aims to demonstrate that this uncertainty on the lift predictions can be linked to higher-order flow patterns that can emerge post-stall. It focuses on the influence of the number of sinusoidal leading-edge tubercles included in the model on the predictions of "bi-periodic" or "tri-periodic" flow structures, and of the associated hydrodynamic performance.

2 Methodology

Simulations of the flow over NACA 0021 hydrofoil models with unmodified leading edge and with sinusoidal leading edge of peak-to-peak amplitude of 10% of chord length and wavelength of 50% of chord length (see Fig. 1) were carried out for a Reynolds number of 120,000. The computations were performed using OpenFOAM 2.4 with a finite-volume discretization of the steady RANS equations. Spalart–Allmaras turbulence model was used to solve the problem in non-dimensional form with the SIMPLE algorithm. The flow domain was discretized with a hexahedral structured C-mesh refined near the hydrofoil to obtain typical maximum and average y^+ values of about 0.68 and 0.25, respectively. The resulting number of cells was 3.25 millions per tubercle included in the model. A no-slip boundary condition was applied on the hydrofoil surface, and standard velocity inlet and pressure outlet boundary conditions were specified on the freestream outer boundaries. A symmetry boundary condition was used on both ends of the hydrofoils along the spanwise direction to discount the tip vortices effects on the flow properties. Simulations were performed for hydrofoils with 0.5, 1, 1.5, 2, 3, 4, 6 and 8 trough-to-trough and crest-to-crest sinusoidal leading-edge tubercles, and unmodified hydrofoils of corresponding spans to evaluate the lift and drag coefficients at angles of attack between 0 and 25°.

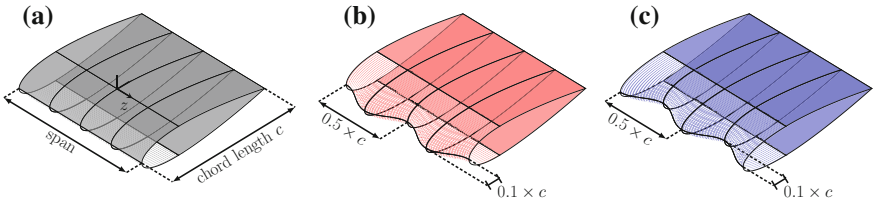

Fig. 1 Characteristics of the NACA 0021 hydrofoil models with **a** unmodified leading edge, **b** trough-to-trough sinusoidal leading edge and **c** crest-to-crest sinusoidal leading edge. The models shown include two tubercles

3 Results and Discussion

The lift and drag curves in Fig. 2a, b show that stall for the standard hydrofoil is characterized by abrupt and severe loss of lift and increase in drag between angles of attack of 13° and 14°. For the scalloped hydrofoil, stall is occurring for a lower angle attack but leads to a smaller drop in lift. Post-stall, the lift and drag coefficients corresponding to the hydrofoil with a sinusoidal leading edge do not increase linearly with the angle of attack. As shown in Fig. 2c, d, the predictions of lift and drag coefficients can vary significantly depending on the number of tubercles included in the model and on the location, crest or trough of the tubercles, where the symmetry boundary condition is applied. By contrast, the predicted lift and drag coefficients for the unmodified hydrofoil remains constant for increasing span-to-chord-length ratios because of the flow's pseudo two-dimensionality.

For the scalloped hydrofoil, including only 0.5, 1 or 1.5 tubercles in the model appears to be too restrictive to allow predictions of relevant three-dimensional flow structures. With two or more tubercles, the location of the symmetry boundary condition has a significant impact on the periodicity of the flow structures predicted. Thus, for four trough-to-trough tubercles included in the model, a flow structure developing over tubercles pairs and being repeated along the span can be distinctly predicted, as

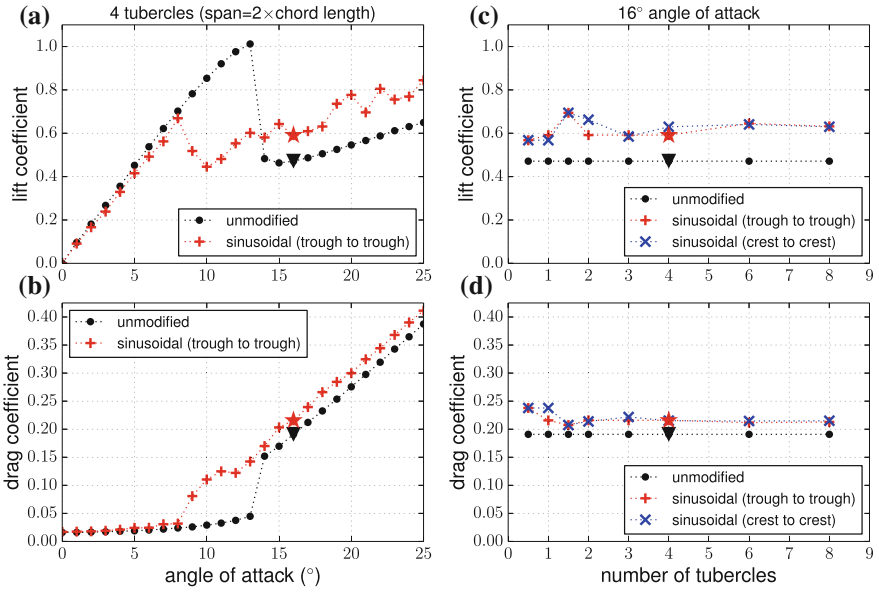

Fig. 2 Predictions for NACA 0021 hydrofoil at Reynolds number 120,000: **a** Lift coefficient and **b** drag coefficient as a function of angle of attack for four tubercles included in the model, and **c** lift coefficient and **d** drag coefficient at 16° angle of attack as a function of the number of tubercles included in the model. ▼ and ★ indicate data points found in both left and right graphs

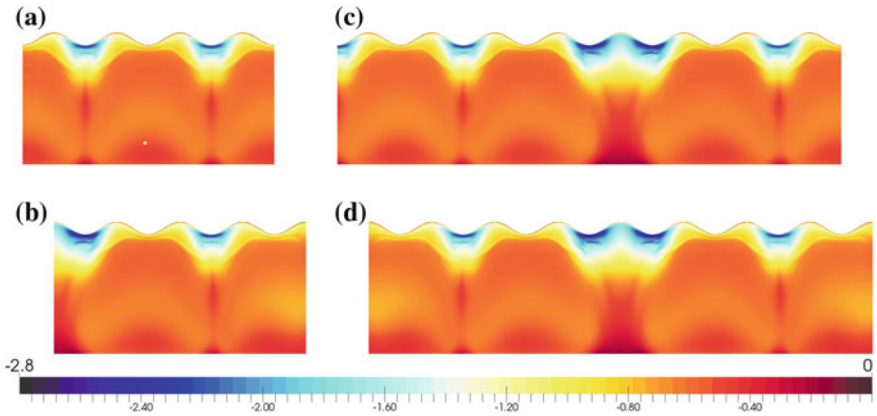

Fig. 3 Coefficient of pressure on the suction surface of the NACA 0021 hydrofoil models with sinusoidal leading edge of peak-to-peak amplitude of 10% of chord length and wavelength of 50% of chord length (Reynolds number 120,000 and 16° angle of attack): simulations carried out with **a** four trough-to-trough tubercles, **b** four crest-to-crest tubercles, **c** eight trough-to-trough tubercles and **d** eight crest-to-crest tubercles

indicated by the pressure-coefficient contours in Fig. 3a. This predicted "bi-periodic" flow pattern is in agreement with previous experimental observations [3] and CFD simulations [1, 2]. In Fig. 3b however, the predicted flow structure appears to differ on one of the two tubercles pairs for four crest-to-crest tubercles included in the model, suggesting that higher-order flow patterns might emerge. Indeed, for eight tubercles included in the model, the simulations allow prediction of a flow structure developing over three tubercles pairs and being repeated symmetrically along the span, as shown in Fig. 3c, d. As the number of tubercles increases, the effect of the imposed symmetry location, crest or trough of the tubercles, is diminished since the increased spanwise width of the flow domain provides the capacity to predict systematically "tri-periodic" flow structures.

Consequently, the estimated lift coefficient converges to a unique value when six or more tubercles are included in the model, as shown in Fig. 2c, d. The patterns generated by the leading-edge tubercles are associated to more complex flow separation and recirculation on the suction surface of the hydrofoil, particularly at high angles of attack. For instance, in the "tri-periodic" structure, the friction lines shown in Fig. 4c, d suggest that the fluid flowing over one of the crests remains attached to the surface of the hydrofoil almost down to the trailing edge. On the other hand, for the stalling unmodified hydrofoil, flow separation occurs at the leading edge, uniformly along the span. Therefore, the standard hydrofoil remains substantially more efficient pre-stall for moderate angles of attack while the tubercles provide superior performance at high angles of attack.

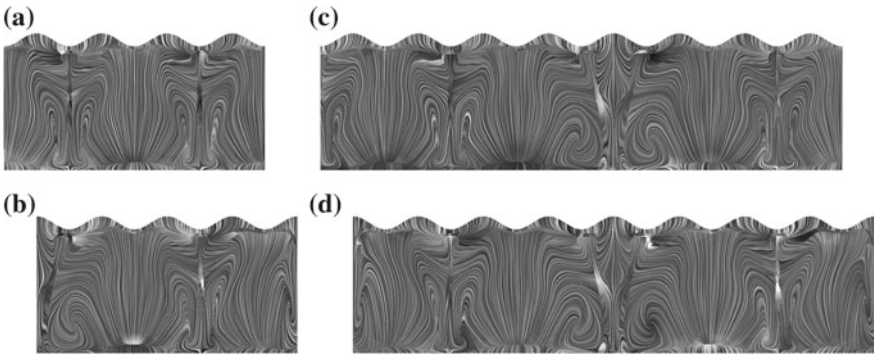

Fig. 4 Friction lines on the suction surface for the cases shown in Fig. 3

4 Conclusions

The flow over a NACA 0021 hydrofoil with leading-edge protuberances was numerically simulated to investigate the influence of the number of sinusoidal leading-edge tubercles included in the hydrofoil model on the lift and drag coefficients. At post-stall angles of attack, characteristic "bi-periodic" flow patterns cannot be systematically predicted when less than six tubercles are included. In this case, the location, crest or trough of the tubercles, of the symmetry boundary condition can affect the type of flow pattern developing along the span, leading to a significant uncertainty on the lift and drag values. With more than six sinusoidal protuberances, the symmetry condition effect is mitigated so that tri-periodic flow structures and more consistent hydrodynamic performance can be predicted.

Acknowledgements This work was supported by resources provided by The Pawsey Supercomputing Centre with funding from the Australian Government and the Government of Western Australia.

References

1. Cai C, Zuo Z, Liu S, Wu Y (2015) Numerical investigations of hydrodynamic performance of hydrofoils with leading-edge protuberances. Adv Mech Eng 7:1–11
2. Câmara JFD and Sousa MM (2013) Numerical study on the use of a sinusoidal leading edge for passive stall control at low Reynolds number. In: 51st AIAA aerospace sciences meeting
3. Custodio D (2007) The effect of humpback whale-like leading edge protuberances on hydrofoil performance. MSc thesis, Department of Mechanical Engineering, Worcester Polytechnic Institute, MA
4. Fish FE, Weber PW, Murray MM, Howle LE (2011) The tubercles on humpback whales' flippers: application of bio-inspired technology. Integr Comp Biol 51:203–213
5. Hansen KL, Kelso RM, Dally BB (2011) Performance variations of leading-edge tubercles for distinct airfoil profiles. AIAA J 49:185–194

On the Thresholds of Vortex Identification Methods

Yiqian Wang and Song Fu

Abstract Several vortex identification methods along with a newly proposed Ω method are examined in the Burgers vortex and the Sullivan vortex. Of particular interest is the physical meaning of the parameter, especially the thresholds. While all the methods are capable of capturing precise vortex boundaries in these two analytical vortices, only the parameter Ω seems to have a clear physical meaning, i.e. to what extent the local fluid particles tend to rotate like a rigid-body. Therefore, the parameter Ω might be helpful and informative when utilized to investigate the interaction of vortical structures.

Keywords Threshold · Vortex identification · Ω method

1 Introduction

The ambiguity introduced by choosing a threshold when employing vortex identification methods like Q, λ_2, Δ and λ_{ci} [2, 8] corrupts the objectivity of vortex dynamics study. For example, Smith et al. [6] hold the idea that a myriad of hairpin type vortices dominate wall adjacent region of near-wall turbulence and low-speed streaks are generated by the passage of hairpin vortices. This hierarchy of hairpin vortices and vortical packets are also believed to play a significant role in fully-developed turbulence [1] and during transition [4, 7]. However, other researchers like Schlatter et al. [5] denies the dominance of hairpin vortices in fully developed turbulent boundary layers. This disagreement might result from the difference of chosen thresholds utilized by different researchers. Thus, to identify the vortical structures without an ambiguous threshold is of great importance in the study of turbulence generation and sustenance mechanism.

Recently, a new Ω vortex identification method proposed by Liu et al. [3] is claimed to be able to capture vortical structures with a uniform threshold in

Y. Wang (✉) · S. Fu
School of Aerospace Engineering, Tsinghua University, Beijing 100084, China
e-mail: yiqianw@mail.tsinghua.edu.cn

Y. Zhou et al. (eds.), *Fluid-Structure-Sound Interactions and Control*, Lecture Notes in Mechanical Engineering,
https://doi.org/10.1007/978-981-10-7542-1_6

various flows. The parameter Ω is expected to be 1 in regions with rigid-body rotation and 0 in uniform flows. Along with other criteria mentioned above, these vortex identification methods are applied to several exact vortex solutions and analysis on the thresholds is given.

2 The Burgers Vortex

In a Burgers vortex, the velocity components written in cylindrical coordinates is

$$\begin{aligned} V_r &= -ar \\ V_\theta &= \frac{\Gamma_0}{2\pi r}[1 - e^{-\frac{ar^2}{2\nu}}] \\ V_z &= 2az \end{aligned} \tag{1}$$

where Γ_0 is the circulation, a the axisymmetric strain rate, and ν the kinematic viscosity. Apply the vortex identification methods to the Burgers vortex, we get

$$\mathrm{Q} = a^2(\mathrm{Re}^2\eta(\tilde{r}) - 3) \tag{2}$$

$$\Delta = \frac{a^6\mathrm{Re}^2\eta(\tilde{r})}{27}[9 + \mathrm{Re}^2\eta(\tilde{r})] \tag{3}$$

$$\lambda_2 = a^2(1 - \mathrm{Re}^2\eta(\tilde{r})) \tag{4}$$

$$\Omega = \frac{0.5}{1 - 2\mathrm{Q}/(a\mathrm{Re}e^{-\tilde{r}^2/2})^2} \tag{5}$$

where $\mathrm{Re} = \Gamma_0/2\pi\nu$,$\tilde{r} = r\sqrt{a/\nu}$, and the auxiliary function $\eta(\tilde{r})$ is defined as

$$\eta(\tilde{r}) = \frac{1}{\tilde{r}^4}((1 + \tilde{r}^2)e^{-\tilde{r}^2/2} - 1)(1 - e^{-\tilde{r}^2/2})$$

Apply the criteria to a Burgers vortex with $a = 1s^{-1}$, $\nu = 0.02m^2/s$ and $\Gamma_0 = 5m^2/s$ (thus Re = 39.79), and the criterion values distribution along radial direction is shown in Fig. 1, and the identified locations of vortex boundaries by these criteria are listed in Table 1.

The red dashed lines in Fig. 1 indicate the thresholds of corresponding methods based on its original ideas. However, thresholds with magnitude much larger than zero (like 1000 or 10000) are used in practical applications. On the other hand, the Ω method is able to use a uniform threshold that a bit larger than 0.5 (like 0.52) to identify vortices in various applications [3].

As expected, the parameter Ω equals 1 on the center of the Burgers vortex where rigid-body rotation happens, and approaches 0 as r becomes larger from Fig. 1. The variation of Ω is smooth and logical. Thus, for a Burgers vortex the parameter Ω can

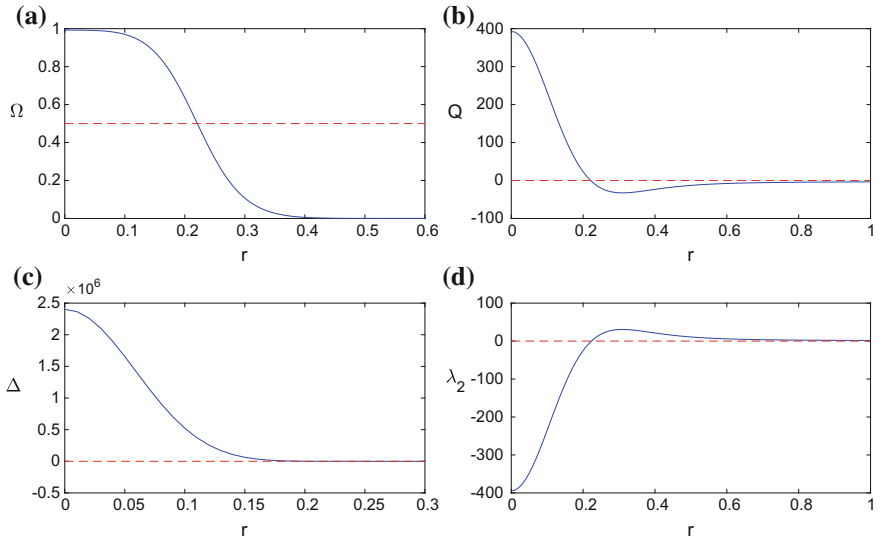

Fig. 1 Vortex criteria test by a Burgers vortex

Table 1 Calculated radius of the Burgers vortex by different criteria

	$r(V_\theta max)$	Ω	Q	Δ	λ_2
r_0	0.2241	0.2208	0.2208	0.2358	0.2230

be a local measure that to what extent the fluid motion tend to be rigid-body rotation. However, the ranges of parameters in other methods are not normalized. Although a larger parameter represents stronger swirling strength, the absolute physical meaning of the parameters is unclear. In addition, Q, Δ and λ_2 tend to be zero as r becomes larger while the the thresholds based on the original ideas of these criteria are zero. This might cause problems when the Burgers vortex domain of interest is too large. The identified boundary radii are given in Table 1. $r(V_\theta max)$ is the radius where the maximum circumferential velocity locates. And the radii of the Burgers vortex identified by Ω and Q methods are identical which results from the clear relationship between the two parameters expressed by Eq. 5. The radii predicted by Δ and λ_2 methods are a little larger, but also smaller than $r(V_\theta max)$. One particular problem with the Δ method is that the gradient at its threshold is near zero, which will cause the iso-surface becomes rough in visualization softwares.

3 The Sullivan Vortex

The Sullivan vortex is a two-celled vortex aimed to describe the flow in an intense tornado with a central downdraft. Its mathematical form is

$$\begin{aligned} V_r &= -ar + \frac{6\nu}{r}\left[1 - \exp\left(-\frac{ar^2}{2\nu}\right)\right] \\ V_\theta &= \frac{\Gamma_0}{2\pi r}\frac{H(ar^2/2\nu)}{H(\infty)} \\ V_z &= 2az\left[1 - 3\exp\left(-\frac{ar^2}{2\nu}\right)\right] \end{aligned} \tag{6}$$

where $H(\eta) = \int_0^\eta \exp\left(-s + 3\int_0^s \frac{1-e^{-\tau}}{\tau} d\tau\right) ds$ and thus $H(\infty) = 37.905$. Apply the criteria to a Sullivan vortex with $a = 1\,\mathrm{s}^{-1}$, $\nu = 0.02\,\mathrm{m}^2/\mathrm{s}$ and $\Gamma_0 = 5\,\mathrm{m}^2/\mathrm{s}$, the parameters of the methods along radial direction r are shown in Fig. 2 and the radii of identified inner and outer vortex boundaries are shown in Table 2.

Despite the difference in the radii as shown in Table 2, the methods are all capable of identifying the inner cell and outer cell vortex. The physical meaning of parameter Q, Δ and λ_2 is still unclear, especially for λ_2 method that the three eigenvalues represented by black dotted line (λ_1), blue line (λ_2) and green starred line (λ_3) in Fig. 2. It can be seen that the first and second eigenvalues connect at two locations,

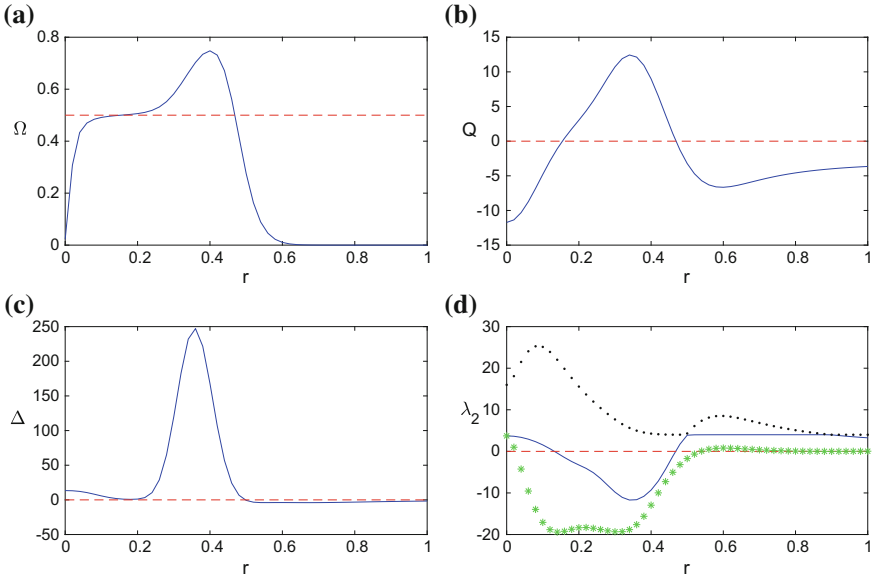

Fig. 2 Vortex criteria test by a Sullivan vortex

Table 2 Calculated radius of the Sullivan vortex by different criteria

	Ω	Q	Δ	λ_2
r_{0in}	0.1542	0.1542	0.1807	0.1323
r_{0out}	0.4689	0.4689	0.4969	0.4678

which means the eigenvalues' magnitude alternates. Thus the physical meaning of λ_2 is unclear. On the other hand, The parameter Ω still ranges from 0 to 1. The maximum Ω in this Sullivan vortex is around 0.7477, which relates to the chosen a, ν and Γ_0. Therefore, for the Sullivan vortex the parameter Ω can still be a local measure of the level fluids rotate like rigid-body.

4 Conclusions

The Burgers vortex and Sullivan vortex are examined with vortex identification methods including Ω, Q, Δ and λ_2 methods. It is concluded for the Burgers vortex and the Sullivan vortex, the parameter Ω could be a indication of to what extent the local fluid particles tend to rotate like a rigid-body, while parameters in other methods could not. Therefore, the Ω parameter might be helpful and informative in investigating vortex interactions in wall-bounded transitional and turbulent flows.

Acknowledgements This work was supported by the National Natural Science Foundation of China (Grant No. 11702159) and Project Funded by China Post-doctoral Science Foundation (Grant No. 2017M610876).

References

1. Adrian RJ (2007) Hairpin vortex organization in wall turbulence. Phys Fluids 19(4):1601–1618
2. Jeong J, Hussain F (1995) On the identification of a vortex. J Fluid Mech 173:303–356
3. Liu C, Wang Y, Yang Y et al (2016) New omega vortex identification method. Sci China Phys Mech 59(8):1–9
4. Liu C, Yan Y, Lu P (2014) Physics of turbulence generation and sustenance in a boundary layer. Comput Fluids 102:353–384
5. Schlatter P, Li Q, Orlu R et al (2014) On the near-wall vortical structures at moderate Reynolds numbers. Eur J Mech B-Fluid 48:75–93
6. Smith CR, Walker J, Haaidari A et al (1991) On the dynamics of near-wall turbulence. Phil Trans R Soc A 336(1641):131–175
7. Wang Y, Al-dujaly H, Yan Y et al (2016) Physics of multiple level hairpin vortex structures in turbulence. Sci China Phys Mech 59(2):1–11
8. Zhou J, Adrian RJ (1999) Mechanisms for generating coherent packets of hairpin vortices in channel flow. J Fluid Mech 387:353–396

Flow Structures Around a Finite Wall-Mounted Cylinder Having an Inclined Hole

Hiroka Rinoshika and Akira Rinoshika

Abstract To study the effect of a hole on the wake structures of a low aspect ratio circular cylinder, an inclined hole going from the front face to the top end face is drilled inside cylinder having height H and diameter D of 70 mm (an aspect ratio $H/D = 1$). In order to compare the flow structures between the hole and no-hole cylinders, the PIV measurement of Reynolds number of 8,570 is carried out in a water tunnel. Furthermore, to evaluate the position effect of the hole, three kinds of the hole cylinders having different height of hole from the flat plate are used. It was found that the separation region of the hole cylinder on the top face is evident smaller than that of the standard cylinder. An area of a high negative u-component velocity was observed in a rear recirculation region by using the hole, indicated a strong separation flow. The Reynolds shear stresses were evidently suppressed by the blowing flow from the hole, but their distribution spread out.

Keywords Passive flow control · PIV · Vortex · Wake flow

1 Introduction

The wake flow behind a cylinder of low aspect ratio exhibits a complex three-dimensional flow structures, such as tip-vortices, a horse shoe vortex and arch-type vortex [1, 4] that is different from two-dimensional wake flow structures [2]. The fundamental researches concerning controlling vortex-induced vibration of short and surface-mounted cylinders are few in the literature. It has practical interest in various engineering applications, such as suppressing noise and drag to design automobile, structural vibrations, and increasing drag in heat exchangers and offshore structures. Recently, Rinoshika et al. [3] studied a passive control method for a short cylinder that has an inclined hole drilled from the top face to the rear

H. Rinoshika · A. Rinoshika (✉)
Department of Mechanical Systems Engineering, Yamagata University, 4-3-16 Jonan, Yonezawa-Shi, Yamagata 992-8510, Japan
e-mail: rinosika@yz.yamagata-u.ac.jp

Y. Zhou et al. (eds.), *Fluid-Structure-Sound Interactions and Control*, Lecture Notes in Mechanical Engineering,
https://doi.org/10.1007/978-981-10-7542-1_7

face. It is made to produce blowing and suction flows, and effectively leads to the reduction of the rear recirculation zone of cylinder.

To control the separation region of the top face and the rear vortices of cylinder, this study developed another passive flow control method, in which an inclined hole drilled from the front side face to the free-end face is applied to originate blowing flow on the free-end face for increasing drag in the offshore structures. Firstly, the controlling and non-controlling flows around a short circular cylinder placed on a flat plate are measured by PIV in a circulation water tunnel. Then the time-averaged streamlines and velocity components and Reynolds shear stresses are compared between the standard and hole cylinders.

2 Experimental Setup

Figure 1a shows a short standard circular cylinder model having diameter D and height H of 70 mm (with an aspect ratio $H/D = 1$), which is placed on a ground plane. A circular cylinder model with an inclined hole having a diameter of $d = 10$ mm, as shown in Fig. 1b, is proposed in order to control the wake flow of three-dimensional cylinder. The inclined hole, called the controlling hole (CH), is drilled from the front side face to the top face. To study the effect of the CH position, the central locations of the CH on the front side face are varied at $h = 20$, 35 and 50 mm and the central location of the CH on the top face is fixed at $L = 30$ mm. The experiment is carried out in a circulating water tunnel with a constant free stream velocity of $U = 0.16$ m/s, which corresponds to Reynolds

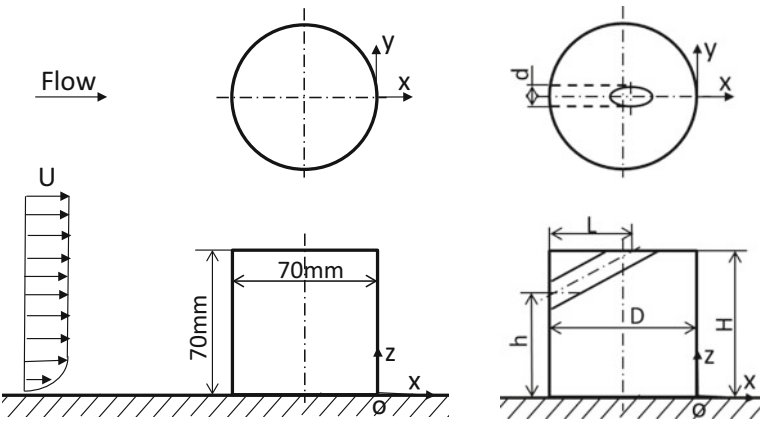

Fig. 1 Experimental models and setup

number Re ($\equiv UD/\nu$) = 8,570. The high-speed PIV measurements are adopted, and 6,000 digital images are analyzed by PIV software. PIV interrogation window size of 24 × 24 pixels with 50% overlap is used.

3 Results and Discussion

The contours of the normalized time-averaged streamwise (u-component) velocity and the mean streamlines around the standard cylinder (no-hole) and three kinds of CH cylinders in the (x, z)-plane, obtained from the measured instantaneous velocity, are shown in Fig. 2. In order to visualize the rear recirculation region, the negative contours of u-component velocity are only plotted, and white region represents positive u-component velocity.

Comparing the streamlines of the standard cylinder with CH cylinders, the small separation zone on the free-end face is reduced because of the flow blowing from the CH. With increasing height of the CH or decreasing the angle of the CH with the streamwise direction, the recirculation region on the free end surface becomes smaller. It is because the flow velocity blowing from the CH increases. However,

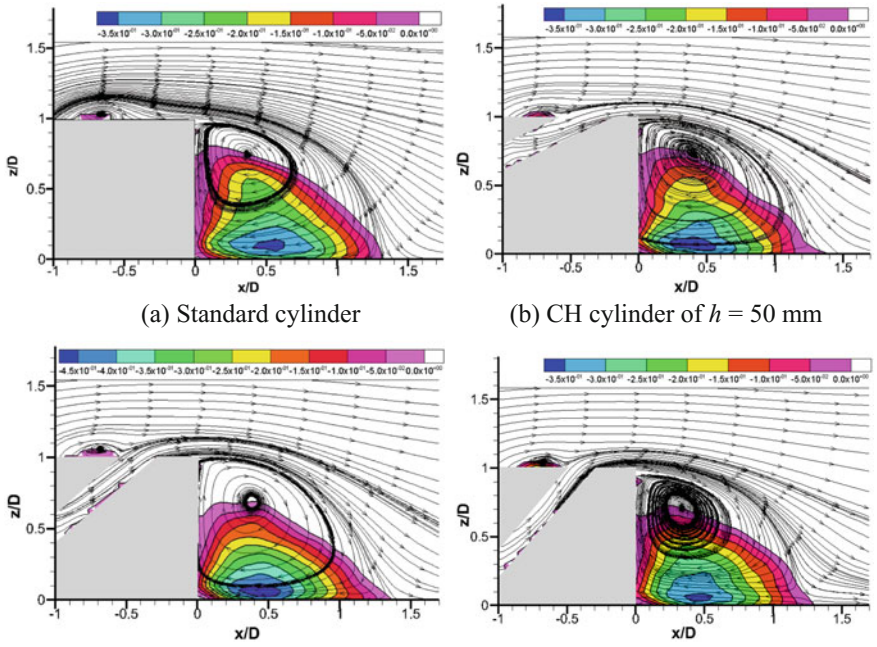

(a) Standard cylinder (b) CH cylinder of h = 50 mm

(c) CH cylinder of h = 35 mm (d) CH cylinder of h = 20 mm

Fig. 2 The time-averaged streamlines and contours of mean streamwise velocity $\bar{u}/U$ in the (x, z)-plane

a large vortex (separation zone) originated from side of the rear face and leading edge of the top face, is slightly increased in the case of the CH. As indicated in the negative contours of u-component velocity, no evident variation of the region of negative u-component velocity can be found, but stronger negative u-component velocity is observed in the case of CH cylinder of $h = 35$ mm. It implies that the blowing flow of the CH increases the strength of recirculation behind the cylinder and may lead to increase of drag, which have important applications in heat exchangers, offshore structures and reducing Tsunami energy.

Figure 3 shows the normalized Reynolds shear stress contours $\overline{u'w'}/U^2$ around the standard cylinder and CH cylinder with different height holes in the (x, z)-plane, obtained from the measured instantaneous velocity fields. Making comparison with the standard cylinder, although the Reynolds shear stress is decreased by using CH, the region of the Reynolds shear stress in the rear recirculation zone increases and distributes to the cylinder and flat plate.

From above results, it is clearly that the angle or position of the CH effects or changes the structures of wake flow, and controls the separation region and Reynolds stresses.

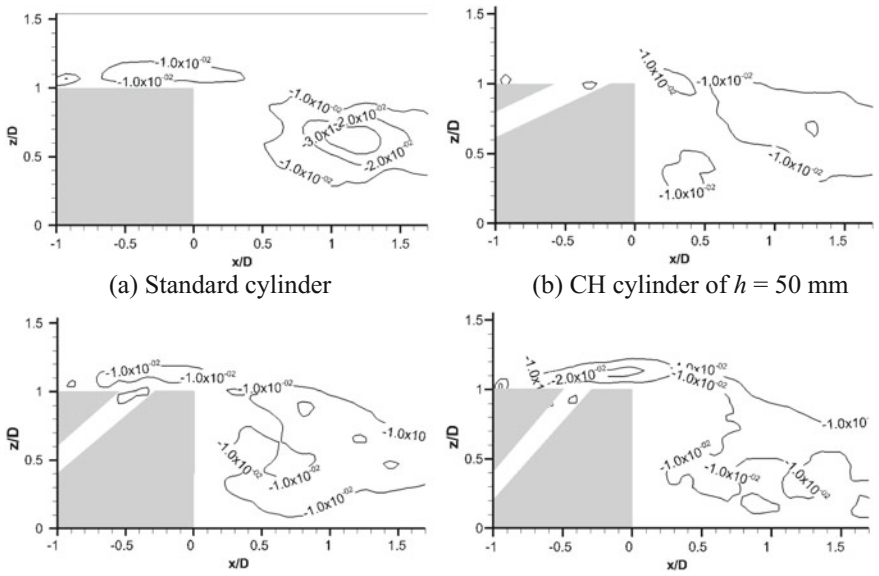

(a) Standard cylinder (b) CH cylinder of $h = 50$ mm

(c) CH cylinder of $h = 35$ mm (d) CH cylinder of $h = 20$ mm

Fig. 3 The contours of Reynolds shear stress in the (x, z)-plane

4 Conclusions

For studying the effect of an inclined hole on the wake flow structures of a circular cylinder having one aspect-ratio, the PIV measurements are performed. By making a comparision with the wake flow of the standard cylinder, the following conclusions can be obtained.

(1) The separation region of the top face is evident smaller than that of the standard cylinder by using the CH.
(2) An area of a high negative u-component velocity appears in a rear recirculation region in the case of CH cylinder of $h = 35$ mm, which indicates a strong separation flow.
(3) The Reynolds shear stresses are evidently reduced by the flow blowing from the CH, but the region of the high Reynolds shear stress in the rear recirculation zone increases.

Acknowledgements The authors wish to acknowledge support given to him by Grant-in-Aid for Scientific Research (C) (no.16K06067) from the Japanese Society for the Promotion of Science.

References

1. Goncalves RT, Franzini GR, Rosetti GF, Meneghini JR, Fujarra ALC (2015) Flow around circular cylinders with very low aspect ratio. J Fluids Struct 54:122–141
2. Rinoshika A, Zhou Y (2005) Orthogonal wavelet multi-resolution analysis of a turbulent cylinder wake. J Fluid Mech 524:229–248
3. Rinoshika H, Rinoshika A, Fujimoto S (2017) Passive control on flow structure around a wall-mounted low aspect ratio circular cylinder by using an inclined hole. Bull JSME J Fluid Sci Technol 12(1):1–13
4. Sumner D (2013) Flow above the free end of a surface-mounted finite-height circular cylinder. A review. J Fluids Struct 43:41–63

Effects of Reduced Frequency on the Behaviors of Burst Point Around a Pitching Double Delta Wing

Jian Liu, Haisheng Sun, Zhitao Liu and Zhixiang Xiao

Abstract The dynamic behavior of burst point (BP) around delta wing (DW) during oscillation has been a hot topic for its close relationship with the stability and control of an aircraft. Delayed detached eddy simulation (DDES) combined with rigid moving mesh techniques was implemented to investigate the dynamic response of the BP around an 80°/65° double delta wing (DDW) during sinusoidal pitching motion at critical angle of attack (AOA). The effects of reduced frequency (RF) on the performance of BP were discussed in detail. The movement of BP is locked in the frequency of pitching motion with a large phase lag. The time-averaged location, oscillation amplitude and phase lag are significantly determined by RF. The time-averaged location reaches its most downstream at RF of 0.2. When the RF is near 0.2, the Root-mean-Square (rms) of displacement of BP is much larger. The phase lag increases linearly with the growth of RF.

Keywords DDES · Double-delta wing · Burst point · Reduced frequency Phase lag

1 Introduction

It is well known that the flow over DW is dominated by a pair of primary stream-wise vortices, which play an extremely significant role in generating considerably additional lift at high AOA. However, when the AOA increases to a certain value, vortex breakdown happens. Especially, when the DW is taking a pitching motion, the flow particularly the BP lags behind the AOA [4]. A few researchers put great enthusiasm into the dynamic behavior of BP [1, 3, 7].

J. Liu · Z. Xiao (✉)
School of Aerospace Engineering, Tsinghua University, Beijing, China
e-mail: xiaotigerzhx@tsinghua.edu.cn

H. Sun · Z. Liu
Low Speed Aerodynamics Institute, China Aerodynamics Research and Development Center, Mianyang, China

Y. Zhou et al. (eds.), *Fluid-Structure-Sound Interactions and Control*, Lecture Notes in Mechanical Engineering,
https://doi.org/10.1007/978-981-10-7542-1_8

Nevertheless, most of researches on dynamic response of BP mentioned above are based on experiments. Numerical investigations are much fewer. Consequently, a solver based on finite volume (FV) was developed to investigate the unsteady flows around a pitching DDW. Here, the focus was put on the dynamic behavior of BP during sinusoidal pitching motion and the effects of RF on the response of BP.

2 Numerical Methods and Our Code

The control equations are the integral URANS equations based on rigid moving mesh technique [5]. DDES [2] based on k-ω-SST model was applied to simulate the vortex breakdown flows. The detailed formulations and constants of DDES can be found in the literature by Spalart [8]. The inviscid flux is calculated by the S-TVD scheme with adaptive dissipation [9]. The adaptive function, ϕ, is calculated by the ratio of DDES length scale to that of the RANS:

$$\phi = \tanh\left(\frac{C_1}{1-C_2}\cdot\max(l_{DDES}/l_{RANS}-C_2,0)\right) \tag{1}$$

Detailed performance analysis can be found in related reference [5].

Our in-house code UNITs (***U***nsteady ***N***av***I***er-s***T***okes ***s***olver) [9] used here is a FV solver based on multi-block structured mesh. The viscid flux is dispersed by the 2nd order central difference scheme. Low-upper symmetric Gauss-Seidel (LU-SGS) method with Newton-like sub-iteration in pseudo time is taken as the time marching method to achieve 2nd order accuracy. Message-passing-interface (MPI) technique is applied to improve computational efficiency.

3 Case Description and Computation Sets

A double-delta wing (DDW) with 80° swept strake and 65° swept main wing during pitching motion was considered. The model and the mesh in the leeward side are shown in Fig. 1. The total number of cells is about 11 M and the grid scale in the leeward side is about 0.015 C, where C is the mean aerodynamic chord.

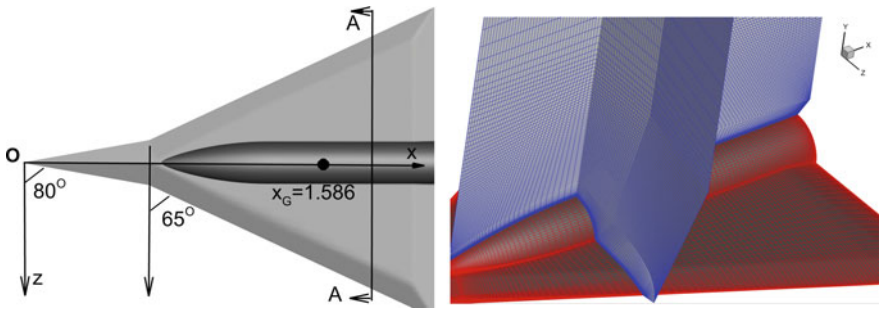

Fig. 1 80°/65° DDW model and distribution of mesh in the leeward side

The angle of attack of pitching motion is determined by $\alpha(t) = \alpha_o + \alpha_m sin(2kt)$, where $\alpha(t)$ is the instantaneous incidence; α_o is the balanced incidence and set to be 36°; α_m is the pitching amplitude and equal to 6°; and $k = \omega C/2U$ is the reduced frequency (RF) and ranges from 0.1 to 0.5. The free-stream velocity U is 40 m/s and the Reynolds number is 1.3×10^6. The normalized time step $\Delta t = \Delta t^* \times U / C = 0.008$. All the computations were run for eight cycles and the last six cycles were used for analyzing.

4 Results and Discussions

4.1 Dynamic Response of Unsteady Flows in One Pitching Period

In the computation range, the movements of BP are locked in the frequency of pitching motion, and have a time lag to the instantaneous AOA. Figure 2 presents the spectrum of $\bar{x}_b(t)$ and its stream-wise velocity u_b(t) when the RF is 0.4. The dominant frequency St is equal to 0.127, which is in accordance with the RF of pitching motion ($k_b = \pi St = 0.4$). The corresponding amplitude $x_{b,Am1}$ and root-mean-square $x_{b,rms}$ are about 0.256 C and 0.207 C, respectively. The stream-wise velocity of BP, $u_b = d\bar{x}_b/dt$ is calculated by a 2nd order central difference. The dominant frequency is also 0.127 and the corresponding amplitude is about $0.21U_\infty$.

Figure 3 demonstrates the dynamic response of BP in one pitching period. The BP is determined by the appearance of negative spanwise vorticity (as P1 denotes in Fig. 3c–f).

At t1, the AOA is at 30° and will increase. The BP locates at the equilibrium position and is going to move downstream with maximum speed (Fig. 3c). At t2,

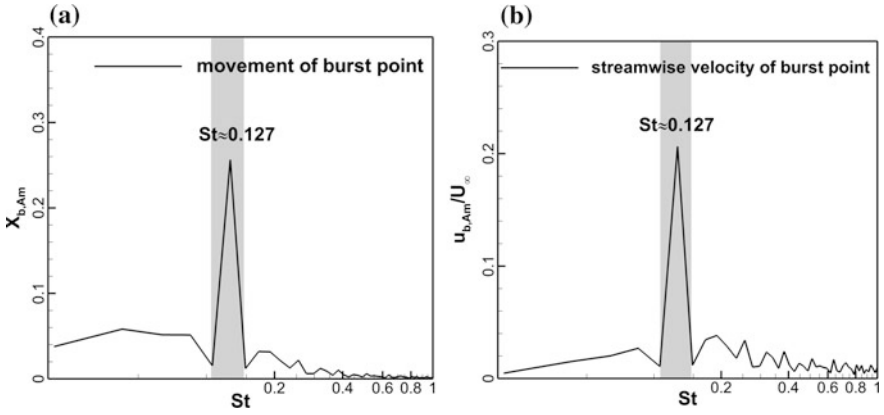

Fig. 2 Spectrum of stream-wise movement and velocity of BP

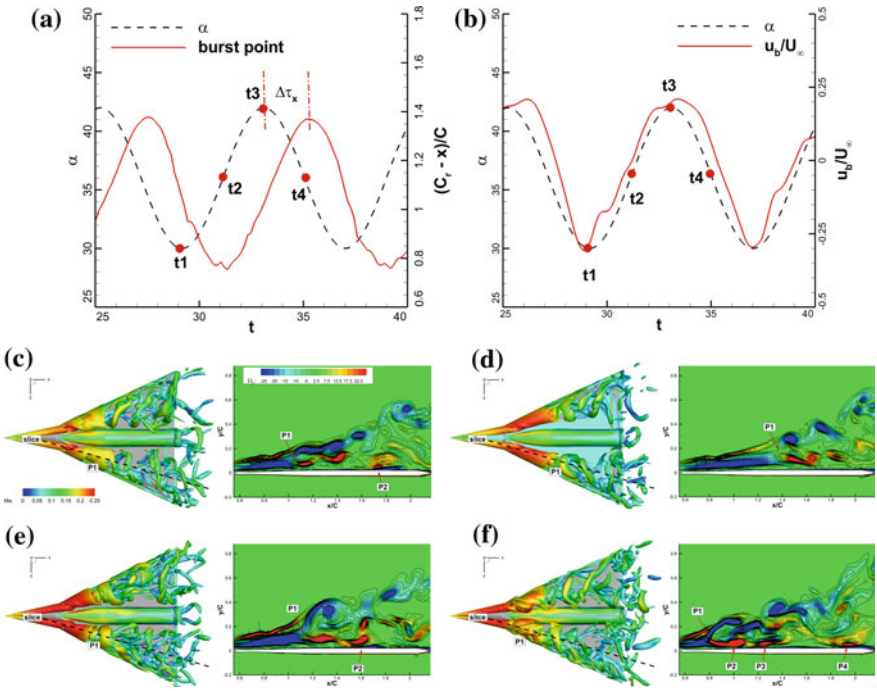

Fig. 3 Evolution of vortex breakdown flows in one period

the AOA arrives at 36°. The BP reaches the most downstream position and its stream-wise velocity almost becomes zero (Fig. 3d). At t3, the AOA increases to 42°. The BP returns to its equilibrium position, but it moves upstream with the maximum velocity (Fig. 3e). At t4, the AOA recovers to 36° and will decrease. The BP moves to the most upstream position. It can be observed that the streamwise movement of BP lags behind the AOA with phase lag of −90°. Thus, the behavior of both $\bar{x}_b(t)$ and u_b(t) can be simplified as sinusoidal functions:

$$\begin{aligned} \bar{x}_b(t) &\approx x_{b,aver} + x_{b,Am1}\sin(2kt + \Delta\phi_x) = x_{b,aver} + x_{b,Am1}\sin(2k(t - \Delta\tau_x U_\infty / C)) \\ u_b/\mathrm{U}_\infty &= \frac{d\bar{x}_b}{dt} \approx x_{b,Am1} \times 2\mathrm{k}\cos(2kt + \Delta\phi_x) \approx u_{b,Am1}\sin(2kt + \Delta\phi_u) \end{aligned} \tag{2}$$

4.2 *Effects of RF on Dynamic Behavior of BP*

Time-averaged location ($x_{b,\ aver}$), oscillation amplitude ($x_{b,\ Am1}$), RMS of fluctuation ($x_{b,rms}$) and phase lag($\Delta\phi$) at different RF ($0.1 \leq k \leq 0.5$) are plotted in Fig. 4. All the pitching motions can postpone the vortex breakdown. When RF is smaller than

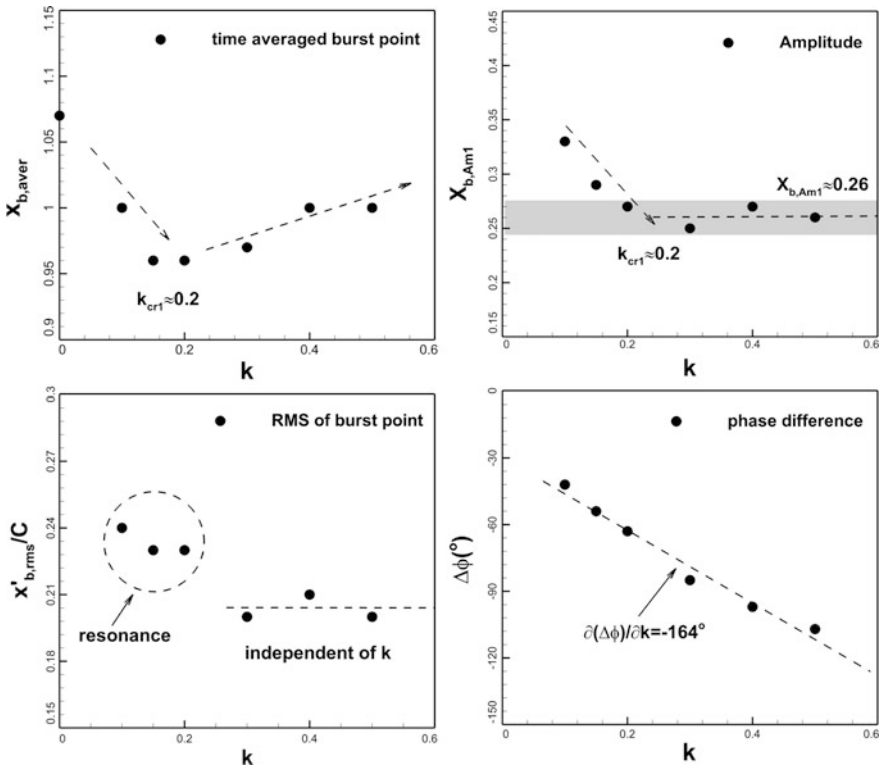

Fig. 4 Performance of dynamic response of burst point varying with RF

$k_{cr1} \approx 0.2$, $x_{b,\ aver}$ moves downstream as it increases. Then the BP reaches the most downstream position at k_{cr1}. When the RF increases continuously, $x_{b,\ aver}$ moves upstream. $x_{b,\ Am1}$ decreases with RF until it reaches k_{cr1}. When RF is larger than k_{cr1}, $x_{b,Am1}$ approaches to 0.26 and is independent of RF. When RF is near the natural frequency of burst point in the stationary case ($k \approx 0.2$, equivalent to $St = k/\pi \approx 0.06$, Liu 2016), resonance effect occurs, and the $x_{b,\ rms}$ reaches the largest value. But for RF larger than 0.3, $x_{b,rms}$ is approximately 0.2 and independent of it. Similar phenomenon was also observed by Menke and Gursul [6].

It has been found that the phase lag of burst point decreases linearly with RF within a certain range.

5 Conclusions

A solver based on the rigid moving mesh and DDES techniques has been implemented to simulate the unsteady flows around a pitching DDW. The focus are put on the dynamic behavior of BP and the effects of RF. It has been found that the

temporal evolution of BP is approximately a sinusoidal curve accompanied with a phase lag to the AOA. The phase lag decreases linearly with the growth of RF. When the RF is equal to the natural frequency of BP in the stationary state, the BP reaches the most downstream position and the r.m.s. of displacement is much larger.

Acknowledgements The investigations presented in this paper are supported by the National Natural Science Foundation of China (Grant No. 11372159) and the National Key Technologies R&D Program of China (Grant No. 2016YFA0401200).

References

1. Ericsson LE (1996) Pitch rate effects on delta wing vortex breakdown. J Aircraft 33(3): 639–642
2. Gritskevich MS et al (2012) Development of DDES and IDDES formulations for the k-ω shear stress transport model. Flow Turbul Combust 88:431–449
3. Gursul I (2000) Proposed mechanism for time lag of vortex breakdown location in unsteady flows. J Aircraft 37(4):733–736
4. Gursul I (2005) Review of unsteady vortex flows over slender delta wings. J Aircraft 42(2): 299–319
5. Liu J et al (2016) Vortex breakdown flows around a double-delta wing during pitching motion based on DDES. In 6th Symposium on Hybrid RANS-LES Methods, Sept. 26–28, Strasbourg, France
6. Menke M, Gursul I (1999) Nonlinear response of vortex breakdown over a pitching delta wing. J Aircraft 36(3):496–500
7. Rockwell D et al (1988) On unsteady flow structure from sweep eddies subjected to controlled motion. F. J. Seiler (ed.) Research Lab, USAF Academy, CO, TR-88–0004, pp 299–312
8. Spalart PR (2006) A new version of detached-eddy simulation, resistant to ambiguous grid densities. Theor Comput Fluid Dyn 20(3):181–195
9. Xiao ZX et al (2012) Numerical dissipation effects on massive separation around tandem cylinders. AIAA J 50(5):1119–1136

Drag Reduction of an Ahmed Body Using Combined Steady Blowings

K. Liu, B. F. Zhang and Y. Zhou

Abstract Active drag reduction of an Ahmed body with slant angle of 25° has been experimentally investigated at a Reynolds number *Re* of 1.67×10^5, based on the square root of the body cross-sectional area. A combination of steady blowing is deployed along the upper and two side edges of the rear window and the upper edge of the vertical base, resulting in a maximum reduction in drag by 25%, which is higher than those reported in the literature for the same body. Measurements are conducted using particle image velocimetry. A marked modification is identified on the separation region over the rear window, the upper and lower recirculation bubbles behind the vertical base, and the C-pillar vortices, which is connected to the high drag reduction.

Keywords Ahmed body · Drag reduction · Combined actuations
Steady blowing

1 Introduction

The lasting high fuel costs as well as environmental issues of global warming and air pollution highlight the necessity and urgency of searching for new technologies to reduce aerodynamic drag and hence fuel consumption in automotive industry. The generic Ahmed body [1] is perhaps the most widely used simplified car model

K. Liu
State Key Laboratory of Aerodynamics, China Aerodynamics Research and Development Center, Mianyang Sichuan, China

K. Liu · Y. Zhou (✉)
Institute for Turbulence-Noise-Vibration Interactions and Control, Shenzhen Graduate School, Harbin Institute of Technology, Shenzhen, China
e-mail: yuzhou@hit.edu.cn

B. F. Zhang
Department of Mechanical Engineering, The Hong Kong Polytechnic University, Hong Kong, China

Y. Zhou et al. (eds.), *Fluid-Structure-Sound Interactions and Control*, Lecture Notes in Mechanical Engineering,
https://doi.org/10.1007/978-981-10-7542-1_9

in the active drag reduction investigations of vehicles. The wake of an Ahmed model with a slanted surface (φ) of 25°, corresponding to the high drag regime, comprises a separation bubble on the rear window, a pair of longitudinal C-pillar vortices at the side edges of the slanted surface and a recirculation torus behind the vertical base. Controlling the interactions between the three types of coherent structures is the key of drag reduction techniques. Numerous studies have been performed on the active drag reduction of an Ahmed body ($\varphi = 25°$), though achieving a rather limited success. Most of the previous studies focused on controlling one of the three types of coherent structures in the wake, neglecting the other two and their interactions. This work aims to develop an effective active drag reduction technique for this body based on a combination of steady blowings, thus manipulating all three types of coherent structures and maximizing drag reduction. Extensive measurements are also conducted to understand flow physics behind control.

2 Experimental Details

Experiments were carried out in a closed circuit wind tunnel with a test section of 5.5 m long, 1.0 m high and 0.8 m wide. The flow non-uniformity is about 0.1% and the longitudinal turbulence intensity is about 0.3% for a free-stream velocity U_∞ = 15 m/s. The experimental setup is schematically shown in Fig. 1a. A flat plate with a semi-elliptical leading edge is installed horizontally, 0.1 m above the test section floor, as a raised floor to control the boundary layer thickness. The vehicle model is a ½-scaled Ahmed body [1], with a slant angle φ of 25°. The model is supported by four cylindrical struts of 15 mm in diameter. The gap between the model and the raised floor is 25 mm. The blockage ratio of the model frontal surface A to the test section above the raised floor was around 4.0%. Three steady blowing actuations are implemented over the rear end of the model for drag reduction (Fig. 1b). Actuation S1 is produced by one array of micro-jets along a line parallel to and

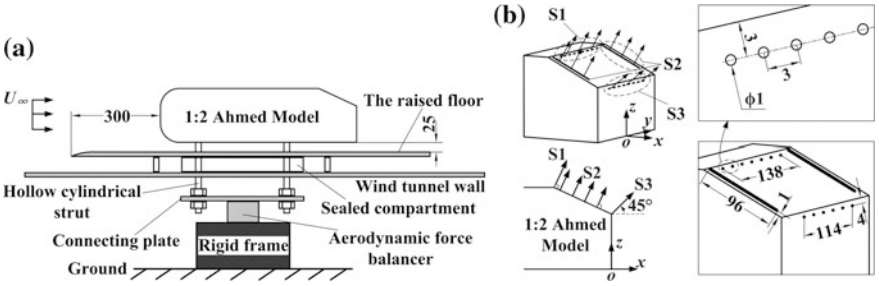

Fig. 1 Schematics of experimental setup. **a** Schematic of aerodynamic drag measurement setup. **b** Schematic description of steady actuations S1, S2 and S3 on the rear end. The length unit is mm

3 mm downstream of the upper edge of the rear window. Actuation S2 is generated through a pair of slots along the two side edges of the rear window. Both S1 and S2 are blowing normally to the slanted surface. Actuation S3 is generated by one array of micro-jets along a line parallel to and 4 mm below the upper edge of the base, and is blowing upwards at an angle of 45° with respect to the free-stream direction. The right-handed Cartesian coordinate system (*x, y, z*) is defined in Fig. 1b. In this paper, superscript asterisk '*' denotes normalization by $\sqrt{A}(= 0.167$ m). Experiments were carried out at $U_\infty = 15$ m/s, corresponding to $Re = 1.67 \times 10^5$. Mean aerodynamic loads were measured by a six-component force balance with an accuracy of 0.01 N. PIV measurements were performed in the *x*-*z* plane at $y^* = 0$ and the *y*-*z* plane at $x^* = -0.1$.

3 Results and Discussion

3.1 Drag Reduction

A combination of S1, S2 and S3 is deployed to control simultaneously the separation region and C-pillar vortices over the rear window and the recirculation bubbles behind the vertical base. In the combined actuations, the momentum coefficients $C_{\mu 1}$ of S1 and $C_{\mu 2}$ of S2 were fixed at 3×10^{-3} and 1.9×10^{-2}, respectively, at which a significant reduction in drag by 15.8% was obtained provided that S1 and S2 were simultaneously implemented. Figure 2 presents the dependence of drag coefficient variation ΔC_D on the momentum coefficient $C_{\mu 3}$ of S3. The drag gradually decreases with increasing $C_{\mu 3}$, reaching the maximum drag

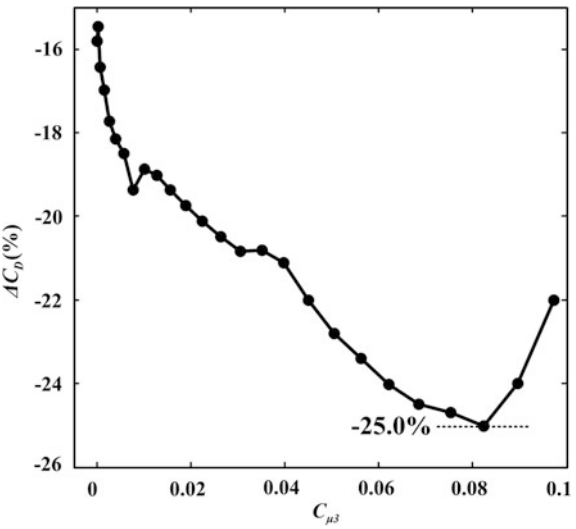

Fig. 2 Drag coefficient variation versus $C_{\mu 3}$ based on the optimal combination of S1 and S2

reduction of 25% at $C_{\mu 3} = 8.2 \times 10^{-2}$. The obtained maximum reduction in drag is higher than those reported in literature for the same Ahmed body. Above this critical momentum coefficient, the drag increases for higher $C_{\mu 3}$.

3.2 *Effects of the Combined Actuations on Flow Structure*

Figure 3 shows time-averaged sectional streamlines and the velocity magnitude in the symmetry plane ($y^* = 0$) with the combined actuations at $C_{\mu 1} = 3 \times 10^{-3}$, $C_{\mu 2} = 1.9 \times 10^{-2}$ and $C_{\mu 3} = 8.2 \times 10^{-2}$, as compared with the base case of the uncontrolled flow. The flow structures with control exhibit a number of changes from the time-averaged structures in the base flow. Firstly, in the absence of control, the flow separates at the upper edge of the rear window and then reattaches on the slanted surface, forming a small separation region, and the flow remains attached on the rear window downstream (Fig. 3a). When the actuation is switched on, the streamlines show a significantly increased separation region over the rear window, with its streamwise extent reaching $x^* = 0$ (Fig. 3b). Secondly, the recirculation region behind the base is enlarged longitudinally, with the saddle point S moving downstream from $x^* = 0.54$ to $x^* = 0.59$. Furthermore, the two foci of the streamlines behind the base, marked by "F1" and "F2", are shifted farther downstream, reaching $x^* = 0.4$. The length of the reverse flow region behind the base is increased by 39.2%. Since two recirculation bubbles are pushed far away from the vertical base, their effect on the wall pressure is reduced, leading to a pressure recovery on the vertical base.

The contours of time-averaged streamwise vorticity $\overline{\Omega}_x^*$ in the y-z plane of $x^* = -0.1$with and without active control are examined in Fig. 4 in order to understand the effect of the control on the longitudinal structures in the wake. In the base flow, there is one vorticity concentration at each side of the rear window, with its

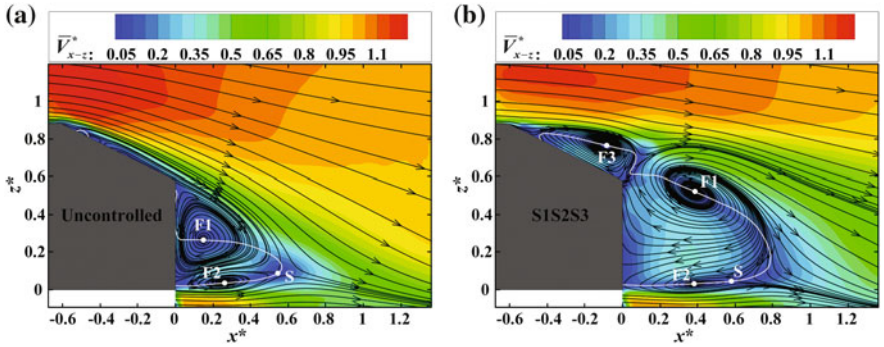

Fig. 3 PIV-measured mean streamlines and velocity magnitude for **a** uncontrolled and **b** controlled flows in the x-z plane $y^* = 0$. White line is the contour line for streamwise velocity $U = 0$ m/s

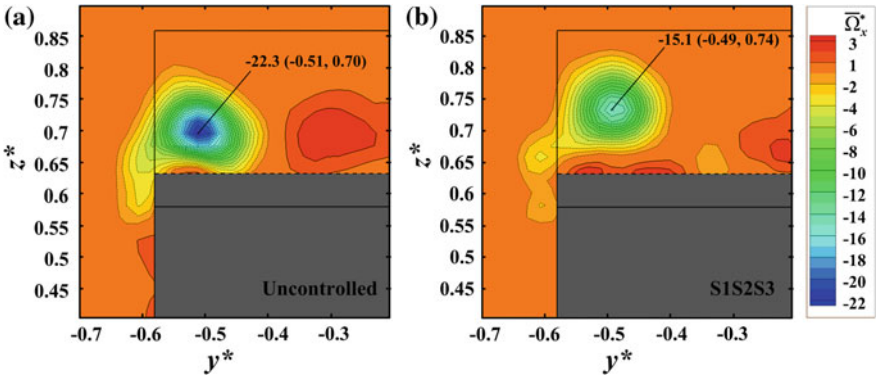

Fig. 4 PIV-measured mean vorticity contours for **a** uncontrolled and **b** controlled flows in the y-z plane $x^* = -0.1$

maximum magnitude reaching 22.3, which corresponds to the C-pillar vortices (Fig. 4a). When the control is applied, the maximum vorticity concentration is decreased to 15.1 (Fig. 4b). Meanwhile, the location of the maximum vorticity concentration is pushed away from the slant surface, from $z^* = 0.70$ to $z^* = 0.74$, as compared with its counterpart in the uncontrolled case. This result is consistent with Bruneau et al.'s [2] numerical study on drag reduction of an Ahmed body ($\varphi = 25°$). They found that the steady slot blowing at the two sides of the rear window was effective in breaking the C-pillar vortices through increasing the swirl of vortices and pushing them away to get diffused.

4 Conclusions

In this work, drag reduction of an Ahmed body with a slant angle of 25° has been experimentally investigated using combined steady blowing actuations, and a maximum drag reduction up to 25% has been achieved, higher than previous reports on the same body. With the control, the separation region over the rear window expands in both streamwise and transverse directions. Behind the vertical base, the recirculation region is longitudinally enlarged under control with two recirculation foci moving downstream away from the base. The C-pillar vortices are weakened dramatically and deflect away from the rear window, indicating a local pressure recovery on the rear window and a reduced vortex drag. To conclude, this control strategy has been demonstrated effective in drag reduction of a 25° Ahmed body by manipulating all the major coherent structures in the wake.

Acknowledgements YZ wishes to acknowledge support given to him from NSFC through grant 11632006 and from Scientific Research Fund of Shenzhen Government through grant JCYJ20140417172417119.

References

1. Ahmed SR, Ramm G, Faltin G (1984) Some salient features of the time-averaged ground vehicle wake. SAE Technical Paper No.: 840300, USA
2. Bruneau CH, Creusé E, Depeyras D, Gilliéron P, Mortazavi I (2011) Active procedures to control the flow past the Ahmed body with a 25° rear window. Int J Aerodyn 1:299–317

Control of the Aerodynamic Forces of a Cantilevered Square Cylinder with Free-End Suction

H. F. Wang, S. Peng and S. Q. Li

Abstract Steady slot suction is applied near the leading edge of the free end of a cantilevered square cylinder to investigate its effects on the aerodynamic forces. The slot suction significantly changes the flow separation on the free end and also the aerodynamic forces on the entire cylinder span. The best control result appears at the suction coefficient $Q = 1$ ($Q = U_s/U_\infty$, where U_s is the suction velocity at the slot, and U_∞ is the oncoming flow velocity), with the fluctuation drag and lift reduced by 17.8% and 45.5%, respectively. At $Q = 1$, the shear flow at the leading edge is weakened and reattaches on the cylinder free end, which results in stronger momentum transport between the free-end shear flow and the wake, thus suppressing the vortex shedding and aerodynamic forces efficiently.

Keywords Cantilevered square cylinder · Aerodynamic forces
Flow control

1 Introduction

The flow around a wall-mounted cantilevered cylinder is highly three dimensional and characterized by the interactions among spanwise vortices, tip vortices and base vortices [4]. Both the tip and base vortices induce downwash and upwash flow in the near wake, which attenuate the spanwise Karman vortex shedding [5]. A number of investigations suggest that the flow over the free end of a cantilevered cylinder and the flow around its both sides form a connected arch type vortex structure in the near wake [2, 3]. The two 'legs' of this arch type structure may be shed symmetrically or alternately into the wake. When alternating vortex shedding occurs, the lift on the cylinder fluctuates with large amplitude and bears obvious periodicity. On the other hand, when symmetrical vortex shedding occurs,

H. F. Wang (✉) · S. Peng · S. Q. Li
School of Civil Engineering, Central South University, Changsha, China
e-mail: wanghf@csu.edu.cn

Y. Zhou et al. (eds.), *Fluid-Structure-Sound Interactions and Control*, Lecture Notes in Mechanical Engineering,
https://doi.org/10.1007/978-981-10-7542-1_10

thefluctuation of lift is considerably suppressed and has no obvious periodicity. These two states occur randomly in the near wake [5].

To reduce the aerodynamic forces and also the flow induced vibration (FIV) of a 2D slander structures, a lot of methods have been investigated. Choi et al. [1] classified these control methods into three groups, i.e. passive, active open-loop, and active closed-loop controls. Many passive devices, such as helical wire, longitudinal groove, etc., and active open-loop controls, such as steady and time-periodic blowing/suction, etc., have been successfully applied to bluff body flow. Note that, for a 2D structure, the flow manipulation techniques are generally applied along its spanwise direction. For a cantilevered square cylinder, considering the spanwise flow is connected by the flow over the cylinder free end, it is interesting to know whether it is possible to reduce the aerodynamic forces via the flow control at the cylinder free end.

2 Experimental Details

A square cylinder with the width $d = 40$ mm and the aspect ratio $H/d = 5$ was mounted on the bottom wall of a wind tunnel. The test section of the wind tunnel was 450 mm wide, 450 mm height and 1200 mm long. The blockage ratio caused by the model was about 3.9%. The oncoming flow velocity (U_∞) was 12 m/s, corresponding to a Reynolds number based on U_∞ and d of 27,400. The thickness of the boundary layer on the wind tunnel wall was about 10 mm. That is, most of the cylinder span was immersed in the uniform oncoming flow.

A suction slot was set at the cylinder free end, 1 mm downstream from its leading edge, to control the shear flow over the free end and test its effects on the aerodynamic forces on the cantilevered cylinder. The width and length of the slot were 1 mm and 36 mm, respectively. The tested model and definition of the coordinate system are shown in Fig. 1. A steady suction was established using a vacuum pump. A volume flowmeter was used to monitor flow rate driven by the pump. Consequently, the averaged suction velocity U_s at the slot could be calculated based on the volume flow rate and the area of the slot. The suction velocity, which was documented using a hot wire, was quite uniform along the slot. The suction ratio Q was defined as $Q = U_s/U_\infty$, which ranged from 0 to 4 in the present experiments.

The pressure distribution was measured at different spanwise positions, i.e. at $z^* = 1$, 2, 3, 4 and 4.5. In the present paper, the superscript "*" indicates the normalization with U_∞ and/or d. At each z^*, there were 20 pressure taps distributed circumferentially on the model. The aerodynamic forces on the cantilevered cylinder could be evaluated from the interrogation of the pressure measurement results. The shear flow was measured with Cobra probe along z direction at different positions on the free end as marked by A1 ~ A7 in Fig. 1. Note that, A1 was located at the leading edge of the free end.

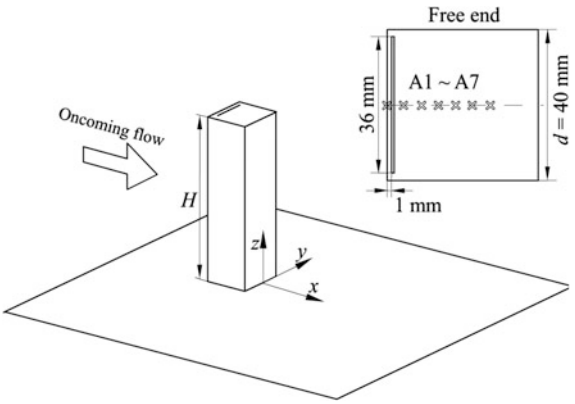

Fig. 1 Experimental setup

3 Results and Discussion

Figure 2 shows the dependence of the mean drag (C_d) and also the fluctuating drag and lift (C_d' and C_l') on Q. The steady slot suction near the leading edge of the free end has significant effects on the overall aerodynamic forces on the tested cylinder. Obviously, C_d, C_d and C_l' all reduce with the increase of Q from 0 to 1. The minimum of C_d, C_d'

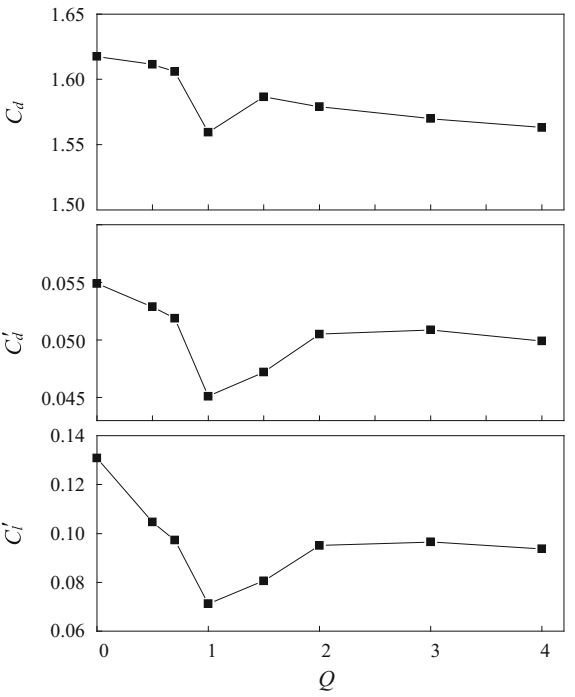

Fig. 2 The overall aerodynamic forces at different Q

and C' presents at $Q = 1$. With further increase of Q, these forces rise again and almost keep constant at $Q > 2$. Generally, C_d' and C' are more sensitive to Q, compared with C_d, which reduce by about 17.8 and 45.5% at $Q = 1$ relative to those at $Q = 0$. On the other hand, the maximum reduction of C_d at $Q = 1$ is only 3.6%.

The local aerodynamic forces (C_d, C_d and C_l) at different spanwise positions are shown in Fig. 3 for three typical suction ratios, i.e. $Q = 0$, 1 and 3. For the case without control, the maximum of C_d appears at $z^* = 4$, i.e. near the cylinder free end, and reduces with the bottom wall approached. With the application of slot suction, C_d reduces at all z^*, especially near the free end. The maximum reduction of C_d is about 5.4%, which occurs at $z^* = 4.5$ with $Q = 1$. At $Q = 3$, the C_d along the cylinder span almost overlaps with that at $Q = 1$. The effects of the slot suction on C_d and C_l are far more remarkable relative to C_d. The slot suction reduces C_d and C_l not only near the free end but also at the mid-span and even near the cylinder base. For example, the maximum reduction rates of C_d at $z^* = 1$, 2, 3, 4 and 4.5 are 16.4%, 21.3%, 25.7%, 24.2% and 24.5%, respectively. The corresponding maximum reduction rates of C_l at these spanwise locations are 34.0, 43.9, 51.5, 61.2, 57.6%. Generally, the reduction rates of both C_d' and C_l' are larger at larger z^*. Interestingly, the reduction rate is still quite remarkable at $z^* = 1$, which is far away from the cylinder free end. This observation suggests that the steady slot suction at the leading edge of the free end can significantly suppress the fluctuating forces over its entire span. The pressure fluctuation on the side faces and leeward face reduces remarkably with the application of the suction. The minimum fluctuation occurs at $Q = 1$, consistent with aerodynamic forces shown in Fig. 3. Interestingly, the St number of the flow does not change with Q (These results are not shown because of length limit.).

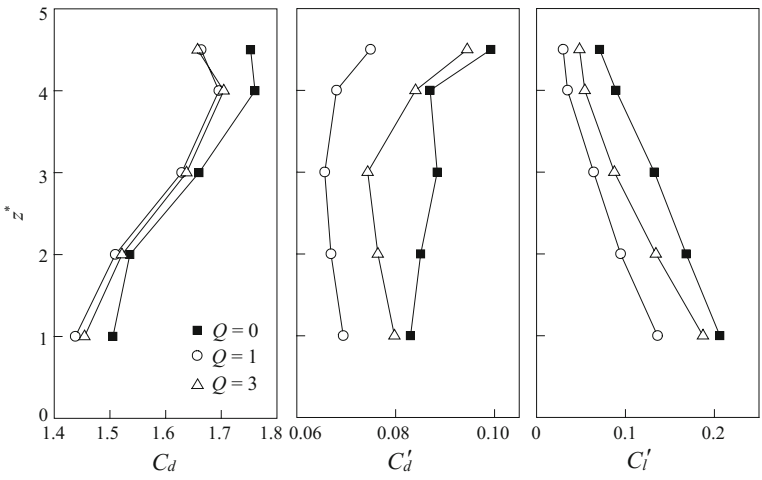

Fig. 3 The local aerodynamic forces at different z^*

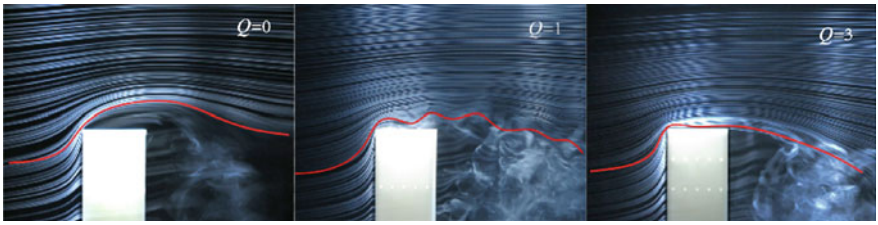

Fig. 4 Flow visualization of free-end shear flow

Figure 4 shows the flow visualization of the free-end shear flow at $Q = 0$, 1 and 3. For the case without control, the shear flow separates at the free-end leading edge and overshoots the cylinder. This shear flow forms the downwash flow at about $1d$ downstream from the cylinder and interacts with the spanwise shear flow in the near wake. For $Q = 1$, the shear flow separates at the leading edge of the free end and reattaches on it, as shown in Fig. 4. This shear flow becomes quite unstable, characterized by a wavy fluctuation as moving downstream. With further increase of Q to 3, the flow separation is completely suppressed, with the shear flow fully attaches on the cylinder free end. Moreover, the wavy motion at $Q = 1$ disappears, suggesting that the free-end shear flow becomes more stable at $Q = 3$.

Figure 5 presents the distribution of $\overline{U^*}$ and u^*_{rms} over the cylinder free end. The z^* in Fig. 5 indicates the spacing between each measurement point and the free end. Considering the measurement range of the Cobra probe is a 90° corn area, the data at the point where the mean flow direction exceeds this measurement region are rejected, as shonw in Fig. 5. For $Q = 1$, the flow separation is weakened. A reattachment occurs between A5 and A6, about 25 mm downstream of the leading edge. For $Q = 3$, the flow separation disappears completely. As shown in Fig. 5, the turbulence fluctuation over the free end is stronger in the case with $Q = 1$ relative to that with $Q = 3$, which may result stronger momentum transport

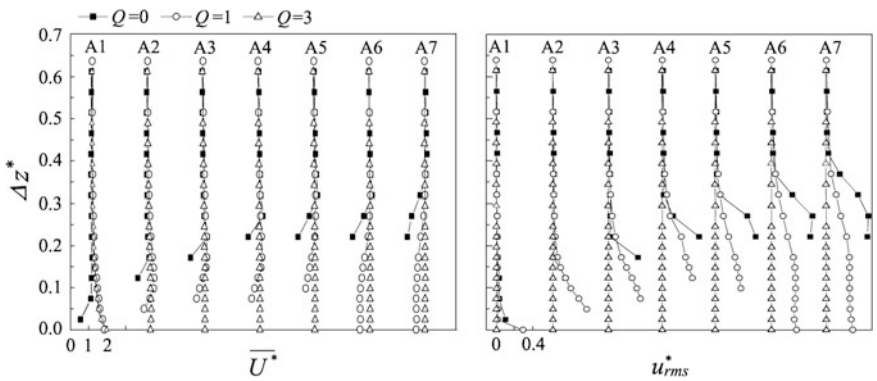

Fig. 5 Distribution of $\overline{U^*}$ and u^*_{rms} over the cylinder free end

between the free-end shear flow and the near wake for the former. The stronger momentum transport may suppress the spanwise vortex shedding more effectively, thus resulting in smaller aerodynamic forces for $Q = 1$.

4 Conclusions

The slot suction near the leading edge of the free end acts to accelerate the shear flow on it, and suppress flow separation over the free end. At $Q = 1$, the separated flow is weakened and reattaches on the free end; on the other hand, the flow fully attaches on the free end at $Q = 3$. The slot suction can suppress the aerodynamic forces not only near the free end, but also over the entire cylinder span. At the suction ratio $Q = 1$, the maximum reduction of these aerodynamic forces occurs, with C_d reduced by 3.6%, and $C_{d'}$ and $C_{l'}$ reduced by 17.8% and 45.5%, respectively.

Acknowledgements Financial support from the NSFC through Grants 11472312 is acknowledged.

References

1. Choi H, Jeon WP, Kim J (2008) Control of flow over a bluff body. Annu Rev Fluid Mech 40:113–139
2. Kawai H, Okuda Y, Ohashi M (2012) Near wake structure behind a 3D square prism with the aspect ratio of 2.7 in a shallow boundary layer flow. J Wind Eng Ind Aerody 30:196–202
3. Krajnovic S (2011) Flow around a tall finite cylinder explored by large eddy simulation. J Fluid Mech 676:294–317
4. Sumner D, Heseltine JL, Dansereau OJP (2004) Wake structure of a finite circular cylinder of small aspect ratio. Exp Fluids 37:720–730
5. Wang HF, Zhou Y (2009) The finite-length square cylinder near wake. J Fluid Mech 638:453–490

Jet Control Using the Coaxial Type DBD-PA by Burst Modulation

M. Akimoto, H. Matsumori and M. Kimura

Abstract In this study, a jet control using the coaxial type DBD plasma actuator (=DBD-PA). The coaxial type DBD-PA is an axisymmetric nozzle, and the jet is ejected from this nozzle. DBD-PA is driven by burst modulation control and the induced flow is intermittently generated. The coaxial type DBD-PA controls the jet by controlling vortex generation in the jet. We control the jet at Reynolds number Re = 10,000. As a result, the induced flow of the coaxial type DBD-PA synchronizes vortex generation of the jet in a specific burst modulation control frequency range. This phenomenon is the phenomenon of lock-in. Driving the coaxial type DBD-PA with burst modulation, it is possible to generate an axisymmetric vortex within frequency of burst modulation control in which the phenomenon of lock-in occurs. Consequently, the jet is controlled by the coaxial type DBD-PA within frequency of burst modulation control in which the phenomenon of lock-in occurs.

Keywords Jet · DBD-PA · Phenomenon of lock-in · Visualization

1 Introduction

Jet is one of the typical flow modes occurring in nature and industry [1]. Depending on the state of the jet flow at the nozzle exit, behavior such as vortex generation and coalescence changes greatly [2]. In this study, we control the jet flow ejected from nozzle by an induced flow of the coaxial type DBD-PA (DBD: Dielectric Barrier Discharge, PA: Plasma Actuator). The coaxial type DBD-PA is an axisymmetric nozzle, and the jet is ejected from this nozzle. When AC high voltage is applied to

M. Akimoto (✉) · M. Kimura
Department of Mechanical Engineering, College of Science and Technology, Nihon University, 1-8-14 Kanda-Surugadai, Chiyoda-ku, Tokyo, Japan
e-mail: akimoto.masato@nihon-u.ac.jp

H. Matsumori
Department of Mechanical Engineering, Graduate School of Science & Technology, Nihon University, 1-8-14 Kanda-Surugadai, Chiyoda-ku, Tokyo, Japan

Y. Zhou et al. (eds.), *Fluid-Structure-Sound Interactions and Control*, Lecture Notes in Mechanical Engineering,
https://doi.org/10.1007/978-981-10-7542-1_11

DBD-PA, the induced flow from DBD-PA is generated. DBD-PA is driven by burst modulation control and the induced flow is intermittently generated. This intermittently generated induced flow controls the jet. The coaxial type DBD-PA controls the jet by controlling vortex generation in the jet.

2 Experimental Details

Figure 1 is the coaxial type DBD-PA. DBD-PA is configured two copper electrodes and a dielectric. Electrodes place on the front and back of the dielectric. The coaxial type DBD-PA nozzle is made of machinable ceramics of dielectric constant 9 and the two electrodes are made of phosphor bronze of 0.5 mm thickness. The coaxial type DBD-PA nozzle of diameter is $d = 10$ mm. And the converging nozzle with a contraction ratio of 6.25 attaches to the tip the coaxial type DBD-PA nozzle. Applying AC high voltage to the coaxial type DBD-PA occur dielectric barrier discharge. As shown in Fig. 2, the induced flow that is used jet diffusion control and diffusion promotion is generated from the nozzle inner electrode side.

Figure 3 shows an over view of the experimental apparatus. In this study, we conduct experiments in the jet at Reynolds number $Re = 10{,}000$. Compressor supplies Air to experimental apparatus. Then, the mass flow controller adjusts air

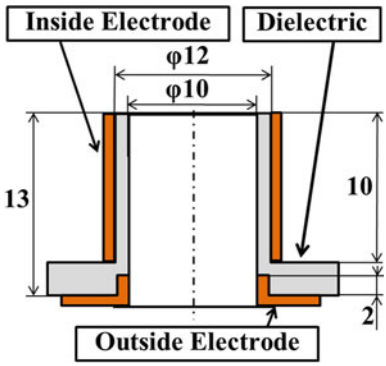

Fig. 1 The coaxial type DBD-PA

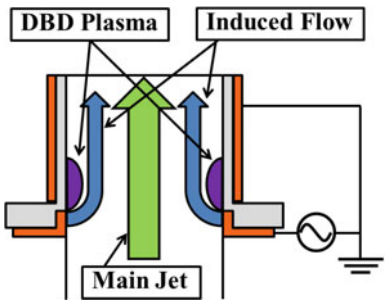

Fig. 2 Flow and DBD plasma

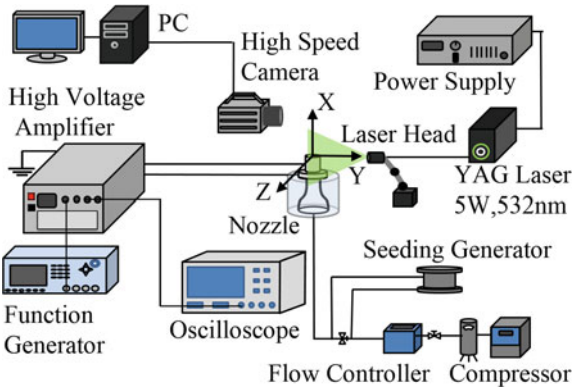

Fig. 3 Experimental apparatus

flow rate. Passing through the seeding generator, adjusted air is mixed tracer particles for visualization. Here, tracer particles are corn oil with a particle size of about 1 μm. To rectify the flow of adjusted air, pass through an air filter with a filtration degree of 5 μm and a pipe for run-up. This pipe for run-up of an inner diameter is 25 mm and of a length is about 1.2 m. After that, air jet out vertically upward from the coaxial type DBD-PA nozzle attached the converging nozzle.

Visualization of the jet is conducted by laser sheet scattered light technique with YAG laser. And the jet is photographed by the high speed camera. Here, frame rate of the high speed camera is 12,000 fps. The function generator generates AC waveform. Here, AC waveform is sine wave. The high voltage amplifier boosts this AC waveform. The high voltage amplifier boosts AC high voltage $V_{p\text{-}p}$ (peak to peak) = 16 kV. The AC high voltage waveform is applied to the coaxial type DBD-PA.

Figure 4 shows burst modulation control parameter of AC high voltage applied to the coaxial type DBD-PA. Here, f_{burst}: the frequency of the on-off cycle of AC high voltage waveform of burst modulation control. Burst ratio of burst modulation control in all experimental conditions is 50%. The f_{burst} is determined on basis of the natural vortex frequency f_n. Here, f_n: the frequency of naturally generated vortices of a free jet at plasma off. The f_n at Re = 10,000 is searched by measured frequency of flow velocity fluctuation of the free jet with laser doppler velocimeter. As a

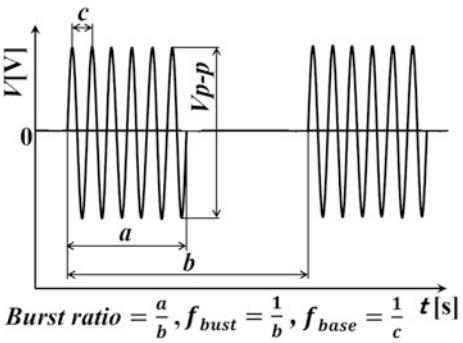

Fig. 4 Burst modulation control parameter

result, the f_n of Re = 10,000 is 1984 Hz. In addition, this f_n is confirmed by counted the naturally generated vortices. The high-speed camera photographs the free jet at Re = 10,000 of XY plane. The naturally generated vortices of the free jet are counted at a height x/d = 0.5 from nozzle exit using this moving image for 1.0 s. f_{base}: AC high voltage driving frequency is about 7 kHz. This study is investigated effect on the jet from change in the f_{burst}. The influence of change in the f_{burst} is evaluated by searched the f_{vortex}. Here, f_{vortex}: frequency of generated vortices of plasma excited jet. The f_{vortex} is searched by counted the generated vortices of plasma excited jet at a height x/d = 0.5 from nozzle exit using moving image for 0.1 s.

3 Results and Discussion

Figure 5 shows the searched result of f_{vortex} at Re = 10,000. The vertical axis of graph is the ratio of f_{burst} and f_{vortex}, the horizontal axis of graph is the ratio of f_n and f_{burst}. This graph can be divided into three sections of $f_{burst} < f_{vortex}$, $f_{burst} = f_{vortex}$, $f_{burst} > f_{vortex}$. Within $f_{burst} = f_{vortex}$ ($f_{vortex}/f_{burst} = 1$), the induced flow of the coaxial type DBD-PA synchronizes f_{burst} and f_{vortex} [3]. This phenomenon is the phenomenon of lock-in [2]. Driving the coaxial type DBD-PA with burst modulation, it is possible to generate an axisymmetric vortex within frequency of burst modulation control in which the phenomenon of lock-in occurs. Consequently, the jet is controlled by the coaxial type DBD-PA within frequency of burst modulation control in which the phenomenon of lock-in occurs.

Figure 6 shows XY plane of jet visualization image at Re = 10,000. Figure 6a is the free jet of plasma off. The free jet is not controlled. The free jet generates vortices in an unsteady cycle. In Fig. 6b is $f_{burst} = 0.3f_n$ = 595 Hz. This condition generates a large vortex and a small vortex near the nozzle of the jet in an unsteady

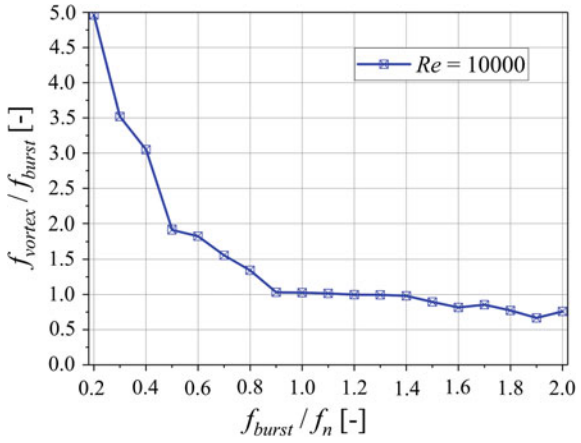

Fig. 5 Relationship between f_{vortex}/f_{burst} and f_{burst}/f_n

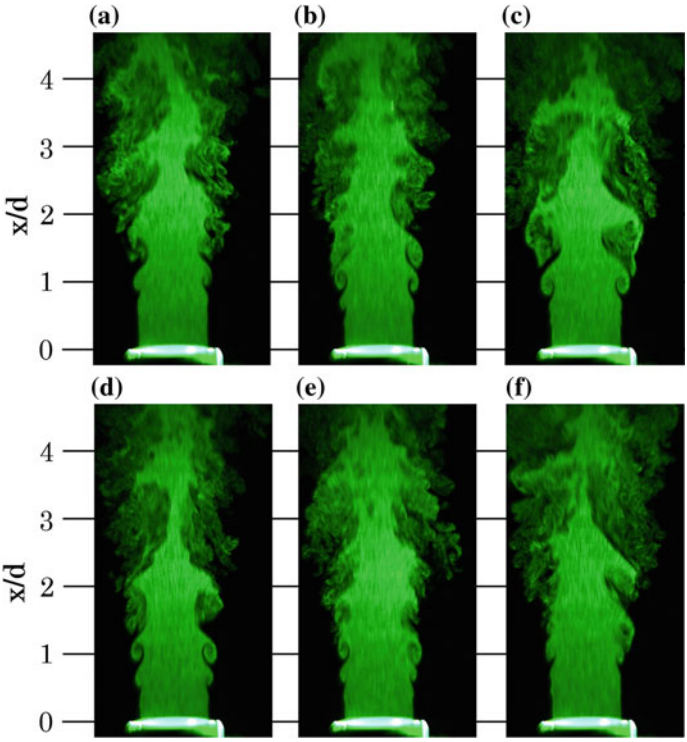

Fig. 6 XY plane of jet visualization image at Re = 10,000. **a** Plasma off. **b** $f_{burst} = 0.3f_n$ = 595 Hz. **c** $f_{burs} = 0.9f_n$ = 1786 Hz **d** $f_{burst} = 1.0f_n$ = 1984 Hz. **e** $f_{burst} = 1.4f_n$ = 2778 Hz. **f** $f_{burst} = 2.0f_n$ = 3968 Hz

cycle. We consider that the induced flow of the coaxial type DBD-PA generates a large vortex and Shear layer instability of jet generates a small vortex. In Fig. 6c–e, the jet is controlled by driving the coaxial type DBD-PA frequency of burst modulation control in which the phenomenon of lock-in occurs. Figure 6c is $f_{burst} = 0.9f_n$ = 1786 Hz, the phenomenon of lock-in begins with this f_{burst}. Figure 6d is $f_{burst} = 1.0f_n$ = 1984 Hz, this f_{burst} is the natural vortex frequency. When the coaxial type DBD-PA driving condition is $f_{burst} = 0.9f_n$ or $1.0f_n$, these conditions generate large vortices near the nozzle of the jet in a steady cycle and these vortices coalescence develop large-scale vortex ring compared to other experimental conditions (Fig. 6a, b, e, f). Figure 6e is $f_{burst} = 1.4f_n$ = 2778 Hz, the phenomenon of lock-in ends with this f_{burst}. This condition generates a small vortex near the nozzle of the jet in a steady cycle. Figure 6f is $f_{burst} = 2.0f_n$ = 3968 Hz. This condition generates a small vortex near the nozzle of the jet in an unsteady cycle. We consider that frequency of the induced flow of the coaxial type DBD-PA is higher than other conditions and the generation of vortex can not follow.

4 Conclusions

The coaxial type DBD-PA is driven by burst modulation control and the intermittently generated induced flow control the jet. As a result, following knowledge is obtained.

1. By the phenomenon of lock-in, the induced flow of the coaxial type DBD-PA synchronizes vortex generation in the jet in a specific burst modulation control frequency range. Consequently, the jet is controlled by the coaxial type DBD-PA within frequency of burst modulation control in which the phenomenon of lock-in occurs.
2. Driving the coaxial type DBD-PA with burst modulation control generates a large vortex near the nozzle of the jet in a steady cycle and these vortices coalescence develop large-scale vortex ring.

Acknowledgements This work was supported by Grants-in-Aids for Scientific Research from the Japan Society for the Promotion of Science (JSPS) (C) KAKENHI 16K06131.

References

1. Nobuhide K (2004) Hunryu no chiteki noudou seigyo heno tyosen. Mech Eng Congr Jpn (MEJC) 8:85–86
2. Hiroaki S et al (1999) Active control of axisymmetric jet with an array of micro electro-magnetic flap actuators. Trans Jpn Soc Mech Eng Part B 65(639):106–113
3. Masato A et al (2017) Control of jet by the coaxial type DBD plasma actuator—change vortex structure of jet by burst actuation. J Vis Soc Jpn 37(8):21–31

Unsteady Flow Structure Behind A Low-Drag Ahmed Body

Yingchao Zhang, Bingfu Zhang and Yu Zhou

Abstract Unsteady flow structure behind an Ahmed body with a slant angle of 35°, corresponding to the low-drag regime, has been experimentally investigated at Re of 6.59×10^4. Measurements are conducted using single hotwire and flow visualization techniques. The major flow characteristics are examined. A total of five distinct Strouhal numbers (St) have been identified in the wake, as the case of the high-drag regime. Two detected over the rear window are linked to vortices generated along the roof and side surfaces of the model, respectively, and two found near the ground surface are ascribed to vortices produced by the struts (wheels) of the body. The fifth one, with $St = 0.3$, captured behind the base is distinct from its counterpart found in the high-drag regime and a physical explanation is proposed for this St.

Keywords Ahmed body wake · Unsteady flow structure · Vehicle model Strouhal number

1 Introduction

There has been recently a renewed interest in finding new technologies to reduce aerodynamic drag and hence fuel consumption in automotive industry because of the lasting high fuel costs in the past few years as well as the issue of global

Y. Zhang
State Key Laboratory of Automotive Simulation and Control,
Jilin University, Changchun, China

Y. Zhang · B. Zhang
Department of Mechanical Engineering, The Hong Kong Polytechnic University,
Hung Hom, Kowloon, Hong Kong, China

Y. Zhou (✉)
Institute for Turbulence-Noise-Vibration Interaction and Control, Shenzhen
Graduate School, Harbin Institute of Technology, Shenzhen, China
e-mail: yuzhou@hit.edu.cn

Y. Zhou et al. (eds.), *Fluid-Structure-Sound Interactions and Control*, Lecture Notes in Mechanical Engineering,
https://doi.org/10.1007/978-981-10-7542-1_12

warming. Active control of aerodynamic drag reduction calls for a thorough understanding of the unsteady wake of vehicles. The Ahmed body is perhaps the most widely used simplified vehicle model in the active drag reduction research. This body may be classified as high drag and low drag bodies, corresponding to the rear slant angle of $\varphi < 30°$ and $\varphi > 30°$, respectively. In spite of previous investigations on the wake of the low-drag Ahmed body, the overall picture on this flow remains elusive. For example, the data of Strouhal numbers *St*, based on the square root of the frontal area A, is rather scarce in the literature. Most of previous investigations were focused on the high drag regime, as summarized in Zhang et al. [2, 3]. For the low drag regime only one St (=0.27) was reported for $\varphi = 35°$ [1]. This work aims to improve our understanding of the wake of a low-drag Ahmed body and conduct a relatively thorough experimental investigation on the unsteady flow structures, including St, in this flow.

2 Experimental Setup

Experiments were conducted in a closed circuit wind tunnel. A 1/3-scaled Ahmed body with a rear slant angle of $\varphi = 35°$ was placed on a raised floor, which was used to control the boundary layer thickness, as schematically shown in Fig. 1. The coordinate system is defined following the right-hand rule such that its origin is at the lower edge of the vertical base in the symmetry plane. Extensive hotwire and flow visualization measurements were carried out at a Reynolds number Re ($\equiv U_\infty \sqrt{A}/\upsilon$, where U∞ and υ are the free-stream flow velocity and kinematic viscosity and A is the frontal area, respectively) of 6.59×10^4.

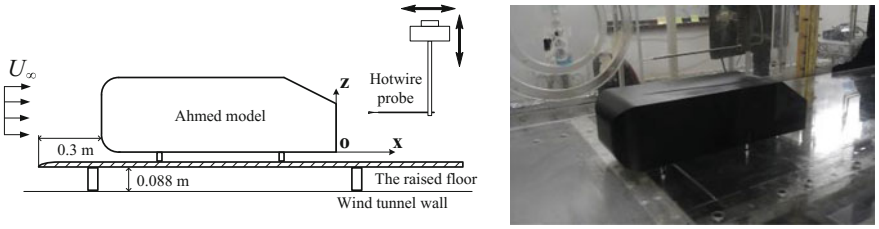

Fig. 1 Experimental arrangement (left) and Ahmed body in wind tunnel (right)

3 Results and Discussion

Figure 2 presents a typical photograph captured from flow visualization in the plane of symmetry ($y^* = 0$) over the rear window. During flow visualization, smoke is released simultaneously from three points, as indicated in the figure. Asterisk denotes normalization by $\sqrt{A}$ in this paper. The flow separates at the upper edge of the rear window, rolling up to form span-wise vortices behind the upper edge of the slanted surface. Two recirculation flow regions, one above the other, are formed in the wake. It is interesting to note the presence of an anti-clockwise secondary recirculation bubble, albeit small, near the lower edge of and over the slanted surface, whose formation appears resulting from the motion of the upper recirculation of the vertical base, as indicated by a sketch. This bubble produces a flow reversal along the slanted surface and may contribute to a pressure recovery on the surface.

Figure 3a presents the power spectral density function E_u of u measured at H1-H7 in the plane ($x^* = -0.36$, $z^* = 0.85$). One peak is evident at St = 0.19 in E_u (Fig. 3b) from position H3 to H5 and from I3 to I5 ($x^* = -0.09$, $z^* = 0.85$). Another unsteady structure at St = 0.27 is detected near the side edge of the rear window. As found by Zhang et al. [3], the unsteady flow structures at St = 0.19 and 0.27 originate from the shear layers developed over the roof and the side face of the model, respectively. Two more unsteady structures have also been detected at St = 2.21 and 1.79 from E_u measured behind the base (near the ground surface),

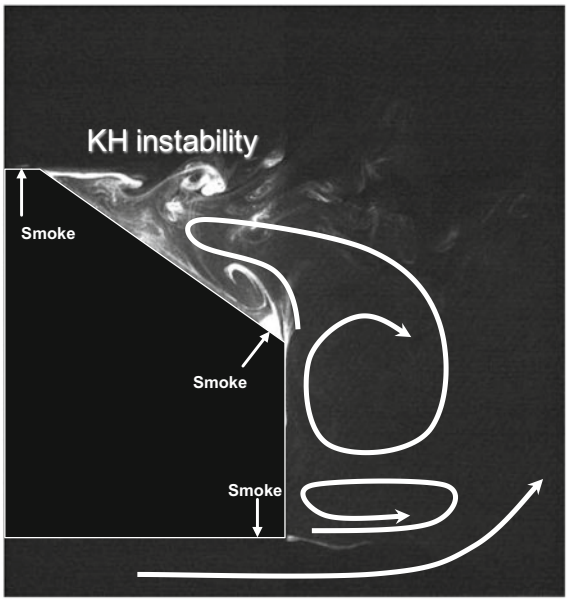

Fig. 2 Typical photograph captured from smoke flow visualization

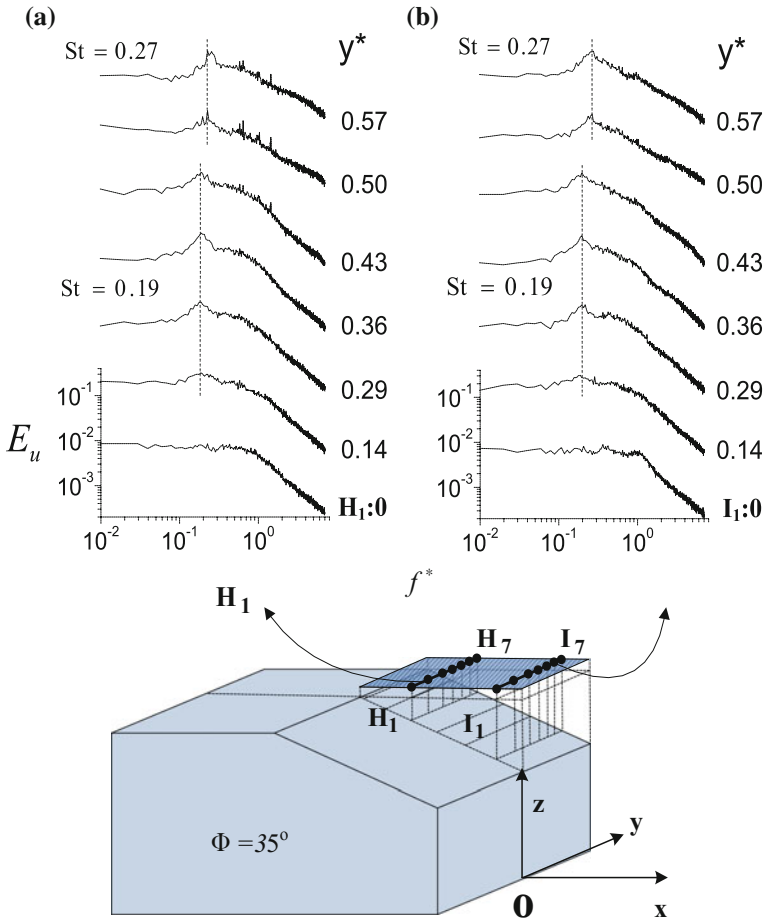

Fig. 3 Power spectral density function Eu of the hotwire signal measured along **a** H1-H7 (x* = −0.36, z* = 0.85), **b** I1-I7 (x* = −0.09, z* = 0.85), respectively, over the slant surface

which are ascribed to vortices shed from the upstream and downstream struts, respectively, under the model, which simulate vehicle wheels. Those structures are found around high drag Ahmed body by Zhang et al. [3], its location and frequencies are same with reported by Zhang et al. [3].

Behind the vertical base, a predominant peak is observed in E_u at St = 0.30 for various downstream locations in the plane of y* = 0 (Fig. 4). This frequency is observed for the first time. Careful analysis of both E_u measured at different locations and photographs from flow visualization indicates that this frequency results from the quasi-periodical emanation of fluid parcels from the lower recirculation region behind the vertical base. This frequency has not been found around

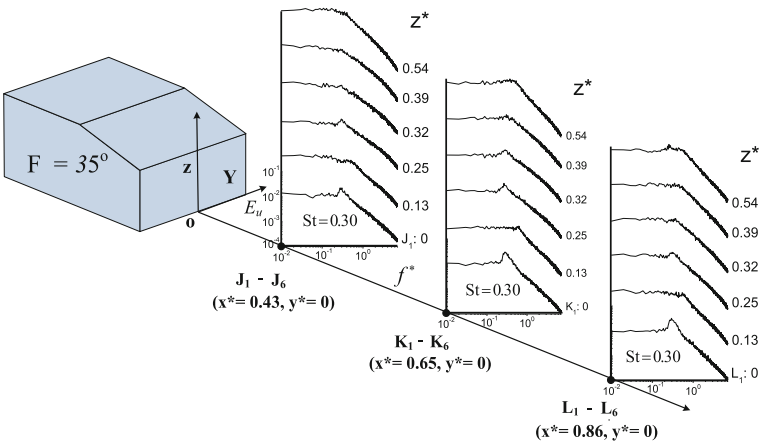

Fig. 4 Power spectral density function Eu of the hotwire signal measured along J1-J6 (x* = 0.43), K1-K6 (x* = 0.65,), L1-L6 (x* = 0.86,) in plane of y* = 0

high drag Ahmed model. The speculated reason is the slanted surface make the air flow pass the up surface and bottom surface with differents directions and velocities, so there will be form different flow structures.

4 Conclusions

Unsteady flow structures and their predominant frequencies have been investigated in the wake of an Ahmed body with a slant angle of 35°. The shear layer separated from the upper edge of the rear window rolls up, forming spanwise vortices. A total of five distinct St are identified in the wake of the body. Two are detected at St = 0.19 and 0.27 over the rear window. The former is connected to the hairpin vortices formed at the roof of the body, and the latter is linked to the side vortices generated along the side surface. Two are detected at St = 2.21 and 1.79 near the ground surface and are ascribed to the vortices produced by the struts of the body. One predominant frequency of $St = 0.30$ is captured for the first time behind the vertical base, which is attributed to the structures emanated from the lower recirculation bubble behind the base.

Acknowledgements Authors acknowledge support from the Hong Kong Scholar Program and China Postdoctoral Science Foundation through grants 2012M510874, 2012T50314 and 2014M551180. Supports from Research Grants Council of HKSAR through grant GRF 531912 and from Shenzhen Government through grant JCYJ20130329154125496 are also gratefully acknowledged.

References

1. Tunay T, Sahin B, Ozbolat V (2014) Effects of rear slant angles on the flow characteristics of Ahmed body. Exp Therm Fluid Sci 57(2014):165–176
2. Zhang BF, To S, Zhou Y (2014) Strouhal numbers of unsteady flow structures around a simplified car model. In: Zhou Y, Liu Y, Huang L, Hodges D (eds) Fluid-structure-sound interactions and control. Springer, Berlin, Heidelberg, pp 179–184
3. Zhang BF, Zhou Y, To S (2015) Unsteady flow structures around a high-drag Ahmed body. J Fluid Mech 777:291–326 (2015)

Trident Convection in a Cube

M. Kodama, M. Nobuhara, K. Tatsumoto, H. Tanigawa and K. Hirata

Abstract The authors numerically investigate the influence of the forced oscillation upon the three-dimensional thermal convection in a cubic cavity heated from one wall and chilled from its opposite wall in the gravity and zero-gravitaty fields without/with a forced sinusoidal oscillation. The direction of the forced oscillation is parallel to the temperature gradient direction. In addition, the direction is parallel to the direction of the gravity, in the gravity field. The authors assume incompressible fluid with a Rayleigh number $Ra = 8.0 \times 10^4$ in the gravity field without the forced oscillation or $Ra = 1.0 \times 10^4$ in the gravity field and a Prandtl number $Pr = 7.1$ (water). The forced-oscillation parameters are a vibrational Rayleigh number Ra_η and a non-dimentional forced-oscillation frequency ω. In the gravity field, $Ra_\eta = 1.0 \times 10^5$ and $\omega = 5.0 \times 10^0$, and in the zero-gravity field, $Ra_\eta = 1.1 \times 10^5$ and $\omega = 5.0 \times 10^0$. As a result, supposes reports a new flow structure in laminar and steady thermal convection, which consists of a pair of trident currents, namely, three ascending streams and three matching descending streams in a cube heated from a bottom wall and chilled from its opposite top wall. This flow is rather robust. Then, it can be observed in a stationary cube under the gravity, and can be observed in an oscillating cube under the gravity or zero gravity besides.

Keywords Rayleigh-Bénard convection · Natural convection
Convective instability

M. Kodama · M. Nobuhara · K. Tatsumoto · K. Hirata (✉)
Department of Mechanical Engineering, Doshisha University, 1-13 Tatara Miyakodani, Kyotanabe, Kyoto, Japan
e-mail: khirata@mail.doshisha.ac.jp

H. Tanigawa
Department of Mechanical Engineering NIT, Maizuru College, Maizuru, Kyoto 625-8511, Japan

Y. Zhou et al. (eds.), *Fluid-Structure-Sound Interactions and Control*, Lecture Notes in Mechanical Engineering,
https://doi.org/10.1007/978-981-10-7542-1_13

1 Introduction

Thermal convection is a key phenomenon for heat and mass transfer and mixing. Bénard [1] considered a horizontal layer. After Bénard, a lot of researchers have studied practical problems of thermal convection.

Here, we considers thermal convection in a cavity (or a container). One of the simplest cavities is a cube. Especially for thermal convection in a cube, for example Pallares et al. [2–4] numerically showed three-dimensional flow structures in the cubic cavity for moderate Rayleigh numbers $Ra < 6.0 \times 10^4$. They reported seven different steady-flow structures; namely, four kinds of single-roll structures (referred to as S1, S2, S3 and S7), two kinds of four-roll structures (referred to as S5 and S6), and one kind of a toroidal-roll structure (referred to as S4).

In this report, we reports a new flow structure in laminar and steady thermal convection as one facet of conductive diversity. This flow structure involves three downwelling and three matching upwellings in a cube heated from below and chilled from above, as well as our past studies [5–8] This flow structure is not transient but stable. So, it is commonly observed in various situations, such as in a stationary cube under the gravity and in an oscillating cube under the gravity or zero gravity besides.

2 System Modelling

2.1 Model and Governing Equation

Figure 1 shows the current model. The model is the flow in a cubic cavity with a length scale H^*. We analyse the thermal convection assuming incompressible flow with a constant Prandtl number $Pr = 7.1$ (water) in the non-gravitational field. A pair of opposed walls are taken to be isothermal, and the temperature one of them (hereinafter, referred to as a cold wall) is greater than the other (hereinafter, referred

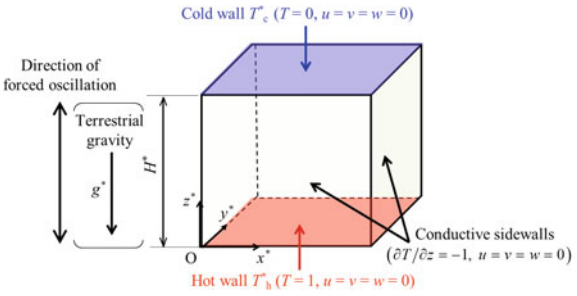

Fig. 1 Computational domain, together with coordinate system and boundary conditions

to as a hot wall). The four walls beside the cold and hot walls (hereinafter, referred to as sidewalls) are conductive.

The governing equations are the continuity equation, the dimensionless Navier-Stokes equations with the Boussinesq approximation and a dimensionless energy equation. They are as follows;

$$\nabla \cdot u = 0 \tag{1}$$

$$\frac{Du}{Dt} = -\nabla p + Pr\Delta u + Ra_\eta PrT \sin \omega t \mathbf{e}_z \tag{2}$$

and

$$\frac{DT}{Dt} = \Delta T \tag{3}$$

where $u = (u, v, w)$, t, p, T, $\boldsymbol{e}_z$ and ω denote velocity vector, time, pressure, tempera-ture, the unit vector in the z direction and (angular) frequency, respectively. We the definitions of Ra_η and Pr in the following subsection.The governing equations Eqs. (1)–(3) are solved by a finitedifference method based on the MAC method with the FTCS scheme using a staggeredmesh system.

2.2 Governing Parameter

Non-dimensional governing parameters are as follows;

$$\begin{aligned} Ra_\eta &= \frac{\eta^* \beta^* \left(T_{\mathrm{h}}^* - T_{\mathrm{c}}^*\right) H^{*3}}{\nu^* \alpha^*}, \; pr = \frac{\nu^*}{\alpha^*}, \; \omega = \frac{\omega^* H^*}{\alpha^*} \text{ and} \\ Ra &= \frac{g^* \beta^* \left(T_h^* - T_c^*\right) H^{*3}}{\nu^* \alpha^*}, \end{aligned} \tag{4}$$

where β^*, $\nu^*$and η^* denote thermal expansion coefficient, kinetic viscosity and acceleration amplitude, respectively. In the present study, Pr is fixed to 7.1 (water). The test ranges of Ra_η and ω are from 5.0×10^3 to 1.1×10^4 and from 1.0×10^0 to 1.0×10^3, respectively.

As global indicators, we considers such physical quantities as a spatially-averaged kinetic energy $\overline{K}$. These are defined as follows.

$$\overline{K} = \frac{1}{V} \iiint \left\{ \frac{1}{2} \left(u^2 + v^2 + w^2\right) \right\} dxdydz \tag{5}$$

3 Results and Discussion

3.1 Flow Structure Sα

Figure 2 shows a result of the present computations for $Ra = 8.0 \times 10^4$ and $Pr = 7.1$, being based on many preliminary computations over wide ranges of system parameters. The figure is a perspective view looking downward. Three-dimensional flow structure is visualised by iso-kinetic-energy surfaces of $0.38 \times K_{max}$, where K_{max} is the maximum value of kinetic energy K.

Brightness of the surfaces represents the value of w which is shown as a legend on the lower right of the figure. The flow visualisation based on K is more suitable for the concerning laminar problem to grasp the whole three-dimentional structure, than other physical quantities such as velocity vector $\boldsymbol{u}$, temperature T, vorticity vector and the second invariant of the velocity-gradient tensor.

From Fig. 2, we can see a pair of trident currents on thermal convection in a cube, which consist of three ascending streams and three matching descending streams. we name this flow structure Sα. Until now, this trident convection in a cube have not been reported, mainly because of the dependency of initial condition. According to past studies [5, 6], we usually expect another flow structure with two ascending and two descending streams which is referred to as S5 for $Ra = 8.0 \times 10^4$ and $Pr = 7.1$. Actually, the author observes the S5, if we start our computation with such an initial condition as the conductive state or if we compute with very-slowly increasing/decreasing Ra from zero/infinity.

However, this initial-condition dependency does not necessarily mean weak stability of the trident convection. As an example for this, we can consider the time development of $\overline{K}$ for $Ra = 8.0 \times 10^4$ and $Pr = 7.1$ in a stationary cube under the gravity. we regard $\overline{K}$ as a global indicator representing the system's state. $\overline{K}$ is defined by such a physical quantity as a spatially-averaged value of K over the whole volume of a cube. Then, as initial condition, we use the steady solution of S2 with a relatively-small $\overline{K} = 20.2$ for $Ra = 1.0 \times 10^4$ and $Pr = 7.1$, instead of the

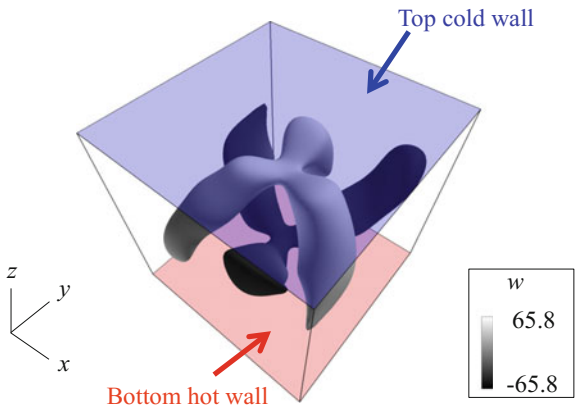

Fig. 2 Perspective view (look-down view) of the flow structure visualised by iso-kinetic-energy surfaces of $0.38 \times K_{max}$ for $Ra = 8.0 \times 10^4$ and $Pr = 7.1$. The value of w is represented by gray scale

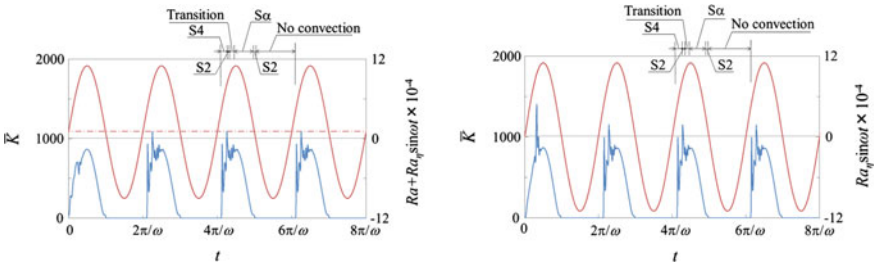

(a) Case I **(b)** Case II

Fig. 3 Time development of $\overline{K}$, together with $Ra + Ra_\eta \sin \omega t$ in figure (**a**) and $Ra_\eta \sin \omega t$ in figure (**b**). In each figure, — denotes $\overline{K}$, and — denotes $Ra + Ra_\eta \sin \omega t$ or $Ra_\eta \sin \omega t$ -·- in figure (**a**) is at Ra = 1.0×10^4 and the S5. In both the samples, the duration times of the S9 are effectively long with enough large values of $\overline{K}$

S5 or instead of the conductive state. Such time development of $\overline{K}$ show that the trident convection steadily and permanently appears at $t > 0.06$, after the initial transient process where another flow structure of one ascending and one descending streams (the S2) is dominant.

As another example to show the durability of the trident convection, we cosider the thermal convection in an oscillating cube instead of a stationary cubeunder the gravity or zero gravity. More specifically, the forced sinusoidal oscillationis parallel to the given temperature gradient direction. Figure 3a is a sample of the forcedly-oscillating cube under the gravity. Figure 3b is another sample of the forcedly-oscillating cube under zero gravity. Both the samples are rigorously periodic except for the first start-up period of computation at $t < 2\pi/\omega$, while we see high-frequency fluctuations due to higher harmonics. Then, we consider only the third period at $t = 4\pi/\omega - 6\pi/\omega$ in each figure. There exist the time-intervals where $\overline{K}$ becomes completely zero (or in the conductive state) each forcing cycle. Convective motion always starts with the S4 in each forcing cycle. We can confirm the appearance of the trident convection S9 at $t = (4\pi + 1.01)/\omega - (4\pi + 2.07)/\omega$ in Fig. 3a and at $t = (4\pi + 1.49)/\omega - (4\pi + 2.95)/\omega$ in Fig. 3b, together with other flow structures like the S2, the S4.

4 Conclusions

To summarise, we have reported a pair of trident currents on thermal convection in a cube. This previously-unidentified flow is rather robust, and can be observed not only in a stationary cube under the gravity, but also in an oscillating cube under the gravity and zero gravity. This finding implies a diversity of three-dimensional Rayleigh-Bénard convection, even if we suppose laminar and steady flow with very simple boundary condition.

References

1. Bénard MH (1900) Étude expérimentale des courants de convection dans une nappe liquide—régime permanent: tourbillons cellulaires, J de Phys, 3^{e} Série 513–524 (in French)
2. Pallares J, Cuesta I, Grau FX, Giralt F (1996) Natural convection in a cubical cavity heated from below at low Rayleigh numbers. Int J Heat Mass Trans 39:3233–3247
3. Pallares J, Grau FX, Giralt F (1999) Flow transitions in laminar Rayleigh-Benard convection in a cubic cavity at moderate Rayleigh numbers. Int J Heat Mass Transf 42:753–769
4. Pallares J, Cuesta I, Grau FX (2002) Laminar and turbulent Rayleigh-Bénard convection in a perfectly conducting cubical cavity. Int J Heat Fluid Flow 23:346–358
5. Hirata K, Tanigawa H, Nakamura N, Fujita S, Funaki J (2013) On the effect of forced-oscillation amplitude upon the flow in a cubic cavity heated below. J Fluid Sci Technol 8:106–119
6. Hirata K, Fujita S, Okaji A, Tanigawa H (2013) Thermal convection in an oscillating cube at various frequencies and amplitudes. J Therm Sci Technol 8:309–322
7. Hirata K, Tatsumoto K, Nobuhara M, Tanigawa H (2015) On g-jitter effects on three-dimensional laminar thermal convection in low gravity. Mech Eng J 2(5):15–00268
8. Tatsumoto K, Nobuhara M, Tanigawa H, Hirata K (2015) Thermal convection inside an oscillating cube analysed with proper orthogonal decomposition. Mech Eng J 2(2):15–00018

Effect of Ventilation on the Velocity Decay of Cavitating Submerged Water Jet

Guoyi Peng, Takayuki Itou, Yasuyuki Oguma and Seiji Shimizu

Abstract High-speed water jet shows a peculiar processing property in cutting of submerged objects but its processing ability decreases quickly with the increase of standoff distance. Aiming at to improve the performance of submerged water jet an experiment investigation on the velocity distribution of cavitating submerged jet is carried out by PIV method where micro bubbles are used as flow tracers. Further, a sheathed orifice nozzle with ventilation hole is developed and the effect of air ventilation is investigated. The result reveals that the core velocity of no-ventilation cavitating jet is higher than ventilated ones near the sheath exit. However it becomes reverse at the downstream when $x/d \geq 40$. The core velocity of ventilated jets decays much slowly compared to the case of no-ventilation jet. Air ventilation is demonstrated to be an effective way to enhance the perframnce of submerged water jets.

Keywords Water jet · Ventilation · Bubbly flow · Velocity profile

1 Introduction

High-speed water jets, where pressured water or fluid mixture is jetted from a small nozzle at high speed, have been developed and widely applied to many fields of industry for its peculiar processing property [5]. However, the processing ability of water jet decreases quickly with the increase of standoff distance, especially in the case of submerged working condition. In order to ensure the effective standoff of submerged water jet a new way of sheathed nozzle, where a pipe-like sheath is set to the exit of a jet nozzle, has been proposed and its effectiveness has been con-

G. Peng (✉) · Y. Oguma · S. Shimizu
Department of Mechanical Engineering, College of Engineeing, Nihon University, Koriyama 963-8642, Japan
e-mail: peng@mech.ce.nihon-u.ac.jp

T. Itou
Graduate School of Engineeing, Nihon University, Koriyama 963-8642, Japan

Y. Zhou et al. (eds.), *Fluid-Structure-Sound Interactions and Control*, Lecture Notes in Mechanical Engineering,
https://doi.org/10.1007/978-981-10-7542-1_14

firmed via various experiments [4]. But the flow structure of submerged water jet is still unclear for the difficulty to observe the inner of cavitation bubble clouds [1, 3]. In order to improve the performance of submerged water jets further investigations on the flow structure of submerged water jets become a practical requirement [2].

In the present work, the velocity distribution of submerged water jets issuing from a sheathed orifice nozzle is measured by PIV method, where micro bubbles involved in jet flow are used as tracing particles [6]. In order to further enhace the processing ability of submerged water jet a sheathed orifice nozzle with ventilation hole is proposed and the effect of air ventilation on the velocity distribution of jet flow is investigated. The decay of core velocity along the centrial axis is compared under difference air ventilation flowrate and the effectivity of ventilation on submberged processing by water jet is discussed.

2 Experimental Apparatus and Method

Figure 1 shows the schematic diagram of an opentype submerged water jet experimental device. The water tank is made of acrylic acid resin and a sheathed nozzle (1.0 mm in diameter) is located at the center of the square bottom. The tank is full of clear water and the water depth is kept to the level of 750 mm by using an overflow pipe. The nozzle is connected to a plunger pump with a high-pressure hose. A sheath pipe (3.0 mm in diameter) is mounted at the exit of the nozzle where a ventilation hole leading to the inlet of the sheath pipe is arranged, and a ventilation hose is connected to the ventilation hole. The output pressure of the plunger pump is adjustable from 0.5 to 21.0 MPa and the inject pressure P_i is monitored in real-time by a pressure sensor set just in front of the nozzle. Pressured clear water supplied by a plunger pump is injected into the still water upward vertically. When the pressure at the inlet of sheath pipe decreases to the atmospheric pressure

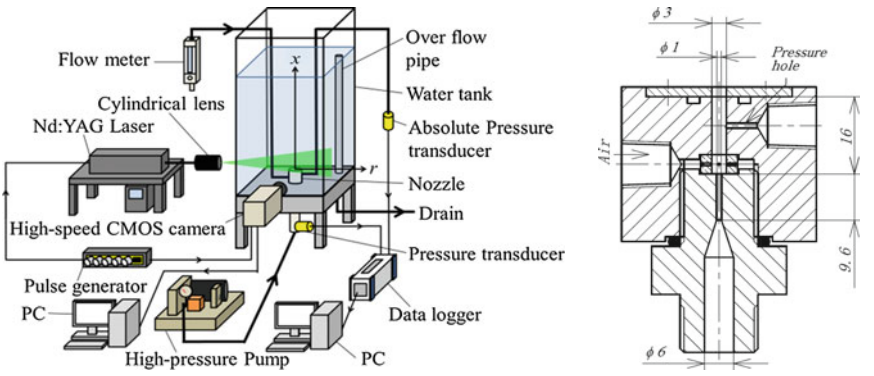

(a) Submerged water jet apparatus **(b)** Ventilation nozzle systeme

Fig. 1 Scheme of experimental device

air will be naturally suctioned and small bubbles may be generated around water jet under the effect of ventilation. The ventilation air flowrate is adjusted by a flowrate adjasting valve. The vacuum pressure in the sheath is measured by an absolute pressure sensor and the ventilation air flowrate Q_{air} is done by area flowmeter. As an index of the pressure decrease at the nozzle throat, cavitation number σ of the water jet device is defined as follows.

$$\sigma = \frac{p_o - p_v(T_\infty)}{P_i - p_o} \tag{1}$$

where P_i denotes the jet injection pressure, and p_o does the surrounding static pressure at the nozzle exit under the effect of water depth to the water sureface. p_v does the saturated vapor pressure under the surrounding temperature T_∞.

Visualization observation and velocimetry are performed by using a 2D PIV system. High-speed water jet issuing from the nozzle is irradiated by a sheet laser light (Lee Laser: LDP-100MQG, 5.0 mJ at 10 kHz) through the nozzle axis, and micro bubbles involved are used as flow tracers. Temporal flow fields are observed and recorded with a high-speed CMOS camera (Photron: FASTCAM SA-NX2, 1024 × 1024 pixels, 12-bit gray level) and the observation area of the CMOS camera is fitted to the central axial behind the sheath exit (image area: 31 mm × 31 mm). The frame rate of photographing is 5000 s^{-1}. For description of the flow field a cylindrical coordinate system (z, r, θ) is adopted, where the origin is located at the nozzle exit and coordinates z and r are respectively set along the streamwise direction and the radial direction. The components of velocity vector in the z, and r directions are denoted as u, v respectively. Then, the magnitude of velocity vector is defined by $V = (u^2 + v^2)^{1/2}$. Velocity analysises are performed by applying the direct cross-correlation algorithm based on the Gaussian peak fitting technique.

3 Results and Discussions

Experiments were perfomed under condition that the time-averaged injection pressure is set to $P_i = 1.1$ MPa. The static pressure at the nozzle exit is estimed to be 0.1 Mpa, and thus the cavitation number is calculated to be $\sigma = 0.1$. Figure 2a shows, as an example, an instantaneous visualization picture of jet flow without air ventilation ($Q_{air} = 0$), where cavitation bubbles are observed to be bright spots. The velocity vector distribution at the same moment obtained by PIV abalyszing of tracer's motion is indicated by arrows. Figure 2b shows an instantaneous flow filed observed by high-speed camera as well as the velocity vector distribution at the same moment when the air-ventilation flowrate is given to be $Q_{air} = 0.5$ L/min for comprason. Their grey levels are diffrent since the volume fraction of gas bubbles are different, and the behavior bubble clouds included in the cavitating jet varies corresponding to the ventilation flowrate.

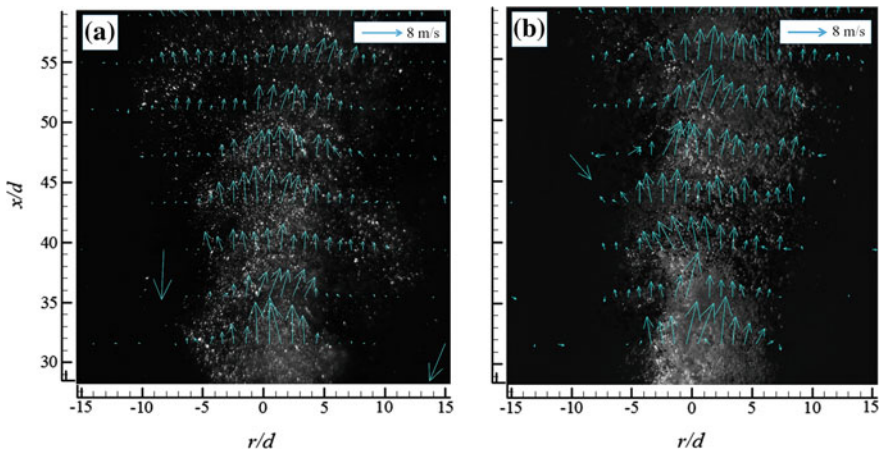

Fig. 2 Instantaneous visualization image and velocity vectors distribution where **a** $Q_{air} = 0$ (no-ventilation) and **b** $Q_{air} = 0.5$ L/min

Figure 3a to d respectively shows the profiles of timely averaged velocity at standoff distances $x/d = 30$, 35, 40 and 50 from the nozzle exit, where symbols •, Δ, □, +, ◇ respectively denote the velocitys when the ventilation flowrate are given to be $Q_{air} = 0$, 0.25, 0.5, 0.75, and 1.0 L/min. Figure 3a demonstrates that the core velocity of jet without ventilation along the axis is higher at $x/d = 30$ compared to ventilated jets while $Q_{air} = 0.25$, 0.5, 0.75, and 1.0 L/min. As the section is close the the sheath exit and the reflection of laser right is very strong and it is difficult to recongnize a small bubble cloud. So, velocity dispersion of PIV analysis is relative large. Figure 3b indicates that the core velocity is almost the same as that of ventilated jet at $x/d = 35$ when $Q_{air} = 0.25$. But at the sections of $x/d = 40$ and 50, the core velocity of no-ventilation jet is smaller than that of all ventilated jets. Thus, the core velocity of ventilated jets decays slowly along the cental axis compared to the case of no-ventilation jet. The effect of ventilation is confirmed it is demonstrated that ventilation is an effective way to delay the decay of core velocity of submerged water jet. Therefor, air ventilation is advantagoud to enhance the perframnce of submerged water jet since the processing ability of water jet closely denpend upon the core velocity.

Figure 3a demonstrates that the thickness of jet is about $8d$ in diameter at the section of $x/d = 30$ and expands to $18d$ approximately at $x/d = 50$. The unilateral expansion angle of the present jet nozzle is estimated about 14.0°.

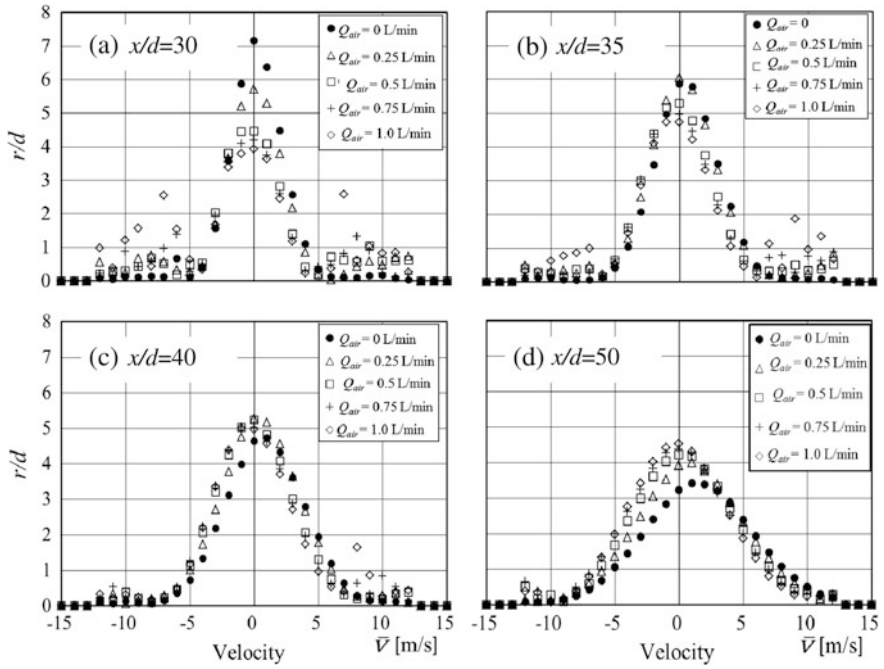

Fig. 3 Time-averaged velocity profiles under different ventilation flowrates

4 Conclusions

The flow structure of cavitating subumerged water jets issuing from a sheathed orifice nozzle has been investigated under ventilation and no-ventilation conditions by PIV method. The result demonstrates that:

(1) The flow patterns of ventilated cavitating jet and no-ventilation cavitating jet are different. In the case of ventilation, the velocity profile near the nozzle exit is relative flat and bubble clouds reaches far downstream.
(2) The core velocity of ventilated jets decays much slowly compared to the case of no-ventilation jet, and air ventilation is helpful to to extend the effective processing standoff distance of submerged water jet.

Acknowledgements This work was partly supported by JSPS, Grant-in-Aid for Scientific Research (C) (No. 17K06169), and the PIV system was equipped by the key equipment expansion foundation of Graduate School of Engineering, Nihon University.

References

1. Peng G, Oguma Y, Shimizu S (2015) Visualization observation of cavitation cloud shedding in a submerged water jet. In: Proceedings of 3rd FSSIC. Springer, Berlin, Heidelberg, pp 229–234
2. Peng G et al (2016) Numerical analysis of cavitation cloud shedding in a submerged water. J Hydrodyn 28(6):986–993. https://doi.org/10.1016/S1001-6058(16)60700-X
3. Sato K et al (2013) High speed observation of periodic cavity behavior in a convergent-divergent nozzle for cavitating water jet. J FCMV 1:102–107. https://doi.org/10.4236/jfcmv.2013.13013
4. Shimizu S et al (2015) Submerged cutting characteristics of abrasive suspension jet. Trans JSME (in Japanese) 81(831):15–00361. https://doi.org/10.1299/transjsme.15-00361
5. Summers D-A (2003) Water jetting technology. CRC Press, pp 642
6. Ziegenhein T, Garcon M, Lucas D (2016) Particle tracking using micro bubbles in bubbly flows. Chem Eng Sci. 153(22):155–164

Turbulent Ramp Flow Control Using Unsteady Blowing Upstream of the Separation Point

P. Sujar-Garrido, J. C. Hao and Y. Zhou

Abstract The control of a two-dimensional turbulent flow separation from a 25°—backward-facing-ramp is experimentally studied using an unsteady upstream blowing through a spanwise slit with a view to reducing the recirculation length. The Reynolds number examined is 9.38×10^4, based on the ramp height h. Three control parameters are examined, i.e. the blowing amplitude, frequency and duty cycle. Extensive measurements of the flow are carried out using PIV, pressure and hotwire techniques. The results are compared with those of the natural flow and under unsteady blowing. The time-averaged recirculation bubble is found to contract in length by 40% under the optimum control parameters, which correspond to a very small fraction of input energy. It is further found that the optimization control frequency is close to the shedding frequency of the uncontrolled shear layer captured at 1 h downstream of the separation point.

Keywords Flow control · Backward-facing ramp · Unsteady blowing actuation

1 Introduction

The control of a separated flow may improve the performances of many engineering devices. Many hydrodynamic means have been developed as periodic excitation in controlling flow separation [1]. An open-loop control is a crucial step to understand the behaviour and response of the natural flow to the imposed forcing. This work aims at studying the control of turbulent flow separation from a backward-facing ramp. We propose to deploy unsteady blowing through a spanwise slit, upstream of

P. Sujar-Garrido
State Key Laboratory of Aerodynamics, China Aerodynamics Research and Development Center, Mianyang Sichuan 621000, China

P. Sujar-Garrido · J. C. Hao · Y. Zhou (✉)
Institute for Turbulence-Noise-Vibration Interactions and Control, Shenzhen Graduate School Harbin Institute of Technology, Xili University Town, Shenzhen 518055, China
e-mail: yuzhou@hit.edu.cn

Y. Zhou et al. (eds.), *Fluid-Structure-Sound Interactions and Control*, Lecture Notes in Mechanical Engineering,
https://doi.org/10.1007/978-981-10-7542-1_15

the flow separation. This ramp flow is dynamically similar to the backward-facing step flow [2], both characterized by a big recirculation bubble [3]. The time-averaged reattachment point is mostly used as a reference parameter to evaluate the control performance of the actuation. Our results demonstrate that the control is highly effective and there is no need to have a high expense of input energy to reduce substantially the recirculation bubble.

2 Experimental Setup

Experiments are conducted in a closed-loop wind tunnel whose test section is $0.8 \times 1.0 \times 5.6\ m^3$, with a speed range of 2–50 m/s and a turbulence intensity level of around 0.3%. The experimental arrangement is schematically shown in Fig. 1, along with the definition of the coordinate system. The ramp model, spanning the entire width of the working section floor, consists of three parts, i.e., the upstream flat plate with a NACA0015 leading edge, the ramp part with a height h of 70 mm and an angle $\alpha = 25°$ with respect to incident flow, and the downstream plate that ends with a rear flap to control the pressure gradient upstream of the separation edge. The actuator is formed by a slit of 1 mm in width (w), covering 2/3 of the spanwise width of the model (L = 540 mm) and located at 2 mm upstream of the separation edge. The unsteady blowing, normal to the wall, may have a frequency of 10–300 Hz and a duty cycle of 10–90%. The model is made with a number of pressure taps longitudinally at mid-span and also transversely for the measurements of the static pressure distribution. The flow is ensured to be

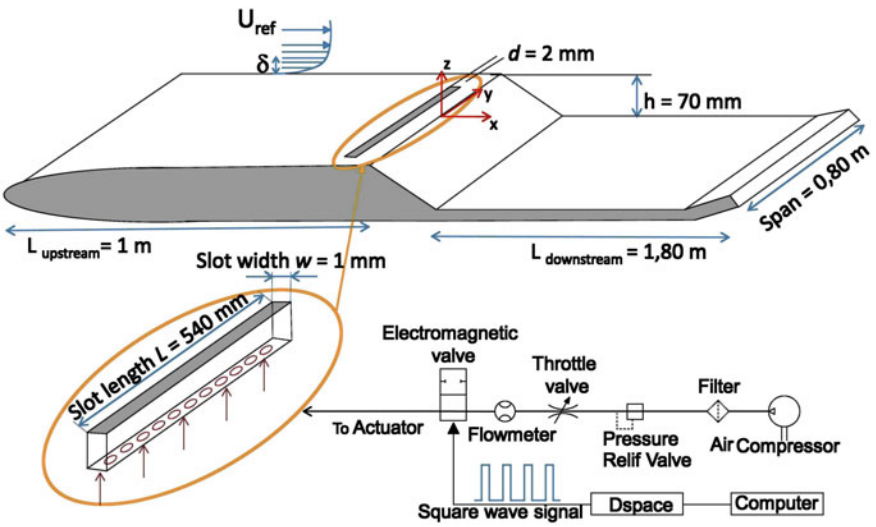

Fig. 1 Schematic of the ramp model and the unsteady blowing jet

two-dimensional. The blowing jet and the boundary layer are documented using a single hot-wire, sampled at a frequency of 2 kHz. The recirculation bubble and flow near the separation and reattachment points were captured using a time-resolved PIV system, consisting of a Litron Laser of 30 mJ, a LaVision CCD camera of 2048 × 2048 pixels^2 and a synchronizer. The CCD camera is placed on a traverse mechanism in order to capture the entire separated-reattached flow from x = −1 h up to 6 h longitudinally. The PIV data were obtained at a frequency of 200 Hz.

3 Results

The natural flow was first examined and compared with the data in the literature. The free-stream velocity (U_{ref}) is 21 m/s, corresponding to an h-based Reynolds number of around 9.38 × 10^4. The major characteristic parameters of the boundary layer are shown in Table 1. The time-averaged reattachment point (X_R) is found to be around 5 h, which is determined from the maximum gradient of the pressure coefficient and/or from the intersection between the line of the time-averaged streamwise velocity $U = 0$ and the downstream plate. Then, the blowing jet was documented in the absence of the ramp flow. The maximum output velocity ($U_{jet\ max}$) produced is around 1 m/s for steady blowing but rises to 1.7 m/s for unsteady mode, depending on the blowing frequency and the duty-cycle. The maximum velocity ratio $U_{jet\ max}/U_{ref}$ is around 0.08 given in Fig. 2a.

Table 1 Turbulent boundary layer characteristics

Location	α	h (mm)	U_{ref} (m/s)	δ (mm)	θ (mm)	Re_h	Re_θ
x = −1 h	25	70	21	15.5	1.4041	9.38 × 10^4	1881

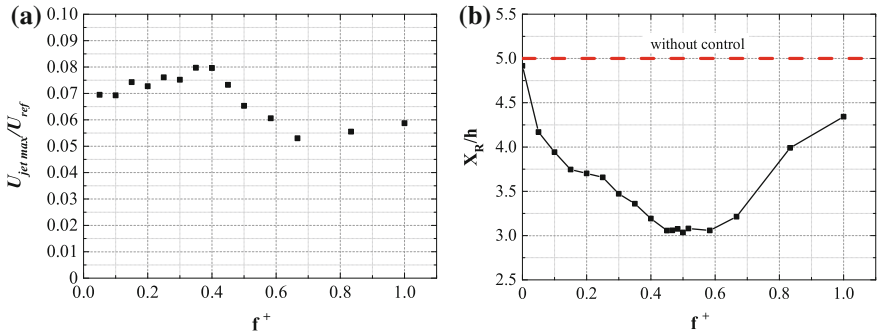

Fig. 2 **a** Dependences of $U_{jet\ max}/U_{ref}$ on f$^+$ at dc = 0.5. **b** Dependence of the mean reattachment area, X_R/h, on f$^+$ at dc = 0.5 (black solid line), compared with the uncontrolled case (red dashed line)

A parametric study was carried out in order to find the optimal actuation parameters for the open-loop control. To this end, one of the two control parameters, i.e. the control frequency f and the duty-cycle dc, was varied while the other was fixed. The dependence of X_R/h on f^+ is given in Fig. 2b given dc = 50%. The superscript + denotes normalization by h and U_{ref}. Evidently, X_R/h depends strongly on f^+ and retreats by up to 40%, compared to the uncontrolled case. Note that the control performance is poor at higher frequencies say $f^+ > 0.7$. It is noteworthy that the optimal f^+ range ($f^+ = 0.4$–0.6) is close to the shedding frequency ($f_s^+ = 0.45$) of the uncontrolled shear layer, measured at 1 h downstream of the separation point using the hot-wire. It seems plausible that the unsteady blowing may have capitalized the natural instability of the shear layer, thus resulting in the substantially reduced X_R/h. The result is consistent with Sujar-Garrido et al. [4], who found that the minimum X_R/h in a step flow control was achieved when the forcing frequency f^+ coincided approximately with the vortex shedding frequency.

Figure 3 compares the flow fields, captured using PIV, with and without control. The sectional streamlines show clearly that the recirculation bubble contracts greatly under control, and the high-level contours of k/U_{ref}^2 increase largely above the line of U = 0 m/s, where k is the turbulent kinetic energy. The observation is similar to that made by Yoshioka et al. [5] who used alternate suction and injection to control a step flow and reduced the reattachment by 30%, which is accompanied by an increase in the Reynolds stress within the shear layer.

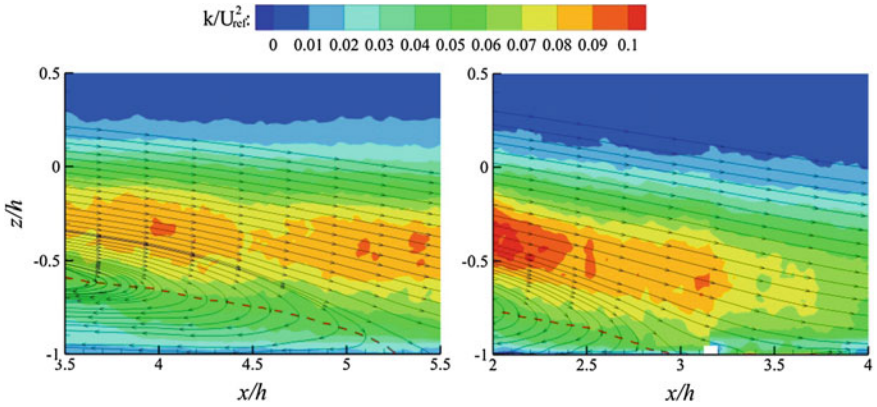

Fig. 3 Sectional streamlines (solid line) overlapped with the iso-contours of the dimensionless turbulent kinetic energy for the uncontrolled (left) and controlled (right, $f^+ = 0.5$) cases. The dashed line denotes the location where U = 0 and determines the mean reattachment point

4 Conclusion

The results, though preliminary, show that unsteady blowing through a spanwise slit placed upstream of the ramp is both effective and efficient in reducing the separation bubble, cutting down the recirculation length by 40% with a very small velocity ratio (<0.1) and a very small momentum coefficient (1.83×10^{-4}). It is found that the control performance depends highly on f^+ and is most effective when f^+ coincides approximately with the frequency of vortex shedding from the ramp. Further data analysis is under way to understand thoroughly the flow physics and control mechanisms behind the effective control.

Acknowledgements The financial support given from Shenzhen Government through grant JCYJ20150625142543469 is gratefully acknowledged.

References

1. Greenblatt D, Wygnanski IJ (2000) The control of flow separation by periodic excitation. Prog Aerosp Sci 36(7):487–545
2. Kourta A, Thacker A, Joussot R (2015) Analysis and characterization of a ramp flow separation. Exp Fluids 56:104
3. Simpson R (1989) Annu Rev Fluid Mech 21:205232
4. Sujar-Garrido P, Benard N, Moreau E, Bonnet JP (2015) Dielectric barrier discharge plasma actuator to control turbulent flow downstream of a backward-facing step. Exp Fluids 56:70
5. Yoshioka S, Obi S, Masuda S (2001) Turbulence statistics of periodically perturbed separated flow over backward-facing step. Int J Heat Fluid Fl 22:393–401

Friction Drag Reduction Mechanism Under DBD Plasma Control

X. Q. Cheng, C. W. Wong, Y. Z. Li and Y. Zhou

Abstract This work aims to understand the mechanism behind friction drag reduction in a dielectric barrier discharge (DBD)-plasma-controlled flat-plate turbulent boundary layer (TBL). Streamwise-oriented DBD plasma actuators are deployed to generate streamwise counter-rotating vortices in the TBL. The variation in the local friction drag is measured using a single hotwire, and the change in the flow structure is captured using a high-speed PIV. At a voltage V_a of only 4.25 kV, the drag reduction over an area (90 mm long and 200 mm wide) behind the plasma actuators reaches 14%. In fact, the drag reduction area stretches longitudinally to about 300 mm or 2000 wall units. The drag reduction is found to be linked to the decrease in the near-wall turbulent kinetic energy production, pointing to that the plasma-actuator-generated streamwise vortices interrupt effectively the turbulence generation cycle, thus stabilizing near-wall velocity streaks and resulting in friction drag reduction.

Keywords Turbulent boundary layer · Drag reduction · Control mechanism DBD plasma control

1 Introduction

Drag reduction in turbulent boundary layers (TBL) has received widespread attention in the literature and its potential benefits in various engineering applications cannot be overlooked. Plasma-based TBL control is attractive to many researchers due to ease in implementation and possible large friction drag reduction.

X. Q. Cheng · C. W. Wong (✉) · Y. Z. Li · Y. Zhou
Institute for Turbulence-Noise-Vibration Interactions and Control,
Shenzhen Graduate School, Harbin Institute of Technology, Shenzhen, China
e-mail: cwwong@hit.edu.cn

X. Q. Cheng
Department of Mechanical Engineering, The Hong Kong Polytechnic University,
Hung Hom, Hong Kong

Y. Zhou et al. (eds.), *Fluid-Structure-Sound Interactions and Control*, Lecture Notes in Mechanical Engineering,
https://doi.org/10.1007/978-981-10-7542-1_16

Choi et al. [1] developed two DBD plasma actuator configurations for generating spanwise wall oscillation and spanwise travelling waves in TBL. They suggested that the plasma-actuator-generated spanwise oscillation and travelling waves could lead to a drag reduction of 45%, though the drag change was not measured in their experiments. Whalley and Choi [2] observed based on the PIV data a wide ribbons of low-speed streamwsie velocity in the viscous sublayer due to the plasma-actuator-generated spanwise travelling waves. They conjectured that the drag reduction is associated with the near-wall flow structures change.

Wong et al. [3] investigated experimentally the effect of plasma-generated streamwise vortices in a flat-plate TBL and achieved a drag reduction of 20% over an area (100 mm long and 200 mm wide) behind the actuators. The drag reduction was found to be enhanced by increasing the voltage V_a of actuators. However, the mechanism of drag reduction was not explained. This work aims to study the drag change under plasma control and the flow control mechanism that is responsible for the drag reduction.

2 Experimental Details

Experiments were conducted in a closed-circuit wind tunnel, which has a test section with $L \times W \times H = 5.6 \times 0.8 \times 1.0$ m. With its leading-edge tripped, a smooth Perspex flat plate (4.8 m long and 0.78 m wide) generates a fully developed TBL under zero streamwise pressure gradient. The TBL thickness δ is 85 mm at 3.2 m downstream from the leading edge of the flat plate, where most measurements are performed (Fig. 1). The x-, y- and z-axis are along the streamwise, wall-normal and spanwise directions, respectively, with their origin at the trailing edge and half-way between the second actuator pair. The freestream velocity $U_\infty = 2.4$ m/s and the Reynolds number $Re_\theta = 1450$, based on the momentum thickness. Each DBD plasma actuator comprises two copper electrodes and a

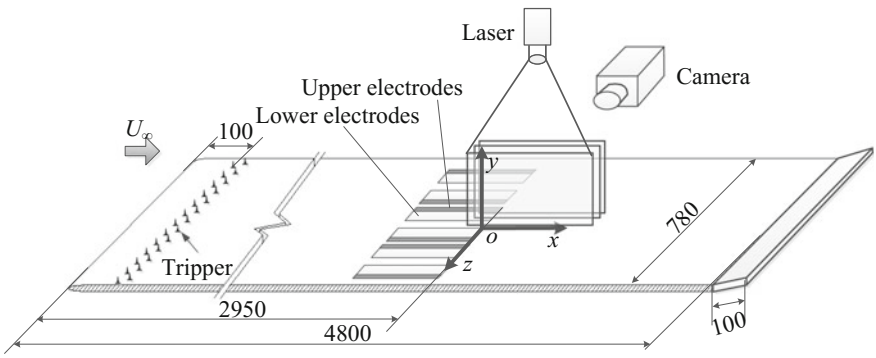

Fig. 1 Schematic of the experimental setup (not to scale; dimensions are in mm)

dielectric panel (one layer of mylar tape sandwiched between two layers of kapton tapes). In the present study, the actuators, required working long hours for detailed flow measurement, are operated at a small V_a (4.25 kV) to avoid breakdown. The streamwise-oriented actuators (configuration B in [3]) generate counter-rotating vortex pairs in the TBL.

The local skin-friction drag was estimated from the single-hotwire-measured mean streamwise velocity gradient in the viscous sublayer. An overheat ratio of 0.6 was used for the hotwire on the constant temperature anemometer. The hotwire signal was sampled at a frequency of 3 kHz (the cut-off frequency was 1 kHz). The sample duration was 40 s, long enough for the convergence of the streamwise mean and fluctuating velocities with and without plasma control. LaVison high-speed PIV system was used to measure the flow field in three *x*-*y* planes. The flow was seeded with the fog, with an average particle size of 1 μm in diameter, generated from peanut oil by a TSI 9307-6 particle generator. Flow was illuminated by a 1.0 mm thick laser sheet generated by a dual beam laser system (Litron LDY304-PIV, Nd:YLF) in conjunction with spherical and cylindrical lenses. A high-speed camera (Imager Pro HS4M) equipped with 180 mm lens was installed underneath the test section to capture PIV images at a framing rate of 300 frames per second. Each image covers an area of 70.46 mm × 70.46 mm, with 2056 × 2056 pixels. Over 2700 pairs of images were captured in each plane to ensure the convergence of the turbulent kinetic energy dissipation and production.

3 Results and Discussions

Since each pair of actuators is identical to another, it is expected that the drag variation is the same behind each pair of actuators when all actuators are operated simultaneously. Therefore, our results are presented only the second or middle actuator pair. In Fig. 2, the local wall shear stress τ_w downstream of the actuators is estimated from the streamwise velocity gradient in the viscous sublayer and the drag change $\Delta c_f = (\tau_{won} - \tau_{woff})/\tau_{woff}$ (where subscripts on and off denote with and without control, respectively). Through integrating the hotwire-measured Δc_f in both *z*- and *x*-directions, the estimated drag reduction over an area of 90 mm × 200 mm behind the plasma actuators agrees reasonably well with the measurement by a force balance [3], which may resolve the friction drag change up to the order of 10^{-4} N, and reaches 14% at a V_a of 4.25 kV. It is worth pointing out that the drag reduction may increase for a higher V_a. Figure 2a shows that the local drag reduction is non-uniform along the z-direction. The downstream variation in Δc_f is examined at three typical locations in Fig. 2a, i.e., the maximum drag increase region (R1), the maximum drag decrease region (R2) and the drag reduction plateau region (R3) which is between the actuator pair. At $x^+ = 167$ and $z^+ = 133$ (R1), the drag reduction is as high as 55%, due to the fact that the upwash side of the plasma-generated streamwise vortices pushes the near-wall low-speed fluid away

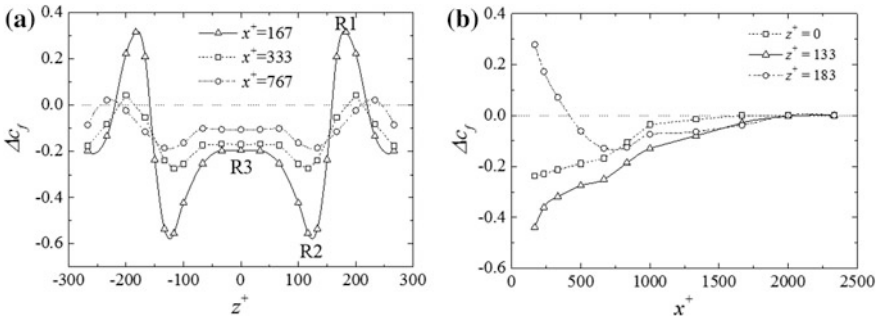

Fig. 2 **a** Spanwise distribution of Δc_f at $x^+ = 167$, 333, 767 downstream of an actuator pair. **b** Streamwise distribution of Δc_f at $z^+ = 0$, 133, 183 downstream of an actuator pair. Control parameters: $V_a = 4.25$ kV, $f = 11$ kHz

from the wall. On the other hand, the R1 occurs on the downwash side of the plasma-generated streamwise vortices due to the entrainment of high speed fluid in the near wall region. At R3, there is about 19% drag reduction; the corresponding turbulent kinetic energy (TKE) production is considerably reduced, as shown in Fig. 3b. The result seems consistent with the observation that the velocity streaks appear stabilized as evident from the flow visualization images captured at $y^+ = 24$ (not shown).

The Δc_f of R2 and R3 is initially significantly negative and resumes gradually to the value of the natural state with increasing x^+ (Fig. 2b) due to the weakened plasma-generated streamwise vortices when advected downstream. Yet Δc_f measured at $z^+ = 183$ drops from a level appreciably positive to negative before approaching the natural state. It is also noteworthy that there is no overshoot after Δc_f reaching zero beyond $x^+ = 2000$.

The dissipation and production of TKE is closely associated with drag reduction in TBL since TKE is an essential element to sustain near-wall turbulence [4]. Figure 3a shows the distribution of $\overline{(du^+/dy^+)^2}$ in the wall-normal direction, extracted from the PIV data. It has been established that this quantity may account for nearly 80% of the total TKE dissipation in the near wall region [5]. Without control, this quantity coincides well with the DNS data obtained in a turbulent channel flow by Antonia et al. [5]. Under control, the $\overline{(du^+/dy^+)^2}$ deviates slightly from that without control at all three z^+ locations.

The maximum TKE production is 0.3 at $y^+ \approx 14$ without control and is larger than that of the controlled case at all three z^+ locations (Fig. 3b). The maximum TKE production is reduced, compared to 0.3, by about 34% at $z^+ = 133$, which corresponds to the largest local drag reduction but by only 10% at $z^+ = 183$, where the positive Δc_f occurs (Fig. 2a). It is noteworthy that the location of the maximum TKE production changes when the control is applied. For instance, at $z^+ = 133$, the maximum TKE production occurs at $y^+ = 18$, due to the upwash of the plasma-generated streamwise vortices but shifts toward the wall at $z^+ = 183$ due to

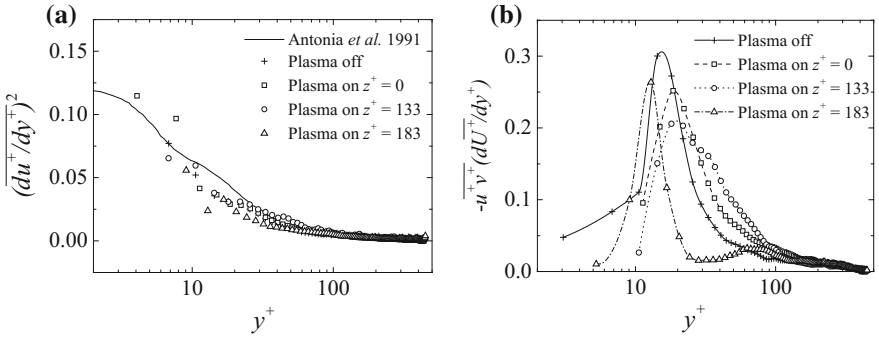

Fig. 3 Variation of **a** $\overline{(du^+/dy^+)^2}$ and **b** $-\overline{u^+v^+}(d\overline{U^+}/dy^+)$ with y^+ (at $x^+ = 167$). Control parameters: $V_a = 4.25$ kV, $f = 11$ kHz

the downwash of the plasma-generated streamwise vortices. One scenario is proposed. The plasma-generated streamwise vortices interact with the TBL, interrupting the turbulence generation cycle, and causing the TKE production to be decreased though not affecting much the TKE dissipation. As a result, the near-wall streaky structures are stabilized, which is consistent with the observed drag reduction.

4 Conclusions

(1) The present investigation demonstrates that the DBD plasma actuators are effective to reduce the skin-friction drag over a flat-plate TBL. At $V_a = 4.25$ kV applied on the actuators, a drag reduction of 14% is achieved over the control area (90 × 200 mm or 600 × 1333 wall units) behind plasma actuators. The percentage drag reduction could be increased further given a higher V_a [3].

(2) The decreased TKE production under the plasma control points to that the plasma-generated streamwise vortices may have altered the near-wall coherent structures and hence the turbulence generation cycle, causing a considerable decrease in the TKE production, though affecting little the TKE dissipation in distinct contrast to the observation made in Bai et al. [6]. As a result, the near-wall streaky structures are stabilized, which is fully consistent with the observed drag reduction.

Acknowledgements C. W. Wong wishes to acknowledge support by the National Natural Science Foundation of China through grant 11502060 and from the Research Grants Council of the Shenzhen Government through grants JCYJ20160531193045101 and JCYJ20150513151706565.

References

1. Choi KS, Jukes T, Whalley RD (2011) Turbulent boundary-layer control with plasma actuators. Philos Trans R Soc A 369:1443–1458
2. Whalley RD, Choi KS (2014) Turbulent boundary-layer control with plasma spanwise travelling waves. Exp Fluids 55:1–16
3. Wong CW, Zhou Y, Li YZ, Zhang BF (2015) Skin friction drag reduction based on plasma-induced streamwise vortices. In: Fluid–structure-sound interactions and control. Springer, Berlin, Heidelberg, pp 139–144
4. Suzuki Y, Kasagi N (1994) Turbulent drag reduction mechanism above a riblet surface. AIAA J 32:1781–1790
5. Antonia RA, Kim J, Browne LWB (1991) Some characteristics of small-scale turbulence in a turbulent duct flow. J Fluid Mech 233:369–388
6. Bai HL, Zhou Y, Zhang WG, Xu SJ, Wang Y, Antonia RA (2014) Active control of a turbulent boundary layer based on local surface perturbation. J Fluid Mech 750:316–354

Interaction Between Water or Air-Water Bubble Flow and Tube Bundle—Effects of Arrangement of Tube Bundle and Void Fraction

Toshihiko Shakouchi, Takeshi Kitamura, Koichi Tsujimoto and Toshitake Ando

Abstract Water or air-water bubble flow passing through tube bundle can be seen in many industrial equipments such as heat exchanger and chemical equipment. In addition, tube bundle can be used as a flow-straightener, -mixer, -resistor, and -damping device. In this study, the effects of tube arrangement of equally or unequally spaced in-line and staggered tube bundle and of void fraction on the flow characteristics such as flow pattern and flow resistance of a tube or tube bundle are examined experimentally.

Keywords Tube bundle · Effects of tube arrangement · Water or air-water bubble flow · Flow resistance

1 Introduction

Tube bundle is used widely in many industrial fields such as heat exchanger, chemical equipment, flow-straightener, -mixer, -resistor and -damping device. There are many studies on the improvement of performance but almost all are for equally spaced tube bundle [1, 2]. It is expected that using the tube bundle with an unequal interval the flow and heat transfer characteristics are changed and the performance will be improved. Shakouchi et al. [3] studied the flow and heat transfer of gas-liquid flow passing through a single row tube bundle with unequal interval tube pitch and showed the heat transfer efficiency of an uneaqul interval could be enhanced.

In this study, the effects of tube arrangement of equally or unequally spaced in-line and staggered tube bundle and of void fraction on the flow characteristics are examined by flow visualization using tracer method, velocity measurement by

T. Shakouchi (✉) · T. Kitamura · K. Tsujimoto · T. Ando
Graduate School of Engineering, Mie University, Kurimamachiya-cho 1577, Tsu-shi, Mie 514-8507, Japan
e-mail: shako@mach.mie-u.ac.jp

Y. Zhou et al. (eds.), *Fluid-Structure-Sound Interactions and Control*, Lecture Notes in Mechanical Engineering,
https://doi.org/10.1007/978-981-10-7542-1_17

Particle Image Velocimetry, PIV, and the flow resistance of a tube and tube bundle are also examined by pressure measurement.

2 Experimental Apparatus and Procedure

Figure 1 shows the schematic diagram of experimental apparatus, test section. The test section is made of transparent acrylic resin plate and is set vertically. The width, depth and length of the test section are $D = 90.0$, $H = 45.0$, and $L = 1{,}520$ mm, respectively. The tube bundle is consisted of 5 rows and 9 lines of tube of diameter $d = 15.0$ mm. The pitch of tube is equal interval of $p/d = 1.5$, and unequal interval of $p/d = 1.33$, 1.17 which were realized by moving odd numbered rows.

Water or air-water bubble flow introduces into the test section from the bottom after passing through the inlet flow passage with an enough length. The volumetric flow rate of water or air can be adjusted using flow meter and valve (Fig. 2).

A tube has a pressure hole of diameter 0.8 mm at the half depth and which can be rotated around its own axis. Then the pressure around the tube can be measured. The pressure loss Δp_{tl} of the tube bundle was measured by the pressure holes which were located on the middle depth of the side wall of the trst section at the up- and down-stream of distance $5d$ and $27d$ from the first row, respectively.

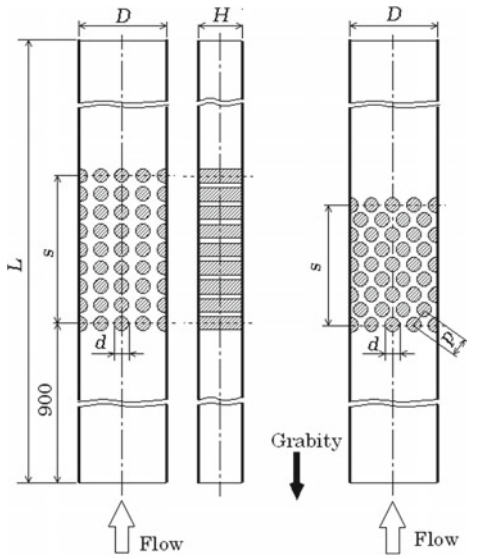

D : width of flow passage, = 90.0mm
H : depth of flow passage, = 45.0mm
d : tube diameter, =15.0 mm
L : length of test section, =1520mm
p : pitch of tube
= 22.5 (p/d=1.5), 20.0 (1.33), 17.5 mm (1.17)
s : length of tube bundle
= 180 mm (in-line)
= 156 mm (staggered)

Re: Reynolds number, $=Ud/\nu = (1.5\sim7.5)\times10^3$
U : mean inlet water velocity
α: apparent void fraction, =0~15%

Fig. 1 Test section (tube bundle)

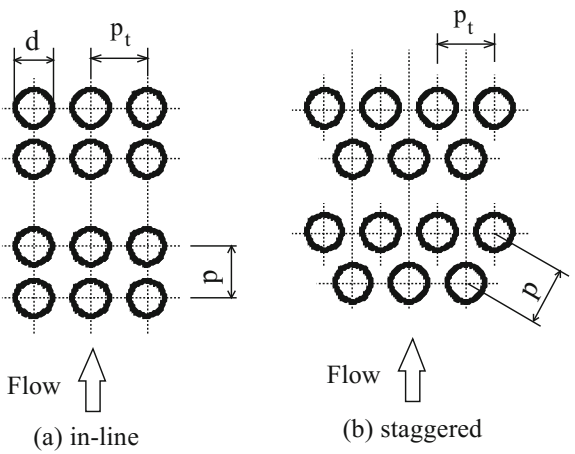

Fig. 2 Arrangement of tube bundle

The visualized flow pattern by a Tracer method was photographed by a high speed video camera. The velocity distribution was measured by Particle Image Velocimetry, PIV, and pressure was measures by pressure hole of diameter 0.8 mm and liquid column manometer or semi-conductor type pressure transducer.

3 Results and Discussions

3.1 Flow Pattern and Velocity Distribution

Figure 3 shows an example of the visualized flow pattern around the 1st to 2nd rows of staggered tube bundle with equal interval of $p/d = 1.5$ where are in the center region of the test section and velocity distribution around the 1st and 2nd

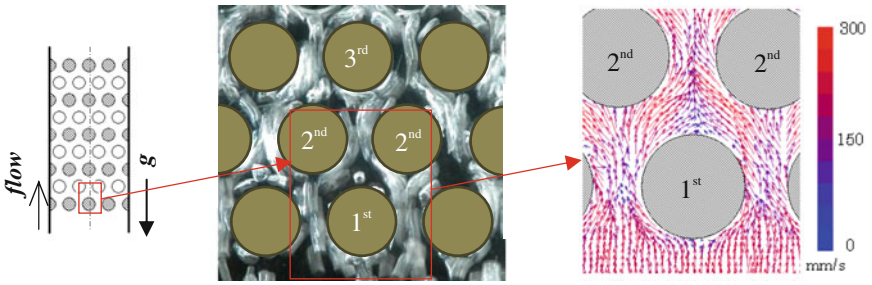

(a) p/d=1.5 (b) Visualized flow pattern (c) Velocity vector of bubble

Fig. 3 Flow pattern and velocity distribution of staggered tube bundle under equal interval of $p/d = 1.50$, $Re = 1.5 \times 10^3$, and $\alpha = 5.0\%$ [**b** shutter speed: 1/60 s., **c** PIV using 96 photos taken by 1/240 frs. with 1/1000 s.]

tubes measured by PIV. The white part in the figure are path of air bubbles. The mean bubble size is $d_b \approx 2.5$ mm. Behind the 1st row tube there is a wake region and bubbles collide near the stagnation points of 1st and 2nd row tubes. The flow pattern for unequal interval of $p/d = 1.17$ was largely different with the equal interval of $p/d = 1.5$. The flow seemed to be hard to flow between the 1st and 2nd row tubes.

3.2 Flow Resistance of Tube and Tube Bundle

3.2.1 Drag of Tube

Figures 4a shows the drag Dr of the center tube for the in-line, $Re = 5.0 \times 10^3$, and $\alpha = 0\%$. Dr was obtained from the pressure distribution around the tube. For equal interval of $p/d = 1.5$ the 1st tube has a large value, but after the 3rd tube Dr increases a little to the downstream. But, for unequal interval of $p/d = 1.33$, 1.17, Dr of the even numbered tube is smaller than the tube just before because it is in the wake region of the tube just before. Figure 4b is the results for staggered array. Dr for $p/d = 1.17$ fluctuates much larger than the in-line array. For bubble flow of $\alpha = 5.0\%$ of the in-line and staggered arrays, Dr for each p/d showed almost the same change although the value was a little different.

3.2.2 Pressure Loss ΔP_{tl} of Tube Bundle

Figure 5a, b show the pressure loss ΔP_{tl} of the tube bundle of the in-line array for Re and α, respectively. For $\alpha = 0\%$, ΔP_{tl} increases with Re rapidly and is almost the same regardless of p/d. But, for the bubble flow ΔP_{tl} of $p/d = 1.17$ becomes a smaller than the others. For example, at $\alpha = 0$, 10% for $p/d = 1.17$ it is smaller about 10, 8% than the others, respectively.

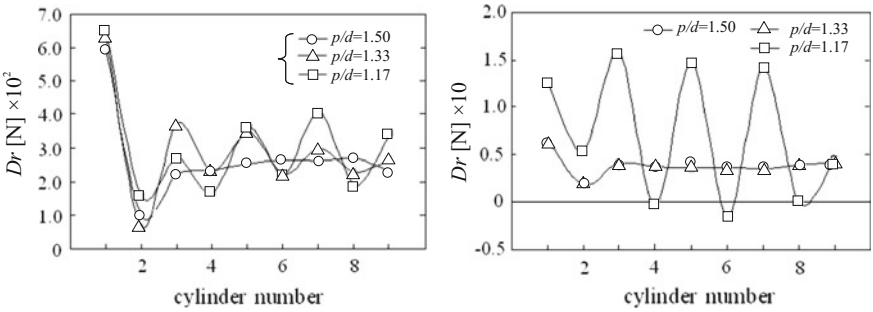

Fig. 4 Drag of center tube, $Re = 5.0 \times 10^3$, $\alpha = 0\%$

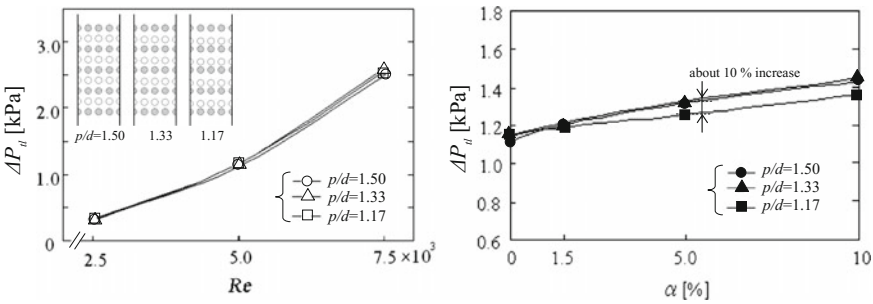

(a) $\alpha = 0$ % (b) $Re = 5.0 \times 10^3$

Fig. 5 Pressure loss Δp_{tl} of tube bundle (in-line)

Figure 6a, b show ΔP_{tl} of the staggered for Re and α, respectively. ΔP_{tl} increases with Re and the $p/d = 1.17$ is much larger than the others. For example, at $Re = (5.0–7.5) \times 10^3$ it is about twice of the others. ΔP_{tl} for bubble flow at $Re = 5.0 \times 10^3$ is almost constant for $\alpha = 0–10.0\%$, but the $p/d = 1.17$ is about twice of the others.

3.3 Flow Fluctuation

Figure 7 is the power spectral density of the pressure fluctuation at the center between the 2nd and 3rd tubes for the staggered, $Re = 5.0 \times 10^3$, $\alpha = 5.0\%$. Two dominant frequencies of $f_d = 1.0$ and 2.0 Hz are appeared. For $\alpha = 0\%$, the 2nd dominant frequency of $f_d = 2.0$ Hz did not appear.

For the in-line and $\alpha = 0\%$, two dominat frequency of $f_d = 1.0$ and 3.0 Hz, and for $\alpha = 5.0\%$ two f_d of 1.0 and 2.0 are appeared. The fluctuation characteristics are different by the arrangement of tube bundle and void fraction.

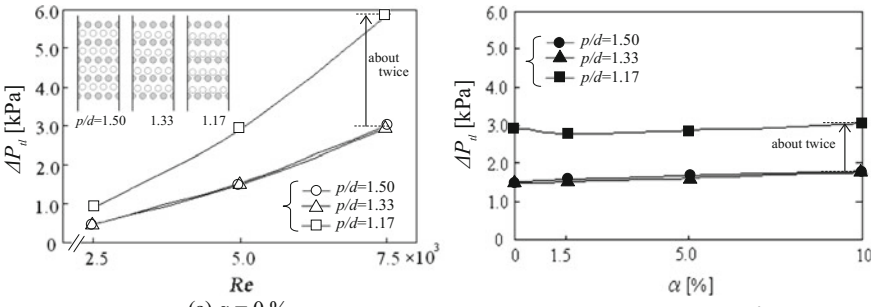

(a) $\alpha = 0$ % (b) $Re = 5.0 \times 10^3$

Fig. 6 Pressure loss of tube bundle (staggerd)

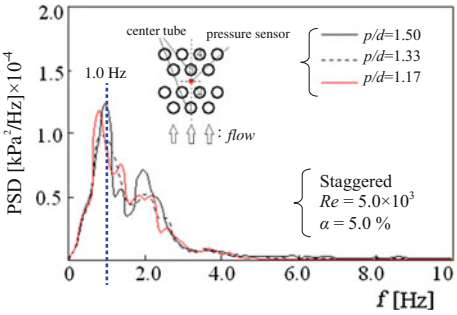

Fig. 7 Pressure fluctuation between 2nd and 3rd tube

4 Conclusions

In this study, the effects of tube arrangement with an equal or unequal interval of the tube bundle and of void fraction on the flow characteristics were examined.

The pressure loss ΔP_{tl} of the tube bundle for the in-line and $\alpha = 0\%$ was independent of p/d, but for bubble flow of $Re = 5.0 \times 10^3$ the $p/d = 1.17$ was about 10% smaller ΔP_{tl} than the others. ΔP_{tl} for the staggered of $p/d = 1.17$ was about twice of the others. The dominat frequency of flow fluctuation was in the range of $f_d = 1.0$–3.0 Hz, and the fluctuation characteristics were different by the arrangement of tube bundle and void fraction.

References

1. Buyruk E (1999) Heat transfer and flow structures around circular cylinders in cross-flow. J Eng Environ Sci 23:299–315
2. Noghrehkar GR et al (1999) Investigation of two-phase flow regimes in tube bundles under cross flow conditions. Int J Multiph Flow 25(5):857–874
3. Shakouchi T et al (2010) Flow and heat transfer of gas-liquid two-phase flow through a single row tube bundle (effects of unequal space pipe pitch arrangement). Jpn J Multiph Flow 23 (5):555–561

Longitudinal Vortex Wind Turbine: Effect of the Blade Lengths

W. Hemsuwan, K. Sakamoto and T. Takahashi

Abstract The longitudinal vortex wind turbine (LV-WT) is a novel propeller type, but the turbine blade is the circular cylinder. The blade is driven by lift force of the longitudinal vortex (LV). This work is to examine a simple single-cylinder blade to suppress the negative driving-force portion by cutting and keeping only the useful area. Unsteady Reynolds-Averaged Navier-Stokes (URANS) simulation is used for investigation. For the original single blade, the positive driving force was generated around the dominance of the LV at the crossing section. Meanwhile, the negative driving force appears far from the ring regime. When the original blade is diminished to avoid the unpleasant parts, the negative regions are suppressed completely. The distribution of the aerodynamic forces along the blade length is symmetric for the length extended equally. Final, the equally extended blade with the length of three times of the ring width is built and tested in the wind tunnel. The tendency of the experimental data and the CFD results correlate very well.

Keywords Wind turbine · Circular cylinder propeller · Longitudinal vortex Longitudinal vortex induced steady lift force · Wake

W. Hemsuwan
Graduate School of Engineering, Nagaoka University of Technology, Nagaoka, Niigata, Japan

K. Sakamoto
Department of Science of Technology Innovation, Nagaoka University of Technology, Nagaoka, Niigata, Japan

T. Takahashi (✉)
Department of Mechanical Engineering, Nagaoka University of Technology, Nagaoka, Niigata, Japan
e-mail: ttaka@nagaokaut.ac.jp

Y. Zhou et al. (eds.), *Fluid-Structure-Sound Interactions and Control*, Lecture Notes in Mechanical Engineering,
https://doi.org/10.1007/978-981-10-7542-1_18

1 Introduction

A newly developed innovative wind/water turbine (WT) with the circular cylinder blades driven by the longitudinal vortex has been firstly presented by [3] that was called the "*longitudinal vortex wind/water turbine: LV-WT.*" Two major components of this turbine are the circular cylinder blades and a ring-shaped plate. The photograph and schematic diagrams of this system are shown in Fig. 1. The ring plate is located behind the cylinder by retaining a suitable gap between them. The longitudinal vortex (LV) is generated at the crisscross region of the ring regime, but it is not stably existing. However, once the cylinder moves along the ring plate, the LV stably exists at the backside of the cylinder and moves with the cylinder. The driving lift force is produced steadily due to the aerodynamic effect of the LV. The mechanical structure of the LV-WT system is very simple compared with the Magnus WT, which is driven by the Magnus force of the spinning cylinders that are powered by the built-in motors for employing the Magnus effect [1] and the extra energy for spinning is also required. Whereas, it is unneeded for the LV-WT.

In this study, the original single blade will be investigated in order to avoid the negative portion. The effect of the blade lengths will be examined by using the URANS simulation.

2 Numerical Modeling

In order to investigate the effect of the blade lengths on the performance of the LV-WT, the original single cylinder blade in Fig. 1b is divided into the two blades. The parameters of the blade extension ratios l_1/W and l_2/W shown in Fig. 1c are accomplished using the URANS simulation with the moving mesh model. The numerical region is divided into the two domains, an inner circular domain and an outer rectangular domain. The inner domain encloses the cylinder blades which is defined as the moving zone, while the outer domain contains the ring plate, the tunnel walls, the inlet and outlet which is defined as the stationary. The 3D

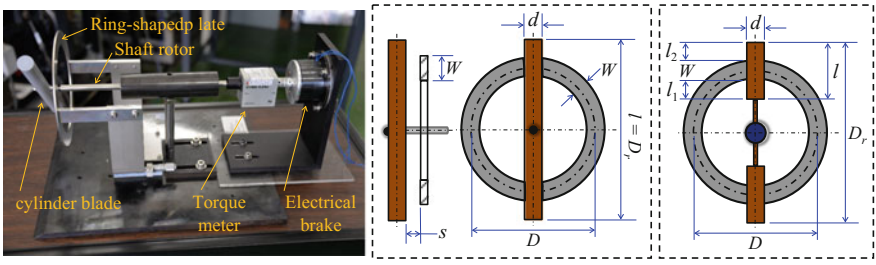

(a) Photograph of experimental apparatus (b) Single cylinder blade WT (c) Two cylinder-blades WT

Fig. 1 Photograph of experimental system and schematic diagram of the LV-WT system

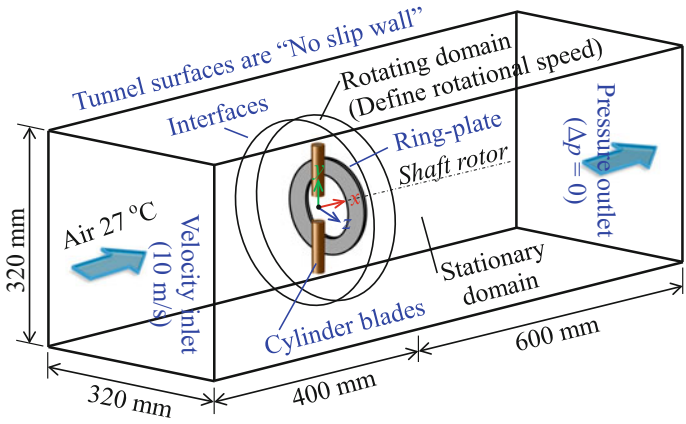

Fig. 2 Schematic diagram of numerical domains and boundary conditions setup

unstructured mesh is calculated by ANSYS-CFX 18.0 based on finite volume method. Figure 2 shows the summary of the CFD domains and boundary condition types. The validations of the mesh resolution and the turbulence model used *SST k-ω* for this calculation had been reported in the previous study [3].

All calculations are performed for the two blades LV-WT system with the free velocity $U_\infty = 10$ m/s (Re = 1.272×10^4 based on the cylinder blade diameter). The cylinder blade diameter $d = 20$ mm, the center diameter of the ring plate $D = 155$ mm, the ratio of the ring width to the blade diameter $W/d = 1$, the gap distance normalized by the blade diameter $s/d = 0.35$, and the tip speed ratio base on the length of the single cylinder blade ($l = 220$ mm) $\lambda = 0.5\omega l/U_\infty = 0.2$. The blade extension ratios l_1/W and l_2/W are varied.

3 Results and Discussion

Flow field around the cylinder blade will be visualized for understanding the aerodynamic driving force. Distribution of the fluid force along the blade length is evaluated to find the effective area in the blade. The best length for the high performance in the experimental investigation in our wind tunnel instrument will be examined, and the CFD results will be compared with the experimental data.

3.1 Flow Visualization

Figure 3 shows instantaneous flow fields around of the cylinder blade on a plane perpendicular to the cylinder axis at the middle of the ring width. The streamline

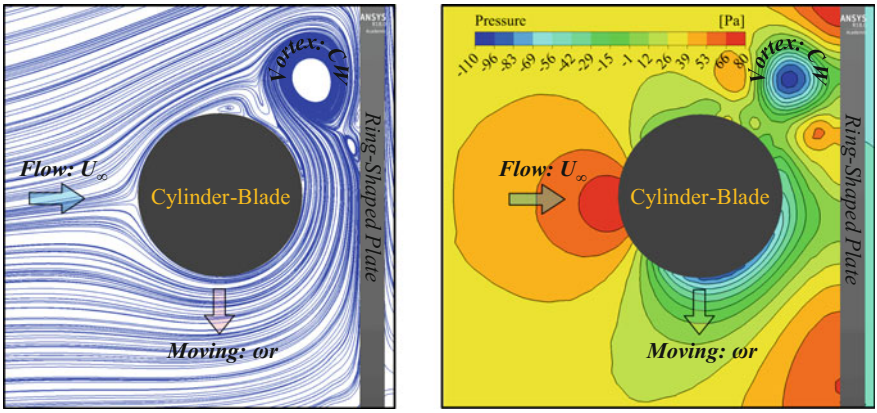

Fig. 3 Instantaneous flow visualizations of the single blade WT on cross section of the cylinder at the middle of the ring width; streamlines visualization (left) and pressure contour (right)

visualization displays a vortex (LV) behind the cylinder blade and locates between the ring plate. The vortex has the rotation direction of $\boldsymbol{Flow} \times \boldsymbol{Motion}_{\boldsymbol{cylinder}}$ (CW for this case) and appears along the cylinder length, but limited by the ring regime. The acceleration flow is found on the moving side due to the strong suction flow of the LV. The net lift force is produced in the moving direction due to the difference of pressure gradient on the cylinder surface that is the aerodynamic effects of this vortex. Outside of the LV regime is the subcritical flow, the disturbance of the wake behind the cylinder bluff body produces the drag force, the steady lift cannot be generated in this region, and it will reduce the performance of the turbine.

3.2 Force Distributions Along the Cylinder-Blade Length

The distribution of the aerodynamic force acting on the cylinder surface along the blade length is evaluated to examine the effective length of the blade. One of the cylinder blades is split into the very short segments with an equally lengthwise of $\Delta l = 0.02d$, the forces acting on each segment are evaluated by integrating the stress acting on their cylindrical surface. The components of the force coefficients on the small sectional blade i are given by; $C_{t,i} = F_{t,i}/0.5\rho A_i {U_\infty}^2$ and $C_{a,i} = F_{a,i}/0.5\rho A_i {U_\infty}^2$. Where, $F_{a,i} = F_{x,i}$ is the force in the axial direction of the rotor shaft, and $F_{t,i} = M_{x,i}/r_i$ is the force in the tangential direction of the rotor plane at rotor radius r_i. When, $M_{x,i}$ is the summation moment due to pressure and stress force, and $A_i = d\Delta l$ is the frontal area of the cylindrical segment.

The tangential and axial force coefficients; $C_{t,i}$ and $C_{a,i}$ of the small blade elements are plotted along the normalized blade length r/R as shown in Fig. 4. For the original single-blade, the values of C_t and C_a near the origin ($r/R = 0$) are similar to the subcritical flow over a stationary cylinder that is the time-averaged of $C_t = C_l =$

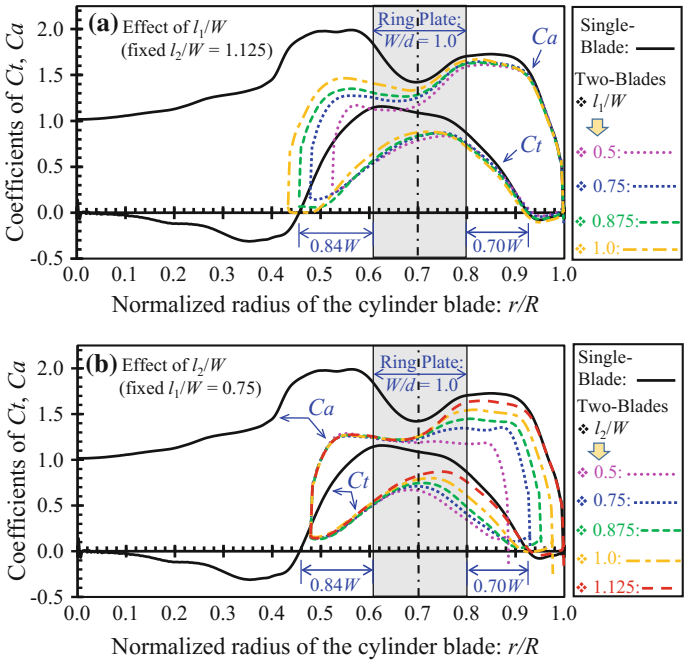

Fig. 4 Distribution of force coefficients C_t and C_a along the cylinder blade length; **a** effect of parameter l_1/W (fixed $l_2/W = 1.125$), **b** effect of parameter l_2/W (fixed $l_1/W = 0.75$)

0 and $C_a = C_d \approx 1.2$ [2]. The negative driving force appears at about $r/R = 0.1$–0.45 as seen in the distribution of C_t. This region is the subcritical flow exterior LV regime where the effective drag is produced but the steady lift cannot be generate. In this case, the negative C_t is the projected net drag from the line of attack of the relative velocity through the tangential direction of the rotor plane. The incline angle of the line of attack is zero at the origin and increases through the blade tip. Therefore, the C_t is zero at the root and strongly reduces into the negative values where increasing radius. Near the crossing region (LV regime), the positive driving force is generated by resulting of the LV (Fig. 3), and decreases again near the tip tends to be the negative values when the top length is extended reach to the external flow (subcritical region).

The negative region of the original blade is suppressed by keeping only the useful portions. Figure 4a shows the effect of the inside blade length ratio l_1/W by fixing the tip length equals the original blade ($l_2/W = 1.125$). At the blade top, magnitudes of the C_t and C_a almost match with the original single blade and lower than the original at the inner portion. The tendency of C_t comes to be negative values at the bottom when increasing l_1/W. The positive inner length of $l_1/W = 0.75$ is employed to study the top length effect l_2/W and shown in Fig. 4b. The C_t and C_a of the increasing tip length are higher than the shorter length. The effect of the tip vortex is powerful for cutting the inner portion. However, the symmetrical

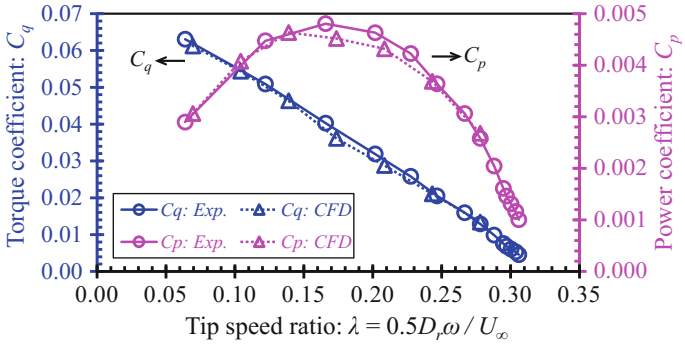

Fig. 5 Comparison between CFD results and experiment data for the $l_1/W = l_2/W = 1$ ($l = 3$ W)

distribution appears on the equally blade extension and the efficiency based on swept area is higher than the single cylinder blade system.

The equally blade extension $l_1/W = l_2/W = 1$ is selected to build for the wind tunnel investigation. The two cylinder-blades are fixed with a hub and a shaft which is connected to the torque meter 0.2 N m UMT II and the electrical brake HB0.5 N m. The torque T and the rotational speed ω of the rotor shaft are measured by the torque meter, while the electrical brake applies a load on the shaft for adjusting the ω. The experimental platform system (Fig. 1) is examined in a low turbulence intensity wind tunnel (0.6% at $U_\infty \geq 2$ m/s and 0.3% for $U_\infty \geq 11.2$ m/s) which has the test section of 0.32 m × 0.32 m × 1 m and the velocity range of 0.5–40 m/s. The ring-type anemometer is set upstream for measuring the U_∞. Both the CFD and experiment are tested for $U_\infty = 10$ m/s, the rotational speed is controlled and varied, and the predicting torque coefficient $C_q = T/0.5\rho R A_r {U_\infty}^2$ is used for comparison. Where $A_r = \pi({D_r}^2 - (D_r - 2l)^2)/4$ is the rotor swept area, $R = D/2$ is the radius of the ring. Power coefficient $C_p = T\omega/0.5\rho A_r {U_\infty}^3$ is estimated and reported in Fig. 5. The tendencies of the C_p and C_q against λ from both the CFD and experimental predictions correlate very well with a small difference. The torque is linearly decreased when increasing tip speed ratio, the maximum power coefficient $C_p \approx 0.005$ at around $\lambda = 0.15$–0.2 in both the experiment and calculation.

4 Conclusions

Flow around the simple single-cylinder blade LV-WT is investigated numerically, with a focus on the effective area of the blade to suppress the negative portions. The results are following:

1. The single cylinder blade, the flow visualization shows the mechanism of the steady lift force generation that is produced by the suction flow of the LV. The positive driving force is generated around the crossing area where is the LV

regime, and outlying regions are the subcritical flow that the negative driving force is produced.
2. The negative region is suppressed by keeping only the useful portions, but the driving force near both tip ends are lower than the original case due to the tip effect. The equally blade extension of $l_1 = l_2 = W$ is selected and built for the wind tunnel and computational investigations. The experimental and numerical predictions have a good agreement of the value and tendency. The effect of the free ends will be investigated in the future in order to increase the efficiency of the system.

Acknowledgements This work was supported by MEXT KAKENHI grant number JP16685247.

References

1. Bychkov NM, Dovgal AV, Kozlov VV (2007) Magnus wind turbines as an alternative to the blade ones. J Phys Conf Ser 75(012004):1–7
2. Schlichting H, Gersten K (2000) Boundary-layer theory, 8th edn. Springer, Berlin, Germany
3. Takahashi T, Yoshitake Y, Sakamoto K, Hemsuwan W (2016) An innovative wind/water turbine with circular propeller driven by longitudinal vortex. In Proceeding of the 15th WWEC2016 TOKYO conference, Japan. PS-A-5

Quantitative Investigation on the Formation of Counter-Rotating Vortex Pairs from the Inclined Jet in Crossflow

C. Dai, Z. Shu and J. Mi

Abstract This study investigates by LES the formation and evolution of counter-rotating vortex pair (CRVP) from a streamwise-inclined 35° turbulent jet in a laminar crossflow (JICF). A new method is developed by which the JICF consists exclusively of a jet marked by artificial XH_2O and crossflow by real H_2O. Predictions by LES agree well with the experimental results of (Dai et al., Int J Heat Fluid Flow 58:11–18, 2016) [3]. It is shown that the flow patterns, visualized by the three-dimensional flow topologies, vary with the velocity ratio (*VR*) considerably. The hairpin vortices are illustrated to be actually the instantaneous forms of the time-averaged CRVP. Analysing the jet mass fraction distributions around the jet exit finds that the CRVP mainly comes from the coherent structures within the nozzle for $VR = 0.5$ and from the shear vortex at the jet/crossflow interface for $VR = 2.0$.

Keywords Jet · Crossflow · CRVP · XH_2O · LES

1 Introduction

The interaction of a jet with the oncoming crossflow, also known as JICF, exists extensively in nature and is highly important in many industrial applications, such as chimney flow, plume dispersions and film cooling in turbines. Due to its great importance for industry, a large number of experimental and numerical studies have been performed over the past decades. Detailed reviews can be referred to the article by Mahesh [6]. Bidan and Nikitopoulos [1] and Cambonie [2] considered the normal JICF at low VR values experimentally. However, the flow structures of an inclined JICF are very different, compared to the normal cases, where coherent structures developed in the inclined nozzle are not formed. Besides, previous

C. Dai · Z. Shu · J. Mi (✉)
Department of Energy & Resource Engineering, College of Engineering, Peking University, Beijing, People's Republic of China
e-mail: jmi@pku.edu.cn

Y. Zhou et al. (eds.), *Fluid-Structure-Sound Interactions and Control*, Lecture Notes in Mechanical Engineering,
https://doi.org/10.1007/978-981-10-7542-1_19

studies often used some separation method of variables to distinguish contributions from different sources to the origin of CRVP. For instance, [5] conducted three simulation cases to interpret how the jet-mainstream shear layer and the in-tube boundary layer together affect the formation of CRVP. Nevertheless, the JICF is commonly considered strongly coupling and nonlinear, any simple separation method of variables is unlikely to capture the real nature of this pattern. As a result, the formation and evolution of large-scale vortical structures of JICF, especially those counter-rotating vortex pairs (CRVPs), are still of much debate. Note that the RANS models have a poor prediction for the anisotropy JICF problem and DNS has the limitation of huge computational costs. So, the LES model is adopted using a new method, where the JICF consists exclusively of a jet marked by artificial XH2O and crossflow by real H2O, to investigate the formation and evolution of CRVP in JICF at various velocity ratios.

2 Apparatus and Procedures

2.1 Computational Details

The present LES is conducted within the same domain as in our previous study [3]. It is implemented in the commercial solver Ansys Fluent using a WALE Subgrid-scale model with second-order accuracy for both spatial and temporal discretization (spectral synthesizer method). Figure 1a shows the calculation domain whose inclined nozzle diameter $D = 10$ mm. After a mesh sensitivity validation, the whole mesh is structured and contained in total 4.2 million cells, of which the dimensionless distance $y^+ < 1.0$. The crossflow develops as it enters the main flow channel and forms a laminar approaching boundary layer. And its shape factor derived from the ratio of the boundary layer displacement thickness to the momentum thickness remains 2.3 at $X/D = -3.0$ in the symmetric plane at $Y/D = 0$. In order to quantify those contributions of the mainstream boundary layer, shear layer and the in-tube jet boundary layer to the formation of CRVP, a new simulation method is proposed by marking the jet by artificial XH_2O and the crossflow by real H_2O. The artificial XH_2O has the same physical properties as the real H_2O. The mass transfer process is governed by the species transport model with full multi-component diffusion. Three typical velocity ratios $VR = 0.5$, 1.0 and 2.0 are considered with the density ratio $\rho_j/\rho_\infty = 1$ and the Reynolds number $Re = 1712$ based on the jet diameter and free-stream velocity (constant 0.172 m/s); here $VR = \rho_j U_j / \rho_\infty U_\infty$, where ρ_j and ρ_∞ denote the jet and crossflow fluid densities while U_j and U_∞ denote the corresponding mean velocities, respectively. The time step varied from 1 ms at $VR = 0.5$–0.2 ms at $VR = 2.0$. Thousands of time steps are calculated to obtain sufficient data for convergent statistics, based on residuals of less than 10^{-6}. Details of other calculation settings can refer to [3].

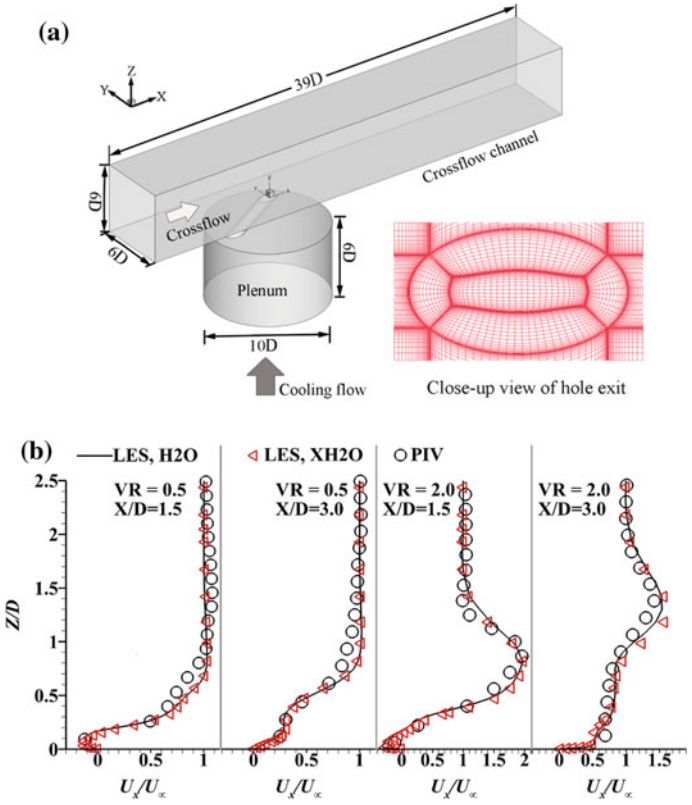

Fig. 1 **a** The computation domain for LES. The coordinates *X*, *Y* and *Z* correspond respectively to the streamwise, spanwise and vertical directions of the flow; **b** lateral profiles of the time-averaged velocity U_x normalized by U_∞ in the symmetric plane at $X/D = 1.5$ and 3.0 for $VR = 0.5$ and 2.0. Symbols: ——, H_2O; Δ, XH_2O; ○, PIV

2.2 Validation of the Modeling

Figure 1b shows lateral profiles of U_x/U_∞ from the present LES prediction and the PIV measurement of [3], for $VR = 0.5$ and 2.0 at $X/D = 1.5$ and 3.0 in the symmetric plane at $Y/D = 0$ of the JICF. Profiles for the case of jet marked by H_2O and that by XH_2O almost coincide. Evidently, the predicted velocities at most locations are within 6.9% of the measured values, validating the utilization of LES for the JICF. More specifically, however, some discrepancies (no more than 18.8%) exist in the shear layer and the boundary layer of the flow at different locations for both velocity ratios. This is not unexpected because the limitation of PIV often occurs in the shear layer and the near wall boundary layer region, where the bad particle tracing characteristic exists.

3 Results and Discussion

To visualize the vortical structures, the Δ-criterion method of vortex identification, firstly proposed by Dallmann [4], is used here. The present flow is incompressible and hence for the Δ-criterion, vortices are identified as flow regions with positive second invariant of the velocity gradient tensor, $\Delta P/\rho = \Omega_{ij}\Omega_{ij} - S_{ij}S_{ij} > 0$, where $\Omega_{ij} = (u_{i,j} - u_{j,i})/2$ denotes the rotation-rate tensor and $\Omega_{ij} = (u_{i,j} + u_{j,i})/2$ the stress tensor.

3.1 Effects of Velocity Ratios on Vortical Structures

Figure 2 shows the jet mass fraction (X_j) contours on the instantaneous iso-surfaces of $\Delta P/\rho = 100/s^2$ for $VR = 0.5$ (up) and $\Delta P/\rho = 200/s^2$ for $VR = 2.0$ (down), each at two time instants. Evidently, the unsteady large-scale vortical structures change drastically from $VR = 0.5$ to $VR = 2.0$. For the low velocity ratio, the hairpin vortices dominate the JICF with their head after their legs below $Z/D = 1.0$ throughout the flow field. As the velocity ratio rises to $VR = 2.0$, the canonical CRVP structures, marked as inverse hairpin vortex recover, with their head ahead of their legs below $Z/D = 2.5$ downstream from the nozzle exit. It need to be mentioned here that the hairpin vortex occurring for $VR = 0.5$–2.0 are actually responsible for the time-averaged CRVP as their instantaneous form is similar to the CRVP, which is illustrated in Fig. 3. Note that the horseshoe legs formed from the crossflow boundary layer, travel on both sides of the jet for $VR = 0.5$ while they pass through under the inverse hairpin vortex for $VR = 2.0$. This is caused by the suction of the low pressure region just downstream of the jet exit and the strong entrainment of the CRVP. Besides, it is observed that the hairpin vortices, denoted as A and B in Fig. 2, both break down a bit farther downstream of $X/D = 5.0$ for $VR = 0.5$ and 2.0.

3.2 Origins of CRVP at Different Velocity Ratios

Since it has been mentioned above that the hairpin vortex is the instantaneous form of the temporally averaged CRVP, we will focus on the formation and evolution of the hairpin vortex to investigate the origins of CRVP at different velocity ratios, through analyzing the jet mass fraction distributions near the jet exit.

Different from the conclusion by Mahesh [6] that the hairpin vortex is formed from the crossflow boundary layer separation when overwhelming the jet for the lower VR, the hairpin vortex is observed to come mainly from coherent structures generated within the inclined nozzle and in-tube boundary layer at the lateral side of the nozzle; the coherent structures form its head and the lateral counter-rotating

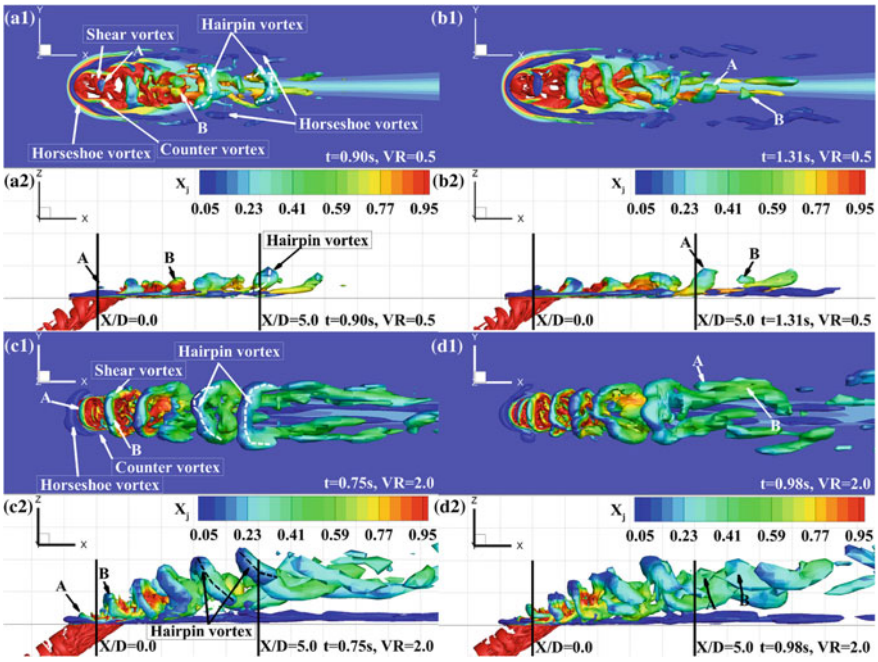

Fig. 2 Jet mass fraction (X_j) contours on the instantaneous iso-surfaces of $\Delta P/\rho = 100/s^2$ for $VR = 0.5$ and $\Delta P/\rho = 200/s^2$ for $VR = 2.0$ at different time instants

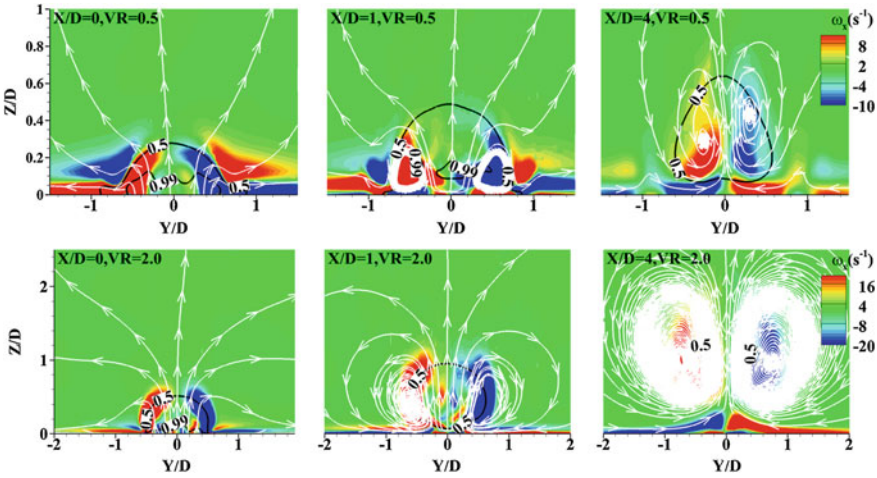

Fig. 3 Contours of time-averaged streamwise vorticity ω_x with the time-averaged streamtraces (white arrowhead lines) and time-averaged iso-curves of jet mass fraction (X_j) (black curves) for $VR = 0.5$ and $VR = 2.0$ in different YZ-planes at $X/D = 0$, 1 and 4

vortices develop its legs. As we can see in Fig. 3, the majority of the time-averaged streamwise vorticity ω_x is enveloped within the iso-curves of $X_j = 0.5$. The jet-crossflow shear layer just contributes a little to the formation of the hairpin vortex head, as the tip of the hairpin vortex comes out from the iso-surfaces of $X_j = 0.5$ at few positions downstream of the exit.

However, for the higher *VR*, the jet-crossflow shear layer becomes dominant in forming the CRVP. It can be seen from Fig. 3 that only a little part of the time-averaged streamwise vorticity contours are immersed within the iso-curves of $X_j = 0.5$, especially in the plane of X/D = 4. In fact, the coherent vortical structures from the inclined nozzle is detrimental to the formation of CRVP because the spanwise vorticity of the coherent structures is opposite to that of the jet-crossflow shear layer. A little further away from the exit but before X/D = 4, the coherent vortex is completely annexed by the shear vortex.

4 Conclusion

The present LES calculations have demonstrated that the unsteady large-scale vortical structures change drastically with different velocity ratios. For $VR = 0.5$–2.0, the hairpin vortex is observed to dominate the JICF and to be actually the instantaneous form of the time-averaged CRVP. The origin of the CRVP is different for the two values of *VR*. For $VR = 0.5$, the CRVP mainly results from the coherent structures within the nozzle while it derives mainly from the shear vortex at the jet/crossflow interface for $VR = 2.0$.

Acknowledgements The authors acknowledge the support of the National Key Research and Development Program of China (No. 2016YFB0600605).

References

1. Bidan G, Nikitopoulos DE (2013) On steady and pulsed low-blowing-ratio transverse jets. J Fluid Mech 714:393–433
2. Cambonie TAJ (2014) Transition scenario of the round jet in crossflow topology at low velocity ratios. Phys Fluids 26(8):084101. https://doi.org/10.1063/1.4891850
3. Dai C, Jia L, Zhang J, Shu Z, Mi J (2016) On the flow structure of an inclined jet in crossflow at low velocity ratios. Int J Heat Fluid Flow 58:11–18. https://doi.org/10.1016/j.ijheatfluidflow.2015.12.001
4. Dallmann U (1983) Topological structures of three-dimensional vortex flow separation. In: 16th fluid and plasmadynamics conference. Fluid dynamics and co-located conferences. American Institute of Aeronautics and Astronautics. https://doi.org/10.2514/6.1983-1735
5. Li H, Ghaly W, Hassan I (2016) The formation of counter-rotating vortex pair and the nature of liftoff-reattachment in film-cooling flow. Fluids 1(4):39. https://doi.org/10.3390/fluids1040039
6. Mahesh K (2013) The interaction of jets with crossflow. Annu Rev Fluid Mech 45(1):379–407. https://doi.org/10.1146/annurev-fluid-120710-101115

Measurement of Velocity Field of an Abrasive Fan Jet by PIV

Y. Oguma, G. Peng and S. Shimizu

Abstract Water jets issuing from a fan jet nozzle (Fan Jets: FJs) are widely used in cleaning, decontamination of radiological substances, and removal of plasma spray coating and asbestos. The material removal performance of abrasive suspension jets issuing from a fan jet nozzle (Abrasive Fan Jets: AFJs) are much higher than that of FJs. In the present study, flow structure and velocity distribution of AFJs are investigated by using PIV method to clarify the material removal characteristics of AFJs.

Keywords PIV · Water jetting technology · Flow visualization
Abrasive fan jet · Fan jet

1 Introduction

Water jets issuing from a fan jet nozzle (Fan Jets: FJs) are widely used in cleaning, decontamination of radiological substances, and removal of plasma spray coating and asbestos. The material removal performance of abrasive suspension jets issuing from a fan jet nozzle (Abrasive Fan Jets: AFJs) is much higher than that of FJs [1].

There are some reports on AFJ and FJ. Xu and Summers [2] and Shimizu et al. [3] have investigated the flow structure and erosion characteristics of FJs at a high injection pressure. Shimizu et al. [4] have investigated the flow structure of AFJ and FJ. Material removal characteristics of AFJ was related to the standoff distance and the traverse velocity. Particle image velocimetry (PIV) has been used to measure velocity distribuiton of FJs [5–7]. However, the velocity distribuiton of AFJs have not been clarified sufficiently.

Y. Oguma (✉) · G. Peng · S. Shimizu
Department of Mechanical Engineering, College of Engineering, Nihon University, 1, Nakagawara, Tokusada, Tamura-Machi, Koriyama, Fukushima 963-8642, Japan
e-mail: oguma-y@mech.ce.nihon-u.ac.jp

Y. Zhou et al. (eds.), *Fluid-Structure-Sound Interactions and Control*, Lecture Notes in Mechanical Engineering,
https://doi.org/10.1007/978-981-10-7542-1_20

In the present study, the flow structure and velocity distribuiton of AFJs are investigated by using PIV method to clarify the material removal characteristics of AFJs.

2 Experimental Apparsatus

As shown in Fig. 1, the FJ nozzle used in the present experiments has an elliptical outlet hole in a triangular notch on the outlet face. The major and minor axes of the nozzle are 1.37 and 0.72 mm, respectively. The equivalent diameter of nozzle is approximately $d_e = 1$ mm.

Figure 2 shows the experimental PIV system used to measure the velocity distributions of AFJs and FJs. AFJ and FJ are formed using an abrasive suspension jet (ASJ) system. Detailed information of the ASJ system used in this study can be found in a previous study by Shimizu et al. [8]. In the case of AFJ, a high-pressure slurry is generated in the mixing unit of the pressure vessel by discharging high pressure water and stirring up abrasive particles. High-pressure slurry is discharged from the nozzle head. In the cases of FJ, only water are filled in the pressure vessel. The injection pressures P_i are 10 MPa for both cases. Abrasive used in the experiments is garnet having a mesh designation of #220. Abrasive concentration and density of abrasive slurry are calculated from the measured volume and mass of slurry collected using a pipe catcher. Average abrasive concentration is 12.7 wt%. Density of average abrasive slurry is 1,078 kg/m^3 during observation of the AFJ. The velocity distribuitons of the AFJs and the FJs are measured using a high-speed CMOS camera and a laser light sheet system. Tracer particles, such as nylon particles, are not used in these measurements; instead, water droplets, lumps and abrasive particles are used as tracers. Observation area of the high-speed

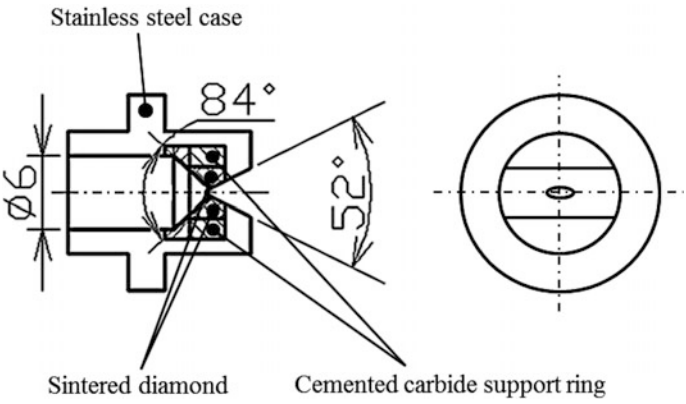

Fig. 1 Fan jet nozzle

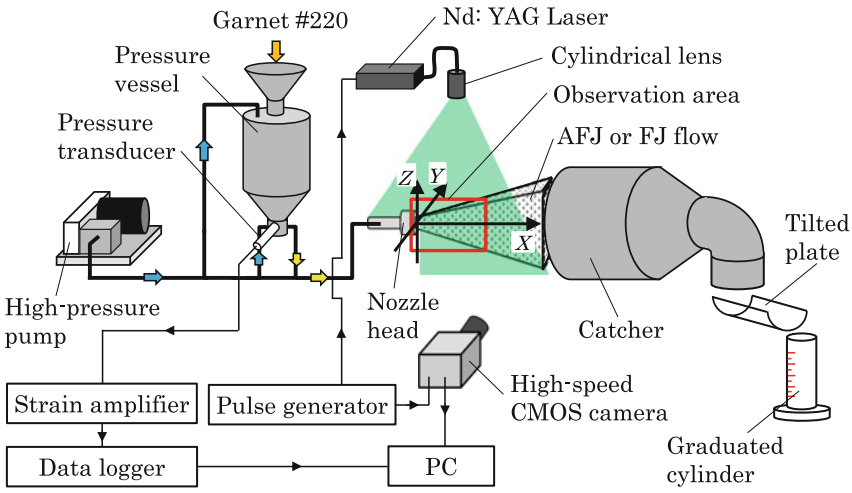

Fig. 2 Experimental setup

CMOS camera is in the region the near nozzle head (image area: 108 mm × 108 mm).

Origin of the coordinate system is on the nozzle outlet plane and *X*-, *Y*-, *Z*-axis are taken on the jet center axis, the nozzle minor axis, and the major axis, respectively. The instantaneous velocity component of *X*, *Y* and the *Z*-direction is designated by *u*, *v*, *w* respectively. A laser light sheet with a thickness of approximately 2 mm is used to illuminate the jet cross-section vertical to the *XY*-plane along the *X*-axis.

3 Results and Discussion

3.1 Instantaneous Visualization and Velocity Distributions

Figure 3 shows the instantaneous images and velocity distributions of (a) AFJ and (b) FJ. Irregular reticulated structures are observed from nozzle exit to the region further downstream of AFJ and FJ. In the case of AFJ, the reticulated pattern appears to be dominated by the *Z*-directional structures. In the case of FJ, the irregular reticulated structure pattern appears to be dominated by the *X*-directional structures. The magnitude of instantaneous velocity is defined by $V = (u^2 + w^2)^{1/2}$. The velocity vectors of AFJ and FJ are nearly constant in *Z*-direction.

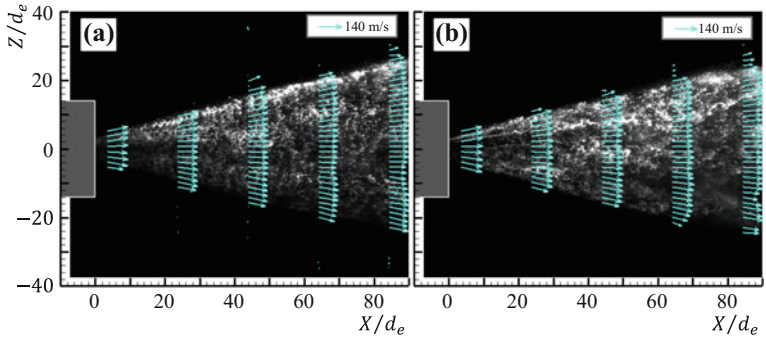

Fig. 3 Instantaneous visualization images and velocity distribuitons: **a** AFJ, **b** FJ

3.2 Time Average Velocity and Velocity Fluctuation Distribuitons

Figure 4a, b show the time-averaged velocity and the root-mean-square of velocity fluctuation distribuitons normalized by the theoretical jet velocity V_{th} at different locations along the X/d_e-axis. The theoretical issuing velocity V_{th} is calculated by Bernoulli's equation using injection pressure and the fluid density (water or abrasive slurry). The theoretical jet velocity V_{th} of the AFJ and the FJ are 137 m/s and 141 m/s respectively. The time average velocity distributions are obtained in the upper side of the AFJ and the FJ ($Z/d_e = 0-40$) because liquid droplets and abrasive particles are clearly observed at this area.

Generally the non-dimensional time averaged velocity distributions $\bar{u}/V_{th}$ and $\bar{w}/V_{th}$ of the AFJ are almost the same as the those of FJ. In the central part of the jets, the time averaged velocities $\bar{u}/V_{th}$ remain nearly constant with varying Z/d_e. The time averaged velocities $\bar{w}/V_{th}$ are largest at the outer edge of the jets and reach maximums of approximately 0.2. The non-dimensional velocity fluctuation distributions u_{rms}/V_{th} and w_{rms}/V_{th} of the AFJ are almost the same as the those of FJ. The velocity fluctuation distributions u_{rms}/V_{th} and w_{rms}/V_{th} near the outer edge of the jet are large, but are small in the central part of the jets.

It is known that velocity fluctuation also differs when the flow structure is different. However, instantaneous visualization image of AFJ and FJ in the Fig. 3 show completely different flow structures mutually. In the past research, fractal analysis was used to evaluate flow structure of FJ [9]. Fractal analysis quantitatively evaluates flow structure. Evaluation of the flow structure of AFJ and FJ by this fractal analysis will be the future subjects.

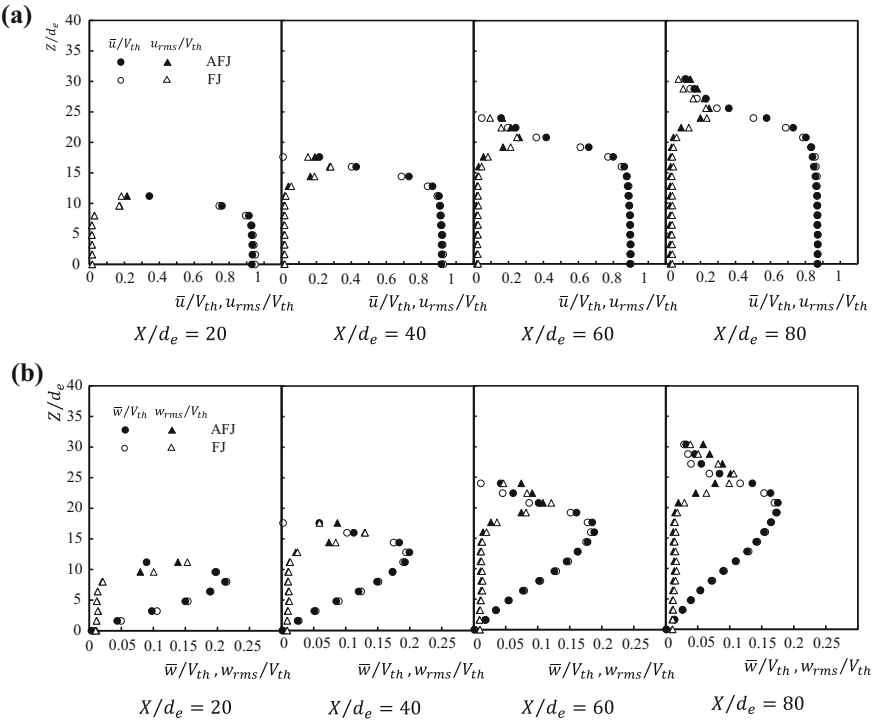

Fig. 4 Distribuitons of dimensionless time averaged velocity components and velocity fluctuation: **a** $\bar{u}/V_{th}$, u_{rms}/V_{th} and **b** $\bar{w}/V_{th}$, w_{rms}/V_{th} at different standoffs

4 Conclusions

In this study, flow structure and velocity distribuiton of an AFJ have been investigated using PIV method to clarify the material removal characteristics of AFJ. The main conclusions are given as follows.

1. The flow patterns of AFJ and FJ are different. Particularly, in the case of AFJ, irregular reticulated structures are observed at the nozzle exit.
2. The normalized velocity ($\bar{u}/V_{th}$ and $\bar{w}/V_{th}$) and velocity fluctuation (u_{rms}/V_{th} and w_{rms}/V_{th}) of AFJ shows almost the same as those of FJ.

References

1. Shimizu S, Suzuki T, Peng G (2014) Material removal characteristics of an abrasive fan jet. Water Jetting, BHR Group, pp 215–221

2. Xu J, Summers DA (1994) Experimental evaluation of the performance of fan jet systems. Jetting Technology, Mechanical Engineering Pub, pp 37–46
3. Shimizu S, Kato H, Liang D, Kido M. (2004) Flow structure and erosive characteristics of water jet issuing from a fan jet nozzle. J Jet Flow Eng 21(3):4–10 (in Japanese)
4. Shimizu S, Ito H, Hori S, Peng G (2012) Abrasive suspension jet issuing from a fan jet nozzle. Water Jetting, BHR Group, pp 395–403
5. Ding L, Shimizu S, Kido M (2003) Removal of plasma sprayed ceramic coatings by plain water jets. In: Proceedings of 7th Pacific Rim international conference on water jetting technology, pp 413–420
6. Fujisawa N, Yamagata T, Hayashi K, Takano T (2012) Experiments on liquid droplet impingement erosion by high-speed spray. Nucl Eng Des 250:101–107
7. Oguma Y, Peng G, Shimizu S (2017) Evaluation of velocity field of water fan jet by PIV. J Jet Flow Eng 33(1):10–18. (in Japanese)
8. Shimizu S, Sagami S, Peng G, Kakizaki T (2009) Experimental abrasive suspension jet system for rescue operation. J Jet Flow Eng 26(2):11–16 (in Japanese)
9. Sawamura T (2005) Study on analysis of fan-type water jet structure by fractal dimension. J Jet Flow Eng 22(3):21–26 (in Japanese)

Effect of Micro-bubbles on a Turbulent Boundary Layer

H. L. Cao, W. Guo, X. H. Li and Y. Zhou

Abstract Micro-bubble is one of the most promising methods for reduction of skin friction drag. The injection of gas bubbles into a turbulent boundary layer may have multiple impacts on the turbulent flow structure. This work aims to understand the interaction between micro-bubbles and the turbulent boundary layer, especially the effect of the bubble layer thickness on the skin-friction drag reduction. Large eddy simulation was conducted for a turbulent boundary layer over a flat plate, injected with micro-bubbles, with a view to reduce skin-friction drag. The Reynolds number Re_θ examined was 1430 based on the momentum thickness θ and free-stream velocity U_∞. A three-dimensional perturbation method was deployed to generate a turbulent boundary layer within a short distance of inflow.

Keywords Large-eddy simulation · Microbubble drag reduction
Boundary layer

1 Introduction

The use of micro-bubble as a way to reduce skin friction in turbulent flows has been a focus for researchers in the expectation that which is applicable to ships. Previous experimental work has shown it can reduce the skin friction by as much as 80% [5, 7]. Ferrante and Elghobashi [2, 3] reported their direct numerical simulation study to explain the mechanisms of drag reduction in a microbubble-laden spatially developing turbulent boundary layer, and also the Reynolds effect on drag reduction. Our objective in the present paper is to further explain the interaction between micro-bubbles and the turbulent boundary layer, especially the effect of the micro-bubble layer thickness on the skin-friction drag reduction.

H. L. Cao (✉) · W. Guo · X. H. Li · Y. Zhou
Shenzhen Graduate School, Harbin Institute of Technology, Shenzhen, China
e-mail: caohualilmy@163.com

Y. Zhou et al. (eds.), *Fluid-Structure-Sound Interactions and Control*, Lecture Notes in Mechanical Engineering,
https://doi.org/10.1007/978-981-10-7542-1_21

2 Simulation Method

It is well understood that the inner layer of the turbulent boundary layer has low speed streaks, while the outer layer has large scale coherent structures. In order to reproduce turbulent flow numerically, here we follow Sandham et al. [6] method, in which the streamwise and wall-normal fluctuations were generated with one mode in the inner region and three modes in the outer region. Disturbances in the inner region (denoted as $\hat{u}^{\text{inner}}$) represents lifted streaks, with a peak at a location of $y^+_{p,j}$, while the outer region disturbances (denoted as $\hat{u}^{\text{outer}}$) represent three-dimensional vortices. The disturbances can be written as follows:

$$\hat{u}^{\text{inner}} = c_{1,0} y^+ e^{-y^+/y^+_{p,0}} \sin(\omega_0 t)\ \cos(\beta_0 z + \varphi_0) \tag{1}$$

$$\hat{v}^{\text{inner}} = c_{2,0} (y^+)^2 e^{-(y^+/y^+_{p,0})^2} \sin(\omega_0 t)\ \cos(\beta_0 z + \varphi_0) \tag{2}$$

$$\hat{u}^{\text{outer}} = \sum_{j=1}^{3} c_{1,j} y/y_{p,j} e^{-y/y_{p,j}} \sin(\omega_j t)\ \cos(\beta_j z + \varphi_j) \tag{3}$$

$$\hat{v}^{\text{outer}} = \sum_{j=1}^{3} c_{2,j} (y/y_{p,j})^2 e^{-(y/y_{p,j})^2} \sin(\omega_j t) \cos(\beta_j z + \varphi_j) \tag{4}$$

where subscripts $j = 0, 1, 2, 3$ are mode indices, y^+ is the y^- coordinate in wall units and the $c_{i,j}$ are constants. Forcing frequencies are denoted by ω_j, spanwise wave numbers by β_j, and phase shiftes by φ_j.

Figure 1 shows a schematic of the turbulent boundary flow over a flat plate. The large-eddy simulation (LES) used presently is applied to a computational domain of $10\delta \times 3\delta \times 3\delta$ (δ is the turbulent boundary thickness) with a grid of 148 × 90 × 90 points, uniformly distributed in the streamwise and spanwise directions and stretched in the wall-normal direction (Fig. 1b). The grid resolution for inflow is approximately $\Delta x^+ = 38$ and $\Delta z^+ = 18$ with 10 points in the viscous sublayer ($y^+_{\min} = 0.61$). Superscript + denotes normalization by wall units, e.g. $U^+ = U/u_\tau$ and $y^+ = y u_\tau/\upsilon$, where U is the streamwise mean velocity, u_τ is the wall friction velocity and υ is the kinematic viscosity of fluid. At the lower wall, a no-slip condition was used for the velocity components, and at the upper surface, a free-slip boundary condition was applied. Periodic boundary conditions were used in the spanwise direction.

Figure 2 shows the comparison for the mean streamwise velocity $< U >^+$ and three Reynolds stresses $< u'^2 >^+$, $< v'^2 >^+$ and $< u'v' >^+$ at $x = 9\delta$, where $Re_\theta = 1430$. In this paper, $< >$ represents spatial averaging in the spanwise (z) direction in addition to time averaging of the enclosed quantity. The mean velocity profile is in good agreement with experimental profile obtained by Degraaff and

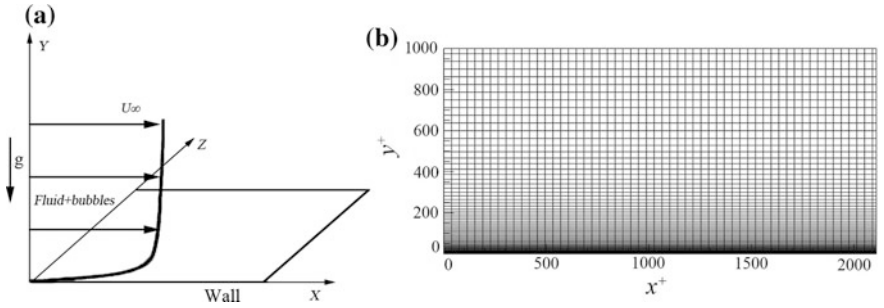

Fig. 1 **a** Schematic of turbulent boundary layer flow over a flat plate **b** typical computational grid

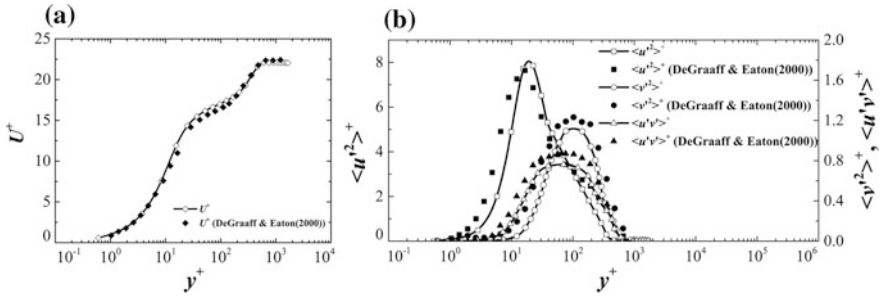

Fig. 2 Comparison between the LES simulation and measurements at $x = 9\delta$: **a** the streamwise mean velocity; **b** Reynolds stresses, at $Re_\theta = 1430$

Eaton at the same Re_θ [1]. The difference in the magnitude of the peak of $< v'^2 >^+$ and $< u'v' >^+$ is probably due to experimental uncertainty. Degraaff and Eaton [1] indicate a 10% error in the measured value of $< u'v' >^+$. The results provide a validation for the single-phase simulation.

Then, the micro-bubbles are introduced at the inlet along with the fluid through the wall. The bubbly air-liquid flows are treated by Mixture model. The size of micro-bubble is 40 μm. Two parameters are investigated, i.e. the inlet air volume fraction $\Phi_{v,in}$ and micro-bubble layer thickness h^+ (micro-bubble layer thickness along with y-direction (Fig. 1a)).

3 Results and Discussion

The effect of micro-bubbles may depend on whether the turbulent boundary layer is on the lower or upper side of the plate. This work is focused on the turbulent boundary layer over the lower side. Given $\Phi_{v,in} = 0.1$, the ratio C_f/C_{f0} from calculation and measurement [4] are 0.855 and 0.857, respectively, where C_f and C_{f0}

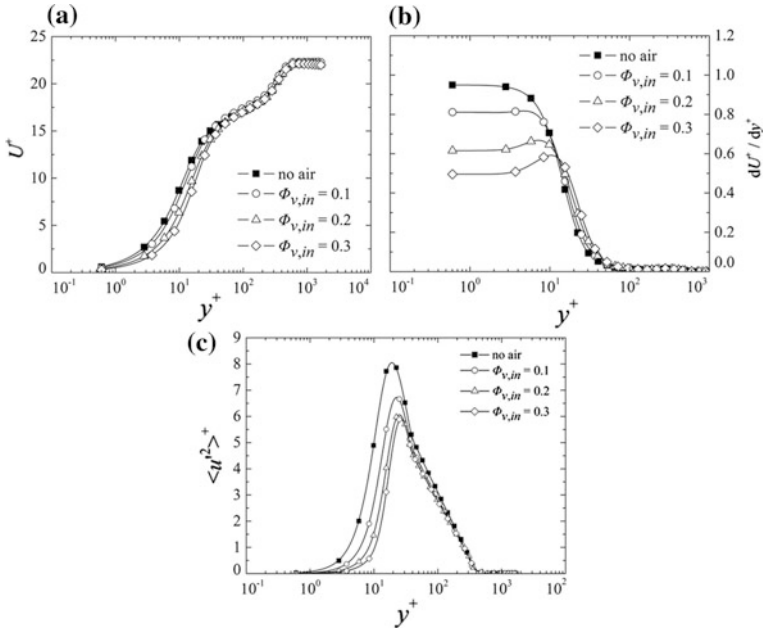

Fig. 3 **a** Mean streamwise velocity; **b** mean streamwise velocity gradient; **c** Reynolds stress at $x = 9\delta$

are the skin-friction coefficients with and without the presence of micro-bubbles. As $\Phi_{v,in}$ increases from 0.1 to 0.3, the average drag reduction increases from 14.5 to 48.6%. Figure 3 shows the profiles of U^+, dU^+/dy^+ and $<u'^2>^+$ for different $\Phi_{v,in}$. The effect of the micro-bubbles is appreciable for $y^+ \leq 10$. The dU^+/dy^+ decreases significantly (Fig. 3b) with the increase in $\Phi_{v,in}$, implying a drag reduction. The viscous layer grows gradually in thickness with an upward shift of the buffer layer, resulting from the rising bubbles which distribute themselves within the boundary layer. There is a marked decrease in $<u'^2>^+$ (Fig. 3c) for $y^+ \leq 20$ and the peak is shifted slightly away from the wall. It has been observed based on the instantaneous vorticity ω_x contours in the (y, z) plane (now shown) that the streamwise vortical structures are dislocated from the wall due to the presence of the micro-bubbles. Furthermore, the spanwise separation between streaky structures is increased.

The effect of h^+ on the drag reduction is investigated, in which five h^+ values are chosen, i.e., 10, 50, 200, 560 and 850. Figure 4 shows profiles of the mean volume fraction and volume fraction gradient of micro-bubble distribution along the vertical direction at $x = 9\delta$. We can find that the concentration of microbubbles at

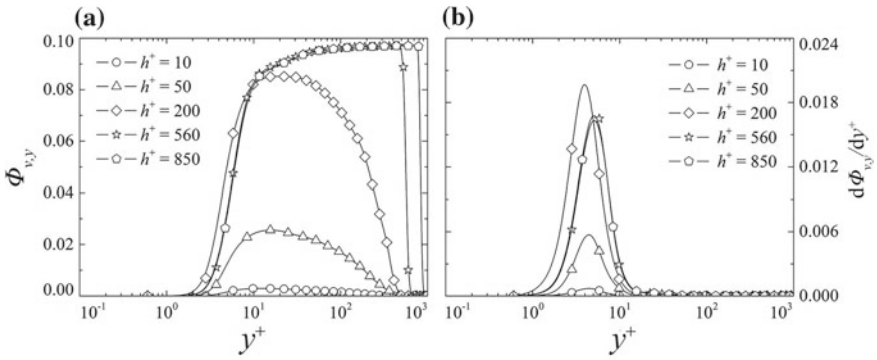

(a) The average volume fraction of micro-bubble; (b) The volume fraction gradient of micro-bubble;

Fig. 4 Profiles of the distribution along the vertical direction at $x = 9\delta$

the near wall region becomes smaller with the increasing of micro-bubble layer thickness h, which is not beneficial to drag reduction. When the micro-bubble was injected into the boundary layer, the large scale vortical structure broke into small scale structure and the vorticity also decreased (Fig. 5a, b). It has been found that, when h^+ is less than 560 (corresponding to the boundary layer thickness), the average volume fraction of bubbles along the x direction decreases and the ability to retain bubbles on the wall is unstable. On the other hand, for $h^+ = 560$ and 850, the thick micro-bubble layer is rather stable; so the bubble layer that is attached to the wall, which is beneficial to drag reduction.

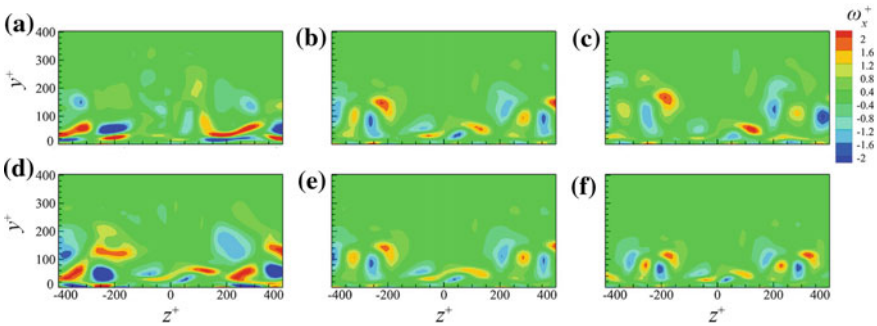

(a) No air; (b) $h^+ = 10$; (c) $h^+ = 50$;(d) $h^+ = 200$;(e) $h^+ = 560$;(f) $h^+ = 850$

Fig. 5 Instantaneous streamwise vorticity at $x = 9\delta$ in y-z plane

4 Conclusion

This study shows that the presence of micro-bubbles acts to decrease the streamwise mean velocity near the wall and to push away the streamwise vortical structures from the wall, thus producing drag reduction. The drag reduction is strongly dependent on the micro-bubble layer thickness h^+. The result shows that the optimum micro-bubble layer thickness is $h^+ = 560$, which corresponds to the boundary layer thickness.

Acknowledgements Financial support by Scientific Research Fund of Shenzhen Government through grant JCYJ20160531192108351 is gratefully acknowledged.

References

1. Degraaff DB, Eaton JK (2000) Reynolds-number scaling of the flat-plate turbulent boundary layer. J Fluid Mech 422:319–346
2. Ferrante A, Elahobashi S (2004) On the physical mechanisms of drag reduction in a spatially developing turbulent boundary layer laden with microbubbles. J Fluid Mech 503:345–355
3. Ferrante A, Elahobashi S (2005) Reynolds number effect on drag reduction in a microbubble-laden spatially developing turbulent boundary layer. J Fluid Mech 543:93–106
4. Madavan NK, Deutsch S, Merkle CL (1983) Reduction of turbulent skin friction by microbubbles. Tech Memorandum 10:1–38
5. Merkle CL, Deutsch S (1992) Microbubble drag reduction in liquid turbulent boundary layers. Appl Mech Rev 45(3):103–127
6. Sandham ND, Yao YF, Lawal AA (2003) Large-eddy simulation of transonic turbulent flow over a bump. Int J Heat Fluid Flow 24(4):584–595
7. Sanders WC, Winkel EW, Dowling DR, Perlin M, Ceccio SL (2006) Bubble friction drag reduction in a high Reynolds number flat plate turbulent boundary layer. J Fluid Mech 552:353–380

Numerical Simulations on Film Cooling Effectiveness from Two Staggered Rows of Coolant Jets

Z. Shu, C. Dai and J. Mi

Abstract This paper reports numerical simulations of the film cooling performance and flow structure from two staggered rows of coolant jets. The RANS modeling is conducted for the cases that are validated by and matched to the measurements of Sinha et al. (J Turbomach 113:442, 1991) [8]. The cooling effectiveness of two rows of jets is calculated for blowing ratios of 0.5 and 1.0. It is found that the interaction of counter-rotating vortex pairs (CRVPs) generated by two rows of jets enhances the cooling effectiveness significantly. Moreover, the calculations quantify the contribution from each row of coolant jets to the overall cooling performance and find that the second row makes more contribution than does the first row.

Keywords Jet in crossflow · Film cooling · RANS

1 Introduction

The modern gas turbine engines operate at extremely high temperature to improve efficiency. Often, the achievable temperature exceeds the metallurgical limit of the turbine blades' material, urgently requiring for effective blade cooling technique. As one of the most common and widely used techniques, film cooling has been investigated both experimentally [8, 9] and numerically [3, 4, 7] over half a century. The simple configurations cannot meet the demand as the cooling effectiveness decreases gradually downstream due to jet lift-off and mixing with hot freestream. Therefore, several studies were conducted with complex configurations of holes, such as sister holes proposed by Ely and Jubran [2] and two rows of holes investigated by Jung and Hennecke [6].

Z. Shu · C. Dai · J. Mi (✉)
Department of Energy & Resource Engineering, College of Engineering, Peking University, Beijing, China
e-mail: jmi@pku.edu.cn

Y. Zhou et al. (eds.), *Fluid-Structure-Sound Interactions and Control*, Lecture Notes in Mechanical Engineering,
https://doi.org/10.1007/978-981-10-7542-1_22

The previous studies have not yet investigated the process of interaction and also not quantified the contribution of each row of holes. The present work is to fill the deficit. A novel numerical method developed by Dai et al. [1] is applied to quantify contribution from each row to the overall cooling performance with a two staggered rows of coolant jets. In that method, the working fluids from various sources are marked by different artificial fluids with identical physical properties.

2 Computational Details

The work of Sinha et al. [8] is taken as the benchmark for the present work. The schematic of film cooling geometry and the boundary condition are provided in Fig. 1a, b. The streamwise, spanwise and vertical coordinates are denoted by X, Y and Z, respectively, with their origin at the jet exit center of side hole in the first row. The computational domain extends from freestream to two staggered rows of holes and two coolant plenums. The holes, each with diameter of $D = 12.7$ mm and length of $1.75D$, are inclined at 35° to the XY-plane. The ratios $P/D = 3.0$ and $S/D = 10.0$, where P = pitch and S = spacing. The velocity and temperature of freestream are 20 m/s and 300 K. The coolant temperature is 250 K to satisfy the constant density ratio of $DR = 1.2$. By varying the coolant velocity, we simulate the cases at blowing ratios of $M = 0.5$ and 1.0, where $M = DR(V_c/V)$. The Reynolds-Averaged Navier-Stokes (RANS) equations are solved with Ansys Fluent. The realizable k–ε model combined with the SIMPLEC algorithm are used to predict the film cooling effectiveness, while the QUICK solution scheme is applied to improve the calculation accuracy. Furthermore, to quantify contributions of the coolant jets from the first and second rows to the cooling effectiveness, a novel newly-developed simulation method is applied. The working fluid from the freestream and the first-row and second-row jets are marked, respectively, by real material air, artificial material air-row1 and air-row2. The artificial materials have the same physical properties as the real air. The cooling performance is mainly focused on the adiabatic effectiveness defined by

$$\eta = (T_\infty - T_{aw})/(T_\infty - T_c) \tag{1}$$

where T, T_c, and T_{aw} are the temperatures of the freestream, coolant jets and adiabatic wall. The laterally averaged film cooling effectiveness $\bar{\eta}$ is calculated by integrating the cooling effectiveness along Y-direction of the wall, defined by

$$\bar{\eta} = \frac{1}{6\mathrm{D}} \int_0^{6\mathrm{D}} \eta(\mathrm{X}, \mathrm{Y}) \mathrm{dY}. \tag{2}$$

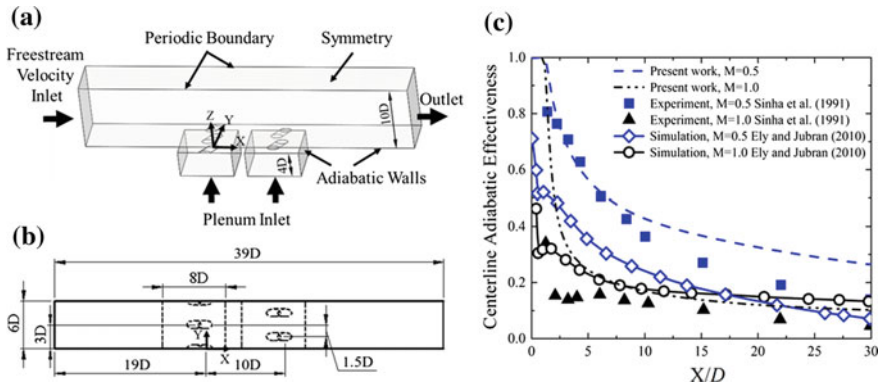

Fig. 1 Physical domain and boundary conditions: **a** 3-D, **b** top view; **c** Streamwise variation of the centerline adiabatic effectiveness

3 Results and Discussion

3.1 Validations

To validate the model setting of computation, Fig. 1c compares our predictions of the centerline adiabatic effectiveness η of a single row of holes for $M = 0.5$ and 1.0 with the measurements of Sinha et al. [8]. Displayed are also the predictions of Ely and Jubran [3]. Our numerical results agree reasonably well with the experimental data for the two cases, despite the overprediction occurring for $M = 1.0$ at all X and for $M = 0.5$ at $X > 8D$. The similar overprediction was found by Johnson et al. [5] and Khajehhasani and Jubran [7]. The reason is that the k–ε model of turbulence improperly uses the isotropic assumption of eddy diffusivity, see Johnson et al. [5]. Below, the interaction of jets from two staggered rows is investigated with the same settings.

3.2 Adiabatic Cooling Effectiveness

Figure 2a compares the streamwise variations of the lateral average of η for two rows of jets at $M = 0.5$ and 1.0. Evidently, the cooling effectiveness is higher for $M = 0.5$ than for $M = 1.0$ all the way at $X/D < 25$. It is also demonstrated that the cooling becomes more effective downstream from the second row ($X > 10D$) in both cases. Figure 2b shows distributions of local η to quantify the cooling performance in the whole adiabatic wall. For $M = 0.5$, the jets are closely attached to the wall and penetrate to the freestream. The cooling effectiveness drops gradually downstream as coolant mixes with hot freestream. For $M = 1.0$, as the flow proceeds downstream, the cooling effectiveness starts with a very low value near the

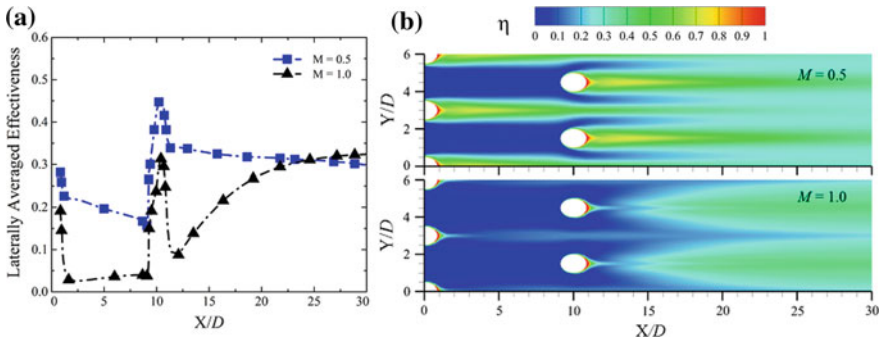

Fig. 2 Effectiveness of two row jets for $M = 0.5$ and 1.0: **a** streamwise variation of laterally averaged effectiveness; **b** contours of local adiabatic film cooling effectiveness

hole exit and then increases monotonically. The reason follows. As jets penetrate into the freestream, their lift-off occurs initially, due to high momentum. Consequently, almost no coolant touches and cools the surface. Farther downstream, the original lift-off coolant jets are reattached to the wall, thus increasing the cooling effectiveness. The effectiveness of $M = 1.0$ is even higher than that for $M = 0.5$ at $X > 25D$ because of larger coolant mass.

3.3 *Interaction of Two-Row Jets*

Figure 3 displays distributions of the streamwise vorticity together with streamlines at various locations for $M = 1.0$. The figure shows evolutions of counter-rotating vortex pairs (CRVPs) generated from the two rows of holes. As seen in Fig. 3c, d, the nearby CRVP of the first row is spinning in opposite direction, which pushes the CRVP of the second row closer to the wall. Besides, the gap of the second row of holes is filled by the coolant from the first row, then the CRVP of the second row entrains the relatively low temperature coolant instead of the hot freestream. Therefore, the entrainment of the CRVP make the coolant from both rows more uniform in lateral direction, see Fig. 4a and b. Here, X_{c1} and X_{c2} represent the coolant mass fractions from the first and second row, respectively. The lift-off and reattachment also can be observed. The reattachment occurs sufficiently downstream of both rows but is more pronounced downstream of the second row due to the interaction of jets. Figure 4c shows the total mass fraction of coolant X_c $(= X_{c1} + X_{c2})$ and local cooling effectiveness η. Since cooling effectiveness is closely related to the local mass fraction of coolant, η is almost identical with X_c. To quantify the contribution of each row, Fig. 4d displays the lateral distributions of $\eta_1 = X_{c1}/X_c\eta$ and $\eta_2 = X_{c2}/X_c\eta$, i.e., the cooling effectivenesses from the first and

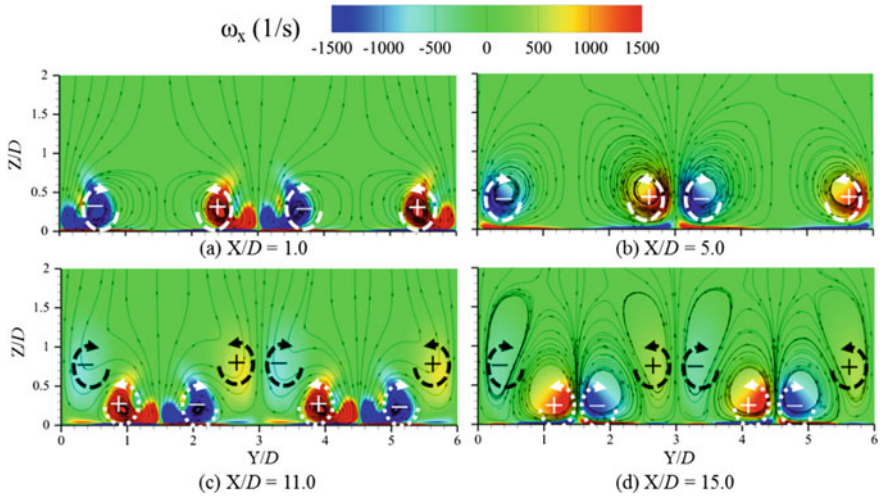

Fig. 3 Streamwise vorticity and streamline distribution for $M = 1.0$ at **a** $X/D = 1.0$, **b** $X/D = 5.0$, **c** $X/D = 11.0$ and **d** $X/D = 15.0$

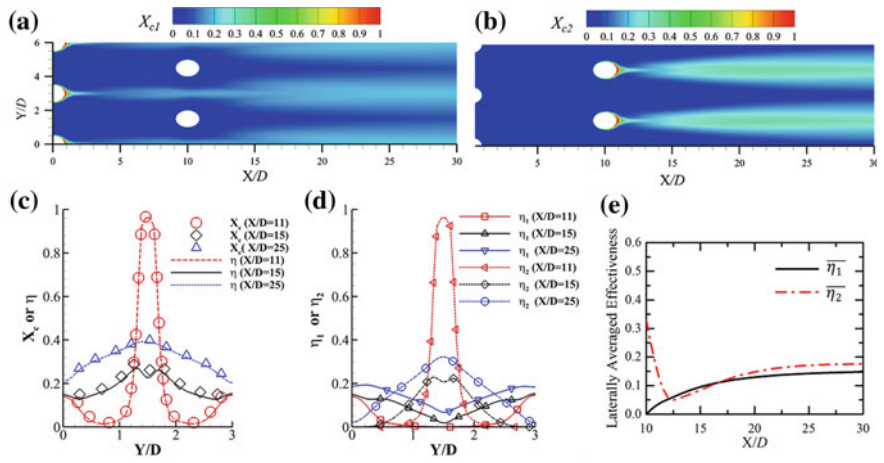

Fig. 4 Local mass fraction distributions of coolant from **a** the first row X_{c1} and **b** the second row X_{c2}. **c** Total mass fraction of coolant X_c and η at $X/D = 11$, 15 and 25. **d** Cooling effectiveness generated by coolant of the first row η_1 and that of the second row η_2 at $X/D = 11$, 15 and 25. **e** Laterally averaged cooling effectiveness of the first row $\overline{\eta_1}$ and the second row $\overline{\eta_2}$

second row, while Fig. 4e reports on the average cooling effectiveness $\overline{\eta_1}$ and $\overline{\eta_2}$ at different locations. Clearly, η_2 is much higher than η_1 downstream of the second row at $1D < Y < 2D$ but is lower at the sides of the hole exit. Generally, see Fig. 4e, the average contribution of the second row is greater than that of the first row.

4 Conclusion

This numerical work has investigated the film cooling performance and flow structure from two staggered rows of jets. The significant interaction of two rows results mainly from the entrainment between the CRVPs of two rows, making the coolant mass distribution more uniform laterally than the single row injection. By quantifying the contribution from each row to the overall cooling performance, the second row is found to make more contribution than does the first row.

Acknowledgements The support of National Key Research and Development Program of China (No.: 2016YFB0600605) is gratefully acknowledged.

References

1. Dai C, Shu Z, Mi J (2017) Quantitative investigation on the formation of counter-rotating vortex pairs from the inclined jet in crossflow. In: The 4th symposium on FSSIC-No. 112 (accepted)
2. Ely MJ, Jubran BA (2008) A numerical study on increasing film cooling effectiveness through the use of sister holes. In: ASME conference proceedings 2008, pp 341–350
3. Ely MJ, Jubran BA (2010) A parametric study on the effect of sister hole location on active film cooling flow control. ASME
4. Goldstein RJ, Eckert ERG, Burggraf F (1974) Effects of hole geometry and density on three-dimensional film cooling. Int J Heat Mass Transf 17:595–607
5. Johnson PL, Shyam V, Hah C (2011) Reynolds-averaged Navier-Stokes solutions to flat plate film cooling scenarios. Nasa/Tm
6. Jung K, Hennecke DK (2001) Curvature effects on film cooling with injection through two rows of holes. Tro-Mp-069(I) 069, 6 1–14
7. Khajehhasani S, Jubran BA (2014) Numerical assessment of the film cooling through novel sister-shaped single-hole schemes. Numer Heat Transf Part A: Appl 67:414–435
8. Sinha AK, Bogard DG, Crawford ME (1991) Film-cooling effectiveness downstream of a single row of holes with variable density ratio. J Turbomach 113:442
9. Yazid MH, Hamidon BS, Razali A (2015) An experiment investigation of film cooling effectiveness of sister hole of cylindrical shaped hole film cooling geometry on a flat plate surface, pp 3–7

Three-Dimensional Time-Averaged Flow Fields in the Turbulent Wake of a Surface-Mounted Finite-Height Square Prism

R. Chakravarty, N. Moazamigoodarzi, D. J. Bergstrom and D. Sumner

Abstract The wake of a three-dimensional (3D) time-averaged flow field over a surface-mounted finite-height square prism of aspect ratio AR = 3 at a Reynolds number Re = 500 has been investigated using Large Eddy Simulation (LES). The topological characteristics and interactions between the dynamic structures in the prism wake were assessed using planar streamlines and the second invariant vortex identification criterion. The shear layer from the prism free end, which descends into a pair of counter-rotating tip vortices due to downwash, is seen in the streamwise planes in the wake. Other features identified in the simulation include the mean recirculation zone behind the prism and a complex set of discrete streamwise vortex tubes in the wake.

Keywords Finite square prism · Wake · Second invariant · Streamlines Vortex structures

1 Introduction

The flow over surface-mounted finite-height square prisms has several industrial applications, including flows over buildings and chimneys. Studying these flows also serves to advance the understanding of turbulent bluff-body wakes. The wake flow configuration is dependent on the prism's aspect ratio (defined as AR = H/D where H and D represent the prism height and width, respectively), the boundary layer thickness (δ) on the ground plane, the incidence angle of the prism (α), and the Reynolds number (Re). While several studies have examined the planar mean flow topologies at higher Reynolds numbers and aspect ratios, fewer studies have focused on analyzing the complete 3D (three-dimensional) flow fields [1, 2], and an improved understanding of the vortex structures at lower Reynolds numbers is still

R. Chakravarty · N. Moazamigoodarzi · D. J. Bergstrom (✉) · D. Sumner
Department of Mechanical Engineering, University of Saskatchewan, Saskatoon, Canada
e-mail: don.bergstrom@usask.ca

Y. Zhou et al. (eds.), *Fluid-Structure-Sound Interactions and Control*, Lecture Notes in Mechanical Engineering,
https://doi.org/10.1007/978-981-10-7542-1_23

needed. This study examines the mean flow in the wake of a surface-mounted finite-height prism of AR = 3 at a lower Reynolds number of Re = 500, with the prism oriented at $\alpha = 0°$ using Large Eddy Simulation (LES).

2 Computational and Flow Visualization Methodologies

The filtered Navier-Stokes equations with a finite-volume discretization on a collocated grid were solved using the fractional-step method. An algebraic multigrid method was used to accelerate the solution of the pressure-correction equation. The subgrid-scale (SGS) stress terms were modeled using a localized Dynamic Smagorinsky Model. A structured, Cartesian grid with 128 × 144 × 96 control volumes in the x (freestream), y (spanwise) and z (transverse) directions, respectively, was used to discretize the flow domain. The prism was located approximately $3D$ from the inlet plane with a thin boundary layer inflow condition. The mean flow was computed over approximately 15 periods of the flow based on a Strouhal number of St = 0.12.

To resolve flow structures in a 3D field and to study their contribution to the overall flow dynamics, Chong et al. [3] identified a vortex as a region where the magnitude of the vorticity exceeds that of the strain-rate, i.e. regions showing positive values of the second invariant of the velocity gradient tensor, and called this parameter the Q-criterion or the second invariant. The second invariant successfully isolates regions of rotational vorticity in flows dominated by shear effects.

3 Results and Discussion

Figure 1 shows some important features of the mean flow field using x-vorticity contours in two vertical (y-z) planes in the prism wake (at $x/D = 2.5$ and 6.5) with the velocity vectors at its mid-height (i.e. $y/D = 1.5$). The figure shows the evolution of a pair of counter-rotating tip vortices in the upper part of the wake. Further downstream, the effects of downwash push these vortex structures closer to the ground plane.

Figure 2 shows the planar spanwise streamlines at three locations, at the free end ($y/D = 3$), mid-plane ($y/D = 1.5$), and near the ground plane ($y/D = 1$); the streamlines are superimposed with plane-normal y-vorticity contours. Flow separates from the leading edges of the prism without reattachment onto the side walls of the prism. All planes show symmetric spanwise vortex formation about the transverse midplane ($z/D = 0$), confirming results previously seen for such flows with a thin incoming boundary layer. The mean recirculation length is the shortest for the plane closest to the free end with its foci being closest to the prism trailing edge. The mid-plane has an elongated and thick symmetric recirculation zone with its foci moving further downstream. In the plane closest to the ground plane,

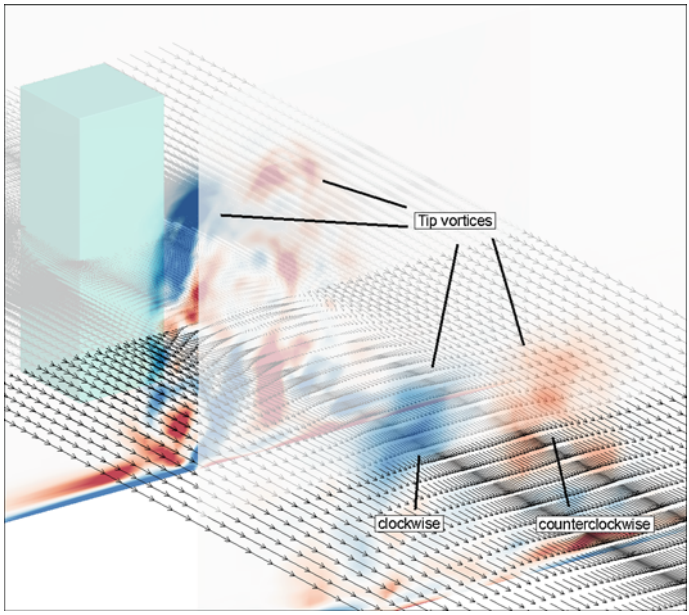

Fig. 1 Mean x-vorticity contours in two vertical planes in the prism wake (at $x/D = 2.5$ and 6.5) and the mean velocity vectors in the horizontal mid-plane (at $y/D = 1.5$)

the recirculation zone is shorter due to the influence of the ground plane. However, the foci are located farther downstream compared to those in the plane closer to the free end.

Figure 3 shows the z-vorticity contours for the vertical streamwise (x-y) planes superimposed on the mean streamlines at $z/D = 0$ and $z/D = 0.5$. The flow is characterized by flow separation from the leading edge. A strong recirculation zone develops in the upper portion of the near-wake. At the prism-wall junction, the horseshoe vortex forms upstream, and the N_w vortex identified by [4] for a circular cylinder forms downstream. The foci of the mean recirculation zone in the vertical plane move farther downstream in the side plane, possibly due to the increased influence of momentum from the freestream flow closer to the sides of the prism. At a location close to the ground plane, the side plane shows the growth of a second vortex structure due to the opposing effects of the upwash from the ground plane and the free end downwash.

Figure 4 shows the iso-surface of the Q-criterion ($Q = 100$) coloured with normalized streamwise velocity (u/U), where U represents the freestream velocity. Flow separation at the leading edge of the free end and along the vertical leading edges of the sides of the prism is clearly noticeable, similar to that seen in previous studies [5, 6]. A distinct horseshoe vortex is visible near the ground plane upstream and along the sides of the prism. The separating shear layers are reconfigured in the near-wake to form distinct streamwise vortex tubes. The side wall shear layers and the shear layer from the free end evolve together into a pair of tip vortices.

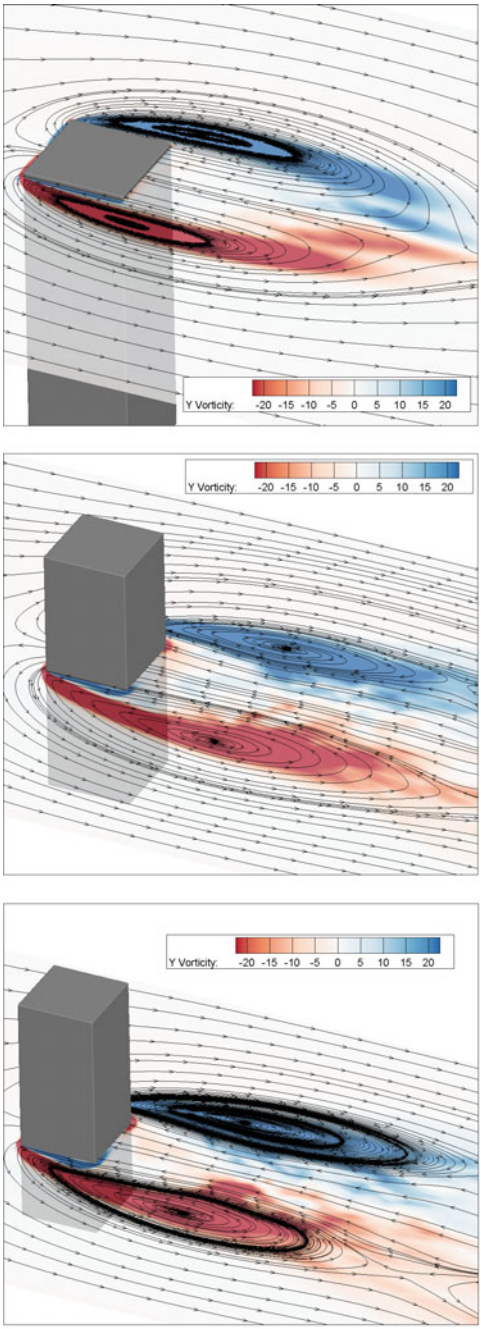

Fig. 2 Mean streamlines in three horizontal planes in the prism wake (at $y/D = 3$, $y/D = 1.5$ and $y/D = 1$) superimposed with y-vorticity contours

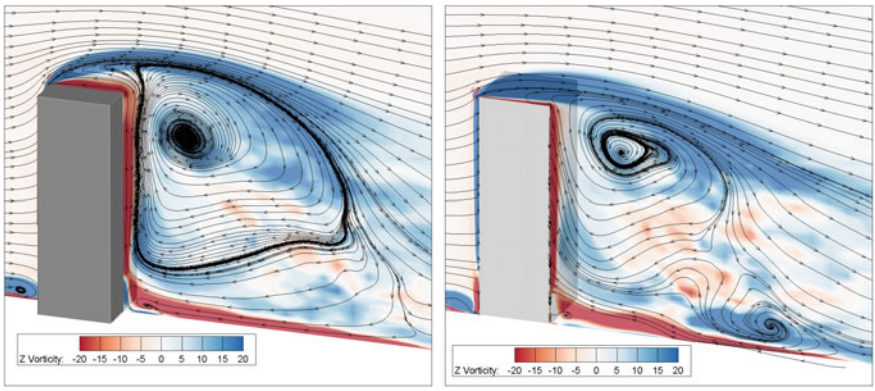

Fig. 3 Mean streamlines in two vertical planes (at $z/D = 0$, and $z/D = 0.5$) in the prism wake superimposed with z-vorticity contours

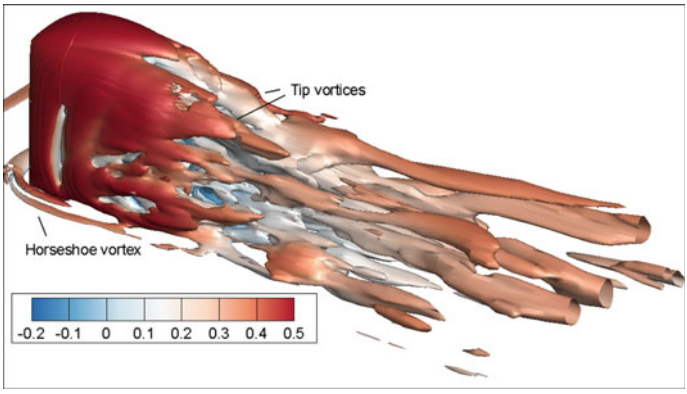

Fig. 4 Q-criterion iso-surface ($Q = 100$) contoured with normalized (u/U) velocity in the wake

Farther downstream, a second pair of streamwise vortex tubes is seen emerging from the base of the prism. The larger vortex structures persist downstream.

4 Conclusions

The mean flow over a surface-mounted finite-height square prism was studied using LES at Re = 500 using streamlines and the Q-criterion. Major flow features include free end shear layers descending into a pair of counter-rotating tip vortices due to downwash in the streamwise planes; a recirculation zone behind the prism trailing edge; and a complex set of vortex structures in the wake aligned mostly in the streamwise direction.

References

1. Saha AK (2013) Unsteady flow past a finite square cylinder mounted on a wall at low Reynolds number. Comput Fluids 88:599–615
2. Saeedi M, Wang BC (2016) Large-eddy simulation of turbulent flow around a finite-height wall-mounted square cylinder within a thin boundary layer. Flow Turb Combust 97(2): 513–538
3. Chong MS, Perry AE, Cantwell BJ (1990) A general classification of three-dimensional flow fields. Phys Fluids A: Fluid 2(5):765–777
4. Krajnović S (2011) Flow around a tall finite cylinder explored by large eddy simulation. J Fluid Mech 676:294–317
5. Wang HF, Zhou Y, Chan CK, Lam KS (2006) Effect of initial conditions on interaction between a boundary layer and a wall-mounted finite-length-cylinder wake. Phys Fluids 18(6): 065106
6. Wang HF, Zhou Y (2009) The finite-length square cylinder near wake. J Fluid Mech 638: 453–490

Jet Diffusion Control Using Plasma Actuators

Influence of Plasma-Induced Flow Instability on Jet Diffusion

Norimasa Miyagi and Motoaki Kimura

Abstract The present study investigated the jet diffusion mechanism using a coaxial dielectric barrier discharge plasma actuator. A coaxial plasma actuator was installed at a nozzle exit to promote mixing, and a hotwire sensor was used to measure the jet velocity fluctuations downstream of the nozzle exit. It was found that the jet velocity near the nozzle exit exhibited three different fluctuation modes depending on the duty cycle of the plasma actuation. Modifications to the flow structure and the corresponding mechanism under different actuation conditions are described in this paper.

Keywords Jet · Mixing · Plasma actuator · Flow control

1 Introduction

Jets are essentially unstable due to the presence of a free shear layer, and as a result their flow structure is extremely complex. Recent studies have examined fluid control techniques using plasma actuators based on atmospheric pressure dielectric barrier discharge (DBD) [1, 4] and the use of plasma actuators for jet control [5].

In the present study, a DBD plasma actuator was used for diffusion control in the initial region of the jet. As shown in Fig. 1, a coaxial plasma actuator was fixed to the nozzle exit to promote mixing immediately before ejection. Instability of the jet was promoted during intermittent control when driven at integer multiples of the preferred frequency of the jet. The vortices were generated near the nozzle, and the

N. Miyagi (✉)
Junior College of Nihon University, Narashinodai 7-24-1,
Funabashi City, Chiba, Japan
e-mail: miyagi.norimasa@nihon-u.ac.jp

M. Kimura
Department of Mechanical Engineering, College of Science and Technology,
Nihon University, Chiyoda, Japan
e-mail: kimura@mech.cst.nihon-u.ac.jp

Y. Zhou et al. (eds.), *Fluid-Structure-Sound Interactions and Control*, Lecture Notes in Mechanical Engineering,
https://doi.org/10.1007/978-981-10-7542-1_24

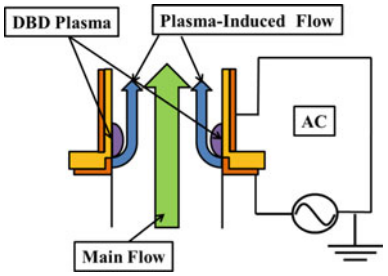

Fig. 1 Schematic diagram of coaxial plasma actuator for jet control

potential core region collapsed earlier [2]. In our previous work we focused on visualization experiments and PIV analysis [3]. However, we did not examine the instability caused by plasma-induced flow on the free shear layer of the jet. In the present study, the velocity distribution and fluctuation were measured using a hot wire velocity meter to determine the influence of the induced flow on the diffusion of the jet.

2 Experimental Details

Figure 2 shows the experimental apparatus, and the experimental conditions are presented in Table 1. A cylindrical plasma actuator was attached to the nozzle exit for diffusion control of the jet. The flow velocity was set to $V_0 = 1.54$ m/s. The Reynolds number was approximately 1000 based on the jet velocity and the nozzle exit diameter ($d = 10$ mm). The initial fluctuation frequency was $fd = 75$ Hz when the actuator was off. The drive frequency for the plasma actuator was set based on the fluctuation frequency. The plasma generator was operated at a comparatively

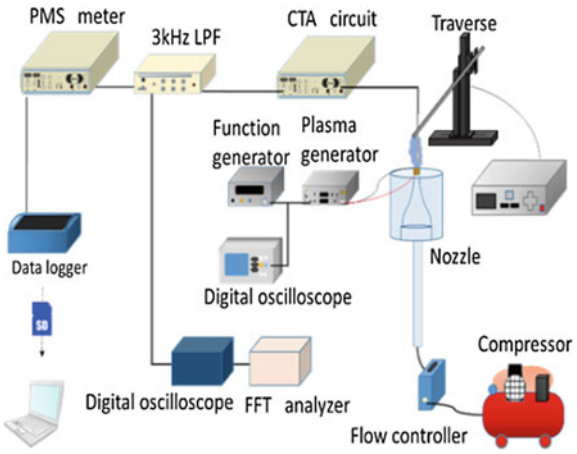

Fig. 2 Experimental apparatus

Table 1 Experimental conditions

Jet fluid	Air
Nozzle diameter d	10 mm
Issuing velocity V_0	1.54 m/s
Flow rate Q	7.4 L/min
Reynolds number Re	1024
Drive frequency f_d	75 Hz
Input voltage $V_{p\text{-}p}$	12.0 kHz
Duty ratio	0, 10, 30, 50, 70, 90, 100%

low power (applied frequency f = 4 kHz, applied voltage E = 6.0 kV). The duty ratio, which is a ratio of the time when the plasma was turned on to the cycle time, was varied from 0 to 100%. The origin of the coordinate system was set at the center of the mainstream jet, with the axial direction defined as the x direction and the radial direction defined as the r direction. The hot wire was traversed to axial and radial direction. The electrical signal from the hot wire velocity meter was passed through a low pass filter (cut off frequency 3 kHz) to remove electric noise, observed with an oscilloscope or FFT analyzer and stored at a sampling rate of 10,000 samples/s.

3 Results and Discussion

3.1 Initial Conditions

Figure 3 shows the cross-sectional velocity profile near the nozzle exit for x/d = 1. The black, red, green, and blue symbols indicate duty ratios of 0, 10, 50 and 90%, respectively. The results show that when the duty ratio is 90%, the acceleration near

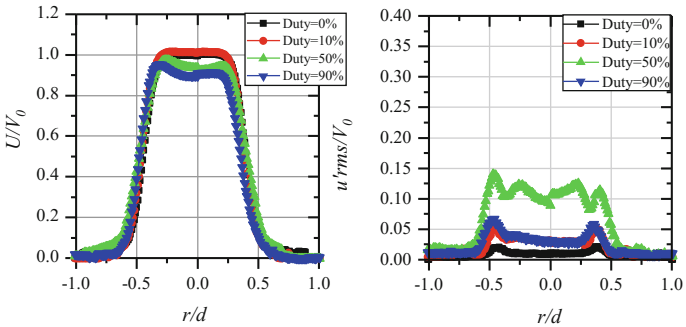

(a) Velocity profile (b) Turblent profile

Fig. 3 Cross-sectional velocity profile for $x/d = 1$ The black, red, green, and blue symbols indicate duty ratios of 0, 10, 50 and 90%, respectively

the wall due to the plasma-induced flow is small. The main flow velocity is reduced by 5–10% due to the influence of the induced flow. When the duty ratio is 10%, a periodic disturbance is generated in the shear layer immediately after ejection. Similarly, even when the duty ratio is 90%, which is an almost continuous flow state, velocity fluctuations occur. When the duty ratio is 50%, velocity fluctuations occur across the entire nozzle exit area. This suggests that the intermittent induced flow develops as a pulsating fluctuation at the nozzle exit and that there are three types of fluctuations that depend on the duty ratio.

Figure 4 shows the duty-ratio dependence of the Strouhal number for the initial velocity distribution. The black symbols indicate the Strouhal number for column mode, which is based on the center velocity and the nozzle exit diameter. The red symbols show the results for shear layer mode, which is based on the center velocity and the momentum thickness. As the duty ratio increases, the Strouhal number in column mode also increases, indicating that the center velocity decreases due to the pressure loss resulting from the increasing plasma-induced flow. In shear layer mode, the Strouhal number is constant for a duty ratio of 0–60%. When the duty ratio is greater than 80%, the Strouhal number is high because the induced flow is high.

3.2 *Flow Structure*

Figure 5 shows the center velocity fluctuations along the flow direction. The peaks in each plot correspond to the potential core region, the transition region, and the fully developed region. In each case, jet diffusion is generated early due to excitation by the plasma actuator. When the duty ratio is 10–30%, the plasma induced flow was increasing as the duty ratio increases. The shear layer develops earlier by the periodic disturbance by the plasma actuator. When the duty ratio is between 40 and 70%, the center velocity fluctuation is greater even in the initial region. Because it was provided a relatively large velocity fluctuations of the plasma induced flow by switching plasma-on and plasma-off. Though the fluctuation in the center

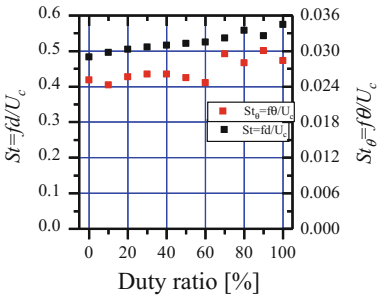

Fig. 4 Dependence of Strouhal number and velocity fluctuation on duty ratio. The black symbols indicate the Strouhal number for column mode. The red symbols show the results for shear layer mode

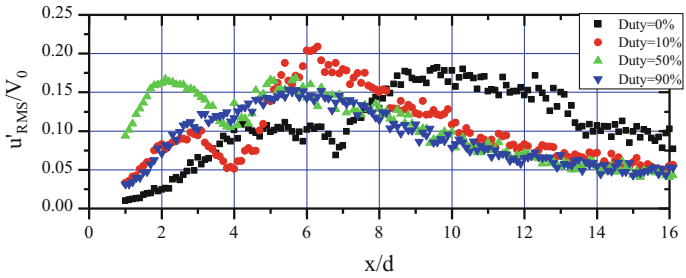

Fig. 5 Center velocity fluctuation profiles. The black, red, green, and blue symbols indicate duty ratios of 0, 10, 50 and 90%, respectively

velocity was large and led to the formation of a pulsating jet. When the duty ratio is between 90 and 100%, plasma induced flow was like an accelerated flow near the wall in the nozzle. This flow develops early in the shear layer due to instability, and becomes fully developed without passing through a transition region.

4 Conclusions

A coaxial DBD plasma actuator was applied to jet diffusion control and the duty ratio and intermittency of the plasma-induced flow were varied. The results showed that the velocity distribution could be controlled by the plasma-induced flow and the following conclusions were reached.

1. When the duty ratio was 10–30%, cyclic disturbance was present in the free shear layer of the jet. The velocity fluctuation became larger as the duty ratio increased.
2. When the duty ratio was 40–80%, the fluctuation in the center velocity was large and led to the formation of a pulsating jet.
3. When the duty ratio was 90–100%, shear layer instability occurred as the influence of the induced flow increased.

References

1. Corke TC, Enloe CL, Wilkinson SP (2010) Dielectric barrier discharge plasma actuators for flow control. Annu Rev Fluid Mech 42:505–529
2. Kimura M, Asakura J, Onishi M, Sayou K, Miyagi N (2013) Jet diffusion control by using a coaxial type DBD plasma actuator. In: Proceedings of ICJWSF2013 4th international conference on jets, wakes and separated flow, vol 79, no 806, pp 2041–2052 (CD-ROM)

3. Miyagi N, Kimura M (2015) Diffusion control in circular jet using coaxial type DBD plasma actuator. In: ASME/JSME/KSME 2015 joint fluids engineering conference, Volume 1A: Symposia, Part 2. https://doi.org/10.1115/ajkfluids2015-14711
4. Moreau E (2007) Airflow control by non-thermal plasma actuators. J Phys D Appl Phys 40 (3):605–636
5. Narayanaswamy V, Raja LL, Clemens NT (2010) Characterization of a high-frequency pulsed-plasma jet actuator for supersonic flow control. AIAA J 48(2):297–305

Flow Characteristics of Multiple Round Jets Issuing from In-line Nozzle Arrangement

Hiroshi Teramoto and Takahiro Kiwata

Abstract This research reports on an experimental investigation of the flow characteristics of multiple round jets issuing from 6 × 6 in-line nozzle arrangement at low-Reynolds number, $Re \approx 4 \times 10^3$, with five spacing ratios of $l/d = 1.5, 2, 3, 4$ and 5 (where d is a diameter of nozzle, and l is a spacing between the center of nozzles). The mean and fluctuating velocities of the jet flow were measured by constant-temperature type hot-wire anemometer. We found that the bending of the outside jet decreases with increasing the spacing ratio l/d. In the further downstream, the multiple jets merge into a single jet flow and the merging of multiple jets occur more downstream with increasing the spacing ratio l/d. In the case of the small spacing ratio, the maximum velocity of merged jet increases and the merged jet spreads from the near field of jet exit.

Keywords Multiple jets · Confluent jet · Flow interaction · Hot-wire anemometry

1 Introduction

The multiple jets are used in various applications, such as air ventilation system, multiple-jet gas burner, fuel injection nozzle and exhaust stacks and so on. The multiple jets were investigated by a number of researchers to improve the performance of devices. Okamoto et al. [1] researched on the interaction of the parallel twin circular turbulent jet. They showed that the twin-jet interacts and joins in the form of an ellipse at the downstream distance, and it becomes close to a circular jet at far downstream distance. Nasr and Lai [2] investigated the influence of acoustic

H. Teramoto (✉)
Graduate School of Natural Science and Technology,
Kanazawa University, Kanazawa, Japan
e-mail: teramoto@ryuko.ms.t.kanazawa-u.ac.jp

T. Kiwata
School of Mechanical Engineering, Kanazawa University, Kanazawa, Japan

Y. Zhou et al. (eds.), *Fluid-Structure-Sound Interactions and Control*, Lecture Notes in Mechanical Engineering,
https://doi.org/10.1007/978-981-10-7542-1_25

excitation to the two parallel plane jets. Ghahremanian et al. [3] and Svensson et al. [4] showed that the multiple round jets issuing from an array also merge and develop into a single round jet similar to the confluent twin-jet. Although the multiple jets exist in various applications, the relation between the arrangement of multiple round jets and the flow structures is not clear. The objective of this research is to clarify an influence of spacing ratio l/d (where d is a diameter of nozzle, and l is a spacing between the center of nozzles) on the flow characteristics of multiple round jets issuing from 6 × 6 in-line nozzle arrangement.

2 Experimental Apparatus and Method

Figure 1 shows a schematic diagram of multiple round nozzles and locations of measurements. Specification of multiple round nozzles and experimental conditions are shown in Table 1. The nozzle diameter was $d = 6.0$ mm, and the nozzles were arranged 6 × 6 square matrix in-line arrangement. The spacing ratio of the multiple round nozzles was varied in the range of $1.5 \leq l/d \leq 5$. Also, the coordinate system and the shape of nozzles are shown in Fig. 1. Measurements of mean and fluctuating velocities were made with cross- and single-wire probes, and hot-wire anemometers of the constant-temperature type with linearized output. The output signals of the hot-wire anemometer were converted by a 12-bit A/D converter with sampling frequency of 10 kHz, and 10×10^4 items of data were stored. The hot-wire anemometer was calibrated by a Pitot static pressure tube and an inclined

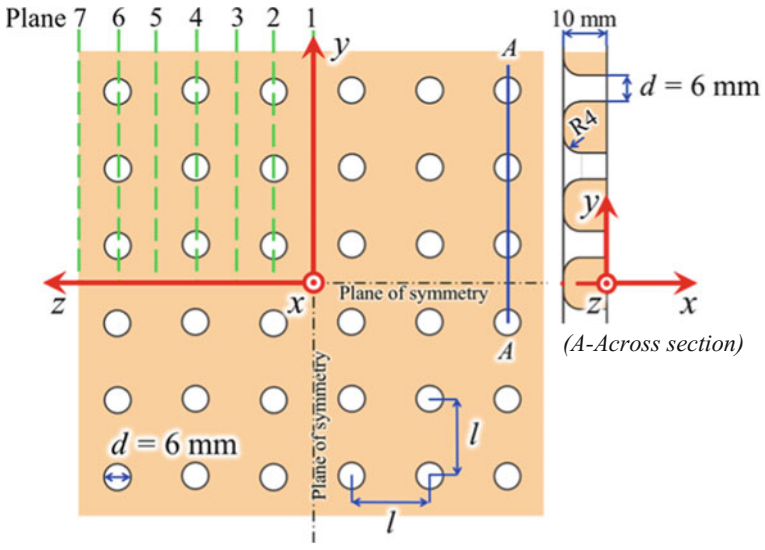

Fig. 1 Schematic diagram of 6 × 6 in-line arrangement of multiple round nozzles

Table 1 Specification of multiple round nozzles and experimental conditions

Nozzle diameter, d [mm]	6				
Nozzle spacing, l [mm]	9.5	12	18	24	30
Spacing ratio, l/d	1.5	2	3	4	5
Reynolds number, Re	4×10^3				
Bulk velocity, U_b [m/s]	9.4				

tube manometer. A computer-controlled 3-dimensional traversing mechanism was used for probe positioning. Experiments were performed under a computer control for the automated data acquisition. The mean and fluctuating velocities and spectrum of fluctuating velocity were obtained by using a personal computer and an FFT analyzer, respectively. The bulk velocity, U_b, was defined as the spatial averaged velocity at nozzle exit. Reynolds number, Re, based on the diameter of the nozzle d and the bulk velocity U_b is about 4×10^3. The uncertainties of the mean velocity component and fluctuating velocity component were about 1.1% and 4.3% respectively.

3 Results and Discussion

3.1 Mean and Fluctuating Velocity Distributions

Figure 2 shows the downstream development of the streamwise mean velocity $\overline{u}/U_b$ and the streamwise velocity fluctuation u'_{rms}/U_b profiles for $l/d = 1.5$, 3 and 5 at the cross section of Plane 2. Each jets have been formed by multiple round nozzles and the potential core exists in the near field of each nozzle exit. The potential core is maintained until $x/d \approx 5$ in the case of $l/d \geq 3$. For $l/d = 1.5$, the potential core of each jets disappear early, because each jets strongly interact with adjoining jets. In downstream of $x/d > 20$, the multiple jets merge and form a single jet flow whose mean streamwise velocity profile has a flat region. The velocity fluctuation increases at the position which have large velocity gradient such as shear layers between the ambient fluid and the perimeter of multiple jets, and the adjoining jets. The velocity fluctuation at the side of ambient fluid becomes larger than that at the side of center of multiple jets.

Figure 3 shows the profiles of the streamwise mean velocity and streamwise fluctuating velocity anew. The vertical axis of each graphs are modified to y/l. At $x/d = 0.08$, the streamwise velocity profiles agree with each other. At $x/d \lesssim 10$, the velocity fluctuations for $l/d = 5$ between adjoining jets are lower than the other spacing ratio. Therefore, the merging of multiple jets with the large spacing ratio occurs more downstream. At $x/d = 60$, the maximum velocity of merged jet for $l/d = 1.5$ is larger than that of the other spacing ratio. In the case of the small spacing ratio l/d, the maximum velocity of merged jet increases.

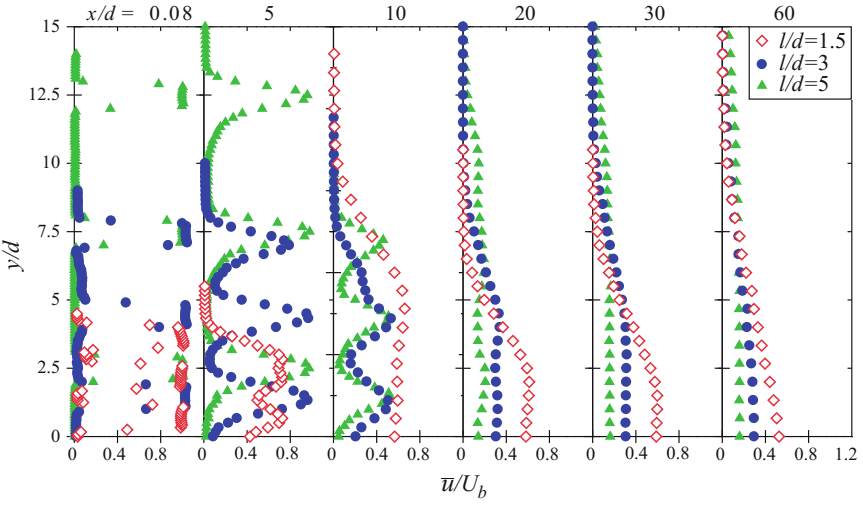

(a) Streamwise mean velocity $\bar{u}/U_b$ *vs.* y/d

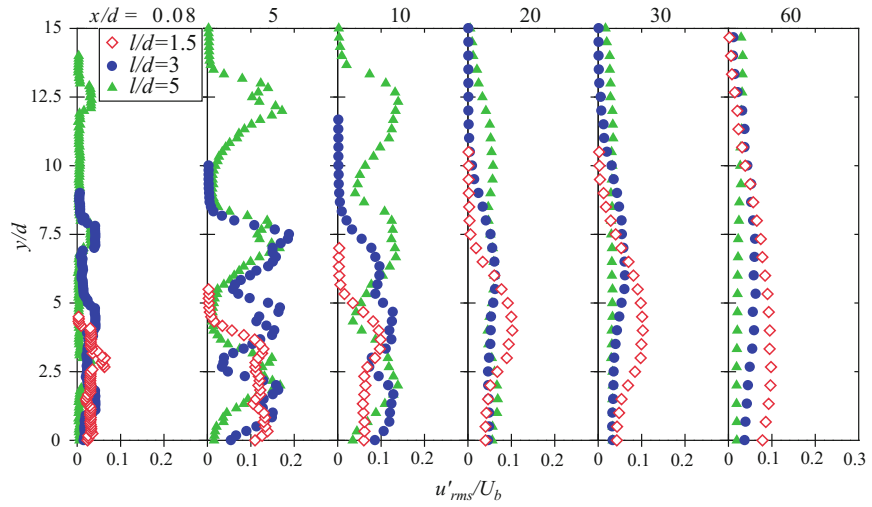

(b) RMS value of streamwise velocity fluctuations u'_{rms}/U_b *vs.* y/d

Fig. 2 Profiles of streamwise mean velocity and velocity fluctuation (Plane 2, *y*-axis: *y*/*d*)

3.2 Velocity Peak Positions and Spreading of Multiple Jets

As shown in Fig. 4, the round jets at the side of the center of the arrangement and the ambient fluid are defined as "inside jet" and "outer jet". The jet between inside jet and outside jet is defined as "middle jet". Figure 5 shows the three peak positions of the mean streamwise velocity profiles at the cross section of Plane 2. Three

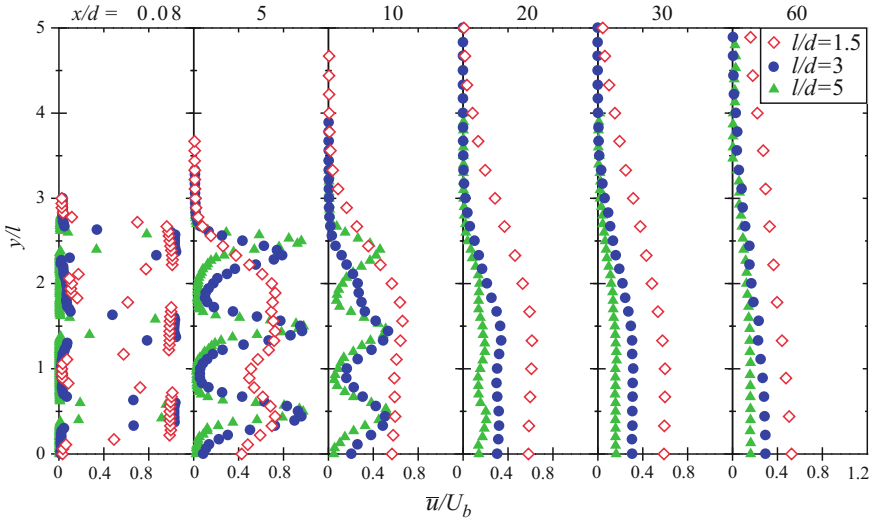

(a) Streamwise mean velocity $\overline{u}/U_b$ *vs.* y/d

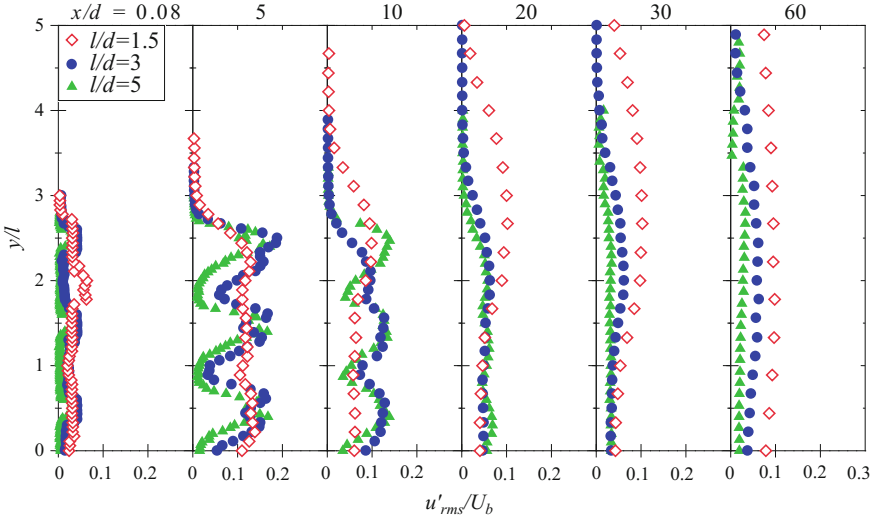

(b) RMS value of streamwise velocity fluctuations u'_{rms}/U_b *vs.* y/d

Fig. 3 Profiles of streamwise mean velocity and velocity fluctuation (Plane 2, *y*-axis: *y*/*l*)

jet peak positions show agreement with each nozzle spacing ratio. This result represent that the flow field of the multiple jets has similarity. The peak positions of outside jets are bend toward to the center of the flow. It is the influence of the entrainment between outside and middle jet. In addition, the outside jet peak disappears at $x/l \approx 4$. It indicate that the outside jets merge with adjoining jets such as

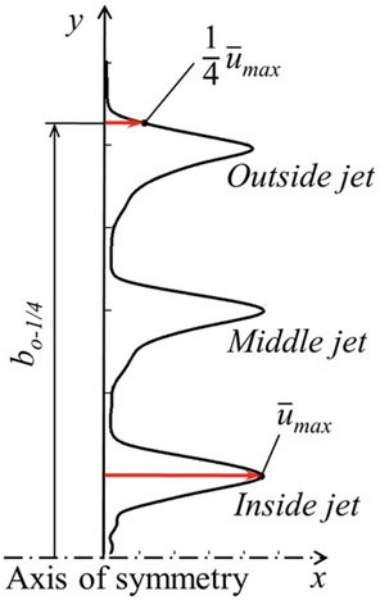

Fig. 4 Definition of jet positions

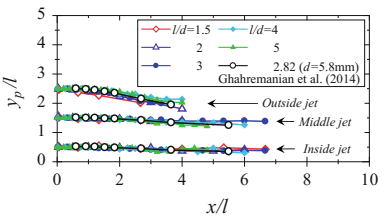

Fig. 5 Peak positions of mean streamwise velocity (Plane 2)

middle jets. The peak positions of middle and inside jets exist until $x/l \approx 6$. From this result, all jets merge fully and develop as a single flow at $x/l \gtrsim 6$.

Figure 6 shows the spread of the multiple jets for all of the spacing ratio, $l/d =$ 1.5, 2, 3, 4 and 5 at the cross section of Plane 2. The width of $b_{o\text{-}1/4}$ is defined as the y-coordinate of $\bar{u} = \bar{u}_{max}/4$ for the outer jet, where $\bar{u}_{max}$ is the maximum velocity at the measured cross sections (as shown in Fig. 4). In the near field of the nozzle exits, $x/l \lesssim 4$, the width of multiple jet flow shrinks. This result shows good agreement with the experimental data by Ghahremanian et al. [3]. In downstream of $x/l \gtrsim 10$, the width of $b_{o\text{-}1/4}$ increases gradually. In the case of $l/d \leq 2$, the multiple jet flow spread becomes large with decreasing spacing ratio l/d. On the other hands, the spacing ratio of $l/d \geq 3$, the change of the width of $b_{o\text{-}1/4}$ with respect to x/l does not depend on spacing ratio l/d.

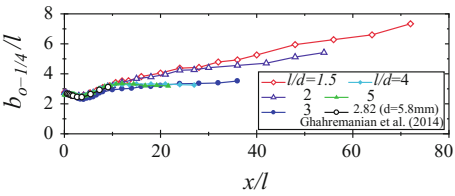

Fig. 6 Spread of multiple jets (Positions of $\bar{u} = \bar{u}_{max}/4$, Plane 2)

4 Conclusions

The influence of the spacing ratio *l*/*d* on the flow characteristics of multiple round jets were investigated experimentally. The following conclusions can be drawn:

(1) The bending of the outside jet decreases with increasing the spacing ratio *l*/*d*, and the merging of multiple jets occur more downstream.
(2) In the case of the small spacing ratio *l*/*d*, the maximum velocity of merged jet increases.
(3) In downstream, the spread of merged jet for $l/d \geq 3$ hardly depend on the spacing ratio *l*/*d*.
(4) The flow characteristics of multiple round jets depend on the spacing between the centers of nozzles *l*.

Acknowledgements This work was supported by JSPS KAKENHI Grant Number JP16K6071.

References

1. Okamoto T, Yagita M, Watanabe A, Wakamura K (1985) Interaction of twin turbulent circular jet. Bulletin of JSME 28(238):617–622
2. Nasr A, Lai JCS (1997) Two parallel plane jets: mean flow and effects of acoustic excitation. Exp Fluids 22:251–260
3. Ghahremanian S, Svensson K, Tummers MJ, Moshfegh B (2014) Near-field mixing of jets issuing from an array of round nozzles. Int J Heat Fluid Flow 47:84–100
4. Svensson K, Rohdin P, Moshfegh B, Tummers MJ (2014) Numerical and experimental investigation of the near zone flow field in an array of confluent round jets. Int J Heat Fluid Flow 46:127–146

Mixing Control of a Round Jet by a Local Sound Wave

N. Nakamura and A. Muramatsu

Abstract Acoustic excitation, moving tabs, a plasma actuator and so on have been presented as methods of active control for a jet. In this study, a round jet is locally excited by a local sound wave radiated from a loudspeaker inputting a sine wave. The excited frequencies were determined with reference to the preferred frequency in the column mode of the jet. The jet was visualized using planar laser Mie scattering. Mean velocity and turbulent intensity on the jet centerline were measured using a hot wire anemometer. As a result, it is found that the acoustic excitation produces anisotropy to the spatial development of the jet, and changes of the flow structure by the frequency of the sound wave. For exciting at the preferred mode, one side of the jet expands and the other side becomes narrow. For exciting at 1/2 frequency of the preferred mode, the asymmetric structure appears in the jet.

Keywords Jet · Flow control · Sound wave · Acoustic excitation
Free shear layer

1 Introduction

Jets are widely used in industrial fields, such as mixing, combustion, heat transfer and so on. Many researchers and engineers have done studies for mixing between the jet and the surroundings [1]. Adding periodic disturbance to the jet with a sound wave is considered to be an effective method to control the mixing between the jet and the surroundings [1]. In previous studies, there are many methods adding the sound waves to the whole jet by a loudspeaker [2, 3]. It is necessary to locally give

N. Nakamura
Major of Aerospace Engineering, Graduate School of Science & Technology,
Nihon University, 7-24-1 Narashinodai, Funabasi, Chiba, Japan

A. Muramatsu (✉)
Department of Aerospace Engineering, College of Science & Technology,
Nihon University, 7-24-1 Narashinodai, Funabasi, Chiba, Japan
e-mail: amura@aero.cst.nihon-u.ac.jp

Y. Zhou et al. (eds.), *Fluid-Structure-Sound Interactions and Control*, Lecture Notes in Mechanical Engineering,
https://doi.org/10.1007/978-981-10-7542-1_26

the jet the disturbance to control the local structure of the jet. The purpose of this study is to experimentally examine the changing of the flow structure and mixing when the shear layer in the initial region of the jet is locally excited with a sound wave. The streamwise sections of the jet are visualized to see the changed flow structure.

2 Experimental Apparatus and Method

Figure 1a shows experimental apparatus for manipulating the flow structure of the jet. An air jet is vertically issuing from a round nozzle having an exit diameter of $D_0 = 8$ mm into the ambient air. A loudspeaker is mounted in a speaker box as shown in Fig. 1a, and a sound wave is added to the jet shear layer through a pipe with an inner diameter of 10 mm. The center of the pipe outlet is radially and axially located at 3 D_0 apart from the center of the nozzle exit.

Experimental conditions are shown in Table 1. The Reynolds number of the jet is $Re = 1{,}500$ (the issuing velocity on the jet centerline $U_{c0} = 2.81$ m/s). The preferred frequency of the jet column at the Re of 1,500 is $f_v = 180$ Hz. Therefore, excited frequencies f_s are set to 90 Hz (= 0.5 f_v), 180 Hz (= f_v), and 360 Hz (= 2.0 f_v). The St_s in the Table 1 is a non-dimensional excited frequency. The excited intensity is indicated with a nondimensional velocity fluctuation u'_s/U_{c0}, where the u'_s is the rms value of velocity fluctuation at the outlet of the speaker box and the U_{c0} is the jet velocity. The value of u'_s/U_{c0} is set to a constant and 36.2%. The input signal to the loudspeaker is a sine wave. Two streamwise cross sections of the jet are visualized using a planar laser Mie scattering. The two visualized sections are shown in Fig. 1b. The cross Sect. 1 is the incident direction of sound waves and the cross Sect. 2 is vertical to the cross Sect. 1. Mean velocity and velocity fluctuation on the jet centerline are measured using a hot wire anemometer.

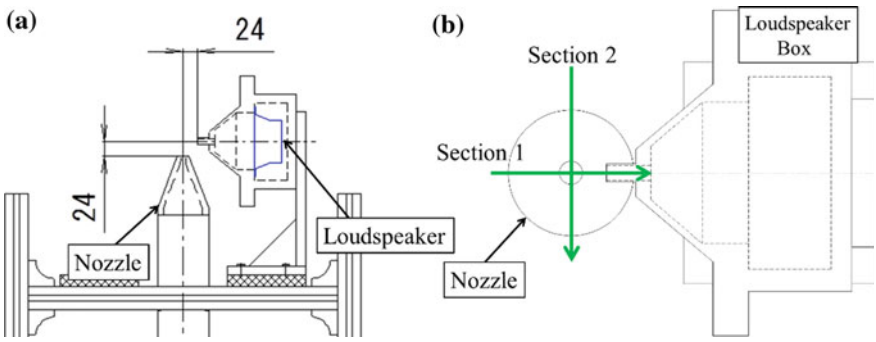

Fig. 1 **a** A loudspeaker and a round nozzle, **b** Two visualized sections on the jet centerline

Table 1 Experimental conditions

Jet gas	Air
D_0 [mm]	8
Re [–]	1500
U_{c0} [m/s]	2.81
f_s [Hz]	0, 90, 180, 360
St_s [–]	0, 0.26, 0.51, 1.03
u'_s/U_{c0} [%]	36.2
Input signal for sound wave	Sine wave

3 Experimental Results and Discussion

3.1 The Visualized Streamwise Sections of the Jet

Figure 2 shows two cross sections for visualized jets without and with excitation. In Figs. 2, 3, and 4, the x and r are axial and radial coordinates respectively, and the origin is the center of the nozzle exit. At the exciting cases in the visualized cross Sect. 1 (the top of Fig. 2), the vortex rings in the jet are inclined due to the advance of the vortex at the incident side of the sound wave. At the excitation frequencies $f_s = 180$ and 360 Hz in the Sect. 1, the width of the jets slightly becomes narrower than the width in the Sect. 2 (the bottom of Fig. 2), with the spatial development of the jet. When the jet is excited at $f_s = 90$ Hz, the jet is meandering, as shown in the visualized Sect. 1. After that the vortex ring peels off at a constant height, so that the jet spreads widely. Asymmetric structure appears clearly in the jet. On the other hand, it is found that, in the Sect. 2, the jet is flowing in symmetrical structure. Focusing on the generation frequency of the vortex rings, in the case of the excitation frequencies $f_s = 180$ and 360 Hz, the generation frequencies of the vortex rings coincide with the preferred frequency. In the case of $f_s = 90$, the generation frequency of the vortex rings coincides with the excitation frequency.

3.2 Measured Mean Velocity and Velocity Fluctuation on the Jet Centerline

Figures 3 and 4 show the distributions of non-dimensional mean velocity and velocity fluctuation on the jet centerline. In the case of the unexcited jet, the mean velocity U_c/U_{c0} almost maintains at constant, and the value of U_c/U_{c0} is about 0.99 at the position of $x/D_0 = 10$. The velocity fluctuation u'_c/U_{c0} gradually increases, and its value becomes about 6% at $x/D_0 = 10$. For the acoustically excited jets except for $f_s = 360$ Hz, the velocity fluctuations increase and the potential cores become extremely short, as compared with the unexcited jet. Particularly, at $f_s =$

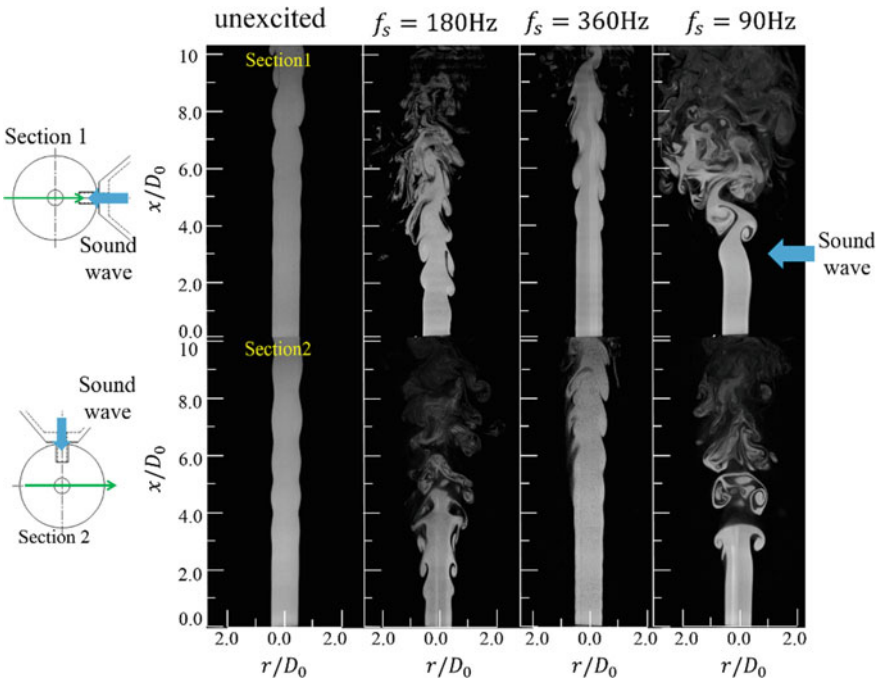

Fig. 2 Visualized air jets

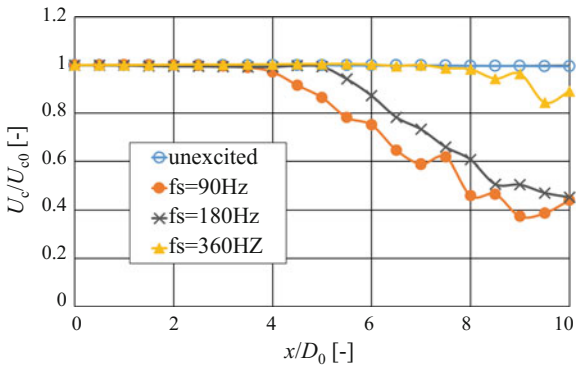

Fig. 3 Axial distributions of mean velocity on the jet centerline (Air, Re = 1500, f_s = 0, 90, 180, and 360 Hz)

90 Hz, the length of the potential core is shortest and the mean velocity greatly decreases from the position of $x/D_0 = 4.0$. At $f_s = 180$ and 360 Hz, the mean velocities decrease from the position of $x/D_0 = 5.0$ and 8.0, respectively. In the early stage of the jet ($x/D_0 < 3$), the velocity fluctuation is most amplified spatially at the $f_s = 180$ Hz. For $x/D_0 > 3$, the velocity fluctuation is most amplified spatially

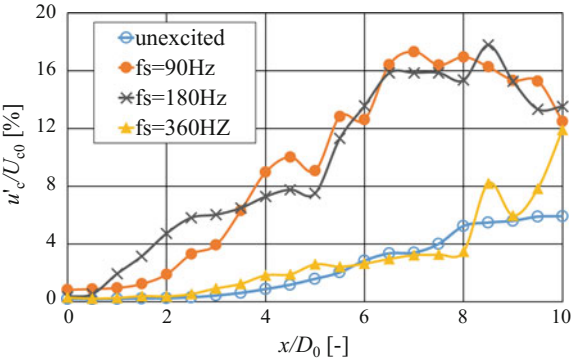

Fig. 4 Axial distributions of velocity fluctuation on the jet centerline (Air, $Re = 1500$, $f_s = 0$, 90, 180, and 360 Hz)

at the $f_s = 90$ Hz and the mean velocity decays extremely. The velocity fluctuation is not most amplified at the $f_s = 360$ Hz and is close to the velocity fluctuation in the unexcited jet. The difference of the visualized jets and the distributions of the mean velocity are understood from the variation of the velocity fluctuations.

3.3 Half Radius of the Jets

Figure 5 shows the half radii for the unexcited jet and the excited jet at $f_s = 180$ Hz. For the unexcited jet, in the measured range, the half radii hardly change. For the excited jet, the half radius on the incident side of sound wave in the Sect. 1 decreases at the $x/D_0 = 3$ of the sound wave incident position. Also, at $x/D_0 = 4$, the half radii decrease, and then at $x/D_0 = 6$, the jet flow leans to the left. In the cross Sect. 2, the half radii extremely increase to the downstream. It is also found that anisotropy occurred in the spacial development process of the jet from the result of half radii.

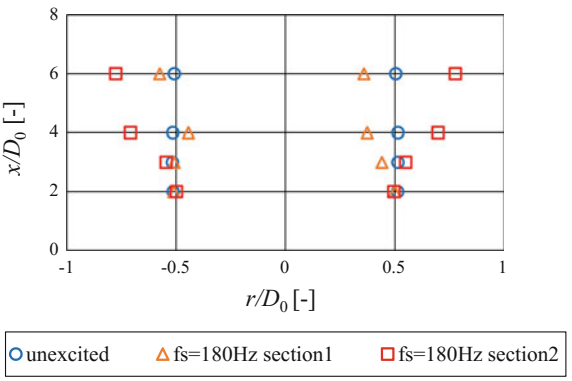

Fig. 5 Half radii of the jets

4 Conclusions

The jet shear layer was locally excited by a sound wave. In the excited jets, the vortex rings are inclined due to the advance of the vortices at the incident side of the sound wave. In the jets for excited frequencies of preferred mode and its double, the width of the jet in the section of the incoming sound waves slightly becomes narrower than the width in the perpendicular section, with the spatial development of the jet. When the jet is excited at 1/2 frequency of the preferred mode, asymmetric structure appears at the section of the incident sound wave in the jet.

References

1. Toyoda K (2005) Vortices in jets. Nagare 24:151–159 (in Japanese)
2. Sato H (1959) The stability and transition of a two-dimensional jet. J Fluid Mech 7:53–80
3. Zaman KBMQ, Hussain AKMF (1980) Vortex pairing in a circular jet under controlled excitation. J Fluid Mech 101:449–491

Measurement of Wall Shear Stress on an Airfoil Surface by Using the Oil Film Interferometry

Y. Yoshioka and Y. Szuki

Abstract In this study, measurement of wall shear stress on an airfoil surface under the lifting condition by using oil film interferometry (OFI) is performed. Reynolds number of the airfoil flow is 8×10^4. Silicon oil and sodium lamp are used for Fizeau fringes formation. The 300–600 images with time interval snap shot in 1–2 s depends on velocity by digital camera are acquired for the calculation of thickness of oil film and moving velocity on surface of it. Also, airfoil surface is covered with PET film for more clearly Fizeau fringes. Time-averaged wall shear stress measured by OFI are compared to numerical simulation by the LES. Maximum difference in the distributions between by the OFI and by the LES has at $x/C = 0.58$, and it has $C_f = 0.00439$ by the OFI and $C_f = 0.00455$ by the LES.

Keywords Flow measurement · Wall shear stress · Boundary layer

1 Introduction

Measurement of wall shear stress with high accuracy is important for evaluating friction drag on vehicle or turbomachinery. Although oil film interferometry (OFI) is a direct method and it need not complicated apparatus, wall shear stress can be measured with high accuracy. OFI has developed by Tanner et al., Znoun et al., Dressler, Imai et al. and Ruedi. It is applied for studying on boundary layer flow developed on a channel or a flat plate. The authors aim for OFI applying for many objects with various shapes in wind tunnel test. In this study, it is performed that time-averaged wall shear stress acting on suction surface of an airfoil is measured by using the OFI technique and the results are compared to the large eddy simulation (LES) calculation [1].

Y. Yoshioka (✉) · Y. Szuki
Department of Mechanical Engineering, College of Science & Technology, Nihon University, Tokyo, Japan
e-mail: csys14028@g.nihon-u.ac.jp

Y. Zhou et al. (eds.), *Fluid-Structure-Sound Interactions and Control*, Lecture Notes in Mechanical Engineering,
https://doi.org/10.1007/978-981-10-7542-1_27

2 Experimental Details

2.1 OFI Technique and Oil Viscosity Calibration

A series of Fizeau interferometric fringes which has same principle to Newton's ring are observed by monochromatic light irradiation to oil film formed on surface of flat plate in uniform flow. Oil film thickness can be calculated from a pitch of the fringes and velocity on the oil film surface can be calculated from moving velocity of the fringes to downstream. Then, friction on surface of the flat plate can be estimated based on Newton's law of friction by using the oil viscosity calibrated because velocity gradient can be computed from the velocity and the pitch. Silicone oil is generally used for the OFI. Since the properties of the silicone oil change depending on the temperature, viscosity calibration is conducted. The calibration is performed with Ubbelohde viscometer in a water tank controlled in temperature. The temperature is changed from 15 to 40 °C assuming room temperature. K type thermocouple and data logger is used for water temperature. Three kinds of silicone oil which have 50, 100 and 300 CS are measured in the calibration.

2.2 Experimental Apparatus

The low noise wind tunnel facility with Goettingen type at Nihon University is used for this study. It has nozzle exit of 300 mm × 200 mm cross section, maximum wind speed of 28 m/s, non-uniformity and turbulence intensity of the main flow are 1.5% or less and 0.5% or less, respectively. Airfoil model which has NACA0012 section, chord length of 60 mm and span length of 120 mm is used. The airfoil is vertically installed in the test section of the wind tunnel at 100 mm downstream from the nozzle exit as shown in Fig. 1. It sets to wind speed of 20 m/s and angle of attack of 12° under the lifting condition. The angle of attack is geometric and is not effective for main flow. Effective angle for main flow is estimated about 9°. The Reynolds numbers of $\mathrm{Re} = 8 \times 10^4$ is given based on the chord length C and the wind speed U. An end of the airfoil is fixed to the ground, but the other end is in the main flow and tip vortex is formed. Therefore, the measurement is performed at the middle span to avoid the influence of the tip vortex.

A sodium lamp is used as the light source and the angle between the light source and the airfoil surface is set to 23.4°. Also, the angle between the camera and airfoil surface is set to 18.3°. A thermal anemometer is used for measurement of mainstream flow velocity. In order to observe Fizeau fringes more clearly, a PET film with a thickness of 0.05 mm is put to the suction surface of the airfoil. 300–600 images are taken at intervals of 1–2 s per measurement by digital camera and image analysis is performed by using MATLAB from the images.

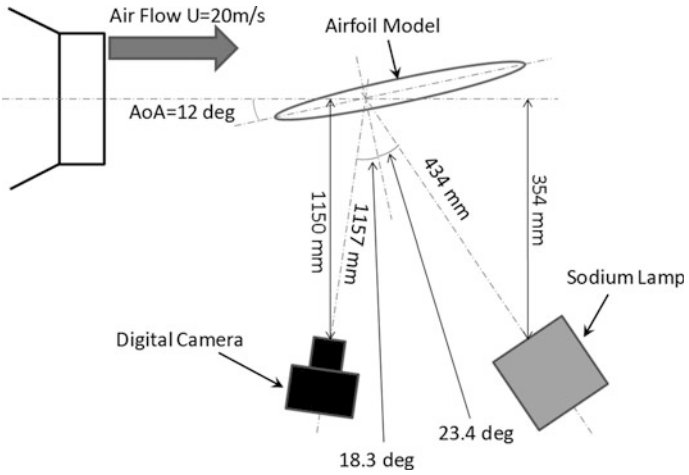

Fig. 1 General view of the test section

3 Results and Discussion

3.1 Oil Viscosity Calibration

The results of oil viscosity calibration for the temperature dependence are shown in Fig. 2. It is clear of temperature dependence characteristics of the three kinds of oils from Fig. 2.

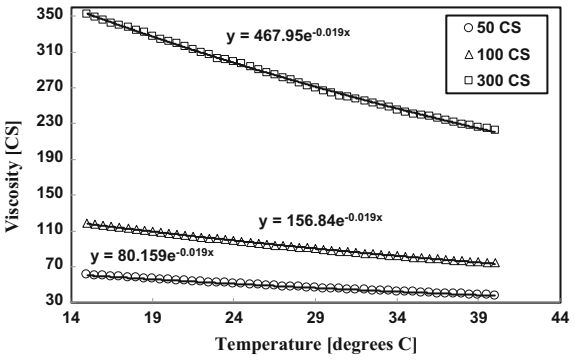

Fig. 2 Calibration carve of viscosity on temperature dependence

3.2 *Measurement of Wall Shear Stress on the Airfoil Surface*

Because Fizeau fringes cannot be observed under the condition of oil painted to the airfoil surface directly as shown in Fig. 3, the experiment is carried out under the PET film put on the airfoil surface. And Fizeau fringes generation can be observed clearly as shown in Fig. 4.

Also, because the model surface does not have monotonous color for wire cut electric spark, image processing that has difference between each images and background image and square brightness on images for improving of detection Fizeau fringes are performed. The pictures of without the differential image processing and with it are shown in Figs. 5 and 6. Fizeau fringes can be detected more clearly with the differential image processing than without it.

Fig. 3 The fringes image without PET film

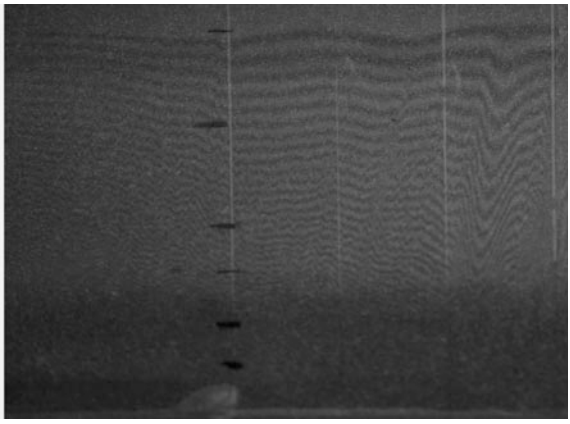

Fig. 4 The fringes image with PET film

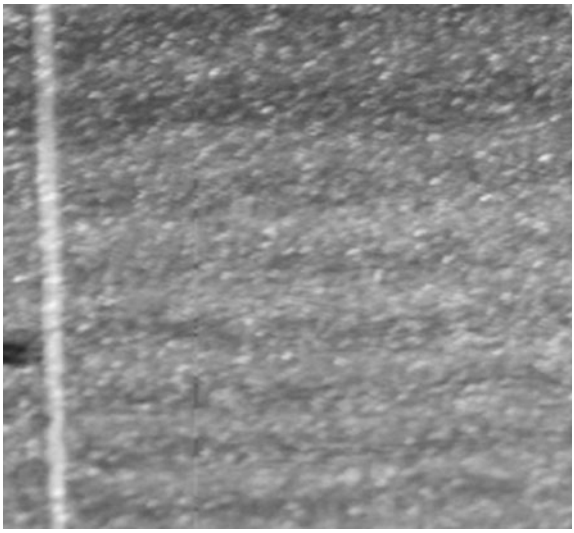

Fig. 5 An image without the processing

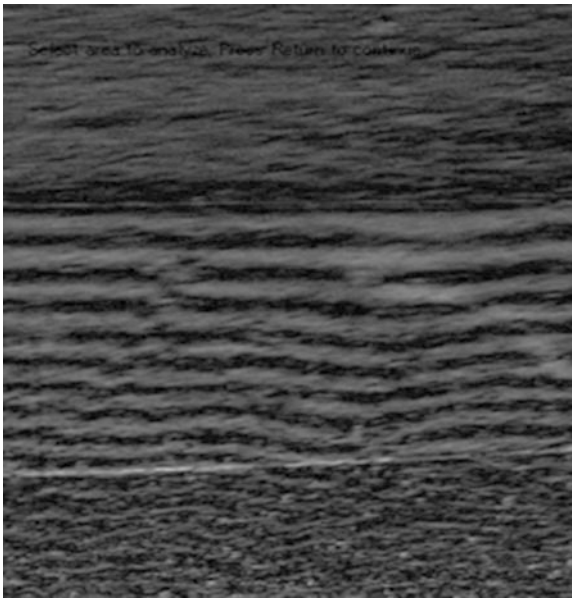

Fig. 6 An image with the image processing

Effect on local skin friction coefficient C_f by different kinematic viscosity is shown in Fig. 7. Local skin friction coefficient C_f has 0.0067 in case of 50 CS, 0.0062 in case of 100 CS and 0.0064 in case of 300 CS at $x/C = 0.33$ which is normalized position from leading edge of the airfoil by the chord length. C_f value in case of 50 CS is larger than in case of the other viscosity. It is considered that this is

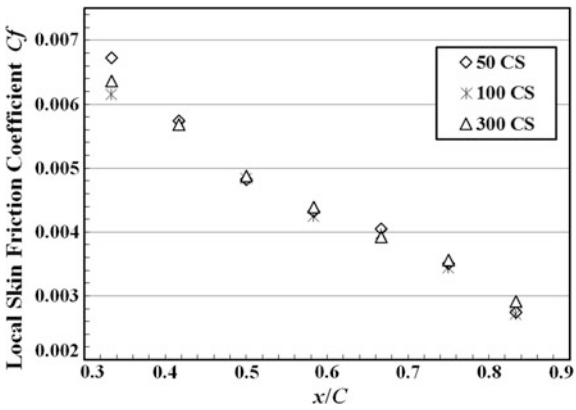

Fig. 7 Effect on local skin friction coefficient by different kinematic viscosity

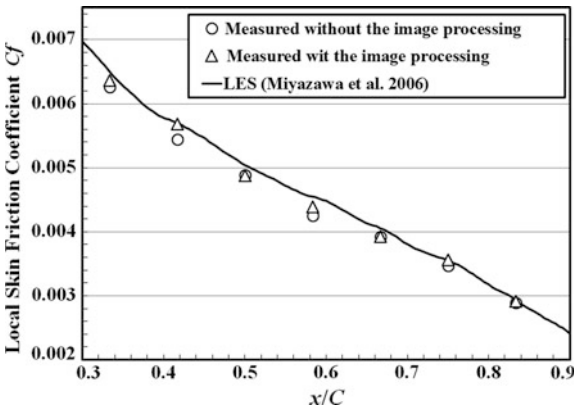

Fig. 8 Comparison between experimental and calculated local skin friction coefficient (Measured: 300 CS)

because of gravity and the oil of 50 CS is not suitable for the airfoil flow in this experimental condition. Experimental and calculated local skin friction coefficient C_f distributions are shown in Fig. 8. Experimental C_f value is measured with the 300 CS oil and calculated C_f value is computed with LES [1]. C_f value in case of 300 CS is used for comparison of the LES result because the OFI result in case of 300 CS is smaller difference between experimental and calculated C_f value than in case of 100 CS. It can be seen that C_f value and tendency that the local skin friction coefficient decreases from $x/C = 0.33$ to $x/C = 0.83$ toward the trailing edge between by the OFI and by the LES are in good agreement. C_f value is 0.00439 by the OFI but 0.00455 by the LES at $x/C = 0.58$, and the difference between in the OFI and in the LES is largest at the position.

4 Conclusions

Wall shear stress acting on the suction side of the airfoil at $x/C = 0.33$ to 0.83 is measured by oil film interferometry (OFI) in the airfoil flow with $\mathrm{Re} = 8 \times 10^4$. And the measured result is compared to calculated result with large eddy simulation by Miyazawa et al. As a result, the following findings are obtained. The visibility of Fizeau fringes generation can be improved by the PET film put on the airfoil surface. Distributions of local skin friction coefficient between by the OFI and by the LES are in good agreement, and they have same tendency that the local skin friction coefficient decreases toward to the trailing edge of the airfoil. Maximum difference in the distributions between by the OFI and by the LES has at $x/C = 0.58$, and it has $C_f = 0.00439$ by the OFI and $C_f = 0.00455$ by the LES.

Acknowledgements A part of this research was subsidized by FY2012 Grant-in-Aid for Young Scientists B issue No. 2582005 "Advanced wall shear stress measurement method using oil film interferometry". We received partial support from Prof. Nagib of IIT in analysing OFI. Also, we received support from Mr. Watanabe of the University of Tokyo for the image processing.

References

1. Miyazawa M et al (2006) Aeroacoustic simulation of a flow around a 2-D Aerofoil (1st report, validation of a large Eddy simulation of separated and transitional flow around an aerofoil). Trans JSME Ser B 72(721):2140–2147
2. Tanner LH, Blows LG (1976) A study of the motion of oil films on surfaces in air flow with application to the measurement of skin friction. J Phys E Sci Instrum 9:194–202
3. Znoun ES, Nagib H, Durst F (2009) Refined relation for turbulent channels and consequences for high-re experiments. Fluid Dyn Res 41:021405
4. Dressler KM (2010) Channel flow as a platform to validate oil film interferometric wall-shear measurements. Master's Thesis
5. Imai S et al (2009) Coherent structure and their contribution to turbulent intensity in turbulent channel flow. In: Proceedings of fluids engineering conference 0218
6. Ruedi JD (2009) Accurate and independent measurements of wall-shear stress in turbulent flows. In: 62nd Mtg of the American Physical Society division of fluid dynamics

A New Method for the Formation of Free Jets with Long Laminar Regions

J. Zayko, A. Chicherina, S. Teplovodskii, A. Reshmin and V. Vedeneev

Abstract A new method for the formation of free jets with long laminar regions using a small-size device is proposed. A free jet with a 0.12 m diameter at Reynolds numbers in the range of 2000–12560 is experimentally studied using thermoanemometer measurements of velocity and turbulent fluctuations profiles and laser visualisation of the flow. It is shown that the designed technology forms the free jet with a laminar region length of 5.5 jet diameters for an optimal regime with Re $\sim$ 10000. Numerical simulation of the flow in the forming unit and an inviscid hydrodynamic instability analysis of the jet with calculated profiles have been conducted to explain the existence of the optimal regime.

Keywords Laminar jet · Free jet · Turbulence transition delay

1 Introduction

Free jets and other shear flows occur often in nature and various technologies and are widely studied. Turbulent jets and their breakdown have been thoroughly studied over several decades in the context of many industrial applications, including mixing, combustion, noise generation, etc.: [1–3]. Laminar jets are much less studied due to their immediate breakdown at normal conditions.

Batchelor and Gill [4] first analysed the equation for an infinitesimal inviscid disturbance of a unidirectional round jet, using the instability condition [5], which is that the expression $Q(r) = ru'/(n^2 + \alpha^2 r^2)$ should have a numerical maximum at some point in the flow. Here n and α are the azimuthal and axial wavenumbers of the Fourier component of the disturbance, u is the mean axial velocity and r is the

J. Zayko (✉) · A. Chicherina · S. Teplovodskii · A. Reshmin · V. Vedeneev
Lomonosov Moscow State University, Moscow 119991, Russia
e-mail: zayko@imec.msu.ru

Y. Zhou et al. (eds.), *Fluid-Structure-Sound Interactions and Control*, Lecture Notes in Mechanical Engineering,
https://doi.org/10.1007/978-981-10-7542-1_28

radial coordinate. Round jets of the "top-hat" profile, which represents the jet profile near the orifice, and the self-similar "far-downstream" profile, obtained in [6], were examined. For the cylindrical vortex sheet which is a limit form of the "top-hat" profile, the flow is unstable for all values of n and α. The disturbance, which grows most rapidly, corresponds to $\alpha \to \infty$, and does not depend on n. For the "far-jet" profile, it was shown [4] that only the sinuous modes ($n = 1$) are growing.

The critical Reynolds number Re_{cr} for an axisymmetric jet was found in [7], where this type of free shear layers with respect to linear azimuthally periodic disturbances with $n = 1$ was investigated. The "far-downstream" profile was examined, and the critical Reynolds number Re_{cr} was determined to be 37.9. Later [8] three types of jet profiles, which represented jet development from the profile near the orifice to the fully-developed jet profile were numerically studied. The first was the "top-hat" profile, the second represented the initial mixing region and the third described the developed annular mixing region. Disturbances with $n = 0$ and $n = 1$ were considered. For $n = 1$, the critical Reynolds number 37.64 was obtained ($\alpha = 0.44$, $\omega = 0.1$), which is close to the result of [7]. Such a low value of Re_{cr} explains the almost immediate break-up of free jets near the orifice at normal conditions.

Numerous more recent studies have been devoted to the control of submerged jets, and to the suppression of turbulence in free shear layers of such jets: [9, 10]. An extensive review of investigations of the subsonic jet flows instability, turbulent structures generation, propagation of disturbances and the influence of an acoustic field on jet structure is given in [11].

An experimental apparatus used by different authors to obtain round jets with long laminar region often consists of grids or honeycombs for turbulence reduction, and a long tube, where the parabolic Poiseuille profile is formed at the tube outlet end: [12, 13]. However, it is impossible to use such technology in practice for the formation of jets with diameters of ~0.1 m or larger because the tube would be several meters or more in length. That is why the crucial issue in the creation of laminar jets of large diameters is the jet forming device, whose size should be comparable with the jet diameter.

In this study, we investigate a new method for the formation of free gas jets with a diameter of 0.12 m, in which the transition to turbulence occurs at the distance of 5.5 jet diameters (for the optimal velocity regime) from the orifice. The forming device has a compact size; its length is only ~1.5 of the jet diameter.

2 Experimental Apparatus and Test Conditions

The experimental apparatus is shown in Fig. 1. The flow from (1) the pipe line enters the forming device, whose first part is a cylindrical channel of 0.04 m in diameter and 0.16 m in length, where the flow is laminarised when it passes through (2) a perforated plate and (3) a bushing with metal grids. The second section of the forming device, a short diffuser, is located at the distance of 0.06 m downstream of the

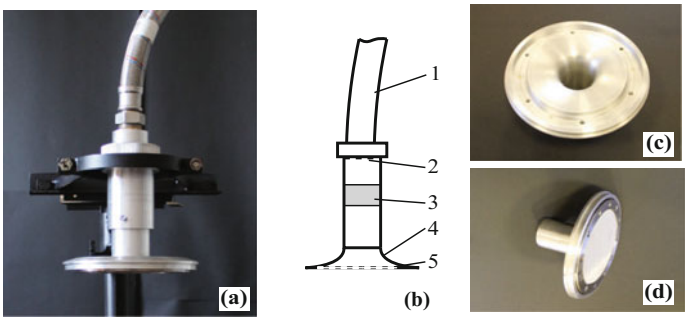

Fig. 1 **a** The photograph and **b** the sketch of the forming device, **c** the short round diffuser without and **d** with the metal grids package at the outlet

bushing. At the length of 0.04 m, the flow expands to the diameter of $D = 0.12$ m through (4) the short diffuser, from which the jet flows to the ambient medium. The diffuser wall profile and (5) a metal grids package at the diffuser outlet provide the velocity profile with almost constant velocity at the central jet core of ~0.05 m in diameter and low turbulence intensity.

Velocity profiles and turbulent fluctuations are measured by the thermoanemometer DISA 56C01 CTA with a hot-wire sensor Dantec Dynamics 55P11. The jet is visualised using glycerin mist and a laser KLM-532.

To analyse the flow inside of the diffuser at different velocities, and its impact on the jet velocity profile and the distance to breakdown, a numerical simulation of Navier-Stokes equations is conducted. Basing on the calculated jet velocity profiles, we analyse the inviscid hydrodynamic instability of the jet, which qualitatively predicts the distance to the jet breakdown.

3 Results

For various velocity regimes, we obtained various lengths L_{max} of the laminar region (Fig. 2a). The velocity and velocity fluctuations profiles for the optimal regime with $Re = 9200$ at the distances of 5.5 D and 6 D from the diffuser outlet are shown in Fig. 2b, c (the Reynolds number is based on the diffuser diameter and mean velocity averaged over a cross-section of the jet). Crosses with solid line corresponds to the measurements at the distance of 5.5 D. The intensity of turbulent fluctuations is less than 0.6% in the central part of the jet, which is not very different from the intensity near the orifice. So the jet stays laminar at this distance. Circles with dashed line correspond to the distance of 6 D, where the fluctuations grow and the transition to the turbulence occurs.

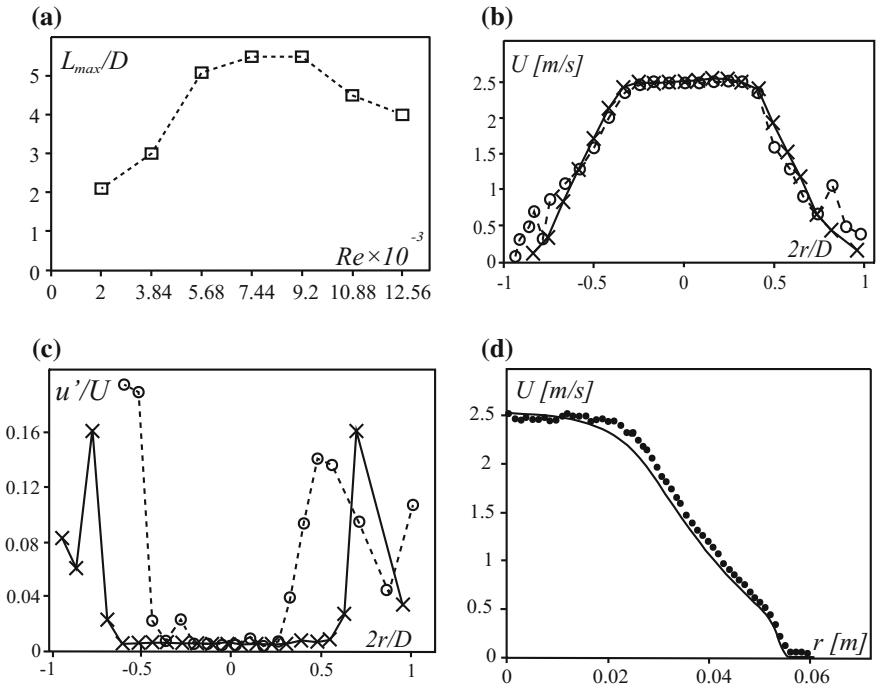

Fig. 2 **a** L_{max}/D versus *Re*, **b** velocity, **c** velocity fluctuations profiles at the distances of 5.5 *D* (crosses with solid line) and 6 *D* (circles with dashed line) from the orifice for $Re = 9200$; **d** comparison of experimental (circles) and calculated (solid line) velocity profiles at the distance of 5 mm from the diffuser outlet for the optimal regime

Numerical simulation of the flow in the diffuser explains the existence of the optimal regime with the longest laminar region. To validate the numerical model, calculated and measured velocity profiles at the distance of 5 mm downstream of the diffuser outlet are compared, and an excellent agreement is seen (Fig. 2d). The increase of the average flow velocity yields local laminar separation of the flow inside of the diffuser, which results in a change of the jet velocity profile that increases growth rates of the most unstable perturbations of the jet.

Figure 3 shows the results of visualisation by a laser sheet. Figure 3a shows the jet at the optimal regime with $Re = 9200$ and the length of laminar region $L_{max} = 5.5\,D$. Figure 3b corresponds to the jet breaking up near the orifice. Velocity time signals from the sensor at the distances of $5.5D$ and $6D$ near the jet axis are also compared (Fig. 3c). The amplitude of the signal at the distance of 5.5 *D*, where the jet is laminar, is ~23 times lower than at the distance of 6 *D*.

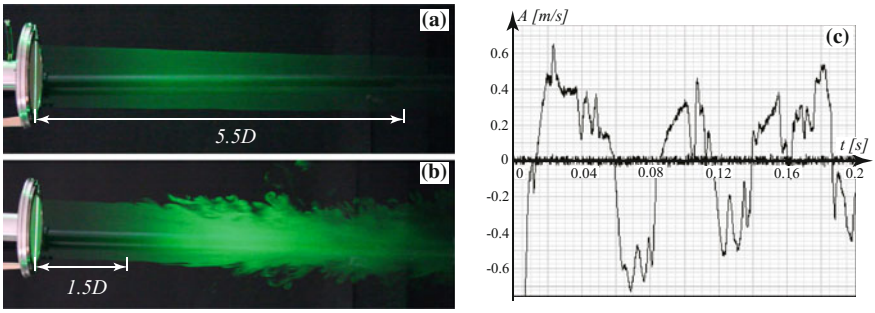

Fig. 3 **a** Jet with laminar region length $L_{max} = 5.5\ D$, **b** jet breaking up near the orifice, **c** comparison of the velocity time signals from the sensor near the jet axis for the optimal regime at the distances of 5.5 and 6 D

4 Conclusions

The main advantage of the proposed technology for laminar jet formation is a compact forming device of 1.5 jet diameters in size. We demonstrate a laminar jet with a diameter of ∼0.1 m and $Re \sim 10\,000$, which is not achievable with other methods of creating of free jets. Laminar initial regions of free jets can be used to organise air curtains, which provide local clean zones with the desired properties in an ambient medium. Wall-free local clean zones can be used in medicine, the medical industry, microelectronics, plasma processing of monocrystal surfaces and other applications. Free jets with long laminar regions can also be used for detailed studies of perturbation growth and transition to turbulence in round jets.

References

1. Drazin PG, Reid WH (2004) Hydrodynamic stability. Cambridge University Press
2. Jordan P, Colonius T (2012) Wave packets and turbulent jet noise. Ann. Rev. Fluid Mech. 45:173–195
3. List EJ (1982) Turbulent jets and plums. Ann. Rev. Fluid Mech. 14:189–212
4. Batchelor GK, Gill AE (1962) Analysis of the stability of axisymmetric jets. J. Fluid Mech. 14(4):529–551
5. Rayleigh L (1892) Scientific papers. Cambridge University Press
6. Landau LD, Lifshitz EM (1959) Fluid mechanics. Pergamon Press (in Russian)
7. Lessen M, Singh PJ (1973) The stability of axisymmetric free shear layers. J. Fluid Mech. 60(3):433–457
8. Morris PJ (1976) The spatial viscous instability of axisymmetric jets. J. Fluid Mech. 77(3):511–529
9. Hussain AKMF, Hasan AZ (1985) Turbulence suppression in free turbulent shear flows under controlled excitation. Part 2. Jet-noise reduction. J. Fluid Mech. 150:159–168
10. Sahu RP, Chatterjee S, Biswas N, Mukhopadhyay A, Sen S (2014) Experimental investigation of the effect of jet inclination of laminar jet. Int. J. Heat Fluid Flow 50:160–168

11. Grek G, Kozlov V, Litvinnko Y (2013) Stability of subsonic stream flows and combustion. Novosibirsk State University press (in Russian)
12. Kozlov G, Grek G, Sorokin A, Litvininko Yu (2008) Influence of initial conditions at the nozzle exit on the structure of round jet. Thermophys. Aeromech. 15(1):55–68
13. McNaughton KJ, Sinclair CG (1966) Submerged jets in short cylindrical flow vessels. J. Fluid Mech. 25(2):367–375

Part II
Fluid-Structure Interaction

Fluid-Structure Interactions of Large Amplitude Vibrations

Woojin Kim and Haecheon Choi

Abstract Fluid-structure interactions of large amplitude vibrations are investigated for flows around an elastically mounted rigid circular cylinder, a long flexible circular cylinder, and the Tacoma Narrows Bridge. The governing equations of fluid flow and structure motion are solved implicitly for a stable solution. Weak coupling is introduced with predictors to simulate fluid-structure interactions without any iteration per time step. For an elastically mounted rigid circular cylinder and a long flexible circular cylinder, large amplitude vibrations are caused by starting vortices generated in the shear layers. On the other hand, for the Tacoma Narrows Bridge, large-amplitude torsional vibrations are maintained in two segments of the deck due to the matching of the dominant frequency of the rotational angles of the deck with that of vortex shedding.

Keywords Fluid-structure interaction · Large amplitude vibration
Circular cylinder · Tacoma narrows bridge

1 Introduction

Fluid-structure interaction (FSI) can cause large amplitude vibrations of structures and serious damage to them. One of the well known examples is the collapse of the Tacoma Narrows Bridge in 1940. At the wind speed of about 18 m/s before the collapse, the middle span of the deck oscillated transversely in eight or nine segments with a frequency of 0.6 Hz, and then torsional vibration occurred in two segments with a frequency of 0.2 Hz [1]. There have been many attempts to explain the cause of the collapse such as flutter of aircraft wings [2], a combination of parametric resonance [3, 4], an aerodynamically induced condition of

W. Kim · H. Choi (✉)
Department of Mechanical & Aerospace Engineering,
Seoul National University, Seoul 08826, Korea
e-mail: choi@snu.ac.kr

Y. Zhou et al. (eds.), *Fluid-Structure-Sound Interactions and Control*, Lecture Notes in Mechanical Engineering,
https://doi.org/10.1007/978-981-10-7542-1_29

self-excitation in a torsional degree of freedom [5], negative damping [6], and structural instability [7], but the cause of the collapse has not been fully understood.

Extremely long risers suffer from severe fatigue damage caused by flow-induced vibration, but understanding the cause of their large amplitude vibration is still limited due to experimental difficulties such as a large facility and relatively complicated instrumentation required [8]. Instead, the fundamental research on vortex-induced vibration has been extensively performed for an elastically mounted rigid circular cylinder [9]. For an elastically mounted rigid circular cylinder, Jauvtis and Williamson [10] observed two triplets of vortices per cycle (2T mode) together with a large amplitude of 1.5 D, and conjectured that the massive vibration of the 2T mode is attributed to the energy transfer from the third vortex of each triplet, where D is the diameter of a circular cylinder. However, Gsell et al. [11] observed two single vortices per cycle (2S mode) instead of the 2T mode, together with the amplitude of 1.2 D.

In the present study, we numerically investigate three examples of fluid-structure interactions of large amplitude vibrations: vibrations of an elastically mounted rigid circular cylinder, a long flexible circular cylinder, and the Tacoma Narrows Bridge, respectively.

2 Numerical Methods

We solve the governing equations of fluid flow and structure motion separately. Before solving the governing equations, the fluid-structure interface is predicted by predictors: explicit and implicit Euler methods to obtain provisional velocity and position of the interface, respectively. The no-slip condition and hydrodynamic force are satisfied and imposed on the provisional interface, respectively [12].

The governing equations of unsteady incompressible viscous flow are the continuity and unsteady three-dimensional Navier-Stokes equations:

$$\frac{\partial u_i}{\partial x_i} - q = 0, \tag{1}$$

$$\frac{\partial u_i}{\partial t} + \frac{\partial u_j u_i}{\partial x_j} = -\frac{\partial p}{\partial x_i} + \frac{1}{\mathrm{Re}} \frac{\partial^2 u_i}{\partial x_j \partial x_j} + f_i, \tag{2}$$

where t is the time, $x_i = (x, y, z)$ are the Cartesian coordinates (streamwise, transverse, and spanwise, respectively), $u_i = (u, v, w)$ are the corresponding velocity components, p is the pressure, Re is the Reynolds number, f_i is the momentum forcing, and q is the mass source/sink. A discrete-forcing immersed-boundary method [13] is used to determine f_i and q. Large eddy

simulation with a dynamic global subgrid-scale model [14] is performed for flows around an elastically mounted rigid circular cylinder and a long flexible circular cylinder. For temporal and spatial discretizations, an implicit fractional step method [15] with linearlization [16] and the second-order central difference method are used, respectively. The size of computational time step is obtained from the maximum Courant-Friedrichs-Lewy (CFL) number condition, CFL $= \Delta t(|u|/\Delta x + |v|/\Delta y + |w|/\Delta z) \leq 1$.

The motion of an elastically mounted rigid circular cylinder is expressed as a mass-damper-spring system [11]:

$$\frac{d^2\zeta_i}{dt^2} + 2\eta\left(\frac{2\pi}{U_R}\right)\frac{d\zeta_i}{dt} + \left(\frac{2\pi}{U_R}\right)^2\zeta_i = \frac{2}{\pi m_R}C_i, \tag{3}$$

where $\zeta_i = (X_C, Y_C)$, $C_i = (C_D, C_L)$, η $(= c_s/2(k_s m_s)^{1/2})$ is the damping ratio, U_R $(= U/f_N D)$ is the reduced velocity, and m_R $(= m_s/m_f)$ is the mass ratio. Here, X_C and Y_C are the streamwise and transverse displacements of the cylinder center, respectively, C_D $(= 2F_D/\rho_f U^2 D L_z)$ and C_L $(= 2F_L/\rho_f U^2 D L_z)$ are the drag and lift coefficients, respectively, F_D and F_L are the drag and lift forces, respectively, ρ_f is the fluid density, U is the free-stream velocity, D is the diameter of a circular cylinder, L_z is the spanwise domain size, c_s is the damping coefficient, k_s is the spring constant, m_s is the structural mass, m_f is the displaced fluid mass, and f_N $(= (1/2)(k_s/m_s)^{1/2})$ is the natural frequency. The Reynolds number $(\mathrm{Re} = \rho_f UD/\mu_f)$ is 4200, the damping ratio is 0, and the mass ratio is 2, where μ_f is the fluid viscosity. The schematic diagram of the computational domain and boundary conditions for flow around an elastically mounted rigid circular cylinder is shown in Fig. 1a. A uniform flow is given at the inlet. The numbers of grid points used are 689 (x) × 897 (y) × 60 (z).

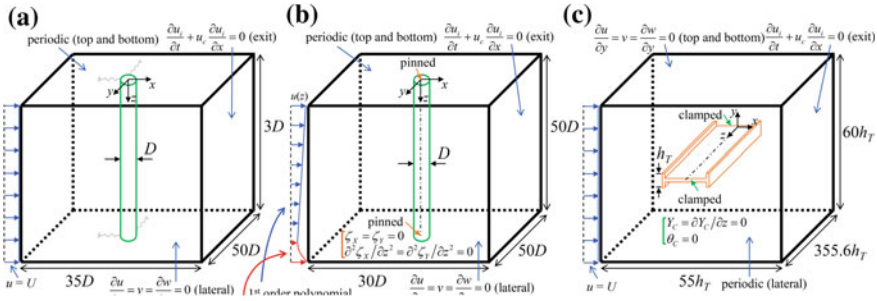

Fig. 1 Schematic diagrams of the computational domains and boundary conditions for flows around **a** an elastically mounted rigid circular cylinder, **b** a long flexible circular cylinder, and **c** the Tacoma Narrows Bridge

A tensioned beam model [17] is used for the motion of a long flexible circular cylinder:

$$\frac{\partial^2 \zeta_i}{\partial t^2} - \omega_c^2 \frac{\partial^2 \zeta_i}{\partial z^2} + \omega_b^2 \frac{\partial^4 \zeta_i}{\partial z^4} = \frac{2C_i}{\pi m_R}, \tag{4}$$

where $\zeta_i = (\zeta_X, \zeta_Y)$, $C_i = (C_{Ds}, C_{Ls})$, ω_c $(= (T_s/m_{ss}U_{max}^2)^{1/2})$ is the tension coefficient, ω_b $(= (E_s I/m_{ss}U_{max}^2 D^2)^{1/2})$ is the bending coefficient, and m_R $(= m_{ss}/m_{fs})$ is the mass ratio. Here, ζ_X and ζ_Y are the streamwise and transverse displacements of the center, respectively, C_{Ds} and C_{Ls} are the sectional drag and lift coefficients, respectively, m_{ss} and m_{fs} are the structural mass and displaced fluid mass per unit length, respectively, T_s is the tension, E_s is the Young's modulus, I is the area moment of inertia, and U_{max} is the maximum inflow velocity. The schematic diagram of the computational domain and boundary conditions for flow around a long flexible circular cylinder is shown in Fig. 1b. At the inlet, a linearly sheared flow is imposed from $z = 0$ $(u = U_{max})$ to $0.92L_c$ $(u = U_{min})$, and the third-order polynomial is given from $z = 0.92L_c$ $(u = U_{min})$ to L_c $(u = U_{max})$ (buffer region) to apply the periodic boundary condition on the top and bottom boundaries following Bourguet et al. [17], where L_c is the length of a long flexible circular cylinder and U_{min} is the minimum inflow velocity. The Reynolds number $(\mathrm{Re} = \rho_f U_{max} D/\mu_f)$ is 4000, $U_{max}/U_{min} = 9$, $L_c/D = 50$, $m_R = 2.55$, $\omega_c = 5$, and $\omega_b = 10$. The numbers of grid points are 641 (x) × 1047 (y) × 768 (z).

A nonlinear model for a suspension bridge [7] is used for the motion of the Tacoma Narrows Bridge:

$$\begin{aligned}
(M_T + 2m_T\xi_T)\frac{\partial^2 Y_C}{\partial t^2} = &-E_s I_T \frac{\partial^4 Y_C}{\partial z^4} \\
&+ H_{0T}\frac{\partial}{\partial z}\left[\frac{2}{\xi_T^2}\frac{\partial Y_C}{\partial z} + \frac{3}{\xi_T^4}\frac{ds_T}{dz}\left\{\left(\frac{\partial Y_C}{\partial z}\right)^2 + \left(l_T\frac{\partial \theta_C}{\partial z}\right)^2\right\}\right] \\
&- \frac{A_T E_s}{L_{cT}}\left[\int_0^{L_T}\frac{1}{\xi_T^3}\left\{\left(\frac{\partial Y_C}{\partial z}\right)^2 + \left(l_T\frac{\partial \theta_T}{\partial z}\right)^2\right\}dz\right]\frac{1}{\xi_T^3}\frac{d^2 s_T}{dz^2} \\
&- \frac{2A_T E_s}{L_{cT}}\left[\int_0^{L_T}\frac{1}{\xi_T^3}\frac{d^2 s_T}{dz^2}Y_C dz\right]\frac{\partial}{\partial z}\left[\frac{1}{\xi_T}\frac{ds_T}{dz} - \frac{1}{\xi_T^3}\frac{\partial Y_C}{\partial z}\right] \\
&+ \frac{2A_T E_s l_T^2}{L_{cT}}\left[\int_0^{L_T}\frac{1}{\xi_T^3}\frac{d^2 s_T}{dz^2}\theta_C dz\right]\frac{\partial}{\partial z}\left[\frac{1}{\xi_T^3}\frac{\partial \theta_C}{\partial z}\right] + \rho_f U^2 h_T \frac{C_{Ls}}{2},
\end{aligned} \tag{5}$$

$$\left(\frac{M_T}{3}+2m_T\xi_T\right)\frac{\partial^2\theta_C}{\partial t^2}=\frac{G_TK_T}{l_T^2}\frac{\partial^2\theta_C}{\partial z^2}+2H_{0T}\frac{\partial}{\partial z}\left[\frac{1}{\xi_T^2}\frac{\partial\theta_C}{\partial z}+\frac{3}{\xi_T^4}\frac{ds_T}{dz}\frac{\partial Y_C}{\partial z}\frac{\partial\theta_C}{\partial z}\right]$$
$$-\frac{2A_TE_s}{L_{cT}}\left[\int_0^{L_T}\frac{1}{\xi_T^3}\frac{\partial Y_C}{\partial z}\frac{\partial\theta_C}{\partial z}dz\right]\frac{1}{\xi_T^3}\frac{d^2s_T}{dz^2}$$
$$-\frac{2A_TE_s}{L_{cT}}\left[\int_0^{L_T}\frac{1}{\xi_T^3}\frac{d^2s_T}{dz^2}\theta_C dz\right]\frac{\partial}{\partial z}\left[\frac{1}{\xi_T}\frac{ds_T}{dz}-\frac{1}{\xi_T^3}\frac{\partial Y_C}{\partial z}\right]$$
$$+\frac{2A_TE_s}{L_{cT}}\left[\int_0^{L_T}\frac{1}{\xi_T^3}\frac{d^2s_T}{dz^2}Y_C dz\right]\frac{\partial}{\partial z}\left(\frac{1}{\xi_T^3}\frac{\partial\theta_C}{\partial z}\right)+\rho_fU^2h_T^2\frac{C_{Ms}}{2l_T^2}, \tag{6}$$

where Y_C and θ_C are the transverse displacement and rotational angle of the center of the deck, respectively, M_T is the mass of the deck per unit length, m_T is the mass of the cable per unit length, ξ_T is the local length of the cable at rest, E_s is the Young's modulus of the deck and cable, I_T is the linear density of the moment of inertia of the cross section of the deck, H_{0T} is the spanwise component of the tension of the cable, A_T is the area of the section of the cable, L_{cT} is the length of the cable, l_T is the half width of the deck, s_T is the position of the cable, G_T is the shear modulus of the deck, K_T is the torsional constant of the deck, C_{Ls} is the sectional lift coefficient, C_{Ms} is the sectional moment coefficient, L_T is the length of the deck, h_T is the height of the deck, ρ_f is the fluid density, and U is the wind velocity. The physical and geometrical parameters are obtained from Arioli and Gazzola [7]: $M_T = 7198$ kg/m, $m_T = 981$ kg/m, $E_s = 210$ GPa, $I_T = 0.15$ m^4, $H_{0T} = 58300$ kN, $A_T = 0.1228$ m^2, $L_{cT} = 868.62$ m, $l_T = 6$ m, $G_T = 81$ GPa, $K_T = 6.44\ 10^{-6}$ m^4, $L_T = 853.44$ m, $h_T = 2.4$ m, $\rho_f = 1.247$ kg/m^3, and $U = 18$ m/s. At rest, the cables reach the equilibrium state due to the balance of tension of the two cables and gravity acting on the deck and two cables:

$$H_{0T}\frac{d^2s_T}{dz^2}=\left[\frac{M_T}{2}+m_T\sqrt{1+\left(\frac{ds_T}{dz}\right)^2}\right]g, \tag{7}$$

where $g = 9.81$ m/s^2. At both ends of the cables, $s(0) = s(L_T) = 72$ m. The schematic diagram of the computational domain and boundary conditions for flow around the Tacoma Narrows Bridge is shown in Fig. 1c. Here, aerodynamic forces are considered only on the deck. The Reynolds number ($\mathrm{Re} = \rho_f U h_T/\mu_f$) is 300. Flow around the Tacoma Narrows Bridge is simulated with an initial condition of the angular velocity of $0.1\sin(2\pi z/L_T)$. The numbers of grid points are 497 (x) × 397 (y) × 2048 (z).

For time advancement, a generalized-α method [18] is applied to the governing equations of the structures. The second-order central difference is used for spatial discretizations of a long flexible circular cylinder and the Tacoma Narrows Bridge. Pinned and clamped boundary conditions are applied to the ends of a long flexible circular cylinder and the deck of the Tacoma Narrows Bridge, respectively.

3 Results and Discussion

3.1 *Flow Around an Elastically Mounted Rigid Circular Cylinder*

Figure 2a shows the trajectory of the center of the elastically mounted rigid cylinder in time. The trajectory has a crescent shape, and the amplitude of the transverse displacement is about 1.2 *D*. At the maximum transverse displacement, two starting vortices generated in the shear layers induce high pressure on the lower side due to strong impingement there but low pressure is distributed on the upper side due to flow acceleration (Fig. 2b and c), which results in a high lift coefficient.

3.2 *Flow Around a Long Flexible Circular Cylinder*

The wavelength of a flexible circular cylinder is $2L_c$. The temporal variation of the contours of instantaneous spanwise vorticity in an $(x - y)$ plane at $z = L_c/2$ is shown in Fig. 3. Similar to the flow around an elastically mounted rigid circular cylinder, starting vortices generated in the shear layers are located on the upper side.

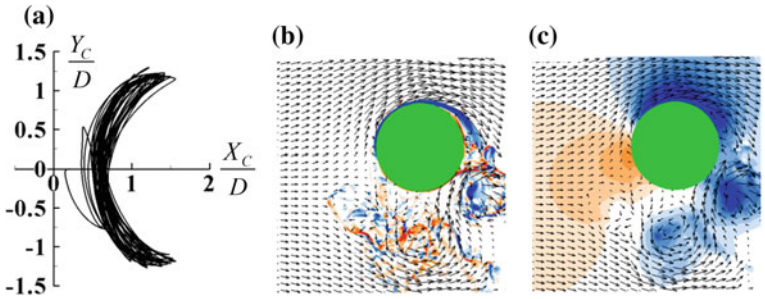

Fig. 2 Elastically mounted rigid circular cylinder: **a** trajectory of the center; **b**, **c** contours of instantaneous spanwise vorticity and pressure at the maximum transverse displacement

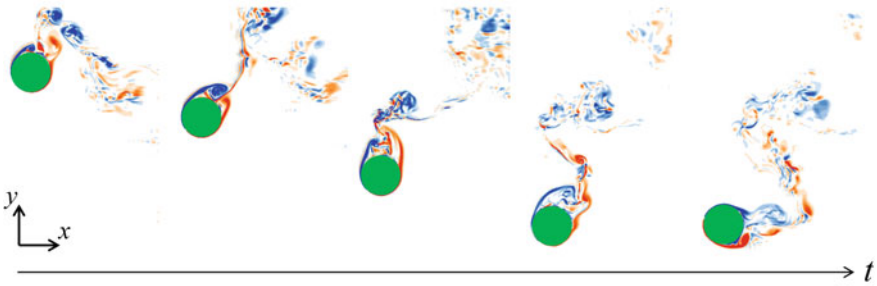

Fig. 3 Long flexible circular cylinder: contours of the instantaneous spanwise vorticity on $(x - y)$ planes at $z = L_c/2$ ($tU_{max}/D = 13.6, 15.9, 18.5, 21.1, 23.6$)

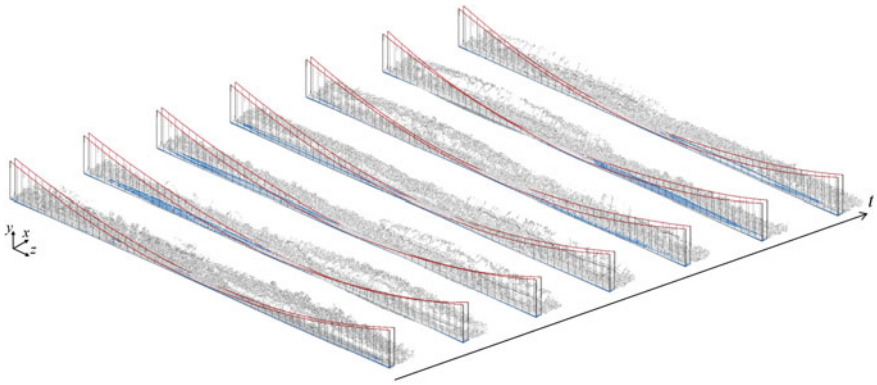

Fig. 4 Tacoma Narrows Bridge: instantaneous vortical structures ($tU/h_T = 45.5, 52.4, 58.9, 64.0, 70.2, 76.7, 82.6$)

3.3 Flow Around the Tacoma Narrows Bridge

Instantaneous vortical structures around the Tacoma Narrows Bridge during one cycle are shown in Fig. 4. Instantaneous vortical structures are generated along both the spanwise and transverse directions. The dominant frequency of the rotational angles of the deck matches with that of vortex shedding.

Acknowledgements This research is supported by National Research Foundation (No. NRF-2016R1E1A1A02921549), Korea.

References

1. Fuller RG, Lang CR, Lang RH (2008) Twin views of the Tacoma Narrows bridge collapse. American Association of Physics Teachers
2. Bleich F (1948) Dynamic instability of truss-sitffened suspension bridges under wind action. Proc ASCE 74:1269–1314
3. Pittel BG, Yakubovich VA (1961) Application of the theory of parametric resonance to explain the collapse of the Tacoma Narrows Bridge (Russian). Uspekhi Mat Nauk 15: 183–184
4. Pittel BG, Yakubovich VA (1969) A mathematical analysis of the stability of suspension bridges based on the example of the Tacoma Bridge (Russian). Vestnik Leningrad Univ 24:80–91
5. Billah KY, Scanlan RH (1991) Resonance, Tacoma Narrows Bridge failure, and undergraduate physics textbooks. Am J Phys 59:118–124
6. Green D, Unruh WG (2006) Tacoma bridge failure: a physical model. Am J Phys 74:706–716
7. Arioli G, Gazzola F (2017) Torsional instability in suspension bridges: the Tacoma Narrows Bridge case. Commun Nonlinear Sci Numer Simulat 42:342–357
8. Wu X, Ge F, Hong Y (2012) A review of recent studies on vortex-induced vibrations of long slender cylinders. J Fluids Struct 28:292–308
9. Bearman PW (2011) Circular cylinder wakes and vortex-induced vibrations. J Fluids Struct 27:648–658
10. Jauvtis N, Williamson CHK (2004) The effect of two degrees of freedom on vortex-induced vibration at low mass and damping. J Fluid Mech 509:23–62
11. Gsell S, Bourguet R, Braza M (2016) Two-degree-of-freedom vortex-induced vibrations of a circular cylinder at Re = 3900. J Fluids Struct 67:156–172
12. Kim W, Lee I, Choi H (2018) A weak-coupling immersed boundary method for fluid-structure interaction with low density ratio of solid to fluid. J Comput Phys 359:296–311
13. Kim J, Kim, D, Choi H (2001) An immersed-boundary finite-volume method for simulations of flow in complex geometries. J Comput Phys 171:132–150
14. Lee J, Choi H, Park N (2010) Dynamic global model for large eddy simulation of transient flow. Phys Fluids 22:075106
15. Choi H, Moin P (1994) Effects of the computational time step on numerical solutions of turbulent flow. J Comput Phys 113:1–4
16. Kim K, Baek SJ, Sung HJ (2002) An implicit velocity decoupling procedure for the incompressible Navier-Stokes equations. Int J Numer Methods Fluids 38:125–138
17. Bourguet R, Karniadakis GE, Triantafyllou MS (2011) Vortex-induced vibrations of a long flexible cylinder in shear flow. J Fluid Mech 677:342–382
18. Chung J, Hulbert GM (1993) A time integration algorithm for structural dynamics with improved numerical dissipation: the generalized-α method. J Appl Mech 60:371–375

Fluid-Structure Interaction and Control Around Vibrating and Morphing Configurations at High Reynolds Number

G. Jodin, N. Simiriotis, A. Aalilija, A. Marouf, Y. Hoarau, G. Harran, J. F. Rouchon and M. Braza

Abstract This study analyses the fluid-elastic instability occurring in turbulent wakes around tandem cylinders as well as the morphing effect in order to control the instability amplification and to improve the aerodynamic performances particularly concerning the Airbus-A320 wing-flap configuration. These studies have been carried out by means of High-Fidelity numerical simulations by using the NSMB—Navier Stokes MultiBlock code (Grossi et al. AIAA J 52(10):2300–2312, 2006) [1], as well as by refined physical experiments, after having built advanced morphing wing prototypes and tested in wind tunnel by using Time-Resolved PIV (TRPIV) and aerodynamic balance measurements. It has been shown that the electroactive morphing concepts are able to provide significant improvements of the aerodynamic performances and to decrease the *rms* of the displacement and of the forces in the case of the tandem cylinders configuration undergoing Flow Induced Vibration.

1 Introduction

The aerodynamic characteristics of airfoils at a chord Reynolds Electroactive morphing using smart materials as Shape Memory Alloys and mini-piezo-actuators distributed under the 'skin' of a lifting structure are able to modify the deformation

G. Jodin · N. Simiriotis · A. Aalilija · A. Marouf · G. Harran · M. Braza (✉)
IMFT-Institut de Mécanique Des Fluides de Toulouse, UMR CNRS 5502, Toulouse, France
e-mail: marianna.braza@imft.fr

G. Jodin · J. F. Rouchon
LAPLACE - Laboratoire de Plasma et Conversion d'Energie – UMR CNRS 5213, Toulouse, France

Y. Hoarau
ICUBE – UMR CNRS 7357 Fluid Mechanics Group, Strasbourg, France

A. Aalilija
Mines-Paritech – CEMEF, Sophia Antipolis, France

Y. Zhou et al. (eds.), *Fluid-Structure-Sound Interactions and Control*, Lecture Notes in Mechanical Engineering,
https://doi.org/10.1007/978-981-10-7542-1_30

capabilities and the vibrational behavior of the solid configuration interacting with the fluid instabilities. By using a hybridization among different classes of electroactive actuators, manipulation of the near-region turbulence structure can be achieved, which is able to modify the fluid-structure system in an optimal way, in order to provide increased performances *at high Reynolds number*.

Regarding the tandem cylinders, a detailed review concerning static cases (e.g. fixed cylinders), can be found in Sumner [2], as well as in the studies [2–4] by Zhou and Yiu [3], Alam and Meyer [4], Elhimer et al. [5] among others. In the present study, the Reynolds number is 166,000 and the pitch ratio (dimensionless distance between the cylinders x/D = 3.75). These parameters have been taken during the European research program ATAAC (Advanced Turbulence Simulations for Aeronautics Applications Challenges), coordinated by Schwamborn (DLR—Germany), in which the group of authors of the present article had participated. The related applications are those of instability and noise reduction in landing gear configurations as well as prevention of fluid-elastic instability in nuclear reactor cooling systems of cylinder bundles. In the present study, the onset of flow induced vibration of the downstream cylinder has been studied numerically. Furthermore, the study by numerical simulation of the behavior of an electroactive piezoactuator located near the separation point of the upstream cylinder on the forces and displacement has been carried out.

Concerning the electroactive morphing behavior around a supercritical wing, the Airbus A320 morphing wing has been studied. The morphing devices are an association of Shape Memory Alloys ensuring high deformations in low frequencies (order of 1 Hz) and piezoactuator patches able to vibrate at higher frequencies (order of 20–200 Hz) and ensuring small deformations (order of several millimeters). These last ones are located near the trailing edge region of the wing. The present association yields a *hybrid electroactive morphing*, able to create simultaneously high cambers in low frequencies and higher-frequency vibrating rear part of the wing, in the context of a *bio-inspired morphing* from large-span hunting birds. A detailed behavior of these morphing concepts can be found in the studies [6–9], by Chinaud et al. [8], Scheller et al. [6, 7], Jodin et al. [9], among other.

2 Methodology and Results

In the present study, the downstream cylinder can freely oscillate in the lift direction, in SDOF (Single Degree of Freedom). The simulations have been carried out by using the blended DDES-OES modelling approach [10, 11] (Detached Eddy Simulation employing the Organised Eddy Simulation [12] in the URANS part near the body's surfaces). This approach is able to take into account turbulence stress anisotropy in the near-region and to provide a smooth passage towards the LES region, by avoiding MSD (Massive Stress Depletion) effects in the interface between URANS and LES. Furthermore, thanks to the OES embedded approach, the formation of coherent structures near the bodies towards the outer region, issued

from flow instabilities coupled with the structural modes, is successfully accomplished. Therefore, the present study allowed the spontaneous onset of an oscillatory motion of the downstream cylinder, the evaluation of the Strouhal number of the body's displacement in relation with the fluid's von Kármán instability created from the upstream cylinder and modulated by the shearing mechanism of the downstream cylinder. This study evaluated these frequency modes as well as the progressive creation of phase-lag between the displacement and the lift force at Scruton number's value 2 and in the reduced velocity range (3–5.5). Furthermore, the present study captured a considerable amplification of the fluid-elastic instability at the reduced velocity's value of 5, characterized by a drastic increase of the displacement's amplitude. This bifurcation has been analyszed in detail by the present study. Moreover, a considerable modulation of the displacement's amplitude can be achieved by applying morphing of the near-separation region of the upstream cylinder. This can be achieved by vibrating piezo-electric patches in the related region.

Figure 1 shows the spontaneous amplification of the vertical displacement of the downstream cylinder for Scruton number 1, as the reduced velocity increases from 2 to 5.

Figure 2 shows a drastic change in the forces and displacement amplitudes at the reduced velocity of 5. This behavior characterizes two different regimes, as shown in the spectra, the first (during the smaller amplitudes evolution) having a fundamental frequency of 0.14 and the second (during the drastic amplitude increase) a frequency of 0.19. These two frequencies correspond respectively to the reattachment and alternating regimes, analyzed in the afore mentioned references. By introducing a vibration region large of order 0.01 D and imposing a vibration frequency equal to the Strouhal number and a quite slight amplitude of the motion of order 10^{-3} D (D being the cylinder's diameter), a significant reduction of the displacement amplitude and of the *rms* of the lift force can be obtained. This effect can be achieved by specific small piezoactuators of MFC type (Micro-Fiber-Composites), as illustrated in the following section (Fig. 3).

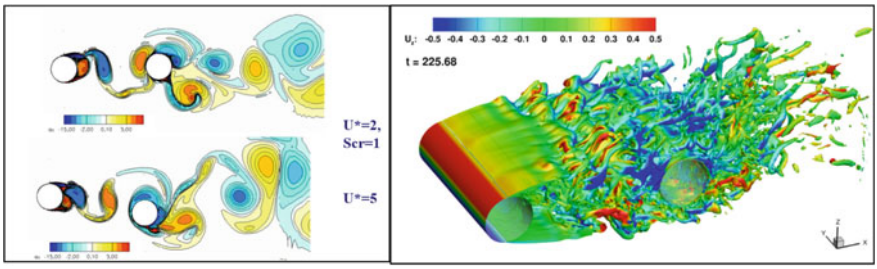

Fig. 1 Iso-vorticity contours at Reynolds number 166,000 showing the vertical displacement amplification of the downstream cylinder as the reduced velocity increases (left). 3D flow structure (right)

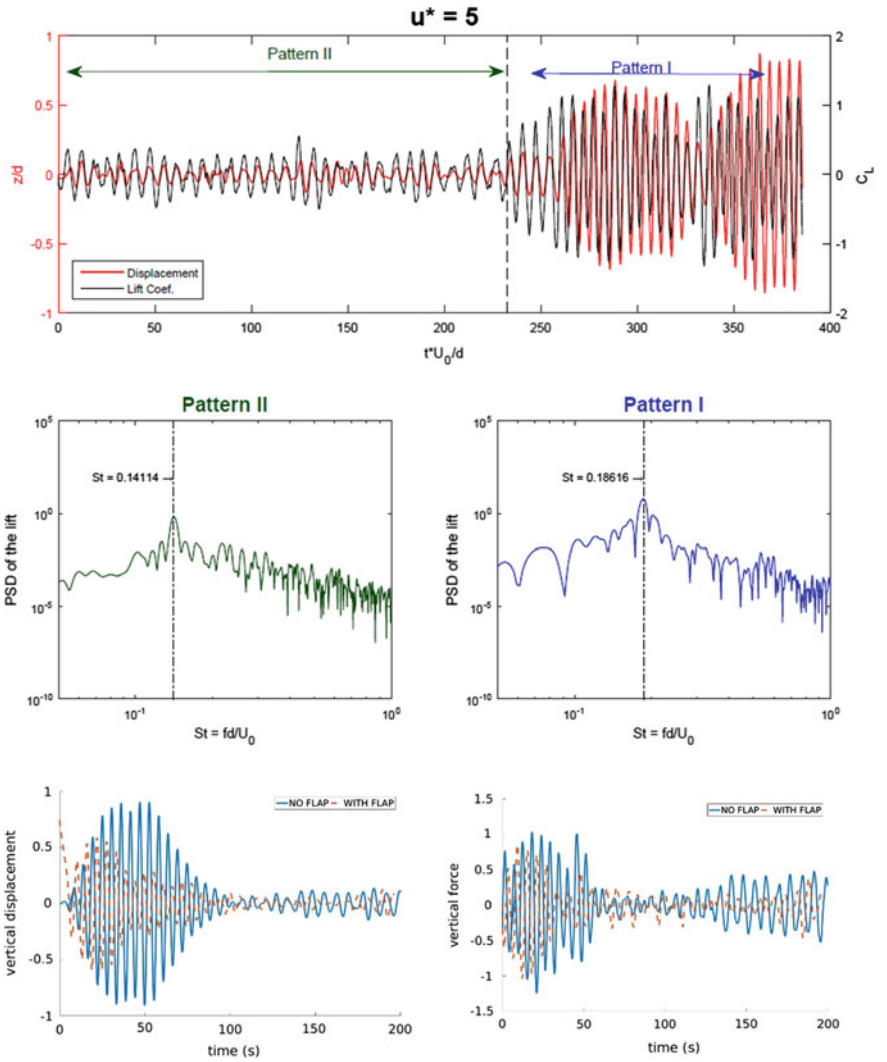

Fig. 2 Up: Time-dependent evolution of the lift force and displacement of the downstream cylinder. Botom: Reduction of the displacement and of the *rms* of the lift oscillations under the effect of the vibrating patch near the upper separation point of the upstream cylinder

Concerning the electroactive morphing effect on the aerodynamic performances of an Airbus A320 wing, the study has been carried out experimentally in the subsonic S4 wind tunnel of IMFT for Reynolds numbers 5,00,000 and 1 Million and angle of incidence 10°, as well as by numerical simulation using the OES approach in the NSMB code as previously, at the Reynolds number 1 Million. The effects of morphing have been studied separately for the trailing edge vibrations as

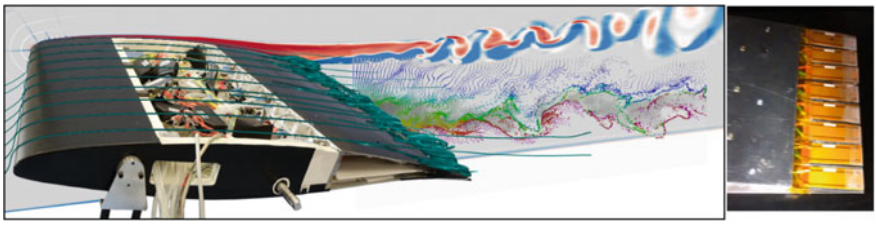

Fig. 3 Shows the A320 morphing prototype, as well as the flow structure in the wake, characterized by shear layer and von Kármán vortex dynamics

well as for the combined Shape Memory Alloys and vibrations. The vibrational action is achieved by MFC actuators (small piezo-patches), disposed along the span near the trailing edge region. The Shape Memory Alloys are composed by Titanium-Nickelium (NitiNol) wires (Fig. 4).

Regarding the instability modulation and aerodynamic performance increase by means of electroactive morphing, this study has shown the ability of manipulating the near-trailing edge turbulence structure around a morphing wing of Airbus-A320 type at Reynolds numbers in the range 1–4 Millions and in subsonic transonic speeds, corresponding to take-off and landing dynamics as well as to cruise speeds respectively. Electroactive hybrid morphing has been applied for different time and length scales of the turbulence structure thanks to hybridization among different classes of electroactive materials: shape memory alloys ensuring large camber of order 15–20% of the chord in low-frequency modes (order 1 Hz) and mini-piezo-actuators distributed in the trailing-edge region along the span, able to apply higher-frequency vibrations (order 100–300 Hz) with low deformations (order of several mm). By means of time-Resolved PIV and high-fidelity simulations, a significant effect of morphing has been detected and optimized in respect of the vibration frequencies (Fig. 5).

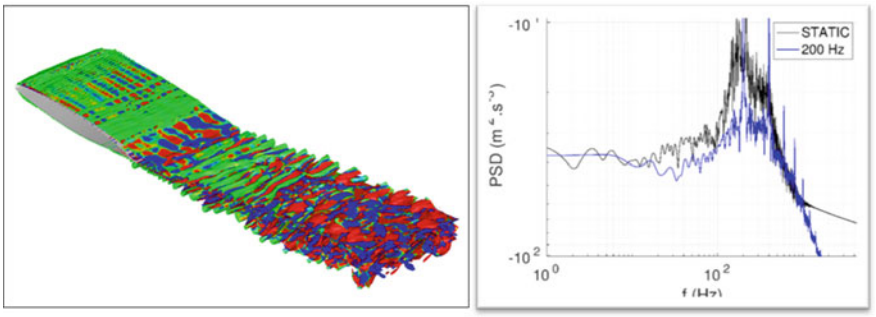

Fig. 4 Shows the three-dimensional flow structure around the A320 wing as well as the morphing effect by optimal vibrations reducing the peak of the shear layer mode. The streaklines are produced on the basis of Time-Resolved PIV (6 kHz)

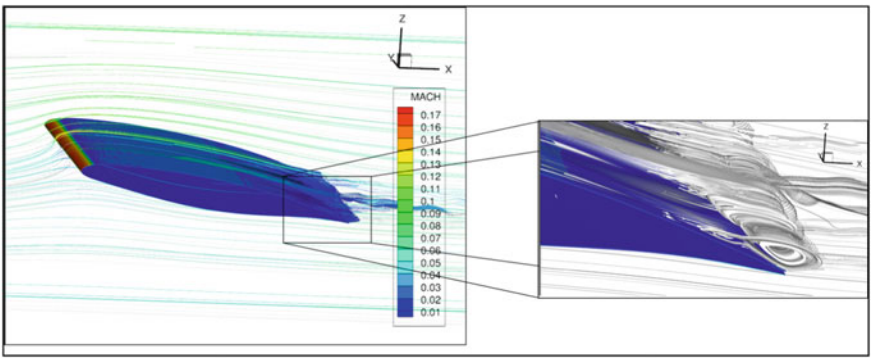

Fig. 5 3D flow structure around the A320 wing by OES simulations [10], as well as the morphing effect on the turbulence spectrum

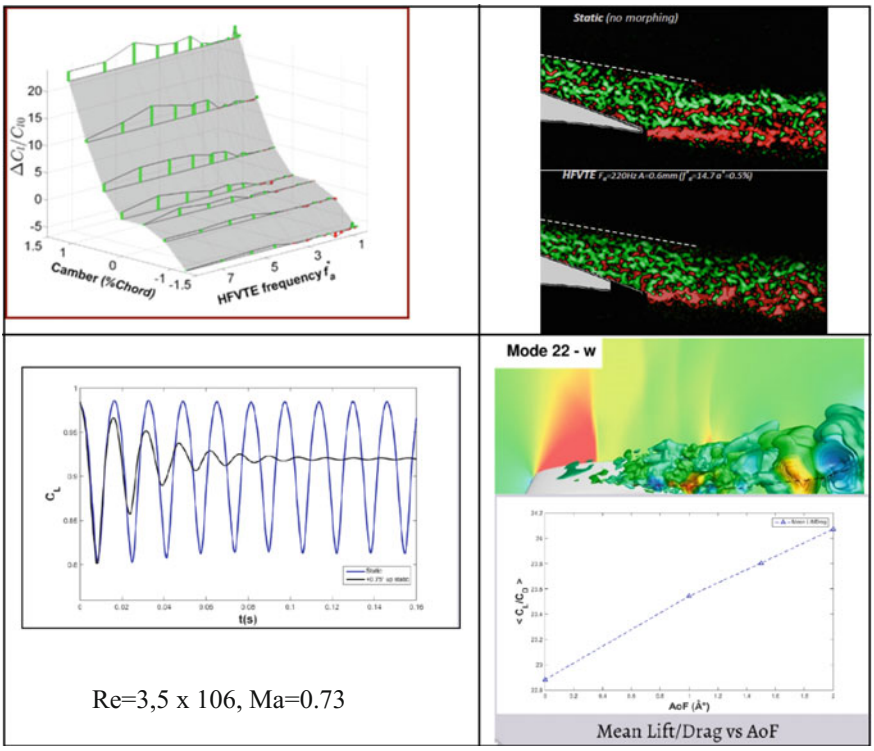

Fig. 6 Up-left: A320 morphing wing—combined effect of camber and vibration—hybrid morphing shows that the vibration associated to camber yields an additional increase of lift of 3% (region indicated by arrow). Up-right: decrease of the near-wake's width thanks to materialization of the eddy blocking effect by means of the morphing. Down_left: Suppression of buffet instability in cruise speed. Down-right: 3D turbulence structure by DDES and shock formation. Increase of lift-to-drag ratio thanks to morphing

The vibrational effect has been studied separately as a first step, as well as the camber effect, then association of both has been finally studied. It has been shown by means of POD and spectral analysis that vibration frequency ranges of order 90 Hz have a considerable impact on vortex breakdown of coherent Kelvin-Helmholtz eddies in the separated shear layers and downstream of the trailing edge. The morphing action introduces smaller-scale eddies between the shear layers and in the near wake, able to create an eddy-blocking effect [12] which operates as an upscale energy transfer and is able to constrict the shear layers and to create thinning of them and reduction of the wake's width, with a consequent reduction of the form drag and of the instability modes which are sources of noise. Moreover, it has been shown that a combined action of camber and of these higher-frequency vibrations is able to further increase lift, beyond the benefit achieved by camber control only (Fig. 6). The present hybrid electroactive morphing which is partly bio-inspired, is therefore able to increase lift by an order of 5% and to reduce drag by an order of 3%.

Concerning cruise speeds in the range of Mach umber (0.7–0.78), it has been shown by high-fidelity simulations that an optimal small trailing edge deformation and vibration frequency operating in the same small amplitudes as previously is able to suppress the transonic buffet instability, to reduce drag and increase the lift/drag ratio (aerodynamic "finesse"), Fig. 6.

The present studies have been part of the http://www.fondation-stae.net/ STAE—RTRA—DYNAMORPH and AIRBUS—ETCT Emerging Technologies and Concepts—Toulouse projects. Details about the morphing activity of the present team can be found in the research platform http://www.smartwing.org.

Acknowledgements The authors thank AIRBUS—Emerging Technologies and Concepts, Toulouse, the Foundation STAE, Sciences et Technologies pour l'Aeronautique et l'Espace, http://www.fondation-stae.net/, as well as the ANR Agence Nationale de Recherche under the project BARESAFE, http://www.agence-nationale-recherche.fr/?Project=ANR-11-MONU-0004, for their financial support. They are grateful to the computing centers CINES, IDRIS and CALMIP for the CPU allocation on their supercomputers.

References

1. Grossi F, Braza M, Hoarau Y (2014) Prediction of transonic buffet by delayed detached-Eddy simulation. AIAA J 52(10):2300–2312
2. Sumner D (2010) Two circular cylinders in cross-flow: a review. J Fluids Struct 26(6):849–899
3. Zhou Y, Yiu MW (2006) Flow structure, momentum and heat transport in a two-tandem-cylinder wake. J Fluid Mech 548:17–48
4. Alam MM, Meyer JP (2011) Two interacting cylinders in cross flow. Phys Rev E 84 (5):056304
5. Elhimer M, Harran G, Hoarau Y, Cazin S, Marchal M, Braza M (2016) Coherent and turbulent processes in the bistable regime around a tandem of cylinders including reattached flow dynamics by means of high-speed PIV. J Fluids Struct 60:62–79

6. Scheller J, Chinaud M, Rouchon JF, Duhayon E, Cazin S, Marchal M, Braza M (2015) Trailing-edge dynamics of a morphing NACA0012 aileron at high Reynolds number by time-resolved PIV. J Fluids Struct 55:42–51
7. Scheller J, Jodin G, Rizzo KJ, Rouchon JF, Duhayon E, Triantafyllou M, Braza M (2016) A combined smart-materials approach for next-generation airfoils. Solid State Phenom 251
8. Chinaud M, Rouchon JF, Duhayon E, Scheller J, Cazin S, Marchal M, Braza M (2014) Trailing-edge dynamics and morphing of a deformable flat plate at high Reynolds number by time-resolved PIV. J Fluids Struct 47:41–54
9. Jodin G, Motta V, Scheller J, Duhayon E, Döll C, Rouchon JF, Braza M (2017) Dynamics of a hybrid morphing wing with active open loop vibrating trailing edge by time-resolved PIV and force measures. https://doi.org/10.1016/j.jfluidstructs.2017.06.015. Accessed 13 July 2017
10. Shinde V, Marcel T, Hoarau Y, Deloze T, Harran G, Baj F, Cardolaccia J, Magnaud JP, Longatte E, Braza M (2014) Numerical simulation of the fluid structure interaction in a tube array under cross flow at moderate and high Reynolds number. J Fluids Struct 47:99–113
11. Bourguet R, Braza M, Harran G, El Akoury R (2008) Anisotropic Organised Eddy simulation for the prediction of non-equilibrium turbulent flows around bodies. J Fluids Struct 24 (8):1240–1251
12. Braza M, Perrin R, Hoarau Y (2006) Turbulence properties in the cylinder wake at high Reynolds number. J Fluids Struct 22:757–771
13. Szubert D, Grossi F, Jimenez-Garcia A, Hoarau Y, Hunt J, Braza M (2015) Shock-vortex shear-layer interaction in the transonic flow around a supercritical airfoil at high Reynolds number in buffet conditions. J Fluids Struct 55:276–302

Multiscale Simulations for Fluid Structure Interaction Problems with Biomedical Applications

Shu Takagi, Kazuya Shimizu, Satoshi Ii, Kazuyasu Sugiyama and Kohei Okita

Abstract A numerical method for massively parallel computing to solve fluid-structure interaction problems was developed and the method was employed for solving the multiscale problems in biomedical applications. As one of the examples, a platelet adhesion process to the vessel wall, which occurs at the initial stage of a thrombosis, was analyzed using the multiscale method of coupling continuum scale finite difference method with the molecular scale Monte Carlo method. The platelets adhesion to the injured vessel wall is caused by the protein-protein binding (GP1b-α on the platelet—VWF on the wall.). This protein-protein binding force is evaluated by Monte Carlo simulation, solving the stochastic process of each biding. Adhered platelets also feel the fluid mechanical force from blood flow and this force is affected by the presence of red blood cells, which causes the drastic change to the adhesion process. As another example of multiscale simulations, ultrasound therapy method using microbubbles are also explained.

Keywords Finite difference method · FSI · Protein-protein binding
Full eulerian formulation · Massively parallel computing · Blood flow
Ultrasound · Microbubbles

S. Takagi (✉) · K. Shimizu
Department of Mechanical Engineering, The University of Tokyo, 7-3-1, Hongo, Bnkyo-Ku, Tokyo 113-8656, Japan
e-mail: takagi@mech.t.u-tokyo.ac.jp

S. Ii · K. Sugiyama
Graduate School of Engineering Science, Osaka University, Osaka, Japan

K. Okita
Nihon University, College of Industry Technology, Chiba, Japan

Y. Zhou et al. (eds.), *Fluid-Structure-Sound Interactions and Control*, Lecture Notes in Mechanical Engineering,
https://doi.org/10.1007/978-981-10-7542-1_31

1 Introduction

Fluid-Structure Interaction (FSI) phenomena are ofter observed in many situations, e.g., biological systems, and industrial processes. The computational Fluid dynamics is more conventionally described in Eulerian frame, while the computational structure dynamics is more straightforward to be described in a Lagrangian way. The coupling of the Fluid and structure dynamics is not always a easy task due to this difference in the numerical framework. In this paper, a full Eulerian approach for the continuum scale fluid-structure coupling and also fluid-membrane coupling problems is introduced and the method is further extended to multiscale problems such as continuum-molecular coupling ones.

Thinking about the analysis using the voxel data converted from the medical image data of MRI or CT, it is straightforward to develop the full Eulerian finite difference methods, which can directly utilize the voxel data to describe the boundary on the fixed Cartesian meshes and avoid complicated process in mesh generation and reconstruction. Sugiyama et al. [9] developed a novel full-Eulerian FSI solver, and it was extended to a fluid and stiff material interaction and fluid and membrane interaction [4, 5, 11]. The method is also suitable for the massively parallel computation [10] and achieved actual speed of 4.5 peta flops, which was the world-fastest FSI simulation in the year of 2012. The method was used to analyse the platelet adhesion process on the injured vessel wall, which corresponds to the initial stage of thrombosis. To simulate this process, the molecular scale protein-protein binding needs to be considered with the blood flow simulation.

As another example of multiscale problems in the medical applications, high intensity focused ultrasound (HIFU) simulations with the utilization of microbubbles for the ultrasound therapy is introduced. In this method, bubble dynamics equations are coupled as small-scale phenomenon in both space and time with the large-scale fluid mechanical or acoustic field equations. These kinds of multiscale methods developed by the authors are explained in this paper.

2 Multiscale Method for Fluid-Structure-Protein Dynamics Coupling

2.1 Full Eulerian Method for FSI Problems

As is mentioned in Introduction, we have been working on a novel numerical method for fluid structure interaction (FSI) problems, which is available for massively parallel computing. Sugiyama et al. [9] developed a full-Eulerian FSI solver with fixed grid system, which is suitable for introducing the voxel type medical image data. In this method, the concept of well-known VOF method for two-phase flows are introduced for fluid and hyperelastic-materials interaction problems. Since the original VOF method using the one-equation Eulerian formulation cannot keep

the information of the material points to link between the reference and current configurations, a method to quantify the amplitude of deformation is required. For this purpose, we introduced Eq. (1), which gives the advection equation for left Cauchy-Green deformation tensor defined on each grid point, and this equation is temporally updated on the fixed grid system.

$$\partial_t \mathbf{B} + (\mathbf{v} \cdot \nabla)\mathbf{B} = \mathbf{L} \cdot \mathbf{B} + \mathbf{B} \cdot \mathbf{L}^T, \quad \text{where} \quad \mathbf{L} = \nabla \mathbf{v}^T. \tag{1}$$

This full-Eulerian approach method has been reviewed by Takagi et al. [11]. The simulation example of large scale parallel computation with $O(10^6)$ flowing RBC-like hyperelastic particles are shown in Fig. 1.

2.2 *Full Eulerian Method for Fluid-Membrane Interaction Problems*

The above-mentioned method was further developed for fluid-membrane interaction problems and applied to the blood flows containing Red Blood Cells and platelets. Ii et al. [4, 5] developed a full Eulerian fluid–membrane interaction method as an extension of the concept proposed by Sugiyama et al. [9]. In this method, a smoothed volume fraction (VOF) function is introduced to express a material phase describing each fluid. This VOF function ϕ chages the value from 0 to 1 within a few computational meshes. A membrane transition region Γ is

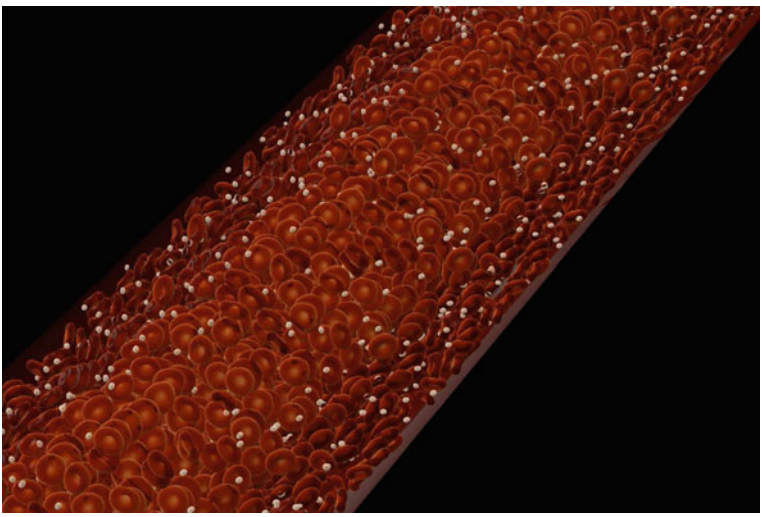

Fig. 1 Large scale parallel computation with $O(10^6)$ deformable hyper elastic particles

expressed as $|\nabla\phi| \leq \varepsilon$, where $|\nabla\phi|$ corresponds to a smoothed Delta function (e.g. [2] and ε is an arbitrarily value depending on the mesh size.

Introducing a basic theory on the finite deformation [1, 8], a set of governing equations with a one equaion formulation for the mixture is given in the Eulerian frame. The discretization of a set of PDEs is given in the finite difference/volume manner, and the SMAC algorithm is employed for the coupling of the pressure and velocity fields using the staggered arrangement. More detailed description on the numerical methods is given in [4, 5].

As one of the examples for the numerical simulations, the flows containing many RBCs and some platelets in an capillary tube are shown in Fig. 2. Snapshots of numerical results at $t = 7.5$, 30 and 75 ms are shown. It is found that the initially-distributed RBCs interact and are mixed in time. Each RBC has a different shape of a parachute type or slipper one reported in both experiment [3] and a numerical simulation [12]. The deformed RBCs tends to flow near the axial center due to a hydrodynamic effect, causing a plasma phase near the wall, so-called the cell-free layer.

2.3 *Multiscale Coupling Method for Simulating the Platelet Adhesion Process*

Thrombosis is one of the most important diseases causing the myocardial and cerebral infarctions. This disease is caused with a very complicated mechanism

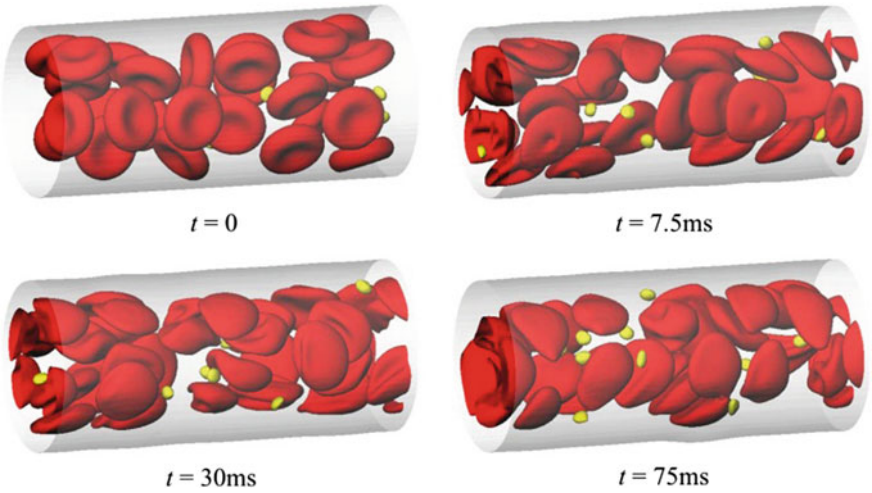

Fig. 2 Simulated results of flowing RBCs and platelets. Reproduced from Ii et al. [4]

affected from molecular scale protein-protein interaction to continuum scale fluid mechanical interaction in blood flow. In the initial stage, platelets start showing the aggregation at the injured wall, where von Willebrand Factor (VWF) is attached. The Glycoprotein, GPIb-α, on the platelet membrane shows ligand-receptor type interaction with this VWF. Through the binding force between GPIb-α and VWF, platelets start showing adhesion around this spot. From this stage, very complicated activated process of platelets and interactions with blood, vessel walls red blood cells, fibrin etc. occur. And, finally, they end up with the occlusion of the vessels.

Here, the numerical model for conducting the initial stage of thrombus formation is explained. To analyze this process, we used the above-explained the full Eulerian fluid-membrane coupling method. The method is further coupled with the stochastic Monte Carlo method for the interactions between GPIb-α and VWF molecules. The basic concept of this multiscale thrombosis simulator is given in Fig. 3.

Using this simulator, the influence of RBCs on the platelets adhesion process was investigated. It was shown from the simulation that the adhesion of platelets does not occur without the presence of RBCs. The velocity fluctuation in the wall-normal direction caused by the presence of RBCs plays an essential role to have the platelets adhesion. The snapshot of the platelet adhesion in the presence of RBCs are shown in Fig. 4.

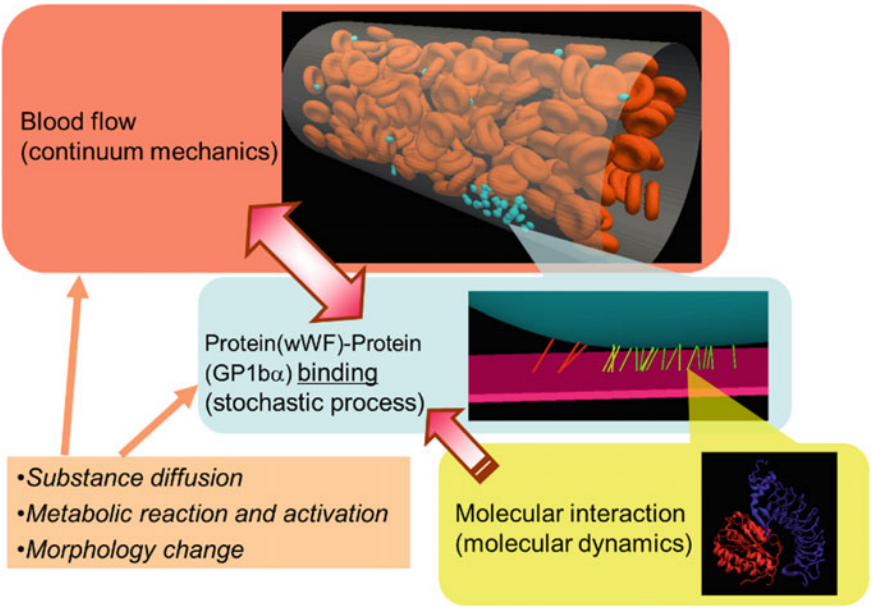

Fig. 3 Concept of multiscale modeling of thrombosis

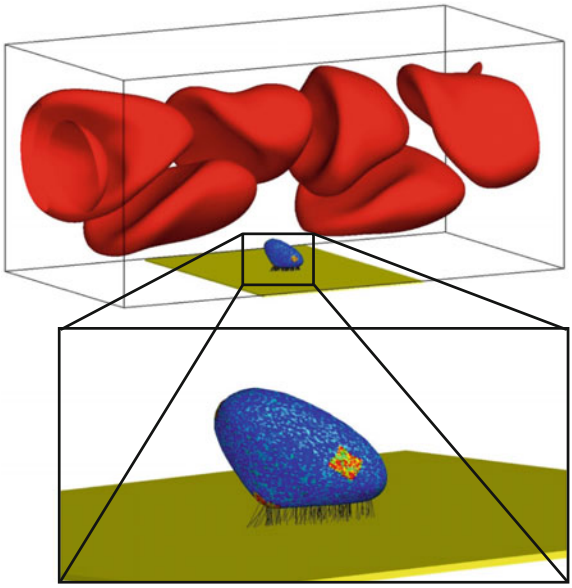

Fig. 4 Simulation result of platelet adhesion in the presence of RBCs

3 Multiscale Simulations of HIFU with Microbubbles

3.1 Microbubble Enhanced HIFU

Ultrasound therapy is a rapidly growing technique, which is expected to be one of the minimally-invasive methods. In ultrasound therapy, High Intensity Focused Ultrasound (HIFU) is used to achieve the local treatment with the high energy deposition. This treatment is known to be enhanced using the ultrasound contrast agent microbubbles [6]. That is, the heat generated by the bubble motion contributes an enhanced localized heating effect, via volume oscillation of bubbles. The behavior of microbubbles in a focused ultrasound field is not well investigated due to the complex interactions between the oscillating bubbles and the ultrasound. Here, as another example of the multiscale coupling method, the simulation method for microbubble-enhanced HIFU is introduced.

3.2 Simulation Model

Numerical simulations were conducted for the focused ultrasound in microbubble mixture gel shown in Fig. 5. For ultrasound propagation, bubbly flow mixture equations are solved as large-scale equations. The basic equations are discretized by a sixth-order finite difference scheme in space and are developed temporally on the basis of the finite-difference time-domain (FDTD) method with orthogonal mesh.

Fig. 5 Simulation Setup

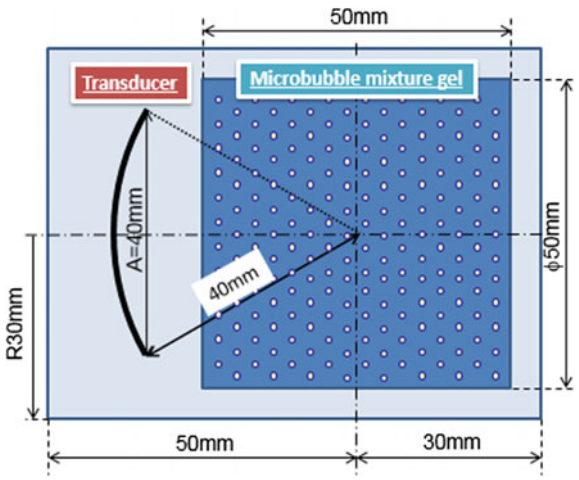

The signed distance function is employed for the shape representation of a transducer in the computational domain. Ultrasound irradiations are represented as the sound source or sink corresponding to the volume fraction of transducer. The perfectly matched layer (PML) is employed to represent the nonreflecting boundary.

For the small-scale bubble behaviors to resolve the rebound of bubble collapse, the bubble dynamics equation given by Eq. (2) is integrated in adaptive time increments that are consistently smaller than the time increment for the integration of the basic equations for the mixture. Bubbles are described by the representative bubble at the Lagrange point x_B and coupled with the mixture phase by the Euler–Lagrange method, which requires the interpolation of physical values between Euler and Lagrange points.

More detail description for the numerical method is given in [7].

$$\rho_L\left[\left(1-\frac{\dot{R}}{c}\right)R\ddot{R}+\left(1-\frac{1}{3}\frac{\dot{R}}{c}\right)\frac{3}{2}\dot{R}^2\right]=\left(1+\frac{\dot{R}_2}{c}\right)\left[P_G-P_S-\frac{2\sigma}{R}-4\mu\frac{\dot{R}}{R}-\frac{4}{3}G\left[1-\left(\frac{R_0}{R}\right)^3\right]\right]$$
$$+\frac{R}{c}\left[\frac{dP_G}{dt}-\frac{dP_S}{dt}+\frac{2\sigma}{R}\frac{\dot{R}}{R}+4\mu\left(\frac{\dot{R}}{R}\right)^2-4\mu\frac{\ddot{R}}{R}-4G\left(\frac{R_0}{R}\right)^3\frac{\dot{R}}{R}\right] \tag{2}$$

3.3 Numerical Results

Numerical simulations were conducted for the different microbubble concentrations. The comparison between numerical results and experimental results are shown in Fig. 6. Both results show good agreements and indicate that the higher

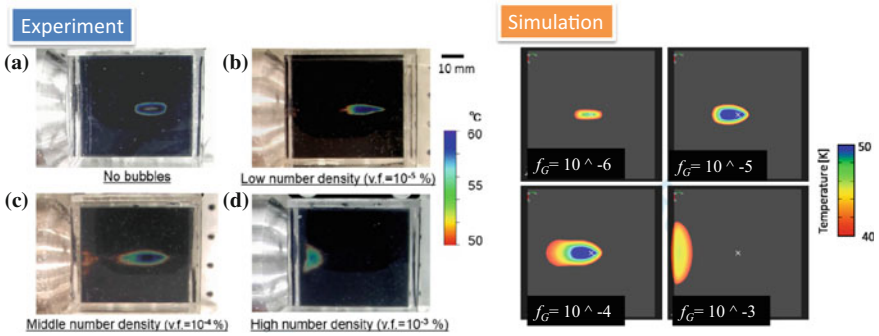

Fig. 6 Temperature rise distribution of HIFU for different bubble concentrations

concentration give the temperature rising spot coming closer to the transducer. This interesting behaviour comes from the fact that each bubble dissipates the energy due to bubble oscillation, and this gives the shielding effect of pressure wave propagating in bubbly liquid mixture with the increase of bubble concentration.

4 Conclusions

In this paper, 2 types of multiscale simulations have been briefly introduced. The present simulation results support some experimental results and help us to understand what is going on in the microscale phenomena. The concept of the present methods is available for many other problems. More detail discussion for the limitation of the methods will be important for the wide area of the applications.

References

1. Barthés-Biesel D, Rallison JM (1981) The time-dependent deformation of a capsule freely suspended in a linear shear flow. J Fluid Mech 113:251–267
2. Brackbill JU, Kothe DB, Zemach C (1992) A continuum method for modeling surface tension. J Comput Phys 100:335–354
3. Gaehtgens P, Duhrssen C, Albrecht KH (1980) Motion, deformation, and interaction of blood cells and plasma during flow through narrow capillary tubes. Blood Cells 6:799–817
4. Ii S, Gong X, Sugiyama K, Wu J, Huang H, Takagi S (2012) A full Eulerian fluid-membrane coupling method with a smoothed volume-of-fluid approach. Commun Comput Phys 12 (2):544–576
5. Ii S, Sugiyama K, Takeuchi S, Takagi S, Matsumoto Y (2012) A computational blood flow analysis in a capillary vessel including multiple red blood cells and platelets. J Biomech Sci Eng 7:72–83
6. Matsumoto Y, Allen JS, Yoshizawa S, Ikeda T, Kaneko Y (2005) Medical ultrasound with microbubbles. Exp Thermal Fluid Sci 29(3):255–265

7. Okita K, Sugiyama K, Takagi S, Matsumto Y (2013) Microbubble behavior in an ultrasound field for high intensity focused ultrasound therapy enhancement. J Acoust Soc Am 134 (2):1576–1585
8. Skalak R, Tözeren A, Zarda PR, Chien S (1973) Strain energy function of red blood cell membranes. Biophys J 13:245–264
9. Sugiyama K, Ii S, Takeuchi S, Takagi S, Matsumoto Y (2011) A full Eulerian finite difference approach for solving fluid–structure coupling problems. J Comput Phys 230(3):596–627
10. Sugiyama K, Ii S, Shimizu K, Noda S, Takagi S (2017) A full Eulerian method for fluid-structure interaction problems. Proc IUTAM 20:159–166
11. Takagi S, Sugiyama K, Ii S, Matsumoto Y (2012) A review of full Eulerian methods for fluid structure interaction problems. J Appl Mech 79(1):010911
12. Zhao H, Isfahani AHG, Olson LN, Freund JB (2010) A spectral boundary integral method for flowing blood cells. J Comput Phys 229:3726–3744

Numerical Investigation of Vortex-Induced Vibration of Circular Cylinder with Multiple Control Rods at Low Reynolds Number

Ming-ming Liu, Ming Zhao, Lin Lu, Bin Teng and Guo-qiang Tang

Abstract Vortex induced vibration of a circular cylinder with multiple small-diameter control rods at a relatively low Reynolds number Re = 200 is numerically investigated in this study. The numerical model is based on the Reynolds-Averaged Navier-Stokes equations. The Arbitrary Lagrangian-Eulerian (ALE) method is employed to consider the motion of the circular cylinders. The Petrove Galerkin Finite Element Method (PG-FEM) is used to discretize the governing equations. The numerical results show that the maximum oscillation amplitude for the small gap ratio of $G/D = 0.1$ is almost the same as that of an isolated circular cylinder. However, for larger gap ratios, the maximum oscillation amplitudes are much smaller. Therefore, the VIV response of the circular cylinder can be successfully suppressed by the six control rods in present study.

Keywords VIV · Suppressed · Multiple cylinders

1 Introduction

The Vortex-Induced Vibration (VIV) can be widely encountered in ocean engineering, civil engineering, chemical industry, aerodynamic engineering and so on. A typical example is the VIV of deep-water risers in petroleum exploration. The oscillatory drag and lift forces on a cylindrical structure will lead to the vibration of the structure, which is an important reason of structural failure. When the vortex shedding frequency is close to the natural frequency, the amplitude of vibration increases significantly and lock-in or synchronization occurs. Many researchers have conducted studies on VIV in the past decades, such as Feng [1], Bearman [2], Williamson and Govardhan [3], Mittal and Kumar [4], Tang et al. [5] and Zhao

M. Liu (✉) · M. Zhao
Western Sydney University, Penrith, Australia
e-mail: M.Liu@westernsydney.edu.au

L. Lu · B. Teng · G. Tang
Dalian University of Technology, Dalian, China

Y. Zhou et al. (eds.), *Fluid-Structure-Sound Interactions and Control*, Lecture Notes in Mechanical Engineering,
https://doi.org/10.1007/978-981-10-7542-1_32

et al. [6]. Efforts have also been made to control VIV. One of the popular methods for VIV control of a cylinder is to attach control devices such as helical strikes, control rods, etc. to the cylinder. Based on our previous numerical examinations for the stationary cylinder group (Lu et al. [7]) the VIV response of a primary circular cylinder with multiple control rods is numerical investigated at a relatively low Reynolds number Re = 200. The effect of the gap between the cylinder and the control rods is examined.

2 Numerical Model

The governing equations for the motion of incompressible viscous Newtonian fluids are the Reynolds-Averaged Navier-Stokes (RANS) equations. The equations can be written in ALE formulation,

$$\frac{\partial u_i}{\partial x_i} = 0 \tag{1}$$

$$\frac{\partial u_i}{\partial t} + \left(u_j - u_j^m\right)\frac{\partial u_i}{\partial x_j} = -\frac{1}{\rho}\frac{\partial p}{\partial x_i} + \nu\frac{\partial}{\partial x_j}\left(\frac{\partial u_i}{\partial x_j}\right) \tag{2}$$

where u_i is the i-th velocity in the x_i-direction by using the Cartesian coordinates ($u_1 = u$ and $u_2 = v$ for $x_1 = x$ and $x_2 = y$, respectively), u_j^m is the velocity of the moving grid, t is the time, p is the pressure, ρ is the fluid density, ν is the kinematic viscosity.

Figure 1 shows a sketch of the computational domain for viscous fluid flow over an elastically mounted circular cylinder with six small control rods. The diameter ratio of the control rods to the primary cylinder is $d/D = 0.24$, where d and D are the diameters of the control rods and the primary cylinder, respectively. The gap between the primary circular cylinder and the control rods is defined as G.

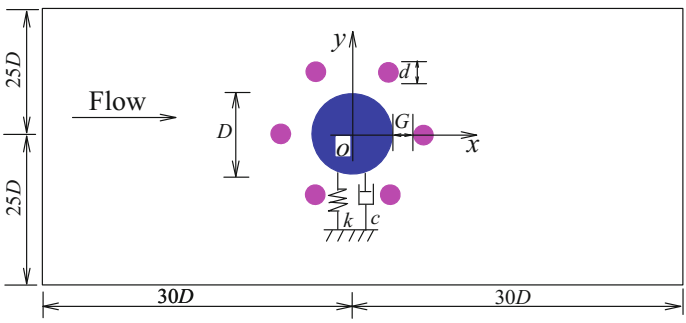

Fig. 1 Computational domain for viscous fluid flow over elastically mounted circular cylinders

The control rods and the primary cylinder are rigidly connected with each other and move together in the fluid.

The motion of the circular cylinders is represented as a mass-spring-damper system. Hence, the motion equation of the circular cylinders in cross-flow direction can be written as,

$$m\ddot{Y} + c\dot{Y} + kY = F_y(t) \tag{3}$$

where m, c and k are the mass of the cylinders, the structural damping and the rigidity of the spring, respectively, $\ddot{Y}$, $\dot{Y}$ and Y are the acceleration, velocity and displacement, respectively and $Fy(t)$ is the total lift force of the primary circular cylinder and control rods.

3 Numerical Results and Discussion

Figure 2 shows the variation of the maximum oscillation amplitude Y_{max} of the cylinder group with the reduced velocity for a constant gap ratio $G/D = 0.7$. The reduced velocity is defined as $U_r = U/f_nD$, where U and f_n are the free-stream velocity and the structural natural frequency, respectively. In Fig. 2, the maximum oscillation amplitude of cylinder group, appearing at $U_r = 6.5$, is about 0.11 D, which is much smaller than the maximum response of an isolated cylinder. Additionally, the lock-in region for the cylinder group is about between $U_r = 5.0$ and 6.5, which is much narrower than that of an isolated circular cylinder. Therefore, both the maximum vibration amplitude and the lock-in region can be significantly reduced by appropriately installing control rods around the primary circular cylinder.

Figure 3 presents the variation of Y_{max}/D with the reduced velocity U_r under different gap ratios (G/D). It can be seen from Fig. 3 that the maximum oscillation amplitude can reach about 0.64 D for the small gap ratio of $G/D = 0.1$, which is almost the same as that of an isolated circular cylinder. However, for larger gap ratios, namely, $G/D = 0.7$ and 1.4, the maximum oscillation amplitudes are much

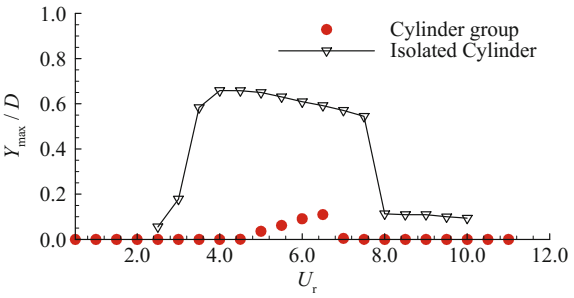

Fig. 2 Variation of Y_{max} with reduced velocity U_r with the gap ratio G/D = 0.7, m* = 2.0, ξ = 0.0

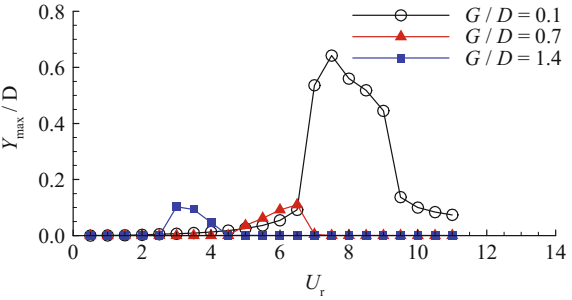

Fig. 3 Variation of Y_{max} with reduced velocity U_r under different gap ration G/D with m* = 2.0, ξ = 0.0

smaller. Both are about 0.1 *D*. The lock-in region moves towards the low reduced velocity with the increase of gap ratio *G*/*D*. The results in Fig. 3 demonstrate that the VIV response of the circular cylinder can be successfully suppressed by the six control rods over a wide range of gap ratio, at least $0.7 \leq G/D \leq 1.4$ for the present study.

4 Conclusions

The numerical results of fluid induced vibration of a circular cylinder with multiple control rods at Re = 200 are presented in this work. The effect of spacing ratio and reduced velocity is investigated.

For small gap ratios, the maximum oscillation amplitude is almost the same as that of an isolated circular cylinder. But the lock-in region is much narrower than that of an isolated circular cylinder.

For large gap ratios, both the maximum oscillation amplitudes and the lock-in region are much smaller than that of an isolated cylinder.

Therefore, numerical results show that the VIV response of the circular cylinder can be successfully suppressed by the six control rods over a wide range of gap ratio for the present study.

References

1. Feng CC (1986) Master's thesis, University of British Columbia
2. Bearman PW (1984) Vortex shedding from oscillating bluff bodies. Ann Rev Fluid Mech 16:195–222
3. Williamson CHK, Govardhan R (2008) A brief review of recent results in vortex-induced vibrations. J Wind Eng Ind Aerodyn 96(6–7):713–735
4. Mittal S, Kumar V (1999) Finite element study of vortex-induced cross-flow and in-line oscillations of a circular cylinder at low Reynolds numbers. Int J Numer Meth Fluids 31(7): 1087–1120

5. Tang GQ, Lu L, Teng B et al (2013) Numerical simulation of vortex-induced vibration with three-step finite element method and arbitrary Lagrangian-Eulerian Formulation. Adv Mech Eng 1
6. Zhao M, Cui Z, Kwok K et al (2016) Wake-induced vibration of a small cylinder in the wake of a large cylinder. Ocean Eng 113:75–89
7. Lu L, Liu M, Teng B et al (2014) Numerical investigation of fluid flow past circular cylinder with multiple control rods at low Reynolds number. J Fluids Struct 48:235–259

The Effect of Aspect Ratio on the Normal Force and Bending Moment Coefficients for a Surface-Mounted Finite Cylinder

A. Beitel and D. Sumner

Abstract A cylinder is constructed to have its aspect ratio (AR = *H/D*) varied between 0.5 and 11 in increments of 0.5. A force balance is used to measure a normal force developed on the free end of the cylinder, along with the drag force and corresponding bending moment. The forces are seen to be influenced by two critical aspect ratios, occurring at AR = 2.5 and AR = 6. The drag coefficient increases rapidly for low AR, is stable between the critical AR, and rises linearly for high AR. The normal force coefficient reaches a plateau between the critical AR. The bending moment coefficient and the point of action for the drag force are stable for AR higher than 6, and increase rapidly at low AR. Below AR = 2.5, the boundary layer is dominant, and above AR = 6, the free end effects begin to reduce as infinite cylinder behaviour is approached.

Keywords Fluid · Bluff body · Finite cylinder · Drag · Normal force Bending moment

1 Introduction

The flow around a surface-mounted finite-height cylinder (Fig. 1) is strongly three-dimensional [4, 5]. The flow field, vortex shedding, surface pressure distributions, and aerodynamic forces are sensitive to the cylinder's aspect ratio, AR = H/D (where H is the cylinder height and D is its diameter), Reynolds number, Re = $U_\infty D/\nu$ (where U_∞ is the freestream velocity and ν is the kinematic viscosity), and the relative thickness of the boundary layer on the ground plane, δ/D (where δ is the boundary layer thickness at the location of the cylinder). Several studies (e.g., [12, 14]) report measurements of the mean drag coefficient, $C_D = 2F_D/(\rho U\infty^2 HD)$

A. Beitel (✉) · D. Sumner
University of Saskatchewan, 57 Campus Drive, Saskatoon, SK, Canada
e-mail: adam.beitel@usask.ca

D. Sumner
e-mail: david.sumner@usask.ca

Y. Zhou et al. (eds.), *Fluid-Structure-Sound Interactions and Control*, Lecture Notes in Mechanical Engineering,
https://doi.org/10.1007/978-981-10-7542-1_33

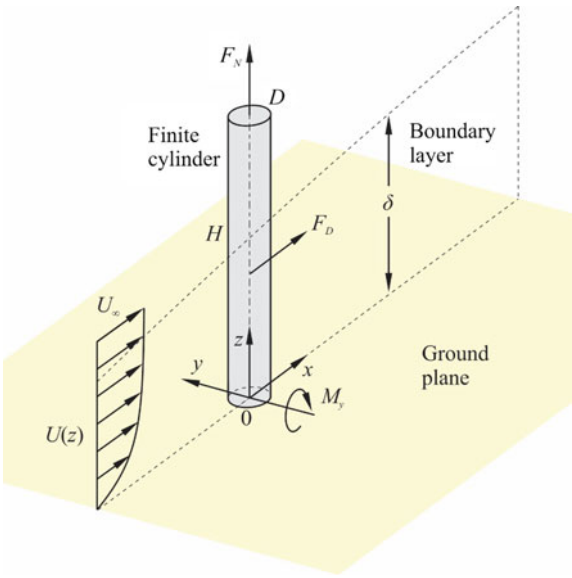

Fig. 1 Schematic of the flow around a surface-mounted finite cylinder. The origin of the coordinate system is at the base of the cylinder

(where F_D is the mean drag force and ρ is the density), which may be obtained directly with a force balance or indirectly through integration of the pressure distribution on the circumferential surfaces of the cylinder, and the variation of C_D with AR, *Re*, and δ/*D*. Pressure distributions on the free-end surface of the cylinder have also been measured [13], but few results have been reported for the corresponding mean normal force coefficient, $C_N = 2F_N/(\rho U\infty^2 \pi D^2/4)$ (where F_N is the mean normal force), which can be obtained from integration of the free-end pressure distribution.

In the present experimental study, small increments of AR are used to study its influence on the mean aerodynamic forces and moments experienced by a finite cylinder, including measurements of the mean normal force coefficient, C_N, and the mean bending moment coefficient, $C_{My} = 2M_y/(\rho U\infty^2 H^2 D)$ (where M_y is the mean bending moment about the cylinder-wall junction, defined as positive in the clockwise direction, as in Fig. 1), which have not been reported extensively in the literature. Results are reported at a single Re and four values of δ/*D* for $0.5 < \text{AR} < 11$. Comparison is made with C_N data obtained by integrating free-end pressure distributions reported in the literature.

2 Experimental Approach

Experiments were conducted in a low-speed wind tunnel using two sets of finite cylinders. The primary set of cylinders, with $D = 48$ mm, had heights which could be increased in steps of *D*/2 to give $0.5 < \text{AR} < 11$ in increments of 0.5. The

second set of cylinders, with $D = 31.5$ mm (similar to [4]), had aspect ratios of AR = 3, 5, 7 and 9. Cylinders were mounted on a six-component force balance, which was used to measure F_D, F_N, and M_y. The relative boundary layer thickness on the ground plane was $\delta/D = 0.6$ for the primary set of cylinders and $\delta/D = 0.9$ for the second set of cylinders. Tests on a turbulent, thick boundary layer yielded measurements for $\delta/D = 1.88$ and $\delta/D = 2.86$ as well. All force measurements were made at a Reynolds number of 6.5×10^4.

3 Results

Figure 2 shows the results for C_D, C_N, C_{My}, and point of action (PoA) as functions of AR. Data are shown for all four cases of δ/D and, in Fig. 2b, for selected C_N data obtained from integrating free-end pressure distribution data found in the literature.

The mean drag coefficient (Fig. 2a) has been reported extensively in other studies, although rarely has a single study focused on a wide range of AR, with a single *Re* and δ/D, and with as small an increment in AR, as in the present study. Figure 2a is one of the few times the overall behaviour of C_D with AR for a finite cylinder has been explicitly shown, though this curve is similar to the one shown by

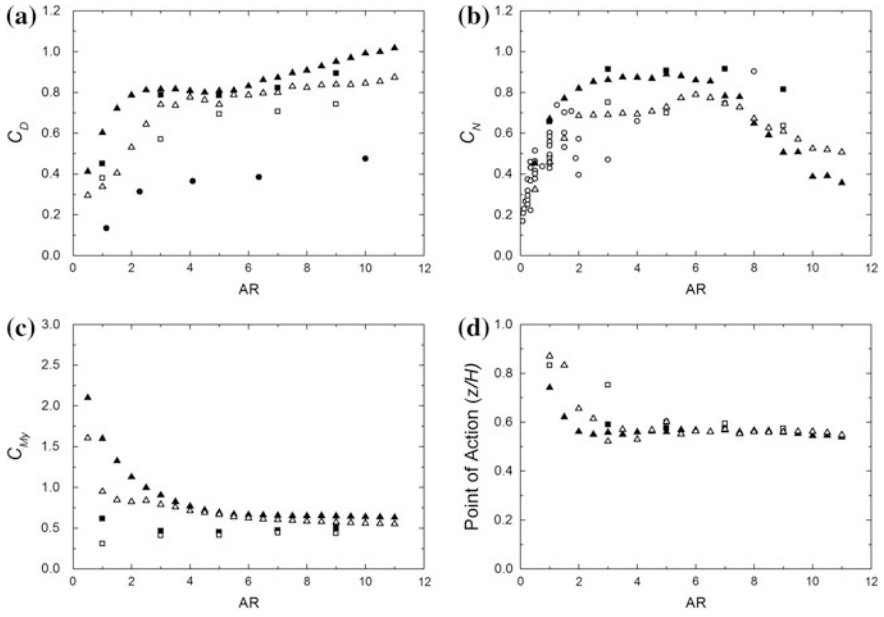

Fig. 2 Aspect ratio effects on the aerodynamic forces for a cylinder. **a** C_D **b** C_N **c** C_{My} **d** Point of action. Force measurements are represented according to relative boundary layer thickness: ▲ $\delta/D = 0.6$, △ $\delta/D = 0.92$, ■ $\delta/D = 1.88$, □ $\delta/D = 2.86$, ◯ existing literature pressures (see References [1–4, 6, 8–11, 15–18])

Sarode et al. [12]. The behaviour of the C_D data seems to indicate two critical aspect ratios, at AR ≈ 2.5 and AR ≈ 6. For AR < 2.5 (the first critical aspect ratio), C_D increases rapidly with an increase in AR. This is the familiar critical aspect ratio for the finite cylinder where the wake is characterized by arch vortex formation and shedding [7]. For 2.5 < AR < 6, C_D is relatively insensitive to AR, indicating a region of stable flow. For AR > 6, however, C_D increases linearly up to the end of the data set (AR = 11). This second critical aspect ratio has not been identified in other studies, but appears to show the influence of the free end flow is reducing in this region, and the cylinder is approaching infinite behaviour. In the thick boundary layer, the second critical AR is less pronounced.

The data for C_N (Fig. 2b) reveal new information. Among the integrated results, which are concentrated mostly for AR < 2 (less than the first critical aspect ratio), there is much scatter due to the wide ranges of Re and δ/D among the different studies, but a clear upward trend. The present experiments provide new data for AR > 2, which show a plateau of the normal force for 2.5 < AR < 6, and a steady decrease in C_N when AR > 6 (above the second critical aspect ratio). Within the thick boundary layer, there is a small peak evident at the second critical AR.

Only one critical aspect ratio is clear from the C_{My} data (Fig. 2c). The mean bending moment coefficient seems to be nearly independent of AR for AR > 6 (the second critical aspect ratio); however, for AR < 6, C_{My} rapidly increases as AR is lowered. The latter trend may be a result of the increasing influence of the boundary layer at lower AR; however, the increase in C_{My} is not obvious for the small-diameter datasets, where δ/D is higher, so further investigation is needed.

The point of action of the mean drag force (Fig. 2d) exhibits similar behaviour to the C_{My} data, acting near the top edge of the cylinder for low AR, and quickly settling out slightly above the mid-height position for AR > 2.5. The rate of change in both C_{My} and PoA is reduced within the thicker boundary layer.

4 Conclusions

The aerodynamic forces on a cylinder, including the drag, the bending moment, and the normal force, are measured for 22 equally spaced aspect ratios within a range from 0.5 to 11. The normal force arises mainly from the pressures on the free end, and does not exceed $C_{\mathrm{N}} = 0.9$. The force readings reveal the existence of two critical aspect ratios where the flow conditions may change. Below AR = 2.5, the boundary layer flow is dominant upstream, with symmetric vortex shedding in the wake, and forces are reduced. The stable flow region is between AR = 2.5 and AR = 6, and the force coefficients are constant in this range. Above AR = 6, the effects of free end flow are reduced, causing the normal force to fall, and the drag force to follow a linear increase towards the value for an infinite cylinder.

References

1. Dobriloff C, Nitsche W (2009) Surface pressure and wall shear stress measurements on a wall mounted cylinder. Imagin Measur Methods Vol NNFM 106:197–206
2. ESDU (1981) ESDU 81017 Mean forces, pressures and moments for circular cylindrical structures: finite-length cylinders in uniform and shear flow. ESDU International plc, s.l
3. Hiwada M et al (1984) Heat transfer from a finite circular cylinder on a flat plate: in the case of cylinder length larger than the turbulent boundary layer thickness. Trans JSME 50:733–742
4. Kawamura T et al (1984) Flow around a finite circular cylinder on a flat plate. Cylinder height greater than turbulent boundary layer thickness. Bull JSME 27:2142–2151
5. Krajnovic S (2011) Flow around a tall finite cylinder explored by large eddy simulation. J Fluid Mech 676:294–317
6. Majumdar S, Rodi W (1989) Three-dimensional computation of flow past cylindrical structures and model cooling towers. Build Environ 24:3–22
7. Okamoto S, Sunabashiri Y (1992) Vortex shedding from a circular cylinder of finite length placed on a ground plane. Trans ASME J Fluids Eng 114:512–521
8. Ozmen Y (2013) Effect of parapets to pressure distribution on flat top of a finite cylinder. Winds Struct 17(5):465–477
9. Ozmen Y, A E (2017) Wind pressures on different roof shapes of a finite height circular cylinder. Wind Struct 24(1):25–41
10. Purdy DM, Maher FJ, Frederick D (1967) Model studies of wind loads on flat-top cylinders. Proc Am Soc Civil Eng J Struct Div 379–395
11. Rödiger T, Knauss H, Gaisbauer U, Krämer E (2007) New research in numerical and experimental fluid mechanics VI, vol NNFM 96, pp 121–128
12. Sarode R, Gai S, Ramesh C (1981) Flow around circular- and square-section models of finite height in a turbulent shear flow. J Wind Eng Ind Aerodyn 8:223–230
13. Sumner D (2013) Flow above the free end of a surface-mounted finite-height circular cylinder: A review. J Fluids Struct 43:41–63
14. Sumner D, Heseltine J, Dansereau O (2004) Wake Structure of a finite circular cylinder of small aspect ratio. Exp Fluids 37:720–730
15. Tsutsui T (2012) Flow around a cylindrical structure mounted in a plane turbulent boundary layer. J Wind Eng Ind Aerodyn 104–106:239–247
16. Tsutsui T, Igarashi T, Nakamura H (2000) Fluid flow and heat transfer around a cylindrical protuberance mounted on a flat plate boundary layer. JSME Int J Ser B 43:279–287
17. Uematsu Y, Choong Mo K (2008) Wind-tunnel study of wind loads on circular cylindrical structures (in Japanese). J Wind Eng 33(1):17–25
18. Yoshida M, Hongo T (1983) Experimental study of wind forces on buildings, Part 3: Wind tunnel study of wind forces on flat roofs with long span (in Japanese). Ann Rep Kajima Inst Constr Technol 31:119–126

Numerical Investigation on Performance Improvement by Using a Runner with Splitter for a Francis Turbine

J. J. Feng, F. Z. Lin, G. K. Wu, P. C. Guo, G. J. Zhu and X. Q. Luo

Abstract In this paper, three-dimensional turbulent flow fields in a low specific speed Francis turbine have been obtained by CFD methods, and the performance prediction for the turbine have been made based on the simulation results. Two types of runner have been compared for the turbine: a conventional runner with uniform blades and another runner with splitter blades. The comparison of results shows that by adding splitter blades, the inlet vortex on the suction surface of the long runner blade is inhibited obviously, leading to an increase in turbine efficiency. Furthermore, the minimum pressure on the runner blade with splitter is higher than for the conventional runner, resulting in a better cavitation performance. In addition, the turbulence kinetic energy and vorticity for the runner with splitter are also smaller than that of the conventional runner.

Keywords Francis turbine · Splitter · CFD · Performance

1 Introduction

Francis turbine has a wide range of application of head, and it also has the advantages of simple structure, high efficiency and good anti-cavitation performance [1]. The runner of a high working head and a low specific speed Francis turbine has a large difference in the inlet and outlet radius due to the longer blade, which leads to the flow area at the runner inlet is much greater than at the runner outlet. This can produce flow separation at the runner inlet, especially at part-load conditions. In order to control the inlet area and not to affect the outlet, adding a splitter is a good solution to this problem [2]. CFD technology has been widely used in performance prediction of hydraulic turbines, including hydraulic efficiency [3], cavitation [4] and pressure fluctuations [5].

J. J. Feng (✉) · F. Z. Lin · G. K. Wu · P. C. Guo · G. J. Zhu · X. Q. Luo
Institute of Water Resources and Hydro-Electric Engineering, Xi'an University of Technology, Xi'an 710048, People's Republic of China
e-mail: jianjunfeng@xaut.edu.cn

Y. Zhou et al. (eds.), *Fluid-Structure-Sound Interactions and Control*, Lecture Notes in Mechanical Engineering,
https://doi.org/10.1007/978-981-10-7542-1_34

2 Numerical Procedures

The model turbine for a hydropower plant with a maximal head of 500 m is chosen for investigation. Two kinds of model runners are designed for this model turbine while keeping the rest flow components the same: a conventional runner with uniform blades and runner with splitter blades. The runner diameter for both runners is $D_1 = 0.55$ m. The conventional runner has 17 blades, and the runner with splitter blades has 15 long blades (main blades) and 15 short blades (splitter blades). The model turbine has 23 stay vanes, 24 guide vanes and an elbowed draft tube. Figure 1 shows the 3D model for the turbine, together with mesh views. The total numbers of grid nodes are 6.9 million for the turbine with conventional runner, and 7.1 million for the turbine with runner with splitter.

The internal flow fields inside the Francis model turbines were simulated by using ANSYS CFX-16.0. For boundary conditions, a constant total pressure was defined at the casing inlet, with flow direction normal to the inlet surface. At the outlet of the draft tube, mass flow rate was specified. Smooth and no-slip condition was imposed on walls. Three interfaces were introduced to connect different domains in simulations. Second order accuracy was chosen for space discretization method and advection terms. The SST turbulence model was utilized to close the time-averaged N-S equations.

3 Results

The turbine parameters of the optimal point are $n_{110} = 61$ r/min and $Q_{110} = 152$ L/s, defined in Eq. (1). In numerical simulations, five operating points at $n_{110} = 61$ r/min are selected. including the best efficiency point. During simulations, the head used for CFD is the same with the one for the model test, which is $H = 30$ m.

$$n_{11} = nD_1/\sqrt{H}, Q_{11} = Q/(D_1^2\sqrt{H}) \tag{1}$$

(a) 3D model (b) Mesh for runner with splitter (c) Mesh for conventional runner

Fig. 1 Computational domains and mesh view

Figure 2 shows the turbine efficiency curves obtained from CFD simulations both for the turbines with conventional runner and runner with splitter, and the experimental results for the case of runner with splitter have been also given for comparison. The hydraulic efficiency is defined in Eq. (2).

$$\eta = \frac{M \cdot \omega}{\rho \cdot g \cdot Q \cdot H} \tag{2}$$

where: M is the torque on the runner blades, ω is the rotational velocity, Q is the flow rate and H is the working head for the whole turbine.

It is found that the CFD results are consistent with the experimental ones, and the former is slightly higher than the later. Over the whole range, the turbine efficiency by runner with splitter is higher than the one by conventional runner, denoting that the design with splitter can improve the energy conversion inside the runner of the turbine.

Figure 3 gives the comparison of runner efficiency and hydraulic loss in the runner between both types of runner. The runner efficiency is calculated with Eq. (1), with the head in the runner. The runner with splitter has a higher runner efficiency and lower hydraulic loss in the runner than the conventional runner, denoting that the former has a better energy conversion efficiency.

Figures 4 and 5 give the comparisons of relative velocity vectors at midspan of the runner both at the best efficiency point and one part-load operation condition $0.65Q_{110}$. It can be observed that the flow structure has been improved by the splitter at the runner inlet, especially at the part-load condition where the flow separation near the runner leading edge has been removed.

The comparison of minimal pressure on runner blade surface for two types of runner has been plotted in Fig. 6 for different operating conditions. It can be observed that the runner with splitter can have a bigger minimum pressure than the

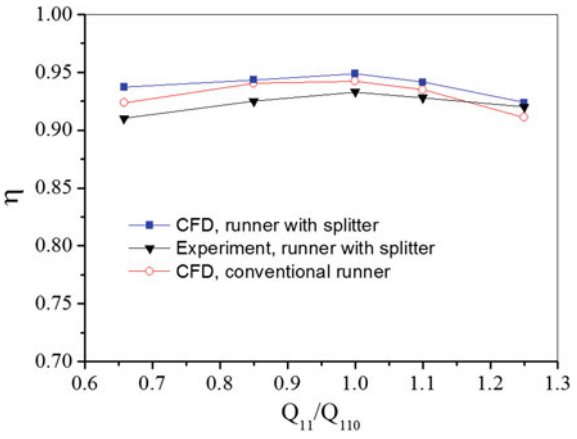

Fig. 2 Comparison of turbine hydraulic efficiency

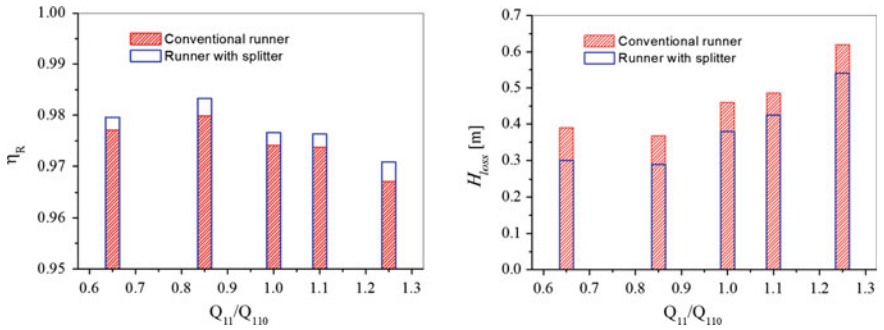

(a) Runner efficiency (b) Hydraulic loss in runner

Fig. 3 Comparison of runner efficiency and hydraulic loss in runner

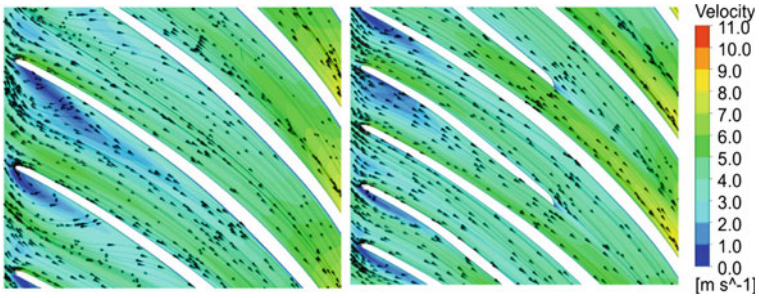

(a) Conventional runner (b) Runner with splitter

Fig. 4 Velocity vectors in runner at Q_{110}

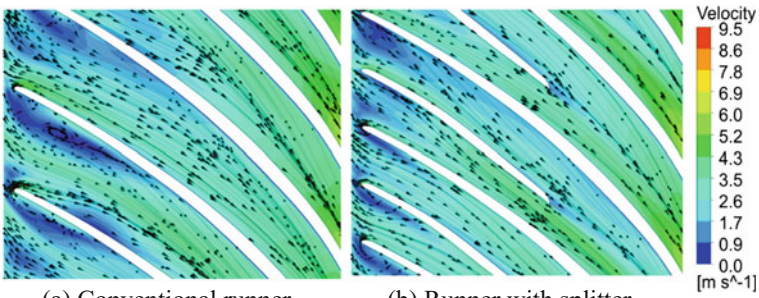

(a) Conventional runner (b) Runner with splitter

Fig. 5 Velocity vectors in runner at $0.65Q_{110}$

conventional runner at all shown operating conditions, denoting that the anti-cavitation performance of the runner with spiller is better than that of the conventional runner.

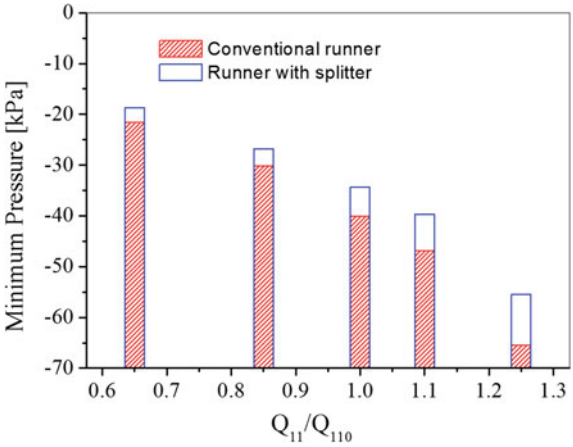

Fig. 6 Minimal pressure on runner blade surface

Figure 7 shows the distribution of turbulence kinetic energy at mid-span of the runner under the optimal condition. For the conventional runner, the turbulence kinetic energy near the blade leading edge is the highest, and the high value propagates downstream along the blade pressure side. Compared to the one for conventional runner, the turbulence kinetic energy for the runner with splitter is much smaller, resulting in a lower energy dissipation and a higher efficiency.

Figure 8 represents the comparison of vorticity in the runner. The vorticity in the conventional runner decreases first and then increases. For the runner with splitter blade, the vorticity core in the flow passage from the inlet to the outlet is partitioned and becomes relatively thin due to the cutting effect of the splitter blade. Therefore, the design of splitter blade successfully reduces the vorticity generation in the runner. In addition, the decrease of vorticity at runner outlet has great effect on the hydraulic loss of the draft tube, which has greatly improved the performance of hydraulic turbine.

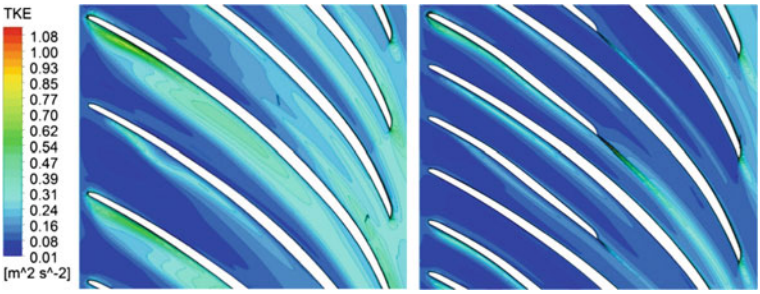

(a) Conventional runner (b) Runner with splitter

Fig. 7 Turbulence kinetic energy contours at runner midspan for Q_{110}

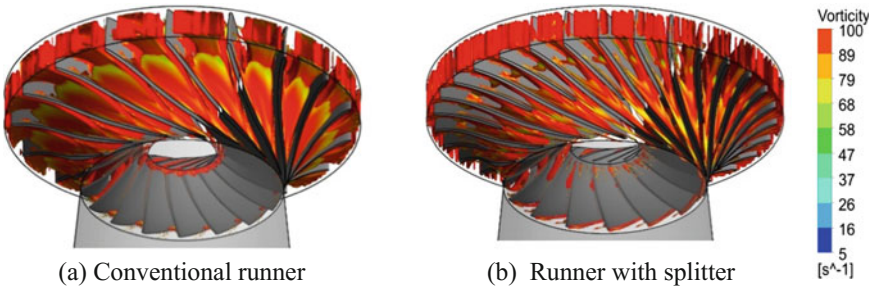

(a) Conventional runner (b) Runner with splitter

Fig. 8 Distribution of vorticity in runner at 65% Q_{110}

4 Conclusions

The turbine performances of two types of runner have been predicted with the help of CFD code CFX 16 for a Francis turbine. The internal flow fields are analyzed and compared. Main conclusions are summarized as follows:

(1) The design of the splitter blade improves the hydraulic efficiency of the unit and improves the output of the unit. The calculated results are in good agreement with the experimental results.
(2) The minimum pressure on the runner blade with splitter is higher than for the conventional runner, resulting in a better cavitation performance.
(3) The turbulence kinetic energy and vorticity for the runner with splitter are both smaller than that of the conventional runner.

Acknowledgements This research was supported by the National Natural Science Foundation of China (Grant Nos. 51679195, 51479167 and 51339005).

References

1. Zhang ZL (2003) Development trend of high head Francis turbine and hydraulic characteristics. China Water Resour 4:59–60
2. Qian ZD, Li W (2012) Analysis of the effect of cone form of Francis turbine pressure pulsation. J Hydroel Eng 31:278–291
3. Xin Z, Wu JH, Chang JS (2010) Analysis and performance prediction of three dimensional turbulent flow in Francis turbine. Trans Chin Soc Agric Eng 26:118–124
4. Trivedi C, Cervantes MJ, Gandhi BK (2014) Experimental investigations of transient pressure variations in a high head model Francis turbine during start-up and shutdown. J Hydrodyn 26:277–290
5. Zhang HM, Zhang LX (2012) Numerical simulation of cavitating turbulent flow in a high head Francis turbine at part load operation with OpenFOAM. Proc Eng 31:156–165

Numerical Simulation on the Vortex-Induced Vibrations on Four Cylinders in a Square Arrangement

T. Pearcey, M. Zhao and Y. Xiang

Abstract This paper present a numerical study of vortex-induced vibration of four rigidly connected cylinders in a square arrangement in an oscillatory flow. The cylinders are elastically mounted and are only allowed to vibrate in the cross-flow direction. The gap between two neighbouring cylinders is $3D$, where D is the cylinder diameter. The Reynolds number and Keulegan–Carpenter (KC) are kept at constants of 2×10^4 and 10, respectively. The reduced velocity is in the range of 1–15. The vibration amplitude and frequency are compared with those of a single cylinder. Two lock-in regimes of the reduced velocity are found to be the same as that of a single cylinder. Between the two lock-in regimes, the vibration amplitude is zero because of the symmetric vortex shedding flow pattern.

1 Introduction

Multiple cylindrical structures are frequently used in the offshore engineering. For example, a Tension Leg Platform (TLP) is often supported by four cylindrical columns in a square arrangement. It is important to understand the effects of the vortex-induced vibrations (VIV) of the structures as the vibrations can lead to structural failure. Offshore structures experience surface waves in the ocean environment. The fluid flow due to ocean waves is generally represented by an oscillatory flow when the interaction between waves and cylindrical structures is studied. Numerical studies on the flow behaviour on four circular cylinders have been mainly focused on steady flows, and most of them are limited to the cases with low Reynolds numbers ($Re < 500$) such as [1–3, 5]. No studies of VIV of four cylinders in an oscillatory flow have been reported based on our understanding. In the present study the VIV of four circular cylinders in a square arrangement is numerically investigated. The Reynolds-Averaged Navier-Stokes (RANS)

T. Pearcey (✉) · M. Zhao · Y. Xiang
School of Computing, Engineering and Mathematics, Western Sydney University, Penrith, NSW 2751, Australia
e-mail: 17254885@student.westernsydney.edu.au

Y. Zhou et al. (eds.), *Fluid-Structure-Sound Interactions and Control*, Lecture Notes in Mechanical Engineering,
https://doi.org/10.1007/978-981-10-7542-1_35

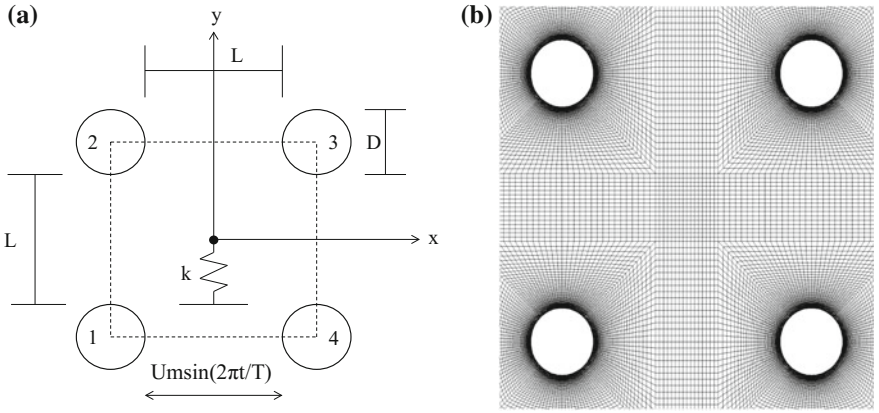

Fig. 1 **a** A sketch of the four rigidly connected, elastically mounted cylinders; **b** Computational mesh near the cylinders

equations are solved for simulating the flow and the equation of motion are solved for the vibration of the cylinders. The effect of the reduced velocity on the response of the cylinders will be investigated.

The configuration of the four circular cylinders is shown in Fig. 1a, where D is the cylinder diameter, L is the distance between two adjacent cylinders. The velocity is given as sinusoidal flow by the equation:

$$u = U_m \sin(2\pi t/T) \tag{1}$$

where U_{m} and T are the amplitude and period of the oscillatory fluid velocity, respectively. A Cartesian coordinate system is fixed at the centre of the cylinder system in the neutral position and the x-axis is parallel to the oscillatory flow direction. The cylinders are rigidly coupled together elastically mounted in the fluid flow.

2 Numerical Method

The two-dimensional incompressible Reynolds-Averaged Navier-Stokes (RANS) equations are the governing equations for solving the fluid flow. To account for the moving surfaces of the cylinders due to VIV, the Arbitrary Langrangian Eulerian (ALE) scheme is used when solving the RANS equations. In the ALE scheme, the mesh can move independently to the fluid velocity. The RANS equations with the ALE scheme are written as:

$$\partial u_i/\partial x_i = 0 \tag{2}$$

$$\partial u_i/\partial t + \left(u_j - \hat{u}_j\right)\partial u_i/\partial x_j = -(1/\rho)(\partial P/\partial x) + \partial/\partial x_j\left(2\nu S_{ij} - \overline{u_i' u_j'}\right) \tag{3}$$

where $x_1 = x$ and $x_2 = y$ are the Cartesian coordinates in the in-line and transverse directions of the flow, respectively, u_i is the fluid velocity in the x_i-direction, p is pressure, ρ is the fluid density, $\hat{u}_j$ is the mesh velocity, ν is the kinematic viscosity, S_{ij} is the mean stress tensor and $\overline{u_i' u_j'}$ is the Reynolds stress tensor. The SST k-ω turbulence model is used to close the RANS equation. The Reynolds number, $\mathrm{Re} = U_\mathrm{m} D/\nu$ and KC number, $\mathrm{KC} = U_\mathrm{m} T/D$ affect the VIV in oscillatory flow, the other parameters that affect the VIV are the mass ratio, $m^* = m/m_d$, where m is the total mass of the four cylinders per unit length, m_d is the mass of the displaced fluid, the reduced velocity, $V_\mathrm{r} = U_\mathrm{m}/f_\mathrm{n} D$, f_n is the structural natural frequency in vacuum, and the structural damping factor, $\zeta = c/c_\mathrm{cr}$, c is the damping coefficient and c_cr is the critical damping coefficient. In this study, the damping factor is zero, the mass ratio is fixed at 2, Re and KC are kept at a constant 2×10^4 and 10, respectively. Simulations are conducted for reduced velocities between 1 and 15.

The one-degree-of-freedom equation of motion for the cylinders displacement is

$$m\ddot{Y} + c\dot{Y} + kY = F_y \tag{4}$$

where k is the spring stiffness, Y,$\dot{Y}$ and $\ddot{Y}$ are the displacement, the velocity and the acceleration of the four cylinders, respectively, and F_y is the sum of the fluid forces on the four cylinders in the cross-flow direction. The forces are calculated by integrating the shear stress and pressure over the cylinder surfaces.

A square computational domain with a boundary length of $100D$ is used in the numerical simulations. The four cylinders are located at the center of the computational domain. The computational domain is divided into four-node quadrilateral finite elements and the computational mesh near the cylinders is shown in Fig. 1b, there are 132 nodes along the surface of each cylinder and the total element number is 70,300.

The boundary conditions need to be specified in the numerical simulations. At the left and right boundaries, the oscillatory flow velocity is given as in Eq. (1). On the cylinder surface, the velocity of the fluid is the same as the vibration velocity of the cylinder. Symmetric boundary condition is used on the top and bottom boundaries, i.e. the transverse velocity and the pressure gradient in the normal direction of the boundary are zero. The turbulence quantities are $k = 0.001 U_m^2$ and $\omega = 1\ \mathrm{s}^{-1}$.

3 Results and Discussion

The vibration of a four cylinder system is found to start later than that of a single cylinder. Figure 2 shows the variation of the maximum displacement with the reduced velocity. The maximum amplitude A_max is defined as the maximum value

of |Y|. The Amax/D for a single isolated cylinder is also plotted in Fig. 2 for comparison. It can be seen that two lock-in ranges of the reduced velocity are $3 \leq V_r \leq 6$ and $9 \leq V_r \leq 15$, respectively. The multiple lock-in was also found in the experimental studies [4]. When $V_r = 7$ and 8, the vibration amplitudes of a single isolated cylinder is very small, while those of the four-cylinder system are zero.

Figure 3 shows the nondimensional vorticity contours for $V_r = 5$, 10 and 7. At $V_r = 5$ and 10, where the maximum amplitudes occur, the vortex shedding of the four cylinders are found to be in phase with each other and vortices are only shed from the bottom side of each cylinder. At $V_r = 7$, where the vibration amplitude is zero, the vortex shedding from the top two cylinders is in anti-phase with that from the bottom two cylinders, leading to a zero lift force and vibration amplitude.

Figure 4 shows the Fast Fourier Transform (FFT) spectra of the vibration displacement. The dashed curve in the figure represents the f_{nw}/f_w, where f_{nw} is the natural frequency measured in the fluid and f_w is the oscillatory flow frequency. It can be seen that the vibration is dominated by $f/f_w = 1$ and 2 in first and second lock-in regimes, respectively. Between $V_r = 10$ and 15 the vibration is mutli-mode. The cylinders typically vibrate at a single frequency in the first lock-in regime.

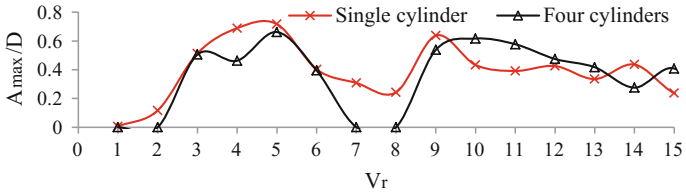

Fig. 2 Comparison of maximum amplitude response

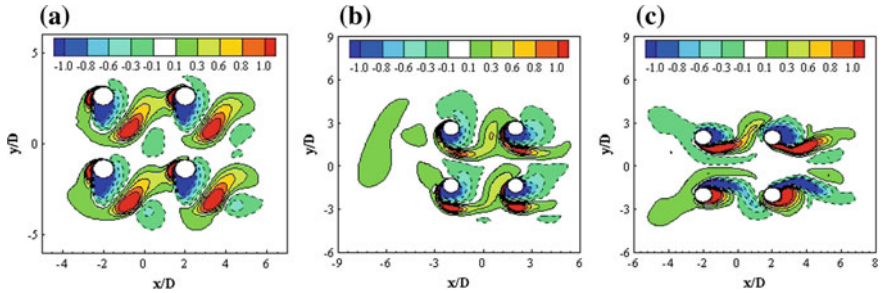

Fig. 3 Vorticity contours. **a** $V_r = 5$ and $t = 24.6T$, **b** $V_r = 10$, $t = 24.65T$, **d** $V_r = 7$ and $t = 25.3T$

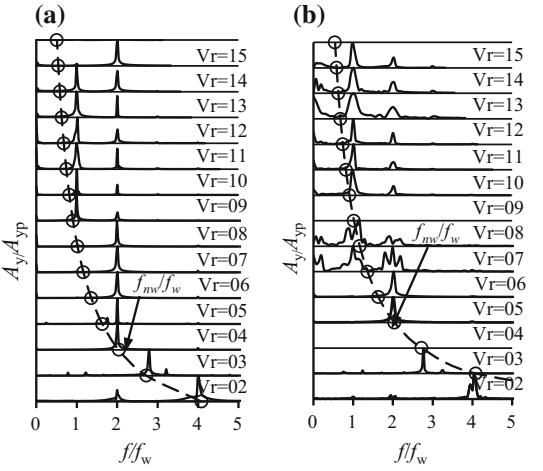

Fig. 4 FFT of **a** Single cylinder and **b** Four cylinders with a gap of 3*D*

4 Conclusions

Oscillatory flow past four cylinders in a square arrangement is numerically simulated with a gap of 3*D*, *KC* of 10 and reduced velocities in the range of 1–15.

Similar to the single cylinder case, two lock-in regimes are found and the vibration frequency in the two lock-in regimes are $f/f_w = 1$ and 2, respectively. The vortex shedding flows of the four cylinders are found to synchronize in the lock-in regime, resulting a vibration amplitude and frequency similar to that of a single cylinder case. At Vr = 7 and 8, which are the boundary between the two lock-in regimes, the vibration amplitude is zero, because of the symmetric vortex shedding pattern.

References

1. Anagnostopoulos P, Dikarou Ch (2011) Numerical simulation of viscous oscillatory flow past four cylinders in square arrangement. J Fluids Struct 27:212–232
2. Anagnostopoulos P, Dikarou Ch (2012) Aperiodic phenomena in planar oscillatory flow past a square arrangement of four cylinders at low pitch ratios. Ocean Eng 52:91–104
3. Chern MJ, Shiu WC, Horng TL (2013) Immersed boundary modeling for interaction of oscillatory flow with cylinder array under effects of flow direction and cylinder arrangement. J Fluids Struct 43:325–346
4. Kozakiewicz A, Sumer BM, Fredsøe J, Hansen EA (1997) Vortex regimes around a freely vibrating cylinder in oscillatory flow. Int J Offshore Polar Eng 7:94–102
5. Tong F, Cheng L, Zhao M, An H (2015) Oscillatory flow regimes around four cylinders in a square arrangement under small KC and Re conditions. J Fluid Mech 769:298–336

Vibration Initiation of a Cylinder in the Wake of Another

B. Qin, Y. Liu, Md. Mahbub Alam and Y. Zhou

Abstract This paper presents the cross-flow induced vibration response of a both-end-spring-mounted circular cylinder (diameter D) placed in the wake of a rigid circular cylinder of a smaller diameter d. The cylinder diameter ratio d/D and the spacing ratio L/d are 0.4 and 2.0, respectively, where L is the distance between the center of the upstream cylinder to the forward stagnation point of the downstream cylinder. The focus is given to investigate how the initiation of the vibration occurs, gaining insight into physics in the transition period where the cylinder starts to vibrate. The transition period can be divided into pre-initial, initial and late transitions. The role of added mass, added damping and work done in the transition process is studied in detail.

Keywords Flow induced vibration · Vibration initiation · Added mass Energy transfer

1 Introduction

Previous investigations have mostly been concerned with two rigid circular cylinders in tandem [1]. Bokaian and Geoola [2] surveyed flow-induced vibration (FIV) of a cylinder immersed in the wake of a fixed identical upstream cylinder, where the downstream cylinder is free to oscillate laterally. The FIV of a pair of cylinders in tandem has been investigated by Assi et al. [3, 4] for $L/d \geq 4.0$ at $m^* \zeta = 0.018$, where the mechanism of the origin of the downstream cylinder lift forces has been elucidated. Divergent vibration was observed for $L/d = 4.0$ –6.0 with increasing reduced velocity U_r, and constant vibration amplitude was for

B. Qin · Y. Liu · Md.Mahbub Alam (✉) · Y. Zhou
Shenzhen Graduate School, Institute for Turbulence-Noise-Vibration Interaction and Control, Harbin Institute of Technology, Shenzhen, China
e-mail: alamm28@yahoo.com; alam@hit.edu.cn

Md.Mahbub Alam
Digital Engineering Laboratory of Offshore Equipment, Shenzhen, China

Y. Zhou et al. (eds.), *Fluid-Structure-Sound Interactions and Control*, Lecture Notes in Mechanical Engineering,
https://doi.org/10.1007/978-981-10-7542-1_36

$L/d > 6.0$. A review of the literature indicates that previous investigations have mostly been with two identical diameter cylinders at a low mass-damping $m^* \zeta$ value, where m^* is the mass ratio and ζ is the damping ratio. A systematic study on the influence of the upstream cylinder size (diameter d) on FIV of a downstream cylinder of diameter D has been documented by Alam et al. [5] at $d/D = 0.2$–1.0 and $L/d = 1.0$–5.5. Violent vibrations were generated for $d/D = 0.2$–0.8, $L/d < 1.5$–5.5 depending on d/D. Many issues were unaddressed. For example, how the vibration is initiated? What are the parameters responsible for the instability to generate the vibration? What are their roles? The objectives of the present investigations are to investigate (i) the initiation of vibration and characteristics during the generation of the vibration, and (ii) the roles of added damping, added mass and energy transfer when the cylinder starts to vibrate. $d/D = 0.4$ and $L/d = 2.0$ are chosen for the detailed investigation.

2 Experimental Details

FIV experiments were carried out in a low-speed, closed-circuit wind tunnel. A schematic diagram of the experimental setup is shown in Fig. 1. Investigation was made for $d/D = 0.4$ and $L/d = 2.0$ where violent vibration is erupted. The upstream cylinder was fixed at both ends and the downstream cylinder was allowed to vibrate in the transverse direction only. A standard laser vibrometer was used to measure the vibration displacement (Y) and vibration frequency (f_{osc}) of the downstream cylinder. The ζ, $m^* \zeta$, and natural frequency of the cylinder (f_n) were estimated to be 0.043, 15.05, and 10.23 Hz, respectively. Connecting both pressure scanner and laser vibrometer systems to the same data-acquisition computer enabled simultaneous measurements of lift force and displacement.

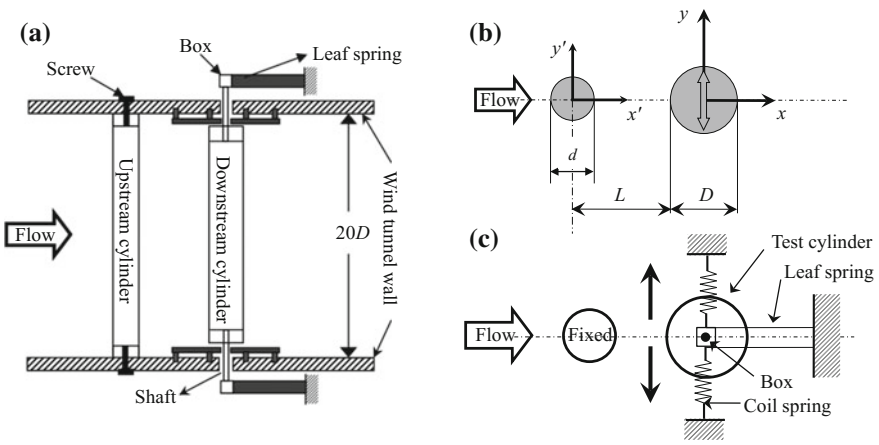

Fig. 1 **a** Experimental setup, **b** definition of symbols, **c** the test cylinder support system

3 Results and Discussion

3.1 Force and Vibration Characteristics

For two tandem cylinders with $d/D < 1$, VE (vortex excitation) is generated for the downstream cylinder at $U_r \approx 5.0$ and a violent vibration divergent with increasing U_r is unveiled at larger U_r, which is excited by the switching gap shear layers from one side to the other of the downstream cylinder [5]. Presently $U_r = 41.4$ corresponding to $A/D = 0.48$ is chosen to investigate the violent vibration initiation.

Two scenarios are examined to investigate the process when the cylinder vibration starts and grows in amplitude. (I) The flow is increased continuously from $U_r =$ (arbitrary) to a value 41.4 and then remains constant. The velocity was increased at a rate of 0.84 m/s/T_n, where $T_n = 1/f_n$. (II) Given a flow that is adequate to produce a large amplitude vibration ($U_r = 41.4$), the cylinder is kept fixed and then suddenly released. In both cases, Y_0/D grows from zero to its stable value, where Y_0 is the displacement amplitude. Time histories of Y/D, lift force coefficient C_L, 20 Hz low-pass-filtered C_L, and f_{osc}/f_n in the transition process for cases I and II are presented in Fig. 2, which is characterized by three stages. In the pre-initial stage, Y_0/D is very small and lift force coefficient C_L is dominated by the fluctuation at the vortex shedding frequency. Meanwhile, f_{osc}/f_n grows gradually. In the initial transition stage, Y_0/D grows rapidly (positive curvature), accompanied by an

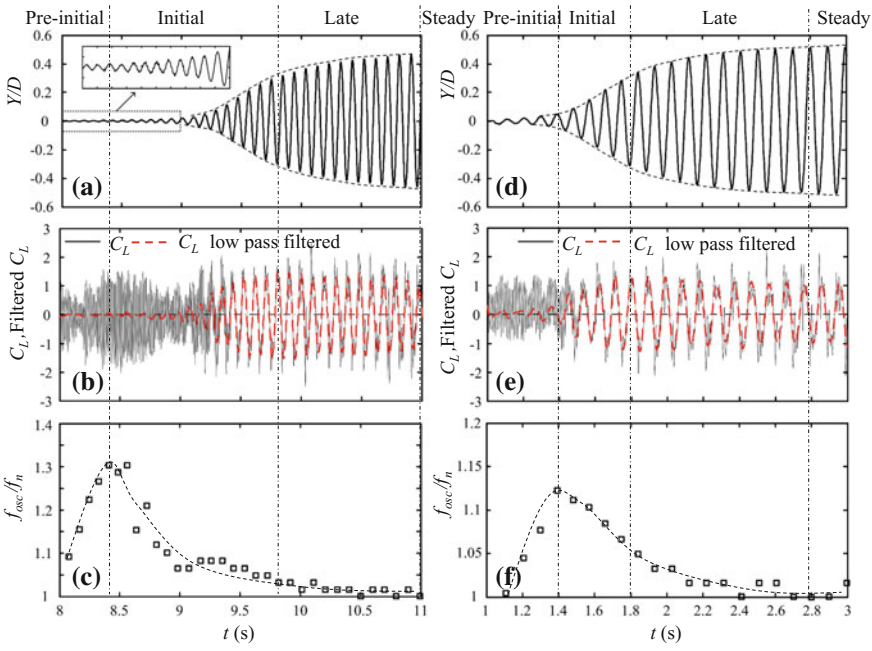

Fig. 2 Time histories of Y/D, C_L and f_{osc}/f_n in the transition process for cases I (**a**–**c**) and II (**d**–**f**). Dashed red lines in (**b**) and (**e**) are 20 Hz low-pass-filtered C_L

exponential rise in C_L amplitude. C_L fluctuation at the shedding frequency weakens and that at the oscillation frequency grows. Meanwhile, f_{osc}/f_n drops. In the late transition stage, the growth in Y_0/D slows down (negative curvature), C_L is dominated by cylinder oscillation frequency and filtered C_L amplitude decreases, along with reduced f_{osc}/f_n.

3.2 Energy Transfer and Added Mass

Figure 3a, d shows the variations of energy transferred from the fluid to the cylinder motion W_f, energy dissipated by the structural damping W_d, and total energy transfer W_t ($=W_f + W_d$) calculated over one period. W_f and W_d rise and decline, respectively, in the initial and late transitions, and become invariant after the late transition. W_t grows rapidly in the initial transition regime, reaching a maximum before declining in the late transition regime. $W_t > 0$ means that the energy transferred from the fluid to cylinder is larger than the energy dissipated through the structural damper. Therefore, the excess energy is used to enlarge Y_0/D in the initial regime with $W_t > 0$. In the late transition regime, the slowing down of Y_0/D growth is complemented by W_t declination, essentially $W_t > 0$. As Y_0/D becomes constant, $W_t \approx 0$.

Finally, added mass ratio m_a^* and added (or flow-induced) damping ratio ζ_a variations from estimated C_L in phase with acceleration ($\ddot{Y}$) and velocity ($\dot{Y}$),

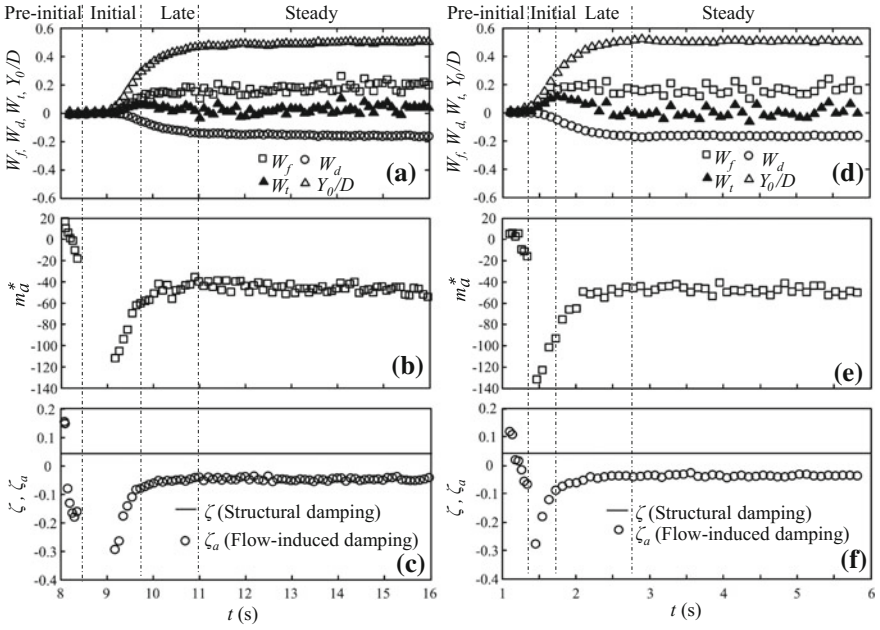

Fig. 3 Time histories of W_f, W_d, W_t, Y_0/D, m_a^* and ζ_a in each period: (**a–c**) case I, (**d–f**) case II

respectively, are presented in Fig. 3b, c, e, f. For case I, m_a^* and ζ_a are based on the shedding frequency in the pre-initial regime, and on the vibration frequency for other regimes. Interestingly, both m_a^* and ζ_a being positive at $t = 8$ s experiences a drastic drop in the pre-initial regime. It may be inferred that the vibration is initiated by m_a^* and ζ_a being negative at the shedding frequency. At $t = 8.4$–9.0 s, both added mass and added damping cannot be calculated. Then at $t > 9.0$ s, m_a^* and ζ_a experience rapid increases in the initial transition and mild increases in the late transition regime, resulting in a reduced f_{osc}/f_n (Fig. 2c). They attenuate in the steady regime where $m_a^* \approx -47$ and $\zeta_a \approx -0.043$ that is equal in magnitude of the structural damping ζ, i.e., $\zeta + \zeta_a = 0$ (Fig. 3c). A similar observation is made for case II (Fig. 3e, f). Thus, it can be concluded that during the increase of the vibration amplitude, the cylinder sustains an effective negative damping ratio ($\zeta + \zeta_a < 0$), while at the stable vibration amplitude, $\zeta + \zeta_a = 0$.

4 Conclusions

The transition period can be divided into pre-initial, initial and late transitions. In the pre-initial regime, Y_0/D is very small, C_L is dominated by the vortex shedding frequency, f_{osc}/f_n augments, W_t is negligible, and ζ_a and m_a^* both plummet. The Y_0/D increases in the initial transition, with C_L amplitude soaring exponentially, f_{osc}/f_n declining, and both ζ_a and m_a^* escalating. W_t grows rapidly, reaching a maximum before declining in the late transition regime. The growth of W_t thus corresponds to that of Y_0/D. On the other hand, the increase in Y_0/D occurring at a negative curvature characterizes the late transition where C_L amplitude declines, f_{osc}/f_n wanes, and both ζ_a and m_a^* keep rising very slowly. The slowing down (negative curvature) of Y_0/D growth is complemented by W_t declination, essentially $W_t > 0$. As Y_0/D becomes constant, $W_t \approx 0$. The natural vortex shedding becoming dominant in pre-initial transition regime initiates the vibration, both shedding and oscillation frequencies in C_L play role in the initial transition regime, and oscillation frequency takes control in the late transition regime.

Acknowledgements Alam wishes to acknowledge the support given to them from National Natural Science Foundation of China through Grants 11672096 and from Research Grant Council of Shenzhen Government through grant JCYJ20160531191442288.

References

1. Alam MM, Moriya M, Takai K, Sakamoto H (2003) Fluctuating fluid forces acting on two circular cylinders in a tandem arrangement at a subcritical Reynolds number. J Wind Eng Ind Aerodyn 91:139–154
2. Bokaian A, Geoola F (1984) Wake-induced galloping of two interfering circular cylinders. J Fluid Mech 146:383–415

3. Assi GRS, Bearman PW, Meneghini JR (2010) On the wake-induced vibration of tandem circular cylinders: the vortex interaction excitation mechanism. J Fluid Mech 661:365–401
4. Assi GRS, Bearman PW, Carmo BS, Meneghini JR, Sherwin SJ, Willden HJ (2013) The role of wake stiffness on the wake-induced vibration of the downstream cylinder of a tandem pair. J Fluid Mech 718:210–245
5. Alam MM, Qin B, Zhou Y (2016) A cylinder vibration induced by shear layers of another of smaller diameter. In: Lecture notes in mechanical engineering, FSSIC. Springer, pp 389–394

Power Output of Spring-Mounted Lifting Plates in a Cross Flow

S. A. Maaskant, R. M. Howell and A. D. Lucey

Abstract In this paper, a twin cantilever system is spring-mounted on a bearing and investigated experimentally in a cross flow in a wind tunnel; two types of bearing are used, cylindrical with one degree of freedom and spherical with three. By comparing the two systems, it is found that the spherical bearing system is slightly more unstable and operates at a higher oscillation frequency, hence having more favourable conditions for energy harvesting. The physical manifestation of the destabilising effect of the spherical bearing is seen in the yawing *figure-of-eight* forward and backward motion of the cantilevers about the mount, which can be observed by looking directly down on the set-up. For the range of spring stiffnesses used in this investigation, the power producing capabilities of both systems continue to increase as system natural frequency reaches higher values.

1 Introduction

The phenomenon of flutter, while most commonly known for its destructive effect, has recently been investigated as a viable mechanism for harvesting renewable energy. Flutter is a dynamic instability caused by fluid flow passing over a flexible surface, that in axial flow can occur either through constructive interference between the pressure forces of the fluid and the plate velocity, or by the fluid pressure coalescing two or more translational *in vacuo* modes of the structure. When flutter occurs in a cross flow, only the latter exists and requires that the fluid pressure couples at least one *in vacuo* torsional mode with at least one *in vacuo* translational mode; in the system herein, the plates are too short to twist themselves and this rotation is provided by the hinge mount.

S. A. Maaskant · R. M. Howell (✉) · A. D. Lucey
Fluid Dynamics Research Group, Department of Mechanical Engineering,
Curtin University of Technology, GPO Box U1987, Perth, WA 6845, Australia
e-mail: richard.howell@curtin.edu.au

Y. Zhou et al. (eds.), *Fluid-Structure-Sound Interactions and Control*, Lecture Notes in Mechanical Engineering,
https://doi.org/10.1007/978-981-10-7542-1_37

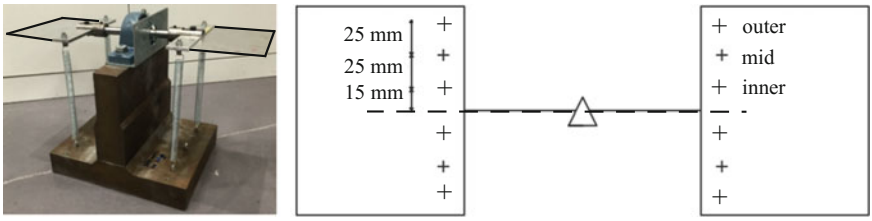

Fig. 1 Left: the fluid-structure system under consideration. Right: spring fixture positions

Piezoelectric devices that utilise this phenomenon have been well studied e.g. see [1]. A more robust approach is to harvest energy through a spring mount, an axial flow example of which can be seen in [2]. In the present study, a twin cantilever system is spring-mounted on a bearing and investigated experimentally in a cross flow in a wind tunnel, see the left-hand side of Fig. 1. Two types of bearing are used: cylindrical with one degree of freedom and spherical with three. The system that is most unstable would therefore yield more favourable conditions for energy harvesting. The results presented herein were generated in [3, 4] that respectively investigated the use of cylindrical and spherical bearings for this set-up. Similar experimental set-ups were investigated in [5, 6]; both of these latter investigations utilised cylindrical bearings and the free stream fluid was water.

2 Experimental Design

The right-hand side of Fig. 1 shows the spring fixture positions of the twin cantilever system; 4 springs were always attached, one in each quadrant and at the same position in each quadrant i.e. either the inner, mid or outer positions. The cylindrical system is only free to rotate about its pitch axis when exposed to the uniform cross flow, whereas the spherical system rotates about each of the pitch, roll and yaw axes and hence has three rotational natural frequencies, respectively Ω_s^P, Ω_s^R and Ω_s^Y. The wind tunnel was of cross section 457 mm × 457 mm and was capable of producing flow speeds ranging from 4 to 29 m/s. The cantilevers were aluminium plates of dimensions 0.5 mm × 120 mm × 150 mm (thickness × length × width). Results were taken at the critical velocity U_c where fluid forces outweigh the opposing forces caused by elastic bending of the plate. An upper value of U_c was recorded—when possible—where the set-up produced a self-starting motion; the flow speed was then reduced and a lower value of U_c was recorded, denoting the lower bound of the hysteresis loop. At each value of U_c, the frequency f_c and angle of rotation (pitch) θ_c were also recorded through the use of a high speed camera.

3 Results

Results for $\Omega_s^P > 20$ rad/s are shown in Fig. 2. The cylindrical and spherical systems are represented by the points ▲ and • respectively and the filled and hollow markers are for the upper and lower values of U_c respectively. The solid quadratic best fit lines are for the cylindrical system while the broken lines are for the spherical system. For results with $\Omega_s^P < 20$—not shown here—the flutter oscillation becomes intermittent and prone to divergence.

Figure 2a–c show that in both cases as Ω_s^P increased U_c increased and so f_c also increased; however, θ_c remained fairly constant as seen in Fig. 2c. As might be expected, the values of f_c do not show much difference between the large amplitude and small amplitude motions. The system's overall ability to generate power is proportional to the *power factor* $(\Omega_s^P)^2\theta_c^2\omega_c$; this is derived from the relationship of power output being equal to the product of moment and the rate of angular rotation. This is plotted in Fig. 2d where it can be seen that as Ω_s^P increased the power factor also increased. This trend is significant as it shows that there is still greater potential for the system to generate power above the spring stiffnesses already tested. However, this cannot continue to be true indefinitely because as $\Omega_s^P \to \infty$ then $\theta_c \to 0$.

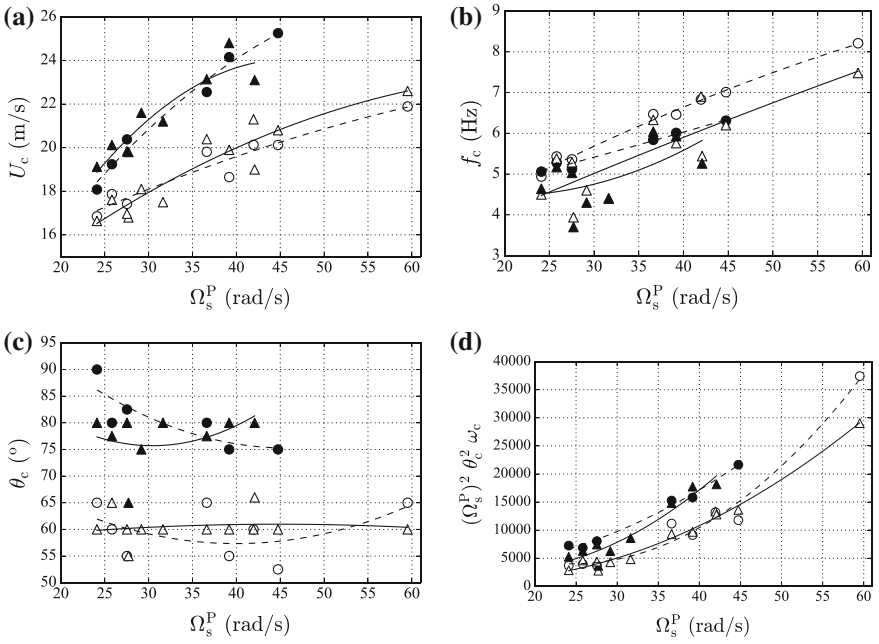

Fig. 2 Effect of bearing type on the fluid-structure interaction: variation with Ω_s^P of **a** U_c, **b** f_c, **c** θ_c and **d** power factor; cylindrical bearing —▲—, spherical bearing —•—; filled and hollow symbols - upper and lower U_c respectively; $15.89 < \Omega_s^R < 24.14$ and $0.55 < \Omega_s^Y < 1.51$

Clearly it is desirable to achieve high power factors for low values of U_c. Therefore efficiencies can be calculated by dividing the power factor by the power available from the free stream, calculated via the kinetic energy flux. The trend found, not shown here, is the same as that in Fig. 2d.

By comparing the two data sets, it can be seen that the spherical bearing system is slightly more unstable and operates at a higher oscillation frequency, hence having more favourable conditions for energy harvesting. The physical manifestation of the effect of the spherical bearing was seen in the yawing *figure-of-eight* forward and backward motion of the cantilevers about the mount, observed by videoing from directly above the set-up.

4 Conclusions

We have investigated experimentally in a wind tunnel a twin cantilever system, spring-mounted on a bearing in a cross flow. Two types of bearing were used: cylindrical with one degree of freedom and spherical with three. By comparing the two systems, it is found that the spherical bearing system is slightly more unstable and operates at a higher oscillation frequency, hence having more favourable conditions for energy harvesting. The physical manifestation of the effect of the spherical bearing was seen in the yawing *figure-of-eight* forward and backward motion of the cantilevers about the mount, which can be observed by looking directly down on the set-up. For the range of spring stiffnesses used in this investigation, the power producing capabilities of both systems continue to increase as system natural frequency reaches higher values. Current experimental work now focusses on investigating higher values of Ω_s^P to find the limit to the favourable increase in power production efficiency.

References

1. Li S, Yuan J, Lipson H (2011) Ambient wind energy harvesting using cross-flow fluttering. J Appl Phys 109, Paper no: 026104
2. Howell RM, Lucey AD (2015) Flutter of spring-mounted flexible plates in uniform flow. J Fluids Struct 59:370–393
3. Gehrmann P (2015) Energy harvesting from dual shaft mounted galloping surfaces in air flow. 4th year project, Curtin University, Perth, Australia
4. Maaskant S (2016) Energy harvesting from the fluid-structure interaction of a galloping twin cantilever in cross flow. 4th year project, Curtin University, Perth, Australia
5. Fernandes AC, Armandei M (2014) Low-head hydropower extraction based on torsional galloping. Renew Energy 69:447–452
6. Stappenbelt B, Johnstone AD (2016) Torsional galloping marine current energy extraction. In: 20th Australasian fluid mechanics conference, 5–8 Dec, 2016. Perth, Australia

Effect of Structural Stiffness on the Stability of Pulsatile Poiseuille Flow Through a Compliant Channel

K. Tsigklifis and A. D. Lucey

Abstract We study the asymptotic stability of steady and pulsatile Poiseuille flow through a compliant channel to investigate the effect of wall structural stiffness on the different instability branches that may exist in the Fluid-Structure Interaction (FSI) system. We implement both vertical (V) and axial-vertical (AV) structural displacement models in which the dynamics are respectively controlled by the vertical stiffness and its ratio to the axial stiffness. It is shown that reducing the wall stiffness in the axial direction causes destabilisation of the inflectional instability (II) while reducing vertical stiffness causes Divergence (D) modes to yield the critical instability. Finally, it is shown that pulsatile Poiseuille flow at the low-frequency modulation used herein is more unstable regarding the inflectional instability but more stable regarding the Divergence instability than the steady Poiseuille flow for the range of wall stiffness and streamwise disturbance wavenumber studied in the present work.

Keywords Pulsatile plane Poiseuille flow · Compliant channel
Aero-/hydro-dynamic stability

1 Introduction

In recent years attention has been given to the stability of modulated unsteady base flow through rigid [1] and compliant channels [2] due to potential applications in engineered and biomechanical systems. Our previous work [2] has systematically studied the linear stability of pulsatile Poiseuille flow through a relatively stiff compliant channel revealing the stabilising role of compliance over the entire range of modulation frequencies for $\Lambda \leq 5$, where Λ is the amplitude of the pressure-gradient

K. Tsigklifis (✉) · A. D. Lucey
Fluid Dynamics Research Group, Department of Mechanical Engineering, Curtin University of Technology, GPO Box U1987, Perth 6845, Australia
e-mail: k.tsigklifis@curtin.edu.au

Y. Zhou et al. (eds.), *Fluid-Structure-Sound Interactions and Control*, Lecture Notes in Mechanical Engineering,
https://doi.org/10.1007/978-981-10-7542-1_38

modulation relative to the pressure gradient of the steady plane Poiseuille flow. The instability mechanism at low modulation frequency $Wo = L^*(\omega_f^*/\nu_l^*)^{1/2} = 5$, where Wo is the Womersley number, L^* the half distance between the channel walls, ω_f^* the forcing angular frequency of the periodic pulsation and ν_l^* the kinematic viscosity of the fluid, is due to the inflectional velocity profile during the deceleration phase of the fundamental cycle. At higher modulation frequencies the Stokes layer combines with wall compliance to exercise a stabilising effect. Here and hereafter, * denotes a dimensional quantity.

In the present work, we extend the findings in [2] to investigate the extent to which wall compliance can be used for flow stabilisation. Accordingly, we evaluate the time-asymptotic stability of the pulsatile flow at a fixed $\Lambda = 3$ and $Wo = 5$ as we systematically reduce the wall stiffness. Our purpose is to identify and track all the different instability branches of the fluid-structure interaction (FSI) system, namely, the Inflectional Instability (II) (that exists within the corresponding rigid-walled system) and flow-induced wall-based instabilities such as Travelling-Wave-Flutter (TWF) and Divergence (D). We implement both vertical (V) and axial-vertical (AV) displacement lumped-mass models for the compliant walls in order to permit the identification of instability modes but also to assess the validity of the vertical (V) displacement model (that is most often used in compliant-wall studies) for the present FSI system. Finally, we compare the instability branches of the pulsatile flow with those predicted by the temporal stability of the corresponding steady Poiseuille flow.

2 System Modelling

We consider the plane pulsatile Poiseuille flow between two compliant walls separated by $2L^*$ distance. The flow field is then characterized by the Reynolds number, $Re = U_0^* L^*/\nu_l^*$, with U_0^* the maximum magnitude of the velocity of the steady plane Poiseuille flow and the Womersley number, Wo, with the Navier-Stokes equations taking the form,

$$\frac{Wo^2}{Re}\frac{\partial \mathbf{U}}{\partial t} + \mathbf{U}\cdot\nabla\mathbf{U} = -\nabla P + \frac{1}{Re}\nabla^2\mathbf{U}. \tag{1}$$

Decomposing the base velocity field into steady and time-dependent parts, $\mathbf{U}_B(\mathbf{x},t) = \overline{\mathbf{U}(\mathbf{x})} + \mathbf{U}'(\mathbf{x},t)$ and taking into account that each part satisfies independently, the fluid momentum Eq. (1) and the no-slip boundary condition on the channel walls, we obtain for the base steady velocity part, $\overline{U_x} = 1 - z^2$, while the time dependent part of the base flow is given by

$$U_x{}' = \frac{\mathrm{i}\Lambda}{Wo^2}\left[1 - \frac{\cosh\left(\mathrm{i}^{3/2}Woz\right)}{\cosh\left(\mathrm{i}^{3/2}Wo\right)}\right]\exp(-\mathrm{i}t) + \frac{\mathrm{i}\Lambda}{Wo^2}\left[\frac{\cosh\left(\mathrm{i}^{1/2}Woz\right)}{\cosh\left(\mathrm{i}^{1/2}Wo\right)} - 1\right]\exp(\mathrm{i}t), \tag{2}$$

where z is the coordinate normal to the flow direction.

We proceed by decomposing the velocity field into a base flow field and a field of small-amplitude disturbances which have a spatial exponential form, $\mathbf{U}(x,z,t) = \mathbf{U}_B(z,t) + \varepsilon\hat{\mathbf{u}}(z,t)\exp(\mathrm{i}\alpha x) + \text{c.c.}$ and $P(x,z,t) = P_B(x,t) + \varepsilon\hat{p}(z,t)\exp(\mathrm{i}\alpha x) + \text{c.c.}$, where $\varepsilon \ll 1$, α is the disturbance wavenumber in the streamwise direction, while the amplitudes of disturbance velocity and pressure, $\hat{\mathbf{u}}(z,t)$, $\hat{p}(z,t)$ depend on time and c.c. denotes the complex conjugate. Upon substituting these into the governing Eq. (1) and the continuity equation, expanding in powers of ε, subtracting the base velocity and pressure fields and eliminating the pressure disturbance, we obtain the time-dependent Orr-Sommerfeld equation,

$$Wo^2\frac{\partial}{\partial t}\mathscr{L}\hat{u}_z = \left(\mathscr{L} - \mathrm{i}\alpha Re U_{x,B}\right)\mathscr{L}\hat{u}_z + \mathrm{i}\alpha Re\frac{\partial^2 U_{x,B}}{\partial z^2}\hat{u}_z, \tag{3}$$

where $\mathscr{L} = \partial^2/\partial z^2 - \alpha^2$.

For the compliant-wall dynamics, we use the one-dimensional isotropic Kirchhoff plate equation with additional terms to account for a dashpot-type damping and a uniformly distributed spring foundation. Combined with the normal and tangential force balance on the two compliant walls, we obtain for the vertical and axial degrees of freedom, respectively,

$$-p(x,z=\mp1,t) + \frac{2}{Re}\frac{\partial u_z}{\partial z}(x,z=\mp1,t) - \frac{2}{Re}\frac{\partial U_{x,B}}{\partial z}(z=\mp1,t)\frac{\partial \eta_{z,s}}{\partial x} = C_I\frac{\partial^2\eta_{z,s}}{\partial t^2} + C_{Dz}\frac{\partial\eta_{z,s}}{\partial t} + C_K\eta_{z,s} + C_B\frac{\partial^4\eta_{z,s}}{\partial x^4}, \tag{4}$$

$$\pm\frac{1}{Re}\left(\frac{\partial u_z}{\partial x}(x,z=\mp1,t) + \frac{\partial u_x}{\partial z}(x,z=\mp1,t)\right) = C_I\frac{\partial^2\eta_{x,s}}{\partial t^2} + C_{Dx}\frac{\partial\eta_{x,s}}{\partial t} - C_A\frac{\partial^2\eta_{x,s}}{\partial x^2}, \tag{5}$$

where $\eta_{z,s}(x,t)$, $\eta_{x,s}(x,t)$ are the vertical and axial displacements of the two compliant surfaces ($s = 1, 2$ lower/upper surfaces) and $p(x, z = \mp1, t)$ is the non-dimensional pressure disturbance on the compliant walls. $C_K, C_B, C_I, C_A, C_{Dz}, C_{Dx}$ are respectively the dimensionless spring-foundation stiffness, flexural rigidity, wall inertia, in-plane stiffness and structural damping of the walls in the vertical and axial direction

respectively, made dimensionless through the maximum magnitude of the velocity of the steady part of the base flow, U_0^*, the half distance between the two plates, L^*, and the angular frequency of the pulsations, ω_f^* for the case of the pulsatile Poiseuille flow. Finally, it is noted that the characteristic time-scale for the case of steady Poiseuille flow is defined through the half distance between the two plates and the maximum magnitude of the base-flow velocity U_0^* and that Eq. (5) becomes redundant for the 1-DOF vertical-displacement model (V).

Using the spatial wavetype decompositions $\eta_{z,s}(x,t) = \hat{\eta}_{z,s}(t)exp(\mathrm{i}\alpha x) + \text{c.c.}$, $\eta_{x,s}(x,t) = \hat{\eta}_{x,s}(t)exp(\mathrm{i}\alpha x) + \text{c.c.}$, the system of Eq. (3) with the boundary conditions Eqs. (4), (5) and the linearized kinematic boundary conditions on the interface [2], is cast in the form of the following initial value problem,

$$\frac{d\hat{\mathbf{v}}}{dt} = \mathbf{Q}(t)\hat{\mathbf{v}},\ \ \hat{\mathbf{v}} = \{\hat{c}_{z,s}, \hat{\eta}_{z,s}, \hat{c}_{x,s}, \hat{\eta}_{x,s}, \hat{\mathbf{u}}_z^T\}^T,\ \ \hat{\mathbf{v}}(t=0) = \hat{\mathbf{v}}^0, \tag{6}$$

where $\hat{c}_{z,s} = \mathrm{d}\hat{\eta}_{z,s}/\mathrm{d}t$, $\hat{c}_{x,s} = \mathrm{d}\hat{\eta}_{x,s}/\mathrm{d}t$ and $\mathbf{Q}$ is periodic in time with fundamental period T, due to the imposed periodic base velocity $\mathbf{U}_B$. The time-asymptotic stability of the pulsatile flow is then studied through extraction of the eigenvalues (Floquet multipliers) of the monodromy matrix calculated from the fundamental solution matrix at the end of the fundamental period of base-flow modulation [2]. Finally, the temporal asymptotic stability of the boundary-value type steady Poiseuille flow is studied through eigenvalue extraction of the generalized eigenvalue problem.

The dynamics for the 1-DOF vertical-displacement model (V) are controlled by the dimensionless stiffness, characterised by the dimensionless free-wave speed of the vertical motion, $K_V = (4C_KC_B)^{1/4}/C_I^{1/2} = (4K^*E^*h^*/(12(1-\nu^2)))^{1/4}/(\rho_s^*L^{*2}\omega_f^{*2})^{1/2}$. Parametrisation of the 2-DOF axial-vertical displacement model (AV) additionally includes the ratio of the vertical to axial stiffness, $R_{VA} = K_V/K_A = (K^*h^*(1-\nu^2)/(3E^*))^{1/4}$, where $K_A = (C_A/C_I)^{1/2}$ is the dimensionless free-wave speed of axial motion. K^*, E^*, h^*, ρ_s^* are respectively the spring foundation stiffness, elastic modulus, thickness and density of the compliant walls while ν is the material Poisson ratio.

3 Results and Discussion

As reference properties for the variations of compliant-wall stiffness investigated herein, we select $R_{VA} = 0.12$ and $K_V = 607$ used in [2], the results of which are shown as blue lines in Fig. 1 where we plot the neutral-stability curves for the pulsatile and steady Poiseuille flows in the Re-wavenumber plane. Figure 1a, b show the predictions for the compliant-wall restricted to vertical displacements (V) while Fig. 1c, d show corresponding predictions for the compliant wall having both vertical and axial displacements (AV). These curves feature the well-known inflectional instability (II) loop and the appearance of travelling-wave flutter (TWF) at

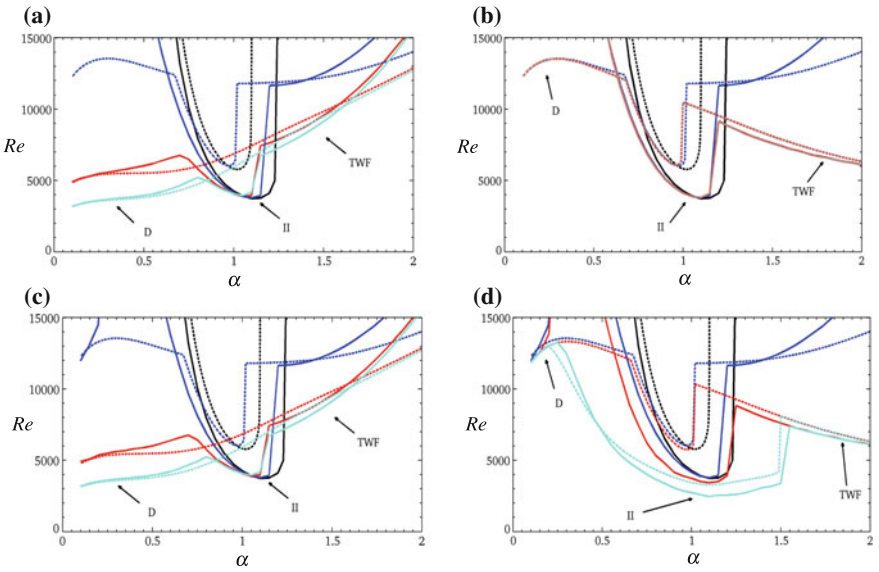

Fig. 1 Variation of the Reynolds number at instability onset with streamwise wavenumber, α, for $Wo = 5$, $\Lambda = 3$ for two wall models: vertical displacement only (V) in (**a**) and (**b**) and axial-vertical (AV) in (**c**) and (**d**). Wall stiffness is varied through changing the dimensional spring foundation stiffness K^* in (**a**) & (**c**) [Legend: cyan: $R_{VA} = 0.068, K_V = 341$, red: $R_{VA} = 0.08, K_V = 409$, blue: $R_{VA} = 0.12, K_V = 607$, black: Rigid walls] or changing the dimensional elastic modulus E^* in (**b**) and (**d**) [Legend: cyan: $R_{VA} = 1.2, K_V = 61$, red: $R_{VA} = 0.675, K_V = 108$, blue: $R_{VA} = 0.12, K_V = 607$, black: Rigid walls]. The solid lines are for pulsatile Poiseuille flow and the dashed lines for steady Poiseuille flow

higher wavenumbers. We reduce wall stiffness through either (i) the spring foundation stiffness K^* in Fig. 1a, c that only reduces the stiffness in vertical displacement, or (ii) the dimensional elastic modulus E^* in Fig. 1b, d that reduces wall stiffness for both vertical and horizontal components of displacement, the latter being more pronounced. Throughout, it can be seen that reducing wall stiffness causes destabilisation of TWF at high wavenumbers and the appearance of Divergence (D) instability at low wavenumbers. It is seen that the critical values for Divergence onset at low wavenumbers are very similar between pulsatile and steady Poiseuille flow for the case where only the vertical stiffness is reduced as seen in Fig. 1a, c.

In Fig. 1d the AV-model results also show that compliant walls with reduced levels of axial stiffness lead to destabilisation of the II mode because this effect is absent if axial motion is suppressed as in Fig. 1b. This difference holds for both the pulsatile and steady flows even though modulation has the stronger destabilizing effect. We note that the II mode yields the critical (lowest) Reynolds number for destabilisation of the FSI system in both Fig. 1b, d. By contrast, the results of Fig. 1a, c for which the stiffness in the axial direction is held constant but vertical wall stiffness is reduced, show a slight stabilisation of the II mode (relative to results for a rigid channel) for the

pulsatile flow and a stronger stabilization of the II mode for the steady flow, because, overall, the wall has become more flexible. However, the TWF and D modes become more unstable with increased wall compliance because their instability mechanisms are primarily dependent upon out-of-plane (bending) waves at the fluid-solid interface. This can be deduced by the close agreement between the results of the AV and V wall models in Fig. 1a, c. It is also noted that D modes of higher wavenumber are stabilized by the pulsation. Finally, it is seen that the D mode ultimately yields the critical Reynolds number for plate-spring compliant walls that are more flexible in bending than in axial deformation. Accordingly, stabilising compliant-walls should be selected with properties that restrict axial motion (to avoid II destabilisation) while being flexible in out-of-plane deformation (stabilising for II) but not so flexible as to be destabilised by wall-based instabilities (D and TWF).

4 Conclusions

We have studied the asymptotic stability of pulsatile and steady Poiseuille flow through a compliant channel for a range of structural stiffness at fixed modulation frequency, $Wo = 5$ and dimensionless pressure-gradient pulsation amplitude, $\Lambda = 3$. The structural stiffness is controlled by two parameters when using the axial-vertical (AV) structural model, namely, the vertical stiffness and the ratio of the vertical to axial stiffness and by one parameter, the vertical stiffness, when implementing the vertical (V) structural model. We have shown that the pulsatile flow is more unstable regarding the inflectional instability but more stable regarding the Divergence instability than the steady flow for the range of the structural stiffness and streamwise disturbance wavenumber, α, studied in the present work. In addition, reducing the wall stiffness in the axial direction causes destabilisation of the inflectional instability (II), while reducing the vertical stiffness is slightly stabilusing for II but renders the FSI system prone to Divergence (D) instability.

References

1. Kerczek CH Von (1982) The instability of oscillatory plane Poiseuille flow. J Fluid Mech 116:91–114
2. Tsigklifis K, Lucey AD (2017) Asymptotic stability and transient growth in pulsatile Poiseuille flow through a compliant channel. J Fluid Mech 820:370–399

Numerical Study of Fluid-Structure Interaction of Microvasculature

S. H. Liu, T. X. Chi, S. Tian, Z. D. Su, Y. Liu and X. Y. Luo

Abstract Blood flow oscillations of 0.001–0.2 Hz are called vasomotion whose physiological mechanism has not been understood. This vasomotion can mirror human body conditions and initiate the pathogenesis sequence in some diseases. In the preliminary measurement of blood flow oscillations in radial artery at the wrist, a strong power spectral density (PSD) at ∼0.1 Hz was found, indicating that low frequency flow oscillations play a dominate role in radial pulse pattern. To understand the interaction between vasomotion and cardiac rhythm in radial artery, numerical simulations were carried out. It is found that the natural frequency of the system decreases with the complexity of microvasculature system, and the inlet oscillating velocity interacts with the natural frequency to generate subharmonics. As the natural frequency in the constructed vessel system can be as low as 0.37 Hz, we speculate that the natural frequency of actual microcirculation is much lower, and the mechanism of vasomotion is actually due to the interaction of cardiac rhythm and microvasculature natural frequency.

Keywords FSI · FFT · Wavelet · Microvasculature

S. H. Liu · T. X. Chi · S. Tian · Y. Liu (✉)
Department of Mechanical Engineering, The Hong Kong Polytechnic University, Hung Hom, HK, China
e-mail: mmyliu@polyu.edu.hk

S. Tian · Z. D. Su
College of Metrology and Measurement Engineering, China Jiliang University, Hangzhou, China

X. Y. Luo
School of Mathematics and Statistics, University of Glasgow, Glasgow, UK

Y. Zhou et al. (eds.), *Fluid-Structure-Sound Interactions and Control*, Lecture Notes in Mechanical Engineering,
https://doi.org/10.1007/978-981-10-7542-1_39

1 Introduction

The radial stretch of the ascending aorta brought about by left ventricular ejection initiates a pressure wave that is propagated down the aorta and its branches. The typical heart rate is ~1 Hz. However, in our preliminary laser Doppler Flowmetry (LDF) measurement of blood flow oscillation in radial artery at the wrist, we found that the power spectral density (PSD) at 0.001–0.1 Hz is much higher than that at heart rate (Fig. 1a), indicating that low frequency flow oscillations play a dominant role in radial pulse pattern. Spectral intervals of blood flow oscillation are related to several types of activities, ~1 Hz is related to cardiac activity, ~0.3 Hz is related to respiratory activity, and 0.001–0.2 Hz is related to endothelial and myogenic activities. Vasomotion is spontaneous time-dependent contraction and relaxation of micro arteries, and there is evidence that microcirculation may mirror the vascular function of other parts of the body and the microvascular abnormalities may initiate the pathogenesis sequence in some diseases [3]. Thus, the thorough understanding of the interaction between vasomotion related and cardiac activity related pressure waves would enable us to develop novel diagnostic technique. In this research, the experimental and numerical studies are carried out to understand the interaction

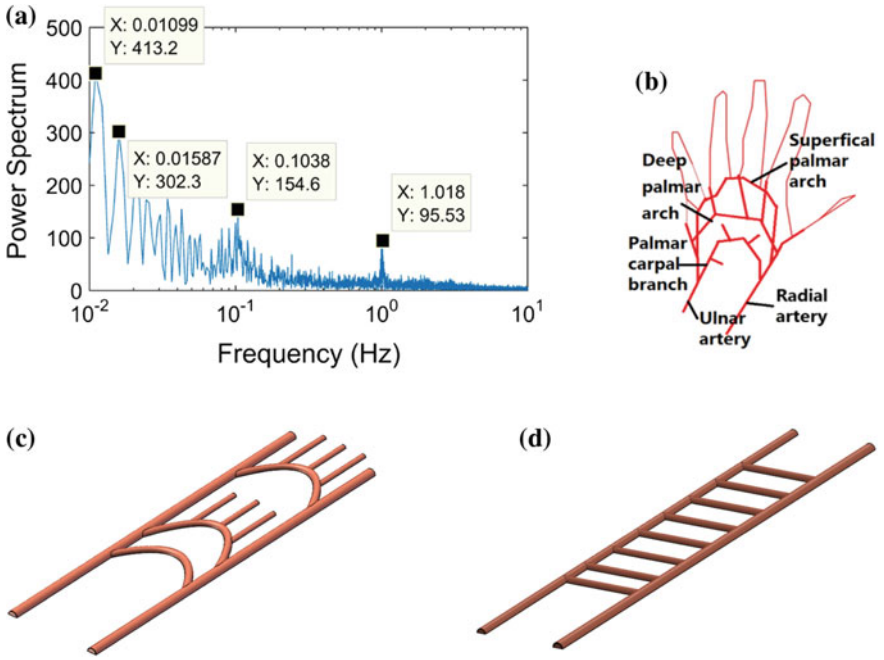

Fig. 1 Previous knowledge and numerical models: **a** FFT analysis of measured LDF signal, **b** real vessels in hand, **c** numerical vessel structure in hand, **d** connected tube model

between vasomotion and cardiac rhythm in radial artery at the wrist, which is an attractive fluid-structure interaction research topic in itself.

2 Methodology

The blood vessel model of the palmar arch is shown as Fig. 1b, the two examples of constructed models are indicated in Fig. 1c, d, and in our simulation the numbers of connected tubes in the Fig. 1d is 5, 6, 8, 16 and 32. The diameter of vessels is set to be 0.02 m. The density of the blood is set as 1050 kg/m^3, and dynamic viscosity is 4×10^{-3} kg/m s. The blood is considered as Newtonian fluid, as the current study is focused on the spectral characteristics, and the non-linearity of viscosity does not have significant effect on spectral analysis. The numerical models were built in ANSYS, and were calculated with CFX. The actual velocity waveform was used to simulate the inlet velocity with different frequencies [2]. The no-slip wall boundary condition was adopted. The calculated and measured time series were analyzed by Fast Fourier Transformation (FFT) and morlet wavelet analysis.

3 Results and Discussion

3.1 Natural Frequency of Microvasculature

Every vibration mode has its own characteristic frequency, which depends on the geometry, the mass density, and the tethering of the arterial system [1]. For the vasculature model in Fig. 1c, the root mean square (RMS) of oscillating pressure at different inlet frequencies is tabulated in Table 1. The RMS of oscillating pressure increases dramatically from 1.0 to 1.87 Hz and then decreases gradually, indicating the natural frequency of the vasculature is 1.87 Hz.

Using the same method, the natural frequency of systems in Fig. 1d with different number of connected tubes are investigated. As shown in Fig. 2, the natural frequency is 2.29 Hz for single connected tube, 0.67 Hz for 16 connected tubes, and 0.37 Hz for 32 connected tubes, indicating that the natural frequency decreases with the complexity of the microvasculature. The real human microvasculature is much more complicated than the vasculature in Fig. 1d, therefore, we speculate that the natural frequency of human microvasculature is lower than 0.37 Hz. We wonder if the low frequency vasomotion is due to the interaction between cardiac rhythm and natural frequency of vasculature.

Table 1 Pressure RMS for different frequencies

Frequency (Hz)	0.072	1	1.87	10	25	50
RMS (Pa)	0.0107	8.4077	68.0392	29.9428	10.1772	6.9592

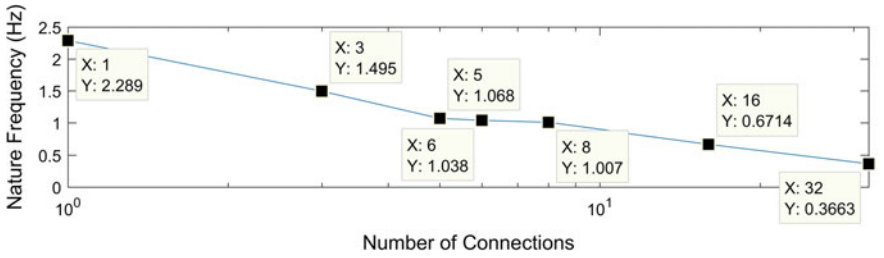

Fig. 2 Natural frequency for connected tube models

3.2 *Interaction Between Inlet Oscillating Velocity and Natural Frequency*

Figure 3a, b illustrate the FFT analysis for the 16-connected-tube model with two different inlet frequencies. When the inlet frequency is 0.67 Hz (natural frequency), the PSD is dominant, and the PSD at lower subharmonic frequency is much lower than that at 0.67 Hz. When the inlet frequency is 1.0 Hz, the PSD at lower subharmonic frequency is comparable to that at inlet frequency. To further investigate the effect of inlet frequency on lower subharmonics, we carried out the simulation with various inlet frequencies, i.e., 0.67 Hz, 1.0 Hz, 2.0 Hz, 10 Hz, 25 Hz and 50 Hz, respectively. The ratio of PSD at lower subharmonic frequency to that at inlet frequency is tabulated in Table 2. When the inlet frequencies are far away from the natural frequency, for example at 10, 25 and 50 Hz, the PSD ratio at lower subharmonic is quite low, only 2–5%. When the inlet frequencies are at natural frequency or its harmonic, for example at 0.67 and 2.0 Hz, the PSD ratio at lower subharmonic is about 10%. When the inlet frequency is at 1.0 Hz, the PSD ratio can be 95%. The similar phenomenon can also be found in the cases with 32 and 8 connections These findings indicate that the interaction between inlet oscillating

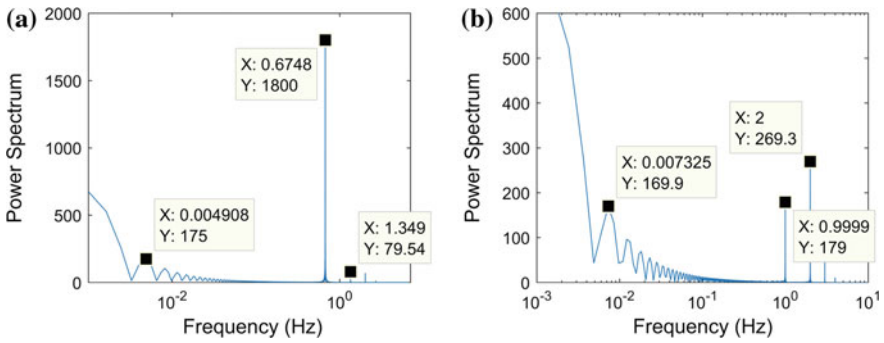

Fig. 3 Sixteen-connections FFT analysis: **a** 0.67 Hz, **b** 1.0 Hz

Table 2 Ratio between subharmonic PSD and inlet frequency PSD

Inlet f (Hz)	0.67	1	2	10	25	50
Sub/inlet	0.10	0.95	0.15	0.02	0.03	0.05

flow and natural frequency of vasculature is very strong, and would affect the flow oscillating pattern.

In real human vasculature, the natural frequency should be lower than 0.37 Hz, the typical inlet frequency is 1.0 Hz, and the interaction between inlet frequency and natural frequency would generate strong oscillation at subharmonic frequencies. As the frequency of vasomotion is 0.001–0.1 Hz, we could speculate that the so-called vasomotion is initiated by the subharmonic oscillation, and this oscillation triggers the myogenic and endothelial activities.

4 Conclusions

The numerical simulation of blood flow in microvasculature has been carried out, and the spectral analysis leads to following conclusion: (i) the natural frequency of vasculature has significant effect on vasomotion at lower frequency; (ii) the natural frequency of the system decreases with the complexity of system; (iii) the interaction between natural frequency and inlet oscillating frequency would generate lower subharmonic oscillation in vasculature which is the mechanism of vasomotion.

Acknowledgements Supports given by HKRGC PolyU 5202/13E and PolyU G-YBG9 & G-UACM are gratefully acknowledged.

References

1. Lin Wang YY, Jan MY, Shyu CS et al (2004) The natural frequencies of the arterial system and their relation to the heart rate. IEEE Trans Biomed Eng 51(1):193–195
2. Mills CJ, Gabe IT, Gault JH et al (1970) Pressure-flow relationships and vascular impedance in man. Cardiovasc Res 4(4):405–417
3. Rossi M, Carpi A, Di Maria C et al (2006) Spectral analysis of laser Doppler skin blood flow oscillations in human essential arterial hypertension. Microvasc Res 72(1–2):34–41

On the Vortex Dynamics in the Wake of High-Speed Low-Damping Galloping Cylinders

L. Gan, H. O. Claydon, Q. Y. Wang and S. J. Xu

Abstract In this work, we focus on the vortex evolutions in the wake behind three non-axisymmetric rigid cylinders under high-speed, low-damping galloping in a wind tunnel. Laser displace sensor is used to measure the displacement amplitude and two branches of amplitude curves are observed—rising and falling range of galloping range. Particle Image Velocimetry is then used to investigate coherent vortex structures in the wake. It has been found that a D-section cylinder has a galloping response at the lowest free stream velocity, which also has the smallest formation length and recirculation bubble length when at static condition. The wake widths show a similar growth rate, which is independent of the galloping amplitudes.

Keywords High-speed galloping · Low-damping · Amplitude spectra
Vortex dynamics · PIV

1 Introduction

Flow induced galloping is a well known phenomenon associated with non-axisymmetric sectional slender bluff-bodies exposed in high velocity cross flows. While there have been extensive experimental studies trying to understand it, most of them either focused on the structure responses or the qualitative vortex patterns (modes) in vortex induced vibration (VIV, happens at lower free stream velocities) regime [1]. In this work, we conduct experimental investigations trying to tackle quantitative vortex evolution in the wake of the galloping non-circular cylinders, aiming for both initial and terminal branches of the amplitude response curves. Our primary interest is the use of the large vibrating amplitude for potential applications in flow mixing and energy harvesting.

L. Gan (✉) · H. O. Claydon
Department of Engineering, Durham University, DH1 3LE, Durham, UK
e-mail: lian.gan@durham.ac.uk

Q. Y. Wang · S. J. Xu
AML, School of Aerospace Engineering, Tsinghua University, Beijing 100084, China

Y. Zhou et al. (eds.), *Fluid-Structure-Sound Interactions and Control*, Lecture Notes in Mechanical Engineering,
https://doi.org/10.1007/978-981-10-7542-1_40

2 Experimental Method and Results

Aluminium cylinders of three cross-sectional shapes are spring mounted horizontally in a wind tunnel (outside) so that the vibration is in the transverse direction; see Fig. 1a. The length/diameter ratio $L/D = 15$, which gives a blockage ratio $\phi = 6\%$ in the wind tunnel so that the flow two-dimensionality is well preserved. The system's natural frequency f_n and damping ratio ζ are determined from the free oscillation amplitude A_y measured by a Baumer laser displacement sensor, which operates at 1kHz with a resolution of 50 μm, and is also used to measure A_y in the galloping states. The system's natural frequency is given in Table 1 and they result in similar Scruton numbers $Sc \equiv (4\pi m\zeta)/(\rho D^2) \approx 10$, with m being mass per unit length and ρ being the density of air.

The wind tunnel velocity is set at $U_\infty \approx 3 - 15$ m/s. The A_y responses are presented in Fig. 1b. We target high reduced speed conditions, i.e. $U_\infty/Df > 20$, where f is the vibration frequency. For the D-section cylinder (DS), $A_y/D > 2.2$ where spring limit is reached at $U_\infty/Df \approx 25$, suggesting the widest response compared to the

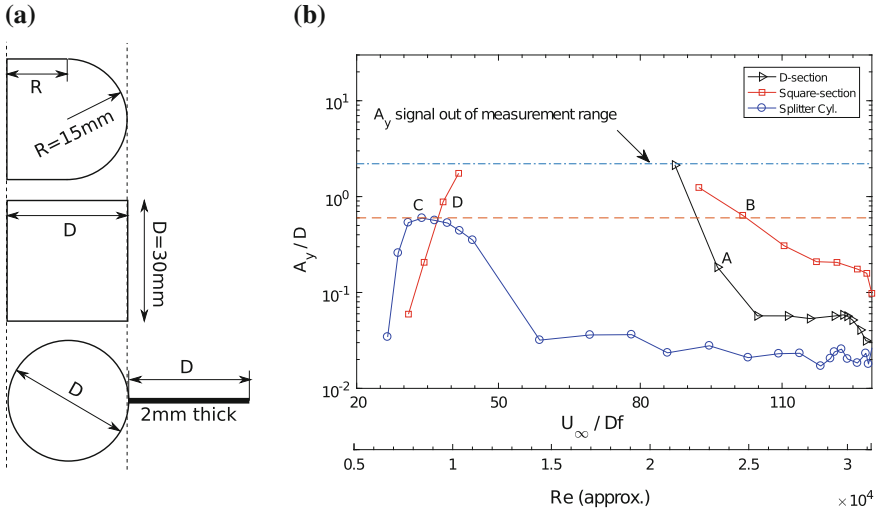

Fig. 1 **a** The cylinder cross sectional shapes; from top to bottom: D-section (DS), square-section (SQ) and Splitter plate-section (SP). The flow comes from the left to the right. **b** Dependence of the oscillation amplitude on the reduced velocity, U_∞ ramps up from low value. The PIV measurement are conducted at the condition near A–D

Table 1 System natural properties

	D-section	Square-section	Splitter plate
f_n (Hz)	3.96	3.74	4.03
$\zeta(\times 10^{-4})$	3.53	3.73	5.65

other two cylinders. Based on the quasi-steady theory, the critical wind speed of galloping is $U_g \equiv 2Scf_nD/a_g$, where $a_g = -\mathrm{d}C_L/\mathrm{d}\alpha(0) - C_D(0)$. It is well documented in [2, 3] that over a wide testing conditions and cylinder shapes, $-6 \lesssim \alpha_g \lesssim -1$, which gives $0.4 \lesssim U_g \lesssim 2.5$. It has also been shown in [1, 3] that for general bluff bodies in high Re flows, the Strouhal number $St \equiv f_sD/U_\infty \sim 0.1$, where f_s is the vortex shedding frequency, which infers the Kármán-vortex resonance wind speed $U_r \equiv f_nD/St \sim 1$. The ratio $U_g/U_r \lesssim 2.5$ and therefore it indicates that the vibration observed is highly likely a full interaction of VIV and galloping.

Particle Image Velocimetry (PIV) measurements are conducted in the near wake area of $6D \times 7D$(streamwise), starting from the downstream vertical dashed line in Fig. 1a. PIV images are processed at 32 pixel interrogation window size with 50% overlap, resulting in a spatial resolution of $D/10$ based on vector spacings. PIV measurements are carried out for each cylinder at both static and galloping conditions, which are measured at $U_\infty = 4.5$ and 12 m/s. In total 800 velocity fields are acquired in each case. The testing points at galloping are indicated in Fig. 1b. It has been found from the A_y spectra (figure not shown) that at these testing points, dominant oscillation frequency matches f_n, which is similar to the VIV resonance for large mass ratio structures [1]. The PIV sample rate is set at 3 Hz for all the cases to allow snapshots to be evenly sampled at all phases (vortex shedding and A_y) of a cycle. This is to ensure that all the ensemble averaged process are not phase-locked. The DS A_y spectra also shows more pronounced (compared to SQ) peaks at higher frequencies (not super-harmonics) at a similar reduced velocity, which suggests a multi-scale vortex shedding. Further time resolved measurements will be useful to understand this mechanism.

From the mean velocity field, the development of the wake width defined at half deficit velocity $H[(1/2)(U_\infty - U_0)]$ is shown in Fig. 2. Evidently, the absolute value of H is strongly correlated with A_y, whereas the growth rate is not. Galloping cases tend to have lower growth rates at the same U_∞ for $x > 3D$, which should be attributed to the intensive near-field mixing between the more segmented vortices and regions outside the wake.

Figure 3 presents the relation between the formation length L_f (determined by the peak value of the transverse velocity fluctuations) and the recirculation bubble size (determined by the stagnation point location) B_s. For static cases at $U_\infty = 12$ m/s, L_f and B_s share a similar size for SQ and DS. Noticeable differences can be observed for other cases. For the galloping cases, it is interesting to see that A_y has no strong influence on B_s and L_f; see the $U_\infty = 12$ m/s cases.

Standard snapshot based proper orthogonal decomposition (POD) is used to track cores of the shed vortices in reduced-order reconstructed vorticity (ω) fields. Subsequently their evolution can be assessed by a conditional average process (not phase averaging). Using DS(F4.5) as an example, Fig. 4a shows a 95% POD energy reconstruction of an instantaneous snapshot (b). The centre of each vortex core in (a) can then be determined after a proper image segmentation process. Comparing Fig. 4a, b, it is not surprising to see that the reduced-order reconstruction shows more organised coherent vortex structures, but the peak ω intensity is lower than that of the true ω. The vortex patterns in the cases shown in Fig. 4 are well pinched-off from the

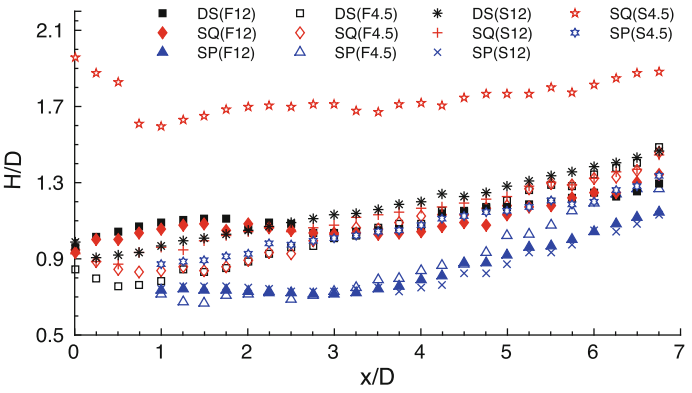

Fig. 2 Development of the wake width H with streamwise distance x. Legend example: DS(F12) stands for static (fixed) DS at $U_\infty = 12$ m/s, SQ(S4.5) for galloping (sprung) SQ at $U_\infty = 4.5$ m/s. This legend system is adopted hereafter

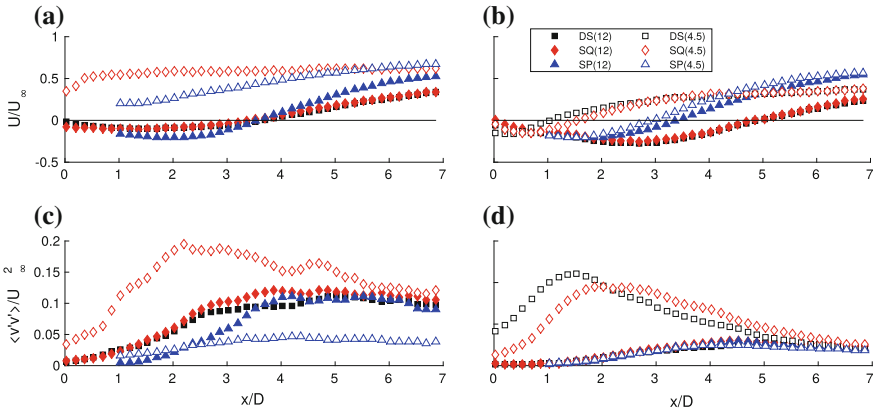

Fig. 3 Recirculation bubble size, defined by the distance of the cylinder centre to the wake stagnation point, which can be determined from the streamwise velocity U along the wake centreline, and formation length, in this case defined by the peak spanwise Reynolds stress $\langle v'v' \rangle$ along the centreline. **a**, **c** galloping cases; **b**, **d** static cases. Legends are shown in (**b**)

shear layers. Their strength can be estimated by the approximated circulation Γ_e. Assuming circular vortices, $\Gamma_e = 2\pi \int_0^{R_t} \omega(r) r dr$, where R_t is the radius subjected to a universal threshold or a relative one of $\omega_t = 0.1\omega_0$, with ω_0 being the peak vorticity intensity. The evolution of Γ_e will be presented in a future work, considering the length of the current manuscript.

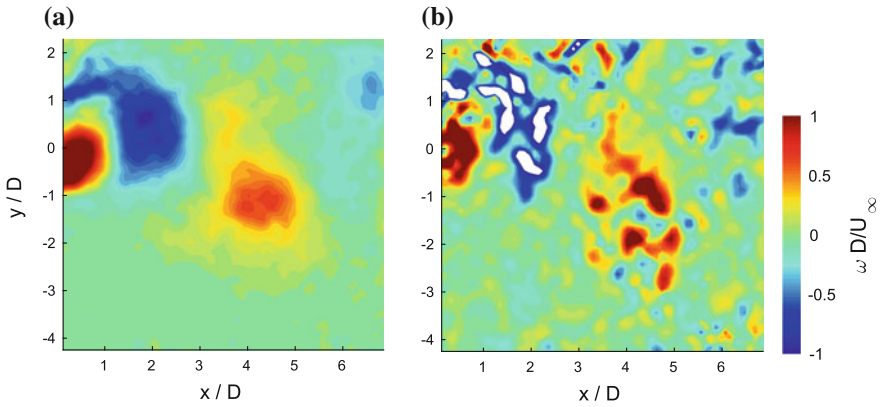

Fig. 4 **a** Reduced-order reconstruction using POD modes of an instantaneous snapshot shown in **b** for DS(F4.5), where **a** contains 95% of the total energy of **b**

3 Conclusion

We present in this paper some wind tunnel measurements of galloping behaviour and wakes behind three non-axisymetric cylinders. The primary results show that DS has the widest galloping response compared to SQ and SP in terms of amplitude A_y. The PIV measurements reveal that SQ and DS exhibit distinguishable differences in terms of formation length, which is potentially associated with the observed different A_y responses. DS shows to have the smallest formation length and recirculation bubble length in fixed conditions. However, DS and SQ share a similar variation trend for the wake width H at static conditions independently to A_y, with SP having a subtly larger growth rate. The H magnitude is approximately proportional to A_y, not surprisingly.

Acknowledgements The authors thank the support from UK Royal Academy of Engineering (NRCP/1415/130) and China NSFC (11472158).

References

1. Williamson CHK, Govardhan R (2004) Vortex-induced vibrations. Annu Rev Fluid Mech 36
2. Wang Q, Song K, Xu S (2015) Experimental study of a spring-mounted wide-D-section cylinder in a cross flow. In: 3rd symposium on fluid-structure-sound interactions and control
3. Mannini C, Marra AM, Bartoli G (2014) VIV galloping instability of rectangular cylinders: review and new experiments. J Wind Eng Ind Aerodyn 132

Active Control of Two-Dimensional Vortex-Induced Vibration of a Circular Cylinder Using a Pair of Synthetic Jets

Chenglei Wang, Fei Duan and Hui Tang

Abstract This paper presents a study on the control of two-dimensional vortex-induced vibration (VIV) of a single circular cylinder at a low Reynolds number of 100 using a synthetic jet (SJ) pair. To facilitate this study, a lattice Boltzmann method based numerical framework is adopted. While its strength is fixed, the SJ pair operates either in phase or anti-phase over a wide excitation frequency range. The effects of the SJ excitation phase difference and frequency are systematically investigated. Simulation results reveal that both the in-phase and anti-phase SJ pairs are able to mitigate the VIV at higher excitation frequencies, while either the cross-flow or streamwise resonance (associated with large-amplitude VIV) may be induced by the SJ pair at lower frequencies.

Keywords Synthetic jet · Vortex-induced vibration · Lattice Boltzmann method

1 Introduction

Asymmetric vortex shedding from a bluff body can cause dynamic loading on the associated structure. When the vortex shedding frequency is close to the structure's natural frequency, large-amplitude vibrations may occur, known as vortex-induced vibration (VIV). When this happens, catastrophic failures to the structure may occure. Since this VIV phenomenon can be widely found in engineering practices, such as airplanes, automobiles and offshore structures, it is necessary to attenuate the VIV to protect relevant structures. For years, numerous flow control methods

C. Wang · H. Tang (✉)
Department of Mechanical Engineering, The Hong Kong Polytechnic University, Kowloon, Hong Kong, China
e-mail: h.tang@polyu.edu.hk

C. Wang · F. Duan
School of Mechanical and Aerospace Engineering, Nanyang Technological University, Singapore 639798, Republic of Singapore

Y. Zhou et al. (eds.), *Fluid-Structure-Sound Interactions and Control*, Lecture Notes in Mechanical Engineering,
https://doi.org/10.1007/978-981-10-7542-1_41

have been used to suppress the asymmetric vortex shedding and VIV, including passive (no power required) and active (power required) schemes, on which Choi et al. [1] has given a comprehensive review.

2 Problem Description and Methodology

This research studies the active control of two-dimensional vortex-induced vibration (VIV) of a circular cylinder using a pair of synthetic jets. The cylinder is immersed in a uniform flow at a low cylinder-diameter-based Reynolds number, i.e., $Re = U_\infty D/\upsilon = 100$, where U_∞ is the freestream velocity, D the cylinder's diameter, and υ the kinematic viscosity. It connects to two identical springs along the cross-flow and streamwise directions, respectively, as depicted in Fig. 1. Hence, the cylinder can move in the two-dimensional space. In order to mitigate its VIV, a pair of synthetic jets (SJs), represented by the two red line sections in Fig. 1, is implemented along the streamwise direction at the leeward surface of the cylinder. Assuming that the upper and lower SJs operate with the same excitation frequency (f_{sj}) and velocity amplitude (U_{sj}), their velocities relative to the oscillating cylinder can be defined as

$$u_{sj}{}^{u} = U_{sj} \sin(2\pi f_{sj} t + \phi_u) \tag{1}$$

$$u_{sj}{}^{l} = U_{sj} \sin(2\pi f_{sj} t + \phi_l) \tag{2}$$

respectively, where ϕ_u and ϕ_l are the operating phase angles of the upper and lower SJs, from which the phase difference between the SJ pair can be defined as

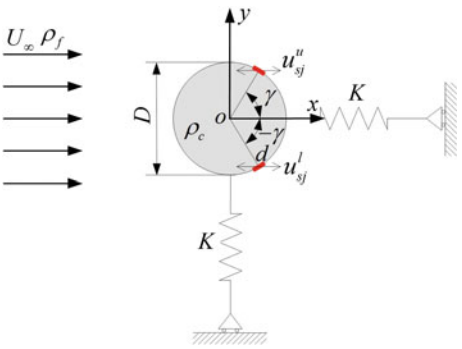

Fig. 1 Schematic of two-dimensionally oscillating cylinder equipped with a SJ pair. The two red line sections represent the SJ pair, U_∞ the freestream velocity, ρf the fluid density, D the diameter of the cylinder, ρc the density of the cylinder, γ the azimuthal angle, $u_{sj}{}^{u}$ and $u_{sj}{}^{l}$ the velocities of the upper and lower SJs relative to the oscillating cylinder, respectively, d the SJ width, and K the stiffness of the spring

$$\Delta\phi = \phi_u - \phi_l \tag{3}$$

Normalizing f_{sj} using the natural frequency of the mass-spring system (f_N) in fluid gives a non-dimensional SJ excitation frequency (f_{sj}^*)

$$f_{sj}^* = f_{sj}/f_N \tag{4}$$

The SJ strength is quantified by a momentum coefficient (C_μ) as

$$C_\mu = 2U_{sj}^2 d/U_\infty^2 D \tag{5}$$

where d is the width of the SJ slots.

This study only focuses on the effects of SJ frequency (f_{sj}^*) on attenuating the cylinder's two-dimensional VIV when the SJ pair operates either in-phase ($\Delta\phi = 0$) or anti-phase ($\Delta\phi = \pi$). Thus, f_{sj}^* varies in the range of 0.4–7, within which various lock-on could be induced [2, 3]; and the other parameters are fixed as: momentum coefficient $C_\mu = 2.149$, SJ location $\gamma = 50°$, the cylinder-fluid mass ratio $m^* = \rho_c/\rho_f = 2.55$, and the reduced velocity $U_r = U_\infty/f_N D = 5.9$. The latter two parameters are chosen in such a way that the cylinder's vibration amplitude is relatively large and difficult to control, as suggested in Du and Sun [4].

To simulate the two-dimensional flow around the cylinder, two major types of numerical solvers exist in literature. One is the Navier-Stokes equation (NSE) based solver rooting in the continuum assumption at the macro scale, and the other is the lattice Boltzmann equation (LBE) based solver describing the collision and redistribution of collections of particles at the meso scale. In contrast with the NSE based solver, it is much easier to write the code for the LBE based solver and to implement the parallel algorithms, originating from its underlying kinetic theory [5]. Therefore, in this study, the incompressible D2Q9 MRT LBE model, i.e., two-dimensional incompressible multiple-relaxation-time lattice Boltzmann equation model with nine discrete velocities, is employed. The MRT multi-block scheme is applied to enhance the computational efficiency while maintaining sound accuracy. Besides, the interpolated half-way bounce back scheme is incorporated to deal with curved boundaries and the corrected momentum exchange method is employed for accurate prediction of the aerodynamic forces on the cylinder.

Throughout this study, the computational domain is set as $60D$(length) $\times$ $20D$ (width) with a uniform flow flowing from the left to the right at a speed U_∞. The circular cylinder is initially placed on the channel centerline and $20D$ away from the inlet boundary. Furthermore, the non-reflecting inlet boundary condition is used at the inlet boundary, whereas the homogenous Neumann boundary condition is implemented at the outlet boundary. On the top and bottom walls, the Dirichlet boundary condition is applied with the x-component velocity U_∞ and y-component velocity 0. The SJ actuators are represented by a number of nodes on the cylinder surface, and the time-dependent SJ velocities are realized through enforcing u_{sj}^u and u_{sj}^l on these nodes. The details of the algorithm and its validation can be found in our previous works [6, 7].

3 Results and Discussion

The variations of the two-dimensional VIV amplitudes (i.e., cross-flow amplitude A_y^* and streamwise amplitude A_x^*) against the excitation frequency of the in-phase ($\Delta\phi = 0$) and anti-phase ($\Delta\phi = \pi$) SJ pair are shown in Fig. 2. Compared to the unforced case where the SJ pair is off, A_y^* can be effectively reduced in two frequency ranges, i.e., $f_{sj}^* < 1.4$ and $f_{sj}^* > 3$, by using the in-phase SJ pair, as shown in Fig. 2a. Within these frequency ranges, the strength of the vortices shed from the upper and lower surfaces of the cylinder can be significantly reduced. The operation of in-phase SJs also results in symmetric wakes as shown in Fig. 3a, which is taken from the case with $\Delta\phi = 0$ and $f_{sj}^* = 1.2$. At frequencies around $f_{sj}^* = 2$, however, A_y^* is augmented, even higher than the amplitude in the unforced case. In this frequency range, the Fast Fourier Transform (FFT) based spectrum analysis for the cylinder's normalized y-displacement (y_o^*) reveals that the cylinder's cross-flow oscillation frequency (f_{vy}^*) is $f_{sj}^*/2$, one half of the SJ excitation frequency. For instance, in the case with $\Delta\phi = 0$ and $f_{sj}^* = 2$, $f_{vy}^* = f_{sj}^*/2 = 1$, as shown in Fig. 4a. Under this condition, the secondary lock-on occurs. As such, f_{vy}^* is close to the system's cross-flow resonance frequency (around 1), causing the occurrence of cross-flow resonance. As for the streamwise amplitude A_x^*, it can be reduced at frequencies greater than about 2 by the operation of in-phase SJ pair, as revealed in Fig. 2b. But it is amplified at $f_{sj}^* < 2$, which mainly stems from the in-phase SJ excitation near the system's horizontal resonance frequency (also around 1). Note that in the case with $\Delta\phi = 0$ and $f_{sj}^* = 2$, FFT is performed over 35 VIV periods, and the sampling rate of FFT is set equal to $35{,}400\Delta t/T_N$, where T_N is the natural period of the mass-spring system in fluid, and Δt the unit time step in the LBM-based simulation. Such FFT parameters remain the same in other cases of this study.

When the anti-phase SJ pair is applied, significant A_y^* reduction is observed at around $f_{sj}^* = 2$ and $f_{sj}^* > 4$, as shown in Fig. 2a. In these frequency ranges the cylinder's cross-flow oscillation frequency (f_{vy}^*) is attracted to the frequency away from the system's cross-flow resonance frequency, and the asymmetric wake is also weakened. This can be confirmed through examining the spectra of the cylinder's

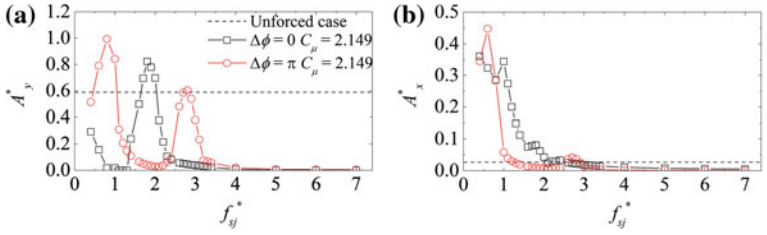

Fig. 2 The variations of the cylinder's cross-flow and streamwise vibration amplitudes (Ay^* and Ax^*) against the normalized SJ excitation frequency (f_{sj}^*) when applying the in-phase ($\Delta\phi = 0$) and anti-phase ($\Delta\phi = \pi$) SJ pair for the two-dimensional VIV control

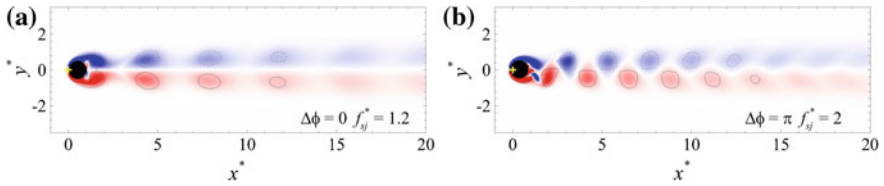

Fig. 3 Wake patterns for a the case with $\Delta\phi = 0$ and $f_{sj}^* = 1.2$, and b the case with $\Delta\phi = \pi$ and $f_{sj}^* = 2$

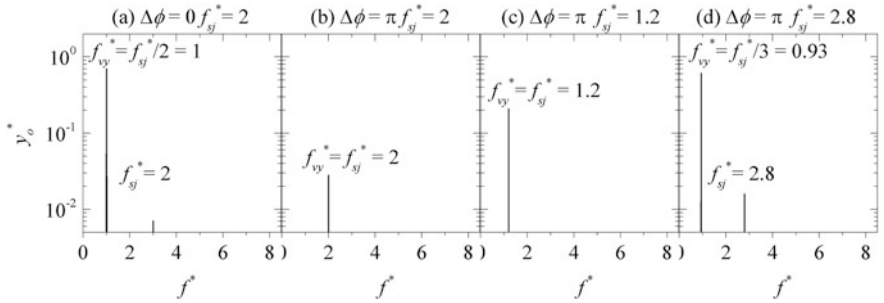

Fig. 4 Frequency spectra of the cylinder's normalized y-displacement (yo^*) for a the case with $\Delta\phi = 0$ and $f_{sj}^* = 2$, b the case with $\Delta\phi = \pi$ and $f_{sj}^* = 2$, c the case with $\Delta\phi = \pi$ and $f_{sj}^* = 1.2$, and d the case with $\Delta\phi = \pi$ and $f_{sj}^* = 2.8$

normalized y-displacement (y_o^*) and instantaneous wake pattern in a representative case (with $\Delta\phi = \pi$ and $f_{sj}^* = 2$), as shown in Figs. 4b and 3b, respectively. On the contrary, the primary ($f_{vy}^* = f_{sj}^*$) and tertiary ($f_{vy}^* = f_{sj}^*/3$) lock-on happen at around $f_{sj}^* = 1$ and 3, respectively, which are evidenced by the spectra of y_o^* in the case with $\Delta\phi = \pi$ and $f_{sj}^* = 1.2$ and the case with $\Delta\phi = \pi$ and $f_{sj}^* = 2.8$, as shown in Fig. 4c and 4d, respectively. Thus, the cross-flow resonance happens as f_{vy}^* approaches 1 or 3, making A_y^* increase a lot in these frequency ranges. Furthermore, the operation of the anti-phase SJ pair at $f_{sj}^* < 1$ allows the development of the system's streamwise resonance, as evidenced by the significant A_x^* increase in Fig. 2b. When $f_{sj}^* > 1$, the anti-phase operation of the SJ pair forces the horizontal oscillation of the system at frequencies away from its natural resonance frequency, so that the cylinder's streamwise VIV is apparently mitigated.

4 Conclusions

This paper investigates the effects of a SJ pair on controlling the two-dimensional VIV of a circular cylinder a low Reynolds number of 100. The SJ pair operates either in phase ($\Delta\phi = 0$) or anti-phase ($\Delta\phi = \pi$) with the momentum coefficient

fixed at 2.149, and its normalized excitation frequency varies from 0.4 to 7. It is found that the SJ pair is able to suppress the two-dimensional VIV at $f_{sj}^* > 4$ effectively, no matter it operates in phase or anti-phase. However, in the lower frequency range, the cross-flow VIV can be augmented by either the in-phase SJ pair operating at around $f_{sj}^* = 2$ or the anti-phase SJ pair operating at around $f_{sj}^* = 1$ and 3, through inducing the secondary, primary and tertiary lock-on, respectively. As for the streamwise VIV, it can also be amplified due to the induced horizontal resonance, when the in-phase SJ pair operates at $f_{sj}^* < 2$ or the anti-phase SJ pair operates at $f_{sj}^* < 1$.

Acknowledgements The authors gratefully acknowledge the financial support for this study from The Research Grants Council of Hong Kong under General Research Fund (Project No.: PolyU 152493/16E).

References

1. Choi H, Jeon W, Kim J (2008) Control of flow over a bluff body. Annu Rev Fluid Mech 40:113–139
2. Wang C, Tang H, Yu S, Duan F (2017) Control of vortex-induced vibration using a pair of synthetic jets: Influence of active lock-on. Phys Fluids 29(8):083602
3. Wang C, Tang H, Yu S, Duan F (2017) Lock-on of vortex shedding to a pair of synthetic jets with phase difference. Phys Rev Fluids 2(10):104701
4. Du L, Sun X (2015) Suppression of vortex-induced vibration using the rotary oscillation of a cylinder. Phys Fluids 27(2):023603
5. Mohamad A (2011) Lattice Boltzmann method: fundamentals and engineering applications with computer codes. Springer, London, pp 1–13
6. Wang C, Tang H, Duan F, Yu S (2016) Control of wakes and vortex-induced vibrations of a single circular cylinder using synthetic jets. J Fluids Struct 60:160–179
7. Wang C, Tang H, Yu S, Duan F (2016) Active control of vortex-induced vibrations of a circular cylinder using windward-suction-leeward-blowing actuation. Phys Fluids 28(5): 053601

Spectral Correlation Study of Skin Blood Flow Oscillation

T. X. Chi and Y. Liu

Abstract Spontaneous rhythmic oscillations in microvessel diameter are known as vasomotion. Vasomotion is the intrinsic property of small arteries and arterioles and is dependent of heartbeat, respiration, or neuronal input. The skin microcirculation is an anastomotic network of vessels with many crucial functions in which the blood flow must be finely regulated and tuned in order to fulfill all the demands of the organism. The laser Doppler Flowmetry (LDF) can be used to measure dynamic changes in skin blood flow over a small area. Traditional Chinese medicine (TCM) considers that there exist acupoints around body which are connected by meridian, and stimulating the acupoint is a typical therapeutic technique in TCM. It was found that stimulating one acupoint could enhance the vasomotion in another acupoint significantly. We argue that the vasomotions in these two acupoints could be correlated to each other. To verify our argument, we used the laser Doppler Flowmetry (LDF) to measure the skin blood flow at two acupoints, and carried out spectral and correlation analyses. It is found that the vasomotions related to myogenic activity are quite strong at acupoints and the correlation is discernable. The vasomotion related to myogenic activity at non-acupoint is much weaker and there is no significant correlation between the acupoint and non-acupoint.

Keywords LDF · Vasomotion · Myogenic

1 Introduction

The spontaneous time-dependent contraction and relaxation of small arteries and arterioles are termed as vasomotion which may have considerable implications in the physiology and pathology of the arterial system. The spectral analysis of human

T. X. Chi (✉) · Y. Liu
Department of Mechanical Engineering, The Hong Kong Polytechnic University, Hong Kong, China
e-mail: 15900011r@connect.polyu.hk

Y. Zhou et al. (eds.), *Fluid-Structure-Sound Interactions and Control*, Lecture Notes in Mechanical Engineering,
https://doi.org/10.1007/978-981-10-7542-1_42

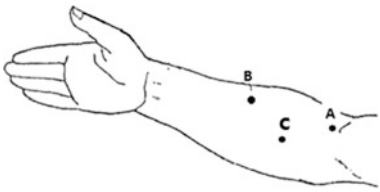

Fig. 1 Two selected acupoints (named Chize (**A**) and Kongzui (**B**)) and one non-acupoint (**C**)

skin blood flow oscillation has revealed five frequency components of vasomotion: the band 0.6–1.8 Hz is due to heart activity, the band 0.2–0.6 Hz is related to respiration, the band 0.06–0.2 Hz is related to myogenic activity, the band 0.02–0.06 Hz is associated to sympathetic activity and the band 0.007–0.02 Hz is more specifically related to endothelial activity [1]. It was found that the vasomotion propagates along arterioles, capillaries and venules in both upstream and downstream directions. Moreover, there is evidence that microcirculation may mirror the vascular function of other parts of the body and the microvascular abnormalities may initiate the pathogenesis sequence in some diseases. In TCM, the acupoints are interrelated to each other, and acupuncturing at one acupoint may affect another acupoint. Several in vivo human studies have found that acupuncturing at one acupoint may increase significantly the myogenic component of flowmotion at another acupoint. To verify whether the vasomotions related to myogenic activity at acupoints are correlated to each other, we selected two acupoints along the same meridian (A and B). In addition, another non-acupoint (point C) is selected as reference (Fig. 1).

2 Materials and Methods

2.1 Measurement Procedure

Two LDF probes were positioned on two selected points. The ambient temperature is set at 23 ± 1 °C in room and sampling rate is 20 Hz equivalent to 0.05 s time interval. Points A−B and Points A−C were measured simultaneously. The measurement time was 20 mins.

2.2 Spectral Analysis

The mainly analytic tools analyzing the LDF signal are usually considered as the linear analysis which include Fast Fourier transform analysis (FFT) and Morlet wavelet analysis. Periodic oscillations of skin blood flow can be quantified directly

by FFT which could reveal the amplitude (energy) of the whole signal at given frequencies. For wavelet analysis, its feature allows us to determine both the dominant modes of blood flow oscillation and how those modes vary in time. For skin blood flow signals, Morlet wavelet analysis breaks down the steady fluctuating time series into its frequency elements and computes the power of signal components in predetermined frequency bands, allowing to measure the amplitude of different flowmotion waves in PU/Hz.

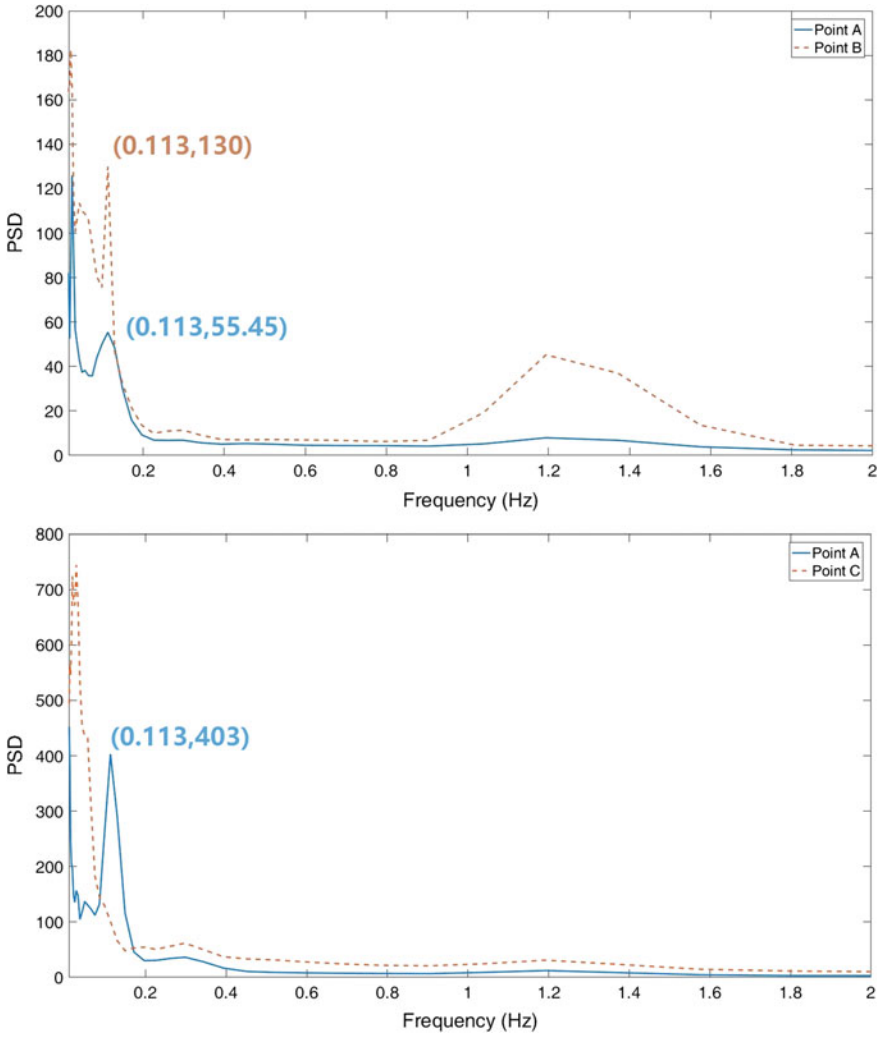

Fig. 2 FFT of Acupoint (**A**),Acupoint (**B**) and Non-acupoint (**C**)

3 Results and Discussion

3.1 FFT and Wavelet Analysis

From FFT analysis, the PSD of acupoint A and B at ~0.1 Hz are dominant on Fig. 2, but not for the non-acupoint C. Thus It could be explained that the skin blood flow oscillation on these two acupoints (A and B) are influenced greatly by the myogenic factor (~0.1 Hz). In addition, all the PSDs of the lower frequency are higher than that of 1 Hz for these three points, indicating the myogenic component

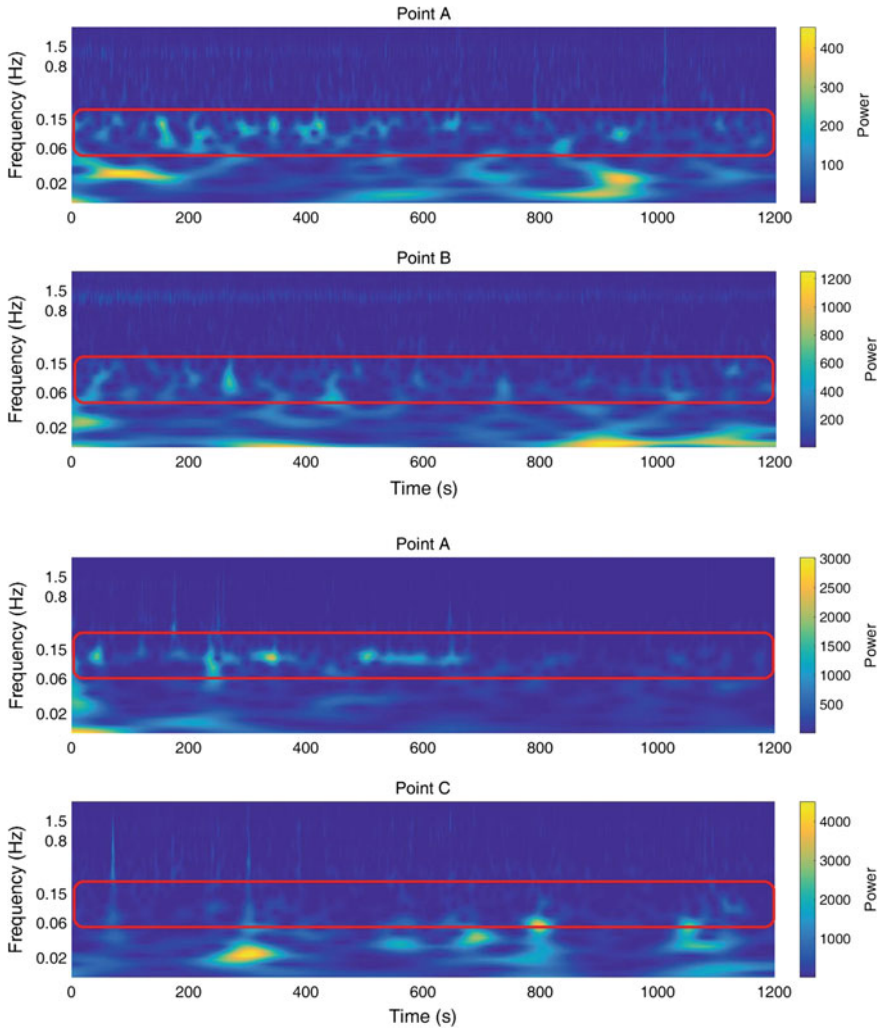

Fig. 3 Morlet Wavelet analysis of Acupoint (**A**) and Non-acupoint (**C**)

of vasomotion is significant. Comparing with the FFT analysis, the wavelet transform does not lose the time-series information of characteristic frequency, and it is obviously that the energy at different frequency varied with time. From wavelet analysis, the Fig. 3 shown that the PSD of acupoint A and B at ~0.1 Hz exhibits periodic behaviour and follows a certain pattern, and the non-acupoint have no significance periodic pattern occurred at ~0.1 Hz. Therefore, the periodic behavior at ~0.1 Hz only exists in acupoints (A and B), and this periodic behavior should follow a certain transmitting direction.

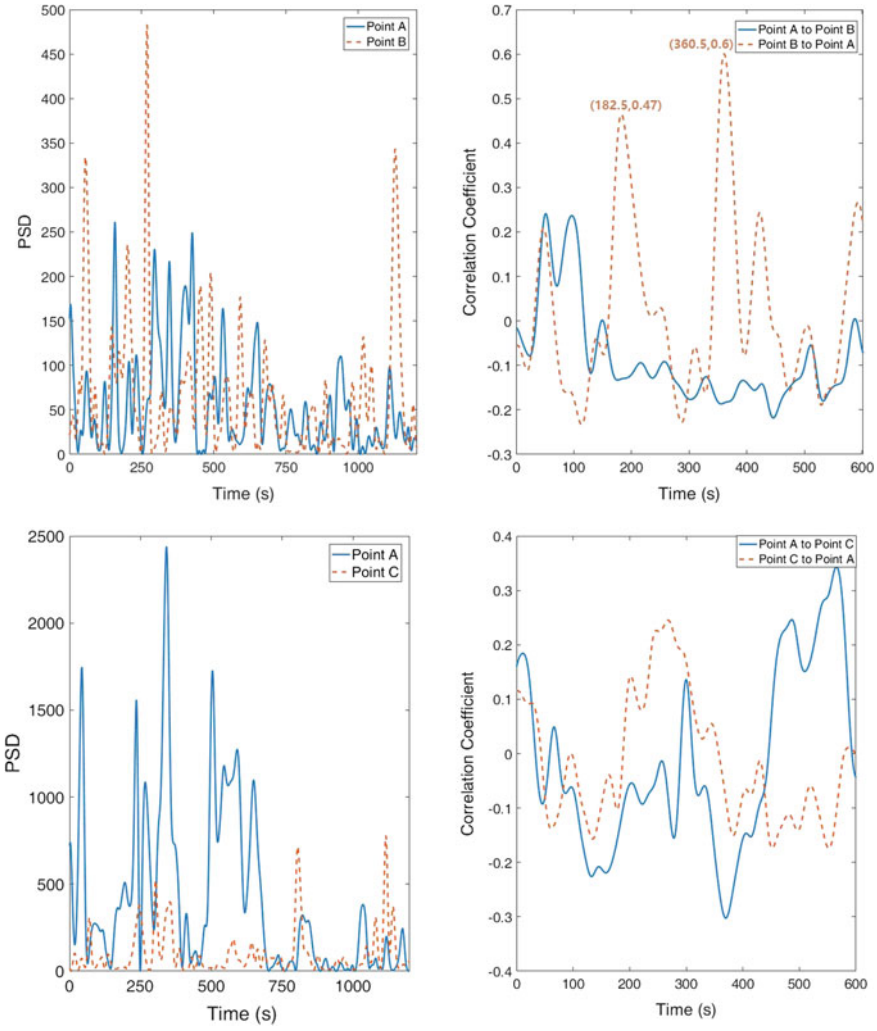

Fig. 4 Extracted PSD from wavelet analysis and phase lag

3.2 *Extracting Characteristic from Wavelet and Correlation Analysis*

Since the PSD at 0.1 Hz in wavelet follows a periodic pattern, if the myogenic vasomotions at acupoints are correlated to each other, the wavelet PSD variations with time should be correlated as well. We extracted the PSD signal at 0.1 Hz from wavelet analyses in Fig. 3, and carried out cross-correlation analysis between these two extracted time series. The PSDs of both acupoints A and B are comparable (Fig. 4), but the PSD of acupoint A is much higher than that of non-acupoint C (Fig. 4). From point A to point B, there is no significant correlation identified; from point B to point A, the maximum correlation can be 0.6 with a phase lag 0.93 π (Fig. 4). Thus, it could be stated that the myogenic factor transmitted from point B to point A. For point A and point C, there is no significant correlation found, indicating the myogenic components in acupoint and non-acupoint are not correlated. Therefore, of the correlation of myogenic related vasomotion only existed between acupoints A and B.

4 Conclusions

The LDF measurement was carried out at acupoint and non-acupoint simultaneously, the spectrum and correlation analyses lead to following conclusion: The myogenic component of vasomotion is dominant in term of PSD; The PSD of myogenic component is much higher in acupoint than that in non-acupoint; There exist correlation of myogenic components between acupoints, but there is no correlation between acupoint and non-acupoint.

Acknowledgements Supports given by HKRGC PolyU 5202/13E and PolyU G-YBG9 are gratefully acknowledged.

Reference

1. Rossi M, Carpi A, Di Maria C et al (2006) Spectral analysis of laser Doppler skin blood flow oscillations in human essential arterial hypertension. Microvasc Res 72(1–2):34–41

Influence of Axial-Flow Turbulence Intensity on Fluid-Structure Interaction for a Flexible Cylinder

C. W. Wong, Z. Y. Lu, X. Zhang and Y. Zhou

Abstract This work aims to investigate experimentally the fluid-structure interaction FSI for a flexible cylinder subjected to axial turbulent flows. Two configurations are considered; a solitary flexible cylinder with simple support ends and is free to vibrate in the transverse direction, another configuration is a non-flexible cylinder which installed parallel and adjacent to the flexible cylinder in various cylinder centre-to-centre pitch P^* (=P/D, where D is the diameter of the flexible cylinder). Investigation on the effect of axial-flow turbulence intensity T_u at 0.7 and 2.9% on the FSI for the two configurations over a range of freestream velocity U_∞ (0.19–2.14 m/s) is performed by means of simultaneous measurement of flexible cylinder vibration and velocity field adjacent to the cylinder. We found that T_u has a strong effect on the flexible cylinder vibration in both configurations. At high $_\infty$ and T_u, we observed substantial interaction of flow structures between cylinders which provokes the buckling of the flexible cylinder at a lower critical velocity compared with its counterpart of a solitary cylinder.

Keywords Fluid-structure interaction · Flexible cylinder · Axial flow

1 Introduction

Flow-induced vibration of cylindrical structures subjected to axial turbulent flows is an important research direction that attracts great attention in the field of nuclear engineering. Fuel elements in a nuclear reactor are subject to the loading of high momentum and axial-flowing coolant, and therefore causing vigorous vibration. Past investigations, e.g., [1, 2], have improved tremendously our understanding of axial flow-induced vibration on a solitary cylinder with simple support ends. Other studies, e.g., [3, 4], hitherto have looked into the flow structures within the rod

C. W. Wong (✉) · Z. Y. Lu · X. Zhang · Y. Zhou
Institute of Turbulence-Noise-Vibration Interactions and Control,
Shenzhen Graduate School, Harbin Institute of Technology, Shenzhen, China
e-mail: cwwong@hit.edu.cn

Y. Zhou et al. (eds.), *Fluid-Structure-Sound Interactions and Control*, Lecture Notes in Mechanical Engineering,
https://doi.org/10.1007/978-981-10-7542-1_43

cluster through measurements of pointwise velocity or velocity field between cylinders. However, these measurements do not provide any information on rod vibration to the turbulent flows, hence limiting our understanding of fluid structure interaction (FSI). To this end, we perform state-of-the art simultaneous measurement of structural vibration and velocity field between cylinders to elucidate the FSI of the cylinders in axial turbulent flows.

2 Experimental Details

Experiments were performed in a vertical water tunnel with a test section of $L \times W \times H = 0.3 \times 0.3 \times 2.0$ m. Figure 1a shows a schematic of the experimental apparatus. The turbulence intensity T_u was approximately 0.7% for the freestream velocity $U_\infty = 0.05$–2.14 m/s. A suspended metallic mesh grid (so called turbulence grid) with the mesh size M of 36.0 mm was installed in the settling section to generate homogeneous turbulence flow field that had a T_u of 2.9%. The solidity of the turbulence grid is 0.38 to avoid the grid-generated jet flows merge together immediately downstream of the grid.

A custom-made flexible circular cylinder made out of silicone rubber and had a length L and outer diameter D of 605.0 and 14.0 mm, respectively, was suspended vertically at $x/M = 20$ (where x denotes the streamwise direction and is originated from the centre of the turbulence grid) using airfoil-shaped supporting structures. The elastic modulus E of the flexible cylinder was 2.78 MPa, therefore, resulting a maximum non-dimensional velocity $u^*(=U\infty L\sqrt{(\rho A/EI)})$, where ρ, A and I are the fluid density, the cross-sectional area of the flexible cylinder and the corresponding second moment of inertia, respectively), of about 6.92. Note that a hollowed circular cylinder (hereafter called rigid cylinder) made out of Fluoro-Ethylene Polymer and had an L and D of 605.0 and 14.4 mm, respectively, was installed parallel and adjacent to the flexible cylinder. A computer-controlled simultaneous measurement of the vibration of the flexible cylinder and the flow field between cylinders were performed based on the laser Doppler vibrometer (LDV) and the particle image velocimetry (PIV) techniques. (Fig. 1b, c). Measurement of the root-mean-square vibration amplitude A_{rms}, the dominant

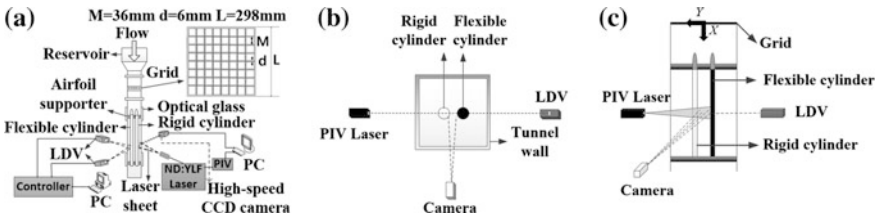

Fig. 1 **a** Overall experimental configuration; **b** synchronized PIV-LDV measurements (top view); **c** side view

frequency ω (=2πf, where f denotes the dominant frequency of vibration), and the flow field around the solitary cylinder was performed. Note that vibration was measured at the mid span of the flexible cylinder. For the twin cylinder configuration, A_{rms}, turbulence kinetic energy in the axial and lateral directions, and the flow field between the cylinders were investigated with different P/D ratios ranging from 1.21 to 1.85. Here, the cylinder pitch P is defined by the spacing between the centres of the two cylinders.

3 Results and Discussions

Figure 2a shows the dependence of the A_{rms}/D on u^* for a solitary flexible cylinder under different T_u. At $T_u = 2.9\%$, the A_{rms}/D in both y- and z-directions is largely increased compared to their counterparts at $T_u = 0.7\%$, due to the turbulence-induced pressure fluctuations around the cylinder that leads to strong deflection in the transverse directions. In general, flow-induced vibration of the solitary cylinder is enhanced at large u^*, however the turbulent flow dominates the response of the flexible cylinder. At $u^* = 5.23$, there is more vorticity along the mid span of the cylinder at $T_u = 2.9\%$ compared with its counterpart at $T_u = 0.7\%$ (Fig. 2b). It can be inferred from Fig. 2b that the small-scale turbulence within the boundary layer around the cylinder produces random, but large pressure fluctuation at $T_u = 2.9\%$, leading to significant influence on the cylinder dynamic response. The ω of the solitary flexible cylinder decreases with increasing u^* (Fig. 2c), and the estimated critical u^* for buckling is larger than 6.92; somewhat similar to that estimated by [2] based on their non-linear model. In practice the solitary flexible cylinder does not buckle at $u^* = 6.92$ based on our observations in the experiments, which is fully consistent with the aforesaid critical u^* for buckling (>6.92). The increased T_u from 0.7 to 2.9% does not produce any significant influence on ω, which suggests that the randomly distributed vorticity is resulted mainly from the near-wall turbulence. In other words, the cylinder vibration cannot change the flow field significantly at $T_u = 2.9\%$.

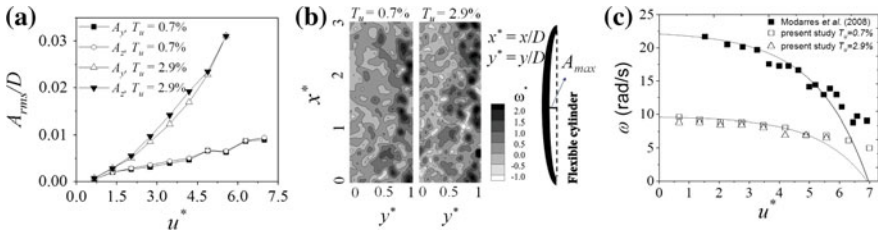

Fig. 2 **a** Dependence of the A_{rms}/D on u^* (solitary flexible cylinder); **b** instantaneous vorticity field w^* around a solitary flexible cylinder ($u^* = 5.23$); **c** dependence of the ω of solitary flexible cylinder on u^*. (The z-axis is perpendicular to both x and y axes)

Figure 3a shows the dependence of A_{rms}/D on u^* for a twin cylinder configuration. At $T_u = 0.7\%$, the A_{rms}/D increases linearly up to a certain u^* for all three cases with different P/D ratios. In general, the presence of the rigid cylinder would influence the flow field along the flexible cylinder, in turn the modified flow field influences the vibration of the flexible cylinder. At $T_u = 0.7\%$, three major observations can be made from Fig. 3a. Firstly, the small P/D ratio (i.e., 1.21) leads to more vigorous interactions of flow structures between cylinders, therefore resulting a larger A_{rms}/D compared with that at larger P/D ratio. Secondly, the gradient change of the A_{rms}/D indicates the onset of buckling of the flexible cylinder. For instance, the buckling should occur at $u^* \approx 5.25$ for the case with P/D ratio of 1.21. It is noteworthy that the critical u^* for buckling decreases with decreasing P/D ratio due to more vigorous interactions of flow structures between cylinders. Thirdly, the flexible cylinder within the twin-cylinder configuration buckles at a lower critical velocity compared with its counterpart of a solitary cylinder. At $T_u = 2.9\%$, A_{rms}/D increases largely at $u^* \geq 2.76$. It can be seen in Fig. 3b, where $P/D = 1.36$, $T_u = 2.9\%$, $u^* = 5.23$, that the vortical structures (region A) which initially ($t = 0$) occur near the flexible cylinder wall interact with the ones from the rigid cylinder ($t = 5$–20 ms), forming larger vortical structures ($t = 25$ ms) that move back to the wall of the flexible cylinder ($t = 30$ ms). Alternatively, some vortical structures (region B) that originate from the wall of the flexible cylinder ($t = 0$) diminish ($t = 25$ ms) due to the interaction of vortices between the cylinders.

Figure 4a shows the dependence of P/D on the k_x ($=0.5\langle u'u' \rangle$, where u' is the streamwise fluctuating velocity). In general, the k_x is the smallest at the mid point between two cylinders, and k_x increases toward the cylinder wall. It can be interpreted that the velocity fluctuations in axial direction, which is probably caused by friction, become strong near the cylinder wall. On the other hand, the k_x near the cylinder wall increases with decreasing P/D (Fig. 4a), while the k_y ($=0.5\langle v'v' \rangle$, where v' is the lateral fluctuating velocity) near the cylinder wall decreases with decreasing P/D (Fig. 4b). In general, the fluid-structure interaction becomes strong

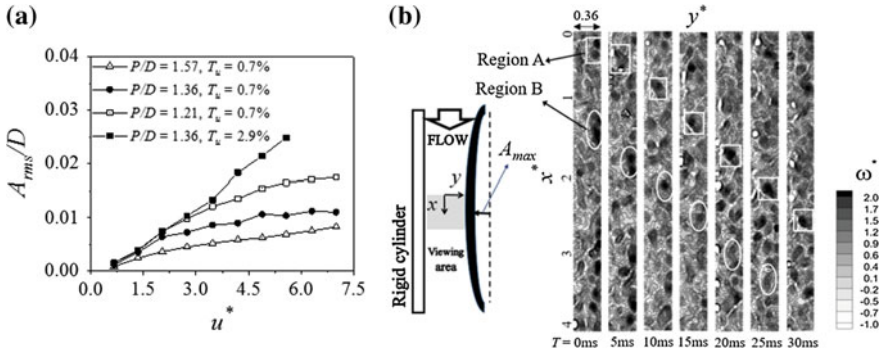

Fig. 3 **a** Dependence of A_{rms} on u^* ($P/D = 1.21$, 1.36, 1.57); **b** instantaneous vorticity field w^* between the cylinders ($P/D = 1.36$, $T_u = 2.9\%$, $u^* = 5.23$)

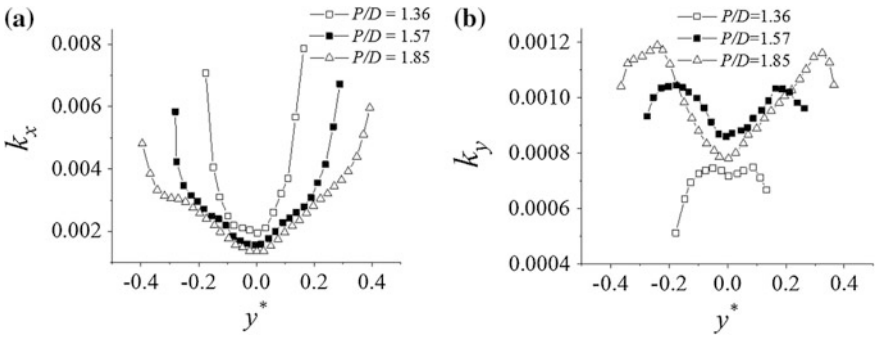

Fig. 4 Dependence of *P*/*D* on the turbulence kinetic energy k at A_{max} position; **a** k_x and **b** k_y (T_u = 0.7%, u^* = 5.23, subscript x and y denote the streamwise and lateral direction, respectively)

with decreasing *P*/*D*. The strong vorticity from the walls of the two cylinders interact about the mid point between two cylinders (e.g., Fig. 3b), and some vortical structures may retreat from the gap and bounce back to the wall of the flexible cylinder. When it happens, the k_y in vortical structures rises toward the wall. As the vortical structures get closer to the wall, k_y in vortical structures may dissipate through changing from large-scale to small-scale turbulence, resulting the reduction of k_y near the wall of the flexible cylinder.

4 Conclusions

(1) For a solitary flexible cylinder, at T_u = 2.9%, the A_{rms}/D in both y- and z-directions is largely increased compared to their counterparts at T_u = 0.7%. The high T_u leads to significant influence on the cylinder dynamic response, however, the critical velocity for buckling of cylinder does not depend on the T_u.

(2) For the twin cylinder configuration at different *P*/*D* ratios, the A_{rms}/D increases linearly up to a certain u^*. The small *P*/*D* leads to more vigorous interactions of flow structures between cylinders, therefore resulting a larger A_{rms}/D. Small *P*/*D* ratio leads to the small critical u^* for buckling. Yet, the flexible cylinder within the twin-cylinder configuration buckles at a lower critical velocity compared with its counterpart of a solitary cylinder. At high T_u, the A_{rms}/D increases largely at $u^* \geq 2.76$. We observe strong interactions of flow structures between cylinders and some flow structures may retreat from the gap and bounce back to the wall of the flexible cylinder, causing vigorous lateral vibration.

Acknowledgements C. W. Wong wishes to acknowledge support by the National Natural Science Foundation of China through grant 11502060 and from the Research Grants Council of the Shenzhen Government through grants JCYJ20160531193045101 and JCYJ20150513151706565.

References

1. Païdoussis MP (2006) Real life experiences with flow-induced vibration. J Fluids Struct 22:741–745
2. Modarres-Sadeghi Y, Païdoussis MP, Selmer C, Grinevich E (2008) Experiments on vertical slender flexible cylinders clamped at both ends and subjected to axial flow. Phil Trans R Soc A 366:1275–1296
3. Domingguez-Ontiveros EE, Hassan YA (2009) Non-intrusive experimental investigation of flow behaviour inside a 5 × 5 rod bundle with spacer grids using PIV and MIR. Nucl Eng Des 239:888–898
4. Caraghiaur D, Anglart H, Frid W (2009) Experimental investigation of turbulent flow through spacer grids in fuel rod bundles. Nucl Eng Des 239:2013–2021

Non-linear Spring-Mounted Flexible Plates in Axial Flow

R. M. Howell and A. D. Lucey

Abstract In this paper we model the fluid-structure interaction of non-linear flutter of a cantilever mounted upon a non-linear spring at the clamp in a uniform axial flow. This permits us to compare results with those from a *hybrid* non-linear system (a linear system mounted on a non-linear spring) and so to assess the change in fundamental physical phenomena owing to the introduction of full non-linear structural- and fluid-mechanics. We use numerical simulation for the non-linear system while our state-space solution of the corresponding linear system is used to guide the choice of parameters in the investigation. We show that above the flow speed of flutter-onset for small disturbances, amplitude growth leads to non-linear saturation so that the system settles into finite-amplitude oscillations. The frequencies of these oscillations evidence the dual-frequency characteristics of mount oscillation observed in physical experiments. When the natural frequency of the mount is low, we show that for a range of increases above the linear critical speed the linear hybrid and non-linear systems evidence the same frequency phenomena. However, the linear hybrid system evidences larger oscillation amplitudes than the non-linear system. Therefore, the stabilising effect of the non-linear structural terms outweighs the destabilising effect of the non-linear fluid terms.

1 Introduction

We model the fluid-structure interaction (FSI) of non-linear flutter of a cantilever of length L mounted upon a non-linear spring at the clamp in a uniform axial flow of speed U_∞. This system is depicted in Fig. 1. The fluid pressure is modelled using a non-linear potential flow method in the absence of a wake. This extends our linear study [1] that presented the stability space in the absence of damping and charted how the dynamics and the critical flutter velocity U_c at a mass ratio of $\bar{L} = 1$ depend

R. M. Howell (✉) · A. D. Lucey
Department of Mechanical Engineering, Fluid Dynamics Research Group, Curtin University of Technology, GPO Box U1987, Perth, WA 6845, Australia
e-mail: richard.howell@curtin.edu.au

Y. Zhou et al. (eds.), *Fluid-Structure-Sound Interactions and Control*, Lecture Notes in Mechanical Engineering,
https://doi.org/10.1007/978-981-10-7542-1_44

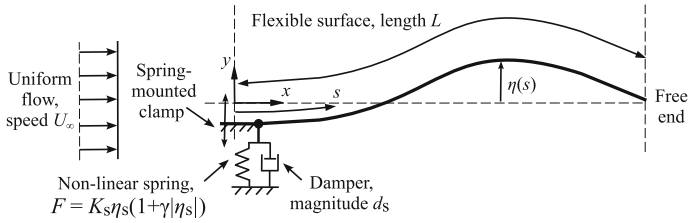

Fig. 1 The fluid-structure systems under consideration

upon the variation in natural frequency of the support of the spring-mass system ω_s. The non-linear spring stiffness is $K_s^* = K_s(1 + \gamma|\eta_s|)$ where γ is a constant that determines the magnitude of the non-linear stiffness contribution, as detailed in [2]. If simple dashpot damping d_s were to be included at the mount, the energy harvesting capabilities from the flutter instability could be measured and the fluid-structure system would then be classified as a type of *flutter mill*, for example see [3].

2 Method

The non-linear Euler-Bernoulli beam equation is presented in [3]. The modified version for the system illustrated in Fig. 1 is

$$\begin{aligned} -\delta p \; = \rho h \frac{\partial^2 \eta}{\partial^2 t} - \rho h \frac{\partial \eta}{\partial s} \int_0^s \left(\left(\frac{\partial^2 \eta}{\partial t \partial s} \right)^2 + \frac{\partial \eta}{\partial s} \frac{\partial^3 \eta}{\partial t^2 \partial s} \right) \mathrm{d}s \\ - \rho h \frac{\partial^2 \eta}{\partial s^2} \int_s^L \int_0^s \left(\left(\frac{\partial^2 \eta}{\partial t \partial s} \right)^2 + \frac{\partial \eta}{\partial s} \frac{\partial^3 \eta}{\partial t^2 \partial s} \right) \mathrm{d}s\mathrm{d}s \\ + B \left[\frac{\partial^4 \eta}{\partial s^4} + \frac{\partial^4 \eta}{\partial s^4} \left(\frac{\partial \eta}{\partial s} \right)^2 + 4 \frac{\partial \eta}{\partial s} \frac{\partial^2 \eta}{\partial s^2} \frac{\partial^3 \eta}{\partial s^3} + \left(\frac{\partial^2 \eta}{\partial s^2} \right)^3 \right] + d_s \frac{\partial \eta_s}{\partial t} + K_s^* \eta_s. \end{aligned} \tag{1}$$

B, ρ and h are respectively the flexural rigidity, material density and thickness of the plate. The plate is discretised into N mass points spaced $\delta s = L/N$ apart where s is the ordinate along the plate. This derivation is based upon the assumption that the plate is inextensible *i.e.* L does not vary and therefore δs is constant. At the downstream end of the plate, conditions of zero bending moment and shear are applied. To enforce a spring-mounted clamp at the upstream end of the plate, the leading edge of the plate must follow the heaving motion of the actuating force from the clamp. These constraints are applied through a *shear-force balance*, as detailed in [1], which couples the plate dynamics to the motion of the spring-mount. This also permits the plate to drive the motion of the mount. A final condition of zero gradient at the leading edge of the plate completes the imposition of the spring-mounted clamp. Finally,

Table 1 Mount oscillation frequencies for increasing $\bar{U}$ with $\bar{\omega}_s = \bar{L} = 1$ and $\bar{\gamma} = 1 \times 10^4$

	Linear			Non-linear		
Δ	$\bar{\omega}_L$	$\bar{\omega}_U$	I_U	$\bar{\omega}_L$	$\bar{\omega}_U$	I_U
0.6	11.1	33.4	0.18	10.6	32.1	0.15
0.8	11.3	34.1	0.20	10.9	32.6	0.17

the last two terms on the right-hand side of Eq. (1) account for damping and spring stiffness at the mount.

The fluid modelling is based on the non-linear boundary-element method detailed in [4] that modelled the non-linear FSI of flow over one side of a flexible, simply supported plate. The plate is discretised into N panels each of length δs, the centre of which coincide with the mass points described above. The non-linear vortex strengths for each panel are found through the no-flux condition, $\{\gamma\} = [I^N]^{-1}\{U_\infty \sin\theta + \dot{\eta}\cos\theta - \dot{\xi}\sin\theta\}$, where θ is the angle of each panel on the plate with respect to the horizontal and $\dot{\xi}$ and $\dot{\eta}$ are the velocities of each panel in the x- and y-directions respectively. This equation is used to solve for the flow field. This is then inserted into the unsteady Bernoulli equation to determine the transmural pressure difference across the plate of $-\delta p = \delta p' + \rho_f[\mathbf{B}_2]\ddot{\eta}\cos\theta$, where $\delta p'$ summarises 10 pressure terms that do not depend on $\ddot{\eta}$, $[\mathbf{B}_2]$ is a matrix that contains the influences of the panels on each other and ρ_f is the density of the free-stream fluid. This pressure formulation is combined with Eq. (1) to generate an equation for the full fluid-structure system in terms of $\ddot{\eta}$ that is solved using a time-stepping, semi-implicit method of solution; this type of initial-value solution is fully detailed in [4].

3 Results

Following [2], results are non-dimensionalised using reference length and time scales $L_r = \rho h/\rho_f$ and $t_r = (\rho h)^{\frac{5}{2}}/(\rho_f^2 B^{\frac{1}{2}})$ respectively. In [2], values of oscillation frequency $\bar{\omega} = \omega t_r$ were obtained of the mount- and tip-oscillation displacement in the absence of damping for the FSI of the hybrid system. These are presented on the left-hand side in the first row of Table 1 for $\Delta = 0.6$ above the linear flutter-onset flow speed U_c (*i.e.* $U_\infty = U_c(1 + \Delta)$) with $\bar{L} = L/L_r = 1$ and $\bar{\omega}_s = \omega_s t_r = 1$. The value $\bar{\gamma} = \gamma L_r$ is set to an illustrative value of 1×10^4. These results show that there are two different frequencies present in the time series of the mount oscillation. The term I_U is the intensity of the higher frequency divided by the intensity of the lower frequency. It can therefore be seen that the lower frequency, associated with single-mode flutter, dominates the oscillation. Its frequency is close to that for the corresponding fixed cantilever at 15.3. The higher frequency is close to the third mode *in vacuo* of the spring mounted cantilever. The equivalent $\Delta = 0.6$ results for

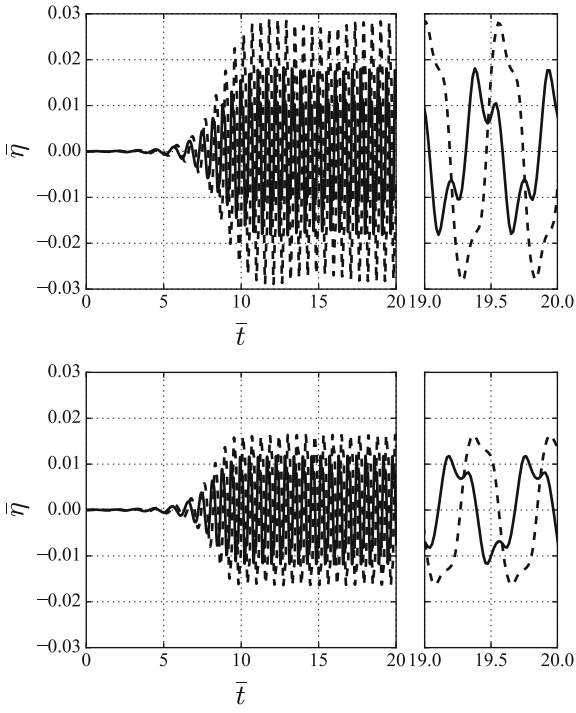

Fig. 2 Displacement in time for $\Delta = 0.8$ with $\bar{\omega}_s = \bar{L} = 1$ and $\bar{\gamma} = 1 \times 10^4$:—Mount, - - Tip. Plate and fluid mechanics: Top - linear, Bottom - non-linear. Small windows show traces from $\bar{t} = 19$ to 20

the non-linear cantilever are shown on the right-hand side in the first row of Table 1: little difference is seen as amplitudes are of a magnitude for which linear mechanics still hold. As shown in the second row of Table 1, similar frequency phenomena are found at $\Delta = 0.8$.

However, there is a difference in displacements. In Fig. 2 we plot $\bar{\eta} = \eta / L_r$ against $\bar{t} = t/t_r$ for the cantilever mount and tip displacements for $\Delta = 0.8$. The similarity of the frequency properties between the bybrid and non-linear models are shown by the mount–and tip-traces in the windows from $\bar{t} = 19$ to 20 on the right-hand side of Fig. 2. The left-hand side figures show that although both systems saturate by $\bar{t} = 10$ for a similar rate of amplitude increase, clearly the final amplitude magnitudes differ, the non-linear system amplitude smaller by a third. Therefore, the stabilising effect of the non-linear structural terms outweighs the destabilising effect of the non-linear fluid terms *i.e.* as displacement increases, the non-linear plate mechanics increase their stiffness non-linearly whereas the fluid forces continue to increase nearly linearly.

Mount and tip amplitudes for a range of Δ are shown in Fig. 3. In both cases, with increasing Δ tip displacement grows at a larger rate than mount displacement. For the non-linear case, the hysteresis loop has reduced in size, now only extending to $\Delta = -0.1$ whereas the linear loop extends to $\Delta = -0.2$.

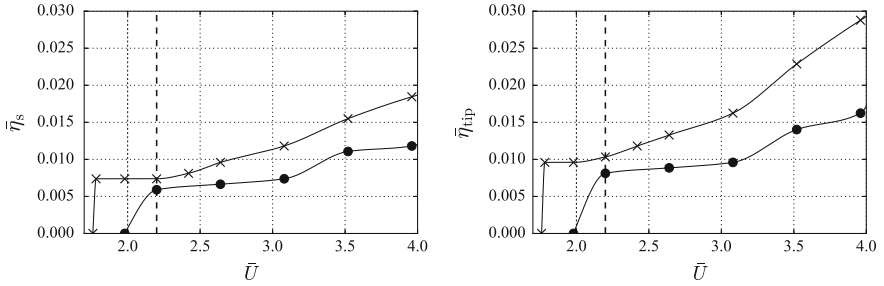

Fig. 3 Maximum displacement for increasing $\bar{U}$ with $\bar{L} = 1$, $\bar{\gamma} = 1 \times 10^4$ and $\bar{\omega}_s = 1$: The vertical dashed lines denote U_c for the linear case. Plate and fluid mechanics: × linear, • non-linear. Left: mount, Right: tip

4 Conclusions

We have presented a model for predicting the two-dimensional stability characteristics of non-linear, spring-mounted cantilevered plates in a uniform flow. The dynamics of the system have been investigated for cases that, for a rigid mounting, would succumb to single-mode flutter at instability onset. In the hybrid system, a non-linear spring at the mount permits dual frequency mount oscillation and saturation of this oscillation with increasing amplitude for increasing flow speed above the linear U_c. The value of the main, low frequency, component of the response lies between the natural frequency of the mount $\bar{\omega}_s$ and the frequency at flutter onset of a fixed cantilever; the higher frequency is close to the third mode *in vacuo* of the spring mounted cantilever.

When the natural frequency of the mount is low, we show that above the linear critical speed the linear hybrid and non-linear systems evidence the same frequency phenomena; however, the mount and tip displacement of the non-linear model is much smaller as the stabilising effect of the non-linear structural terms outweighs the destabilising effect of the non-linear fluid terms. This effect leads to a reduction in the size of the hysteresis loop.

Immediate future work will investigate a range of mount natural frequencies. The inclusion of the effect of the substantial wake that must form at the flow separation point will then be quantified through the inclusion of a discrete-vortex model, similar to the method described in [5]. It is finally noted that the non-linear model will be able to continue to grow to much larger amplitudes at higher values of Δ which augurs well for energy harvesting applications.

References

1. Howell RM, Lucey AD (2015) Flutter of spring-mounted flexible plates in uniform flow. J Fluids Struct 59:370–393

2. Howell RM, Lucey AD (2016) Flutter of a nonlinear-spring-mounted flexible plate for applications in energy harvesting. In: 20th Australasian fluid mechanics conference, Dec 5–8, Perth, Australia
3. Tang L, Paidoussis MP, Jiang J (2009) Cantilevered flexible plates in axial flow: Energy transfer and the concept of flutter mill. J Sound Vib 326:529–542
4. Lucey AD, Cafolla GJ, Carpenter PW, Yang M (1997) The nonlinear hydroelastic behaviour of flexible walls. J Fluids Struct 11:717–744
5. Howell RM, Lucey AD, Carpenter PW, Pitman MW (2009) Interaction between a cantilevered-free flexible plate and ideal flow. J Fluids Struct 25:544–566

Turbulence Intensity Effect on Axial-Flow-Induced Cylinder Vibration

Z. Y. Lu, Y. Zhou and C. W. Wong

Abstract A numerical study is conducted on the effect of inlet turbulent intensity on the axial-flow-induced vibration of an elastic cylinder subjected to axial tubular flow. The cylinder with fix-supported ends is free to vibrate in the lateral direction. While a large eddy simulation is used to calculate the turbulent flow field, the Ansys mechanical + Fluent two-way coupling has been deployed to capture the fluid-structure interaction. The calculation agrees qualitatively with experimental data. Various inlet turbulence intensities, T_u, i.e., 0, 0.3, 5.0 and 10.0%, are examined at two non-dimensional flow velocities, $\overline{U}$, i.e., 3.30 and 7.62. The results show that T_u has a significant effect on the cylinder vibration. At $\overline{U} = 3.30$, the maximum displacement grows with T_u and the vibration is classified as the sub-critical vibration; the instability of cylinder is not induced with increasing T_u. At $\overline{U} = 7.62$, the buckling occurs at $T_u = 0\%$, while the flutter takes place at $T_u = 0.3\%$; both are associated with an asymmetric pressure distribution around the cylinder.

Keywords Axial-flow-induced vibration · Inlet turbulence intensity
Elastic cylinder · Fluid-structure interaction

1 Introduction

Axial-flow-induced vibration of cylindrical structures is frequently seen in engineering. One typical example is that coolant flows through fuel rods in nuclear reactors. The small amplitude vibration produced by flow velocity below the so-called critical velocities for divergence and flutter has been an interest of many

Z. Y. Lu · Y. Zhou (✉) · C. W. Wong
Institute for Turbulence-Noise-Vibration Interactions and Control,
Shenzhen Graduate School, Harbin Institute of Technology, Shenzhen, China
e-mail: yuzhou@hit.edu.cn

Z. Y. Lu
State Key Laboratory of Aerodynamics, China Aerodynamics Research
and Development Center, Mianyang, Sichuan, China

Y. Zhou et al. (eds.), *Fluid-Structure-Sound Interactions and Control*, Lecture Notes in Mechanical Engineering,
https://doi.org/10.1007/978-981-10-7542-1_45

researchers (e.g. [1]). It has been experimentally found that the structural response is sensitive to the flow entrance conditions (e.g. [2]). Furthermore, the incident flow on the clustered fuel rods is always turbulent in practice. However, the information on how the inlet turbulence intensity affects the axial-flow-induced structural vibration is very limited in the literature. This work is to investigate both numerically and experimentally an elastic cylinder subjected to an axial tubular flow with varied incident turbulent intensity T_u. The numerical data is further compared with the experimental data.

2 System Modelling

An elastic cylinder with D in diameter of 0.025 m and $20D$ in length, modelled by Euler-Bernoulli beam, is immersed in a uniform axial tubular flow. Assume an infinitely long cylinder, with no flow separation. The axial flow is confined by a cylindrical wall of the same length as the cylinder and a diameter $12D$, as shown in Fig. 1 where the coordinate system is defined. The cylinder is clamped at both ends so that the end conditions are given by $u|_{z=-10D} = \frac{\partial u}{\partial z}|_{z=-10D} = u|_{z=10D} = \frac{\partial u}{\partial z}|_{z=10D} = 0$. The cylinder may vibrate freely along the x and y directions. The flow boundary conditions at the inlet and outlet are $\nu_{inlet} = (0, 0, \nu_0)$ and $p|_{outlet} = 0$, where ν_0 is the mean axial flow velocity. The non-dimensional velocity $\overline{U}$, time τ, frequency $\bar{f}$ and displacement d_y are defined as follows;$\bar{U} = \nu_0 L\sqrt{\rho A/EI}$,$\tau = t/L^2\sqrt{\rho + \rho_c A/EI}$, $\bar{f} = fL^2\sqrt{(\rho + \rho_c)A/EI}$, $d_y = u_y(z,t)/D$.

The interactions between the axial flow and the structure are studied by solving iteratively the governing equations of both fluid and structural dynamics. The mass conservation and Navier-Stokes equations along with the structural dynamics equation are given below,

$$\nabla \cdot \vec{\nu} = 0 \tag{1}$$

$$\rho\frac{\partial \vec{\nu}}{\partial t} + \rho\left(\vec{\nu} - \vec{\hat{\nu}}\right) \cdot \nabla\vec{\nu} = -\nabla p + \mu\nabla^2\vec{\nu} \tag{2}$$

$$\mathbf{M}\ddot{\vec{u}} + \mathbf{C}\dot{\vec{u}} + \mathbf{K}\vec{u} = \vec{F}(t) \tag{3}$$

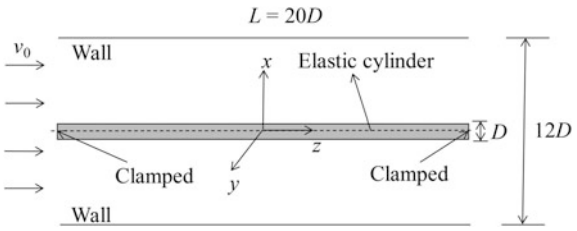

Fig. 1 Schematic model

where t, $\vec{\nu}$, p, ρ, and μ are time, fluid velocity vector, pressure, fluid density and dynamic viscosity of the fluid, respectively; the $\vec{\hat{\nu}}$ refers to the moving mesh velocity vector, and $\mathbf{M}$, $\mathbf{C}$, $\mathbf{K}$, $\vec{\ddot{u}}$, $\vec{\dot{u}}$, $\vec{u}$ and $\vec{F}(t)$ are mass matrix, damping matrix, stiffness matrix, nodal acceleration vector, nodal velocity vector, nodal displacement vector and load vector, respectively. Equations (1)–(3) are iteratively solved by Ansys mechanical + Fluent with two-way coupling [3]. The flow field and the induced forces on the cylinder are solved in each iteration by Ansys Fluent, and then the forces are transferred to Ansys Mechanical to resolving the cylinder displacements. The cylinder displacement is in turn utilized by Fluent to resolving the mesh motion for the next time step. In all cases, there are 6 coupling iterations in each of the 300 subcycles used in the two-way coupling. For turbulent flow, the large eddy simulation (LES) model is applied with Smagorinsky-Lilly for the sub-grid scale (SGS) model, where a Smagorinsky constant C_s is 0.1. The mesh is created by Ansys ICME. To avoid the severe mesh distortion and ensure the mesh quality, the fluid domain is divided into two sub-regions: the inner region where the elements are hexahedrons and the motion of mesh is almost the same as that of the cylinder, and the outer region where the elements are prisms. Grid-refinement studies are performed to ensure that the calculated results are independent of the grid size. The total elements of the mesh in fluid domain are about 688600 for all cases.

3 Results and Discussion

Several values of T_u are examined for $\overline{U} = 3.30$ and 7.62, which correspond to the Reynolds number based on the hydraulic diameter (= 0.275 m) of 5.88×10^5 and 1.36×10^6, respectively. In all cases, the cylinder is initially at its equilibrium position. In order to validate the computational code, axial-flow-induced cylinder vibration measurements were conducted in a vertical water tunnel. Experiments are conducted for the same model and flow conditions to validate our simulations. The test cylinder is made of silicone rubber, as used by Paidoussis [1] and is fixed vertically with both ends attached to symmetric-airfoil-shaped supporting structures [4]. The experimentally measured root-mean-square (rms) non-dimensional displacement, d_{xrms}, by the Laser Doppler Vibrometer (LDV) at the mid span of the test cylinder agrees well with the calculated results at $T_u = 0.3\%$ (Fig. 2).

The d_y at the mid span of cylinder exhibits a considerable dependence on T_u at $\overline{U} = 3.30$ and $\overline{U} = 7.62$ (Fig. 3). At $\overline{U} = 3.30$ and $T_u = 0\%$, d_y is rather small (Fig. 3a), somewhat in an order of 10^{-4}. The maximum d_y grows to about 0.03 and 0.09 at $T_u = 5\%$ and 10%, respectively. Based on the magnitude of d_y ($10^{-3} - 10^{-2}D$), the vibrations under various T_u are considered to be subcritical vibration. Apparently, the maximum d_y increases with increasing T_u. It has been captured by our sequential high-speed PIV images from the parallel experimental investigation that vorticity concentrations may separate from the boundary layer around the cylinder as T_u reaches 2.9%, which may have contributed to the enhanced vibration of cylinder. At $\overline{U} = 7.62$ (Fig. 3b), the cylinder response differently as compared to

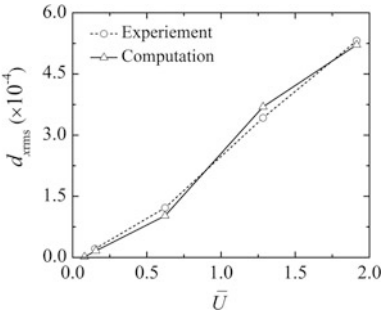

Fig. 2 Comparison of d_{xrms} between computational and experimental measurements ($T_u = 0.3\%$)

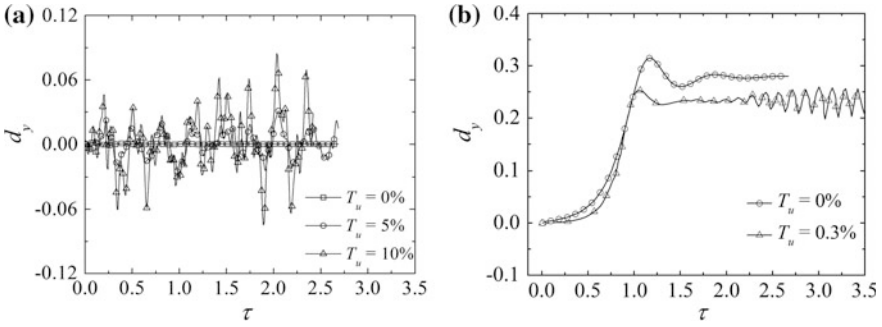

Fig. 3 Time history of d_y at mid-span of cylinder at different T_u. **a** $\overline{U} = 3.30$; **b** $\overline{U} = 7.62$

that at low $\overline{U}$. The d_y increases rapidly at the beginning and eventually reaches a non-zero equilibration vibration state, irrespective of T_u, indicating the occurrence of the buckling instability. The maximum d_y is about 0.3. Given $T_u = 0.3\%$, the buckled cylinder oscillates with an amplitude of about $0.05D$ around its new equilibrium position after $\tau = 2.2$, showing the sign of the flutter instability.

Figure 4 shows the effect of T_u on the d_{xrms} and d_{yrms} along the cylinder span at $\overline{U} = 3.3$ and 7.62. At $T_u = 0\%$, both d_{xrms} and d_{yrms} are very small, about $0.001D$ (Fig. 4a). In addition, at $T_u \geq 5\%$ and $\overline{U} = 3.3$, there exist the second and first modes of subcritical vibration along the x and y directions, respectively. Note that the predominant vibration frequency $\bar{f}$ is a constant (= 3.01), irrespective of T_u, due to the fact that the subcritical vibration has insignificant influence on the flow field. At $\overline{U} = 7.62$, the buckling shape of the cylinder appears to be the first mode of vibration at $T_u = 0\%$, along with the maximum d_{xrms} of about $0.12D$, but changes to the second mode of vibration with the M-shape distribution along the span at $T_u = 0.3\%$ (Fig. 4b). Note that d_{xrms} and d_{yrms} deviate greatly from each other at $\overline{U} = 7.62$, showing the sign of the instabilities of cylinder.

Figure 5 shows instantaneous pressure coefficient (C_p) and vorticity (ω_z^*) contour at the mid span of the buckled cylinder at $\overline{U} = 7.62$ and $T_u = 0\%$. The high and low

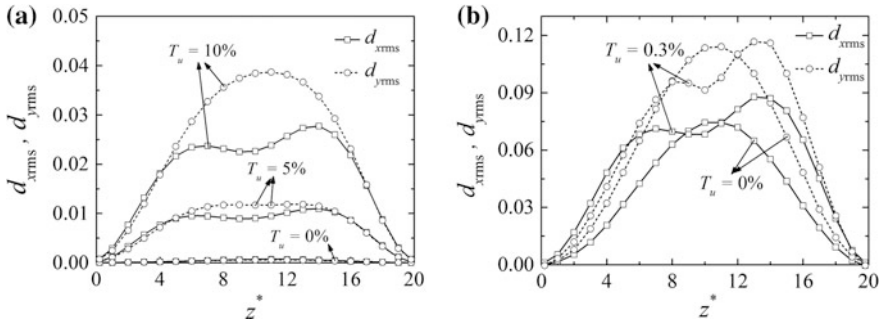

Fig. 4 Root-mean-square non-dimensional displacement. **a** $\overline{U} = 3.30$; **b** $\overline{U} = 7.62$

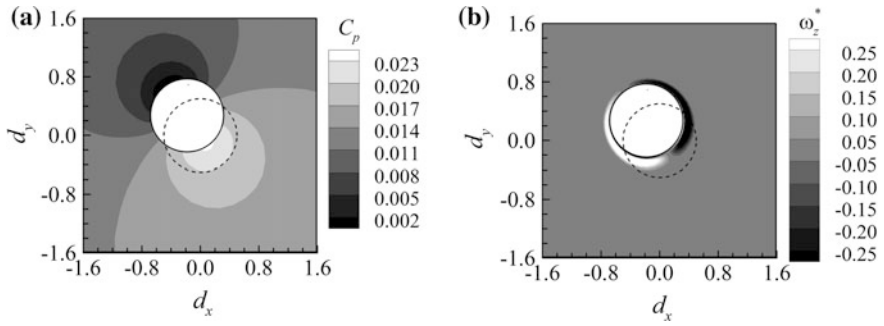

Fig. 5 Instantaneous **a** C_p and **b** vorticity contour at mid span of buckled cylinder. The dotted circle denotes the original position of the cylinder. ($\overline{U} = 7.62$, $T_u = 0\%$)

pressure regions are found at the inner and outer bend of the buckled cylinder, respectively (Fig. 5a). The maximum C_p may reach about 0.023 at the inner bend of the buckled cylinder. The pressure around the cylinder gives rise to the resultant force on the cylinder which causes cylinder deformation. It is noteworthy that the pressure distribution around the cylinder is not symmetrical along the axis perpendicular to the bending direction. This finding is reasonable. As fluid flows from the outer bend to the inner bend caused by the deformation of cylinder, the shear layers around the cylinder (as inferred from the axial vorticity contours, Fig. 5b) are thickened when approaching to the inner bend, thus resulting in the high-pressure region at the inner bend of the cylinder (Fig. 5a).

4 Conclusions

The effect of the inlet turbulent intensity on the axial-flow-induced vibration of an elastic cylinder is investigated numerically. Calculation has been validated through experiments in a water tunnel. This work leads to following conclusions.

1. At $\overline{U} = 3.3$, the cylinder vibration is subcritical, regardless of the level of T_u. Nevertheless, the maximum d_y of cylinder grows with increasing T_u.
2. At $\overline{U} = 7.62$, the d_y grows rapidly at the beginning and eventually reaches a non-zero equilibration vibration state, irrespective of T_u, indicating the occurrence of the buckling instability. At $T_u = 0.3\%$, the cylinder undergoes buckling with negligible vibration amplitude of about $0.003D$, followed by the flutter instability with a sharp increased vibration amplitude about $0.05D$. The buckling and flutter instabilities take place as a result of the asymmetric pressure distribution along the axis perpendicular to the bending direction.

Acknowledgements The financial support from Shenzhen Government through grants JCYJ20150625142543469 and JCYJ20150513151706565 is gratefully acknowledged.

References

1. Paidoussis MP (2004) Fluid-structure interactions: slender structures and axial flow, vol 2. Academic Press, Netherlands
2. Swinson WF, Battiste RL, Luttrell CR, Yahr GT (1993) Follow-up fuel plate stability experiments and analyses for the advanced neutron source. United States Department of Energy. Oak Ridge National Laboratory, Oak Ridge Tennessee. Technical Report No. ORNL/TM–12629
3. Ansys Workbench 15.0 Document (2015) Ansys Inc
4. Païdoussis MP (1966) Dynamics of flexible slender cylinders in axial flow Part 2. Experiments. J Fluid Mech 26:737–751

Experimental Investigation of Flat Plates with Transverse Perforations at Zero Incidence

P. Oshkai, F. Bossi, M. Rahimpour, O. Barannyk and S. Malavasi

Abstract Particle Image Velocimetry (PIV) and direct force measurements are used to investigate the effect of transverse perforations on the flow-induced loading on and the associated flow structure around flat plates that are aligned with the oncoming flow. Plates with different characteristic diameter of the perforations, as well as a reference configuration without perforations are compared in terms of the spectra of the flow-induced forces, frequencies of the trailing edge vortex shedding and boundary layer profiles at the trailing edge at different planes across the perforation patterns for a range of inflow velocities. At high inflow velocities, boundary layer thickness increased as the diameter of the perforations increased and the distance from the perforation to the trailing edge of the plate decreased.

Keywords Perforated plate · Flow-induced loading · Flow-induced vibration PIV

1 Introduction

Rectangular plates aligned with the incoming fluid flow and the associated flow field, flow-induced loading, noise and vibrations have been subjects of a number of studies over the years, which examined the effects of the Reynolds number [6], chord-to-thickness ratio of the plate [5], array configurations [7] and wall confinement [4]. Effects of elasticity and porosity of the leading edge of a semi-infinite plate on radiated acoustic noise were investigated theoretically by [3], and the related experimental measurements of the fluctuating pressure due to flow over a

P. Oshkai (✉) · M. Rahimpour · O. Barannyk
Department of Mechanical Engineering, University of Victoria,
Victoria, BC V8W 2Y2, Canada
e-mail: poshkai@uvic.ca

F. Bossi · S. Malavasi
Department of Civil and Environmental Engineering, Hydraulic Section,
Politecnico di Milano, Piazza Leonardo da Vinci 32, 20133 Milano, Italy

Y. Zhou et al. (eds.), *Fluid-Structure-Sound Interactions and Control*, Lecture Notes in Mechanical Engineering,
https://doi.org/10.1007/978-981-10-7542-1_46

porous surface with flexible bristles were performed by [2]. Directly related to the present study is the investigation of the effect of transverse perforations on loading on plates of finite thickness using direct force measurements [1]. In the present investigation, we employed PIV and direct force measurements in order to provide insight into the physical origin of the flow-induced loading on and the vibrations of the perforated plates.

2 Experimental System and Techniques

The experiments were conducted in a flow visualization water channel with a test section with square cross-section of 45 cm × 45 cm and a length of 250 cm. The flat plates were positioned parallel to the flow. The plates were cantilevered at the top edge and attached to the frame of the water channel by a support structure that incorporated a load cell for direct force measurements (Fig. 1a). Three plates with transverse perforations were considered, in addition to a reference plate with no perforations. The three perforation patterns had the same staggered arrangement, but different perforation diameters $\delta_h = 9.4$, 12.7, 19.5 mm, referred to as patterns P1, P2 and P3, respectively. The spacing between the perforations was also equal to δ_h, so that the three plates had the equivalent area ratio, $(nA_p/A_t)^{0.5} = 0.4$, where n is the number of perforations, A_p is the area of a single perforation, A_t is the total wetted area of the plate. Global measurements of the flow velocity in the vicinity of the trailing edge of the plate were performed using high-speed PIV. A total of 6000 images were recorded during each data acquisition, at the sampling rate of 600 Hz and the spatial resolution of 1.05 vector/mm and 0.54 vector/mm for the solid and perforated plates, respectively. As illustrated in Fig. 1b, three PIV data acquisition planes (DAPs) were defined to characterize the three-dimensionality of the flow. For the case of the solid plate, the data acquisition was performed only in DAP3. In order to study the vortex shedding frequencies, the power spectral density (PSD) of

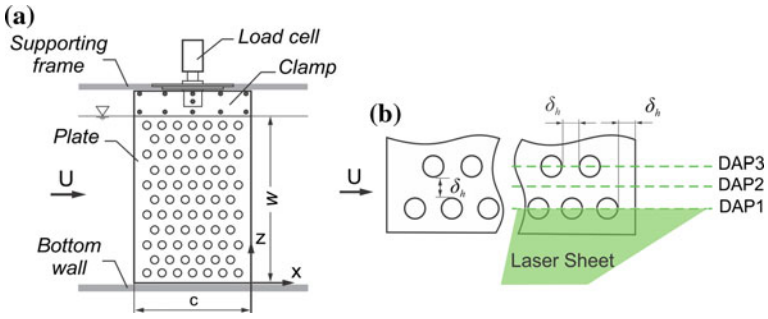

Fig. 1 Schematics of: experimental system (**a**) and the location of PIV data acquisition planes (**b**)

the time signal of the transverse velocity fluctuations (U_y) was calculated. U_y was obtained by subtracting the time-averaged transverse velocity component from that of the instantaneous velocity field.

3 Results and Discussion

3.1 Unsteady Loading

Figure 2 shows the plots of the PSD of the time signals of the unsteady flow-induced torque on the plate (Fig. 2a) as well as the transverse velocity fluctuations $U\,y$ (Fig. 2b), for the plate with the largest perforation diameter (P3). Figure 2b was obtained from the velocity field corresponding to DAP1. With the exception of the case of $U = 0.55$ m/s, the load cell peak frequencies, f_{LC}, (Fig. 2a) and the vortex shedding frequencies, f_{PIV}, (Fig. 2b) both increased linearly with the increase of the inflow velocity. Additionally, at $U = 0.37$, 0.46 and 0.55 m/s, the PSD values of the force signal show an increase (blue symbols in Fig. 2a) at frequencies close to the natural vibrational frequency of the plate ($f_0 = 7.8$ Hz). Figure 2 also shows that, at $U = 0.55$ m/s, f_{LC} and f_{PIV} remained locked-on to the natural vibrational frequency of the plate. As a result, vibrations with 1 mm displacement amplitude were observed at the leading and trailing edges of the plate P3.

3.2 Boundary Layer Profiles

Figure 3 shows the time-averaged boundary layer profiles at the trailing edge of the plate with the largest perforations (P3) for five different inflow velocities, corresponding to the cases presented in Fig. 2. In order to provide a reference, velocity profiles for the solid plate are shown in all plots. The corresponding boundary layer profiles for the plates with smaller perforation diameters (P1 and P2) match those of the solid plate for all values of the inflow velocity, considering the inherent uncertainty of the PIV measurements, and are not presented here. As the perforation diameter increased to $\delta_h = 19.5$ mm, the boundary layer profiles deviated from those corresponding to the solid plate for all inflow velocities. This deviation was particularly pronounced close to the surface of the plate, and it increased with the increase of the inflow velocity. Moreover, larger difference between the boundary layer profiles of the perforated plate and that of the solid plate was observed at DAP1 (Fig. 3a) compared to DAP3 (Fig. 3b). The separating boundary layer corresponding to DAP1 was influenced by the proximity of the most downstream perforation, which was located closer to the trailing edge of the plate in DAP1 than it was in DAP3. From a theoretical standpoint, the fluctuating pressure difference between the upper and the lower surfaces of the plate is proportional to the velocity

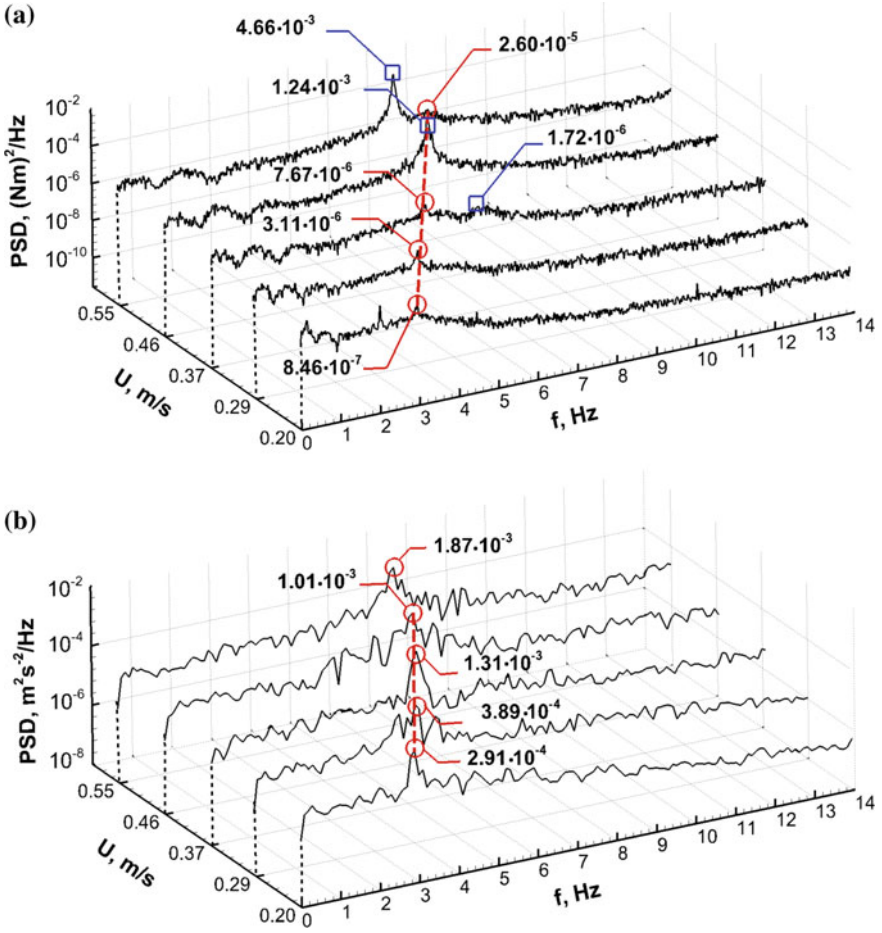

Fig. 2 PSD of the flow-induced loading on plate P3 as a function of the inflow velocity and frequency: direct force measurements (**a**); transverse flow velocity fluctuations in DAP1 (**b**)

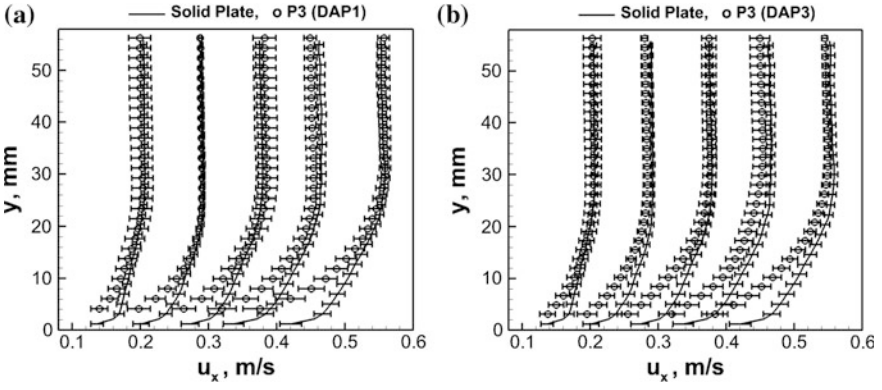

Fig. 3 Boundary layer profiles at the trailing edge of the P3 plate: DAP1 (**a**); DAP3 (**b**)

fluctuations in the perforations [3]. In turn, the pressure difference at the trailing edge governs the process of periodic trailing edge vortex shedding. The present results indicate that the fluctuating pressure difference across the plate was reduced in the vicinity of the individual perforations. Thus, the staggered perforation pattern disrupted the trailing vortex shedding to various degrees along the span of the plate and introduced three-dimensionality to the wake. In the time-averaged sense, increasing the perforation diameter resulted in a wider wake, thus increasing the bluffness of the plate, defined as the ratio of the wake width to the thickness of the plate, following the notation of [8] developed for generalized bluff bodies.

4 Conclusion

The effect of the diameter of the transverse perforations and inflow velocity on the frequency and amplitude of the flow-induced loading was investigated using direct force measurements and PIV. The vortex shedding frequencies were in good agreement with the frequencies of the measured flow-induced loading for all perforation patterns. Thus, it was determined that the trailing edge vortex shedding was the main mechanism of generating the loading on the plates and the resulting flow-induced vibrations. Although not presented in this paper, the frequency of the vortex shedding and of the loading on the plates decreased with the increase of the perforation diameter. The thickness of the boundary layer at the trailing edge also increased with the increasing diameter of the perforations at the highest considered inflow velocities. Therefore, the decrease of the frequency of velocity oscillations in the wake can be attributed to the increase of the boundary layer thickness at the point of flow separation. The largest perforation diameter resulted in a three-dimensional boundary layer whose thickness, as well as the deviation of the velocity profile from the reference case of solid plate, increased with the decrease of the distance of the last (downstream-most) perforation from the trailing edge.

Acknowledgements The authors gratefully acknowledge the financial contribution of PIBI-VIESSE s.r.l. to the Ph.D. scholarship of F. Bossi and financial support of the Natural Sciences and Engineering Research Council of Canada.

References

1. Bossi FC, Barannyk O, Rahimpour M, Malavasi S, Oshkai P (2016) Effect of transverse perforations on fluid loading on a long, slender plate at zero incidence. J Hydrol Hydromech 65
2. Clark I, Devenport WJ, Jaworski J, Daly C, Peake N, Glegg SA (2014) The noise generating and suppressing characteristics of bio-inspired rough surfaces. In: 20th AIAA/CEAS aeroacoustics conference, the AIAA aviation forum, Atlanta, USA, 16–20 June 2014
3. Jaworski JW, Peake N (2013) Aerodynamic noise from a poroelastic edge with implications for the silent flight of owls. J Fluid Mech 723:456–479

4. Malavasi S, Zappa E (2008) Fluid-dynamic forces and wake frequencies on a tilted rectangular cylinder near a solid wall. Meccanica 44:91–101
5. Nakamura Y, Ohya Y, Tsuruta H (1991) Experiments on vortex shedding from flat plates with square leading and trailing edges. J Fluid Mech 222:437–447
6. Okajima A (1982) Strouhal numbers of rectangular cylinders. J Fluid Mech 123:379–398
7. Parker R (1966) Resonance effects in wake shedding from parallel plates: Some experimental observations. J Sound Vibr 4:62–72
8. Roshko A (1955) On the wake and drag of bluff bodies. J Aeronaut Sci 22:124–132

Control of Particle Motion with Ultrasonic Vibration

K. Ouchi and K. Kofu

Abstract The purpose of this research is to control the particles motion by the ultrasonic standing wave in air. In this research, simulation have been compared with experiment for the confirmation of validity and examined the possibility for control of particles motion by ultrasonic standing wave. As the result, simulation corresponded with experiments qualitatively. Also, maximum sound pressure can be increased by converging the acoustic wave with a reflector. Then slow speed particles are more easily affected by acoustic radiation force. But, the motion control of small particle was difficult because acoustic radiation force acting on particle was weak. Additionally, motion of small particle is susceptible to acoustic streaming. Therefore influence of acoustic streaming must be taken into consideration when we want to control the motion of small particle.

Keywords Ultrasonic vibration · Particle motion · Acoustic pressure
Acoustic streaming · Particle size

1 Introduction

If control of particle behaviour with ultrasound becomes possible, agglutination and collection are capable without scratching the particle structure due to non-contact operation. Kozuka [1] has proved that it is possible to control the micro sized particles with ultrasonic. Authors [2] also have been researching experimentally and calculatedly while particle density, diameter, wind speed, sound pressure, vibration frequency are changed. Then we have concluded particle behaviour in the ultrasonic standing wave field can be controlled and the optimum condition regarding

K. Ouchi (✉) · K. Kofu
Nihon University, 1-8-14 Kanda Surugadai, Chiyoda-Ku, Tokyo, Japan
e-mail: cska16006@g.nihon-u.ac.jp

K. Kofu
e-mail: kofu@mech.cst.nihon-u.ac.jp

Y. Zhou et al. (eds.), *Fluid-Structure-Sound Interactions and Control*, Lecture Notes in Mechanical Engineering,
https://doi.org/10.1007/978-981-10-7542-1_47

particle properties has been indicated. But it is not sufficient because the number of condition is few in order to conclude the optimum condition.

Then, the purpose of this study is that particle motion is analysed experimentally and calculatedly while the maximum sound pressure, shape of reflection plate and particle diameter are changed. Then calculation is compared with experiment to investigate the validity of calculation result, and the optimum condition for control of particle motion is tried to propose by checking how the standing wave condition affects on motion.

2 System Modeling and Experimental Apparatus

A schematic diagram of calculation and experimental apparatus is shown in Fig. 1. The conditions used in the analysis are shown in Table 1, and the particles properties are shown in Table 2. Vibration and reflection plate in the figure was set to generate a standing wave field as shown in Fig. 1. Flat and cuved plates are used as the reflector. Vibration mode was expressed as following equation.

$$\Delta y = A_m \sin(\omega t)\cos(kx) \tag{1}$$

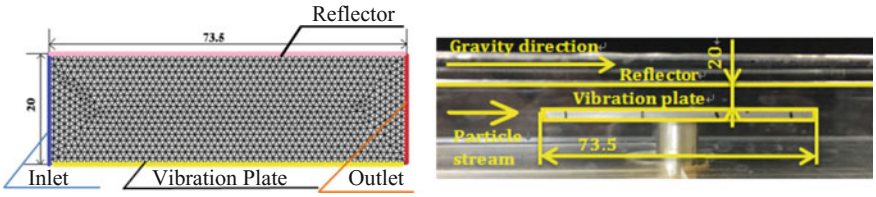

(a) Analysis model (b) Experimental apparatus

Fig. 1 System modeling and experimental apparatus (units in mm)

Table 1 Analysis condition

Domain fluid	Compressible viscous fluid	
Turbulent model	k-ε	
Time dependence	Unsteady	
Vibration frequency (kHz)	19.42	
Flow velocity (m/s)	0.3	0.5
Time step size (s)	0.0001	

Table 2 Particle properties

Material	Diameter (μm)	Density (kg/m^3)
Sodium hydrogen carbonate	40, 60, 80, 100	2200
Calcium carbonate	3, 14, 19, 25	2710
Polystyrene	500	160
Smoke	1	300

where Δy is vibration amplitude, ω is angular velocity, t is time, A_m is maximum vibration amplitude of plate, k is the number of vibration wave on the plate and 3 is employed as k. Comsol mutiphysics 5.2a was used in the study.

In this research, flow direction was corresponded with gravity force. Additionally, in this experiment, the particles are dispersed in the air with an aerosol generator and injected between plates with a compressed air. Then particles were shined with PIV laser and this motion was captured with a high speed camera. In this time, air velocity was employed at 0.3 and 0.5 m/s.

3 Results

3.1 Acoustic Pressure Distribution

Figure 2 shows the experimental result of the generated sound pressure distribution between plates. In this figure two nodes on acoustic pressure in vertical direction between plates appear. Moreover, the maximum sound pressure at the antinode reaches at 1400 Pa in experiment and calculation, and the shape of the sound pressure distribution is almost the same. Therefore this simulation can catch the acoustic pressure distribution corresponding with experiment.

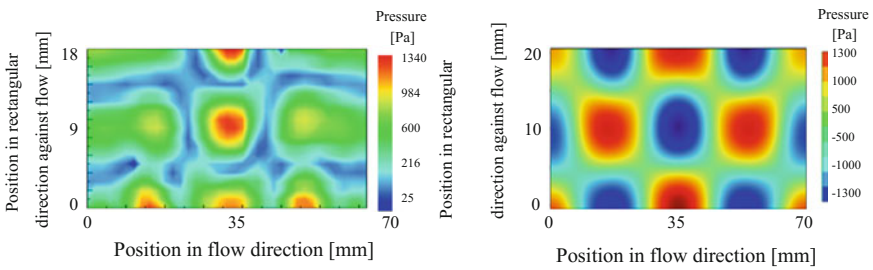

(a) Experiment (b) Analysis

Fig. 2 Acoustic pressure

3.2 *Particle Motion*

Figures 3 and 4 show particles motion which they pass through a standing wave of sound field. In this experiment, the analysed area for particle motion was divided in flow direction because they could not be captured once with high speed camera. Figure 3 shows the particle motion of polyethylene having a particle size of 500 μm at a flow velocity of 0.5 m/s. As a result, particles move to the node. Their particle density is light and diameter is large. Therefore, they can get large acoustic radiation force and it is easy to move because inertial force is small. On the contrary, in Fig. 4, particle of sodium bicarbonate with a particle size of 80 μm could not have the ultrasonic effect because particles flow straight. This reason is assumed as inertial force and acoustic radiation force. Acoustic radiation force decreases in the case of small sized particle. Additionally it is hard to move the particle which density is heavy because inertial force increases. Also, calcium carbonate with d_p = 3 μm is injected into the standing wave field at a velocity of v = 0.3 m/s, and the experimental results and analysis results of the lower part of the field are shown in Fig. 5. As a result of this numerical analysis, the particle behaviour was not affected

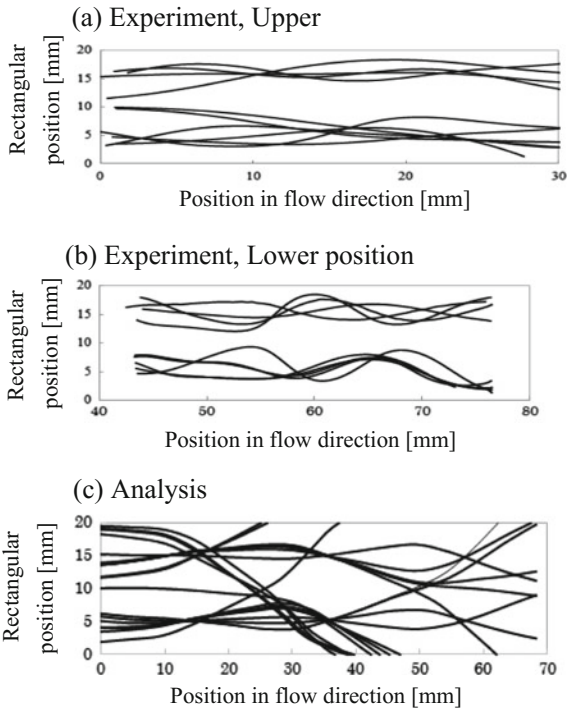

Fig. 3 Particle motion (polyethylene, d_p = 500 μm, P_m = 1810 Pa, v = 0.5 m/s)

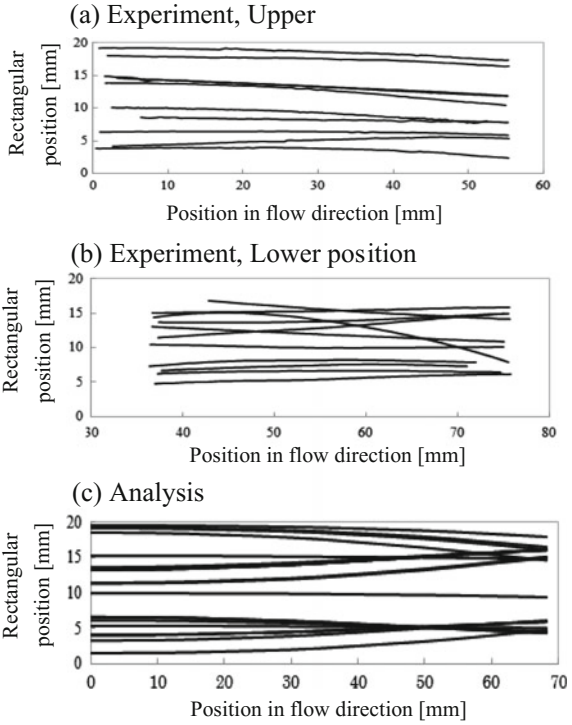

Fig. 4 Particle motion (sodium bicarbonate, d_p = 80 μm, P_m = 1810 Pa, v = 0.5 m/s)

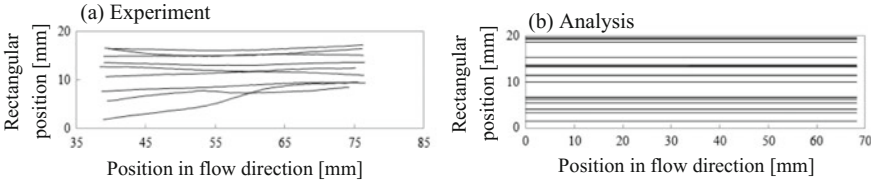

Fig. 5 Particle motion (Calcium carbonate, d_p = 3 μm, P_m = 1810 Pa, v = 0.3 m/s)

by the acoustic radiation force and did not move to the node of the standing wave because the particle diameter is small. On the other hand, in the experiment, the particles near the vibration plate tended to move irregularly and did not match the analysis result. Wada et al. [3] said acoustic flow is generated because acoustic pressure reduces in wave transmission direction due to viscosity and inertia of medium. It is thought that the smaller the particle diameter is, the more it is

susceptible to the influence of the acoustic flow. Therefore it is easy to move by the flow. Since the influence of flow was not considered in this calculation, particle behaviour like the experimental result could not been observed.

3.3 Acoustic Streaming

If Rayleigh type acoustic streaming was observed in the ultrasonic standing wave field, and it is presumed that it influences particle behaviour. Therefore, smoke was injected into the standing wave field of Fig. 3, and the acoustic streaming was examined by capturing the flow of smoke with high speed camera and PIV laser. The experimental results when amplitude of antinode A_m is 1.47 and 7.61 μm are shown in Fig. 6a, b. We did not consider acoustic streaming in this simulation because it requires the large amount of time. The portion of the orange line on the lower side of Fig. 6a, b is the node of the vibration plate. As shown in Fig. 6a, in the range from the left end to the second node, it can be observed that vortexes are generated above the antinode, and this tendency is similar to the Rayleigh type acoustic flow. It is found that the behaviour of micro-sized particles is easily affected by this acoustic flow. Therefore the difference between simulation and experiment appears in Fig. 5. On the contrary, in the range from the second node to the third node, the smoke vortex does not occur neatly. It is thought that the resonance rod was fixed at the center of the vibration plate and it confuses the flow.

On the other hand, as shown in Fig. 6b, it was observed that smoke does not regularly flow in eddy and flows disorderly. It is thought that the flow velocity is too fast. Acoustic streaming occurs due to viscosity and inertia. If amplitude is large, air was pumped under high velocity and inertia increases. As the Reynolds number increases, the sound flow becomes a turbulent, and it is thought that a conventional vortex does not occur.

It was confirmed that the acoustic flow is easy to influence the behaviour of the micro-sized particles, and it was found that the influence of the acoustic flow must be taken into account for the sake of controlling the micro-sized particles motion.

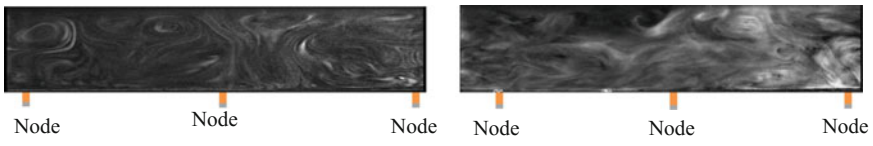

(a) Amplitude of the anti-node, A_m=1.47μm (b) Amplitude of the anti-node, A_m =7.61μm

Fig. 6 Smoke motion by Experiment (d_p = 1 μm, P_m = 1310 Pa)

4 Conclusions

1. Large sized and small density particles are susceptible to the influence of acoustic radiation force, and they are easy to concentrate on nodes.
2. Since the inertial force of large mass particles is large, it is difficult to control behavior.
3. When the particle diameter is small, the influence of the acoustic radiation force is small, and it is difficult to concentrate on the antinode.
4. If the vibration velocity is too fast, the sound flow becomes turbulent and it is difficult to control the small sized particle.

References

1. Kozuka T, Yasui K, Tsujiuchi T, Towata A, Iida Y (2008) Measurement and calculation of acoustic radiation force acting on a minute object in a standing wave field. J Inst Electron Inf Commun J91-A(12):1156–1160
2. Liu X, Suzuki H, Kofu K (2015) Control the Particle motion by ultrasonic standing wave. In: Proceedings of the 6th Asian particle technology symposium, PO02–01:272
3. Wada Y et al (2014) Acoustic streaming in an ultrasonic air pump with three-dimensional finite-difference time-domain analysis and comparison to the measurement. Ultrasonics 54:2119–2125

Part III
Acoustics and Sound-Flow-Structure Interaction

Acoustic Impedance and the Control of Sound Waves

Lixi Huang

Abstract Acoustic impedance is one of the most important parameters for fluid media and is determined by effective mass and elastic modulus. For an acoustic absorber with a shallow depth, the system has high characteristic resonance frequency and its performance is controlled by the system stiffness which is inversely proportional to the depth. This study begins with the analysis of a common porous material as the benchmark and compares with the traditional micro-perforated panels (MPP) before introducing advanced designs. It is shown that MPP can indeed yield similar performance as the porous material when the aperture is very small hence high cost. However, the performance at very low frequencies remains poor. In order to achieve a broadband performance, parallel resonator array is required. This system is shown to reduce system stiffness significantly while the overall mass increase is much smaller than that of a single MPP resonator. Advanced means of reducing system stiffness by electromagnetic forces is discussed, and the physics of a negative dynamic mass is also analyzed.

1 Introduction

Control of sound waves takes two forms, wave reflection and absorption. The latter is more preferable but is harder to achieve at low frequencies. One important application of acoustics is the control of environmental noise which often features heavy low-frequency contents which also spread over a broad frequency band (measured by the ratio of high-to-low frequency limits). For instance, the limits of 100 Hz–1 kHz are used in the examples given in the current study as noise absorption above 1 kHz is easy in existing technology.

L. Huang (✉)
Lab for Aerodynamics and Acoustics, Department of Mechanical Engineering, Zhejiang Institute of Research and Innovation, The University of Hong Kong, Hong Kong, China
e-mail: lixi@hku.hk

Y. Zhou et al. (eds.), *Fluid-Structure-Sound Interactions and Control*, Lecture Notes in Mechanical Engineering,
https://doi.org/10.1007/978-981-10-7542-1_48

The most traditional noise absorber is, of course, the porous sound absorption material (henceforth SAM) which is typically made of glass fiber or rockwool. Porous materials easily accumulate dusts and they may not be acceptable when considerations of hygiene are crucial. Micro-perforated panels (MPP) are used instead as panels are easily cleansed and they are esthetically more appealing. However, the traditional use of MPP is limited to a single resonator formed between the panel and the back cavity. Sound absorption is limited only to a narrow frequency band around the resonance frequency. In what follows, the next section gives a brief review of these with the help of a set of lumped parameters of system mass, resistance and stiffness. Using the concept of system mass and stiffness, the superior performance of the parallel array of MPP resonators is quantified, and the concepts of negative dynamic mass and negative stiffness are also introduced.

2 Reference Absorber and System Parameters

Figure 1a shows the configuration of sound absorption by a layer of SAM with thickness h. For simplicity the study is limited to normal incident sound although the results are easily extended to oblique and random incidence. Figure 1b, 1c illustrate the absorber made of MPPs in series and parallel arrangements, which are discussed in this and next sections, respectively.

Textbook formulation gives the following sound energy absorption coefficient

$$\alpha = 1 - \left|\frac{Z-1}{Z+1}\right|^2, \quad Z = \left.\frac{p}{\rho_0 c_0 u}\right|_{\text{interface}} = \Re + iX, \tag{1}$$

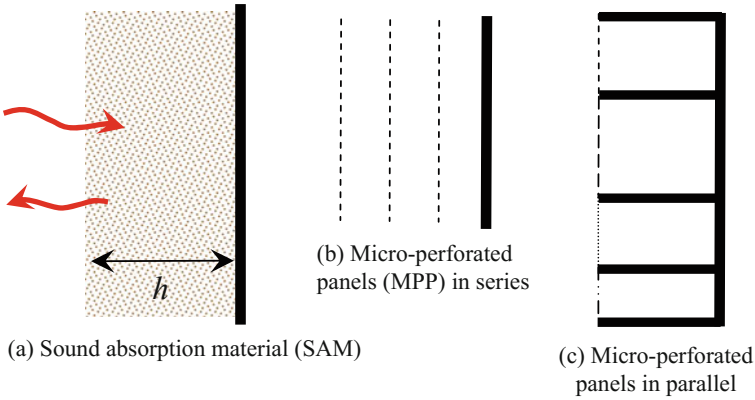

Fig. 1 Illustration of the absorption of normal incident sound by **a** a layer of sound absorption material (SAM) of depth h, **b** micro-perforated panels (MPP) in series and **c** in parallel

where Z is the interface impedance normalized by the air impedance $\rho_0 c_0$. For convenience, Z is decomposed into resistance $\mathfrak{R}$ (real part) and reactance X (imaginary part). Perfect sound absorption, $\alpha = 1$, requires $Z = 1$ or

$$Z = 1: \quad \mathfrak{R} = 1, \quad X = m\bar{\omega} - K/\bar{\omega} = 0 \rightarrow m = K = 0, \tag{2}$$

where m and K are the normalized system mass and stiffness, respectively, and

$$\bar{\omega} = \omega h / c_0 \tag{3}$$

is the dimensionless angular frequency. For the benchmark absorber shown in Fig. 1a, the interface impedance is approximated as follows

$$Z = \frac{\bar{\rho}_{sam}\bar{c}_{sam}}{i\tan(\bar{\omega}/\bar{c}_{sam})} \overset{\cot x \approx x^{-1} - x/3}{\longrightarrow} Z \approx i\left(\frac{\bar{\rho}_{sam}\bar{\omega}}{3} - \frac{\bar{\rho}_{sam}\bar{c}_{sam}^2}{\bar{\omega}}\right), \tag{4}$$

where $\bar{\rho}$ and $\bar{c}$ are the complex density and speed of sound normalized by the air density ρ_0 and speed of sound c_0, respectively, subscripts 'sam' denote sound absorption material, for which the classic Delany and Bazley [2] model is used

$$\begin{aligned} \bar{\rho}_{sam}\bar{c}_{sam} &= 1 + 0.057E^{-0.754} - i \times 0.087E^{-0.732}, \\ \bar{c}_{sam}^{-1} &= 1 + 0.098E^{-0.7} - i \times 0.189E^{-0.595}, \quad E = \rho_0 f / R_f. \end{aligned} \tag{5}$$

Here, R_f is the flow resistivity and parameter E should fall within the range of 0.01 and 1.0 for the empirical formulas to be reliable.

In Eq. (4), the decomposition into real and imaginary parts gives

$$\begin{aligned} \mathfrak{R} &= \mathrm{Re}(Z) = \mathrm{Im}\left(\bar{\rho}_{sam}\bar{c}_{sam}^2\right)/\bar{\omega} - \frac{1}{3}\mathrm{Im}(\bar{\rho}_{sam})\bar{\omega} \\ m &= \mathrm{Re}(\bar{\rho}_{sam})/3, \quad K = \mathrm{Re}\left(\bar{\rho}_{sam}\bar{c}_{sam}^2\right). \end{aligned} \tag{6}$$

For a cavity of pure air, the normalized mass is $m = 1/3$, which in dimensional sense means that one third of the mass of the air column in the cavity is vibrating with the interface. The system stiffness of $K = 1$ means a spring constant of $\rho_0 c_0^2 / h$ for an interface of unit area.

In a real system, the frequency dependency of the interface impedance Z is complex. The resistance $\mathfrak{R}$ is frequency dependent, and the reactance X does not yield a constant mass m and constant stiffness K. For any frequency band of interest, a least-mean-square fit for the reactance X (as a function of frequency) is to be used to analyze the system properties. For a discrete set of frequencies, usually chosen in equal logarithmic intervals with index $j = 1, 2, 3, \ldots, N$, the curve fitting is achieved as follows

$$\begin{bmatrix} m \\ K \end{bmatrix} = \begin{bmatrix} \sum_{j=1}^{N} \bar{\omega}_j^2 & -N \\ N & -\sum_{j=1}^{N} 1/\bar{\omega}_j^2 \end{bmatrix}^{-1} \begin{bmatrix} \sum_{j=1}^{N} X_j \bar{\omega}_j \\ \sum_{j=1}^{N} X_j/\bar{\omega}_j \end{bmatrix}. \tag{7}$$

Note that m and K are dependent on the choice of frequencies and caution must be exercised to interpret the results. When a set of system parameters are thus obtained, a resonant frequency may be obtained as $\bar{\omega} = \sqrt{K/m}$ which is easily translated into a dimensional frequency of $\bar{\omega} c_0/(2\pi h)$ in Hertz.

For all examples presented in this study, the frequency range and the absorber depth are chosen below

$$f \in [100,\ 1000]\ \text{Hz}, \quad h = 0.05\ \text{m}. \tag{8}$$

Figure 2a compares the sound absorption performance for three absorbers: SAM absorber, a single MPP and three MPPs in series, with design parameters given in the figure caption, while the legends (for all sub-figures) are given in Fig. 2c where there is more space for labels. The performance of SAM (solid line) is clearly poor at low frequencies and the same is true for the MPP in series (labelled as MPP-3). Note that the choice of $R_f = 5000\,\text{Pa}\cdot\,\text{s/m}^2$ is made on the basis of achieving some absorption in the low frequency region and an increase of R_f can easily raise the absorption coefficient towards 1 kHz but further suppress the low-frequency absorption. In fact, a systematic optimization scheme was used but the details are not described here for brevity. The main observation here is that the SAM performance is similar to that of MPP-3 (dotted line). The latter consists of 3 layers of MPP, equally spaced over the depth h. It must be cautioned that such panels will be rather expensive to make due to the very small aperture size (0.2 mm) and high perforation ratio specified. The purpose of the comparison is to show that MPPs can indeed achieve the same performance of the porous material but it would be rather expensive. The formulas of Maa [4] are used for the single-aperture impedance (denoted by subscripts '1')

$$\begin{aligned} Z_1 &= \mathfrak{R}_1 + iX_1, \quad \mathfrak{R}_1 = \frac{32\nu t}{c_0 d^2}\left[\left(1 + \frac{K_1^2}{32}\right)^{1/2} + \frac{\sqrt{2}}{32} K_1 \frac{d}{t}\right], \\ X_1 &= \frac{\omega}{c_0} t\left[1 + \left(1 + \frac{K_1^2}{2}\right)^{-1/2} + 0.85\frac{d}{t}\right], \quad K_1 = d\sqrt{\frac{\omega}{4\nu}}, \end{aligned} \tag{9}$$

where d is the aperture diameter, t is the panel thickness, $\nu = 1.5 \times 10^{-5}\,\text{m}^2/\text{s}$ is the kinematic viscosity of air, K_1 is the ratio of diameter to the boundary layer thickness. The panel impedance is Z_1/σ, where σ is the perforation ratio, while the interface impedance is $Z_1/\sigma - i\cot(\bar{\omega})$ from which the absorption coefficient is calculated according to Eq. (1).

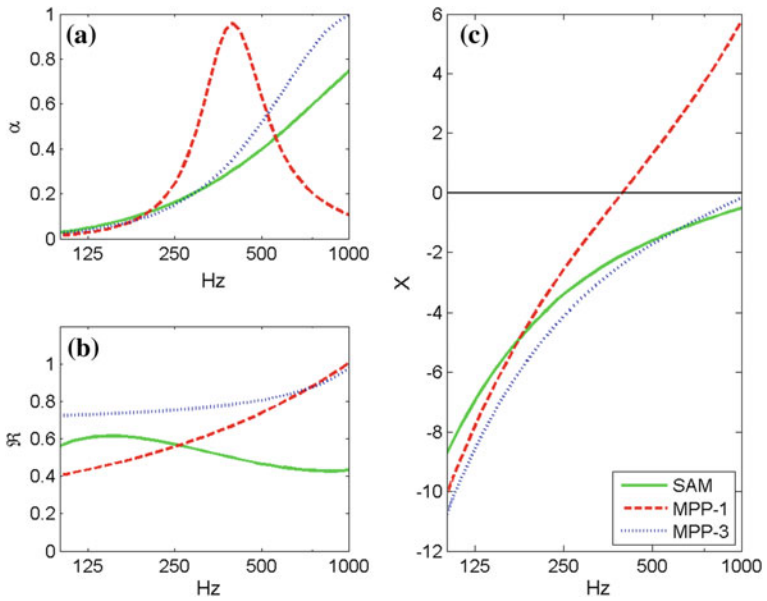

Fig. 2 Sound absorption by perforated panels: single vs a series of panels and comparison with SAM. **a** Absorption coefficients. **b** Resistance. **c** Reactance. The SAM has $R_f = 5000\,\text{Pa}\cdot\text{s/m}^2$; the single MPP resonator has a panel thickness of 0.5 mm, an aperture diameter of 1 mm, and a perforation ratio of 0.4%. The panels in MPP-3 configuration also have a thickness of 0.5 mm, all with an aperture diameter of 0.2 mm, and a perforation ratio of 4%

The dashed-line in Fig. 2a is for the single-MPP absorber with an aperture diameter of 1 mm, and a perforation ratio of $\sigma = 0.4\%$. Here, the very low ratio of σ is chosen in order to amplify (by the factor of σ^{-1}) the grossly inadequate resistance yielded by the aperture diameter of 1 mm. The consequence of such a low perforation ratio is that it also amplifies the virtual mass embedded in X_1. The curve-fitting by Eq. (6) gives $m = 7.58$, $K = 1.0$. The resonance frequency is 392.8 Hz. The high value of mass (compared with the natural cavity acoustic mass of $m = 1/3$) results in a performance drop above the resonance frequency.

Figure 2b shows the resistance for the three configurations. The ideal value of $\Re$ is unity, and the three curves are not too far from that. Figure 2c shows the reactance. The resonance of the single-MPP produces $X = 0$ around 392.8 Hz, while the curves for the SAM and MPP-3 configurations are similar.

As a summary, the following may be said. (i) The performance of the SAM absorber can be matched by MPPs in series, but the panels would be expensive to make. (ii) The single-MPP resonator can be designed to provide a fairly complete absorption at a single frequency and its poor performance elsewhere is caused by the resistance amplification by a low perforation ratio. (iii) Significant sound absorption below around 500 Hz is difficult to achieve by these three configurations.

3 Parallel Sound Absorber

Figure 1c illustrates the parallel absorber which was also reported by Wang and Huang [5] using cavities of various depths. In the current study, a uniform depth of h is used but the summation of acoustic admittance remains unchanged,

$$\frac{1}{Z} = \sum_j \frac{A_j}{Z_{1j}/\sigma_j - i\cot\bar{\omega}}, \quad \sum_j A_j = 1, \tag{10}$$

where A_j is the fraction of the interface area allocated to resonator j. Note that the results predicted by this equation may differ somewhat from a full numerical simulation (such as by Comsol) as the latter takes full account of the inter-resonator coupling which is typically adding virtual mass to the system. Such effects can easily be absorbed by the adjustment of the perforation ratios and are not discussed in detail here. However, the fundamental difference between the parallel arrangement in Fig. 1c and the series arrangement in Fig. 1b deserves some discussions.

The impedance of the series arrangement is a simple addition, while that of the parallel one is the summation of admittance. For the simplest case of two resonators with equal interface area,

$$Z_1 = \Re_1 + iX_1, \quad Z_2 = \Re_2 + iX_2, \quad A_1 = A_2,$$

the overall interface impedance is calculated as follows,

$$Z = 2\frac{Z_1 Z_2}{Z_1 + Z_2} = 2\frac{(\Re_1\Re_2 - X_1X_2) + i(\Re_1X_2 + \Re_2X_1)}{\Re_1 + \Re_2 + i(X_1 + X_2)}.$$

For a frequency between the two resonances where $X_2 = -X_1$, and assuming $\Re_1 = \Re_2$, the following interface impedance is obtained

$$Z = \frac{\Re_1^2 + X_1^2}{\Re_1}.$$

which is purely real. The reactance X_1 is transformed into resistance and it can be much larger than the resistance in each resonator, $|X_1| > \Re_1$ if the two resonance frequencies of the two resonators are far apart. The mechanism for such reactance-to-resistance transformation is explained as follows. When there is no resistance, $\Re_1 = \Re_2 = 0$, any acoustic pressure will drive particle velocities of opposite signs and they sum up to zero total volume flux,

$$u_1 = p/(iX_1), \quad u_2 = p/(iX_2), \quad u_1 + u_2 = 0,$$

as the two resonators form a new resonator, with the first (with lower own resonance frequency) playing the role of mass and the second playing the role of a spring, $X_1 > 0, \quad X_2 = -X_1 < 0$. This inter-resonator resonance is only curtailed

by the resistance $\Re_1 > 0$ which leads to $u_1 + u_2 \neq 0$. The net volume flux thus derived is out of phase with the resistance effect itself and is in-phase with the reactance of the individual resonator.

Figure 3 compares the performance of such a parallel absorber (with 10 resonators) with SAM. Figure 3a shows that an absorption coefficient near 0.5 is possible for frequencies ranging from 100 Hz to 1 kHz (dashed line for the parallel absorber) while the SAM absorber (solid line) can only reach such performance beyond around 500 Hz. The broad bandwidth for the parallel absorber is particularly significant.

However, the resistance data shown in Fig. 3b reveals that the parallel absorber (dashed line) has very high resistance (around 5.0) derived from the component reactance, while the SAM resistance is much closer to the ideal value of $\Re = 1$. Note that this level of resistance is about 4.2 times as high as the average resistance if all the panels were arranged in series. This again proves that the resistance is mainly derived from the reactance of individual resonators. In plain physics, it means that the velocity of the inter-resonator flow is so large that the system resistance is greatly amplified. Details of inter-resonator particle flow were analyzed by Wang and Huang [5] although the frequency bandwidth covered by that study

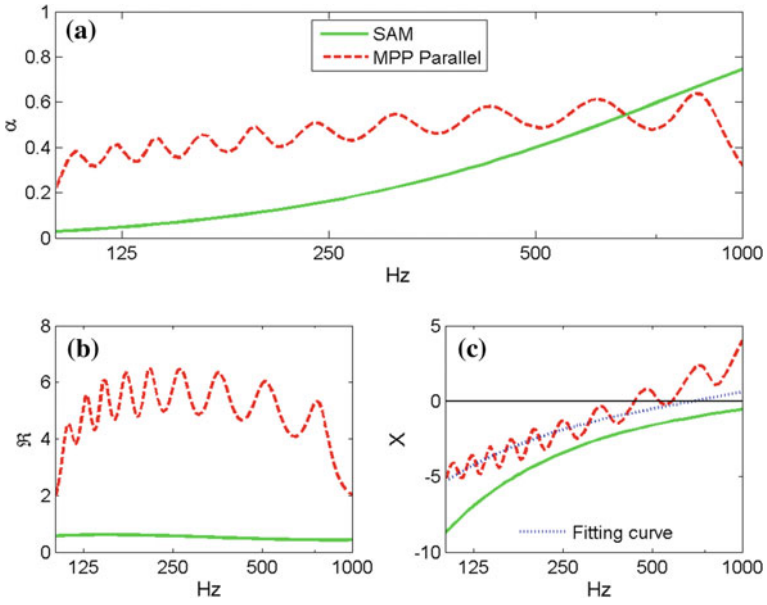

Fig. 3 Parallel MPP array compared with porous medium absorber. **a** Absorption coefficient. **b** Resistance. **c** Reactance. The SAM absorber has $R_f = 5000\,\text{Pa} \cdot \text{s/m}^2$. The parallel absorber of 10 MPPs has an A_p ranging from 0.05 to 0.123, and an aperture diameter from 0.58 to 4 mm

was not as large as in the current example. In this example, this high value of resistance from the parallel absorber is the reason why the absorption coefficient cannot rise above 0.5, unlike the single-resonator performance shown in Fig. 2a as the dashed line.

The reason why the broadband performance in Fig. 3a is possible in the first place is due to the fact that the inertia from one resonator is balanced by the spring from another ($X_1 > 0,\ X_2 < 0$). The cancellation of reactance among the resonators is best illustrated by the system stiffness determined by the least-mean-square fit which is shown as the dotted line in Fig. 3c. This curve is closer to the resonance condition of $X = 0$ than the SAM absorber (solid curve). For the particular example, the system parameters are $m = 1.2628,\ K = 0.5054$. Compared with the single-MPP resonator with $m = 7.58$, the parallel absorber has a rather low system mass. In terms of the more critical parameter of system stiffness, the value is nearly half of the simple cavity. In other words, the effective cavity size is nearly doubled by the parallel arrangement.

4 Advanced Concepts of System Mass and Stiffness Reduction

All configurations analyzed so far are purely mechanical and passive. In such a mechanical system mass can only be added, and it is most easily added by having a perforated panel of low perforation ratio. However, the fact that the parallel resonator with reactance shown in Fig. 3c has such a low system mass reveals that the inter-resonator coupling is able to take away inertia (namely negative dynamic mass) instead of adding to it. The exact mechanism by which this is achieved is complex, but it is likely that the phase angle change associated with the damping is involved. The other known example of negative dynamic mass was revealed by Huang [3]. The page limit here does not allow essential details to be reproduced but a brief summary of physics is necessary. When a flush-mounted piston vibrates on one duct wall, the baffling effect by the opposite duct wall introduces an image source which also radiates to the real piston surface which modifies the radiation impedance of the real piston. The fact that the waves from the image source travel a distance twice the duct height implies a time delay for the damping effect; the wave pressure being a damping term as the product of pressure and velocity carries power. The delayed damping term brings negative dynamic mass, as shown below,

$$\Re u_p(t-\Delta t) = \Re u_p e^{-i\omega\Delta t} \approx \Re u_p - \Re \Delta t\ du_p/dt,$$

where u_p is the piston vibration velocity, $\Delta t = 2h/c_0$ is the time delay, and the negative dynamic mass is simply $-\Re\Delta t$ as it gives rise to a force proportional to the piston acceleration du_p/dt. In the analysis of [3], the actual amount of negative mass is determined by the ratio of piston width to the duct height, and it can be

rather substantial for a wide piston. Having said these, the fact that the piston is assumed to vibrate at a uniform velocity implies a certain structural rigidity and hence structural mass. It is not easily conceivable that the negative mass effect would compensate for the extra structural mass brought by the piston.

The second advanced concept is the negative stiffness rendered by the magnetic force [3]. When a ferromagnetic material is placed in the field of a magnet, the material will be attracted to the magnet and the attraction force increases when the two objects are closer together, giving rise to negative stiffness which does not normally exist in pure mechanical systems. The concept was validated experimentally by Chiu et al. [1] who demonstrated clear resonance frequency shift towards lower frequencies. A very different approach of using a moving-coil loudspeaker diaphragm was proposed by Zhang et al. [6], Zhang and Huang [7] and it was shown that the magnetic force employed in such a design can effectively reduce the cavity stiffness and the cavity volume is estimated to be tripled by the use of the shunt circuit attached to the electromagnetic device.

5 Conclusions

For the purpose of control of sound waves, the acoustic impedance at the sound-absorber interface has two crucial components: system mass and stiffness. The latter controls the performance of the absorber at low frequencies and is determined mainly by the absorber volume. While electromagnetic forces can reduce system stiffness, a pure mechanical system of parallel array of Helmholtz resonators is also capable of significant stiffness reduction. In this study, an absorber designed by this approach delivers higher absorption coefficient from 100 Hz up to 1 kHz. However, the absolute level of the absorption coefficient is seen to be limited by the reactance-derived resistance.

In terms of the system mass, a single MPP resonator is seen to add too much mass that high frequency performance as an absorber is severely damaged. The array resonators, however, are found to yield only a moderate increase of system mass. Negative dynamic mass is also possible via delayed resistance but it remains to be seen if such mechanism can be used to form a practical device.

Acknowledgements The author gratefully acknowledges the funding support from the Department of Science and Technology of Zhejiang Province, China.

References

1. Chiu YH, Cheng L, Huang L (2006) Drum-like silencers using magnetic forces in a pressurized cavity. J Sound Vib 297:895–915
2. Delany M, Bazley E (1970) Acoustical properties of fibrous absorbent materials. Appl Acoust 3:105–116

3. Huang L (2000) A theory of reactive control of low-frequency duct noise. J Sound Vib 238 (4):575–594
4. Maa DY (1998) Potential of microperforated panel absorber. J Acoust Soc Am 104:2861–2866
5. Wang CQ, Huang L (2011) On the acoustic properties of parallel arrangement of multiple micro-perforated panel absorbers with different cavity depths. J Acoust Soc Am 130(1):208–218
6. Zhang YM, Chan YJ, Huang L (2014) Thin broadband noise absorption through acoustic reactance control by electro-mechanical coupling without sensor. J Acoust Soc Am 135 (5):2738–2745
7. Zhang YM, Huang L (2017) Electroacoustic control of Rijke tube instability. J Sound Vib 409:131–144

An Introduction of CARDC 5.5 m × 4 m Anechoic Wind Tunnel and the Aeroacoustic Tests

Xunnian Wang, Jun Zhang, Peng Chen and Zhengwu Chen

Abstract An introduction of 5.5 m × 4 m anechoic wind tunnel in China Aerodynamics Research and Development Center (CARDC, in Mianyang) and some typical experimental results are presented. A C919 1:14 scaled aircraft model test shows that noise sources are mainly located at the landing gear, high-lift device, flap-wing joint points, slat-fuselage conjunction positions. And a 1:8 scaled high speed train model test shows that main noise sources are located at the first bogie and pantograph position.

1 Introduction

Noise emissions from aircraft have become a major factor that can limit growth in the air transportation industry. Communities living near airports are becoming increasingly aware of noise disturbance, and new aviation standard, such as CCAR part 36, has put more stringent regulations on the noise level of the newly designed aircraft. There are various analytical, empirical and numerical tools to help in the design of quieter aircraft [1]. However aeroacoustic measurements in wind tunnels are still required and very necessary. In this paper, an introduction of 5.5 m × 4 m anechoic wind tunnel in China Aerodynamics Research and Development Center (CARDC, in Mianyang) and some typical experimental results are presented.

X. Wang (✉)
State Key Laboratory of Aerodynamics, China Aerodynamics Research and Development Center, Mianyang, China
e-mail: skla_cardc@126.com

J. Zhang · P. Chen · Z. Chen
Key Laboratory of Aerodynamic Noise Control, China Aerodynamics Research and Development Center, Mianyang, China

Y. Zhou et al. (eds.), *Fluid-Structure-Sound Interactions and Control*, Lecture Notes in Mechanical Engineering,
https://doi.org/10.1007/978-981-10-7542-1_49

2 5.5 m × 4 m Anechoic Wind Tunnel

5.5 m × 4 m anechoic wind tunnel is a closed-circuit wind tunnel with a convertible open or closed test section. The open test section is surrounded by an anechoic chamber (27 m × 26 m × 18 m) covered with wedges, which yields more than 99% sound absorption above 100 Hz. The closed test section can be moved from the preparation zone into the chamber using air cushions, which then connects the nozzle and the first diffusion section (with the collector been moved out). The dimension of the closed test section is 14 m × 5.5 m × 4 m. For open test section, the maximum wind speed is 100 m/s, and for closed test section, the maximum wind speed is 130 m/s. The turbulence level in the potential core area is about 0.2% (Fig. 1).

Phased microphone arrays are used to identify the location of aerodynamic noise sources and free-field microphones are used to evaluate the noise level of the source. In open-jet configurations, they are located outside of the jet. CARDC owns two types of microphone arrays: a small aperture microphones array (SAMA, 0.72 m) and a large aperture microphone array (LAMA, 3 m). SAMA consists of 40 GRAS quarter inch microphones, and LAMA consists of 140 GRAS quarter inch microphones. The array design follows the way of Underbrink (2001) to achieve high spatial resolution and large dynamic range capability. A NI-PXIe bus based multi-channel data acquisition (DAQ) system is used to acquire aeroacoustic data. The DAQ system consists of 16 PXIe-4499 data acquisition cards, and each card houses 16 channels, which sums up to 256 channels in total. With the use of a MXI control suite (PXIe-PCIe 8375) and a fibber glass wire, remote data acquiring is realized.

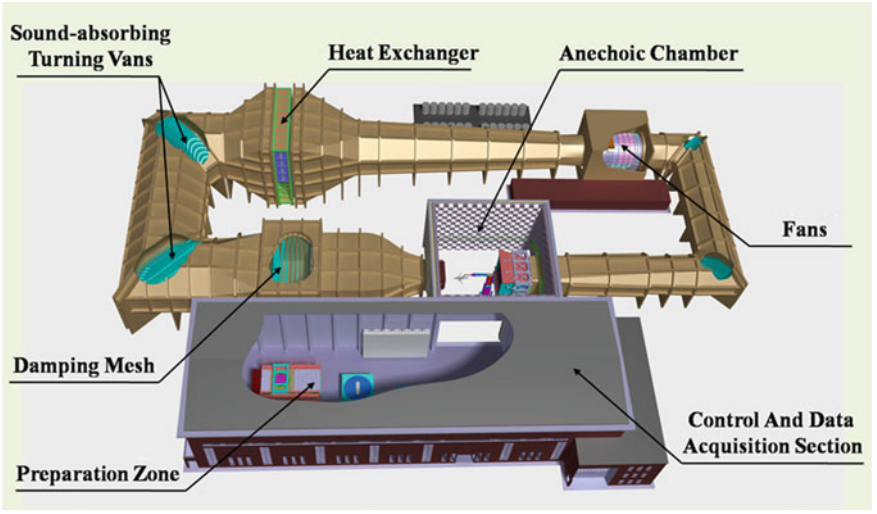

Fig. 1 Sketch of CARDC 5.5 m × 4 m anechoic wind tunnel. By acoustic treatment of driven fan, corner vanes, jet catcher and the first diffusion section, a very low background noise level (75.6dBA, 80 m/s) in the open-jet test section is achieved

3 Data Processing Method

Conventional beamforming algorithm is used to processed the microphone array data to obtain noise map of the source. Firstly, the transient sound signal is transformed into frequency domain using discrete Fourier transform. To reduce the influence of jet noise, the acquired signal is preprocessed using a Chebyshev filter. Secondly, the cross spectrum matrix (CSM) of the microphone array is calculated. The CSM is of Hermite type and its element is given as follows:

$$G_{mm'}(f) = \frac{2}{KW_s T_B} \sum_{k=1}^{K} \left[p^*_{mk}(f) p_{m'k}(f) \right] \tag{1}$$

Here, K is the total number of data blocks and W_s is the window constant. $p_{m'k}(f)$ represents the kth block of data of the mth microphone. Thirdly, the steering vector of scan grids is calculated.

$$\hat{e} = \begin{bmatrix} e_1 & e_2 & \dots & e_M \end{bmatrix}^T \quad e_m = A_m \frac{R_m}{R_c} \mathrm{e}^{j2\pi f \tau_m} \tag{2}$$

where, A_m is the amplitude factor, and R_m is the distance from a scan grid to the mth microphone. R_c is the distance from a scan grid to the center of the array. τ_m is the total delay time. As the open-jet aeroacoustic measurement is subject to shear layer effect, τ_m needs to be corrected. Amiet's method [2] is used for its simplicity and efficiency. Finally, on each scan grid, the output spectrum density is obtained.

$$P(\hat{e}) = \frac{\hat{e}^T \hat{G} \hat{e}}{M^2} \tag{3}$$

The diagonal elements of the cross spectrum matrix can be removed to optimize CSM and improve the quality of beamforming results, and de-convolution algorithms (i.e., CLEAN-SC) can be used to further improve the results.

4 Typical Results and Discussion

A C919 1:14 scaled aircraft model test was performed in CARDC 5.5 m × 4 m anechoic wind tunnel (see Fig. 2). 140 quarter inch G.R.A.S microphones were used to identify the location of noise sources. During the test, the model is on

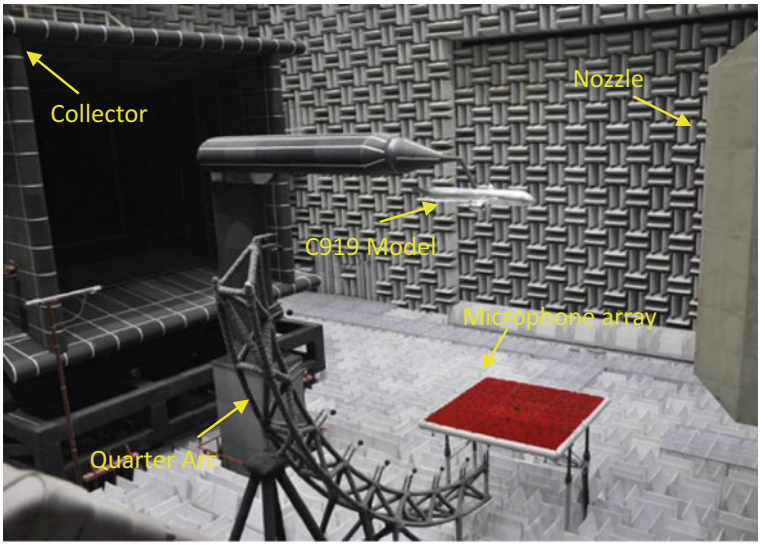

Fig. 2 A C919 1:14 scaled aircraft model test performed in CARDC 5.5 m × 4 m anechoic wind tunnel. The aircraft model is in landing configuration, the wind speed u_0 varies from 40 to 70 m/s, and the angle of attack $\alpha = 0^{\circ}, 3^{\circ}, 6^{\circ}$

landing configuration. The wind speed u_0 varies from 40 to 70 m/s, and the angles of attack $\alpha = 0^{\circ}, 3^{\circ}, 6^{\circ}$.

It can be seen from Fig. 3 that when the angle of attack $\alpha = 0^{\circ}$, the main noise source is located at the landing gear, high-lift device, flap-wing joint points, slat-fuselage conjunction positions. As the analyzing frequency increases, the spatial resolution of noise source is increased too. Fix the wind speed and increase the angle of attack, the main noise source location is changed accordingly. The slat-fuselage noise source level is much stronger than that of other noise sources. Therefore, the slat-fuselage area needs to be carefully treated during design stage.

A 1:8 scaled high speed train model test was performed in CARDC 5.5 m × 4 m anechoic wind tunnel on the design stage for head selection. During the test, themodel is on three-carriage configuration, and key components, e.g., bogies, pantograph, and rail tracks are installed at different test phases.

LAMA is used to identify the location of noise sources and 30 far-field microphones are used to evaluate the far-field noise level of the source. The spectrum is calculated from a single microphone in the middle of the second line (Fig. 4). Figure 5 shows that below 1.5 kHz, the front bogie noise level is stonger than that of the phantograph, and above 2 kHz it is reversed. The phantograph generates tones at 1.5, 3 kHz (1st harmonic) and 4.5 kHz (2nd harmonic), which is thought to be caused by the vortex shedding from the phantograph.

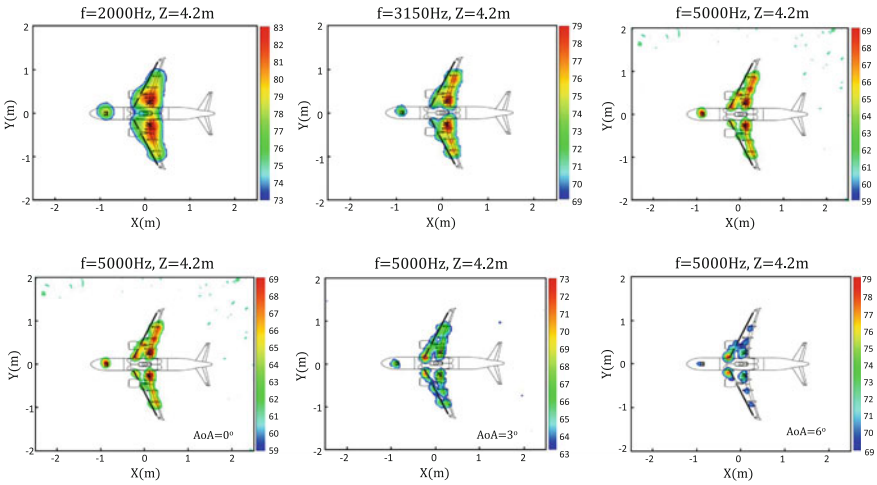

Fig. 3 Noise map of a C919 1:14 scaled aircraft model. (Upper) wind speed $u_0 = 60$ m/s, angle of attack $\alpha = 0°$, $f_0 = 2$, 3.15, 5 kHz; (Lower) wind speed $u_0 = 60$ m/s, $f_0 = 5$ kHz, and angle of attack $\alpha = 0°$, 3°, 6°

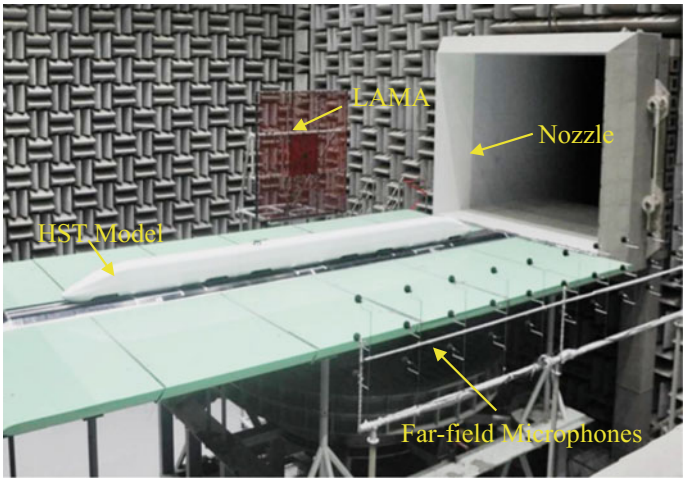

Fig. 4 A 1:8 Scaled high speed train model test performed in CARDC 5.5 m × 4 m wind tunnel. A vertical microphone array and 30 free-field microphones are used to identify noise source and evaluate far-field noise level

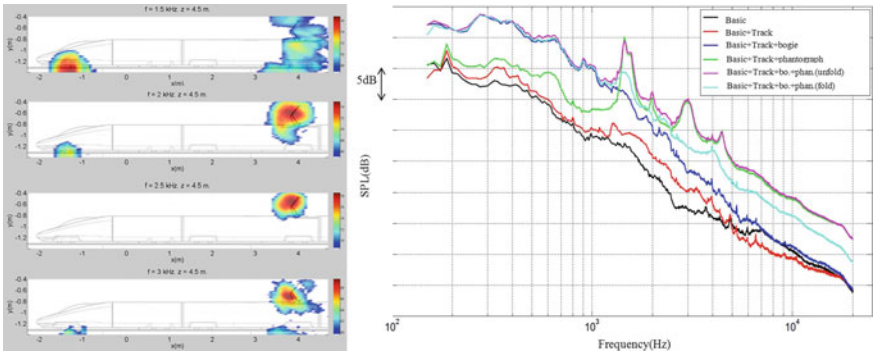

Fig. 5 Noise map of a 1:8 high speed train model (left) and the power spectrum of the far-field noise on different test configurations, $u_0 = 250$ km/h (right)

5 Conclusions

An introduction of CARDC 5.5 m × 4 m anechoic wind tunnel and some typical results are presented. A C919 1:14 scaled aircraft model test shows that noise sources are mainly located at the landing gear, high-lift device, flap-wing joint points, slat-fuselage conjunction positions. And a 1:8 scaled high speed train model test shows that main noise sources are located at the first bogie and pantograph position.

Acknowledgements The research conducted in this paper is supported by National Natural Science Foundation of China (grant No. 11504417).

References

1. Humphreys WM (1998) Design and use of microphone directional arrays for aeroacoustic measurements. AIAA J, 98–0471
2. Amiet RK (1975) Correction of open jet wind tunnel measurements for shear layer refraction. AIAA, 75–532

The Simulation of Tip-Leakage Flow and Its Induced Noise

Shucheng Zhai, Ziying Xion and Hongxing Sun

Abstract In this study, the large eddy simulation (LES) numerical method is applied to simulate the flow filed of a foil with the gap between tip and end plate. The flow field details of three different tip gaps were simulated. The noise source induced by the tip-leakage flow was also predicted by LES method, and then the noise characters of foils with different tip-leakage were calculated by acoustic analogy method using Ffowcs Williams and Hawkings (FW-H) equation. The correlation between noise and vortex was analysed by using the spectral method. This study will give information to rotor tip design.

Keywords Tip-leakage flow · CFD · Noise

1 Introduction

The tip-leakage flow exists extensively in rotary machine such as duct propeller, hydro turbine, jet engine and so on. This kind of high speed separate flow generated by the pressure differentials of rotor surface will induce unwanted vibration and noise which many affect comfort or destroy the structure of ship. So many investigations have be done to bring insight into the mechanism of tip-leakage flow and find method to control it to reduce the negative impact [1]. Many researches focused on the flow characters in tip clearance by numerical or experimental method, and want to explain the correlation between the tip vortex and geometry of the blade tip [2, 3].

The objective of the current work is try to find the correlation between tip-leakage vortex and its induced noise. Firstly to analyse the flow structure of tip vortex generated by NACA 0009 hydrofoil. Secondly to evaluated the noise signal of hydrofoil and investigate the differents between the noise and vorticity spectrum.

S. Zhai (✉) · Z. Xion · H. Sun
National Key Laboratory on Ship Vibration and Noise, China Ship Scientific and Research Center, Wuxi, China
e-mail: zsc_cssrc@163.com

Y. Zhou et al. (eds.), *Fluid-Structure-Sound Interactions and Control*, Lecture Notes in Mechanical Engineering,
https://doi.org/10.1007/978-981-10-7542-1_50

2 Model Details and Computational Method

The investigation model is a NACA0009 profile with a chord of c = 100 mm and a span of 150 mm see in Fig. 1a. This hydrofoil is mounted in the channel with the gap *t* between the blade tip and the wall, as shown in Fig. 1b, c. The incidence of the foil is 10°. The flow filed and radiated noise are simulated by commercial code Fluent in the solving condition that the Reynolds number based on the chord is 1.01×10^6. The upstream velocity at inlet is 10.2 m/s. Three kinds of tip-leakage $t/c = 0.02$, $t/c = 0.05$ and $t/c = 0.1$ are compared to find the differences in radiated noise and any correlation between clearance flow. The unstructured hexahedron meshes, about twenty million cells, are used in simulation, and there are at least 20 cells in clearance to capture the details flow. We use LES method with dynamics SGS model to solve the flow field and also the noise source. Then the wall fluctuating pressure generated by hydrofoil and its endplate is used as a input noise source terms of FW-H equation to predict the far field noise.

3 Results and Discussion

3.1 Flow Stucture

The tip-leakage flow structures of different clearance ratios t/c = 0.02 and t/c = 0.1 are analysed.

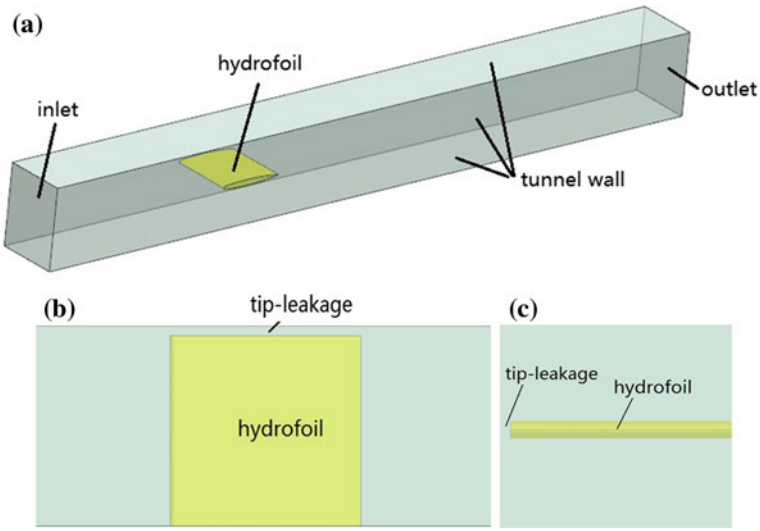

Fig. 1 **a** Computational domains, **b** top view, **c** downstream view of model

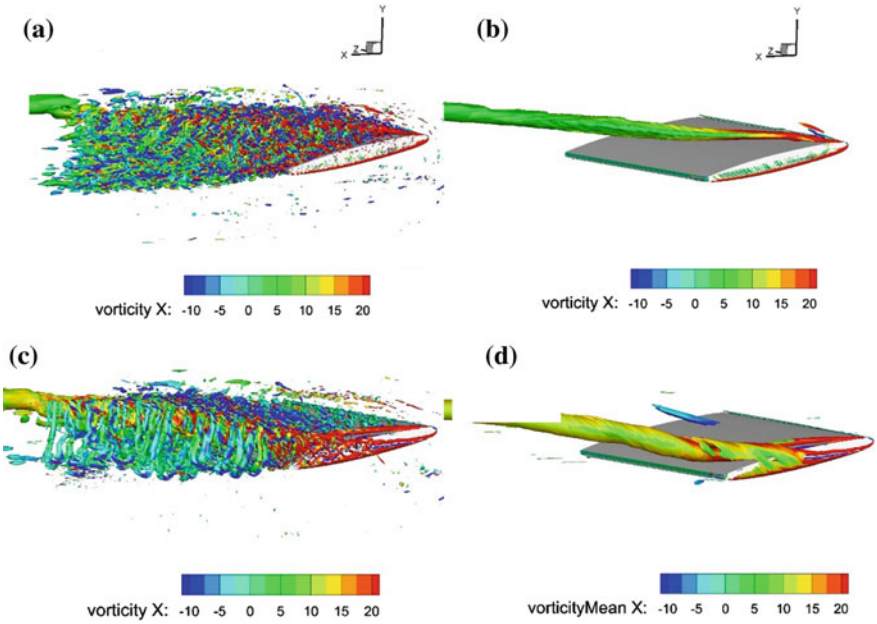

Fig. 2 Instantaneous flow field and averaged flow field: **a** instantaneous flow field of t/c = 0.02 Q = 1 isosurface, **b** averaged flow field of t/c = 0.02 Q = 1 isosurface, **c** instantaneous flow field of t/c = 0.1 Q = 1 isosurface, **d** averaged flow field of t/c = 0.1 Q = 1 isosurface

Figure 2a–d show the instantaneous and averaged flow field which is process using time average on the instantaneous results simulated by LES method. The vortex isosurface is identified by Q criterion and rendered by axial vorticity value. The boundary layer flow structures on hydrofoil, such as hairpin vortex structure as well as in tip clearance, could be seen in instantaneous results. The tip vortex, induced vortex and tip separated vortex are shown clearly in the averaged results. There are some different between t/c = 0.02 and t/c = 0.1 results. The hairpin vortex in tip clearance is richer when t/c = 0.02 and disperse when t/c = 0.1. Comparing with averaged results, when increase the scale of clearance ratio, the flow separated vortex generated on pressure surface of hydrofoil will meet the tip vortex and mixed, then the influence range of tip vortex is increased and shown broken state. This enhanced effect of tip vortex is the mechanism of the hairpin difference shown in different tip-leakage ratios. The flow field validation is in Fig. 3. The calculations are shown good agree with the experimental results [1].

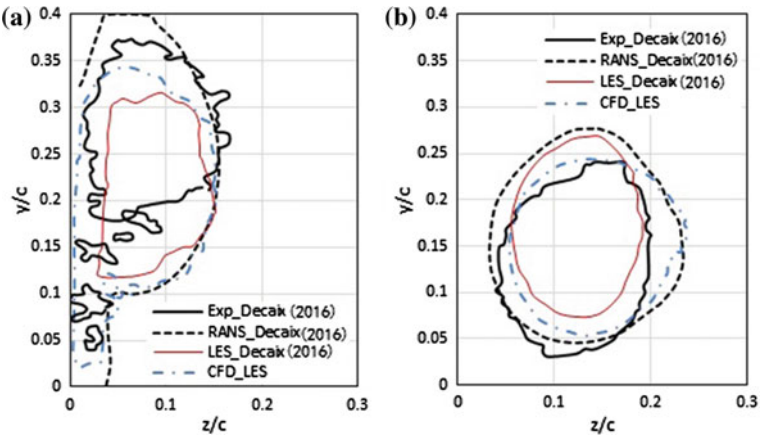

Fig. 3 Tip vortex flow validation: **a** $\omega_x^* = 2$, x/c = 1, t/c = 0.02, vortex isosurface, **b** $\omega_x^* = 4$, t/c = 0.1, x/c = 1, vortex isosurface

3.2 *Noise*

The noise results generated by different tip-leakage ratios t/c = 0.02, t/c = 0.05 and t/c = 0.1 are analysed. The acoustic receiver is at 1 m above the trailing edge on the middle chord. To collect the hydrofoil noise signal within 0.5 s, the sampling frequency is 20 kHz. The crude signal is processed by discrete Fourier analysis with hamming window and filtered by 1/3 octave filter processer.

The hydrofoil tip clearance flow is complex, the pressure gradient and the pressure fluctuation is seriously, so the noise source region contains not only the hydrofoil surface, but also the end plate close to the wing tip. As shown in Fig. 4.

Figure 5a is the 1/3OCT spectrum of foil with three different tip-leakages and the perpendicular distance from the noise calculate point to foil training edge is 1 m. In Fig. 5a, three spectrums show almost the same characters except at 1250 Hz frequency band. There is a strong peak in spectrum of foil with *t/c* = 0.05 and *t/c* = 0.1,

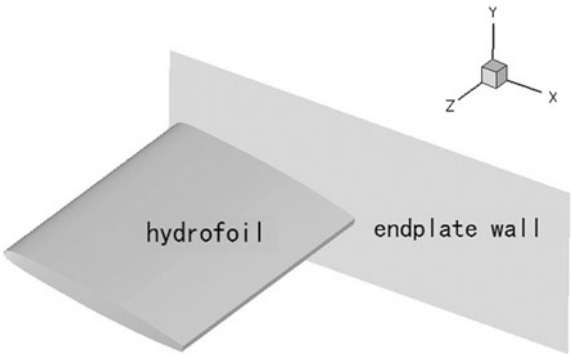

Fig. 4 Schematic diagram of the noise source surface

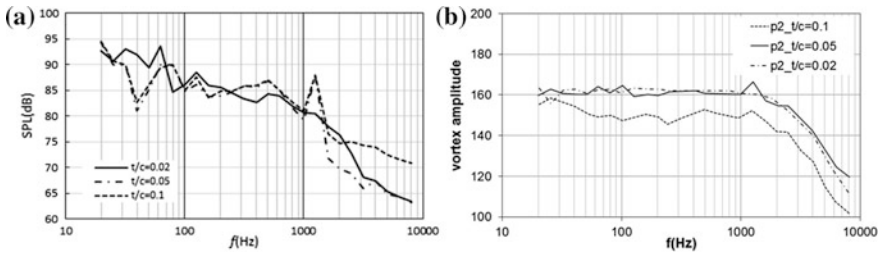

Fig. 5 **a** Acoustic spectrum level of foil with different tip-leakage, $P_{ref} = 1 \times 10^{-6}$ Pa. **b** Votrex spectrum of clearance separated flow

but without this phenomenon shows in $t/c = 0.1$. It is thought that the tip-leakage vortex occurs in the gap between the blade tip and the endplate because of the pressure gradient between the pressure side and suction side of hydrofoil. Some regular vortexes generated in the gap drop from the tip, when increasing the gap scale, which may excite the hydrofoil radiate noise. In order to confirm this speculation, some monitoring points were put close to the gap and to record the vorticity value with time. The spectrum analysis of vorticity time history is shown in Fig. 5b, which indicates that there is a clearly peak in $t/c = 0.05$ and $t/c = 0.1$ line. The frequency band is the same as shown in acoustic spectrum. Figure 6 is the tip vortex isosurface of the Q-criterion coloured by axial vorticity. The tip-separation vortex is well present for large gap $t/c = 0.1$ and vortex shedding could be seen clearly in cross section map. At small gap $t/c = 0.02$, the vortex is much more smaller and keeps away from the hydrofoil surface. When the tip gap is small, the tip endplate will be covered by boundary layer generated by tunnel wall. Then the pressure side vortex is hard to flow over the endplate and there is no influence to suction side vortex. The Strouhal number of the tip-leakage vortex shedding is $\mathrm{St} = ft/u_{\mathrm{inlet}} \approx 1.25$.

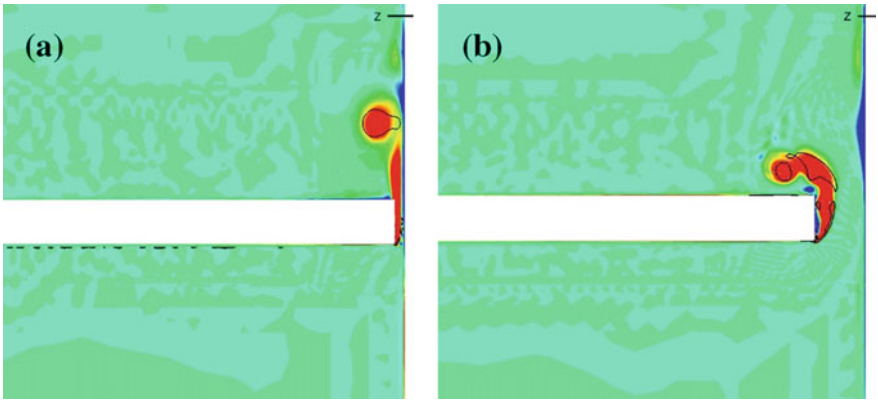

Fig. 6 The axial vorticity contoure of different tip-leakage ratio at the same x position x/c = 0.2, **a** t/c = 0.02, **b** t/c = 0.1

These characters mean that special tip-leakage could excite the acoustic peak because of the tip-separate vortex. Therefore, the results of this paper will give the designer a reference to choose gap scale of the rotary machine.

4 Conclusions

The tip-leakage flow and induced noise are analysed in this study. The LES and FW-H analogy method are used to predict the acoustic of hydrofoil with different tip-leakage ratios ($t/c = 0.02$ to $t/c = 0.1$) and incidence (10°). First, the LES computations are analysed to capture the main character of tip vortex and find their variety law with different tip-leakage ratios.

The noise results are analysed to describe the acoustic peak generated by the tip vortex. It is put in evidence that the vorticity spectrum of tip vortex also show the same peak frequency. For the small gap ($t/c = 0.02$), there is no tip-separation vortices are obervered. For the large gap ($t/c = 0.1$), the tip-separation vortices are distinct. The Strouhal number of tip vortex shedding is about 1.25.

For future works, the investigation of tip induced noise will be tested by hydrophone in laboratory and to verify the relationship between tip-separation and its shedding frequency.

References

1. Decaix J, Balarac M, Dreyer M, Farhat M (2016) RANS and LES computations of the tip-leakage vortex for different gap widths. J Turbul 16(4):309–341
2. Kato H, Taniguchi H, Matsuda K, Funazaki KI, Kato D, Pallot G (2011) Experimental and numerical investigation on compressor cascade flows with tip clearance at a low Reynolds number condition. J Therm Sci 20:481–485
3. You D, Wang M, Moin P, Mittal R (2006) Effects of tip-gap size on the tip-leakage flow in a turbomachinery cascade. Phys Fluids 18(10):683

Influence of Camber on Wall-Mounted Finite Airfoil Tonal Noise Generation

D. J. Moreau, T. F. Geyer, C. J. Doolan and E. Sarradj

Abstract Measurements of flow induced wall-mounted finite airfoil noise have been taken in an anechoic wind tunnel to examine the influence of camber on tonal noise production. The airfoils have an aspect ratio (ratio of airfoil span, L, to chord, C) of $L/C = 2$ and measurements encompass variations in camber of 0–8%. The results include far-field acoustic spectra and sound maps taken with a microphone array that reveal geometry effects on noise production.

Keywords Airfoil noise · Trailing edge noise · Tonal noise · Beamforming

1 Introduction

At low Reynolds numbers, tonal noise may be produced by airfoils with a laminar-transitional boundary layer at their trailing edge. The airfoil tonal noise spectrum is distinct and consists of a primary tone surrounded by multiple equispaced tones [1] commonly attributed to an aeroacoustic feedback loop between acoustic waves generated at the trailing edge and boundary layer instability waves that originate upstream [2]. While tonal noise from symmetric airfoils has been extensively investigated, aerodynamic geometries that include camber and finite span effects have been largely neglected. In an effort to improve our understanding of noise from realistic airfoil designs, this paper presents measurements of tonal noise produced by a wall-mounted finite airfoil with a flat ended tip and varying amounts of camber.

D. J. Moreau (✉) · C. J. Doolan
School of Mechanical and Manufacturing Engineering, UNSW,
Sydney, NSW 2052, Australia
e-mail: d.moreau@unsw.edu.au

T. F. Geyer
Technical Acoustics, BTU Cottbus - Senftenberg, 03046 Cottbus, Germany

E. Sarradj
Institute of Fluid Mechanics and Engineering Acoustics, TU Berlin, Einsteinufer 25,
10587 Berlin, Germany

Y. Zhou et al. (eds.), *Fluid-Structure-Sound Interactions and Control*, Lecture Notes in Mechanical Engineering,
https://doi.org/10.1007/978-981-10-7542-1_51

2 Experimental Method

Experiments were performed in the aeroacoustic open jet wind tunnel at the Brandenburg University of Technology. The facility contains a rectangular nozzle of size 0.28 m × 0.23 m. The test section is surrounded by a chamber that has absorbing walls on three sides and a planar 56 channel microphone array on the ceiling (see Fig. 1).

The airfoil models used in this study have NACA0012, NACA2412, NACA4412, NACA6412 and NACA8412 section profile (0–8% camber at 40% chord). The airfoils were each mounted (one at a time) to a side plate at zero degree (geometric) angle of attack and the side plate was in turn flush mounted to the nozzle (see Fig. 1). The airfoils have a chord of $C = 70$ mm, a span of $L = 140$ mm and an aspect ratio of $L/C = 2$. The side plate has dimensions of 0.36 m × 0.4 m and the airfoils were mounted with their leading edge positioned 0.11 m downstream of the nozzle exit plane. In all tests, the airfoil surfaces were untripped. The wall boundary layer encompasses 6.7% and 3.4% of the airfoil span at $U_\infty = 10$ and 50 m/s, respectively.

Noise data were recorded at flow speeds of $U_\infty = 10$–50 m/s corresponding to Reynolds numbers of $Re_c = 4.6 \times 10^4 - 2.3 \times 10^5$ using the microphone array that was positioned 0.71 m above the NACA0012 airfoil trailing edge. For each channel, 40 s of data were recorded with a sampling frequency of 51.2 kHz. Averaged sound

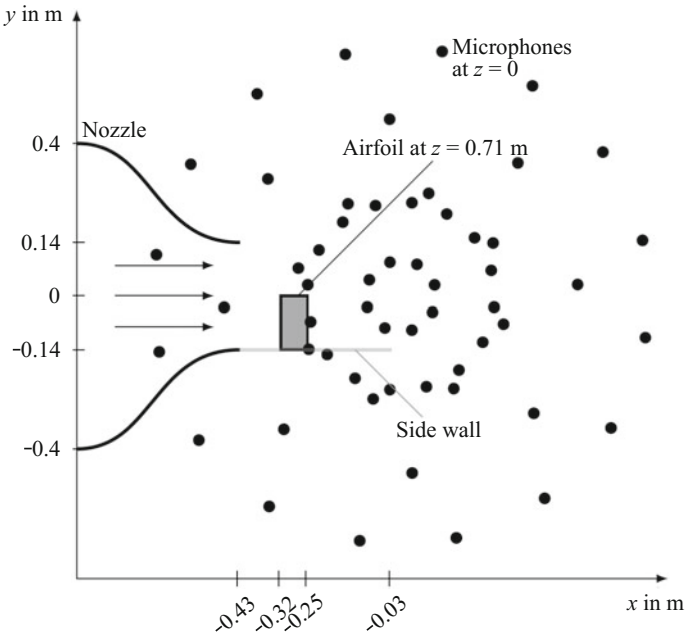

Fig. 1 Top view of the nozzle, test model and microphone array

source contribution maps were calculated and are displayed in 1/3-octave bands. Narrowband spectra have also been obtained by integrating the noise sources in the sound map over a three-dimensional volume encompassing the airfoil.

3 Experimental Results

Figure 2 shows narrowband acoustic spectra for the NACA0012 and NACA8412. Spectral maps for all five airfoils are shown in Fig. 3.

Figures 2 and 3 show camber influences the number and intensity of the tones produced by the airfoils. The highest amplitude tonal noise is produced by the NACA0012 and NACA2412. These airfoils both produce a high amplitude primary tone accompanied by a number of weaker side tones. Harmonics of the fundamental tonal contribution are also visible in the noise spectra. In comparison, the spectra for the NACA4412, NACA6412 and NACA8412 display a set of weaker equispaced tones with the side tones being of similar intensity to the primary tone.

Figure 4 shows sound maps for the NACA0012 and NACA8412 at $U_\infty = 50$ m/s. In Fig. 4, the airfoil is shown as a dotted line, x is the streamwise direction where the flow is from left to right and y is the spanwise direction. The origin is located at the centre of the array.

The sound maps in Fig. 4 show the dominant noise source at 2 kHz is the wall junction, suggesting that the interaction of boundary layer vorticity with the airfoil is responsible for low frequency noise. Higher levels of junction noise are produced

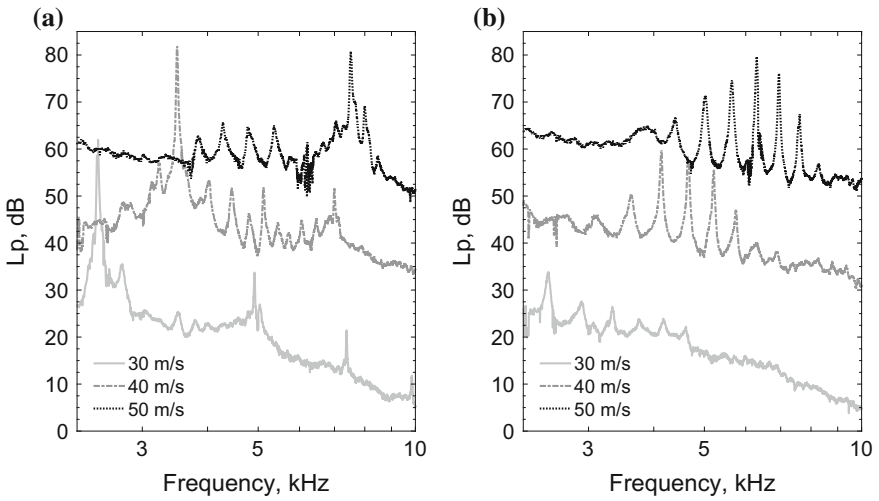

Fig. 2 Narrowband acoustic spectra: **a** NACA0012 and **b** NACA8412. Spectra have been offset by 15 dB with each increase in flow speed

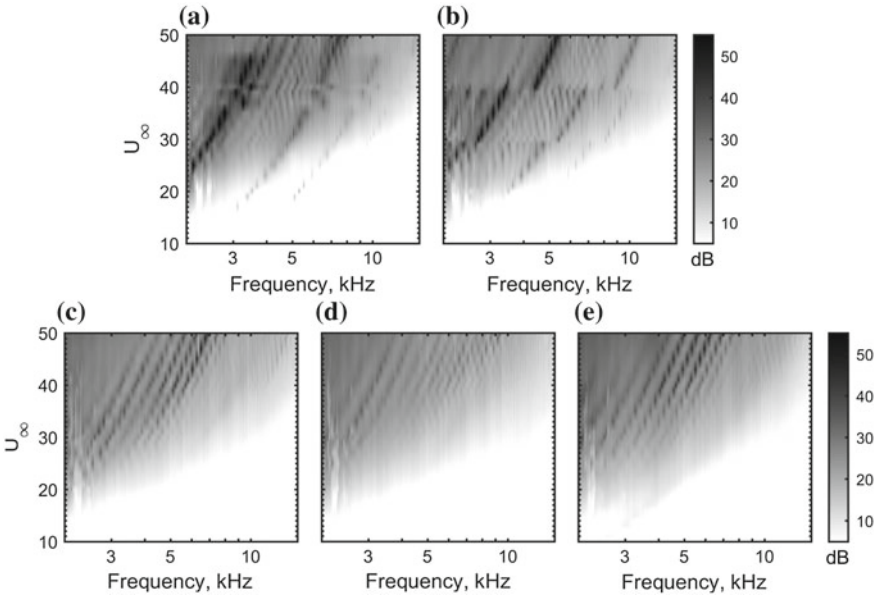

Fig. 3 Tonal noise spectral maps: **a** NACA0012, **b** NACA2412, **c** NACA4412, **d** NACA6412 and **e** NACA8412

by the NACA8412. At frequencies above 2 kHz, the dominant noise source location is the trailing edge. Trailing edge noise distributed along the airfoil span is the primary noise generation mechanism of the NACA0012 at a frequency of 4 kHz. In comparison, the NACA8412 produces high amplitude noise at the trailing edge-wall junction at this frequency.

The NACA0012 and NACA8412 produce primary tones in the 8 and 6.3 kHz 1/3 octave band, respectively (see Fig. 2). The sound maps show that for the NACA0012, tonal noise production is occurring with the trailing edge noise source located in the region near the airfoil's free end. In contrast, tonal trailing edge noise occurs at the mid-span of the NACA8412.

At 16 kHz, both airfoils produce trailing edge noise distributed along the entire span. At this frequency, higher levels of trailing edge noise are produced by the NACA0012. An additional noise source is also detected at the airfoil trailing edge-tip of the NACA8412.

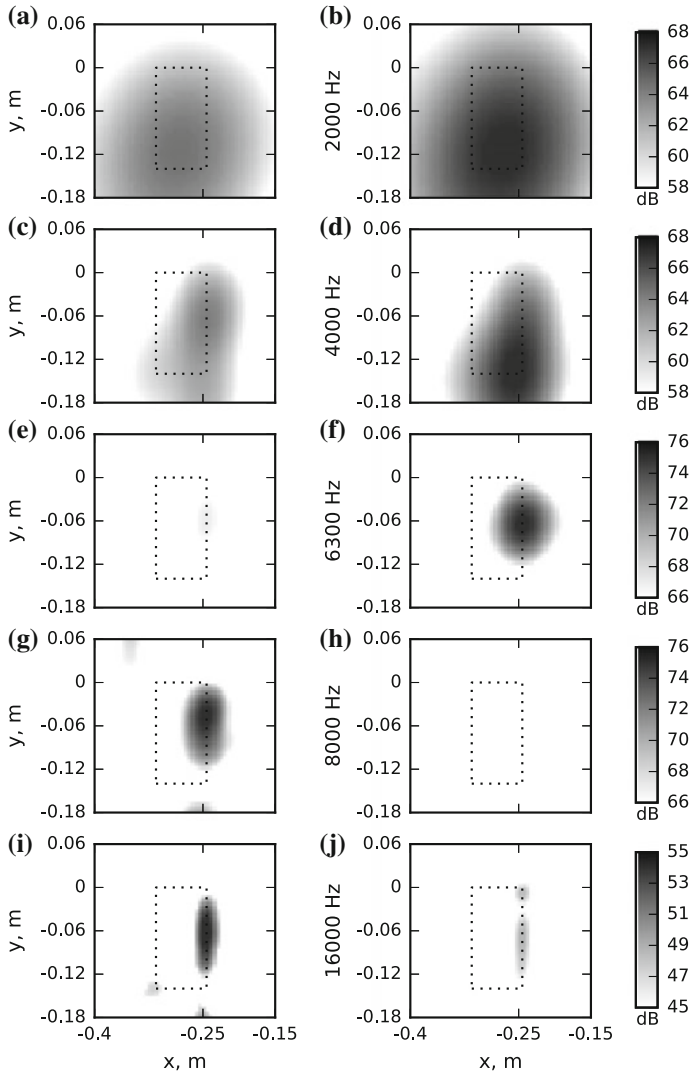

Fig. 4 Sound maps at $U_\infty = 50$ m/s: NACA0012 in (**a**), (**c**), (**e**), (**g**) and (**i**) and NACA8412 in (**b**), (**d**), (**f**), (**h**) and (**j**). The airfoil-wall junction is at $y = -0.14$ and the airfoil tip is at $y = 0$

4 Conclusion

An investigation of the tonal noise generated by wall-mounted finite airfoils with variations in camber has been presented. The results include acoustic spectra and beamforming sound maps that reveal geometry effects on noise production. This work has been supported by the Australian Research Council under DE150101528.

References

1. Moreau DJ, Doolan CJ (2016) Tonal noise production from a wall-mounted finite airfoil. J Sound Vib 363:199–224
2. Arbey H, Bataille J (1983) Noise generated by airfoil profiles placed in a uniform laminar flow. J. Fluid Mech. 134:33–47

Study of Passive Control of Jet Noise by Blind Holes on Nozzle Inner Wall

Z. Shi, J. Lin and H. Lai

Abstract In this paper, the flow characteristics and the noise of a subsonic jet are studied by experimental and computational methods. Blind holes are added to the inner wall of a subsonic round nozzle. Measurements of sound pressure signals are combined with large-eddy simulation to study the flow structures and the noise control. The results show that the porous wall of the subsonic nozzle has changed the vortical structures and the shear layer, and then the radiated sound is changed.

Keywords Aeroacoustics · Jet noise · Porous structure · Sound test

1 Introduction

Jet flow is one of the main noise sources in an aircraft. In nowadays' task of controlling the aircraft noise, revealing and controlling the sound sources in the jet flow seems to be an urgent and the first step. The study of jet noise can be traced back to 1950s when Lighthill [1, 2] published his two-part paper on aerodynamic sound. In those years, the source terms in the acoustic analogy equations were known as the sound source. By so far, the turbulent flow made up of random assortment of small eddies has been recognized as the physical source of the jet noise [4]. As pointed out by Tam et al. [3], large and fine-scale turbulent structures existing in the shear layer of the jet flow are two types of noise sources. It has also been proved that large vortex structures are somewhat the more deterministic jet noise sources by experiment and theoretical deduction [3, 5]. For the purposes of noise suppression, studying the development and evolution of large turbulence structures and seeking the proper way to reduce their noise are just the tasks for jet noise controlling.

Z. Shi · J. Lin · H. Lai (✉)
Key Lab of Pressurized Systems and Safety, Ministry of Education,
East China University of Science and Technology, Shanghai 200237,
People's Republic of China
e-mail: hlai@ecust.edu.cn

Y. Zhou et al. (eds.), *Fluid-Structure-Sound Interactions and Control*, Lecture Notes in Mechanical Engineering,
https://doi.org/10.1007/978-981-10-7542-1_52

In this paper, the inner wall of a subsonic nozzle is changed to be porous by adding blind holes in it. The sound pressure signals in both near and far fields are measured. Sound pressure spectra with different blind holes are compared. In the meantime, large eddy simulation is carried out to find the relationship between the flow structures and the sound signals.

2 Experimental and Numerical Methods

The diameter of the studied nozzle, D_j is 10 mm. Compressed air is supplied by a system with an Unical GS compressor and a gas storage tank, which provides a maximum working flow rate of 1.75 m^3/min. Dwyer GFM-1145 gas flow regulator is used at the exit of gas tank to control the flow rate, which varies from 0 to 1000 L/min in this study. The uncertainty of flow-rate is 1.5% of the full scale. The measurements of noise radiation from the jet are carried out in an anechoic chamber. Sound pressure signals are measured by PCB 377B11 1/2-in. microphones, and its accuracy is ±2 dB in 3.15 Hz–10 kHz. The setting and position of experimental equipment are show in Fig. 1.

The porous wall is produced by a perforated cylinder attached to the lib of the nozzle by a sleeve. The three-dimensional (3D) model of the structure is shown in Fig. 2, while the size of the perforated cylinder is shown in Fig. 3. There are 10 rows of holes in the axial direction, and each row has 6 holes uniformly spaced in the circumferential direction. For simplicity, we use (*H-D*) to distinguish the perforated cylinders, where *H* is the depth of the holes while *D* is their diameter.

Large eddy simulation is carried out for jet flows. Structured grids are generated for calculations. The nodes for the baseline nozzle and the (3-3) porous nozzle are 2.9 millium and 3.9 millium, respectively. The dynamic Smagorinsky-Lilly subgrid-scale model is employed for the closure of turbulence. Stagnant variables of pressure and total temperature are imposed at the nozzle inflow, characteristic

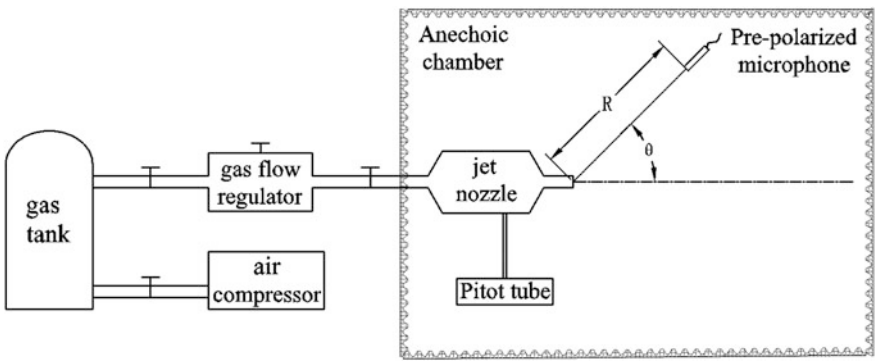

Fig. 1 Schematic of the test rig used to measure the jet noise

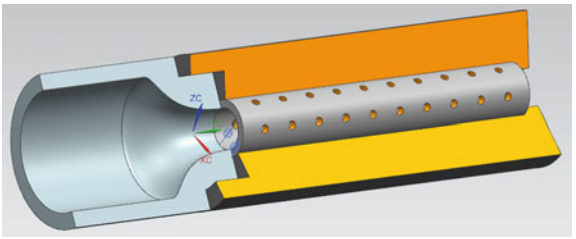

Fig. 2 3D model of the nozzle extension

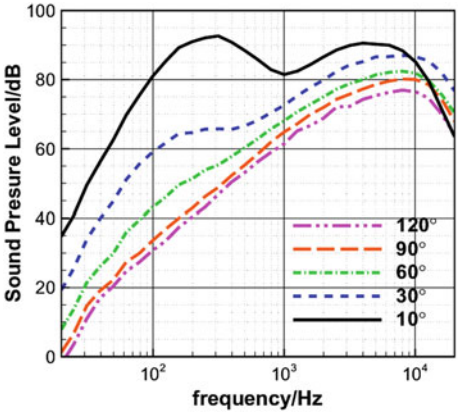

Fig. 3 Near-field sound signals

non-reflection conditions are imposed at other boundaries. The simulations are carried out using a commercial CFD package, the FLUENT.

3 Results and Discussion

The experiments are carried out at the Mach number $M = 0.6$. The dynamic pressure fluctuation measured by Pitot tube is lower than 3%, which confirms the accuracy of the experiment.

3.1 Sound Signal of Subsonic Jet

The near field sound pressure at $30D_j$ and the far field sound pressure at $100D_j$ are measured and shown in the 1/24 octave. Shown in Figs. 3 and 4 are the spectra of sound signals measured at five positions of angle, θ, which is defined as the angle between tested points to the flow direction. The near field spectral curves have a similar trend at most angle. Their peaks are at about 9000–12,500 Hz with the exception of the curve for $\theta = 10°$, whose peak appears at about 4000–5000 Hz.

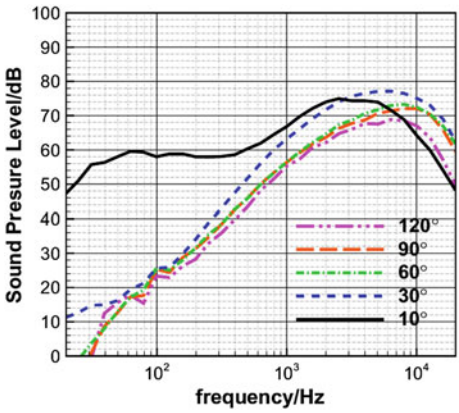

Fig. 4 Far-field sound signals

The OASPL rises with the decrease of angle θ and reaches the maximum overall level for $\theta = 10°$. Jet noise has obvious directivity, as pointed out by Tam [3]. Noises in different frequency-ranges are generated by different sources, which is recognized as large and fine-scale turbulent structures.

3.2 Noise Controlling Effects of Porous Inner Wall

Noise experiment of porous nozzles is compared with the baseline nozzle. The OASPL is presented in Table 1. It is increased in a large part of the cases due to the punishments caused by the blind holes in different situations.

Shown in Figs. 5 and 6 are the substraction of the far-field spectra of the porous nozzles from those of the baseline nozzle. The substraction is mostly influenced by the depth of the blind holes. With shallower holes, the $H = 1$ mm holes for example, the noise in the lower frequency range is enhanced, but the noise in the frequence range of 8000–20,000 Hz is interestingly cut down. For the cases with deeper holes, the $H = 4$ mm holes as shown in Fig. 6, the SPL is cut down by about 0.5–1 dB in the low frequency range, although the noise raises oppositely as a punishment in the high frequency range. With the increase of D, such punishment in the high frequency and the benefits in the low frequency are clearer.

Table 1 The OASPL in the acoustic far field (*unit* dBA)

θ	4-0	4-1	4-2	4-3	1-0	1-1	1-2	1-3
90	80.246	80.187	80.422	82.282	81.055	81.191	81.459	81.62
60	83.966	83.941	84.296	88.105	84.448	84.953	85.447	85.551
30	87.131	86.965	87.259	87.405	87.718	88.094	88.315	88.348
10	86.168	85.958	86.23	86.364	86.806	86.485	86.793	86.572

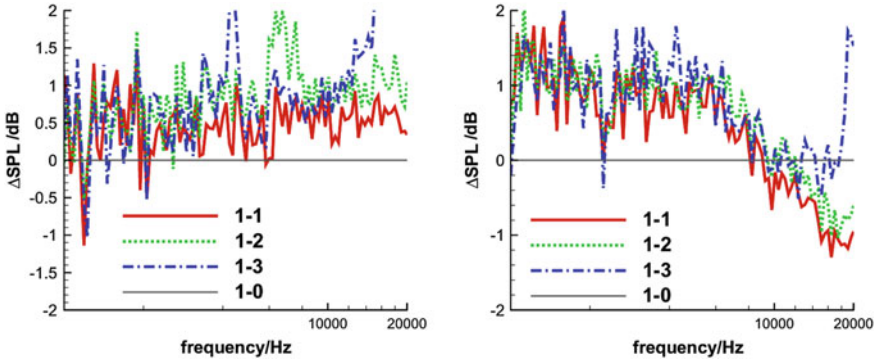

Fig. 5 Substracted spectra of porous nozzles from the baseline. Depth of blind holes $H = 1$ mm

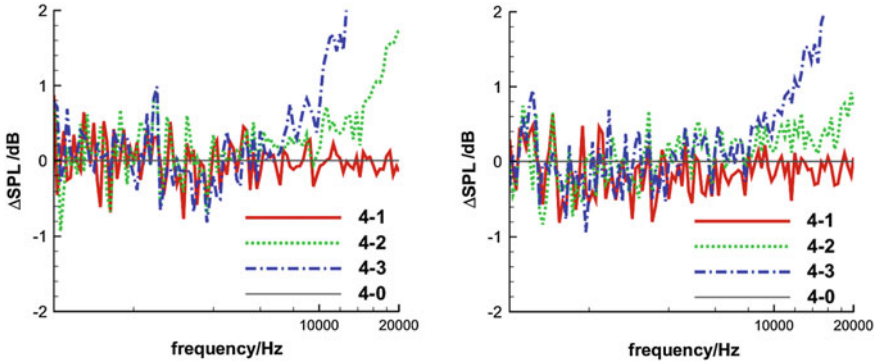

Fig. 6 Substracted spectra of porous nozzles from the baseline. Depth of blind holes $H = 4$ mm

3.3 The Source Flow

The averaged axial velocity distributions at the outlet and along the centerline are shown in Fig. 7. The blind holes have introduced radial disturbance in the jet flow, thus the high velocity zone becomes smaller in the radius. Radial profiles of turbulent fluctuation are shown in Fig. 8. The fluctuation level of radial velocity is weakened by the inner porous wall of the nozzle, which means the weakening of mixing in shear layer. The iso-surfaces of the Q criterion are compared in Fig. 9 to show the vortical structures. Kelvin-Helmholtz instability vortices at the beginning of jet break up into small eddies. The porous inner wall of the nozzle has slightly changed the flow condition by suppressing the large scale vortices. The disappearance spanwise vortices corresponding to the accelerated fragmentation of these vortices. On the other hand, small scale eddies are introduced. As a result, noise reduction in low frequency and punishment in high frequency are observed.

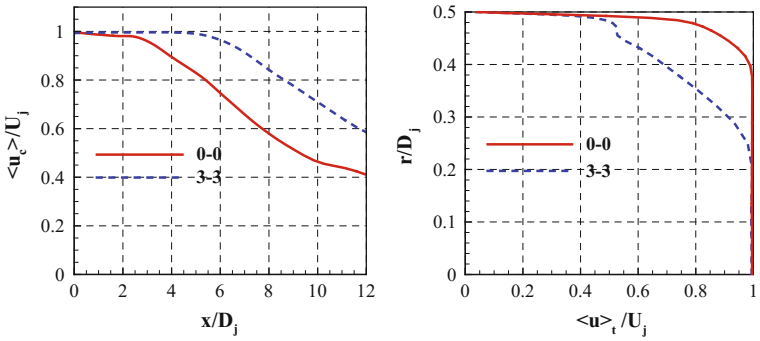

(a) u in cross-section at exit (b) u along nozzle centerline

Fig. 7 Comparison of axial velocity distributions

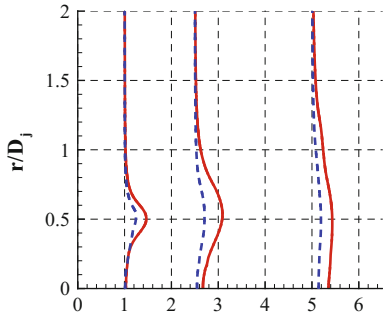

Fig. 8 $4\sqrt{\langle v'^2\rangle_{t\theta}}/U_j$ at $x/D_j = 1$, 2.5 and 5. Meanings of lines are the same with those in Fig. 7

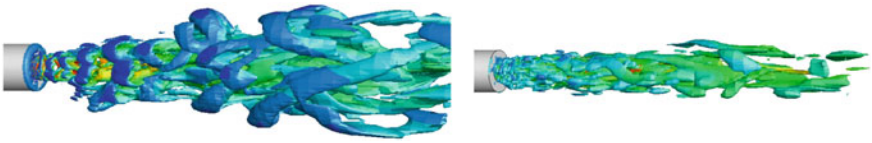

(a) Baseline nozzle (b) Nozzle with porous wall

Fig. 9 Iso-surfaces of Q-criterion

4 Conclusions

This paper studies noise controlling effect of adding blind holes on nozzle inner wall, using experimental and numerical methods for a subsonic jet flow at $M = 0.6$. The results show that low frequency noise is reduced while a punishment appears in

the high frequency noise. The simulations reveal that porous inner wall suppresses the large scale vortical structures, and thus results in noise reduction in low frequency.

Acknowledgements This study is funded by the NSFC under Grant 51576067.

References

1. Lighthill MJ (1952) On sound generated aerodynamically: I. General theory. Proc R Soc Lond Ser A 211:564–581
2. Lighthill MJ (1954) On sound generated aerodynamically: II. Turbulence as a source of sound. Proc R Soc Lond Ser A 222:1–32
3. Tam CKW, Golebiowski M, Seiner JM (1996) On the two components of turbulent mixing noise from supersonic jets. AIAA Paper 1996-1716
4. Tam CKW (1998) Jet noise: since 1952. Theoret Comput Fluid Dyn 10:393–405
5. Zaman KBMQ (1986) Flow field and near and far sound field of a subsonic jet. J Sound Vib 106:1–16

Numerical Study of Shock-Associated Noise in Axisymmetric Supersonic Jet

H. Li, Y. Luo and S. H. Zhang

Abstract Near field screech tone analysis of a typical underexpanded low supersonic circular jet issuing from sonic nozzle have been carried out numerically through solving axisymmetric Navier-Stokes equations directly. Screech tones's spectral information and the dynamic evolution of their corresponding flow structures and acoustic field are presented. Numerical results indicate that axisymmetric A_1 mode and A_2 mode screech tones are generated at the trailing edges of fourth and third shock-cell respectively. It is also found that screech tone's generation is associated with the compressive regions outside jet shear layer closely.

Keywords Axisymmetric supersonic jet · Screech tone · Shock cell DNS

1 Introduction

Most high-speed jet accompanying propulsion systems produces intense radiated jet noise. As well known, imperfectly expanded supersonic jet noise consists of three principal components: turbulent mixing noise, broadband shock-associated noise, and screech tones [8]. The turbulent mixing noise is directly associated with large-scale structures or instability waves in the shear layer; whereas, the broadband shock-associated noise and screech tones are associated with the interaction of these instability waves with the shock cell structures in the jet core. Specially, Powell's pioneering work [3, 4] indicated that screech tone is produced by a self-sustained

H. Li (✉) · Y. Luo · S. H. Zhang
State Key Laboratory of Aerodynamics, China Aerodynamics Research and Development Center, Mianyang 621000, Sichuan, China
e-mail: ustchuli@foxmail.com

Y. Luo
e-mail: yyLuoYong@foxmail.com

S. H. Zhang
e-mail: shzhang@skla.cardc.com

Y. Zhou et al. (eds.), *Fluid-Structure-Sound Interactions and Control*, Lecture Notes in Mechanical Engineering,
https://doi.org/10.1007/978-981-10-7542-1_53

feedback loop. Since then, lots of investigations on screech tone has been conducted via experiments and numerical approaches. Raman [7] provided a concise historical perspective and summary of process in jet screech research during almost 50 years from Powell's discovery. Good understanding of screech generation mechanism and prediction of screech frequency and amplitude are necessary in order to suppress screech tones without performance loss. It is well known that at low supersonic jet Mach numbers axisymmetric mode is the dominant screech mode. The objective of this paper is to examine where and how the screech tones of axisymmetric mode generate in typical low supersonic underexpanded jets.

2 Computational Details

Underexpanded supersonic circular cold jets are studied by direct numerical simulation using fifth order WENO scheme [1] for the axisymmetric Navier-Stokes equations in generalized curvilinear coordinate system. The jet is assumed to be supplied by a convergent nozzle whose designed Mach number is therefore equal to 1. The thickness of nozzle is $0.4D$ and $0.2D$ (where D is nozzle diameter) and the fully expanded jet Mach number is 1.19. The full computational domain is taken from $-5D$ to $40D$ in the streamwise direction and from $0D$ to $18D$ in the radial direction. Beyond the streamwise location of $15D$ and radial location of $6D$, grid cells are stretched and serve as sponge zones. Thompson's characteristic farfield boundary conditions are applied at left boundary and upper boundary regions. At the downstream boundary region, the non-reflecting outflow boundary condition is implemented. At the nozzle exit, the inflow plane is recessed by six cells so as not to numerically restrict or influence the feeback loop. The flow variables on the inflow plane are taken to be uniform corresponding to those at the exit of sonic nozzle. All nondimensional variables ar given as follows:

$$\rho_e = \frac{\gamma(\gamma+1)p_e}{2T_r},\ p_e = \frac{2}{\gamma}\left[\frac{2+(\gamma-1)M_j^2}{\gamma+1}\right]^{\gamma/\gamma-1},\ u_e = \left(\frac{2T_r}{\gamma+1}\right)^{1/2},\ v_e = 0 \quad (1)$$

where γ is equal to 1.4 and T_r is the reservoir temperature. For cold jet assumption, T_r is set to 1. Initially, the whole computational domain except nozzle inlet is set to ambient flow conditions as below:

$$\rho = 1,\ u = 0,\ v = 0,\ p = \gamma^{-1} \quad (2)$$

The unsteady flowfield containing sound waves are obtained and the generation mechanism of axisymmetric mode jet screech tone is investigated.

3 Results and Discussion

3.1 Shock-Cell Structure and Mean Velocity Profiles

A comparison of the present numerical schlieren and experimental schlieren photograph [5] show good agreement in shock cell structures (see Fig. 1). It is observed that the first two shock cells appear to be sharp and clear since the nearby shear layer instability wave is too weak to significantly affect the shock cells. However, when shear layer instability wave reaches the third and fourth shock cells, it has gained sufficient energy through streamwise growth. It interacts with the third and forth shock cells, which result in their deformation and produce screech tones. Figure 2 presents the comparison of our simulated time-averaged density along jet axis with Gao and Li's axisymmetric URANS result [2] and Panda and Seasholtz's experimental result [6]. It is shown that the first four shock cells agree well with the URANS result in both position and amplitude but there are deviations in the rest shock-cells. This is because that URANS method is more dissipative than present method and corresponding grid is more coarser than present grid. Both the present result and Li and Gao's axisymmetric URANS result have discrepancy with the experimental data behind the third shock cell. It results from excessive dissipation of numerical algorithm in the region before the eighth shock cell and axisymmetric N-S equations in the downstream region.

3.2 Screech Tone's Frequency and Sound Pressure Level

The time history of pressure signal is recorded at the selected monitor in the flowfield and later post-processing is to obtain spectral information using Fast Fourier Transformation techniques. Figure 3 displays the sound signal's spectral informations (frequency and SPL) of monitor located at the nozzle exit lip wall. The SPL shows that there are four spikes in the frequency spectrum range of larger than 5000 Hz. The two correspond to screech frequencies of 6567 Hz (128 dB, A_1 mode) and 8637 Hz (123 dB, A_2 mode), while the rest two correspond to frequencies of 12,087 Hz (125 dB, B mode harmonic) and 14310 Hz (123 dB, A_0 mode).

3.3 Axisymmetric Mode Screech Tone's Generation Mechanism

Figures 4 and 5 present the flow structures and acoustic waves related to screech tones of A_1 mode and A_2 mode respectively. In the figures, the part with orange red color is the flow structure characterized by numerical schlieren and the gray part is

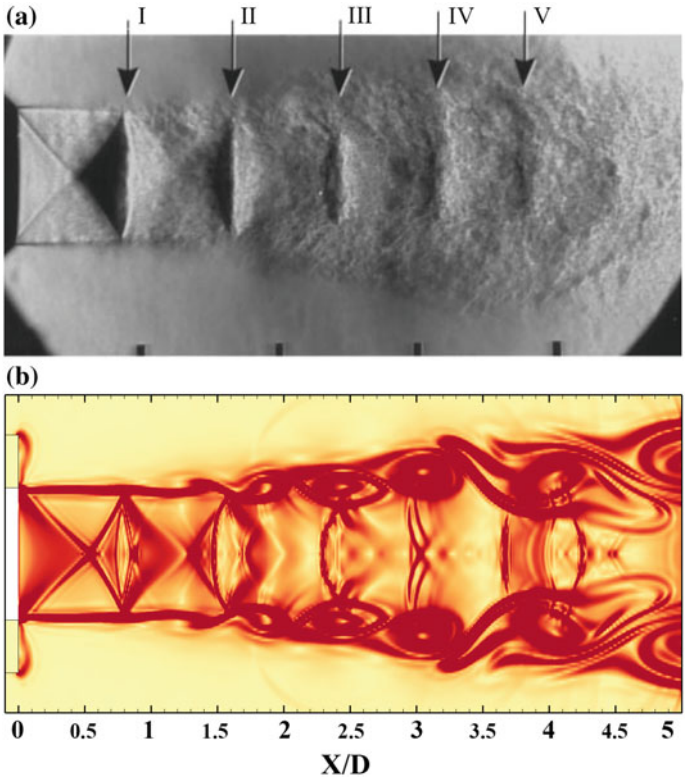

Fig. 1 Numerical schlieren (bottom) for shock cell structure of a supersonic jet at $M_j = 1.19$ and its comparison with experimental schlieren (top)

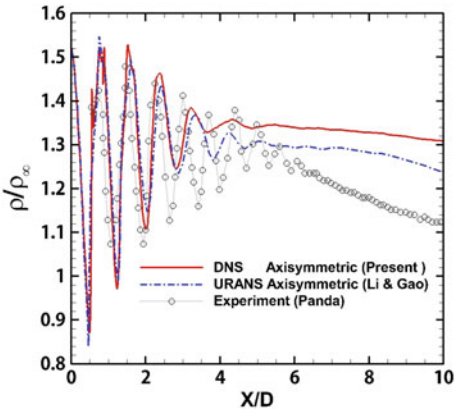

Fig. 2 The time-averaged density along the axis and its comparison with numerical and experimental results of screeching jet at $M_j = 1.19$

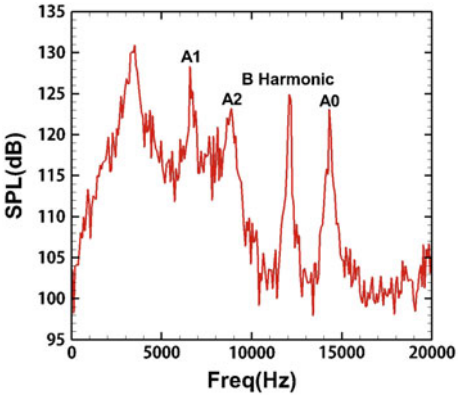

Fig. 3 Spectral analysis of sound signal at the point [0.0, 0.642] on the nozzle exit lip wall

the acoustic field characterized by dilatation. It is shown that screech tones of A_1 and A_2 modes emitted from the regions of third or fourth shock cells.

Figure 6a–f present the spatial and temporal evolution of flow structures and acoustic field corresponding to screech tone of A_2 mode in its complete cycle. At the beginning (t_0) of A_2 mode screech's period (T), a vortex saddle point in the jet shear layer is present at the third shock-cell's trailling edge (streamwise location of $x = 2.43D$ after nozzle exit), where the compressive region outside shear layer and shock tip inside shear layer are connected. As the continuous development of coherent structures in shear layer, such connection will be cut off by the vortices traveling dowstream. After that, the outside compressive region gradually stretches out a tentacle (see Fig. 6b). It will build bridge connection with upstream adjacent compressive region outside of shear layer to form an arc-shaped compressive wave (see Fig. 6c, d), which gradually grows from small to large and develops into screech tone traveling upstream finally (see Fig. 6e). At the same time, shock-tip inside shear layer will continue to interact with developing vortice moving downstream.

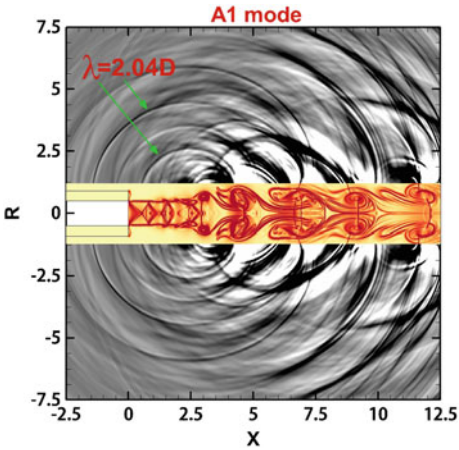

Fig. 4 Flowfield and acoustic field corresponding to the screech of A_1 mode

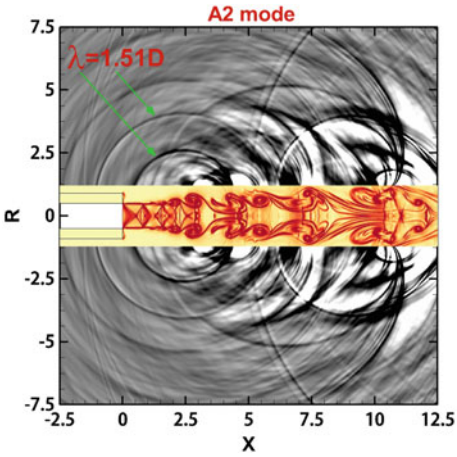

Fig. 5 Flowfield and acoustic field corresponding to the screech of the A_2 mode

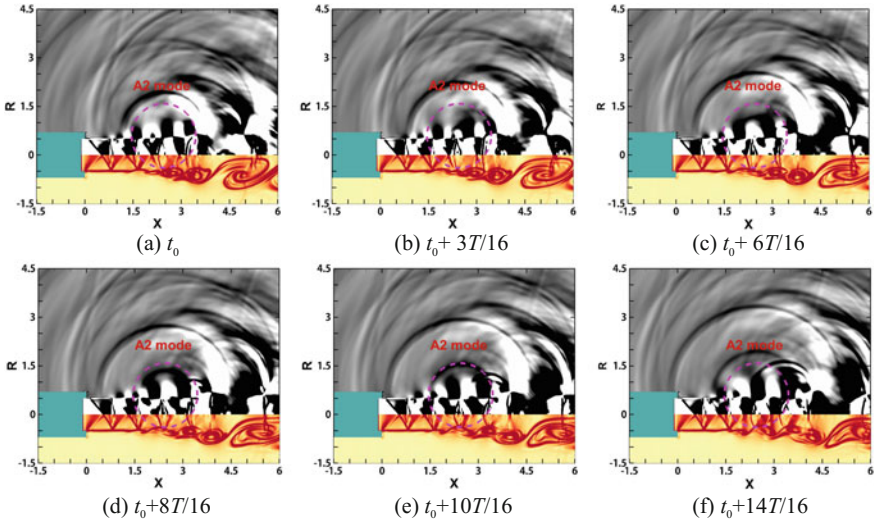

Fig. 6 Spatial and temporal evolution of flow structures and acoustic field associated with screech tone of A_2 mode in its period (the part with orange red color is flow structure characterized by numerical schlieren and the gray part is acoustic field characterized by dilatation (positive value means expansion, white color; negative value means compression, black color))

This interaction can lead shock wave to be bent and straightened, accompanying with shock-tip's backward and forward oscillation. At the ending of the period, an new vortex saddle point forms at original position, where the compressive region outside shear layer and shock tip inside shear layer make links again. As thus, the next A_2 mode screech generation cycle is ready to start.

Although it gives the spatial and temporal evolution of flow structures and acoustic field which describes the A_2 mode screech tone's generation, informations provided by Fig. 6 are not limited to that. At the fourth shock-cell's trailling edge (streamwise location of $x = 3.25D$), another vortex saddle point appears in the jet shear layer (see Fig. 6b), where the nearby flow structures and acoustic field undergo same spatial and temporal evolution as that occurs at streamwise location of $x = 2.43D$. Such dynamic process of evolution also generates acoustic wave (see Fig. 6f), and it should be screech tone of A_1 mode.

4 Conclusions

In this paper, direct numerical simulations of axisymmetric underexpanded supersonic jet issuing from sonic nozzle at jet Mach number of $M_j = 1.19$ are carried out using fifth order finite difference WENO scheme. The frequencies and amplitudes of near-field screech tones, including A_1 and A_2 mode, are obtained. The axisymmetric mode screech tone's generation mechanism is revealed through analyzing the corresponding spatial and temporal evolution of flowfield and acoustic filed in complete cycle. It is concluded that the axisymmetric A_1 mode and A_2 mode screech tones are generated at the trailing edges of fourth and third shock-cell respectively. The investigation also indicates the relationship between screech tones's generation and compressive regions outside jet shear layer.

References

1. Jiang GS, Shu CW (1996) Efficient implementation of weighted ENO schemes. J Comput Phys 126:202–228
2. Li XD, Gao JH (2005) Numerical simulation of the generation mechanism of axisymmetric supersonic jet tones. Phys Fluids 17(085105):1–8
3. Powell A (1953) On the noise emanating from a two-dimensional jet above the critical pressure. Aeronaut Q 4:103–122
4. Powell A (1953) On the mechanism of choked jet noise. Proc Phys Soc Lond B66:1039–1056
5. Panda J (1998) Shock oscillation in underexpanded screeching jets. J Fluid Mech 363:173–198
6. Panda J, Seasholtz RG (1999) Measurement of shock structure and shock-vortex interaction in underexpanded jets using Rayleigh scattering. Phys Fluids 11(12):3761–3777
7. Raman G (1999) Supersonic jet screech: half-century from powell to the present. J Sound Vib 225(3):543–571
8. Tam CKW (1995) Supersonic jet noise. Annu Rev Fluid Mech 27:17–43

Effect of Flow Separation on Acoustic Resonance in In-line Tube Banks

Satoshi Hino, Takahisa Mizoguchi, Hiromitsu Hamakawa, Eiichi Nishida and Eru Kurihara

Abstract In the present paper, the attention was focused on the effect of flow separation, which occurred at upstream of tube banks, on acoustic resonance in In-line tube banks. The flow separation was generated by using the orifice at the upstream of tube banks. We measured the acoustic pressure on the surface of side walls, spectrum, correlation and phase delay of acoustic pressure in the spanwise direction. The height of passage to diameter ratio at the orifice were 0, 2.8, 5.7, 8.6, 11.6, 14.4. When the acoustic resonance of first, second, and third mode occurred, the peak SPLs increased. As the gap velocity increased overall, the acoustic mode number and peak SPLs increased. As height of passage decreased, the peak SPLs decreased and the onset velocity of each mode of acoustic resonance increased. We have also discussed the prediction method to estimate the onset velocity of acoustic resonance with flow separation at upstream of tube banks.

Keywords Acoustic resonance · Vortex · Flow separation · Tube banks Boiler

1 Introduction

Acoustic resonance may occur in heat exchangers such as gas heaters or boilers which contain tube banks [2, 7, 8, 10]. It is generally known that vortex shedding frequency varies with the pitch ratio of the tube arrangement [3, 9, 11–15]. Chen [2], Fitz-hugh [3], Rae and Wharmby [11] have proposed Strouhal number charts for in-line tube banks to estimate the vortex shedding frequency of a heat exchanger at the design stage. On the other hand, the ducts of heat exchanger of power station

S. Hino · T. Mizoguchi · H. Hamakawa (✉) · E. Kurihara
Department of Mechanical Engineering, Oita University, Oita, Japan
e-mail: hamakawa@oita-u.ac.jp

E. Nishida
Department of Mechanical System Engineering, Shonan Institute of Technology, Fujisawa, Japan

Y. Zhou et al. (eds.), *Fluid-Structure-Sound Interactions and Control*, Lecture Notes in Mechanical Engineering,
https://doi.org/10.1007/978-981-10-7542-1_54

were a complicated three-dimensional structure [5, 6]. The proposed Strouhal number may be not effective to predict the acoustic resonance in actual boiler plant due to nonuniformity of incoming velocity at upstream of tube banks. This nonuniformity was caused by the flow separation at upstream of tube banks. Hamakawa et al. [4] have shown the characteristics of acoustic resonance with the flow separation at upstream of tube banks. However, the relation between the flow separation at upstream of tube banks and acoustic resonance was not clear in detail.

The purpose of the present investigation was to clarify the relation between the flow separation at upstream of tube banks and the occurrence of acoustic resonance. We have also discussed the prediction method to estimate the onset velocity of acoustic resonance with flow separation at upstream of tube banks.

2 Experimental Apparatus and Procedure

An schematic view of the experimental apparatus is shown in Fig. 1. The structure of this apparatus is similar to that of a boiler of a power station. The similarities are described in detail in the paper [5, 6]. This apparatus was a subsonic facility with a blower located at its upstream inlet. This was a rectangular duct of 900 mm in width, 150 mm in height, and 1275 mm in length (maximum), and was made of 20 mm thick acrylic plate. Tube banks were installed in the test section. The freestream velocity, U, ranged from 2.5 to 16.5 m/s at the test section inlet.

The in-line tube banks consisted of five rows, with 50 tubes per row. The tube diameter, D, was 9 mm. The tube pitch ratio of tube banks part in the flow direction, L/D, was 2.9, and the transverse direction, T/D, was 2.0. The tubes were 130 mm in length. They were rigidly fixed to both end walls of the test section.

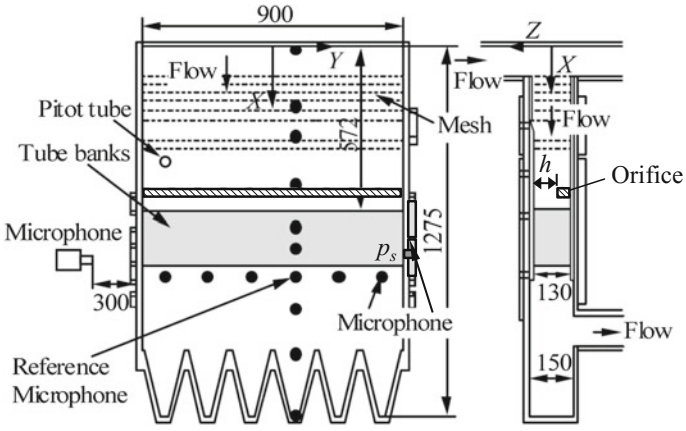

Fig. 1 Experimental apparatus

The flow separation was generated by using the orifice at the upstream of tube banks. The height of passage at the orifice, h/D, were 0, 2.8, 5.7, 8.6, 11.6, 14.4. We have measured the spectra of SPL as parameters of h/D from 0 to 14.4. No flow separation at upstream of tube banks was $h/D = 14.4$ ($h = 130$ mm). We calculated the through flow velocity, U_h, by using continuity equation and the freestream velocity, U. The tube gap velocity of tube banks was defined as $U_g = TU_h/(T - D)$. This gap velocity correlated the actual gap velocity. Reynolds numbers, based on the gap velocity, U_g, ranged from 3.0×10^3 to 1.7×10^4. The time variation of acoustic pressure was measured using a microphone mounted on the side wall as shown in Fig. 1. The amplitude and phase delay of the acoustic pressure fluctuations was measured by setting the reference microphone.

3 Results and Discussion

3.1 Acoustic Resonance with Flow Separation

The time variation of acoustic pressure was measured using a microphone mounted on the side wall as shown in Fig. 1. We calculated the spectrum of acoustic pressure by using Matlab. A single high peak was formed in the spectrum when the acoustic resonance occurred. Figure 2 show the variations of peak frequencies, plotted against the tube gap velocity, U_g, for five heights of passage at the orifice, h/D, respectively. The sizes of the symbols show the levels of peak SPLs. When the acoustic resonance of first, second, and third mode occurred at $h/D = 8.6$, 11.6 and 14.4, the peak SPLs increased respectively. As the gap velocity increased overall, the acoustic mode number and peak SPLs increased. As h/D decreased, St and peak SPLs decreased, and the onset velocity of each mode of acoustic resonance increased.

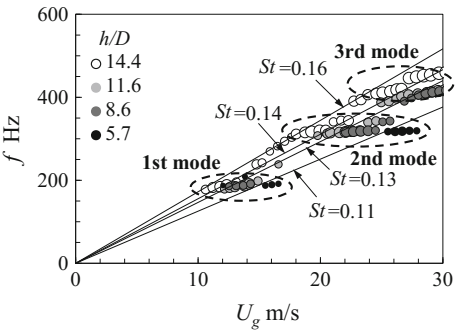

Fig. 2 Variation of peak frequency of SPL against gap velocity

3.2 *Prediction of Onset Velocity of Acoustic Resonance*

Hamakawa et al. [4] have shown the spanwise correlation length of vortex shedding from the last row of tube banks. The spanwise scale of vortex shedding from last row of tube banks became the height of flow passage, h, in present experiment. It is considered that the spanwise correlation scale of vortex became small in the tube banks because the oncoming flow of last row of tube banks was disturbed by the interaction between the vortex shedding from tube and the downstream tube. Therefore, we considered that the spanwise scale of vortex shedding from tube banks closed to the height of flow passage, h, in present experiment. In this situation, the sound intensity is proportional to the freestream velocity raised to the sixth power and the spanwise correlation length raised to the second power [1].

Figure 3a shows the variation of peak SPLs of acoustic resonance against height of passage, h. As h/D increased, peak SPLs increased for all acoustic modes. The peak SPLs of acoustic resonance increased due to the increase of excitation force of acoustic resonance which was proportional to spanwise scale of vortex raised to the seconds power. The rate of increase at the first mode was the largest in all acoustic modes.

Figure 3b shows the variation of gap velocity at peak SPLs as a function of height of passage at the orifice, h. As h/D increased, the gap velocity at peak SPLs decreased for all acoustic modes. The onset velocity of acoustic resonance reduced due to the increase of excitation force of acoustic resonance which was proportional to spanwise scale of vortex raised to the seconds power. The dotted lines are the theoretical results calculated by considering the increase of gap velocity kept the peak SPL. The theoretical results agreed well with the experimental results quantitatively. The variation of gap velocity could be predicted by considering the reduction of spanwise scale of vortex and the increase of gap velocity kept the peak SPLs.

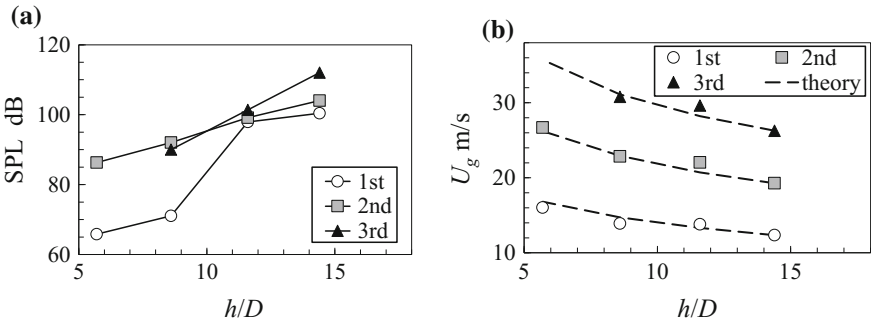

Fig. 3 Variation of peak SPLs and onset velocity of acoustic resonance against height of passage: **a** peak SPL, **b** onset velocity

4 Conclusions

The relation between the flow separation at upstream of tube banks and the occurrence of acoustic resonance were experimentally investigated in in-line tube banks of tube pitch ratio of 2.9. If the flow separation existed at upstream of tube banks, the acoustic resonance occurred from lower freestream velocity compared with no separation. As height of flow passage decreased, the acoustic resonance occurred at lower freestream velocity. When the acoustic resonance of first, second, and third mode occurred, the peak SPLs increased. As the tube gap velocity increased overall, the acoustic mode number and peak SPLs increased. As height of flow passage decreased, Strouhal number and the peak SPLs decreased, and the onset velocity of each mode of acoustic resonance increased for all acoustic modes. The variation of gap velocity could be predicted by considering the reduction of spanwise scale of vortex and the increase of gap velocity kept the peak SPLs.

Acknowledgements The work was partially supported by JSPS KAKENHI Grant Number 17K06232 from the Japan Society for Promotion of Science (in the Japan Ministry of Education and Science) for which the authors wish to express their sincere gratitude.

References

1. Blevins RD (1986) Flow-induced vibration. Robert E. Krieger Publishing Company, Malabar, Florida
2. Chen YN (1968) Flow-induced vibration and noise in tube-bank heat exchangers due to von Karman streets. Trans ASME J Eng Ind Ser B 94:134–146
3. Fitz-hugh JS (1973) Flow induced vibration in heat exchangers. In: Proceedings of UKAEA/NPL international symposium on vibration problems in industry. Keswick, England, Paper 427, pp 1–17
4. Hamakawa H, Hayashi H, Nishida E (2016) Improvement of prediction method of acoustic resonance by considering spanwise synchronization of vortex shedding from tube banks in boiler. J Jpn Boiler Assoc 399:21–26 (in Japanese)
5. Hamakawa H, Matsue H, Nishida E, Fukano T (2008) Acoustic resonance and vortex shedding from tube banks of boiler plant. J Fluid Sci Technol 3(6):805–813
6. Nishida E, Miki M, Sadaoka N, Hamakawa H, Fukano T (2005) Study on acoustic absorbers to suppress acoustic resonance in tube bundles of boiler. Trans JSME 71C(712):3458–3464 (in Japanese)
7. Owen PR (1965) Buffeting excitation of boiler tube vibration. J Mech Eng Sci 7:431–439
8. Païdoussis MP (1982) A review of flow-induced vibrations in reactors and reactor components. J Nucl Eng Des 74:31–60
9. Pettigrew MJ, Gorman DJ (1981) Vibration of heat exchanger tube bundles in liquid and two-phase cross-flow. In: Proceedings of the ASME pressure vessel and piping conference, vol 52, San Francisco, California, pp 89–110
10. Pettigrew MJ, Taylor CE (2003) Vibration analysis of shell-and tube heat exchangers: an overview—Part 2: Vibration response, fretting-wear, guidelines. J Fluids Struct 18:485–500
11. Rae GJ, Wharmby JS (1987) Strouhal numbers for in-line tube arrays. In: Proceedings of the international conference on flow induced vibrations. Bowness-on-Windermere, England, pp 233–242

12. Weaver DS (1993) Vortex shedding and acoustic resonance in heat exchanger tube arrays. In Technology for the 90's. ASME, pp 776–810
13. Weaver DS, Fitzpatrick JA, El Kashlan M (1987) Strouhal numbers for heat exchanger tube arrays in cross flow. J Pressure Vessel Technol 109:219–223
14. Ziada S (2006) Vorticity shedding and acoustic resonance of tube bundles. J Braz Soc Mech Sci Eng 28:186–199
15. Ziada S, Oengören A (1993) Vortex shedding in an in-line tube bundle with large tube spacings. J Fluids Struct 7:661–687

A Frequency Compensation Method to Smooth Frequency Fluctuation for Locating Moving Acoustic Sources

P. Mo, X. Wang and W. Jiang

Abstract The current beamforming approach for locating moving acoustic sources could not correctly evaluate sources with time-dependent frequency fluctuation. The frequency fluctuation is usually caused by the non-constant relative speed between the solid object and the flow. The source frequency varies with time in a certain frequency range, so that the frequency-domain beamforming approach, which only focuses on a fixed narrow frequency band, cannot focus on the fluctuating frequencies. A frequency compensation method is proposed to smooth the frequency fluctuation. Fluctuating frequencies are squeezed into a narrow frequency band, so that a frequency fluctuating source can be treated as a conventional steady source. The method is then integrated into the frequency-domain beamforming approach for moving sources, and is able to identify moving sources with frequency fluctuation. The integrated method is verified by a simulation and an experiment performed on a rotating source.

Keywords Beamforming · Microphone array · Unsteady moving sources Frequency compensation

1 Introduction

Beamforming is now developed to locate moving acoustic sources by removing the Doppler effect in the microphone signals. The de-Dopplerized signals are specially steered to focus on a group of moving points, so as to give the source strength estimation for a source region. Moving beamforming was extensively applied to identify the aero-acoustic noise sources from the passing-by trains [1], the fly-over

P. Mo · W. Jiang (✉)
State Key Laboratory of Mechanical System and Vibration,
Shanghai Jiao Tong University, Shanghai, China
e-mail: wkjiang@sjtu.edu.cn

X. Wang
China Aerodynamics Research and Development Centre, Mianyang, China

Y. Zhou et al. (eds.), *Fluid-Structure-Sound Interactions and Control*, Lecture Notes in Mechanical Engineering,
https://doi.org/10.1007/978-981-10-7542-1_55

aeroplanes [2], and rotating blades [3]. In the current moving beamforming approaches, the moving sources are assumed to be steady and time-independent. However, some of the aero-acoustic noises are actually time-varying. Taking the helicopter rotor noise as example, the frequency fluctuation in the vortex shedding noise is caused by the non-constant relative speed between the blades and the flow. The time-varying source frequencies would disable the current beamforming approaches in determining the source positions and source frequency components. A time-domain frequency compensation method is proposed to smooth the time-dependent frequency fluctuation. The method is integrated into a classic moving beamforming approach [3], so that moving sources with frequency fluctuation could be identified.

2 Frequency Compensation Method

Assume $q(t)$ is the frequency distorted signal following a time-varying frequency shift $f(t)$ with mean frequency $\bar{f}$. The frequency compensation method is performed on the distorted signal as follows.

$$\tilde{q}(t) = q(t) \exp\left(-j2\pi \int_0^t f(\tau) d\tau \right). \tag{1}$$

The frequency compensated signal $\tilde{q}(t)$ is a tonal signal at frequency $\bar{f}$ without frequency fluctuation. To apply this method, the frequency shift $f(\tau)$ should be given in advance. As for the aerodynamic noise induced by the interaction between the blades and the flow, $f(\tau)$ is governed by a physical model that the source frequency is proportional to the normal speed of the relative blade-to-flow speed. The ratio is known as the Strouhal number.

This method is then integrated in the beamforming approach for locating moving sources. A fixed array with M microphones are used record the sound signals, and to scan the moving source region which is discretized into N scanning points. To scan the nth $(n = 1, 2, \ldots, N)$ moving point, the mth $(m = 1, 2, \ldots, M)$ microphone signal $p_m(t)$ is de-Dopplerized to $q_{nm}(t)$ as introduced by Sijtsma et al. [3], so as to remove the Doppler effect caused by the moving source.

$$q_{nm}(\tau) = T_{nm}^{-1}(t, \tau) p_m(t), \tag{2}$$

where T_{nm} is the time-dependent transfer function from the nth moving source to the mth microphone. T_{nm} is defined by

$$T_{nm}(t,\tau)=\frac{1}{4\pi\left|\vec{x}_m-\vec{\xi}_n(\tau)-\vec{U}(t-\tau)\right|\left|1-M_{mn}(\tau)\right|}$$
$$t-\tau=\frac{1}{c}\left|\vec{x}_m-\vec{\xi}_n(\tau)-\vec{U}(t-\tau)\right|. \tag{3}$$

where $\vec{x}_m$ is the fixed position of the mth microphone, $\vec{\xi}_n(\tau)$ is the moving path of the nth source, $\vec{U}$ is the speed of the uniform flow, and $M_{mn}(\tau)$ is the dimensionless source speed projected on the source-to-microphone direction.

To further remove the frequency fluctuation, the previously mentioned frequency compensation method is applied. The frequency compensated source signal is

$$\tilde{q}_{nm}(t)=q_{nm}(t)\exp\left(-j2\pi\int_0^t f(\vec{x}_n,\tau)d\tau\right), \tag{4}$$

where $f(\vec{x}_n,\tau)$ is proportional to the normal speed of the relative blade-to-flow speed for the scanning point at $\vec{x}_n$. Their ratio is determined by the specific Strouhal number.

Beamforming is then performed on the nth scanning point. The elements of the Cross Spectral Matrix (CSM) are calculated by

$$[G_{mm'}(f)]_n=\sum_{k=1}^{K}\left[Q_{nm}^{*}(f)Q_{nm'}(f)\right], \tag{5}$$

where $Q_{nm}(f)$ is the frequency bins of $\tilde{q}_{nm}(t)$ processed by FFT (Fast Fourier Transformation). The elements in Eq. (5) constitute the full CSM G_n. The power spectrum output for the nth scanning point is

$$Y_n=\frac{\vec{e}^{H}G_n\vec{e}}{M^2}, \tag{6}$$

where $\vec{e}=(1\ \ 1\ \ \ldots\ \ 1)^T$ is a reduced steering vector with unit elements.

3 Simulation and Experiment

A numerical simulation is conducted on a counter-clockwise rotating source, as in Fig. 1a. The source rotates on a circle of radius 1 m at a constant rotational speed 60 rpm ($f_{rot}=1$Hz), and emits a sound with frequency distortion $f(\vec{x}_0,t)=4000+200\sin(2\pi f_{rot}t+\theta_0)$. The source strength is 94 dB in sound pressure level (SPL). An array with 56 microphones and 1 m in diameter is placed

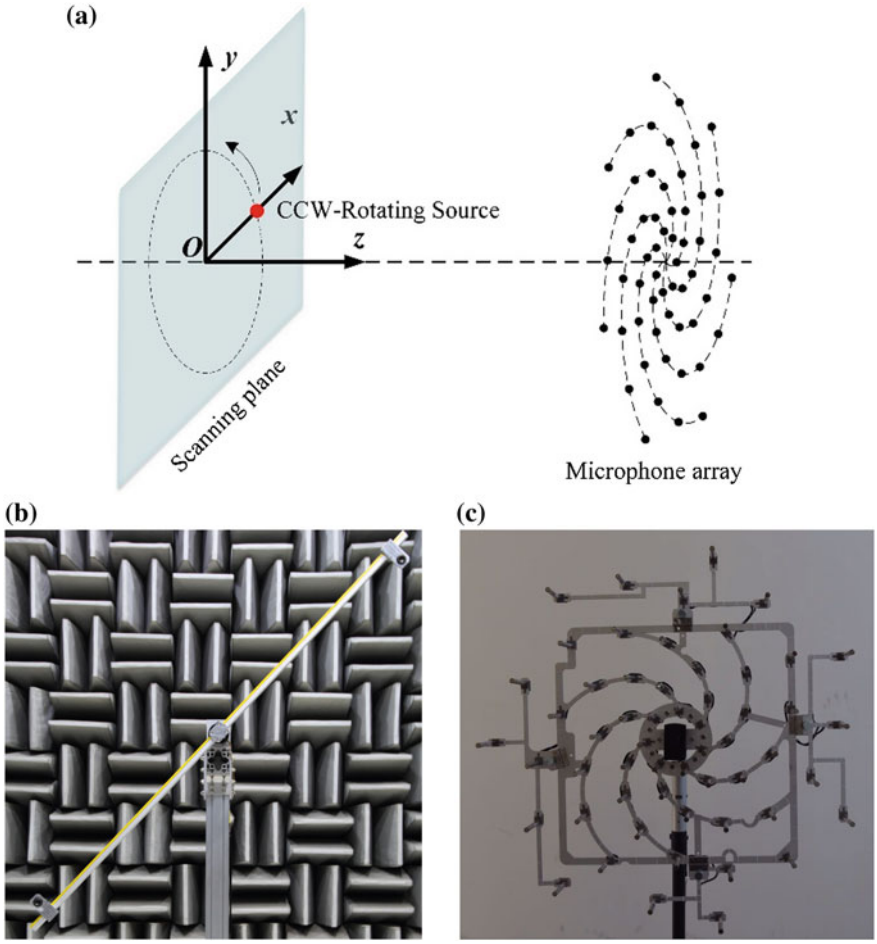

Fig. 1 Setups of beamforming for locating moving sources. **a** schematic description; **b** rotating speakers; **c** an array with 56 microphones and 1 m in diameter

2 m in front of the source plane to record the sound signals. A 2 m × 2 m rectangle scanning plane with a gird size of 0.02 m × 0.02 m is used to cover the rotating source. The sampling rate is 12,800 Hz, and the analyzing time block size is 0.1 s.

On the other hand, a similar experiment is also done in a semi-anechoic chamber, and share the same parameters with the simulation. Two rotating speakers are mounted, but only one actually works, as in Fig. 1b. Figure 1c demonstrates the practical spiral microphone array with 56 half-inch microphones.

The beamforming results of the simulation and the experiment with or without frequency compensation are demonstrated in Fig. 2. Figure 2a is the simulation result without frequency compensation, and Fig. 2b is the beamforming map after

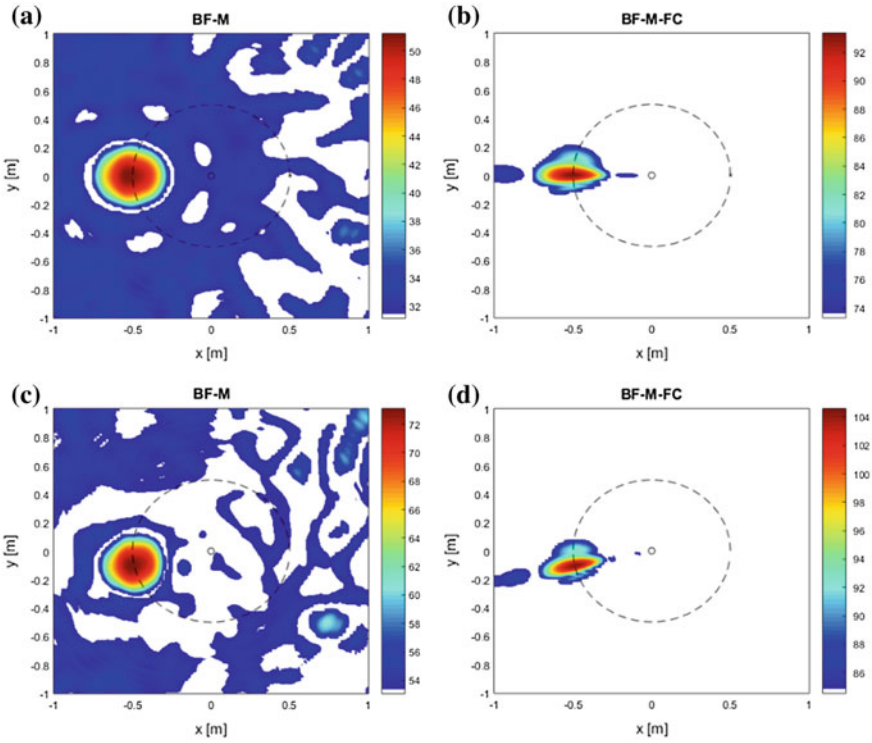

Fig. 2 Beamforming map of a frequency distorted rotating source. **a** simulation without frequency compensation; **b** simulation with frequency compensation; **c** experiment without frequency compensation; **d** experiment with frequency compensation

frequency compensation. By comparing these two figures, it is found that the recovered source strength of the latter map is very close to the actual source strength 94 dB, while the former map has large source leakage in energy. The conventional method only can concentrate on a fixed frequency bin. The other frequency bins are neglected and the frequency components are distorted by performing FFT on the frequency fluctuated signals when applying the conventional method. The frequency compensation method can squeeze the frequencies into a narrow frequency, so that the sources are reconstructed without loss of energy. Similar results are drawn by comparing Fig. 2c, d, which are the experimental results for an actual rotating speaker. The recovered source strength from the source compensation method has less frequency leakage, so its result is more accurate and more reliable.

4 Conclusion

A frequency compensation method is proposed to smooth the frequency fluctuation in moving sources. The integration with the beamforming approach enables it to precisely identify moving sources with frequency fluctuation. The current beamforming approach could only recover a small portion of the source energy, so that the source is likely submerged by large noise. However, the frequency compensation method could recover the fluctuating source with correct source location and strength. It is proved effective and robust to identify moving sources with frequency fluctuation.

Acknowledgements This work was supported by the National Natural Science Foundation of China (Grant No. 11574212).

References

1. Barsikow B (1996) Experiences with various configurations of microphone arrays used to locate sound sources on railway trains operated by the DB AG. J Sound Vib 193:283–293
2. Brusniak L, Underbrink JR, Stoker RW (2006) Acoustic imaging of aircraft noise sources using large aperture phased arrays. In: Proceedings of the 12th AIAA/CEAS aeroacoustics conference, MA, USA
3. Sijtsma P, Oerlemans S, Holthusen H (2001) Location of rotating sources by phased array measurements. In: Proceedings of the 7th AIAA/CEAS aeroacoustics conference, Maastricht, Netherlands

Combustion Oscillation Characteristics of Hydrogen-Rich Fuel

Akane Uemichi, Ippei Kanetsuki and Shigehiko Kaneko

Abstract In this study, combustion oscillation characteristics of hydrogen-rich fuel were investigated. The experimental results fueled by mixture of natural gas and hydrogen show that hydrogen-rich combustion influences on the oscillating frequencies. In the case of only natural gas, the single oscillating frequency around 350 Hz is obtained, and in the hydrogen-containing fuel case, the double oscillating frequencies around 200 and 400 Hz are measured. However, the latter oscillating frequencies could not be derived from the one-dimensional acoustic analysis. Therefore, to figure out these frequencies, the acoustic impedance was measured experimentally and the oscillating frequencies were re-calculated using the measured acoustic impedance as the acoustic boundary conditions. As a result, the 200, 350, and 400 Hz frequencies could be expressed using the acoustic impedances.

Keywords Combustion oscillation · Pressure oscillation · Hydrogen-rich fuel

1 Introduction

Combustion instability in a combustion chamber of a gas turbine has been one of the big problems because the resonance with various parts of a gas turbine leads to weariness or damages when combustion instability occurs [1]. Additionally, it is expected that using unused energy resources such as digestion gas, woody biomass gas, and syngas which have recently been promoted make combustion more unstable. Especially, we focused on hydrogen-rich combustion of natural gas in this study. Since hydrogen does not emit CO_2 at all when it is burned, the hydrogen-containing combustion reduces CO_2 emissions. Therefore, we examined the influence of hydrogen ratio contained in the fuel on combustion instability experimentally and analytically.

A. Uemichi (✉) · I. Kanetsuki · S. Kaneko
Department of Mechanical Engineering, The University of Tokyo,
7-3-1 Hongo, Bunkyo-Ku, Tokyo 113-8656, Japan
e-mail: uemichi@fiv.t.u-tokyo.ac.jp

Y. Zhou et al. (eds.), *Fluid-Structure-Sound Interactions and Control*, Lecture Notes in Mechanical Engineering,
https://doi.org/10.1007/978-981-10-7542-1_56

2 Combustion Oscillation Experiment

The experimental equipment modeling on a micro gas turbine combustor was used [2]. For the fuel, Japanese town gas, 13A, which is equivalent to natural gas and hydrogen was used. The mixed fuel is injected into the combustor through the fuel supply pipe and then mixed with air at the swirler which has a function of a flame stabilizer simultaneously. For pressure fluctuation measurement, a pressure sensor installed on the bottom of the combustor was used. The hydrogen content in the fuel was varied from 0 to 40% in increments of 10%. Air is supplied by the compressor and a throttle to suppress pulsations in the air supply pipe is installed upstream of the swirler (see Fig. 3). Then, the experiment was carried out by decreasing the equivalence ratio starting from stoichiometric ratio down to the ratio corresponding to the extinction point by changing the fuel flow rate and air flow rate adjusting the total flow rate becomes constant of 15 L/s.

In this study, we treated the oscillations after reached the limit cycle. First, to examine the occurrence of combustion oscillation, the root-mean-square $\mathrm{RMS} = \sqrt{\sum_{i=1}^{N} (p_i - \bar{p})^2 / N}$ (N: total number of samples, p_i: pressure of ith sample, $\bar{p}$: average pressure) values of pressure fluctuation were calculated as shown in Fig. 1. Regarding the range of RMS value, variable range does not show much difference regardless the change of hydrogen content in the fuel. Next, to further understand the characteristics of combustion oscillation, the FFT analysis was performed and measured oscillating frequencies are shown in Fig. 2. In the case of 13A 100%, the oscillation frequency around 350 Hz is observed excluding the case of the equivalence ratio around 0.6 corresponding to the extinction point. In 13A 100% case, it should be noted that near the extinction point, the single low-frequency oscillation

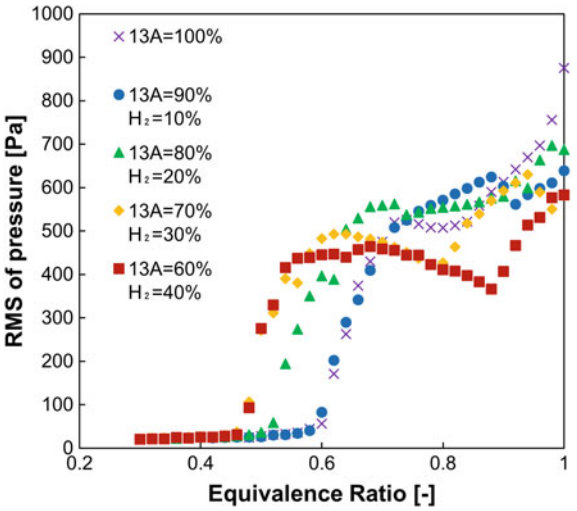

Fig. 1 RMS of pressure at the bottom face of the combustor

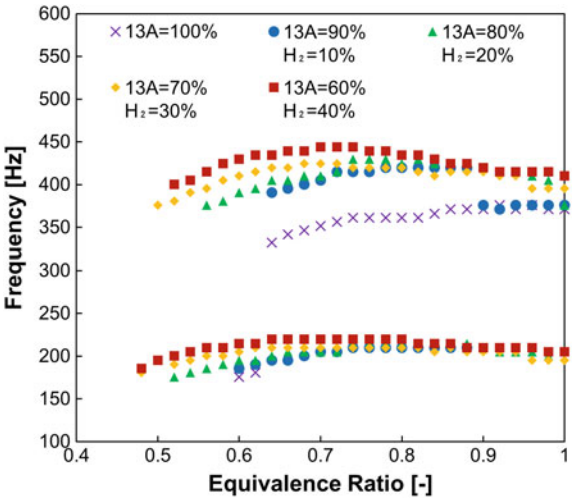

Fig. 2 Measured oscillating frequencies for various fuel mixtures

around 170 Hz was observed because the combustion field has changed near the extinction point. Whereas in the case of the mixture fuel of natural gas and hydrogen, double oscillating frequencies around 200 and 400 Hz are observed.

The oscillating frequency obtained by a simple calculation using the different diameter one-dimensional pipe modeling only the combustion chamber part where the acoustic boundary conditions are one end closed and the other end open is around 350 Hz. It is almost identical to the measured oscillating frequency with the case of only natural gas. However, we could not explain why different double frequencies of 200 and 400 Hz were measured in the case of hydrogen-containing fuel. Then, the oscillating frequencies in the hydrogen-containing case is thought to be the result of acoustic boundary condition change and we decided to investigate the acoustic impedance of acoustic system including the upstream part of the swirler.

3 Measurement of Acoustic Impedance and Acoustic Analysis

To examine the reason of the multiple frequencies observed in the combustor, the acoustic analysis was carried out. Thus, to improve the one-dimensional acoustic analysis, the acoustic impedance of the bottom of the combustor was measured experimentally [3] based on an acoustic network model [4, 5].

In the experiment, the transfer matrix method to measure acoustic impedances is selected, and the frequency range is determined by JIS A1405. Figure 3 shows the schematic of measurement apparatus. As shown in the figure, in the measurement, a loudspeaker supplies acoustic signals generated by a function generator. Then, the

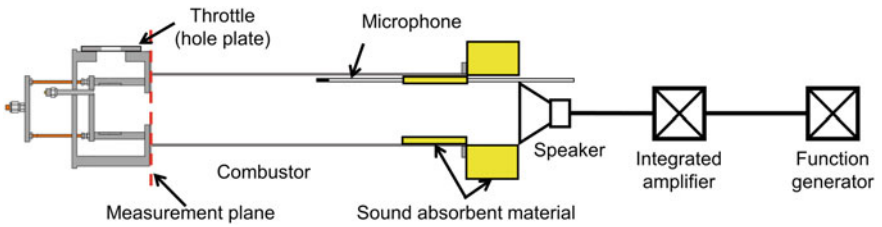

Fig. 3 Schematic image for acoustic impedance measurement

reflected acoustic signals are detected by a microphone. To eliminate the exterior noise, sound absorbent material is attached at the end of the combuster.

Figure 4 shows the acoustic impedance measured under room tempatature. Figure 4a–c show Nyquist plot on the complex plane, gain and phase of the measured acoustic impedance, respectively. As shown in Fig. 4b, a point of a peak where absolute amplitude becomes maximum is around 165 Hz. To accommodate the burned condition based on the unburned situation, the acoustic impedance correction is indispensable. Using the adiabatic flame temperature calculated by CHEMKIN-PRO, the oscillating frequency under burned condition can be estimated around 400 Hz which is 2–3 times of the original frequency under unburned condition; therefore, it is supposed that the throttle located at the upstream of the

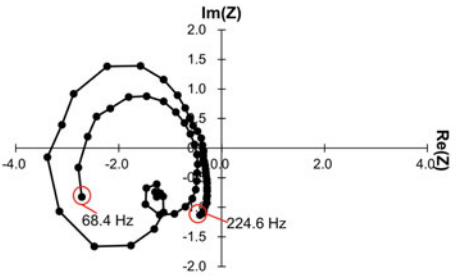

(a) Nyquist plot on the complex plane (Starting point: 68.4 Hz, end point: 224.6 Hz)

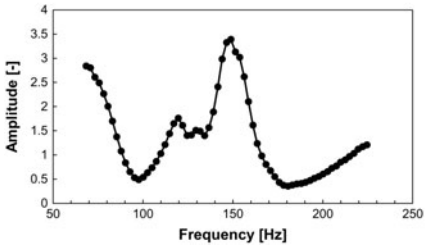

(b) Gain

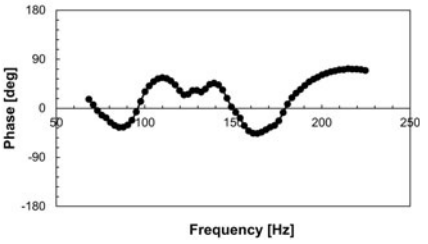

(c) Phase

Fig. 4 Measured acoustic impedance

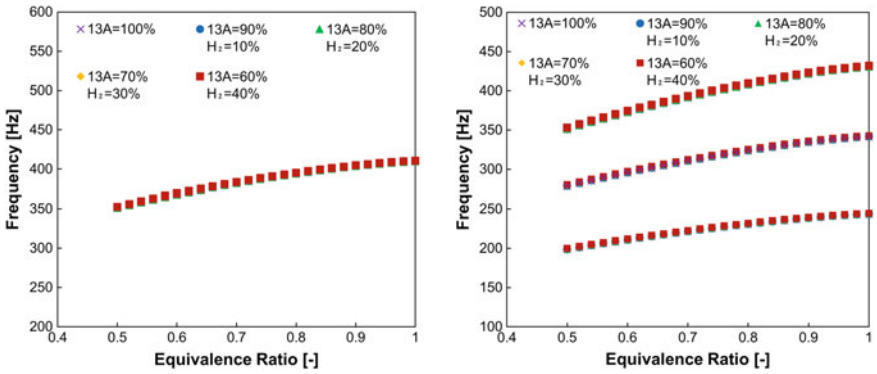

(a) Without the acoustic boundary conditions treatment.

(b) With the acoustic boundary conditions treatment.

Fig. 5 Calculated oscillating frequencies

swirler is the end of the oscillating mode around 400 Hz. Thus, the acoustic boundary conditions were changed by adding hydrogen to the fuel mixtures.

To obtain the oscillating frequencies under burned condition, the one-dimensional acoustic analysis taking account of acoustic impedance were carried out. Since the sound speed is a function of the square root of temperature T, temperature corrected acoustic impedance Z_c can be expressed as $Z_c = f\left(T^{-0.5}\right)$. Therefore, impedance Z_c is very much affected by the accuracy of T. Figure 5 compares the acoustic analysis results between those with and without the acoustic boundary condition which was derived by the measured acoustic impedance. In this calculation, the homogeneous adiabatic flame temperature in the combustor was considered. As a result, in addition to the oscillating frequency of around 350 Hz, the measured frequencies of around 200 and 400 Hz are obtained. It is noted that the acoustic impedance could reproduce the measured oscillating frequencies. However, the difference of the hydrogen content in the fuel mixture is not well expressed in this figure. Furthermore, the reason why the impedance change leads to the frequency change is not revealed. Therefore, other factors influenced by fuel components such as the flame position, the temperature distribution, and the gas properties including the heat capacity should be considered in the further research.

4 Conclusion

In this paper, to understand the combustion oscillation characteristics of hydrogen-rich fuel with natural gas, the experiments and the acoustic analysis were performed. For the acoustic analysis, the acoustic impedances were measured. As a

result, employing the acoustic impedance as the acoustic boundary condition made it possible to express the different oscillating frequencies; therefore, adding hydrogen to the fuel changes the acoustic boundary conditions.

Acknowledgements This work was supported by JSPS Grand-in-Aid for Scientific Research (B) KAKENHI Grant Number 26289053.

References

1. Lieuwen TC, Yang V (2005) Combustion instabilities in gas turbine engine. American Institute of Aeronautics and Astronautics, Inc. https://doi.org/10.2514/4.866807
2. Adachi S, Iwamoto A, Hayashi S et al (2007) Emission in combustion of lean methane-air and biomass-air mixtures supported by primary hot burned gas in a multi-stage gas turbine combustor. Proc Combust Inst 31(2):3131–3138. https://doi.org/10.1016/j.proci.2006.07.239
3. Kato S, Fujimori T, Kobayashi H (2008) Effect of acoustic impedance on one-dimensional linear analysis of combustion oscillation in premixed gas turbine combustor. J Combust Soc Japan 50:72–80 (in Japanese)
4. Han X, Hui X, Qin H et al (2016) Effect of the diffuser on the inlet acoustic boundary in combustion-acoustic coupled oscillation. In: ASME Turbo Expo 2016, June 13–17, 2016 Seoul, South Korea. https://doi.org/10.1115/gt2016-57046
5. Polifke W (2004) Combustion instabilities. VKI Lecture Series

Frequency Domain Beamforming for Monopole and Dipole Sources

J. Z. Gao, X. J. Pan, X. N. Wang and W. K. Jiang

Abstract Beamforming is an imaging technique that locates sources by a phased array system. Conventional source model in beamforming is the monopole, and problematic result may appear towards directional sources. As an alternative, a modified beamforming method is proposed in this paper to extend this technique to dipole sources. The method is developed by predefining orientations and selecting direction of maximum output at each scanning point. Simulation and experiment are conducted to illustrate and verify this method, and results are shown to give a proper location of dipole sources.

Keywords Acoustic imaging · Beamforming · Dipole source

1 Introduction

Beamforming with microphone array has become a popular technique in aeroacoustic measurements. This acoustic imaging method refers to locating sound sources by time delay of different microphone signals in time domain, or phase shift in frequency domain. The main principle of beamforming is to sum the signal emanating from focal position (source position) while minimizing the contribution from out-of-focus locations.

Conventional beamforming (CBF) methods are based on the assumption of monopole source, which is imdirectionally propagated. Actually, the directional source, such as a dipole, is principally responsible for flow induced Aeolian tones in many aeroacoustics systems, e.g., trailing edge and tension rod noise of airplanes. Fixed directional pattern could be found for dipole sources, making it different from

J. Z. Gao · X. J. Pan · W. K. Jiang (✉)
State Key Laboratory of Mechanical System and Vibration,
Shanghai Jiao Tong University, Shanghai 200240, China
e-mail: wkjiang@sjtu.edu.cn

X. N. Wang
China Aerodynamics Research and Development Centre, Mianyang 621000, China

Y. Zhou et al. (eds.), *Fluid-Structure-Sound Interactions and Control*, Lecture Notes in Mechanical Engineering,
https://doi.org/10.1007/978-981-10-7542-1_57

monopole sources applied in conventional beamforming. It has been discovered that beamforming with monopole assumption can be problematic towards dipole sources [2], incorrect source position would be located especially when the source orientation parallels to the array plane. To avoid this situation, correction method was developed with one-dimensional (linear) array [2], two dimensional array [3] and three dimensional array [4], these correction methods are able to identify the source location of dipole with suspected orientation. A more general method towards locating unknown directional sources was introduced by performing a linear combination of eigenbeamformers or sub-beamformers [1] based on spherical harmonic decomposition, however, methods based on decomposition of spherical harmonic function needs either specially designed array or estimation of index/modes to decide accuracy. The generalized inverse algorithm [5] was developed with resolution to be comparable to deconvolution techniques, such as DAMAS and CLEAN. Although it is applicable to general microphone array and realized by more efficient iterate procedure, orientation of the source is limited to the plane parallel to array.

A modified beamforming method for dipole source with arbitrary unknown orientation is introduced in this paper. The main principle of this method is to calculate beamforming result at different pre-defined direction (realized by weighting vector) for each scanning point and the maximum value of different directions is selected as output of the scanning point.

2 Methodology

All sources discussed here is said to be acoustically compact and the frequency f is small enough such that $2\pi f^{*}a/c \ll 1$, which means the radius of source a is a small fraction of wavelength λ with c to be the speed of sound. Only one compact acoustic source is considered at a specified scanning point, so the collocation of two dipoles of perpendicular orientations at same position will not be considered in this paper. Besides, it is important to remind that the beamforming technique discussed here is based on far-field measurement.

The flow-induced dipole source is caused by the interaction between a rigid surface and flow in many aeroacoustic applications. Sound propagation from sth source (coordinate $\mathbf{x}_s$ and orientation $\hat{\boldsymbol{\xi}}_{k_s}$) to mth microphone (coordinate $\mathbf{x}_m$) is given by

$$a_{ms}^{k_s} = \frac{1}{r_{ms}} e^{-jwr_{ms}/c} \left(\hat{\mathbf{r}}_{ms} \cdot \hat{\boldsymbol{\xi}}_{k_s} \right), \tag{1}$$

where $w = 2\pi f$, distance $r_{ms} = |\mathbf{x}_s - \mathbf{x}_m|$, $\hat{\mathbf{r}}_{ms} = (\mathbf{x}_s - \mathbf{x}_m)/r_{ms}$, and c is the speed of sound.

In frequency domain beamforming, array measured data is processed to get the cross-spectral matrix (CSM) at first. Assume a phased array system of M microphones and N scanning points, the expression of conventional beamforming result at nth scanning point is

$$\mathrm{b}_n = \mathbf{w}_n^H \mathbf{C} \mathbf{w}_n, \tag{2}$$

vector $\mathbf{w}_n \in \mathbb{C}^M$ stands for the weighting vector, also named steering vector in other literatures, at nth scanning point with $n = 1, 2, \ldots, N$. The subscribe H indicates the Hermitian conjugate transpose and the M by M matrix $\mathbf{C}$ is the cross-spectral matrix of measured data.

Totally K incoherent dipoles with different orientation are assumed to be located at the same scanning point, then the weighting vector form M microphones of array to nth scanning point at kth orientation is expressed as

$$\mathbf{w}_n^k = \frac{\mathbf{a}_n^k}{\|\mathbf{a}_n^k\|}, \tag{3}$$

where $\mathbf{a}_n^k = \left(a_{1n}^k, a_{2n}^k, \ldots, a_{Mn}^k\right)^{\mathrm{T}}$ and $(\cdot)^{\mathrm{T}}$ stands for transpose. For notational convenience, the nth scanning point with kth orientation is noted as pair (n, k). Inserting weighting vector of Eq. 3 into Eq. 2, the (n, k)th beamforming output, which means kth orientation result at nth scanning point, is given by

$$b_{(n,k)} = \sum_s \left| \mathbf{w}_n^{k\,H} \mathbf{a}_s^{k_s} \right|^2 Q_s, \tag{4}$$

the scalar $Q_s \in \mathbb{R}$ is the power of sth source with k_sth orientation. Final beamforming result of the nth scanning point is the maximum among all K orientations at position $\mathbf{x}_n$

$$\mathrm{B}(\mathbf{x}_n) = \max_k \left\{ b_{(n,k)} \right\}. \tag{5}$$

3 Numerical and Experimental Results

Figure 1a presents the setup of simulation. As illustrated, a 7 × 8 multi-arm spiral array with 56 microphones was applied to coincide with the experiment. A coordinate system is defined with the origin at center of array, the scanning plane parallels to the array at 0.5 m away. For notational convenience, and without loss of generality, the source is located at position (0, −0.2, 0.5) in all cases. The scanning plane is a 1 × 1 m square with grid size of 0.01 × 0.01 m.

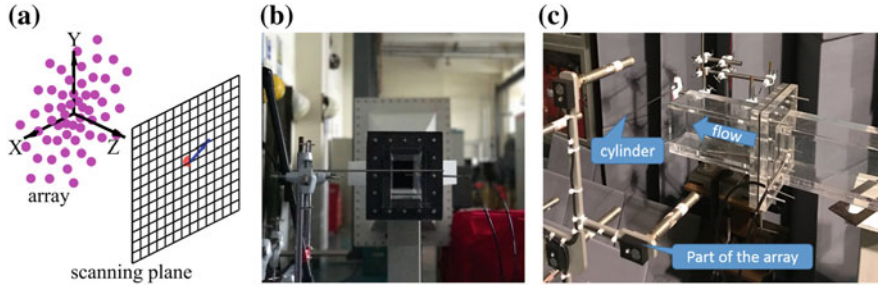

Fig. 1 Sketch of the measurement setup: **a** simulation of a single dipole, **b** and **c** experiment of a dipole with orientation (0, 1, 0)

Three cases of a single dipole source with pre-defined orientation (0, 0, 1), (0, 1, 0) and (1, 1, −0.15) were tested at each scanning point, as indicated in Fig. 2. Results indicates that incorrect interpretation of two source locations is given by conventional beamforming, and on the other hand, dipole source could be properly located for the modified beamforming method although some side lobes may appear, and the lobes could be removed by deconvolution method. The reader is cautioned that the orientation $\hat{\boldsymbol{\xi}}_k = (0, 0, 1)$ is "abnormal" for the reason that directional part $\left(\hat{\mathbf{r}}_{ms} \cdot \hat{\boldsymbol{\xi}}_{k_s}\right) = 0.5$ (constant for all microphones) in Eq. 1, which means propagation of a dipole source is omni-directional at this orientation. i.e., the pre-defined orientation (0, 0, 1) not only represents an orientation of dipole but also a monopole.

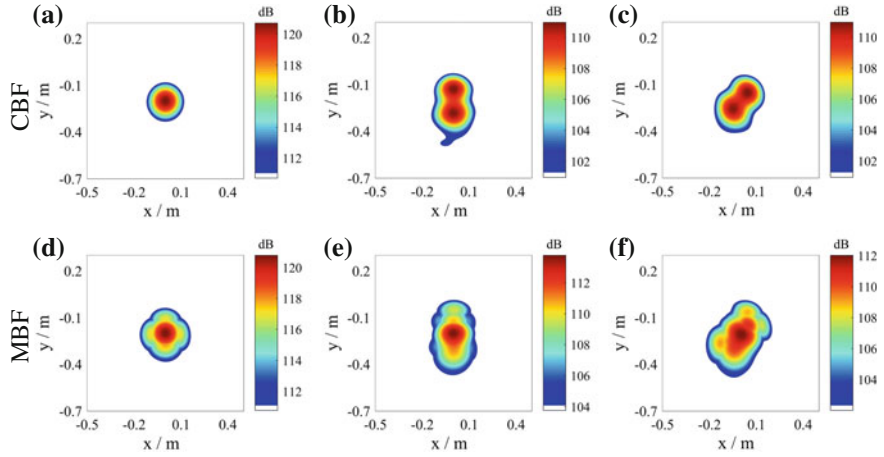

Fig. 2 Simulated results by different methods (rows) of the conventional beamforming (CBF) and the modified beamforming method (MBF) at three orientations: (0, 0, 1), (0, 1, 0) and (1, 1, −0.15) with respect to panels (**a**) (**d**), (**b**) (**e**) and (**c**) (**f**), all results were analyzed at 2000 Hz

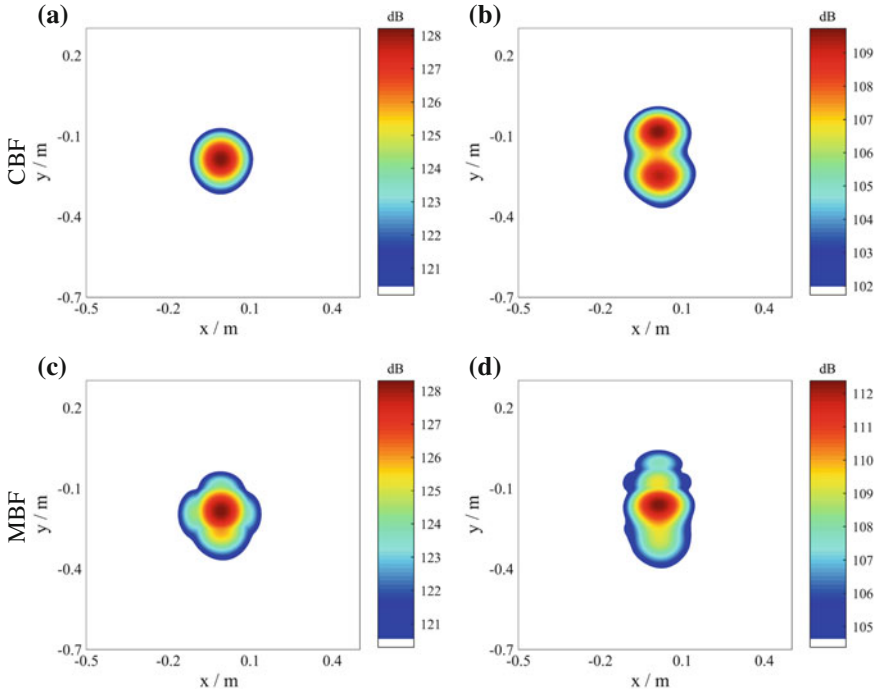

Fig. 3 Comparison of experimental result by the conventional beamforming (CBF) and the modified beamforming method (MBF): **a**, **c** dipole source orientation at (0, 0, 1); **b**, **d** dipole source with orientation (0, 1, 0), source located at same position in all panels

In demonstration of the proposed modified method, experiment was conducted by a 4 mm cylinder fixed in flow, as illustrated in Fig. 1b, c. The flow speed is 44 m/s and cylinder positioned vertically/ horizontally to generate realistic dipole source with orientation (0, 0, 1) and (0, 1, 0). Other parameters remains the same with those in simulation, and results shown in Fig. 3 are in line with the simulation as expected.

4 Conclusion

A modified beamforming method using a phased array has been proposed to locate monopole and dipole sources for arbitrary orientation. This method is realized by pre-defining orientations of each scanning point. Maximum value among all orientations at a scanning point is selected as beamforming result of the position. The modified method is numerically and experimentally verified. It is expected to be applied in situations of directional sources in aeroacoustic measurements.

References

1. Bouchard C, Havelock DI, Bouchard M (2009) Beamforming with microphone arrays for directional sources. J Acoust Soc Am 125(4):2098–2104
2. Jordan P, Fitzpatrick JA, Valiere J-C (2002) Measurement of an aeroacoustic dipole using a linear microphone array. J Acoust Soc Am 111(3):1267–1273
3. Liu Y, Quayle AR, Dowling AP, Sijtsma P (2008) Beamforming correction for dipole measurement using two-dimensional microphone arrays. J Acoust Soc Am 124(1):182–191
4. Porteous R, Prime Z, Doolan CJ, Moreau DJ, Valeau V (2015) Three-dimensional beamforming of dipolar aeroacoustic sources. J Sound Vib 355:117–134
5. Suzuki T (2011) L 1 generalized inverse beam-forming algorithm resolving coherent/ incoherent, distributed and multipole sources. J Sound Vib 330(24):5835–5851

Pulsatile Jet Ejected from Lips

Y. Kubota, K. Sugiyama and O. Mochizuki

Abstract The mechanism of sound generation by lips is studied for basic understandings of biological sound. The sound is similar to buzzing, and is known as a sound which is generated when the trumpet player blows breath to a mouth piece. The sound and vibration of lips are observed experimentally by using a microphone with a high directivity and a high-speed CCD camera. The flow through the opening of lips are observed by using a smoke visualization. The vibration of the lips model is also observed by a high-speed CCD camera with 1000 fps. The lips model shows interesting motion by jetting the compressed air. The cyclic motion of the opening and closing is observed. The frequency of motion relates the natural frequency of the model. The oscillation causes the pulsating sound that is superimposed higher frequencies. The digon shape of nozzle relates the higher frequency sound.

Keywords Pulsatile jet · Lips · Vibration · Sound generation

1 Introduction

The generation mechanism of a sound by lips is studied for basic understandings of biological sound. The sound is similar to buzzing, and is known as a sound which is generated when the trumpet player blows breath to a mouth piece. The player can operate the tone by changing an embouchure and strength of blowing. The nozzle is soft and springy because of lips in this case. Thus, the mutual interaction between the lips and blowing is important for determination of the sound. In past three decades, the control of a jet in engineering points is based on the instability of shear layer. The orderly structure of the jet is enhanced by oscillation with the preferred mode frequency, $f = St\theta U/\theta$ of the shear layer, where f is the initial instability frequency, U is the jet exit velocity, θ is the initial shear layer thickness, and Stθ is a

Y. Kubota (✉) · K. Sugiyama · O. Mochizuki
Toyo University, 2100 Kujirai, Kawagoe, Saitama 350-8585, Japan
e-mail: kubota548@toyo.jp

Y. Zhou et al. (eds.), *Fluid-Structure-Sound Interactions and Control*, Lecture Notes in Mechanical Engineering,
https://doi.org/10.1007/978-981-10-7542-1_58

Strouhal number in the range of 0.009–0.018. The oscillation with small amplitude is given near the sharp edges of the nozzle exit [1] by using sound from a speaker, vibrating thin plates or micro actuators. The increasing entrainment by the enhanced orderly structures promote the mixing and stirring of the fuel gas jet and ambient air, as one of engineering applications. In the other way to control the jet, non-circular nozzle exit is used to stimulate instability not only in the longitudinal direction but in the radial and circumferential directions. The development of the non-circular jet ejected from an elliptic or rectangular exits have been studied experimentally. The mixing by the non-circular jets is larger than that of the circular jet because of the axis switching related to the self-deformation of the non-circular vortex rings. The self-deformation yields the high frequency fluctuations of velocity because of non-linearity. This means that it has a possibility to generate a sound involved higher harmonics. The elliptic jet with aspect ratio of 2 known as the self-excited whistle shows the higher mass entrainment at near position to the exit. The nozzle is made by a hard material like as steel or acrylic resin, and its edge is sharp. Thus, the way to control jets must be based on the inherent character of the shear layer. The inherent frequency of the preferred mode of the thin shear layer separated from the sharp edge of the exit must be obtained to design the control system of the jet in advance. In general, it is difficult to measure the shear layer thickness θ at the exit because it is tremendously thin. The control system requires the micro sensors to detect velocity and pressure fluctuations, micro actuators to impose oscillation to the thin shear layer, and computer to analyze the flow. Moreover, the system needs electric power. Thus, the relation between the supplied power and controlled results is a tradeoff relation. This is a cause that it makes a feasibility of the system hard. The whistle due to feedback mechanism have been studied, but this generates a pure tone. The sound generation mechanism by blowing from lips is considered by comparing with data obtained by our physics model. Therefore, sound making mechanism of living things, especially human, is considered in this paper. The jet which human makes by a springy supple matter suggests a possibility of a new type of adaptive control and application to a reconstruction of the lost vocal cords.

2 Experimental Setup

Lips as a nozzle exit is soft and has no sharp edge. We never control the vibration of lips to make sounds but control the size of hole made with lips and speed of blowing when we whistle. However, if the lips are dry, the whistle is not success. This means the flexibility and vibration of lips are necessary. The mutual interaction between lip-vibration and vortex rings in the blowing jet determines the sound frequency of the whistle. The vibration of lips plays an important role when we play the trumpet. The embouchure is the shape of lips to the mouth-piece of the trumpet. To make sound by the embouchure, hard practice is necessary. When the pressure in a mouth exceeds a force to close lips, the air comes out and the pressure

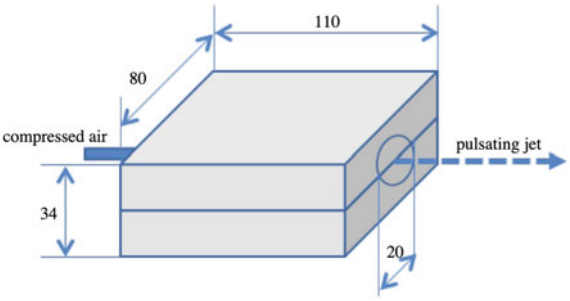

Fig. 1 The konjyak jelly nozzle

goes down. Then, lips close again. The jet becomes pulsatile jet when this occurs in some period repeatedly. The dominant frequency of the pulsatile jet related to the vibration of the opening and shutting of lips must be obtained by the force balance of the pressure and closing force of lips. The mechanical properties, a spring constant, damping characteristic, and Young's modulus, are necessary to estimate the dominant frequency of lips.

The sound and vibration of lips are observed experimentally by using a microphone with a high directivity and a high-speed CCD camera. The flow through the opening of lips are observed by using a smoke visualization.

The experimental setup is shown in Fig. 1. The lips are made by two blocks of a hard konjak jelly. These are put into a box with 80 mm × 110 mm × 34 mm, and the periphery of them are fixed except for a circular hole with 20 mm diameter as shown in Fig. 1. The folder box's size is adjusted to commercially produced konjak that we can buy at shop ordinarily. The compressed air of 2 atm is supplied from the opposite side of the lips nozzle. The stiffness, k, of the konjak jelly is 4 × 102 Pa. The natural frequency, f, is defined by $f = 1/\pi \sqrt{(k/m)}$. Thus, if f is obtained from measurements, the mass of a vibrating substance, m, becomes clear.

The vibration of the lips model is observed by a high-speed CCD camera with 1000 fps. The sound is measured by a condenser microphone having a strong directivity. These data are recorded simultaneously for taking their correlation.

3 Results and Discussion

Some of sequential photos chosen from the high-speed movie is shown in Fig. 2. The interval of each photos is 1/1000 s. The opening and closing of the lips model occurs at a part of the gap in the bounded circle. The maximum opening is 6 mm at the center. The lateral length between the both ends of the opening is 15 mm. The cycle of the opening and closing is 0.008 s; thus, the frequency of the event is 125 Hz. The jet is ejected intermittently by that frequency. The vibrating substantial mass of konjak is estimated from the natural frequency by means of substitution of f and k into the above equation. The result is 0.65 g. Thus, if the vibration area is in the bounded circle, the depth of the substantial volume is 9.5 mm.

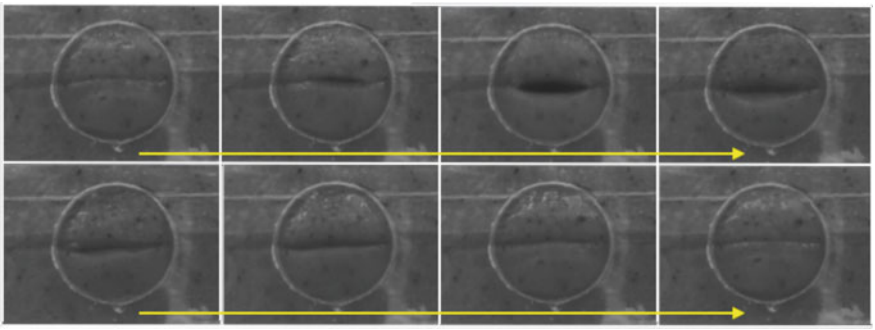

Fig. 2 The one cycle motion of konjyak jelly nozzle. Time interval of photos next to each other is 2 ms. Arrows express time going on

The dominant frequency of the sound is found to be 125 Hz as same as the cycle of the lips by measuring the sound at that interval. This means that the basic sound source is the pulsating jet due to the cycle of the opening and closing. The higher frequency sound is superimposed on the pulsating sound signal. The source of the higher sound is supposed to be related to vortices' interactions in the shear layer of the jet. This jet is very special because the shape of the nozzle is a digon which has two sides and two vertices as shown in the Fig. 2. Two vertices show a singularity because two sides connect discontinuously at the vertex. This is a cause of unpredictable higher harmonics sound due to nonlinear interactions. This will be carried out in the next steps.

It is considered that the velocity of air flow, the konjak jelly's hardness and total mass and the hole's size of the box will affect the natural frequency, the event's frequency and the mass of a vibrating substance. This relationship will be focused in next experiments.

4 Conclusions

The konjak jelly nozzle shows interesting motion by jetting the compressed air. It shows the cyclic motion of the opening and closing. Its frequency relates the natural frequency of the konjak. The oscillation causes the pulsating sound that is superimposed higher frequencies. The cause of higher frequency sound is a digon shape of the nozzle.

Reference

1. Ricota D, Causse R, Misdariis N (2005) Aerodynamic excitation and sound production of blown-closed free reeds without acoustic coupling: the example of the accordion reed. J Acoust Soc Am 117(4):2279–2290

Prediction of Aeolian Tone Radiated from a Tapered Circular Cylinder and Vortex Sound in Wake

Y. Watanabe and Y. Suzuki

Abstract In this paper, Aeolian tone and the related flow field of a circular cylinder (CC) and a tapered circular cylinder (TC1) are predicted using the numerical simulation for incompressible flow. The number of computational grids is 4 million. The Reynolds number based on diameter at middle span and uniform flow velocity is 2.65×10^4. The Aeolian tone spectra are calculated using the formula of FW-H and sound sources around the cylinder are computed based on Powell-Howe vortex sound theory. As a result, comparing these distributions of the sound source, the vortex sound intensity of TC1 is less than of CC in span wise direction. Aerodynamic sound spectra by the experiment and calculation provided good agreement.

Keywords Aeoilan tone · Tapered circular cylinder · CFD · Powell-Howe FW-H

1 Introduction

Recently, aerodynamic noise has become one of the crucial factors in the design of machineries such as high-speed trains, air conditioners, and electronic devices. Aerodynamic noise increase with the 4th to 6th power of flow velocity depending on noise generation mechanisms. One of them is the Aeolian tone based on von Karman vortex shedding in the wake. The Aeolian tone generated from fundamental shape objects such as circular cylinders or square cylinders as shown in pantograph of high-speed train or support on bridge is significant issue for people. Some tapered circular cylinder studies were carried out as one of the passive noise

Y. Watanabe (✉)
Department of Mechanical Engineering, School of Engineering,
The University of Tokyo, Tokyo, Japan
e-mail: yuichiro@iis.u-tokyo.ac.jp

Y. Suzuki
Department of Mechanical Engineering, College of Science & Technology,
Nihon University, Tokyo, Japan

Y. Zhou et al. (eds.), *Fluid-Structure-Sound Interactions and Control*, Lecture Notes in Mechanical Engineering,
https://doi.org/10.1007/978-981-10-7542-1_59

control methods for the Aeolian tone [1, 2]. In the experiment, the Aeolian tone generated from tapered circular cylinder dramatically reduced comparing with circular cylinder. However, the noise reduction mechanism on Aeolian tone are not clarified.

In this study, Aeolian tone and the related flow field of a tapered circular cylinder are simulated and these sound spectra have been evaluated. In order to clarify their sound sources, instantaneous distributions of Powell's sound source are shown from the calculated flow field data.

2 Numerical Method and Prediction of Aeolian Tone

In this study, decouple method on fluid dynamics and acoustics are used with a commercial software of SCRYU/Tetra version 11 which is a solver by finite volume method. The flow field is calculated as an incompressible and viscous fluid with the Large Eddy Simulation (LES) and Dynamic Smagorinsky Model for sub grid scale model. The convection term is calculated by second-order accurate central-difference scheme and the pressure-correction method is SIMPLE. Table 1 shows details of a model specification to compare a Circular Cylinder (CC) with a Tapered Circular cylinder (TC1). Figure 1 illustrates an overview of the TC1 model which

Table 1 Model specification

Model	D_1	D_2	Case name
Tapered circular cylinder	0.5D	1.5D	TC1
Circular cylinder	D	D	CC

Fig. 1 Test model

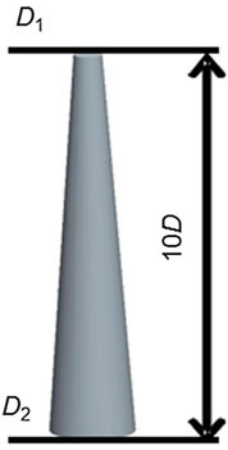

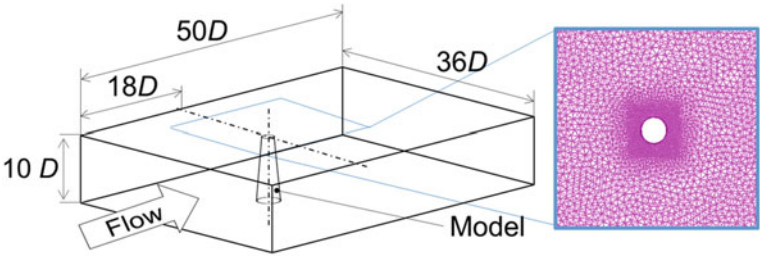

Fig. 2 Overview of computational domain

has diameter D at middle span and span length of $10D$. Figure 2 shows an overview of a computational domain which is $36D \times 50D \times 10D$ in x, y and z directions, respectively. Tetrahedral meshes are used in the domain but prism meshes are used only close to the surface of the CC and TC1. The number of computational grids is approximately 4 million with the minimum grid size of $y^+ = 1$. The Reynolds number based on the uniform flow velocity U and the diameter D at middle span is 26,500. The interval time Δt is about 0.5 ms. The far-field sound at a location 1 m away from the model is computed. These boundary conditions are the uniform velocity of $U = 20$ m/s for inlet, the initial pressure of $P_0 = 0$ Pa for outlet, cyclic boundary conditions of the domain for side domain, and wall conditions with free slip for top and bottom domain. The sound spectra of Aeolian tone are computed based on a formula of Ffowcs Williams and Hawking [3] and sound sources distributions are calculated based on Powell's sound source based on Powell-Howe vortex theory [4].

3 Results and Discussion

3.1 Flow Visualization

Figure 3 shows comparison of measured flow visualization in cross section of diameter and calculated ISO surface of instantaneous visualized vortex structure (vorticity—shear rate) in order to clarify the development of spanwise structure of von Karman vortices for the CC and TC1. The calculation results provided qualitatively good agreement with measured. von Karman vortex is developed regularly along the spanwise direction at CC. The other hand, an vortex shedding inclined to the Z axis of TC1 is developed. According to [5], a specific angle of the vortex shedding has affected on Strouhal number that is calculated by flow velocity around the circular cylinder, due to there are not constant of flow velocity along the spanwise direction. Therefore, it is considered that the inclined vortex shedding contributes to reduction of Aeolian tone generation.

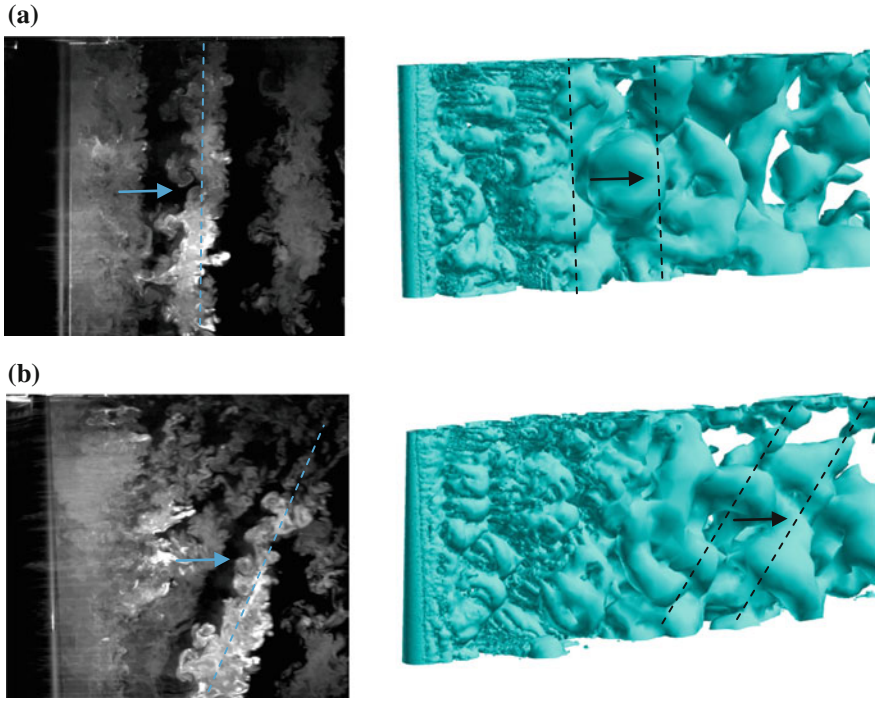

Fig. 3 Instantaneous visualized vortex structure (vorticity – shear rate = 50), **a** CC (Left: measured by Watanabe [2], Right: calculated), **b** TC1 (Left: measured by Watanabe [2], Right: calculated)

3.2 Sound Source of Aeolian Tone

Figures 4 and 5 show an instantaneous distribution of Powell's sound source based on $div(\boldsymbol{\omega} \times \boldsymbol{u})$ which means $\boldsymbol{\omega}$: vorticity and $\boldsymbol{u}$: velocity. It shows ISO surface ($div(\boldsymbol{\omega} \times \boldsymbol{u}) = 1.0 \times 10^7$) of vortex sound intensity with pressure coefficient C_p (Figs. 4a and 5a). The results show sound sources distribute in span wise direction for CC and TC1 (Figs. 4b and 5b). Comparing these distributions of the sound source, the vortex sound intensity of TC1 is less than that of CC in span wise direction. Figures 4b and 5b show that important noise sources are distributed widely in the wake, due to these vortices developed. Furthermore, Figs. 4a and 5a show that another noise sources are distributed in top and bottom regions of the cylinder. This is due to three-dimensional boundary layer by horseshoe vortex [6]. It makes a significant contribution to sound generation along the spanwise direction.

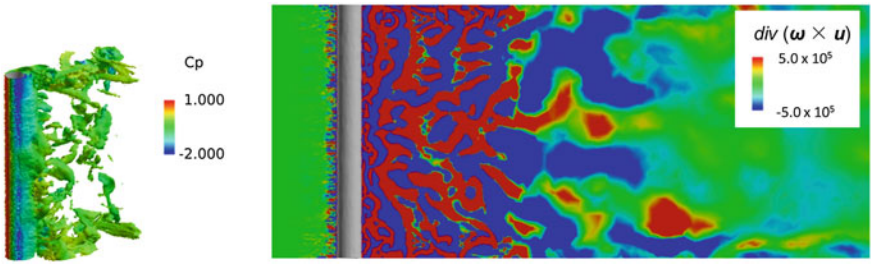

(a) C_p Iso-Surface (b) Instantaneous distribution of Powell's sound source in *XZ* plane

Fig. 4 Sound sources distributions of circular cylinder (CC)

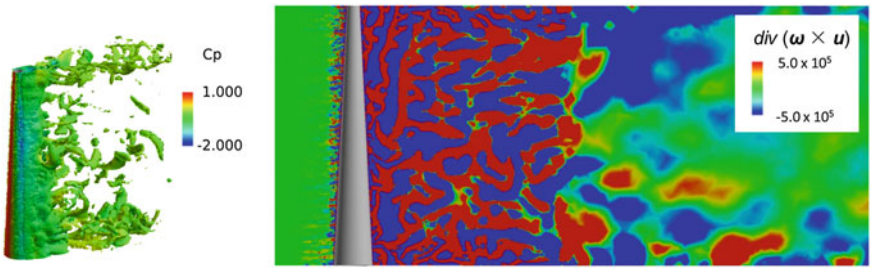

(a) C_p Iso-Surface (b) Instantaneous distribution of Powell's sound source in *XZ* plane

Fig. 5 Sound sources distributions of tapered circular cylinder (TC1)

3.3 Specification of Aeolian Tone

Comparison of aerodynamic sound spectra measured and predicted are shown in Fig. 6a, b. Measured [2] and predicted Aeolian tone for CC contribute to 61.2 dB at 206 Hz ($S_t = 0.206$) and to 66.5 dB at 195 Hz ($S_t = 0.196$), respectively. Both experimental and numerical sound spectra for CC are in good agreement, but the sound spectra for TC1 are not agree because the measured sound pressure level (SPL) of TC1 is almost same as background noise. It can be seen that the peak of Aeolian tone is disappeared in sound spectra and it is decreased SPL due to dissipation von Karman vortex formation for TC1. Its flow velocity is not constant along spanwise direction same as a specific angle of obliquity has affected on Strouhal number around the circular cylinder. Because the vortex shedding with three-dimensional structure makes breakdown of cell structure along the spanwise direction. Sound spectra of TC1 have broadband shape due to the vortex shedding consists of various length scales in the wake.

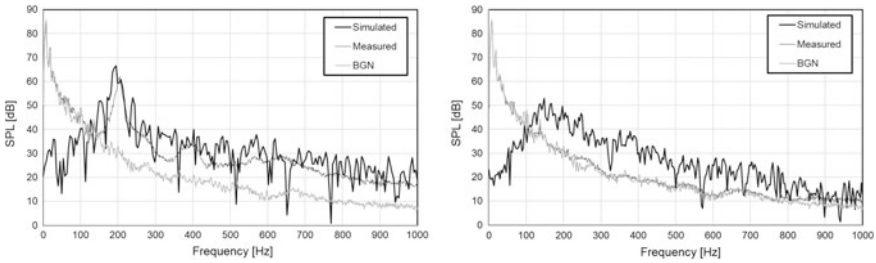

(a) CC (b) TC1

Fig. 6 Comparison of aerodynamic sound spectra

4 Conclusions

Numerical investigations are performed in order to clarify the relationship between the Aeolian tone and flow characteristics for the tapered circular cylinders. As a result, following findings are obtained.

(1) The calculation results of a vortex shedding inclined to the Z axis of TC1 is developed provided qualitatively good agreement with measured.
(2) The important noise sources are distributed widely in the wake, due to these vortices developed. Another noise sources are distributed in top and bottom regions of the cylinder.
(3) The peak of Aeolian tone is disappeared in sound spectra and it is decreased SPL due to dissipation von Karman vortex formation for TC1.

References

1. Fujita H (2010) The characteristics of the Aeolian tone radiated from two-dimensional cylinders. Fluid Dyn Res 42(1)
2. Watanabe Y et al (2014) A study of Aeolian tone radiated from tapered cylinder. In: Abstracts of the 27th ISTP, Aonag villa resort, Krabi, 4–7 Nov 2014
3. Ffowcs Williams JE et al (1969) Sound generation by turbulence and surfaces in arbitrary motion. Phil Trans Roy Soc London: Ser A 264(1151):321–342
4. Powell A (1964) Theory of vortex sound. J Acoust Soc Am 36(1)
5. Yamada A et al (1997) Experimental study on aerodynamic noise generated from two-dimensional models. JSME 63(610)
6. Okuno T et al (1991) Observation of horseshoe vortex in juncture flow. VSJ 11(1)